Development of Ground Penetrating Radar Signal Modeling and Implementation for Transportation Infrastructure Assessment

Amara Loulizi

Dissertation submitted to the Faculty of the
Virginia Polytechnic Institute and State University
in partial fulfillment of the requirements for the degree of

Doctor of Philosophy
in
Civil Engineering

Imad L. AL-Qadi, Chair
Richard M. Barker
Garry S. Brown
Gerardo W. Flintsch
Sedki M. Riad

February 2, 2001

Blacksburg, Virginia

Keywords: pavements, bridge decks, nondestructive evaluation, ground penetrating radar, dielectric constant

Development of Ground Penetrating Radar Signal Modeling and Implementation for Transportation Infrastructure Assessment

Amara Loulizi

(Abstract)

Ground penetrating radar (GPR) technology has been used for the past 20 years for a variety of applications to assess transportation infrastructure. However, the main issue after all these years remains: "How well does GPR work and under what conditions?" Results show that GPR works well for some situations, but is not an appropriate tool for other situations. It is not used currently on a routine basis by the US Departments of Transportation (DOTs) due mainly to difficulties encountered with data interpretation. Data interpretation difficulties are mainly attributed to the fact that images obtained from the reflected signals are not photographs of the features that are beneath the surface being investigated. The images show the amplitude of the radar-reflected signals from the interfaces with different dielectric properties. Therefore, a considerable amount of experience and operator skill may be required to correctly interpret sub-surface radar results. To better understand reflected GPR signals, this research was conducted with the following objectives: to determine the dielectric properties of concrete over the used GPR frequency range; to synthesize the reflected air-coupled radar signals and compare them with measured waveforms; to model and study the effects of simulated defects in concrete on the reflected air-coupled and ground-coupled radar signals; and to validate the research results in the field by predicting layer thicknesses of flexible pavements and detecting moisture in flexible pavement systems. Several concrete slabs, 1.5x1.5 m, were constructed with known thicknesses, simulated defects, and different reinforcement configurations. The concrete mixes included four different bridge deck mixes and one concrete pavement mix used in the State of Virginia. Results have shown that the dielectric constant of concrete is frequency and mix dependent. However, modeling the reflected signals using an average complex dielectric constant over the entire radar frequency range led to modeled waveforms comparable to the measured waveforms. Although air- and water-filled voids did distort the reflected waveforms, a model was developed to predict the reflected waveforms from the simulated defects. Reinforcement

was found to affect the reflected waveforms only when it was oriented in a direction perpendicular to the GPR antennas. A model was also developed to predict the GPR waveforms obtained from flexible pavements. This model could be used in a procedure to measure layer thicknesses more accurately by including losses that occur inside the pavement materials. Two different case studies, where a ground-coupled GPR system was used to locate moisture at different layers, have led to the conclusion that the ground-coupled GPR is a feasible tool to detect moisture inside pavements.

ACKNOWLEDGEMENTS

I would like to express my sincere gratitude to Dr. Imad L. AL-Qadi for his guidance, encouragement, and support during this research. Special thanks are also given to the committee members, Dr. Richard Barker, Dr. Garry Brown, Dr. Gerardo Flintsch, and Dr. Sedki Riad for the time and expertise contributed to the enhancement of this research.

Thanks are also due to Brett Farmer and Dennis Huffman for their assistance with laboratory work.

I would like to thank my friends Samer Lahouar for his great assistance during this research and Agata Pyc for her help during my studies at Virginia Tech.

Sincere gratitude goes to my parents, Achour and Chedlia, my sisters, Mongia and Souad, my brother, Jamel, and all other members of my family for their love and encouragement. Their pride in my accomplishments guided me throughout the best and the worst moments of my work.

Finally, I must thank my wife, Sonia, for her love, belief in me, and constant support. Her guidance, patience and understanding helped me finalize this research.

TABLE OF CONTENTS

LIST OF TABLES

LIST OF FIGURES

Chapter 1. INTRODUCTION

1.1. Background

The United States has approximately 6.3 million kilometers of public roads, with 60% classified as flexible pavement and the remaining 40% consisting of rigid, aggregate (unpaved), and composite pavements (US Department of Transportation, 1999). The road network also has more than 570,000 bridges in service, of which nearly 368,000 have concrete decks (Bettigole and Robinson, 1997). The US public roadway network is traveled by more than 3.8 trillion vehicle-kilometers per year. This makes the US roadway infrastructure system one of the largest in the world. However, this roadway infrastructure is deteriorating at an accelerated rate mainly because most of it was built in the 1940s and is reaching now the end of its service life. It was reported that governmental agencies spend more than 90 billion dollars annually to enhance, rehabilitate, and maintain the roadway infrastructure system (US Department of Transportation, 1999). The average interstate bridge is currently 25 years old, while most other bridges are more than 40 years of age. The national bridge inspection program discovers numerous structurally inadequate bridges in every state. The seriousness of these hazards increases every year as the infrastructure ages and transportation needs increase. The National Transportation Safety Board (NTSB) has criticized the bridge inspection program in several aspects, including lack of trained inspection engineers and a lack of clear guidelines for states to follow.

Deterioration and distress mechanisms of the roadway infrastructure are active under the surface and cannot be accurately assessed by visual inspection. Therefore, a majority of the repair and rehabilitation funds are spent to fix conditions where the deterioration has reached an advanced stage that may jeopardize the structural stability of the facility. Hence, periodic condition assessment of the roadway infrastructure results in better preventive and/or corrective planning, which will preserve its integrity and reduce its life-cycle costs.

Due to the fact that rapidity of measurements, size of sampling, accuracy, and disturbance to users are very important factors in data collection and the inspection process, condition assessments have recently shifted from destructive and direct

measurements to nondestructive and near surface remote sensing. Nondestructive evaluation (NDE) techniques are potentially the most useful techniques for assessing the condition of in-situ pavements and bridge structures. Their importance results from the noninvasive nature of the techniques, the anticipated rapidity of the measurements, non-disturbance to the service during data collection, and the quantitative assessment of the condition.

1.2. NDE Techniques for Roadway Infrastructure Assessment

The NDE techniques used to assess concrete bridge decks include linear polarization techniques, half-cell potentiometer, chain drag test, impact echo, ultrasonic, infrared thermography, acoustic emission, video imaging, and ground penetrating radar. Most of these techniques may also be used for assessing pavements, in addition to falling weight deflectometer (FWD), profilometers, and friction devices.

Linear polarization techniques have been used to measure corrosion current density and therefore predict the state of reinforcement corrosion. Measurements are taken in the linear region of the polarization curve where the applied current to the corroding metal, in an ionic solution, is linearly related to the metal potential. Two devices that are currently used for these measurements are three linear polarization (3LP) and "Gecor." In the 3LP device, shown in Figure 1.1, a counter electrode applies a cathodic current to the steel bar, referred to as a working electrode. A third electrode, known as a reference electrode, detects the potential change in the steel bar/concrete interface. The calculated corrosion current density is interpreted as follows: a value less than 2.2 mA/m^2 indicates that no damage is expected; 2.2 to 10.8 mA/m^2 predicts damage within 10 to 15 years; 10.8 to 108 mA/m^2 predicts damage within 2 to 10 years; and a value greater than 108 mA/m^2 predicts damage in less than 2 years. The "Gecor" device is composed of a corrosion meter and a probe consisting of two sensor electrodes and an external ring guard electrode, used to confine the current. The measured corrosion

Figure 1.1. "3LP" device

current density with this device is interpreted as follows: a value less than 1.1 mA/m^2 indicates a passive corrosion state; 1.1 to 5.4 mA/m^2 indicates a low corrosion state; 5.4 to 10.8 mA/m^2 indicates a moderate corrosion state; and a value greater than 10.8 mA/m^2 indicates a high corrosion state.

Half-cell potentiometer is a method widely used to determine the probability of reinforcement corrosion in concrete bridge decks (ASTM C876-91). The principle of this technique involves measuring the voltage difference between the reinforcing steel and a reference electrode, usually Copper-Copper Sulfate half-cell as shown in Figure 1.2. The reference electrode is placed in contact with the concrete. A potential difference greater than –200 mV indicates more than 90% probability of no corrosion; -350 to –200 mV indicates an uncertain corrosion activity; and less than –350 mV indicates more than 90% probability of active corrosion. This technique is limited when the assessed structures are saturated or some cathodic processes are altered.

Figure 1.2. Half-cell electrode

The chain drag test (ASTM D4580-92) involves dragging a heavy chain, as shown in Figure 1.3, over the bridge deck and listening to the acoustic response from the deck. Areas where delaminations exist would produce distinct acoustic responses different from those obtained in areas with sound concrete. The chain drag test is effective in concrete decks with large delaminations, but the method is very subjective and does not work when the deck is covered with a hot-mix asphalt (HMA) overlay.

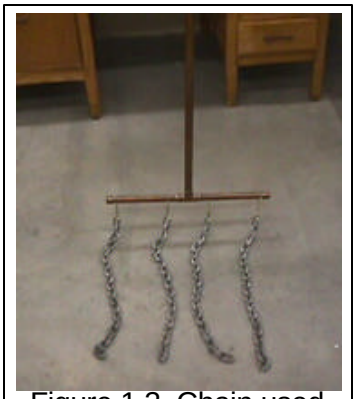
Figure 1.3. Chain used to perform the chain drag test

Impact-echo is based on the use of transient stress waves produced by elastic impact from tapping a small steel ball against the surface of the material under test. The low-frequency stress waves propagate into the material and reflect from flaws or other

interfaces. A transducer placed approximately 150 mm from the impact records surface displacements caused by these reflected waves. The resulting waveform is transformed into the frequency domain using a mathematical process known as Fast Fourier Transform. From the frequency spectrum, transient resonance frequencies, obtained from the multiple reflections of the waves, are identified. These frequency peaks are used to determine the integrity of the structure and to determine the location of flaws using Equation 1.1, which is the basis of the impact-echo method:

$$d = \frac{C_p}{2f} \tag{1.1}$$

where d is the thickness at which the multiple reflections occur, C_p is the speed of the wave (typically 4000 m/s for normal concrete), and f is the frequency. Figure 1.4 shows an impact echo device, while Figure 1.5 shows an impact-echo frequency spectrum obtained from a concrete culvert 165 mm thick. The peak frequency was found to be 12.7 kHz, which corresponds to reflected waves from the bottom of the culvert; therefore, no flaws were present at the location where the impact-echo test was performed. The impact-echo method has been used in many civil engineering applications and the results are very encouraging. Sansalone and Streett (1997) used impact echo for different applications including determination of concrete slab thicknesses, detection of delaminations in bridge decks with and without HMA overlays, determining depth of surface opening cracks, locating unconsolidated concrete, and evaluation of bond quality at internal interfaces.

Figure 1.4. Impact echo device

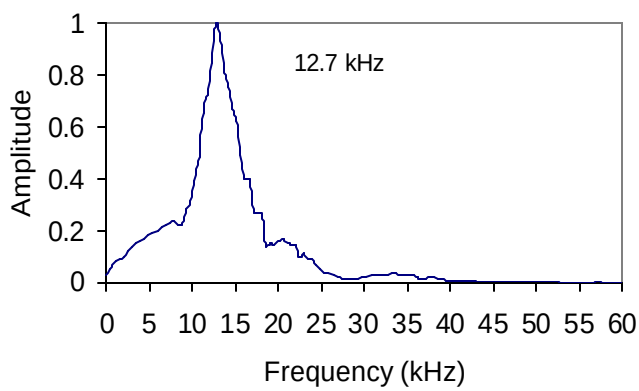

Figure 1.5. Frequency spectrum

Ultrasonic testing uses sound waves with frequencies greater than the human hearing limit (above 20 kHz) to examine materials. The high frequency sound waves propagate well through metals, but not as well in air. The position of a flaw can be determined by measuring the time needed by a pulse of ultrasonic vibrations to travel from a transducer and to be retraced as an echo from the flaw, as shown in Figure 1.6. Sound waves are reflected and/or refracted when there is a contrast in the acoustic impedance between two media. Acoustic impedance is defined as the product of the density of the medium and the speed of the sound wave in that medium. In ultrasonic testing, a "couplant" is usually used to couple the transducer with the structure under test. The coupling would smooth out surface irregularities and eliminate any air between the transducer and the surface. The "couplant" is a grease-like material that fully wets the transducer and the surface of the tested structure.

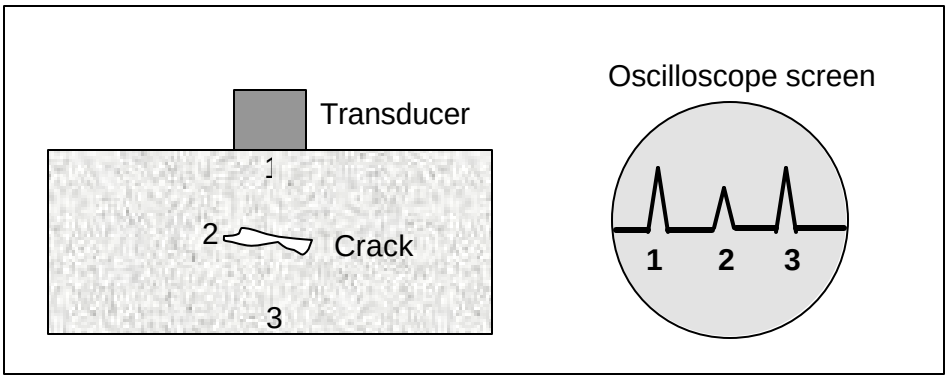

Figure 1.6. Ultrasonic testing with oscilloscope display

Thermography consists of mapping isothermal contour lines on the surface of a material. The technology is based upon the recognition that defects and inhomogeneities would manifest themselves as local hot or cold regions in the isothermal mapping. Therefore, for an anomaly to be detected by thermography, it must create an atypical temperature or a temperature differential at the surface of the test object. Everything in the world with a temperature above absolute zero (-273.15^{o}C) emits some form of radiant thermal energy that can be seen as a temperature pattern with a thermal camera. Figure 1.7 shows a thermography image of a good road section, while Figure 1.8 shows the thermography image from a deteriorated road section. In these images, the warmer the object, the brighter it is shown in the isothermal plot; white is the hottest while black is the coldest.

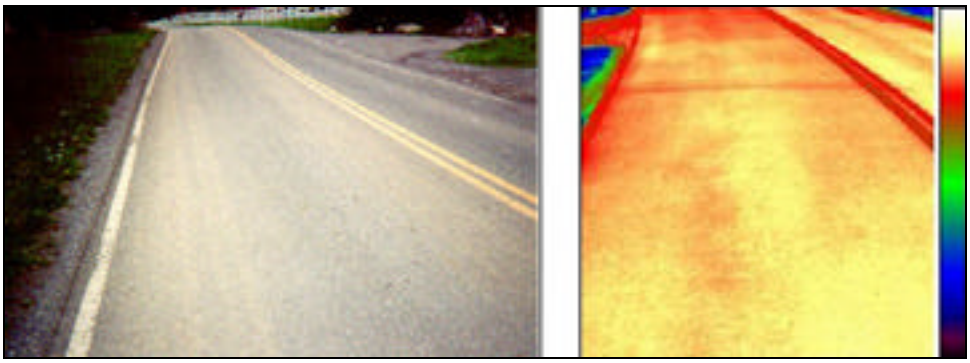

Figure 1.7. Isothermal plot of a good road section

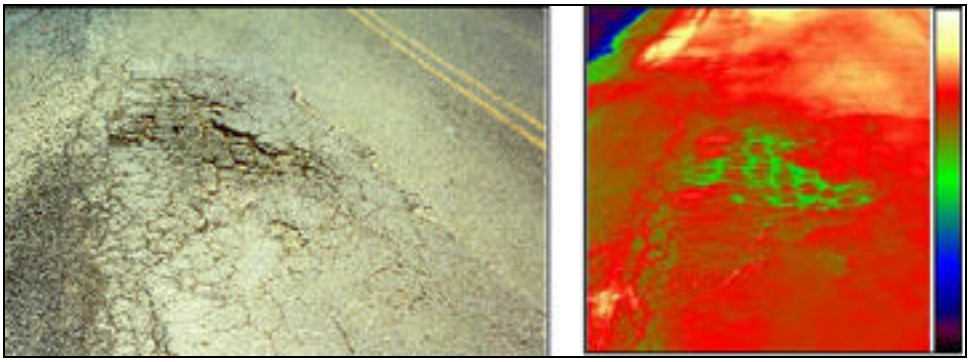

Figure 1.8. Isothermal plot of a deteriorated road section

Acoustic emission refers to the elastic energy, represented by stress waves, that is released by materials when they undergo deformation. The basic process of generation and detection of these waves is shown in Figure 1.9. Sudden movement at the source produces a stress wave, which propagates in the material and excites the sensor. The sensor is a piezoelectric transducer, which converts mechanical energy into electrical energy. The signal from the sensor is amplified, and then measured to produce data for display and interpretation. Acoustic emission is highly dependent on the stress history of the scanned structure, which is also dependent on the material properties and the type of deformation produced during the emission. Elastic materials respond instantaneously to the applied stress, emit, and then stabilize. Viscoelastic materials, on the other hand, take some time to stabilize after the load application. Acoustic emission testing is usually performed under rising load conditions, with the first load application producing more emission than the subsequent loads. This is known as the Kaiser effect, where subsequent loading produces no emission until the previous maximum load is exceeded.

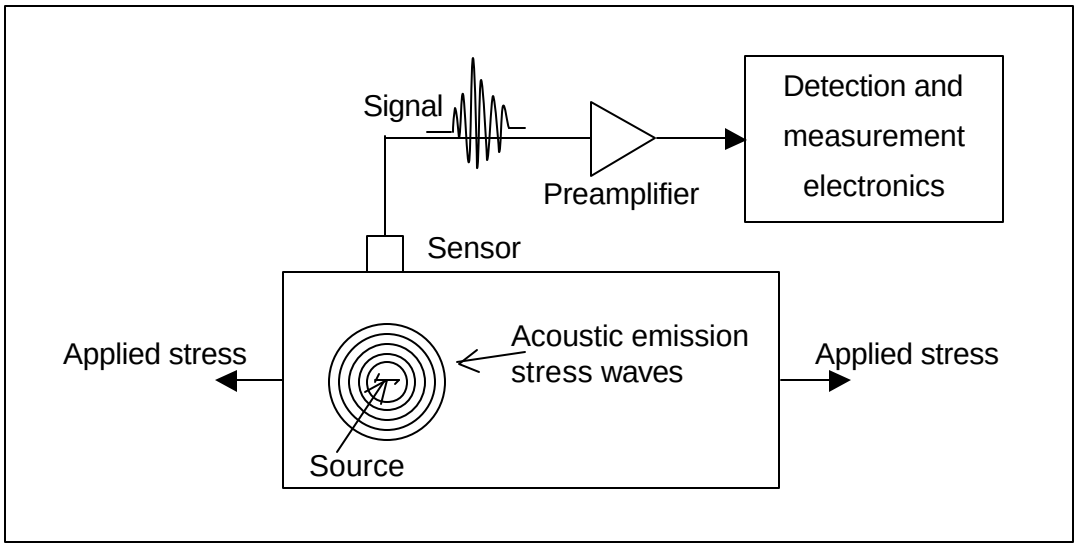

Figure 1.9. Basic principle of the acoustic emission technique (after Pollock, 1989)

The principle of pulsed ground penetrating radar (GPR) is based on transmission of electromagnetic energy and analysis of the reflected pulses from interfaces where there is a contrast in the dielectric properties. Figure 1.10 shows the major components of a pulsed GPR system. A sequence of trigger pulses is generated in the control unit by the radar circuitry. These trigger pulses are sent through the control cable to the antenna, where each trigger pulse is transformed into a bipolar transmit pulse. These transmitted pulses encounter different materials in the subsurface with different dielectric properties. At the interface, signals are reflected back to the surface where the antenna will detect them, and then to the control unit where they are processed and displayed.

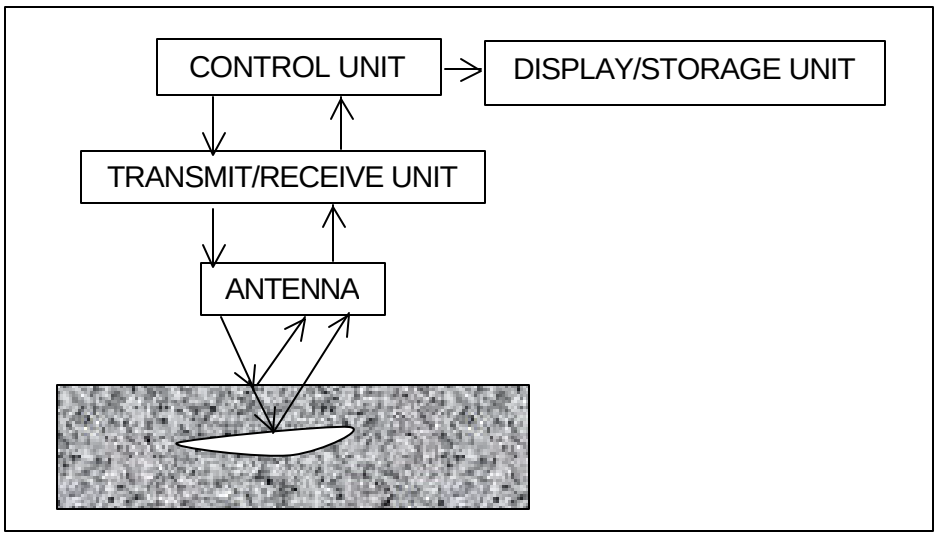

Figure 1.10. Components of a pulsed GPR system

Falling weight deflectometer (FWD) is one of the nondestructive devices that has recently gained widespread acceptance (since the introduction of the static Benkelman beam at the WASHO Road Test in the early 1950s) for the structural evaluation of pavement deflection response (Graves and Drnevich, 1991). This device, shown in Figure 1.11, drops a calibrated mass onto a circular plate (radius 150 mm) in contact with the pavement surface. The magnitude of the applied load and the vertical deformation response of the pavement surface at the center of the loaded plate and at various locations offset from the loaded axis are recorded. Two types of analysis may be performed on FWD data. The simplest and most direct analysis relies on computing a Surface Modulus, E_0, defined as the applied load divided by the measured axial deformation at the center of the loading plate. This value is analogous to a spring constant (N/m) and provides a gross measure of the overall structural value of the pavement system, including the subgrade. A more sophisticated analysis is possible using various techniques of backcalculation, which seek to match the measured deflections to that returned by a mathematical model of layered linear elastic half-space. This technique generally relies upon varying the linear elastic moduli of the component material layers and/or layer thicknesses until a satisfactory match to the observed surface deflection is achieved.

Figure 1.11. FWD loading plate

In digital imaging, high-speed cameras are used to record clear images of the pavement surface at highway speeds. Strobe lights could be synchronized with the cameras to eliminate shadows from overhead objects such as trees, sign poles, and

bridges. Data is processed using image recognition software to classify different types of cracks and their severity level.

Profilometers are used to evaluate pavement roughness, which is a measure of the riding comfort. The International Roughness Index (IRI) is adopted as a common quantitative basis to which different measures of roughness can be compared. This index was developed at the International Road Roughness Experiment held in Brazil in 1982 (Sayers *et al.*, 1986). The IRI is defined as the ratio of the accumulated suspension motion to the distance traveled obtained from a mathematical model of a standard quarter car over a measured profile. It is expressed in units of m/km (in/mile). The longitudinal profile is usually measured using lasers and accelerometers. High-speed laser devices could be mounted over each wheel path to sample at 50-mm intervals, as shown in Figure 1.12.

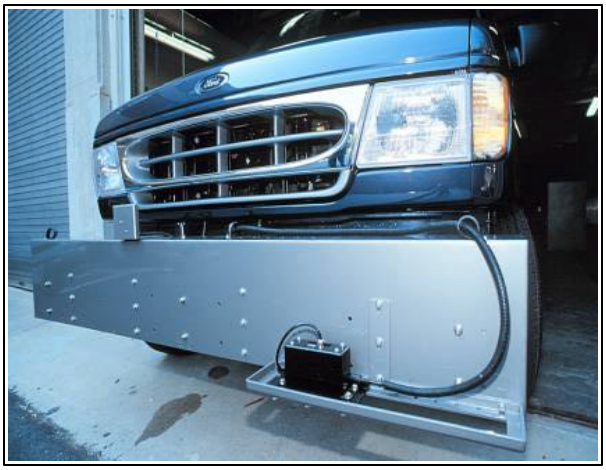

Figure 1.12. Laser device mounted on front of a van to obtain longitudinal profile

There are several devices to measure road surface friction. The principle of measurement differs between these devices, but they all fall within one of five different approaches: deceleration devices, locked wheel devices, side force devices, fixed slip devices, and variable slip devices. Deceleration devices measure the deceleration of the vehicle under full braking. One of the known devices that uses this principle is the Coralba meter. This meter is simply installed in a vehicle preferably equipped with anti-lock brakes. The device measures the deceleration of the vehicle after a sudden and severe brake is performed. Another method, which is similar to using a deceleration device, is the stopping distance method (ASTM E445). Locked-wheel trailers, as shown

in Figure 1.13, are used by more than 40 US States to measure the skid number, defined as 100 times the friction coefficient (ASTM E274). The test tire is installed in a trailer, which is towed behind the measuring vehicle at a speed of 64 km/h (40 mph). Water is applied in front of the test tire, a braking system is forced to lock the tire, and the resistive force is measured. Side force devices maintain the test wheel in a plane at an angle to the direction of motion. The side force perpendicular to the plane of rotation is measured. The British SCRIM, with a wheel yaw angle of 20º, is the most used device of this type. Another system used by at least four US States is the Mu-Meter, which measures the side force developed by two yawed wheels. The Mu-Meter procedure is described as ASTM E670. Fixed slip devices usually operate between 10% and 20% slip. Some of the known equipment that operate with this principle are the FAA friction tester, the Saab Friction Tester, and the Grip Tester. Variable slip devices measure friction as a function of slip between the wheel and the road surface. These devices give maximum information about the frictional characteristics of the tire and road surface. Some of the known variable slip devices are the French IMAG and the Norwegian Norsemeter RUNAR and ROAR systems.

Figure 1.13. Locked-wheel trailer

The above-described NDE techniques have demonstrated high potential as tools for inspecting the roadway infrastructure. However, each method has its own limitations and therefore no method is used currently on a routine basis by the US Departments of Transportation (DOTs); visual inspection is still their number one method to assess and evaluate the condition of roadway infrastructure. Table 1.1 presents a comparison between the performances of NDE technologies when used for bridges. From this table,

GPR seems to be the most appealing technique to assess bridge decks as well as pavements and becomes an important part of any pavement management system (PMS) or bridge management system (BMS). The advantages of using GPR include rapidity of measurements, non-invasive nature of the technique, and the ability to detect defects before they reach an advanced stage.

Table 1.1. Comparison between NDE methods used for bridge inspection

	VI	LP	HCP	CD	IE	UT	IR	AE	GPR
Does HMA overlay need to be removed?	No	Yes	Yes	Yes	No	Yes	No	No	No
Does road or bridge need to be closed?	Yes	Yes	Yes	Yes	Yes	Yes	No	Yes	No
Testing duration	Long	Very Long	Very Long	Long	Very Long	Long	Fast	Long	Fast
Testing speed (km/h)	N/A	N/A	N/A	N/A	N/A	N/A	80	N/A	80
Penetration depth (mm)	0	50	50	50	300	50	100	300	300-2000*
Temperature limitation	No	No	No	No	No	No	Yes	No	No

VI: Visual Inspection LP: Linear Polarization HCP: Half Cell Potential
CD: Chain Drag IE: Impact Echo UT: Ultrasonic
IR: Infrared Thermography AE: Acoustic Emission GPR: Ground Penetrating Radar
* Depends on structural material and frequency of operation

The use of GPR in roadway infrastructure evaluation has been developed over the past 20 years. In rigid pavements, GPR has proven to be feasible to locate dowels (Donohue & Associates, Inc., 1983) and to detect voids or loss of support under slabs (Smith and Scullion, 1993). In flexible pavements, GPR has been found to serve as a tool to detect moisture and stripping in the HMA layer (Rmeili and Scullion, 1997) and to locate moisture in the base layer that leads to structural damage (Smith and Scullion, 1993). Ground penetrating radar is also used to locate changes in pavement structures,

which is necessary information for rehabilitation projects (Maser, 1996a). The most important application of GPR in pavements is the determination of different layer thicknesses. These data are useful for overlay design, predicting pavement life, and as input for other testing techniques such as FWD. For bridges, GPR has been mainly used to detect corrosion-induced delaminations (Clemena, 1983; Maser, 1996b; Barnes and Trottier, 2000)

It is expected that the interest and demand for GPR surveys will grow even more in the near future. However, a number of limitations exist that are related mainly to interpreting the results of GPR testing:

- The images obtained from the reflected signals (using signal-processing packages) are not photographs of the features that are beneath the surface being investigated. The images show the amplitude of the radar-reflected signals from the interfaces with different dielectric properties. These amplitudes are plotted in colors using user-defined color codes. Therefore, a considerable amount of experience and operator skill may be required to correctly interpret sub-surface radar results.
- Extensive amount of data.
- Determination of the exact location of a reflecting feature beneath the surface relies upon a prior knowledge of the dielectric properties of the material. These dielectric properties are also frequency-dependent, and therefore a frequency domain method of analysis is required to accurately measure thicknesses.
- Change of the dielectric constant with depth mainly because of the presence of moisture.
- Losses in the materials, especially due to the presence of moisture or conducting subgrade soils.
- Reflections from thin layers may overlap depending on the GPR system resolution.
- Insufficient dielectric contrast between layers may hinder the detection of the layers underneath.

1.3. Problem Statement

Ground penetrating radar technology has been grossly oversold. A significant amount of attention has been given to the technique without a thorough understanding of its capability. This is a result of the gap existing between the civil and electrical disciplines

involved in the technology. For example, many civil engineers use GPR systems without an understanding of the way the system is working, the capabilities of a specific system, or the electromagnetic properties of the assessed materials. On the other hand, electrical engineers design and build GPR systems without understanding the needs of the civil engineers, which may include the structural component of the pavement or bridge deck as well as the mechanisms of deterioration of the roadway infrastructure. Therefore, limited research has been conducted on GPR data interpretation and on the measurements of the civil engineering materials' dielectric properties.

1.4. Objectives

To address some of the shortcomings of current GPR and solve some of the aforementioned problems, the main objective of this research was to detect flaws in concrete structures quantitatively. This research was conducted with the following objectives in mind:

1- Electrical characterization of different concrete mixes using an air-coupled radar system.
2- Synthesis of reflected air-coupled radar signals and comparison with measured waveforms.
3- Effect of simulated defects in concrete on the reflected air-coupled and ground-coupled radar signals.
4- Modeling of the air-coupled waveforms on concrete with simulated defects.
5- Layer thickness determination in flexible pavements.
6- Feasibility of using a ground-coupled radar system to detect moisture in pavements.

1.5. Scope

This dissertation is divided into six chapters. Chapter one is an introduction. Chapter two presents an overview of the current state of knowledge concerning the use of GPR to assess the road infrastructure. Chapter three presents the experimental program, including a description of the GPR systems used in this study, the performance tests performed on the air-coupled system, the specimen preparation, and the testing procedures. Chapter four presents the testing results as well as data analysis. Conclusions and recommendations are presented in chapters 5 and 6, respectively.

Chapter 2. CURRENT STATE OF KNOWLEDGE

2.1. Introduction

Humans have been exposed to electromagnetic (EM) radiation since the early ages. At those times, the only sources of this type of radiation were natural, such as the sun, thunderstorms, and lightning. Today, the EM spectrum consists of a wide range of EM radiation emanating from a variety of artificial sources, such as electronic circuits with vacuum tubes or transistors, microwave diodes, lasers, magnetrons in microwave ovens, and antennas. These types of radiation may be different in their properties and in the way they are radiated, but they all can be described in terms of their electric and magnetic fields. Therefore, the only fundamental difference among these types of radiation is the frequency and hence the wavelength. The theory of electromagnetism was described in detail by the Scottish physicist James Clark Maxwell in 1873 in his "Treatise on Electricity and Magnetism." The theory of electromagnetism is governed by four equations referred to as Maxwell's equations. These equations are as fundamental to electromagnetism as Newton's law in mechanics, or the laws of thermodynamics for heat.

Radar (Radio Detection and Ranging) is an application of electromagnetic (EM) energy. It was in the early 1900s that the principle of radar was found to be applicable for detecting airborne objects. The principle consists of transmitting EM waves and receiving the reflected signals from any object in the path of the beam. During the Second World War, rapid development of radar technology took place because of its application in the military. It was later discovered that different objects interfere differently with EM energy. The main material properties that have an adverse effect on electric and magnetic fields that constitute the EM wave are permittivity, conductivity, and permeability. It was also discovered that EM waves travel in free space with a constant speed comparable to the speed of light. With these discoveries, radar could be used to detect airplanes, ships, and clouds. In 1926, Hulsenberg used the same principle to detect buried objects; it was the first application in which EM waves were "intentionally" transmitted through solids (Horne, 1993). In 1929, ground penetrating radar surveys were performed in Austria to sound the depth of glacier (Olhoeft, 1988).

Ground penetrating radar technology was forgotten until the late 1950s when a US Air Force plane crashed into the ice in Greenland while it was trying to land; it had misread the altitude given by its radar system "seeing" through ice. This event started investigations into the ability of radar to see into the subsurface, especially for ice sounding, mapping subsoil properties, and locating water table. In the late 1960s, some advances in radar technology were made through NASA lunar investigations when a GPR system was built and flown to the moon to characterize its surface electrical properties. During the Vietnam War, the US Army developed a radar system called "Combat Radar" for locating mines, tunnels, and bunkers. Through further research, this radar system led to the development of other ground probing radar systems used to identify and profile subsurface geological features.

Since the 1970s, GPR has been used in many applications, including locating sewer lines and buried cables (Morey and Harrington, 1972), measuring the thickness of sea ice (Campbell and Orange, 1974), and profiling the bottom of lakes and rivers (Morey, 1974). Since the 1980s, GPR has been used for different applications related to the assessment of roadway infrastructure such as detection of delamination in concrete bridge decks, estimation of pavement layer thicknesses, and detection of moisture inside pavement structures. Prior to discussing the research conducted, an introduction of concrete structure and properties, pavement types, and electromagnetics is appropriate to better understand GPR mechanisms and applications.

2.1.1. Concrete structure and properties

Portland cement concrete (PCC) is the most widely used construction material in the world. It was reported that in 1992, 63 million tons of Portland cement were used to make 500 million tons of concrete (Mehta and Monteiro, 1993). It was also estimated that in 1992, the total world consumption of concrete was three billion tons, or one ton for every living human being (Mehta and Monteiro, 1993). Concrete is widely used mainly because it is durable, cheap, readily available, and can be cast into almost any shape.

Portland cement concrete is a composite material consisting of cement, water, aggregate, and some admixtures. Portland cement is manufactured by crushing calcium carbonate materials (limestone, chalk, marl, seashells) and materials containing silica

(clays, shales) to about 75 μm in size and then mixing them together in a kiln. The mix is then heated to about 1000°C. The reactions inside the kiln produce tricalcium silicate ($3CaO.SiO_2$, abbreviated as C_3S), dicalcium silicate ($2CaO.SiO_2$, abbreviated as C_2S), tricalcium aluminate ($3CaO.Al_2O_3$, abbreviated as C_3A), and tetracalcium aluminoferrite ($4CaO.Al_2O_3.Fe_2O_3$, abbreviated as C_4AF). The final product, called clinker, is then pulverized to particles mostly less than 75 μm in diameter, and approximately 5% gypsum or calcium sulfate is added to control the early setting and hardening reactions of the cement.

Aggregates in PCC occupy 60 to 80 percent of the volume. Characteristics of the aggregates that are significant to PCC technology are gradation (size distribution), moisture absorption, shape and texture, porosity, strength, and the type of deleterious materials present. Coarse aggregates have particles larger than 4.75 mm (retained on #4 sieve), while fine aggregates have particles smaller that 4.75 mm. Usually the size of fine aggregates used in PCC is in the range of less than 75 μm up to 4.75 mm, while the size of coarse aggregates ranges from 4.75 mm to 50 mm, except for mass concrete where the size of aggregates can be as large as 150 mm. Natural mineral aggregate is the most important class of aggregates for making PCC (over 90% of the total aggregate used for making PCC).

An admixture, as defined by ASTM C125, is a material other than water, aggregates, cement, and fiber reinforcement, used as an ingredient of PCC and added to the batch immediately before or during mixing. Admixtures are used in PCC mixes for several reasons (ACI Committee 212, 1981): to increase the plasticity of PCC without increasing the water content (water reducers), to increase the durability of PCC to freeze and thaw (air entrainment admixtures), to retard or accelerate the time of set (retarders and accelerators), to increase the rate of strength development at early ages, to reduce the rate of heat evolution, and to reduce shrinkage. Admixtures are usually grouped into three classes: surface-active chemicals, set-controlling chemicals, and mineral admixtures. Surface-active chemicals, also known as surfactants, are used generally for air entrainment and to reduce the amount of water in PCC mixes. Set-controlling chemicals are used either to retard the setting time or to accelerate the setting time and rate of strength development at early ages. Some chemicals act as retarders when used in small amounts and as accelerators when used in large dosages (Mehta and Monteiro,

1993). Mineral admixtures are siliceous materials, which could be either natural or by-products of the industry. These materials are usually termed pozzolanic materials. A pozzolan is defined as a siliceous or siliceous and aluminous material which in itself has no or small cementing properties, but when it is in a very fine form and in the presence of moisture, reacts with calcium hydroxide (CaOH) at ordinary temperatures to form compounds possessing cementitious properties (Mehta and Monteiro, 1993). By-product materials are the most widely used mineral admixtures. The use of these materials in PCC construction offers the advantage of not wasting these products, which reduces environmental pollution problems. The most widely used by-product admixtures in PCC mixes are fly ash, silica fume, and blast-furnace slag. Fly ash is the residue that results from the combustion of ground or powdered coal, silica fume or microsilica is a by-product of the induction arc furnaces in the silicon metal and ferrosilicon industries, and blast-furnace slag is a by-product of the production of cast iron.

2.1.2. Types of pavements

There are three major types of paved roads: flexible pavements, rigid pavements, and composite pavements. In conventional flexible pavements (Figure 2.1), the top layer is called the wearing surface, which is usually made of a dense graded HMA to resist distortion under traffic and to provide a smooth and skid-resisting riding surface. Under this layer, an HMA base course exists which is made of a lower quality HMA. The base course may be composed of crushed stone, crushed slag, or other untreated or stabilized materials. The subbase course is an optional layer used primarily for economical purposes since it is made of cheaper material than that used for the base. The flexible pavement may consist of all or part of the above layers. In addition, other modified materials of the above layers and/or geosynthetics may be used. The aforementioned layers are supported by the existing or stabilized soil, which is called subgrade. In full-depth flexible pavement, one or more layers of HMA are placed directly on the subgrade.

In rigid pavements, a concrete slab is placed over the existing soil. A base and sub-base, which are typically used, are optional layers. Four different types of rigid pavements are used: Jointed Plain Concrete Pavements (JPCP), which have plain concrete with closely spaced joints (5 to 9m); Jointed Reinforced Concrete Pavements (JRCP), which have longer joint spacing (9 to 30m), but the concrete is reinforced with

wire mesh or deformed bars for shrinkage; Continuously Reinforced Concrete Pavements (CRCP), which have no joints and the concrete is reinforced with bars (however construction joints may exist); and Prestressed Concrete Pavements (PCP), which use prestressed wire strands and no joints. Composite pavements are composed of both HMA and Portland cement concrete.

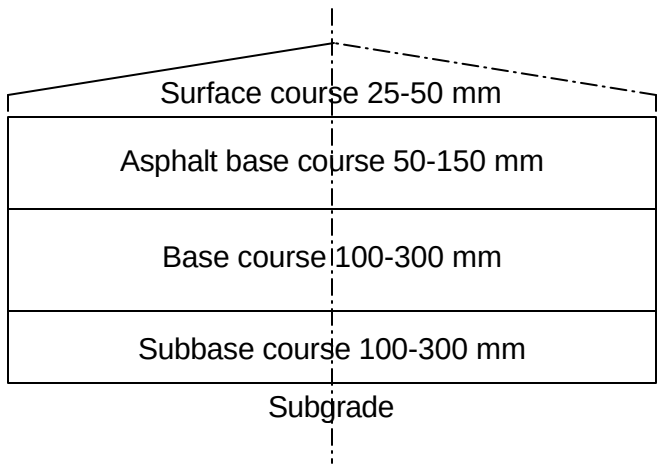

Figure 2.1. Typical cross section of a conventional flexible pavement

2.1.3. Electromagnetics

Most civil engineers are familiar with the mechanical and thermal properties of materials, such as yield strength, modulus of elasticity, and coefficient of thermal expansion. However, their knowledge of electrical and mainly dielectric and magnetic properties of materials is limited. While mechanical properties show the material response to an applied external load, electrical and magnetic properties describe the interaction of a material to applied external electric and magnetic fields, respectively. The main properties of interest in electromagnetics are polarization, conductivity, permittivity, and magnetic permeability. A brief description of these properties is presented.

Polarization occurs in materials when the center of the negative charges in an atom or molecule does not coincide with that of the positive charges when an external electric field is applied. Four different mechanisms of polarization exist, as shown in Figure 2.2. Electronic polarization occurs when the electron cloud shifts off the positive nucleus charge center. Ionic polarization occurs in crystals when the anions and cations are displaced relative to their normal positions. Molecular or dipole polarization refers to the effect that an external applied electric field has on permanent dipoles (e.g. water

molecule). These dipoles tend to reorient themselves so that they will be aligned with the field. Interfacial polarization is the result of the accumulation of the mobile charge carriers at physical barriers (grain or phase boundaries).

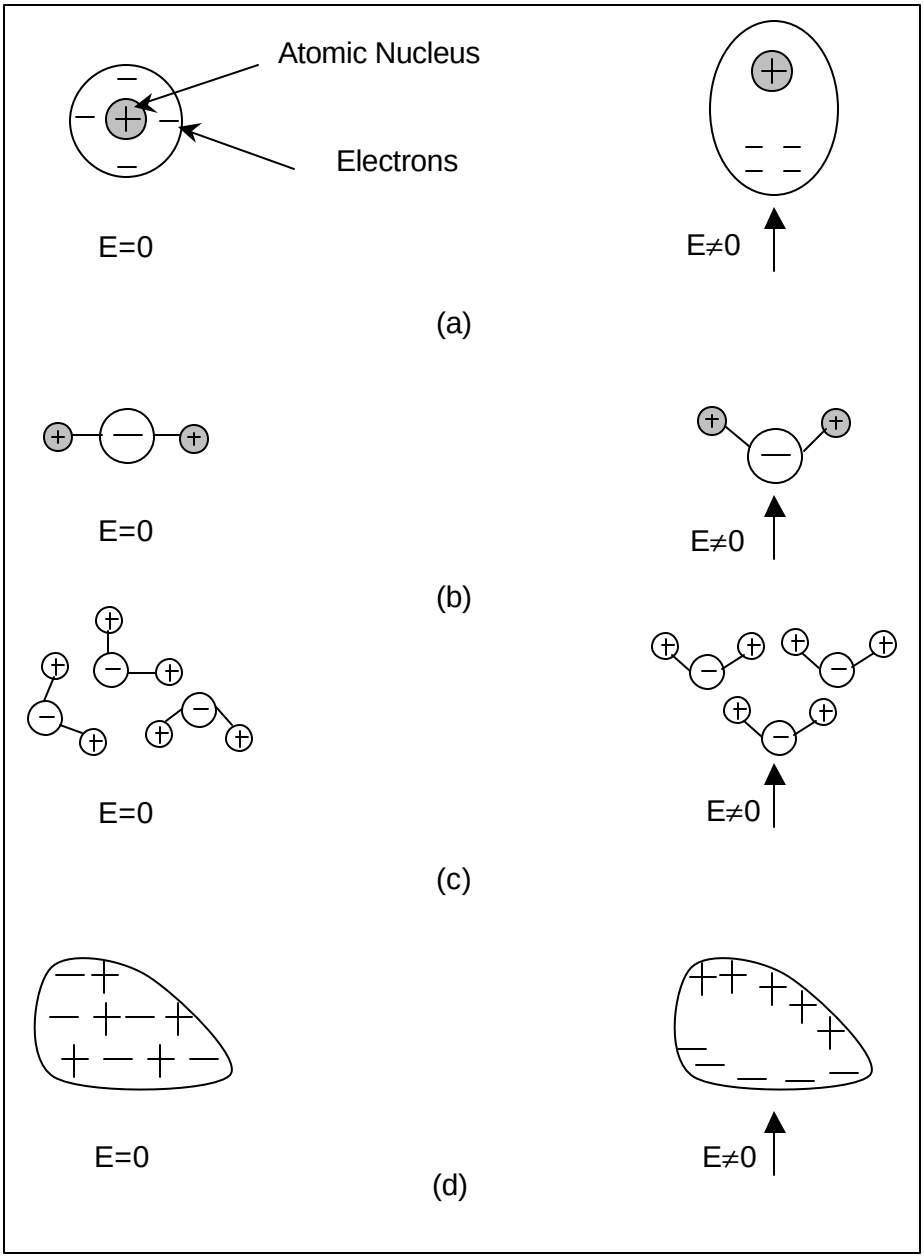

Figure 2.2. Types of polarization: (a) electronic, (b) ionic, (c) molecular, and (d) interfacial (after Scaffer *et al.*, 1995)

Conductivity is the inverse of the resistivity. It is denoted by the letter σ and has units of S/m. This means that conductivity is a measure of a material's ability to conduct electric current. Permittivity, on the other hand, is a property that shows a material's ability to be polarized and therefore its capability of storing a charge when an electric field is applied. The permittivity of free space, which is considered as a reference material, is equal to $\varepsilon_o = 8.854 \times 10^{-9}$ F/m. Permittivity of different materials is expressed as a ratio to ε_o, called relative permittivity or dielectric constant. It is, therefore, a dimensionless quantity and is given as follows:

$$\varepsilon_r^* = \frac{\varepsilon^*}{\varepsilon_0^*} = \varepsilon_r' - j\,\varepsilon_r'' \tag{2.1}$$

The dielectric constant is usually expressed as a complex number where the real part (ε_r') defines the property itself, and the imaginary part (ε_r'') represents the loss due to molecular friction (dielectric loss) and conduction (σ/ω where ω is the angular frequency). The dissipation factor or loss tangent is a measure of the amount of power transformed into heat. Materials with very high loss factors are heated easily and rapidly. The microwave oven principle is based on this property, where the water molecule dipole is excited at a frequency of around 2.4 GHz. The loss factor is defined as the ratio of the imaginary part to that of the real part as shown in Equation (2.2):

$$\tan\delta = \frac{\varepsilon''}{\varepsilon'} \tag{2.2}$$

Magnetic permeability is a measure of the susceptibility of materials to become magnetized. For free space, the magnetic permeability is denoted by μ_0 and is equal to $4\pi \times 10^{-7}$ H/m. The relative permeability of any material is the ratio of the permeability of the material to that of free space. It is, therefore, a dimensionless quantity and is denoted by μ_r. Based on their relative permeability, materials are classified into three groups. Diamagnetic materials are those with a relative permeability less than, but very close to, 1. These materials show very limited interaction with any applied external magnetic field. Examples of diamagnetic materials are copper, silver, and gold. Paramagnetic materials have a relative permeability greater than, but very close to, 1.

These materials also exhibit no interaction with external magnetic fields. Examples of paramagnetic materials are aluminum, magnesium, and platinum. Ferromagnetic materials, on the other hand, have a strong response to applied external magnetic fields. These materials have a relative permeability much greater than 1 and vary with the strength of the applied external magnetic field. Examples of ferromagnetic materials are cobalt, nickel, and annealed iron.

Electromagnetics refers to the study of charges that move with acceleration. Four different fields are involved in electromagnetics: electric field ($\vec{E}$) expressed in V/m, magnetic field ($\vec{H}$) expressed in A/m, electric flux density ($\vec{D}$) expressed in C/m^2, and magnetic flux density ($\vec{B}$) expressed in W/m^2. In free space and without any sources, one can easily derive the wave equations for the electric or magnetic fields. For the electric field, the wave equation is given as follows:

$$\nabla^2 \vec{E} + \omega^2 \mu_0 \varepsilon_0 \vec{E} = 0 \tag{2.3}$$

This is a vector second order differential equation. Two simple solutions to the wave equation are given by the following:

$$\vec{E} = E_0 e^{-j\vec{k}.\vec{r}} \hat{e} \tag{2.4}$$

$$\vec{E} = E_0 e^{j\vec{k}.\vec{r}} \hat{e} \tag{2.5}$$

where $\left|\vec{k}\right|$ is the wave number (in free space, the wave number is $k_0 = \omega\sqrt{\mu_0 \varepsilon_0} = (2\pi/\lambda_0)$), $\hat{k} = \vec{k} / \left|\vec{k}\right|$ represents the direction of the wave propagation, $\vec{r}$ is a position vector, and $\hat{\mathbf{e}}$ represents the direction of the electric field, and therefore the polarization of the wave. These types of waves are called uniform plane waves because planes represent their phase fronts and the amplitude is constant over these planes. To study these types of waves more closely, it is assumed, for simplicity, that the electric field is parallel to the x-axis and is only a function of the z coordinate. The wave is also

assumed to be traveling in free space in the positive z-direction; then $\vec{E} = E_0 e^{-jk_0 z} \hat{x}$. In real space and time, the following equation results:

$$\vec{E} = \mathrm{Re}(E_0 e^{-jk_0 z} e^{j\omega t}) \hat{x} = E_0 \cos(\omega t - k_0 z) \hat{x} \tag{2.6}$$

To find the speed at which the wave travels, the wave phase is set to a constant. This implies that the derivative of this phase with respect to time is zero:

$$\frac{d}{dt}(\omega t - k_0 z) = 0 \Rightarrow \frac{dz}{dt} = \frac{\omega}{k_0} = \frac{1}{\sqrt{\mu_0 \varepsilon_0}} = c = \text{speed of light} \tag{2.7}$$

Materials currently used in roadway structures are considered as slightly conducting media ($\sigma/\omega\varepsilon << 1$) with a relative magnetic permeability equal to 1. To study the behavior of a plane wave traveling through these media, the dielectric constant is considered to be complex, which leads to a complex wave number, k, equal to:

$$k = \omega\sqrt{\mu_0 \varepsilon_0}\sqrt{\varepsilon_r' - j\varepsilon_r''} = k' - jk'' \tag{2.8}$$

The electric field is given as follows: $\vec{E} = E_0 e^{-jk'z} e^{-k''z} \hat{x}$ (2.9)

which represents a plane wave traveling in the positive z-axis with a speed equal to $v = \frac{\omega}{k'}$. As the wave propagates, its amplitude is attenuated exponentially. The penetration depth of the wave is defined as the depth at which the wave falls to e^{-1} of its initial value. Therefore, $e^{-k''z} = e^{-k''\Delta} = e^{-1}$ => $\Delta = 1/k''$. The energy dissipation during propagation could be evaluated by calculating the specific attenuation (α). The specific attenuation in dB/m is given by Equation (2.10):

$$\alpha = 20 \times \log(e^{k''}) = 8.7 \times k'' \tag{2.10}$$

where k" is the attenuation constant (imaginary part of the wave number) and could be approximated by Equation (2.11):

$$k'' \approx \pi \times f \times (\mu_o \times \varepsilon')^{1/2} \times \tan\delta \qquad (2.11)$$

where f is the frequency and tanδ is the loss tangent. Substituting Equation (2.11) into Equation (2.10), the specific attenuation could be approximated by the following equation:

$$\alpha = 27.3 \times f \times (\mu_o \times \varepsilon')^{1/2} \times \tan\delta \qquad (2.12)$$

Figure 2.3 shows an EM wave traveling through two different materials. At the interface, energy will be reflected and transmitted. The plane of incidence of an EM wave is the plane formed by the normal to the flat surface and the incident wave. A transverse electric (TE) wave represents a wave with the electric field perpendicular to the plane of incidence. These types of waves are also called perpendicularly polarized waves, horizontally polarized waves, and S-waves. A transverse magnetic (TM) wave represents a wave with the electric field parallel to the plane of incidence (the magnetic field is therefore perpendicular to this plane). These types of waves are also known as waves with parallel polarization, vertically polarized waves, and P-waves. By satisfying the boundary conditions at the flat surface, one can find the reflection and transmission coefficients of the incident wave:

For TE, the reflection coefficient is the following,

$$\gamma_{\perp} = \frac{-\eta_1 \cos\theta_t + \eta_2 \cos\theta_i}{\eta_1 \cos\theta_t + \eta_2 \cos\theta_i} \qquad (2.13a)$$

and the transmission coefficient is as follows:

$$\beta_{\perp} = \frac{2\,\eta_2 \cos\theta_i}{\eta_1 \cos\theta_t + \eta_2 \cos\theta_i} \qquad (2.13b)$$

For TM, the reflection coefficient is the following,

$$\gamma_{ll} = \frac{\eta_1 \cos\theta_i - \eta_2 \cos\theta t}{\eta_1 \cos\theta_i + \eta_2 \cos\theta t} \qquad (2.14a)$$

and the transmission coefficient is as follows:

$$\beta_{\perp} = \frac{2\ \eta_1 \cos\theta_i}{\eta_1 \cos\theta_i + \eta_2 \cos\theta_t} \tag{2.14b}$$

where η_1 is the wave impedance for medium 1 and η_2 is the wave impedance for medium 2. The wave impedance is defined by $\eta = \sqrt{\frac{\mu}{\varepsilon}}$.

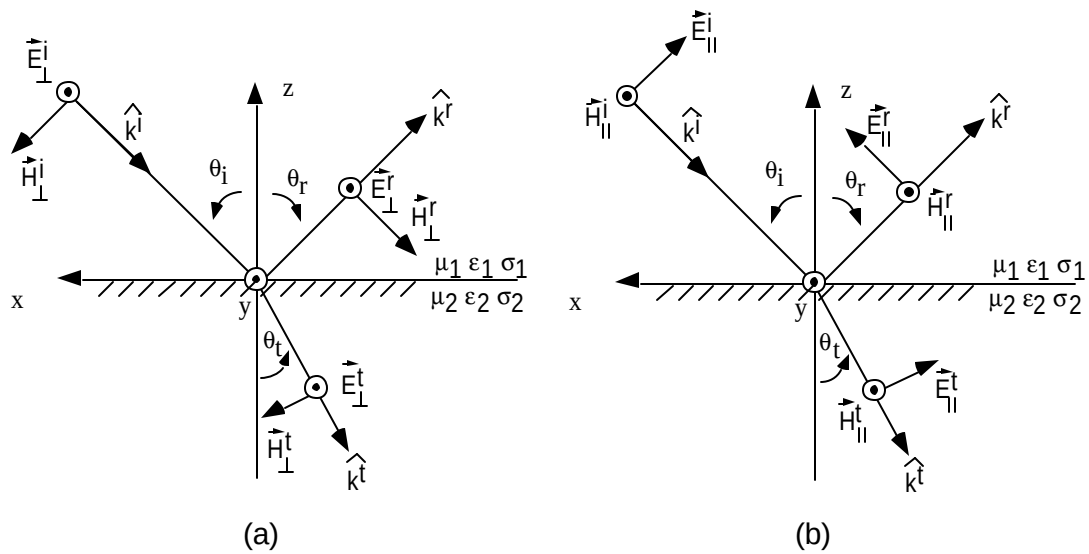

Figure 2.3. Reflection and transmission from a flat surface: (a) TE; (b) TM

Most GPR systems used in civil engineering applications are linearly and horizontally polarized (TE). Since it is assumed that materials in pavement structures are considered to be slightly conducting media with a relative magnetic permeability equal to 1, then the real part of the wave number could be approximated by $k' = \omega\sqrt{\mu\varepsilon}$, and therefore, the speed of propagation of the wave will be as follows:

$$v = \frac{\omega}{k'} = \frac{1}{\sqrt{\mu_0 \varepsilon_0 \varepsilon_r}} = \frac{c}{\sqrt{\varepsilon_r}} \tag{2.15}$$

Thus, if the relative dielectric constant is known, the depth of the reflective interface may be found from the measured return signal time.

At normal incidence ($\theta_i=\theta_t=0°$), the reflection coefficient for a TE wave is the following:

$$r = \frac{\eta_2 - \eta_1}{\eta_2 + \eta_1} = \frac{\sqrt{\varepsilon_{r1}} - \sqrt{\varepsilon_{r2}}}{\sqrt{\varepsilon_{r1}} + \sqrt{\varepsilon_{r2}}} \tag{2.16}$$

Therefore, the degree of reflection at an interface depends on the relative dielectric constants of the two materials. If medium 2 has a higher dielectric constant than medium 1, then r is a negative number, which means that the polarization of the wave is reversed. The higher the absolute value of r (high contrast between the two media), the stronger the reflection, and therefore, the easier the identification between the two media. Equations (2.15) and (2.16) are currently the most important equations used in interpreting ground penetrating radar data obtained from roadway infrastructure assessment.

2.2. Dielectric Properties of Concrete

In 1994, Virginia Tech started a research program to better understand the dielectric properties of concrete and their variations due to changes in concrete ingredients, chloride presence, and concrete deterioration such as alkali-silica reaction (ASR) and freeze-thaw (F/T) damage (Al-Qadi and Riad, 1996). Deterioration in concrete occurs in different forms; thus, a particular deterioration could be detected at a specific frequency. Therefore, an optimal frequency range(s) could be identified for a specific deterioration. To accomplish this, three measuring devices were designed and built at Virginia Tech; these allow for the measurement of concrete complex permittivity over a wideband of frequencies (0.1 MHz to 10 GHz) using time domain and frequency domain techniques. The measuring devices are a parallel plate capacitor (100 kHz to 40.1 MHz), a coaxial transmission line (100 MHz to 1 GHz), and a TEM horn antenna (1 GHz to 10 GHz). Portland cement concrete specimens were cast (in different sizes to accommodate the various measuring devices) at different water to cement (w/c) ratios, with different aggregate and cement types, and different air entrainment levels. The effects of concrete basic properties, maturity (curing), chloride presence, ASR, and F/T damage on the measured dielectric properties and ultrasonic waves were studied. The major findings of that study were as follows:

- The complex dielectric constant of concrete is frequency dependent in the low radio frequencies range, and this dependency is significantly reduced in the microwave frequencies.
- The complex dielectric constant of concrete increases with increasing w/c ratio and/or air content. However, changes in the microwave range are not significant.
- The dielectric constant of concrete decreases with the hydration process.
- Cement and aggregate types have significant effect on the measured complex dielectric constant.

Figure 2.4 shows the measured complex dielectric constant for concrete with limestone at a w/c ratio of 0.45 over the frequency range of 1 MHz to 10 GHz. Figure 2.5 shows the specific attenuation in concrete with limestone at a w/c ratio of 0.45 from 100 MHz to 10 GHz. The graph was obtained by assuming a constant complex dielectric constant over this frequency range with a real part equal to 9 and an imaginary part equal to 0.4. Equation (2.12) was then used to develop the plot. As the graph indicates, as the frequency increases, the specific attenuation increases. Therefore, the high frequency components of the radar pulse will attenuate faster than the low frequency components.

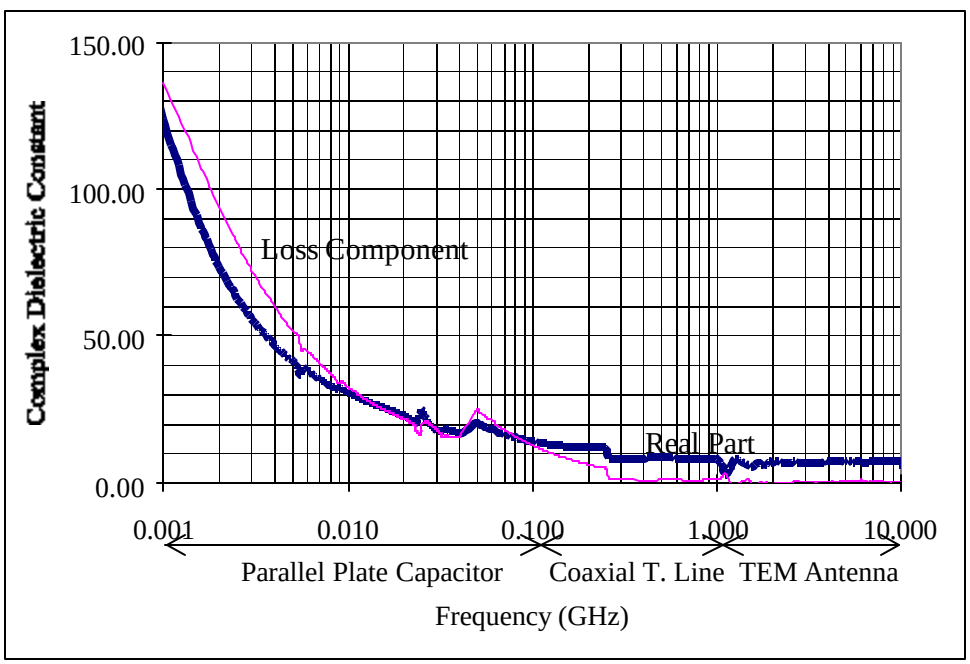

Figure 2.4. Complex dielectric constant for concrete with limestone at 0.45 w/c ratio at the frequency range of 1 MHz to 10 GHz (after Al-Qadi and Riad, 1996)

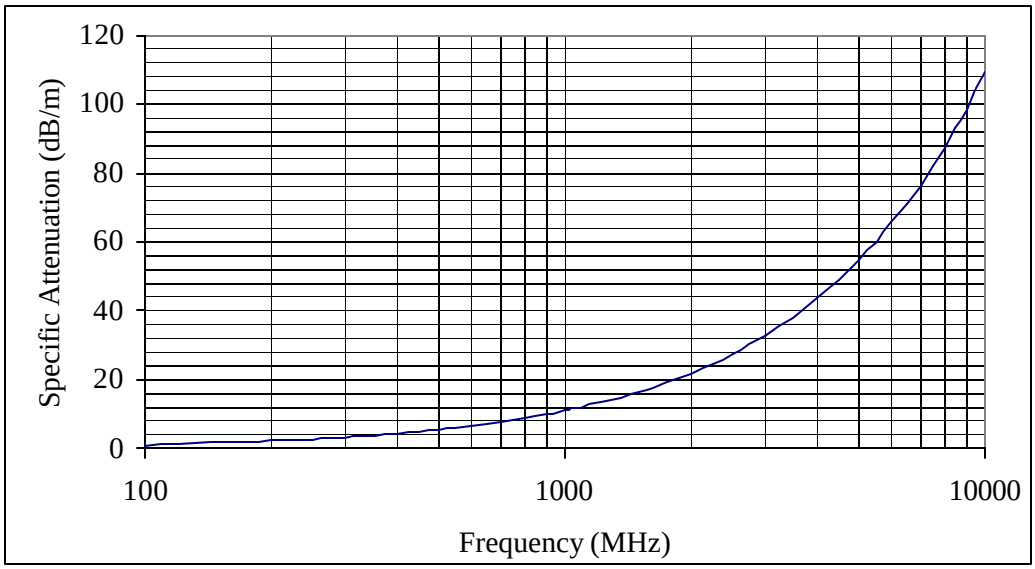

Figure 2.5. Specific attenuation for concrete with limestone at 0.45 w/c ratio at the frequency range 100 MHz to 10 GHz

Another coaxial transmission line was simultaneously but independently designed and developed at the University of Liverpool to electrically characterize concrete in the frequency range of 1 MHz to 1 GHz (Shaw *et al.*, 1993). While the geometry of the line as well as the way data are collected and analyzed is different from the Virginia Tech coaxial transmission line, similar results were found as to the effect of moisture content on the measured concrete dielectric constant. Specimens with high w/c ratios had higher dielectric constants and conductivity due to the high amount of free water.

A large broadband coaxial line was developed by Robert *et al.* (1995) for measuring the complex dielectric constant of concrete from 50 MHz to 1 GHz. Measurements with this line on Teflon were within 5% of the expected value of 2.1 for the real part, while the imaginary part was 0.1± 0.01. The line was used to test PCC with maximum aggregate sizes of 15 mm and 30 mm, and mortar. Only the effect of curing was studied, however. Measurements were taken at curing periods ranging from 1 to 24 days. It was observed that the measured complex dielectric constant for concrete is more frequency-dependent at early curing periods. As the specimens cured, the dielectric constant became stable across the frequency range. The measured complex dielectric constant was found to be higher for specimens with greater w/c ratios and for mortar specimens.

Rhim and Büyüköztürk (1998) also studied the variation of the dielectric constant of concrete with moisture content in the frequency range of 0.1-20 GHz. An open-ended coaxial probe connected to a network analyzer was used for the measurements in the frequency domain. The principle of the coaxial probe is similar to that of a coaxial transmission line. The procedure involved placing the probe on the concrete surface, sending an electromagnetic pulse, and recording the reflected signal. The effect of moisture on the complex dielectric constant was performed by testing cylindrical concrete specimens, 76.2 mm in diameter and 152.4 mm high, with a w/c ratio of 0.45. Four different moisture state conditions were analyzed: wet specimens with free water on the surface, saturated specimens with dry surface, air-dried specimens, and oven dried specimens with no moisture. For the oven-dried specimens, the dielectric constant was relatively constant over the frequency range. The change over the frequency range was significant for the saturated specimens. It was also observed that the dielectric constant for the saturated specimens was almost twice that of the oven-dried specimens, thus showing the effect of moisture on the dielectric constant.

Halabe *et al.* (1993) investigated three models to predict the dielectric properties of concrete by incorporating the electromagnetic properties of its constituents. The studied models are the complex refractive index method (CRIM), the continuous grain size distribution model, and the discrete size distribution model. The predicted concrete complex dielectric constant using the CRIM and the discrete size distribution model were found to be in good agreement with measured values at a high frequency range ($\approx$ 1 GHz). However, at low frequencies, the CRIM model is inapplicable. The continuous grain size distribution model overestimates the attenuation coefficient by 25 to 50%, while it gives good prediction for the real part of the measured concrete dielectric constant.

2.3. Dielectric Properties of Hot-Mix Asphalt

Al-Qadi (1992a) studied the dielectric properties of HMA in the frequency range of 12.4 to 18.0 GHz. His experimental set-up consisted of a focused conical horn antenna and an HP 8510B network analyzer. The focused antenna consisted of two plano-convex lenses mounted back to back, and the network analyzer had a synthesized sweeper that generates microwave signals in a step-sweep mode at 801 frequency modes. Two types of aggregate were used, namely low-absorption limestone and high-absorption

piedmont gravel. Each type of aggregate was used in a dense-graded form and in an open-graded form. One type of binder was used, Conoco AR4000. Specimens were compacted using a kneading compactor in accordance with ASTM Standard D1561. All specimens were approximately 101.6 mm in diameter and 63.5 mm in height, except for the limestone open-graded mixes where another thickness of 101.6 mm was considered. It was found that for dry HMA specimens, the real part of the dielectric constant ranged from 3.7 to 5.2, while the imaginary part ranged from 0.05 to 0.16. For the wet HMA specimens (volumetric water content ranging from 1.2% to 8.2%), the real part of the complex dielectric constant varied from 4.1 to 5.3, and the imaginary part varied from 0.10 to 0.30. A correlation was established between the calculated dielectric constant and the HMA moisture content.

Shang *et al.* (1999) developed an apparatus to measure the dielectric properties of HMA over the frequency range of 0.1 MHz to 1.5 GHz. Their experimental system consisted of an automatic network analyzer (HP 8753D), a sample holder, coaxial cable connections, and data processing software. The coaxial sample holder consisted of a brass tube, two conical sections, and an inner brass center conductor. The brass tube has a length of 457.2 mm and an inner diameter of 101.6 mm. The two conical sections each have a length of 132.3 mm and an inner diameter varying from 11.2 mm to 101.6 mm. The inner brass center conductor is composed of a straight section with a length of 457.2 mm and a diameter of 44 mm, and two tapered sections each with a length of 129.3 mm and an end diameter of 6.12 mm. The HMA specimens were prepared using the Ontario wearing and binding course mixes (HL3 and HL8, respectively). One type of aggregate and three asphalt cement contents were chosen for each mix type: 4.5, 5, and 5.5% for the HL3 mix, and 4.0, 4.5, and 5.0% for the HL8 mix. Specimens were compacted using a gyratory shear compactor. The average bulk specific gravity was 2.44 ± 0.02 for the HL3 mix, and 2.47 ± 0.02 for the HL8 mix. Results indicated that asphalt content and mix type did not significantly affect the measured complex dielectric constant. However, moisture content was found to be a predominant factor on the measured complex dielectric constant. It was found that the average real part of the complex dielectric constant was 6.0 ± 0.15 for the dry specimens, and 6.52 ± 0.99 for the soaked specimens over the frequency range of 8 to 900 MHz.

Field measurements of the dielectric properties of HMA are limited to measuring the wave velocity using known thicknesses and time domain signals. Davis *et al.* (1994) used GPR to determine pavement thickness at six locations in Finland, the United States, and Canada. The average wave velocity from the six sites was reported to be 1.26×10^8 m/s, with a maximum of 1.6×10^8 m/s and a minimum of 0.95×10^8 m/s. Using Equation 2.15, the average dielectric constant for HMA would be 5.7, with a maximum of 10 and a minimum of 3.5. These values represent an average value over the frequency band of the radar system. It is important to note that HMA dielectric properties are highly dependent on the aggregate's dielectric properties.

2.4. Applications

Ground penetrating radar has been used for many applications to assess roadway infrastructure including determining thickness of concrete and flexible pavements, locating reinforcement and dowels in concrete pavements, detecting voids and delaminated areas in bridge decks, locating voids under concrete slabs, evaluating riverbed scour, and detecting buried pipes.

2.4.1. Concrete pavement thickness

Currently the thickness of new concrete pavements is determined from cores, generally taken every 300 m of new lane. This method is time consuming, provides information about the thickness at very limited locations along the pavement, and results in holes, which, even after refilling them, remain as focal points for deterioration. In old pavements, determining the pavement thickness is essential for estimating the structural capacity of the pavement and, therefore, considering the best rehabilitation or maintenance alternative. Ground penetrating radar has been used for determining concrete pavement thickness in many projects. Data for concrete thickness evaluation from Minnesota Road Test Sections revealed that thickness as obtained with GPR correlates well with core data (Maser, 1994). The R^2 of the correlation was 0.76 and the average absolute deviation between GPR and core data was 13.5 mm. It was also found that GPR data over-predicts the concrete thickness. The main limitations were the inadequate contrast between the concrete and the base material, as well as the insufficient power to penetrate through the whole concrete slab.

Seusy *et al.* (1992) reported that radar is able to measure concrete thicknesses up to 420 mm. Their work was performed with an air-coupled system and a ground-coupled system. The air-coupled system was used to estimate the concrete dielectric constant, while the ground-coupled system was used to locate the interface at the bottom of the concrete layer. This is because the ground-coupled system has a lower center frequency than the air-coupled system, and therefore, its penetration depth is greater. However, the resolution of the ground-coupled system was found to be lower than that of the air-coupled system.

2.4.2. Flexible pavement layer thickness determination

Pavement thickness determination is necessary information for many applications related to the flexible pavement evaluation. Some of these applications include designing overlays, inspection of the contractor job in newly built pavements, and structural characterization of existing pavements to estimate their remaining service life. Since a pavement is made of different layers, reflections of the electromagnetic energy are expected at all interfaces. The measured time of reflection from a particular interface will allow the determination of the thickness of the layer above it.

Al-Qadi *et al.* (2001) used GPR technology to assess the condition of the I-81 interstate highway in Virginia from milepost 137 to milepost 154, in both directions, northbound and southbound. Two lanes exist in each direction. The main purpose of the GPR survey was to predict the HMA thickness of the existing pavement system. The HMA thickness determination involved that of the flexible pavement and the overlay on the reinforced concrete section. Two GPR systems were used simultaneously: air-coupled and ground-coupled. The data were collected at 16 km/hr, and the survey was conducted at a scan rate of one scan per 110 mm. To verify the reliability of the GPR predicted thicknesses, cores were taken from several locations. The average error of predicting the HMA thickness was 6.7% and ranged from 1 to 15%. Part of this error could be attributed to the location of measurements, which were not exactly at the core location.

Maser (1996) used GPR (RODAR) and PAVLAYER software to investigate the as-built conditions of pavements. The results of the pavement analysis were compared with several cores and test pits. An accuracy of ±7.5% was found for hot-mix asphalt (HMA)

layers ranging from 51 mm to 500 mm in thickness, and ±12% for granular base layers ranging from 150 mm to 330 mm in thickness.

Mesher *et al.* (1995) used a GPR system called "Road Radar" for pavement thickness determination on three sites: Highway 21 (Alberta, Canada), Interstate Highway 15 (Montana, USA), and Highway 20 (Taivalkoski District, Finland). The system is self-calibrating, can resolve layers as thin as 50 mm with a 2.5 GHz center frequency antenna, and includes a semi-automated software for the processing and interpretation of the large sets of data. The results obtained with the "Road Radar" from all three sites were compared to actual thicknesses obtained from core samples. A linear regression statistical analysis was performed for this purpose. An R^2 value of 0.98, 0.92, and 0.90 were obtained for the three sites, respectively.

2.4.3. Locating reinforcement

The location and cover depth of reinforcing steel in concrete structures has a great effect on the condition of that structure. A thin cover depth would result in rapid reinforcement corrosion, and therefore lead to early deterioration. The principle of GPR in locating reinforcement is the fact that steel is highly conductive and will reflect almost all the incident energy. This means that if the dielectric constant of the concrete is known and the time of the reflected signal is measured, then the depth of the reinforcing bar can be easily found. Bungey *et al.* (1994) studied the effects of the reinforcing steel on the radar signal. Their experimental work was undertaken with a GSSI SIR10 system, which has a 1 GHz transducer. Round steel reinforcing bars ranging in diameter between 6 mm and 32 mm and with a cover depth of up to 280 mm were used. An oil-water emulsion with the dielectric and conductivity properties of concrete was used to allow variation in bar size, depth, and spacing without making concrete specimens. With this set-up, they were able to study 250 different configurations. They concluded that steel bars of any size can be detected when they are spaced at 200 mm or more. For closer spacing, cover depth will be the primary factor for detecting the bars.

Maser (1996) used a radar system manufactured by Pulse Radar, Inc. to investigate the as-built conditions of bridge decks. Cover depths in six bridge decks in Wyoming were determined. The correlation between the radar predictions and the cores had a standard error of 7.9 mm.

Figure 2.6 shows radar data obtained with a GSSI model 3100 ground-coupled antenna (900 MHz), owned by the Roadway Infrastructure Group at Virginia Tech, over Memorial Bridge in Radford, Virginia. The bridge deck has an HMA overlay. The top and bottom reinforcing bars are clearly visible in this scan. The vertical axis indicates the depth of the bar. Figure 2.7 shows additional radar data obtained with Sensors & Software pulseEKKO 1000. From this picture, it is clear that the rebars are located at a depth of 80 to 150 mm, and it is clear that there was improper installation during construction.

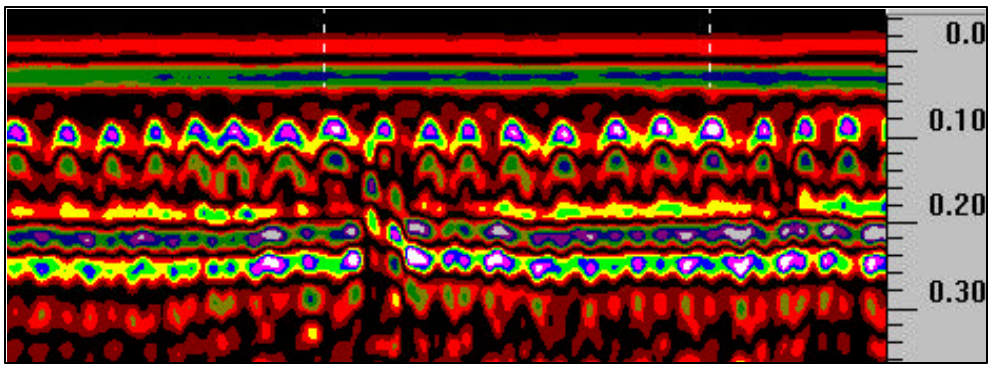

Figure 2.6. Locating reinforcement in bridge deck

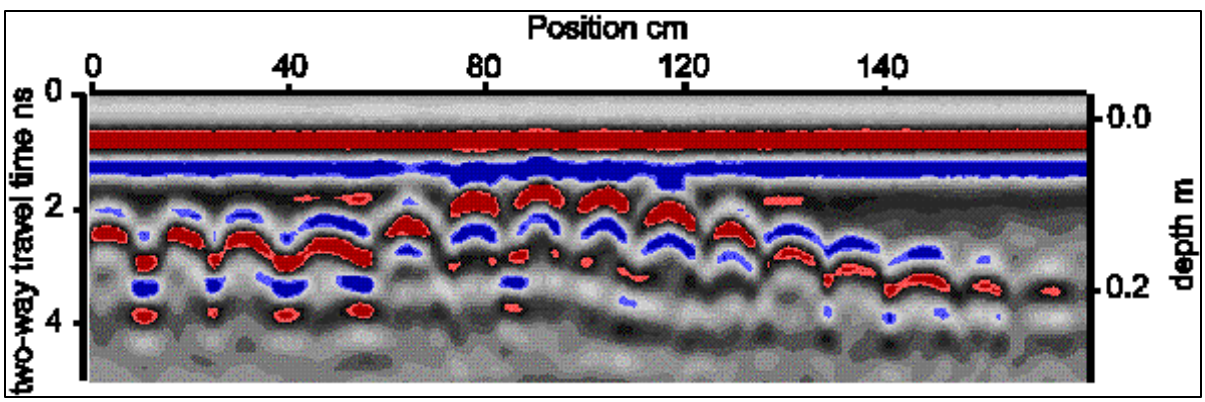

Figure 2.7. Locating reinforcement at different depths (after Sensors & Software)

2.4.4. Locating voids under jointed concrete slabs

Jointed concrete pavements deteriorate mainly near the joints due to increased deflections and stresses and a loss of subsurface support beneath the concrete slab. The loss of support, manifested by the presence of a void under the slab, is created mainly because of pumping. Pumping, defined as the ejection of water and fines

through the joint, happens under the leading slab when the trailing slab rebounds after the passage of a truck load. Ground penetrating radar has been promoted as a tool to detect the loss of support at early ages before the rate of deterioration increases to an advanced level. Studies in the 1980s (Moore *et al.*, 1980; Steinway *et al.*, 1981; Koerner *et al.*, 1982; Clemena *et al.*, 1986; Bomar *et al.*, 1988) used the fact that reflection from the concrete slab/base interface is affected by the presence of air void and/or void filled with water. More recent work in the 1990s (Smith and Scullion, 1993; Scullion *et al.*, 1994; Saarenketo and Scullion, 1994) showed a correlation between the GPR output and the presence of a void. An algorithm was proposed based on setting threshold amplitude on the reflected signal from the slab/base interface as obtained from calibrated measurements. A determination was made that a void exists when the amplitude of the reflected signal is greater than the threshold value.

Sheftick and Bartoski (1997) reported that three short-pulse GPR systems, from different manufacturers, were evaluated at the Pennsylvania Transportation Institute's test track for the ability to detect voids under concrete slabs. Six voids were artificially created in the wheel path of different slabs, before the GPR operators were asked to run their equipment. None of the three GPR personnel were able to locate the artificially created voids, and at least one of the three GPR operators identified a void where none existed. Without knowledge of the slab thickness and the dielectric properties of the concrete, the GPR operators interpreted their data erroneously.

2.4.5. Locating dowels in jointed concrete pavements

The only reported study where GPR was used to locate dowels and measure their depth and spacing dates back to 1983 (Donohue & Associates, Inc.). The use of GPR for this application has been implemented with air-coupled and ground-coupled systems.

2.4.6. Locating delamination in bridge decks

Bridge deck deterioration is primarily caused by chemical or environmental factors such as corrosion of reinforcing steel, alkali-silica reaction, and freeze/thaw damage. Since GPR shows a great sensitivity to moisture (Al-Qadi, 1992), its ability to detect these anomalies is promising. Initial studies to detect delamination in concrete bridge decks were performed using ground-coupled systems, and the data analysis was based on qualitative investigation of the graphical output of the GPR (Clemena, 1983).

Al-Qadi *et al.* (1996) studied the effect of delamination (with and without water) and chloride content on the dielectric properties of concrete over a frequency range of 1 GHz to 10 GHz. Their experimental setup consisted of two transverse electromagnetic (TEM) horn antennas (developed at Virginia Tech), a Tektronix 11801A digital sampling oscilloscope for Time Domain Measurements, and a Hewlett Packard 8510B network analyzer for Frequency Domain Measurements. Concrete slabs (750x600x140 mm) with different defects were evaluated. Air delamination was modeled by placing Styrofoam pieces inside the slabs. The effect of water in delaminated voids on signal response was studied after dissolving and extracting the Styrofoam pieces and filling the voids with water. Although no significant changes in measured complex dielectric constant were noted due to induced delamination, a significant difference was noted in the shift factor for delamination on the order of 6.4 mm thick (smallest thickness used in the study). For slabs with delaminated areas filled with water, an increase in the dielectric constant was observed. In addition, a shift factor and a change in the waveform amplitude were quantitatively identified.

Manning and Holt (1983) reported 26% accuracy in predicting delaminations in bridge decks based on identification of a strong positive reflection at the top reinforcement level.

Büyüköztürk and Rhim (1996) used computer simulations and radar measurements to detect delamination inside concrete. The simulations were based on the finite difference time domain (FDTD) method. Two frequency ranges were used in the simulations: 3.4 to 5.8 GHz, and 2.2 to 7.0 GHz, with bandwidths of 2.4 GHz and 4.8 GHz, respectively. Wideband inverse synthetic aperture radar was used at a frequency of 3.4 to 5.8 GHz to confirm the results of the simulations. They used concrete blocks (305 mm x 101.6 mm in cross section) in which they modeled delaminations embedded at 25.4 to 76.2 mm (distance from the surface to the center of the crack), and ranging in thickness from 3.2 mm to 25.4 mm. The results of this study confirmed that 25.4-mm-thick delaminations could be detected at the different locations with both frequency ranges. The 3.2-mm, 6.4-mm, and 12.7-mm-thick delaminations were difficult to detect at the frequency range of 3.4 GHz to 5.8 GHz, but were visible at the frequency range of 2.2 GHz to 7.0 GHz.

Chen *et al.* (1994) performed experimental work on 15 concrete bridge deck specimens of dimensions 610 x 610 x 150 mm (24 x 24 x 6in.). These specimens were cast in three batches with different internal conditions (air cracks, plain water-filled cracks, saline water-filled cracks, reinforcement, and no reinforcement). They studied the different waveforms obtained with an impulse PS-24 radar system. They also made a comparison of the different specimens' reflected waveforms to determine the effects of the different defects. Their results show that cracks (especially when filled with water) can be easily detected with the radar system.

Halabe *et al.* (1996) studied the radar waveforms obtained from different concrete specimens. These specimens were cast in the laboratory with different internal conditions (air cracks, water-filled cracks, no reinforcement, and with reinforcement) to model the conditions of bridge decks and pavements. Their study showed that cracks 127-mm-deep were difficult to detect because of the attenuation of the wave in the concrete.

Maser (1996b) reported that radar predictions of deteriorated areas in bridge decks were found to be within ± 4.4% of the total deck area when correlated with directly measured quantities. This was based on surveying 32 bridge decks in the New England region.

Hugenschmidt (1997) claimed that GPR is a cost-effective tool to nondestructively inspect bridge decks, and that taking cores and acquiring radar data in their locations could minimize uncertainties of the data interpretation.

In 1995, the Federal Highway Administration (FHWA) initiated a project with Lawrence Livermore National Laboratory (LLNL) to build a GPR system to inspect bridge decks with high cross resolution (30 mm) and wide frequency band (for high range resolution). A system, called HERMES, was developed that meets those requirements. It was reported that HERMES, with its micropower impulse radar (MIR) technology combined with the image reconstruction algorithms (which are based on synthetic aperture techniques), can resolve very thin simulated delamination (Warhus *et al.*, 1994; Warhus *et al.*, 1995; Azevedo *et al.*, 1996; Davidson and Chase, 1999). Figure 2.8

shows a reconstructed image obtained with the HERMES system over a concrete slab made in the laboratory with simulated defects.

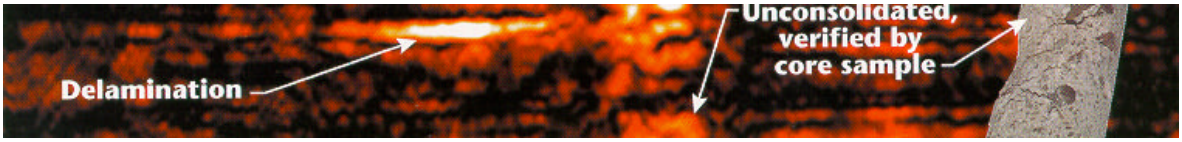

Figure 2.8. Reconstructed image of a concrete slab with simulated defects using the HERMES system

2.4.7. Investigation of bridge scour

Bridge scour refers to the erosion, caused by water flow, of the riverbed near the bridge foundation components. In 1992, Horne studied the feasibility of using GPR for bridge scour investigation as part of a collaboration between Clarkson University and the New York State Thruway Authority. The investigation included several bridge piers and abutments with optimal water and soil conditions. It was found that the 300 MHz antenna was the best antenna for penetrating the silty soil in less than two meters of water. Horne concluded at that time that further research was needed to adopt GPR as a tool for bridge scour investigation (Horne, 1992).

In 1996, Davidson *et al.* showed that impulse radar could be used for a quick and economical investigation of the pre-existing scour pattern. They surveyed three different bridges and were able to localize scour holes in two of them. However, they realized that a prior knowledge of the water conductivity was essential. This is due to the fact that energy penetration is reduced with an increase in water salinity.

Millard *et al.* (1998) carried out several laboratory tests to evaluate riverbed scour using impulse radar. They used a wooden box 2.4 x 1.7 x 0.75 m and they modeled riverbeds using either granular sand bedding material or a clay material. A GSSI SIR2 radar system with a 900 MHz antenna was used. To model a boat-mounted radar system, the antenna was mounted on a specially designed device to allow its free movement across the wooden box. Different concrete piers with different shapes and sizes were placed in the scour hole to determine their effect on the reflected radar signal. Infill of the scour hole was modeled by using fine silty sediment and coarser gravel sediment obtained from the bed of a river (River Dee). The scour hole was constructed using a four-faced pyramid shape with a constant angle of either 120° or 90°. The laboratory tests showed promising results for the use of impulse radar to

evaluate riverbed scour. Following the laboratory study, a field investigation of different masonry bridges in the UK was performed. The authors reported problems in correlating between the radar signal and the spatial location of the boat, in controlling the position of the boat, and in interpreting the radar signal in the presence of infill since it reduces the clarity of the radar image.

2.4.8. Detecting buried pipes

The principle of using GPR to detect buried pipes comes from the differences between the dielectric properties of the pipe and the surrounding soil. This means that steel or cast iron pipes can easily be detected. However, if the pipe is made from a material that has dielectric properties close to that of the soil, then its detection might be difficult. In addition, if the soil is made from a highly conductive material (clay), then the signal penetration is also constrained. Figure 2.9 shows a ground penetrating radar scan over a buried cast iron pipe. The 300-mm pipe is almost 300 mm under the ground surface. The pipe is easily seen in the scan from the hyperbolic shape.

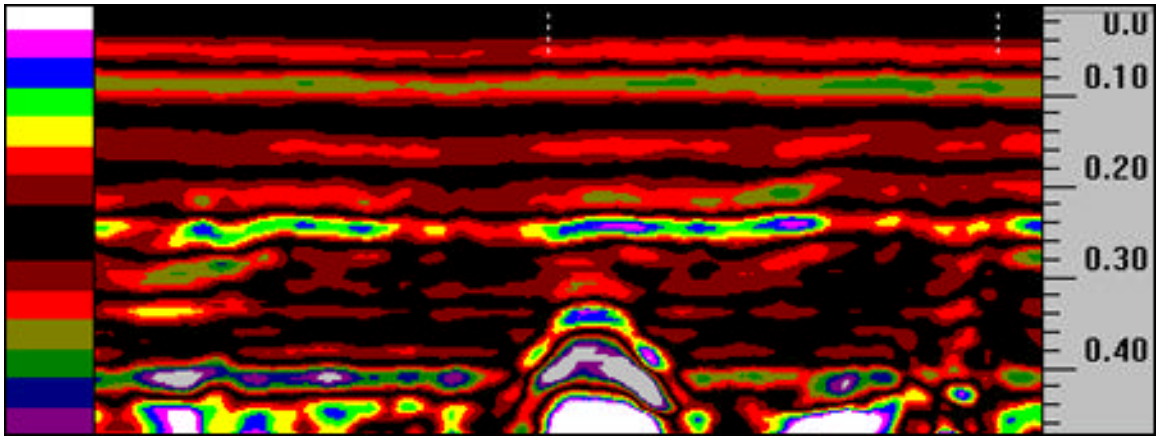

Figure 2.9. Locating buried pipes

Smith and Scott (1989) developed a scale model to experimentally study the capabilities of GPR. The model was 1/3rd full size, and the earth (red clay) was modeled by an emulsion (a mixture of mineral oil, saline solution, and a stabilizing agent). They measured the electric field transmitted by the radar into the earth. They were also able to measure the scattered signals from different pipes buried in the earth. This was done by comparing the responses obtained without the pipes with those obtained when they introduced the pipes. The difference in the signals is the signature of the pipes.

Bourgeois and Smith (1996) used a Smith and Scott scale model to confirm the results calculated with a Finite-Difference-Time-Domain (FDTD) simulation, which they developed to completely model the GPR problem. The physical and electrical parameters of the FDTD analysis were chosen to match those of the scale model. The predicted scattered responses from the buried pipes using the FDTD simulation were similar to those measured with the scale model.

Liu and Shen (1991) investigated numerically, using the Transmission-Line-Matrix (TLM) method, the subsurface radar for detecting dielectric or metal pipes buried in the ground. The main objective of the simulation of the electromagnetic pulse was to improve the design of radar systems and the quality of the output images. They were able to produce images of the scattered signals from different buried pipes (different materials and different depths) by using a reference signal obtained from a ground without any buried pipes.

Conway (1995) used digital signal processing techniques to detect non-metallic pipes buried in a variety of materials. Some of these techniques include signal conditioning, migration, and Hough transform. Using these sophisticated imaging and recognition aspects, it was possible to detect 89 out of 90 targets at 44 sites in New York.

To properly use a GPR system for a specific application, one must have a thorough knowledge of the electromagnetic properties of the scanned materials, know how deep the electromagnetic waves are expected to travel, and know the range and spatial resolution required for the specific application. For these reasons, several GPR systems exist for different applications.

2.5. Currently Available GPR Equipment

Several manufacturers of GPR systems exist in different parts of the world. Presented below are those that are currently used in the market for roadway infrastructure.

Road Radar Ltd: Located in Edmonton, Alberta, Canada, Road Radar Ltd. is a system manufacturer and service provider. Its GPR system has been specifically developed for subsurface inspection of roads and bridge decks. Road Radar typically uses two antennas: a ground-coupled antenna with a center frequency of 1 GHz, and an air-

coupled antenna with a center frequency of 3 GHz. A signal processing software is used to combine information from both antennas for data interpretation. Figure 2.10 shows their system mounted behind a van.

Figure 2.10. Road Radar GPR equipment

Penetradar Corp: Located in Niagara Falls, New York, USA, Penetradar manufactures proprietary GPR systems and uses them to provide inspection services for bridge decks and pavements. Penetradar Corp. also offers a data analysis software. Figure 2.11(a) shows a typical Penetradar GPR system, while Figure 2.11(b) shows some data.

(a)

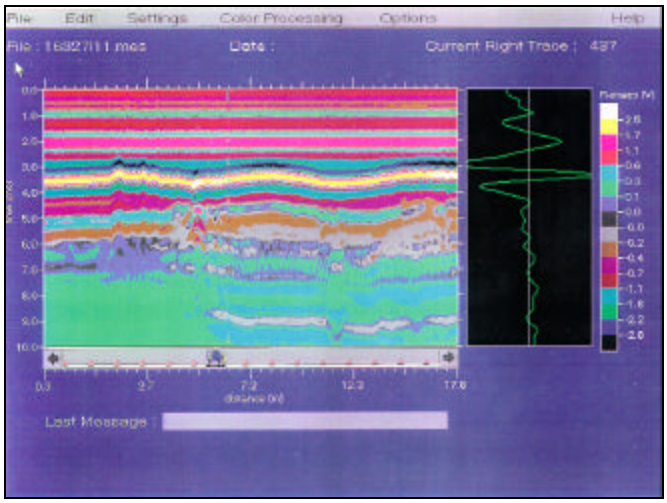

(b)

Figure 2.11. Penetradar GPR equipment (a) control Unit (b) software layout

Sensors & Software, Inc: Located in Mississauga, Ontario, Canada, Sensors & Software, Inc. manufactures, sells, rents, and provides training for several GPR systems. Its pulseEKKO 1000 with a 1200 MHz antenna is used for pavement and bridge deck surveys (Figure 2.12).

Figure 2.12. Sensors & Software pulseEKKO 1000

Pulse Radar, Inc: Located in Houston, Texas, USA, Pulse Radar, Inc. sells GPR equipment and provides highway inspection services. Pulse Radar's antennae are air-coupled horns and are suspended from the front or back of a van.

FHWA HERMES System: The HERMES (High-performance Electromagnetic Roadway Mapping and Evaluation System) is a high-resolution GPR system for bridge deck inspection. The HERMES prototype was developed for the Federal Highway Administration (FHWA) at Lawrence Livermore National Laboratory. An array of sixty-four Micropower Impulse Radar (MIR) modules is housed in a trailer with computers and software. Each element of the array is capable of sending very fast, short pulses at a frequency of 1 to 5 GHz. These pulses penetrate concrete to a depth of up to 300 mm. The system (Figure 2.13) is still under testing by the FHWA.

Figure 2.13. FHWA HERMES GPR system

Geophysical Survey Systems, Inc. (GSSI): Located in North Salem, New Hampshire, USA, GSSI is a manufacturer and service provider. It sells complete systems from 15 MHz to 2 GHz and provides a software package to analyze and process data files. Figure 2.14 shows the GSSI van with a Model 5100 ground-coupled antenna.

Figure 2.14. GSSI GPR equipment (Model 5100 antenna)

The GPR systems that were used in this research are manufactured by GSSI. The control unit is a SIR-10B model, the air-coupled system uses a model 4208 horn antenna, and the ground-coupled system uses a model 3101D antenna. Chapter three presents both systems and the quality control tests performed on the air-coupled system.

Chapter 3. EXPERIMENTAL PROGRAM

3.1. GPR Systems

Both GPR systems used in this research are manufactured by GSSI and have the same control unit, shown in Figure 3.1. For the air-coupled system, the control unit is connected to a transceiver, which is connected to a pair of horn antennas (one is a transmitter and one is a receiver). Figure 3.2 shows the pair of antennas and the transceiver box. For the ground-coupled system, the control unit is directly connected to the monostatic antenna, shown in Figure 3.3. Table 3.1 shows the control unit and antennas specifications.

Figure 3.1. Control unit

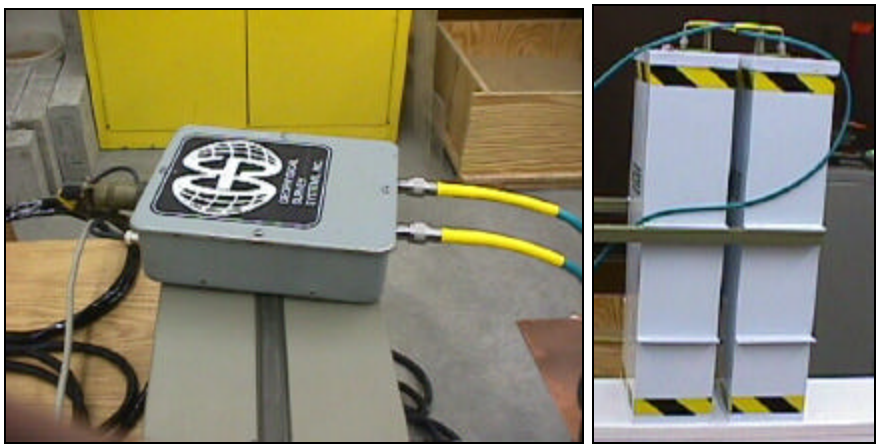

Figure 3.2. Transceiver and horn antennas for the air-coupled system

Table 3.1 GPR system specifications

Radar Parameters:	
Antennas	Can handle up to 2 antenna inputs simultaneously
Sampling frequency rate	up to 100 GHz
Analog quantization	8 or 16 bits, selectable
Analog to digital sampling rate	128, 256, 512, 1024, 2048, 4096 or 8192 samples/scan, selectable
Scan rate	2 to 220 scans/second, selectable
Programmable time window	2-10,000 nanoseconds full scale, selectable
Programmable sampling window increments	10 picoseconds
Dynamic range of time variable gain	150 dB
Dynamic range of input A/D	25 bits
Dynamic range of input averaging filter	48 bits
Dynamic range of DSP	24 bits
Clock frequency of DSP	38.5 MHz
Programmable stacking range	2-32768
Acquisition Software:	
Inputs	Records data from 1 or 2 channels simultaneously, 1 to 4 data channels selectable
Display modes	Linescan (using 16 color bins to represent the polarity and amplitude of the signal), Wiggle plot and Oscilloscope
System setups	Storage of over 50 system setup files for different road types and antenna configurations
Range gain	Manual adjustment from –20 to +120 dB. Number of segments in gain curve is user-selectable from 1 to 8
Vertical filters	Individually filter the scans in the time domain. Low and High Pass, Infinite Impulse Response (IIR), Finite Impulse Response (FIR), Boxcar and triangular filter types are available.
Horizontal filters	Sequentially filter the scans in the spatial domain. Stacking background removal, IIR, FIR, Boxcar and Triangle types are available, as well as Static Stacking modes.
Data Storage	
Hard drive	1.3 GB
Floppy disk drive	1.44 MB
Data transfer	Through parallel cable
Scan size	1 Kb/scan for 16-bit and 512 samples/scan
Antennas:	
Ground-coupled Center frequency Pulse width	Model 3101 900 MHz 1.1 ns
Air-coupled Center frequency Pulse width Pulse repetition	Model 4208, TEM horn antenna 1 GHz 1 ns 400 KHz

Figure 3.3. Ground-coupled antenna

3.2. Performance Tests

Prior to any testing, the performance of the air-coupled GPR system was evaluated. Texas Transportation Institute (TTI) performance specification tests were conducted. These tests include the Noise to Signal Ratio Test, Signal Stability Test, Long Term Signal Stability Test, Variations in Time Calibration Factor Test, End Reflection Test, and Symmetry of Metal Plate Reflection Test (Texas Transportation Institute, 1997). Although these tests are not standards, they are believed to be very beneficial for establishing reference points regarding the system performance.

<u>Noise to signal ratio test</u>

The antennas were positioned at a height of 0.441 m (recommended height from GSSI is 0.45 m ± 0.01 m) above two copper plates (1.22 x 0.91 m each) as shown in Figure 3.4. The radar unit was turned on and allowed to warm up for 15 minutes. The following data collection parameters were used: a Range Gain of 8.0 dB, a Vertical Boxcar Low Pass Filter at 8530 MHz, a Vertical Boxcar High Pass Filter at 500 MHz, a range of 20 ns, 512 Samples per scan, and a scan rate of 80 scans/sec. One scan was collected and is shown in Figure 3.5. The Noise to Signal Ratio is defined by the following equation:

$$NSR = \frac{NoiseLevel\ \ (A_n)}{SignaLevel\ \ (A_{mp})} \tag{3.1}$$

where A_n is the maximum absolute signal level amplitude occurring after the surface echo and A_{mp} is the copper plate return amplitude measured from the peak to the preceding minimum.

Signal stability test

The setup for the Noise to Signal Ratio Test was used again for this test. One hundred scans were recorded. The signal stability is evaluated using Equation (3.2):

$$\frac{A_{max} - A_{min}}{A_{avg}} \tag{3.2}$$

where A_{max} is the maximum amplitude obtained during the 100 scans, A_{min} is the minimum amplitude obtained during the 100 scans, and A_{avg} is the average scan amplitude for the 100 scans.

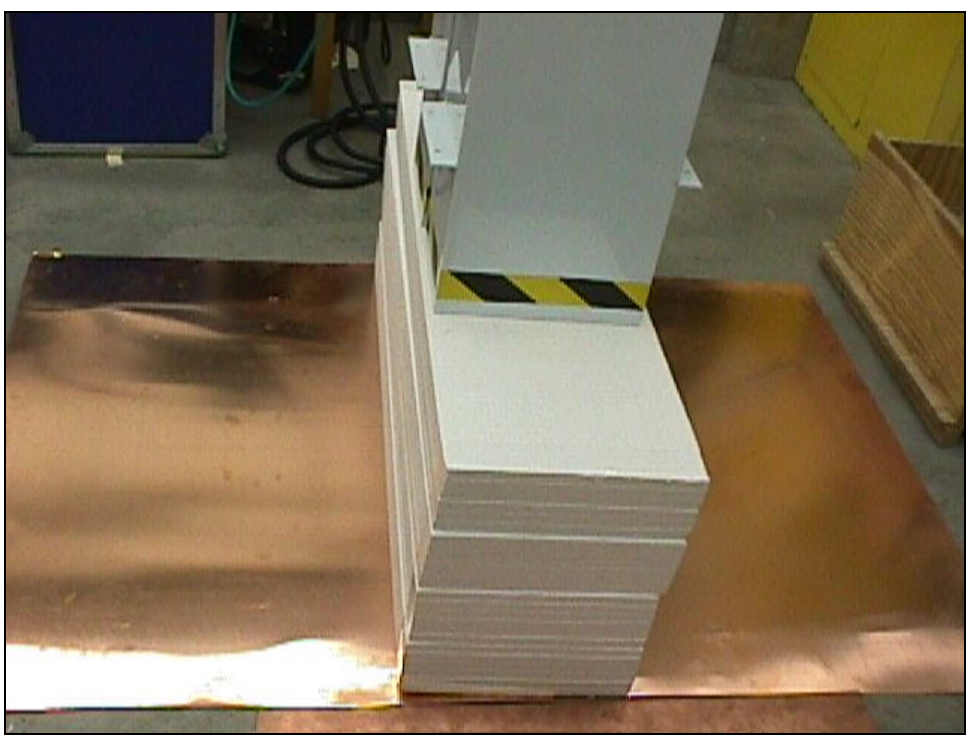

Figure 3.4. Set-up for noise to signal ratio test

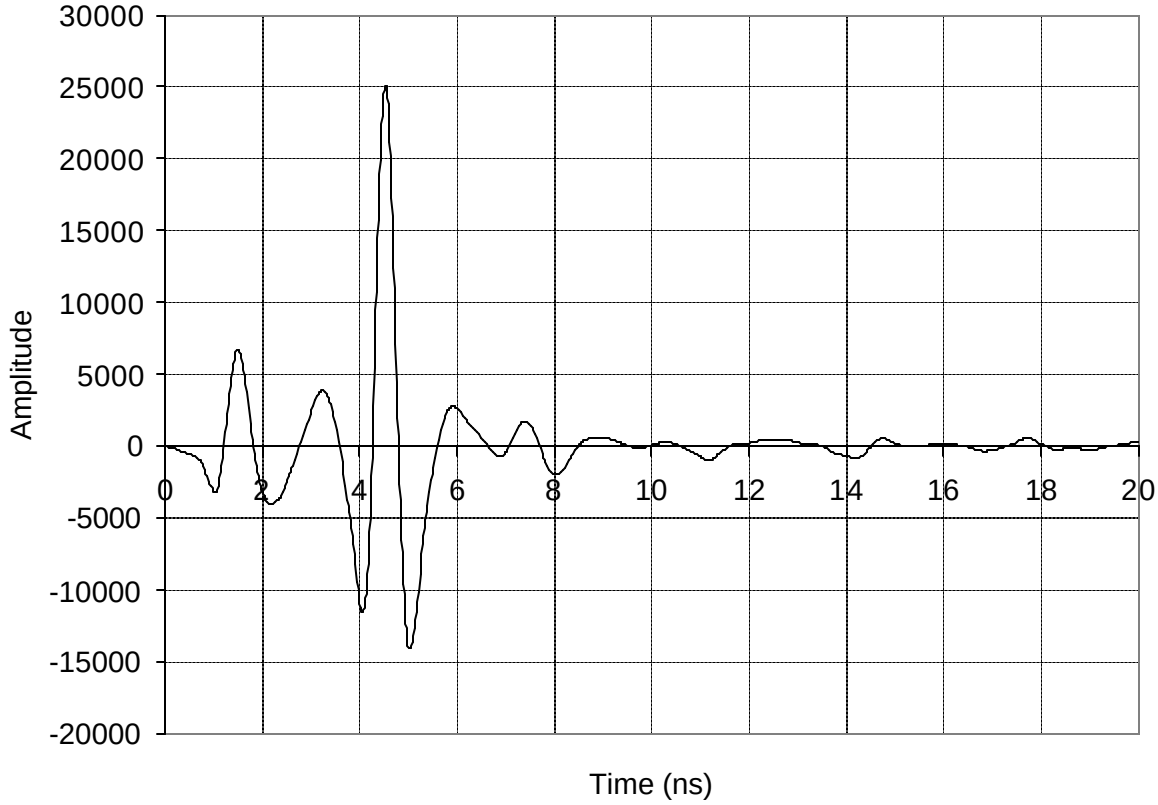

Figure 3.5. Collected waveform for the Noise to Signal Ratio test

Long term signal stability test

Using the Noise to Signal Ratio Test setup, the system was allowed to run continuously for two hours, and a scan was collected every two minutes resulting in a total of 60 scans. The long-term stability is evaluated using Equation (3.3):

$$\frac{A_{max} - A_{20}}{A_{20}} \tag{3.3}$$

where A_{20} is the amplitude measured after 20 minutes (scan number 10), and A_{max} is the maximum amplitude measured from 20 minutes to 120 minutes (scans 11 to 60).

Variations in time calibration factor

Using the setup for the Noise to Signal Ratio Test, the antennas were positioned at three different heights: 0.260 m, 0.406 m, and 0.552 m. A single scan was collected for each

height. The time from the end reflection (reflection at the tip of the antenna) to the reflection from the copper plate is measured for each scan. Figure 3.6 shows the scans for the three different heights. The variation in the time calibration factor is evaluated using Equation (3.4):

$$\frac{c_1 - c_2}{\text{Mean of } c_1 \text{ and } c_2} \tag{3.4}$$

where c_1 is the speed evaluated from scan 1 (height 1 divided by time 1), and c_2 is the speed between heights 2 and 3 [(height 3 minus height 2) divided by (time 3 minus time 2)].

End reflection

This test is evaluated from the Noise to Signal Ratio scan (Figure 3.5). It measures the amplitude of the end reflection and compares it to the measured amplitude of the copper plate reflection. This is done using Equation (3.5):

$$\frac{A_{end}}{A_{mp}} \tag{3.5}$$

where A_{end} is the amplitude of the end reflection, and A_{mp} is the copper plate reflection amplitude.

Symmetry of metal plate reflection

This test is also evaluated from the Noise to Signal Ratio scan. It measures the time from the maximum negative peak following the surface reflection to the zero crossing point.

Results

Table 3.2 shows the results of the performed tests and compares them with the TTI specifications. The end reflection criterion was not met by the GSSI system. This does not affect the accuracy of the measurements, but it does decrease the amount of power transmitted to the assessed structure. This end reflection is also used to measure the height of the antennas above the ground.

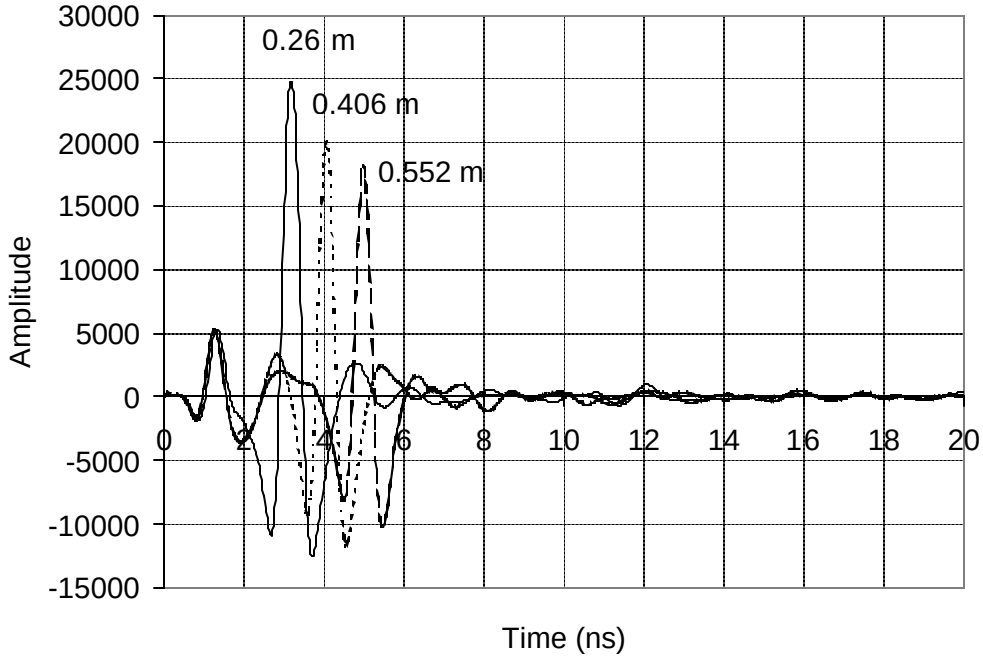

Figure 3.6. Scans from the variation in Time Calibration Factor Test

Table 3.2. Performance test results

Test	Result	TTI Spec.
Noise to Signal Ratio	4.7%	≤ 5%
Signal Stability	1.0%	≤ 1%
Long Term Signal Stability	1.1%	≤ 3%
Variations in Time Calibration Factor	2 %	< 2%
End Reflection	27%	< 10%
Symmetry of Metal Plate	0.59 ns	≤ 0.75 ns

3.3. Signal to Noise Ratio Analysis

Before preparing the specimens for this research, a signal to noise ratio analysis was performed to decide on the thickness of the specimens. This was done for the air-coupled system. The noise power developed in the receiver competes with the desired reflected signal. As long as the returned signal is a few dB above the noise power, the interface could be easily detected. The noise power generated in a receiver is computed as shown in Equation (3.6) (Pratt and Bostian, 1986):

$$P_n = k \times T_n \times B \tag{3.6}$$

where P_n is the noise power in watts, k is Boltzmann's constant = 1.38×10^{-23} W/°K/Hz, T_n is the noise temperature of the source in ºK, and B is the receiver bandwidth in Hz. The term kT_n is called the noise spectral density (W/Hz). The noise temperature, T_n, is characterized by the noise factor through Equation (3.7):

$$T_n = T_0 \times (F - 1) \tag{3.7}$$

where T_0 is a reference temperature used to calculate the standard noise figure and is usually equal to 290°K, and F is the noise factor, which is related to the noise figure, NF (expressed in dB), through Equation (3.8):

$$F = \log^{-1}(NF/10) \tag{3.8}$$

A noise figure of 5 dB is assumed for the calculations. This is a conservative assumption since Edde (1993) reported a maximum noise figure of 5.5dB in systems with frequencies ranging from 8 to 12 GHz. This value for the noise figure yields a noise factor, F, of 3.2. Using Equation (3.7), a noise temperature of 627°K is obtained. The air-coupled system has a bandwidth of approximately 1 GHz, which leads to a noise power, P_n, of 8.6×10^{-12} watts or –110 dBW. Therefore, reflected signals a few dB above –110 dBW would be detectable.

To consider the antenna response as a function of the range, an experiment was performed where a copper plate was placed at different distances from the antennas, and the corresponding waveforms were recorded. The peak to peak amplitude in each waveform was taken as the copper plate reflection at that distance. As seen in Figure 3.7, the amplitude of the reflected signals decreases as the range increases. At a distance of 475 mm from the antennas, for example, there is a reduction of almost 2 dB in the reflected signal. Also, it was noted that at a range of approximately 450 mm, the amplitude is decreasing exponentially with distance. The data were fitted using the following exponential function with an R^2 value of 0.98:

$$y = 48876\, e^{-0.0005x} \tag{3.9}$$

where y is the amplitude of the reflected signal and x is the distance from the antenna in mm.

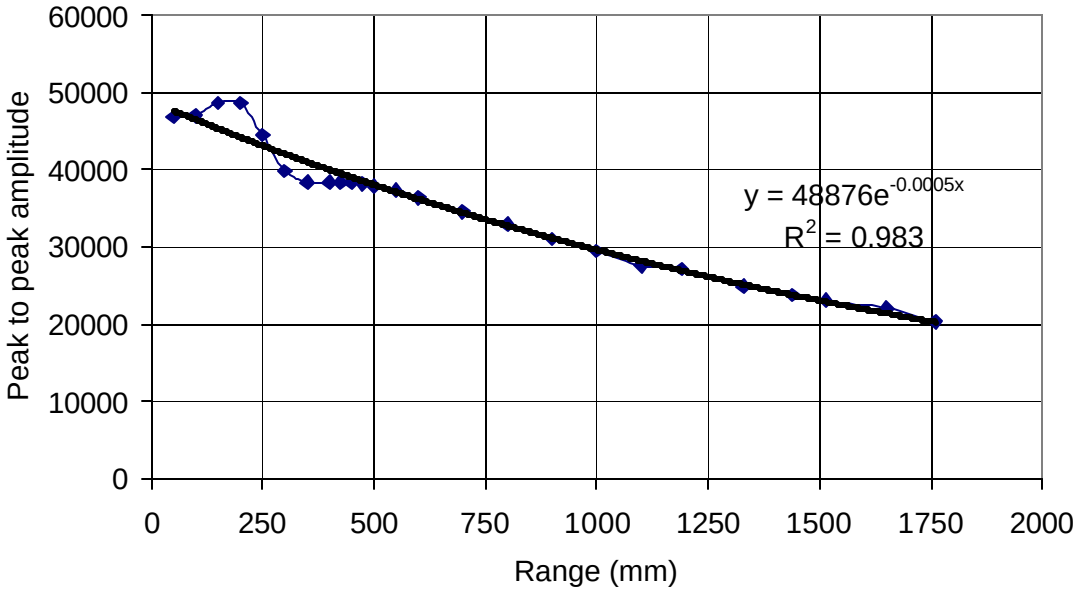

Figure 3.7. Antennas' response as a function of range

To complete the Signal to Noise Ratio analysis, the reflectivity of the interfaces and energy dissipation during propagation through the materials (concrete and HMA) should be considered. Three cases were analyzed as shown in Figure 3.8. Case 1 consists of 127 mm (5 in) concrete slab; case 2 considers an overlay of 76 mm (3 in) of HMA over the concrete slab; and case 3 consists of 102 mm (4 in) of HMA over 102 mm (4 in) of limestone base. The energy dissipation during propagation could be evaluated by calculating the specific attenuation (α) in the materials. Typical values for the dielectric constant and the loss tangent for concrete, HMA, and limestone are shown in Table 3.3 (Al-Qadi, 1992b, Al-Qadi and Riad, 1996). These values were used with a frequency of 1 GHz to estimate the specific attenuation, which is used in computing the Signal to Noise Ratio for the three cases. The voltage reflection coefficient at any interface is calculated using equation (2.16). The power reflection coefficient in decibels is calculated as shown in Equation (3.10a) while the transmission power coefficient is found from Equation (3.10b). Table 3.4 presents the calculated values for all the interfaces found in the three cases.

power reflection coefficient = 10 x log(r^2) (3.10a)

power transmission coefficient = 10 x log(1-r^2) (3.10b)

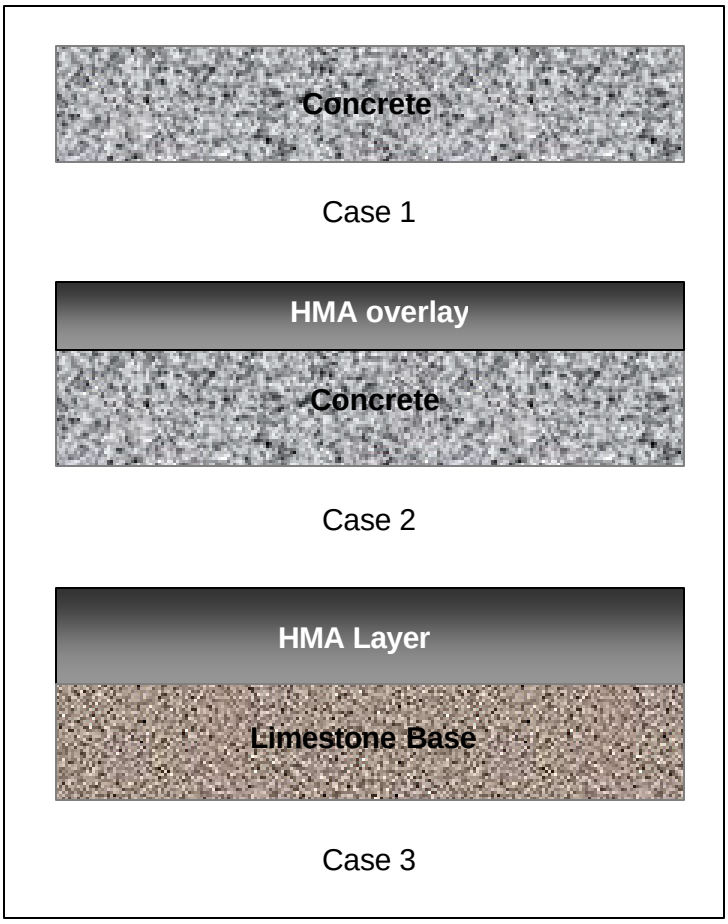

Figure 3.8. Cases for Signal to Noise Ratio analysis

Table 3.3. Typical values for construction materials dielectric properties

Material	e_r'	e_r''	**tan**d	a **(dB/mm)**
HMA	5.4	0.3	0.06	0.04
Concrete	12	2	0.16	0.16
Dry Limestone	4.2	0.14	0.033	0.02

Table 3.4. Power reflection and transmission coefficients at the interfaces

Interface	Reflection Coef.	Power Reflection Coef. (dB)	Power Transmission Coef. (dB)
Air/Concrete	-0.55	-5.2	-1.6
Air/HMA	-0.40	-8.0	-0.8
HMA/Concrete	-0.2	-14	-0.2
HMA/Limestone	0.06	-24.4	-0.02

The antennas were supposed to be 475 mm from the top layer of each case. The system average power as reported by the manufacturer is 820 mW or –0.9 dBW.

Case 1

- Input power = IP = -0.9 dBW
- Antenna response at 0.475 m = $R_{0.455}$ = -2.0 dBW
- Power reflection coefficient = $\Gamma_{a/c}$= -5.2 dBW
- Power transmission coefficient = $T_{a/c}$= -1.6 dBW
- Noise Power = NP = -110 dBW
- α = 1.6 dB/cm
- Thickness = d_c = 0.127 m

Air to Concrete Interface: S-N = IP + $R_{0.475}$ + $\Gamma_{a/c}$ - NP

= -0.9 – 2.0 – 5.2 + 110 = 101.9 dBW

Concrete to Air: S-N = IP + $R_{0.475}$ + $T_{a/c}$ – α_c x 2 x d_c + $\Gamma_{c/a}$ + $T_{c/a}$– NP

= -0.9 – 2.0 – 1.6 – 1.6 x 2 x 12.7 – 5.2 – 1.6 + 110 = 56.2 dBW

These calculated S-N values are high, and therefore both interfaces should be easily detected. The range resolution, given by Equation (3.11), depends on the pulse width and the dielectric property of the material.

$$\Delta R = \frac{\tau \text{ x } c}{2\sqrt{\varepsilon_r}} \tag{3.11}$$

where ΔR is the range resolution in meters, τ is the transmitter pulse width in seconds, c is the speed of light, and ε_r is the dielectric constant. For the GSSI air-coupled system, the transmitted pulse width is approximately 1 ns. If the dielectric constant for concrete

is assumed to be 12, then the range resolution in concrete is calculated to be 43.3 mm. This range resolution is smaller than the concrete thickness, and therefore the signals from both interfaces should not overlap.

Case 2

Air to HMA: $S\text{-}N = IP + R_{0.475} + \Gamma_{a/HMA} - NP = -0.9 - 2.0 - 8 + 110 = 99.1$ dBW

HMA to Concrete: $S - N = IP + R_{0.475} + T_{a/HMA} - \alpha_{HMA} \times 2 \times d_{HMA} + \Gamma_{HMA/c} + T_{HMA/a} - NP$

$= -0.9 - 2.0 - 0.8 - 0.4 \times 2 \times 7.6 - 14 - 0.8 + 110 = 85.4$ dBW

Concrete to Air: $S - N = IP + R_{0.475} + T_{a/HMA} - \alpha_{HMA} \times 2 \times d_{HMA} + T_{HMA/c} - \alpha_c \times 2 \times d_c + \Gamma_{c/a} + T_{c/HMA} + T_{HMA/a} - NP$

$= -0.9 - 2.0 - 0.8 - 0.4 \times 2 \times 7.6 - 0.2 - 1.6 \times 2 \times 12.7 - 5.2 - 0.2 - 0.8 + 110$

$= 53.2$ dBW

The range resolution in HMA is found (from Equation 3.11), to equal 65 mm. Since the calculated S-N from all interfaces are high and the concrete and HMA layers are thicker than the system range resolution, then all interfaces should be easily detected.

Case 3

Air to HMA: $S\text{-}N = IP + R_{0.475} + \Gamma_{a/HMA} - NP = -0.9 - 3.9 - 8 + 110 = 99.1$ dBW

HMA to Limestone: $S - N = IP + R_{0.475} + T_{a/HMA} - \alpha_{HMA} \times 2 \times d_{HMA} + \Gamma_{HMA/L} + T_{HMA/a} - NP$

$= -0.9 - 2.0 - 0.8 - 0.4 \times 2 \times 10.2 - 24.4 - 0.8 + 110$

$= 72.9$ dBW

Since the calculated S-N from both interfaces are high, they should be easily detected.

Theoretically, the Signal to Noise Ratio analysis showed that the considered interfaces might be detected.

3.4. Specimen Preparation

Two types of aggregate (limestone and quartzite) and Type I Portland cement were used to prepare concrete slabs. The slabs were 1.52 x 1.52 m. The thickness was 127 mm for all the slabs except for those planned to study the effect of the slabs' thickness on the radar signal. For those slabs, three thicknesses were considered: 102, 127, and 152

mm. Five different mixes were evaluated: four mixes met VDOT class 30 concrete, used for bridge decks, and one mix met VDOT class 25 paving concrete. All bridge deck mixes had a w/c ratio of approximately 0.41, while the paving mix had a w/c ratio of 0.44. The first mix (referred to as M1) had limestone aggregate and Type I Portland cement. The second mix (referred to as M2) had quartzite fine aggregate, limestone coarse aggregate, and type I Portland cement. The third mix (referred to as M3) had quartzite aggregate, type I Portland cement, and Fly ash. The fourth mix (referred to as M4) had quartzite aggregate, type I Portland cement, and silica fume. The paving mix (referred to as M5) had quartzite aggregate, type I Portland cement, and fly ash. Table 3.5 presents the slab characteristics. Table A1 in Appendix A presents the mix design per m^3 of concrete for all the mixes. Tables A2 and A3 present the physical and chemical analyses, respectively, of the aggregates used in all the mixes as provided by their respective manufacturers. The limestone was provided by ACCO Stone in Blacksburg, VA. The Quartzite was obtained from Sylvastus, VA. Table A4 presents the chemical composition of the different cementitious materials used to prepare the concrete slabs. Type I Portland cement was provided by Roanoke Cement Company. Fly ash with a specific gravity of 2.25 was obtained from American Electric Power. Silica fume (RHEOMAC SF100) with a specific gravity of 2.20 was obtained from Master Builders, Inc.

Figure A1a shows a schematic of a bare concrete slab. Four #5 reinforcing bars were used in these slabs at a distance of 127 mm from the edges, which left a bare concrete area of 1.25 x 1.25 m. A hook was attached to the rebars in order to be able to lift the slabs. Figure A1b shows a schematic of a one-way reinforced slab. The reinforcement consisted of #5 rebars at 200 mm center to center (c-c). Figure A1c shows a two-way reinforced slab. The reinforcement consisted of #5 rebars at 200 mm c-c one way, and #4 rebars at 200 mm c-c the other way. The cover depth for all reinforced slabs was kept constant at 50 mm. Figure A2 shows the forms made for each slab type.

Slabs for mixes M3 and M5 were cast on April 1, 1999. Slabs for mixes M1, M2, and M4 were cast on May 4, 1999. The casting procedure, as shown in Figure A3, was exactly the same for both days. A DE-LOX concrete form coating was first applied to all wooden forms. The ready mix, provided by MARSHALL Concrete, was poured inside the forms using a hopper. A vibrator was then used to avoid honeycombing and to

achieve good consolidation. The slab surface was leveled using an aluminum straight edge, and then it was smoothed using a trowel. Two hrs after casting, wet burlap was placed on top of the slabs for curing. All the slabs were then covered with plastic sheets to keep them moist. Water was sprayed every day for six days on the slabs. Quality control measurements were performed during and after casting including slump test, unit weight, air content, and compressive strength after three, seven, and 28 days. Table A5 presents the results of these quality control tests. All mixes passed the strength requirements for bridge deck mixes and paving mixes. Mix M4 had the highest strength after 28 days (62.3 MPa) because of the presence of silica fume in the mix. After seven days of casting, all concrete slabs were moved out of the lab and were placed on cinder blocks.

Table 3.5. Characteristics of Portland cement concrete slabs

	Mix	M1	M2	M3	M4	M5
Thickness	102 mm			M3S1		
	127 mm	M1S1*	M2S1	M3S2	M4S1	M5S1, M5S2, M5S3
	152 mm			M3S3		
Delamination (Void thickness)	6.4 mm	M1S2	M2S2	M3S4	M4S2	
	12.7 mm	M1S3	M2S3	M3S5	M4S3	M5S4
Reinforcement	One way	M1S4	M2S4	M3S6	M4S4	
	Two ways	M1S5	M2S5	M3S7	M4S5	M5S5
Reinforcement + Void	One Way					M5S6

* Indicates slab identification and characteristics

The delamination in concrete slabs was simulated by inserting Styrofoam pieces, at 50 mm from the surface, with two different thicknesses (6.4 and 12.7 mm). Details of the procedure used to embed these Styrofoam pieces inside the concrete slab are presented in Figure A4. Two small holes were made in each side of the Styrofoam piece. Two plastic conduits (6 mm in diameter) were placed in each prepared hole and taped using duct tape. On the day of casting, the Styrofoam pieces were carefully placed in the center of each slab, above the first lift of the placed concrete. Concrete was then placed on them by hand to avoid breakage of the Styrofoam. After evaluating

the effect of the dry void on the radar signal, water was injected into the delaminated areas after dissolving the Styrofoam pieces using Acetone.

For asphalt over limestone, the air-coupled system was used on an experimental site in Bedford County, VA, where an earlier project was conducted to evaluate the performance of geosynthetics in flexible pavement systems (Loulizi *et al.*, 1999). The 150-m-long secondary road flexible pavement was instrumented in 1994. This tested pavement is composed of nine individual sections. All sections have approximately 90 mm of HMA. The sections were constructed in three groups. Sections one through three have a 100-mm-thick limestone base course (VDOT 21-B), sections four through six have approximately a 150-mm-thick base course, and sections seven through nine have a 200-mm-thick base course. One section in each group was stabilized with geotextile, one was stabilized with geogrid, and the other was kept as a control section. Figure 3.9 shows the layout of the different sections.

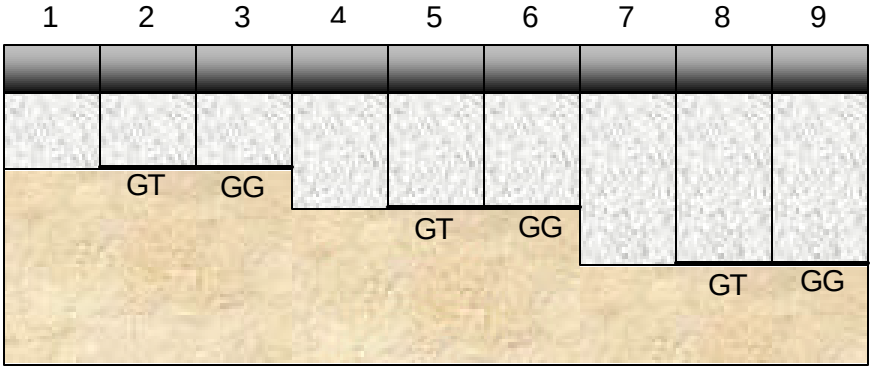

GT: Geotextile; GG: Geogrid

Figure 3.9. Flexible pavement layout in Bedford project

3.5. Data Collection

Data from the concrete slabs were taken regularly using both air- and ground-coupled systems. For the air-coupled system, data were obtained in the following manner. First, a copper plate was placed above one of the slabs (Figure 3.10), and then one hundred radar scans were saved. The saved file was used to obtain the incident wave. Data were then obtained from each slab. For the slabs with reinforcing bars, data were obtained from both directions, parallel and perpendicular to the main rebars. Since the

air-coupled antennas are usually placed at a distance of 475 mm from the surface, Styrofoam pieces with a total thickness of 475 mm were placed on top of the slab surface. The antennas were then placed on top of the Styrofoam pieces. After scanning all the slabs, data were obtained by orienting the antennas into open space, and then taking and saving one hundred scans. This file, referred to as an “end reflection” file, is used to obtain the first reflection caused by the antennas’ coupling. This reflection is subtracted from all collected data. For the ground-coupled system, data were obtained from all the slabs by placing the antenna above the slab and collecting one hundred scans (Figure 3.11).

In Bedford, data from the air-coupled system were obtained above the flexible pavement in all nine sections. Data were collected statically, and one hundred scans from each section were saved.

To determine the feasibility of using the ground-coupled system to detect moisture inside pavement systems, data were obtained from two sites: Laurel, Maryland, and Kernersville, North Carolina. Data were obtained dynamically by driving along the pavement at a speed of approximately 10 km/hr. More details about both sites are given in Chapter four, which presents the testing results as well as data analysis.

Figure 3.10. Air-coupled data collection from concrete slabs

Figure 3.11. Ground-coupled data collection from concrete slabs

Chapter 4. RESULTS AND DATA ANALYSIS

This chapter presents the results of all testing performed during this research. It starts by presenting the data obtained on the concrete slabs described in Chapter 3, and then it presents a method used to predict layer thicknesses in flexible pavements. Finally, the chapter ends by discussing the feasibility of using the ground-coupled system to locate moisture in flexible pavement systems. Data obtained from the constructed concrete slabs were used to develop a method to calculate the dielectric properties of concrete in the frequency range of 0.5 to 1 GHz, to synthesize air-coupled GPR waveforms, and to study the effects of simulated defects in concrete, reinforcing bars, and thickness variation on the reflected air-coupled and ground-coupled radar signals.

4.1. Dielectric Properties of Concrete Using the Air-Coupled Radar System

Data collected from the concrete slabs, described in Chapter 3, using the air-coupled GPR system were used to develop a method to determine the complex dielectric constant of concrete.

4.1.1. Method description

Data collected over the copper plate were used to obtain the incident wave. This is accomplished by first averaging the 100 saved scans. An example of such an averaged scan is shown in Figure 4.1. The end reflection file is then used, and its collected 100 scans are averaged to obtain the first reflection caused by the antennas' coupling, shown in Figure 4.2. The averaged end reflection scan is then subtracted from the averaged copper scan to obtain the scan shown in Figure 4.3. This scan is then multiplied by (–1), and all data points before 1.75 nsec and after 6.65 nsec are set equal to zero. The resulting scan, shown in Figure 4.4, is taken to be the incident wave (Y_i). Data from each concrete slab are also averaged. Figure 4.5 shows the averaged waveform for slab M2S1. The end reflection scan is then subtracted from the averaged waveform, and points before 1.75 and after 8.3 nsec are set equal to zero to eliminate the noise and the reflection obtained from the ground. The obtained scan is the reflected waveform (Y_r) and is shown in Figure 4.6. A Fast Fourier Transform (FFT) algorithm is then used on both signals to achieve the input and reflected frequency spectrums. Using the 20 nsec window, a frequency resolution of 50 MHz is achieved.

To obtain more solutions at smaller frequency steps, zero padding is used on both incident and reflected waveforms. This is performed by adding zeros to the time domain signals so that the scan lengths are 80 nsec. With the zero padding, solutions at 12.5 MHz increments are obtained. The incident frequency spectrum is shown in Figure 4.7. Using the 3 dB criteria, a bandwidth of 0.5 GHz is found (from 0.5 GHz to 1 GHz), as shown in Figure 4.8. Therefore, the dielectric properties of concrete were only determined for this frequency range.

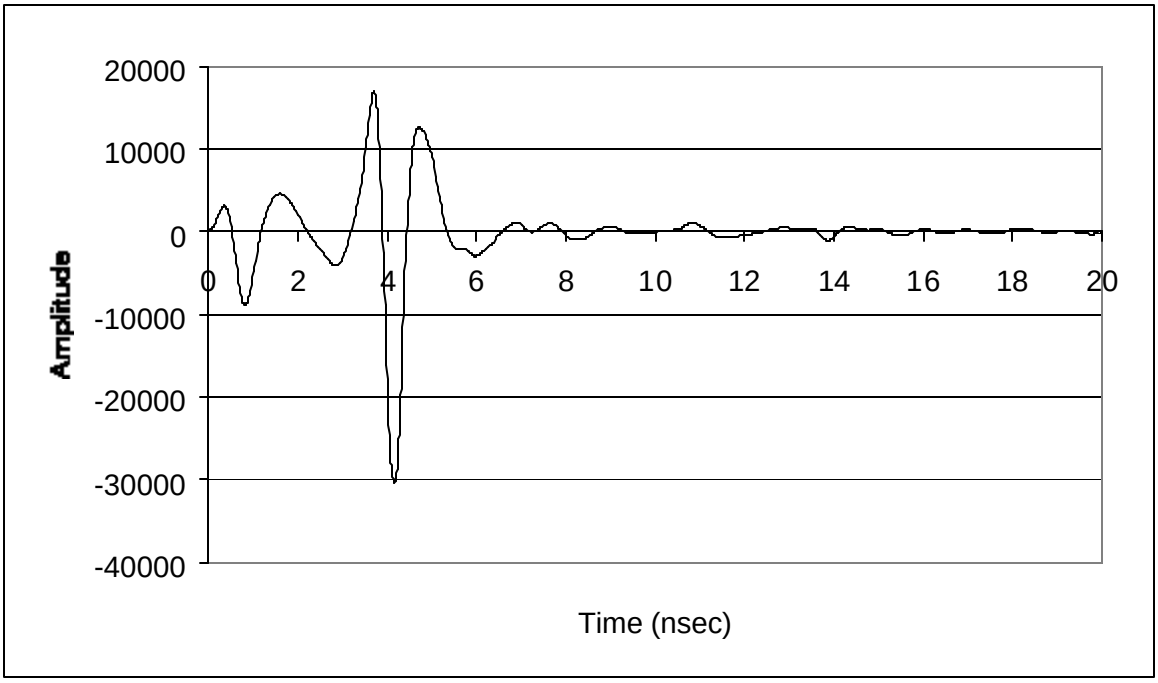

Figure 4.1. Copper plate reflection (averaged scan)

The overall reflection coefficient (Γ) is calculated using Equation (4.1):

$$\Gamma = \frac{FFT(Y_r)}{FFT(Y_i)} = \frac{F_r}{F_i} \tag{4.1}$$

The overall reflection coefficient could also be determined using the reflection model presented in Figure 4.9. As the electromagnetic wave hits the concrete slab surface at an angle of incidence θ_i, some energy will be reflected with a reflection coefficient of ρ_1, and some energy will be transmitted through the interface at an angle θ_t with a transmission coefficient equal to $(1+\rho_1)$. Equation (4.2) gives the reflection coefficient ρ_1:

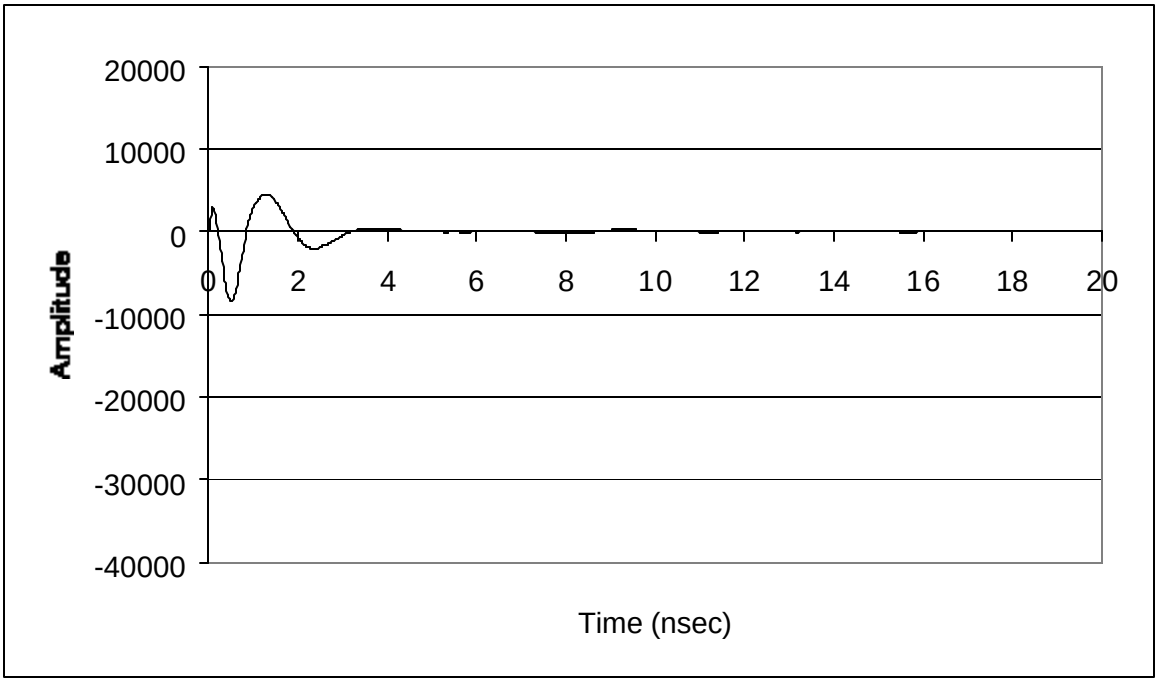

Figure 4.2. End reflection (averaged scan)

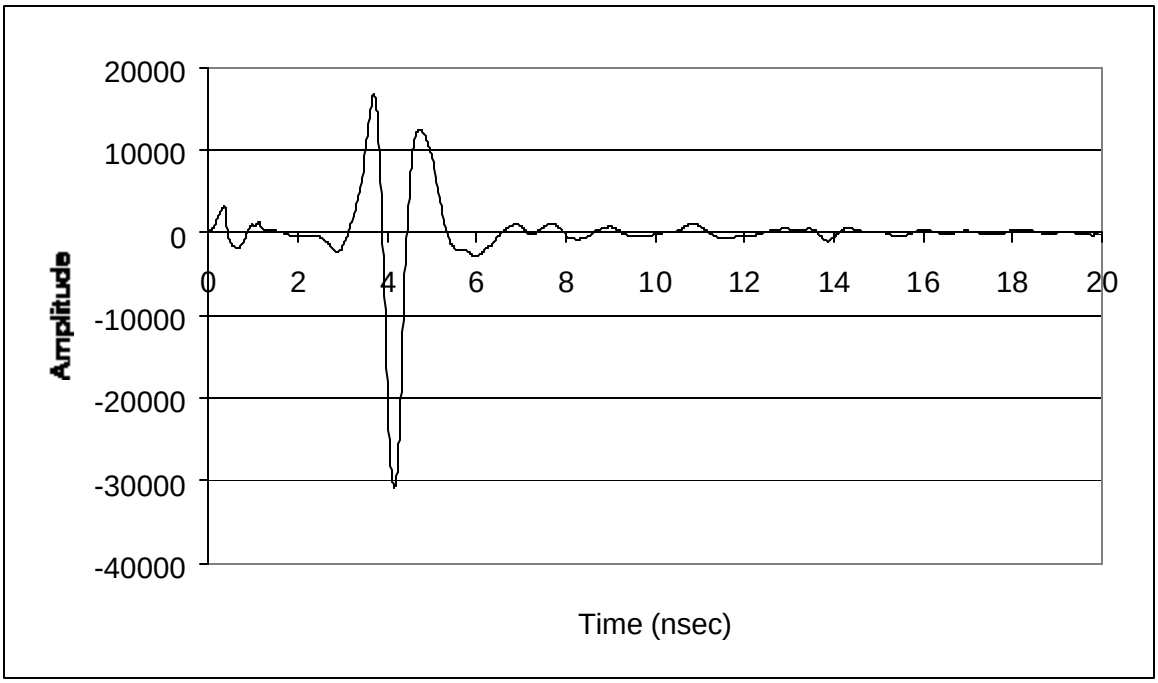

Figure 4.3. Copper plate reflection with end reflection removed

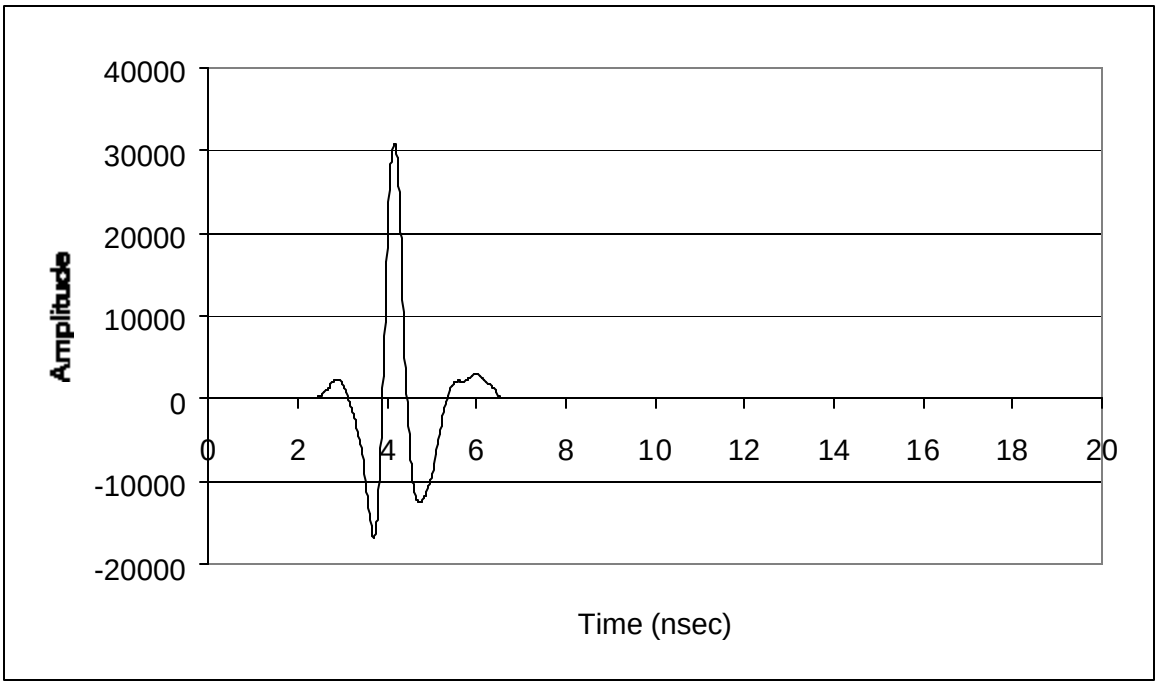

Figure 4.4. Incident waveform

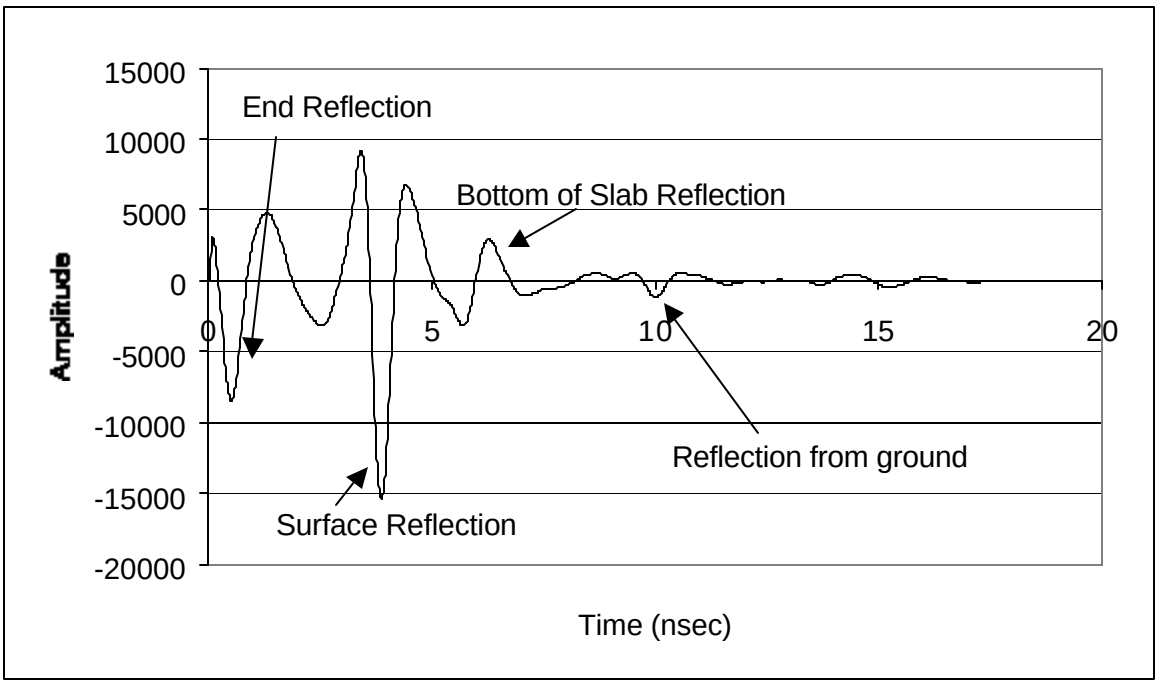

Figure 4.5 Averaged reflected waveform with end reflection

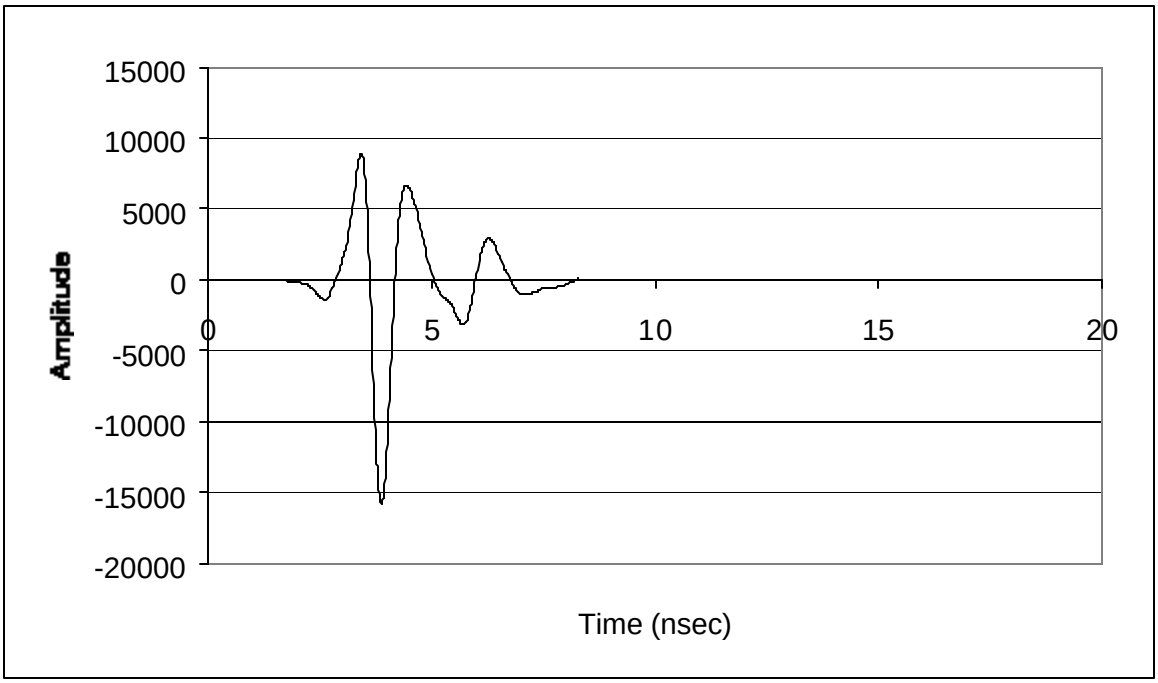

Figure 4.6. Resultant reflected waveform

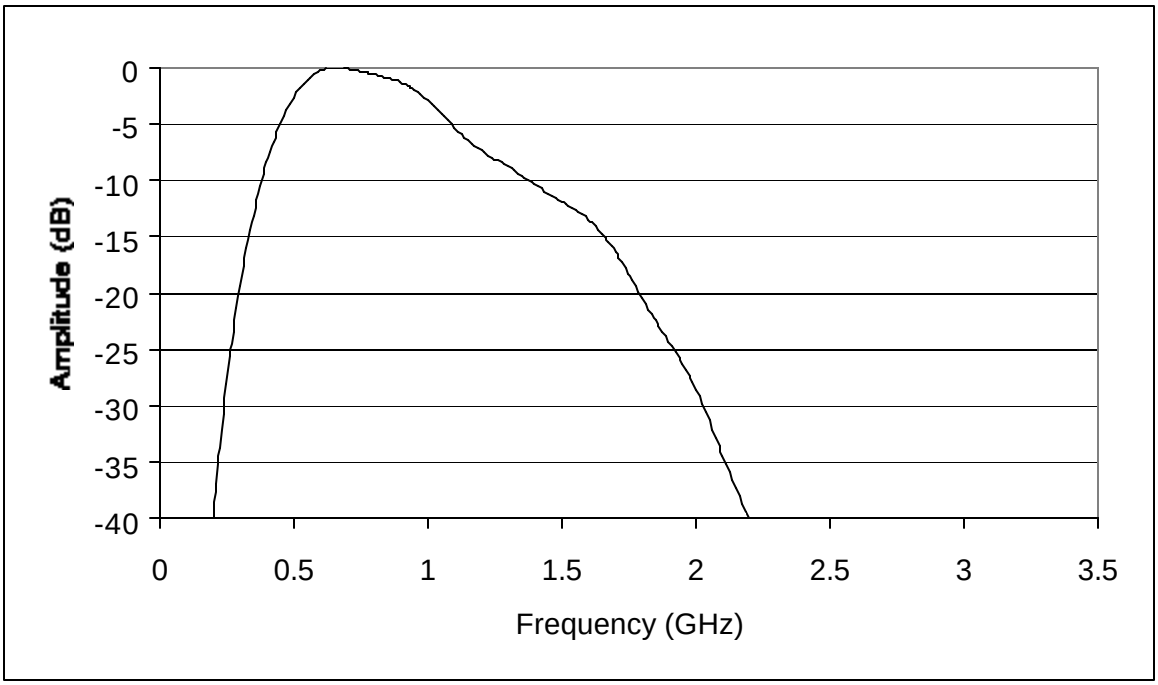

Figure 4.7. Incident frequency spectrum

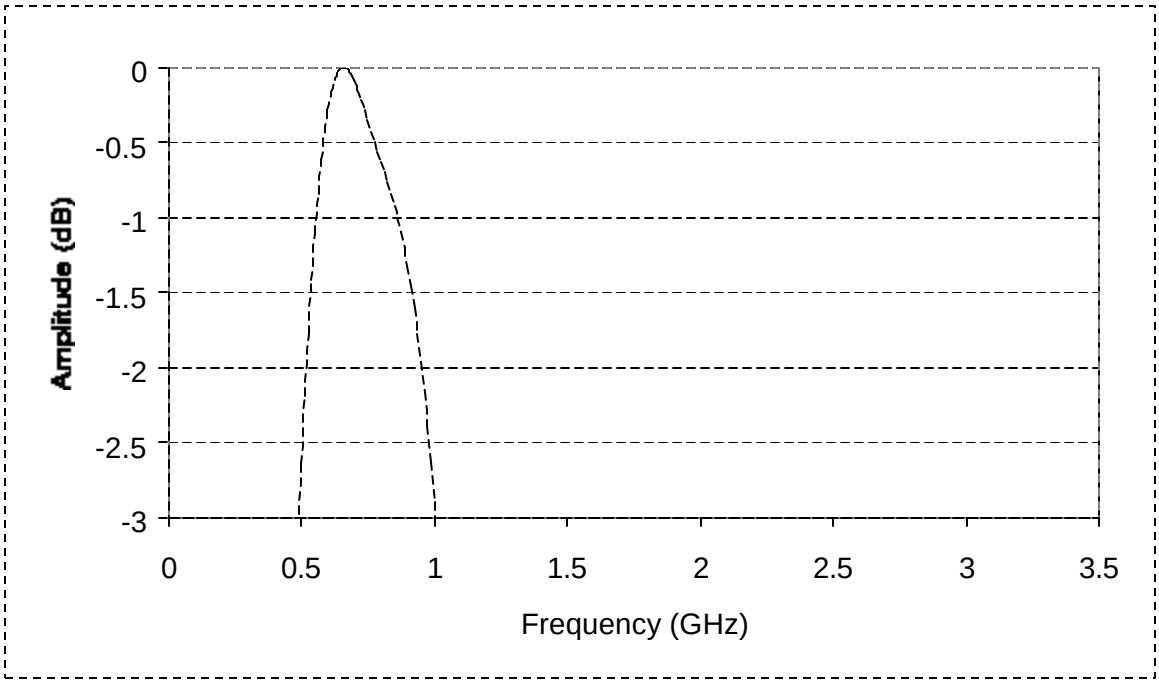

Figure 4.8. Frequency bandwidth

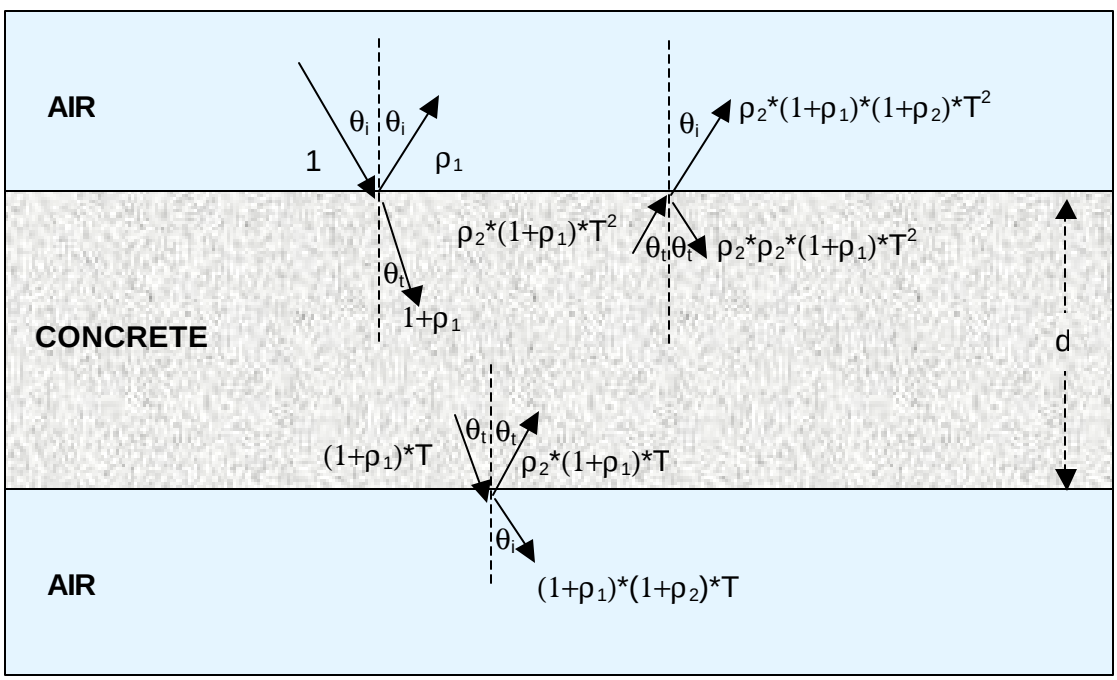

Figure 4.9. Overall reflection model

$$\rho_1 = \frac{\cos\theta_i - \sqrt{\varepsilon_r - \sin^2\theta_i}}{\cos\theta_i + \sqrt{\varepsilon_r - \sin^2\theta_i}} \tag{4.2}$$

where θ_i is the angle of incidence, ε_r is the complex dielectric constant for concrete, and θ_t is the angle of transmission, which is related to the angle of incidence by Snell's law of reflection as follows:

$$\sin\theta_t = \frac{\sin\theta_i}{\varepsilon_r} \tag{4.3}$$

The wave will then propagate through the concrete layer until it reaches the bottom, just before the air interface. At that point, the transmitted wave is multiplied by the propagation factor T given by Equation (4.4):

$$T = e^{-j\frac{\omega}{c}\frac{d}{\cos\theta_t}\sqrt{\varepsilon_r}} \tag{4.4}$$

where ω is the angular frequency, d is the concrete slab thickness (m), c is the speed of light ($3x10^8$ m/sec), and $j^2 = -1$.

At the concrete/air interface, some energy will be reflected with a reflection coefficient of ρ_2 at an angle θ_t and some energy will be transmitted through the interface at an angle θ_i. The reflection coefficient ρ_2 is given by Equation (4.5):

$$\rho_2 = \frac{\cos\theta_t - \sqrt{\frac{1}{\varepsilon_r} - \sin^2\theta_t}}{\cos\theta_t + \sqrt{\frac{1}{\varepsilon_r} - \sin^2\theta_t}} \tag{4.5}$$

The wave will then propagate up through the concrete slab until it reaches the top surface. At that point, energy will be reflected back with a reflection angle of θ_t and

some energy will be transmitted with a transmission angle of θ_i. The transmitted energy will have a coefficient of β_2 equal to:

$$\beta_2 = \rho_2 * (1+\rho_1) * (1+\rho_2) * T^2 \tag{4.6}$$

The overall reflection coefficient is then given by the following:

$$\Gamma = \rho_1 + \beta_2 = \rho_1 + \rho_2 * (1+\rho_1) * (1+\rho_2) * T^2 \tag{4.7}$$

By equating Equations (4.1) and (4.7), one equation would thus be obtained with only one unknown, ε_r, as shown in Equation (4.8):

$$f(\varepsilon_r) = \frac{\cos\theta_i - \sqrt{\varepsilon_r - \sin^2\theta_i}}{\cos\theta_i + \sqrt{\varepsilon_r - \sin^2\theta_i}} + \frac{\cos\theta_t - \sqrt{\frac{1}{\varepsilon_r} - \sin^2\theta_t}}{\cos\theta_t + \sqrt{\frac{1}{\varepsilon_r} - \sin^2\theta_t}} * \left(1 + \frac{\cos\theta_i - \sqrt{\varepsilon_r - \sin^2\theta_i}}{\cos\theta_i + \sqrt{\varepsilon_r - \sin^2\theta_i}}\right) * \left(1 + \frac{\cos\theta_t - \sqrt{\frac{1}{\varepsilon_r} - \sin^2\theta_t}}{\cos\theta_t + \sqrt{\frac{1}{\varepsilon_r} - \sin^2\theta_t}}\right) * e^{-2j\frac{\omega}{c}\sqrt{\varepsilon_r}\frac{d}{\cos\theta_t}} - \frac{F_r}{F_i} = 0 \tag{4.8}$$

When solving Equation (4.8) for ε_r, it was found that multiple solutions exist at each frequency. This is depicted, for example, in Figure 4.10 for slab M2S1 at a frequency of 0.5 GHz and using an angle of incidence θ_i of 15.3°. In this figure, two solutions were found as illustrated with the circles. The solving procedure starts with computing the function $f(\varepsilon_r)$ for different values of ε_r, ranging from 2 to 40 for the real part, and from 0 to 10 for the negative of the imaginary part. The zeros of the function, thus found, are used as initial points in a Gauss-Newton method to find the actual solutions with an accuracy of 10^{-12}. All computations are performed using several functions programmed using the mathematics software MATLAB. The MATLAB listing of these functions is included in Appendix B. Figures 4.11 and 4.12 show all the solutions found for the real and imaginary parts of the complex dielectric constant, respectively, for M2S1. These solutions are sorted to select the best solution based on typical reported values for the complex dielectric constant of concrete. Figure 4.13 shows the chosen solution for

M2S1 from 0.5 to 1 GHz. It should be noted that this data may not be extrapolated to other frequencies. Different dielectric constant values may be obtained at other frequency ranges.

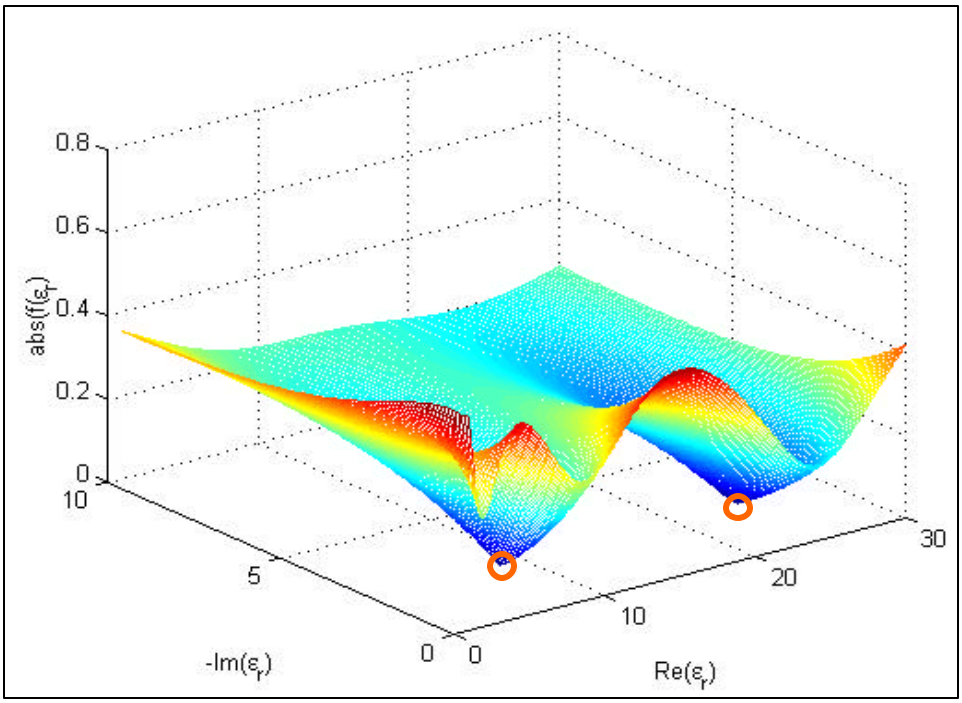

Figure 4.10 Multiple solutions for ε_r at 0.5 GHz (slab M2S1)

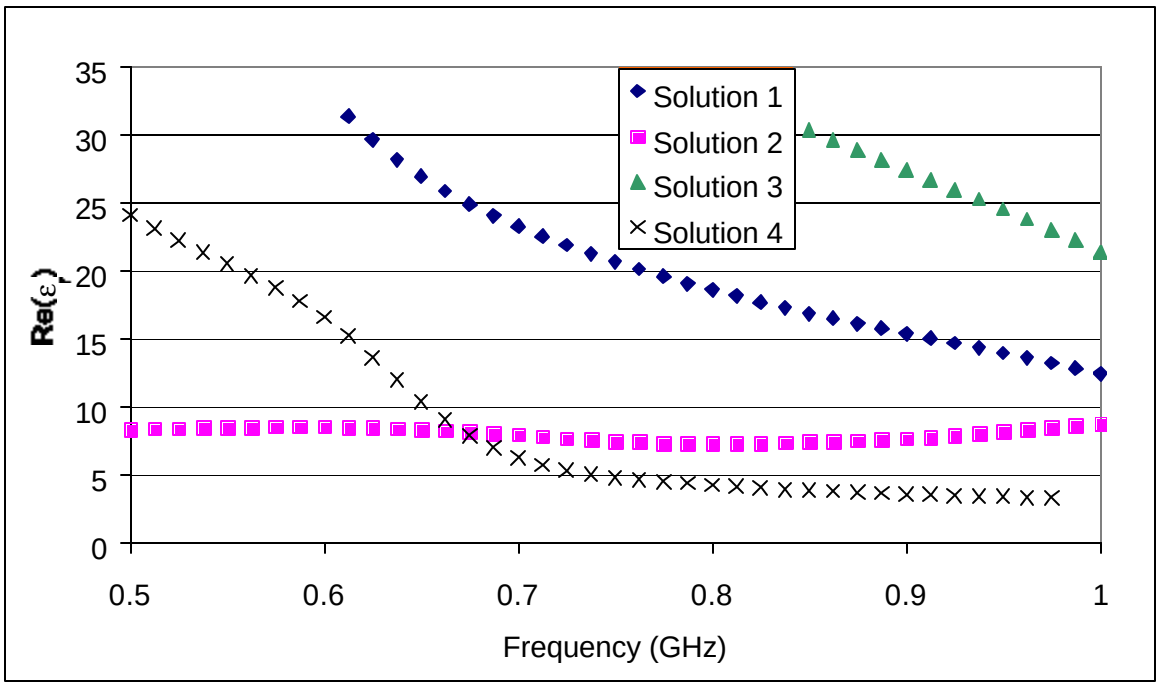

Figure 4.11 Solutions for the real part of ε_r from 0.5 to 1 GHz (slab M2S1)

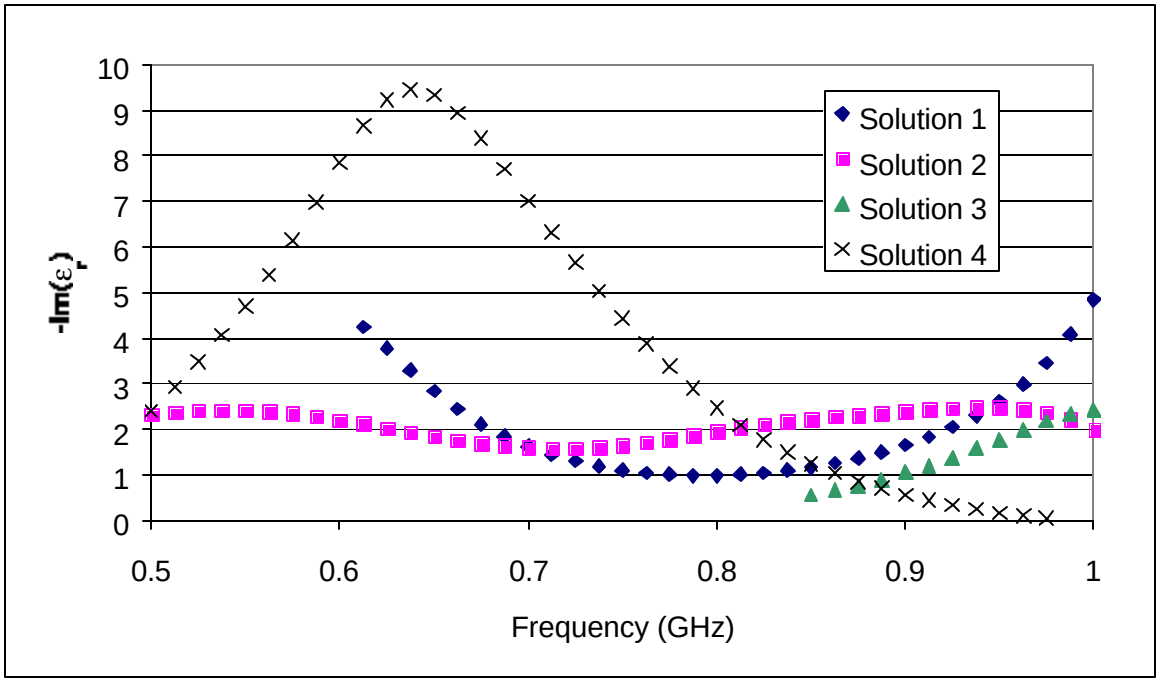

Figure 4.12 Solutions for the imaginary part of ε_r from 0.5 to 1 GHz (slab M2S1)

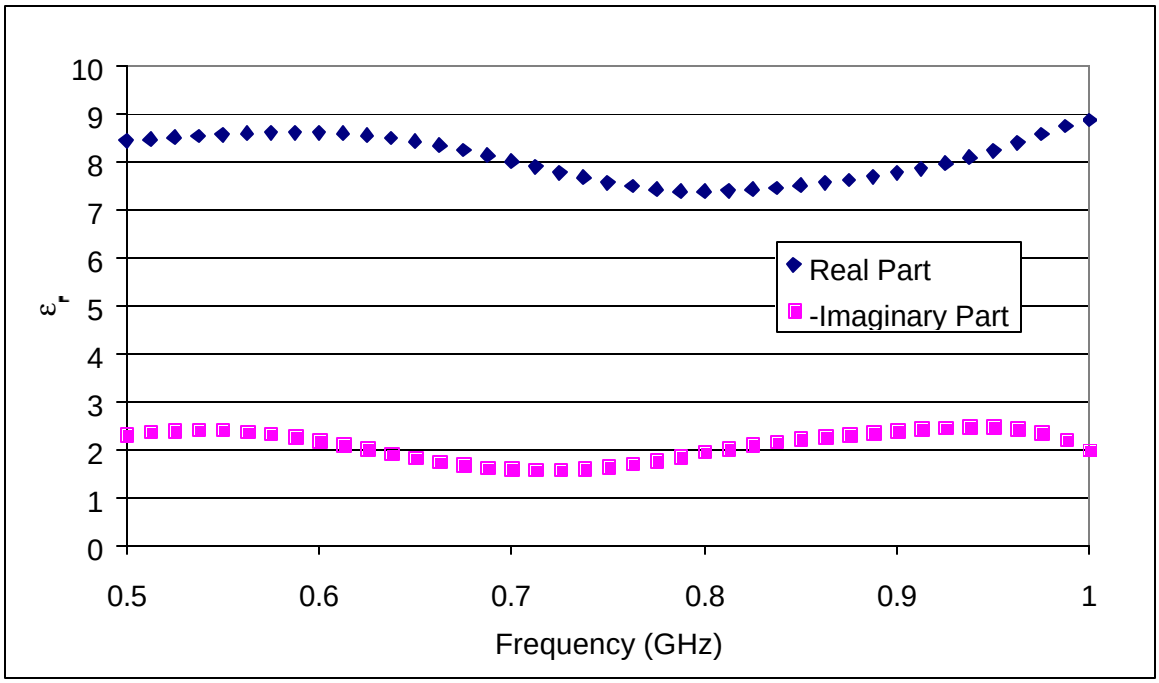

Figure 4.13 Chosen solution for the complex ε_r from 0.5 to 1 GHz (slab M2S1)

4.1.2. Effect of angle of incidence value on the computed complex dielectric constant

The GSSI horn antennas are placed above the concrete slabs as shown in Figure 4.14. The angle of incidence can take several values ranging from 3.0° ($\tan^{-1}(250/475)$) to 26.3° ($\tan^{-1}(235/475)$). The effect of the used value of the angle of incidence on the measured complex dielectric constant is presented below.

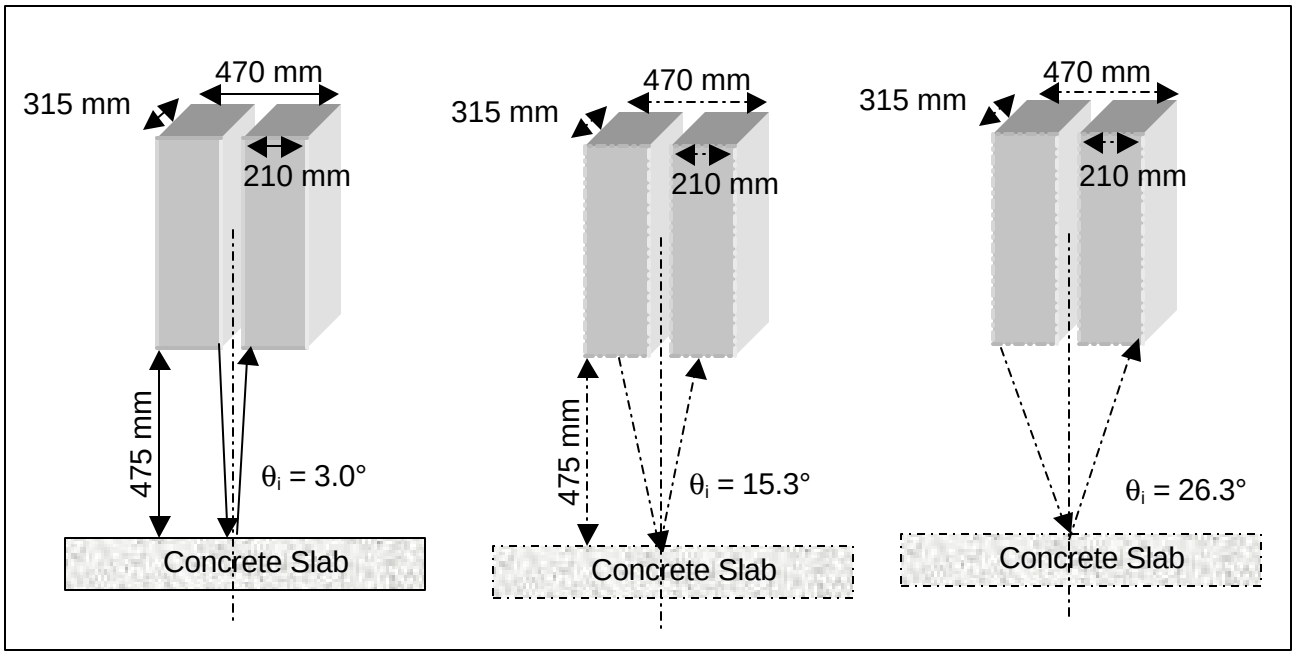

Figure 4.14. Geometry of the air-coupled horn antennas

If the angle of incidence is assumed to be 0 ($\theta_i = 0$), then Equation (4.2) is simplified as follows:

$$\rho_1 = \frac{1-\sqrt{\varepsilon_r}}{1+\sqrt{\varepsilon_r}} \tag{4.9}$$

The angle θ_t will be also equal to 0 (from Equation 4.3); therefore, the propagation factor T in Equation (4.4) becomes the following:

$$T = e^{-j\frac{\omega}{c}d\sqrt{\varepsilon_r}} \tag{4.10}$$

The reflection coefficient ρ_2 becomes equal to the following:

$$\rho_2 = \frac{\sqrt{\varepsilon_r} - 1}{1 + \sqrt{\varepsilon_r}} = -\rho_1 \tag{4.11}$$

If we set ρ_1=-ρ_2=ρ, then Equation (4.6) becomes the following:

$$\beta_2 = -\rho*(1+\rho)*(1-\rho)*T^2 = -\rho*(1-\rho^2)*T^2 \tag{4.12}$$

The overall reflection coefficient is then given by:

$$\Gamma = \rho + \beta_2 = \rho - \rho*(1-\rho^2)*T^2 \tag{4.13}$$

By equating Equations (4.1) and (4.13), one equation would thus be obtained with only one unknown, ρ, as shown in Equation (4.14):

$$f(\rho) = \rho * (1 + (\rho^2 - 1) * T^2) - \frac{F_r}{F_i} = 0 \tag{4.14}$$

where T is set equal to:

$$T = e^{-j\frac{\omega}{c}d\frac{1-\rho}{1+\rho}} \tag{4.15}$$

Equation (4.14) is solved for ρ, and then ε_r is calculated using Equation (4.16):

$$\varepsilon_r = \left(\frac{1-\rho}{1+\rho}\right)^2 \tag{4.16}$$

When solving Equation (4.15) for ρ, it was found that multiple solutions exist at each frequency. This is depicted, for example, in Figure 4.15 for slab M2S1 at a frequency of 0.5 GHz. The two solutions for the complex dielectric constant obtained using θ_i of 15° for slab M2S1 at 0.5 GHz are (24.1 – 2.4j) and (8.4-2.3j). When using a θ_i of 0°, the two obtained solutions are (24.3 – 2.6j) and (8.6-2.4j). This means that the angle of

incidence did not significantly affect the solutions at this frequency. All possible solutions, using θ_i of 0°, for the real and imaginary parts of the complex dielectric constant for slab M2S1 are shown in Figures 4.16 and 4.17, respectively. The chosen solution is shown in Figure 4.18. No significant differences are found between the solutions when using an angle of incidence of 15.3° with those obtained using a 0° angle of incidence. All MATLAB functions used for the case of 0° angle of incidence are presented in Appendix B.

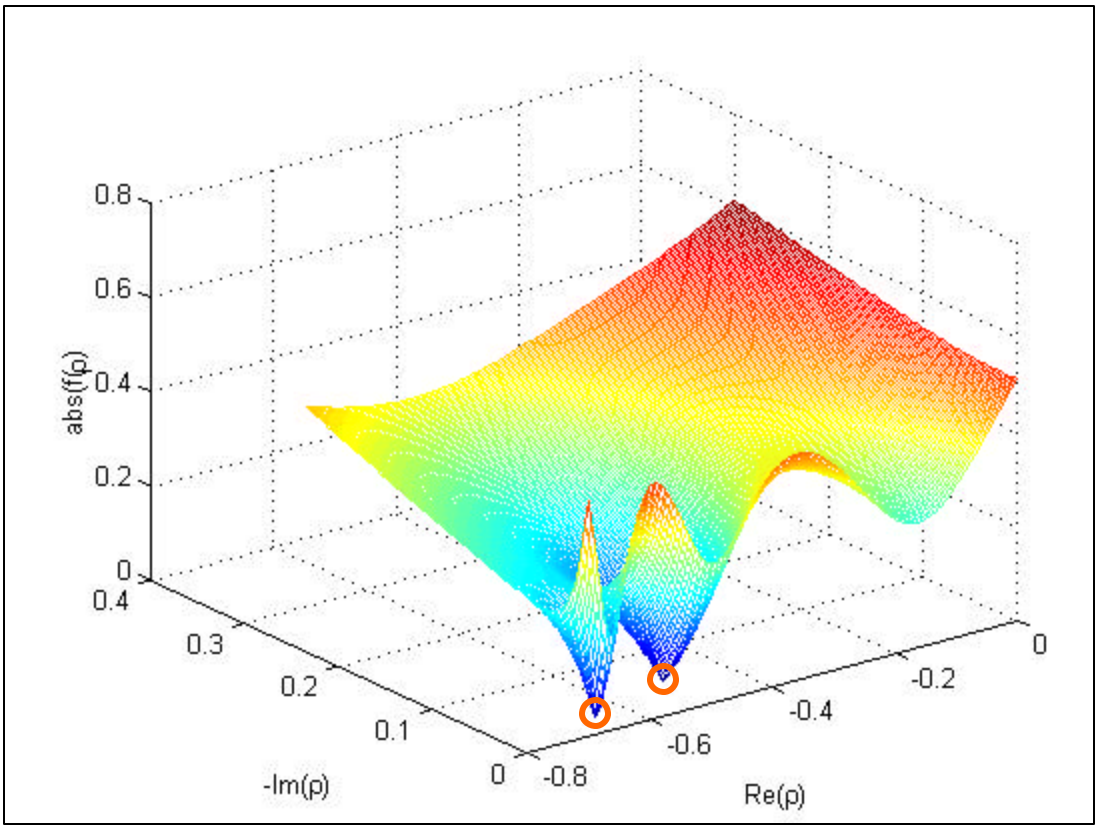

Figure 4.15 Multiple solutions for ε_r at 0.5 GHz using an angle of incidence = 0° (slab M2S1)

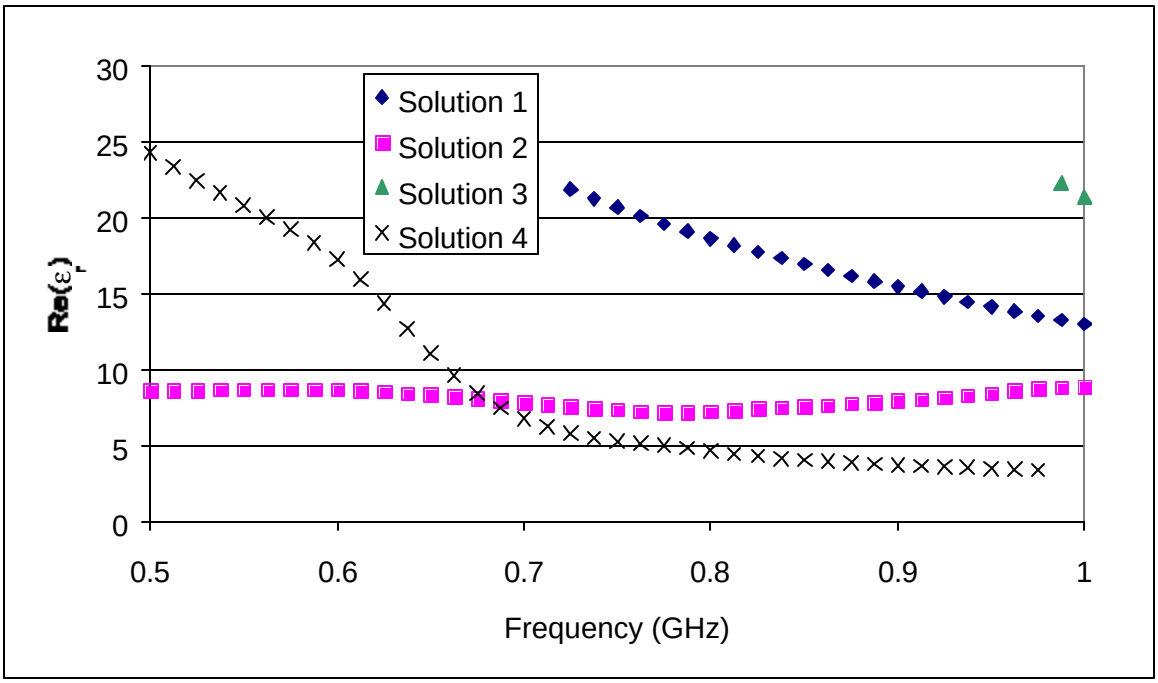

Figure 4.16 Solutions for the real part of ε_r from 0.5 to 1 GHz using an angle of incidence = 0° (slab M2S1)

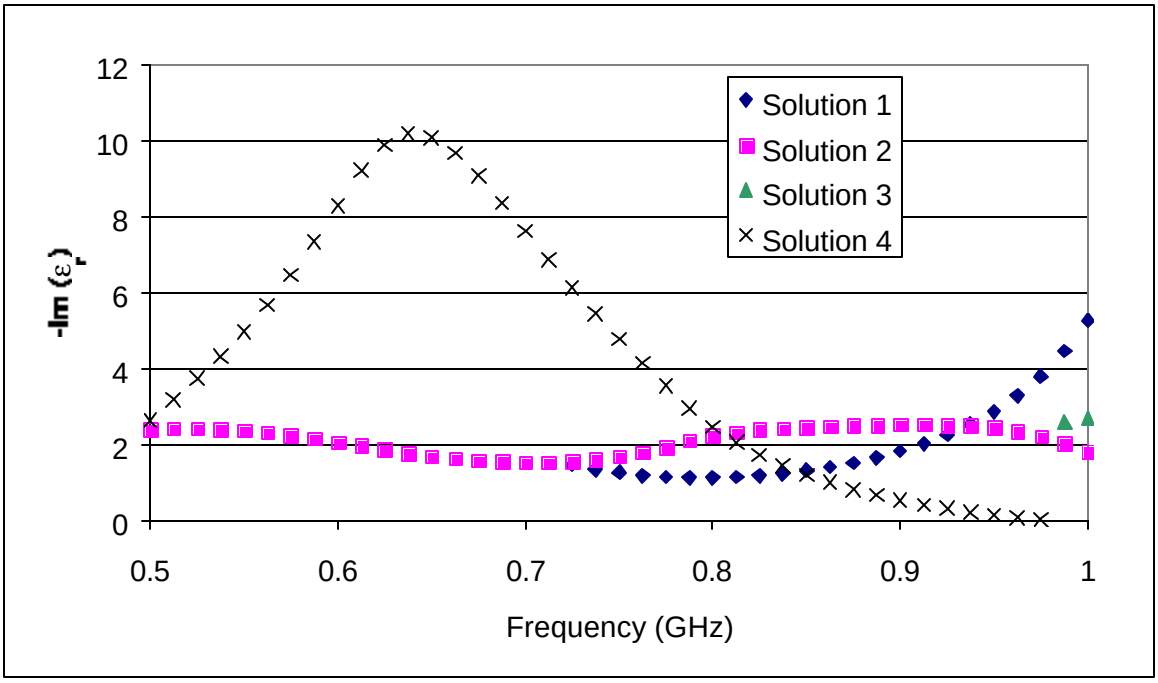

Figure 4.17 Solutions for the imaginary part of ε_r from 0.5 to 1 GHz using an angle of incidence = 0° (slab M2S1)

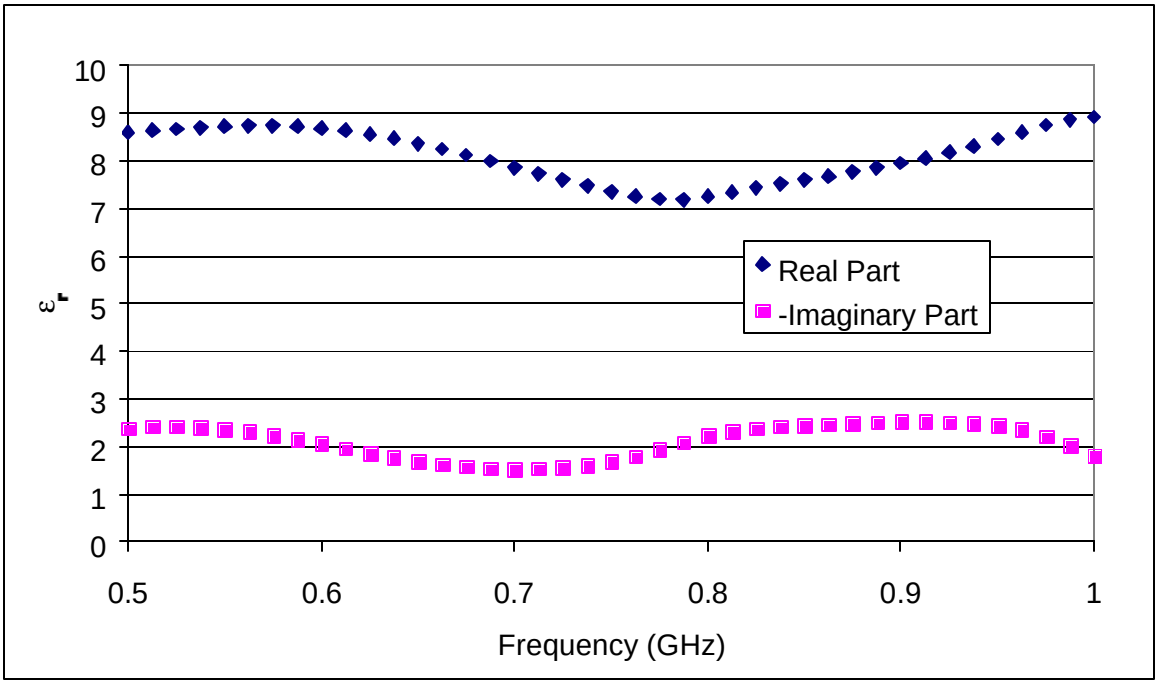

Figure 4.18 Chosen solution for the complex ε_r from 0.5 to 1 GHz using an angle of incidence = 0° (slab M2S1)

To check the effect of other values of the angle of incidence on the computed complex dielectric constant, the method was used at three different frequencies (0.5, 0.75, and 1 GHz) and with seven different values of θ_i (0, 5, 10, 15, 20, 25, and 30°). Figure 4.19 shows the variation of the computed complex dielectric constant with respect to the angle of incidence at 0.5 GHz. At this frequency, both real and imaginary parts of the complex dielectric constant decreased with an increase in the value of the angle of incidence. The maximum value for the real part is 8.60, its minimum value is 8.02, and the average is 8.39. The standard deviation for the real part is 0.22, and the coefficient of variation is 2.6%. For the imaginary part, the minimum value is 2.11, the maximum value is 2.39, and the average is 2.29. The standard deviation for the computed imaginary part is 0.10, and the coefficient of variation is 4.5%.

Figure 4.20 shows the variation of the computed complex dielectric constant with respect to the angle of incidence at 0.75 GHz. At this frequency, the real part increases with an increase in the value of the angle of incidence, while the imaginary part decreases with an increase in the value of the angle of incidence. The maximum value for the real part is 8.09, its minimum value is 7.35, and the average is 7.64. The

standard deviation for the real part is 0.28, and the coefficient of variation is 3.7%. For the imaginary part, the minimum value is 1.35, the maximum value is 1.68, and the average is 1.59. The standard deviation for the computed imaginary part is 0.13, and the coefficient of variation is 8%.

Figure 4.21 shows the variation of the computed complex dielectric constant with respect to the angle of incidence at 1 GHz. At this frequency, the real part decreases with an increase in the value of the angle of incidence, while the imaginary part increases with an increase in the value of the angle of incidence. The maximum value for the real part is 8.91, its minimum value is 8.44, and the average is 8.80. The standard deviation for the real part is 0.17, and the coefficient of variation is 1.9%. For the imaginary part, the minimum value is 1.81, the maximum value is 2.79, and the average is 2.13. The standard deviation for the computed imaginary part is 0.36, and the coefficient of variation is 17%. Based on these results, it was concluded that the value of the angle of incidence does not significantly affect the computed complex dielectric constant. Although an increase in the imaginary part coefficient of variation was noticed, it was expected to be within the measured error range. It was decided that an angle of incidence of 15.3° would be used for all computations.

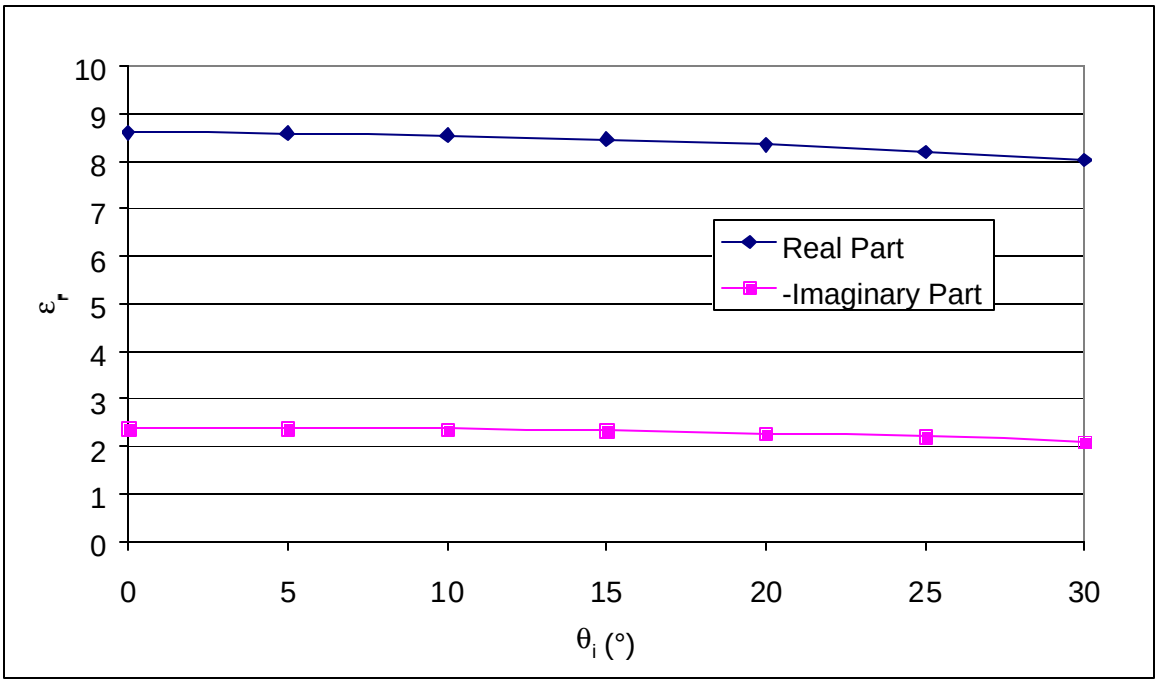

Figure 4.19 Variation of the complex dielectric constant with respect to the value of the angle of incidence at 0.5 GHz (slab M2S1)

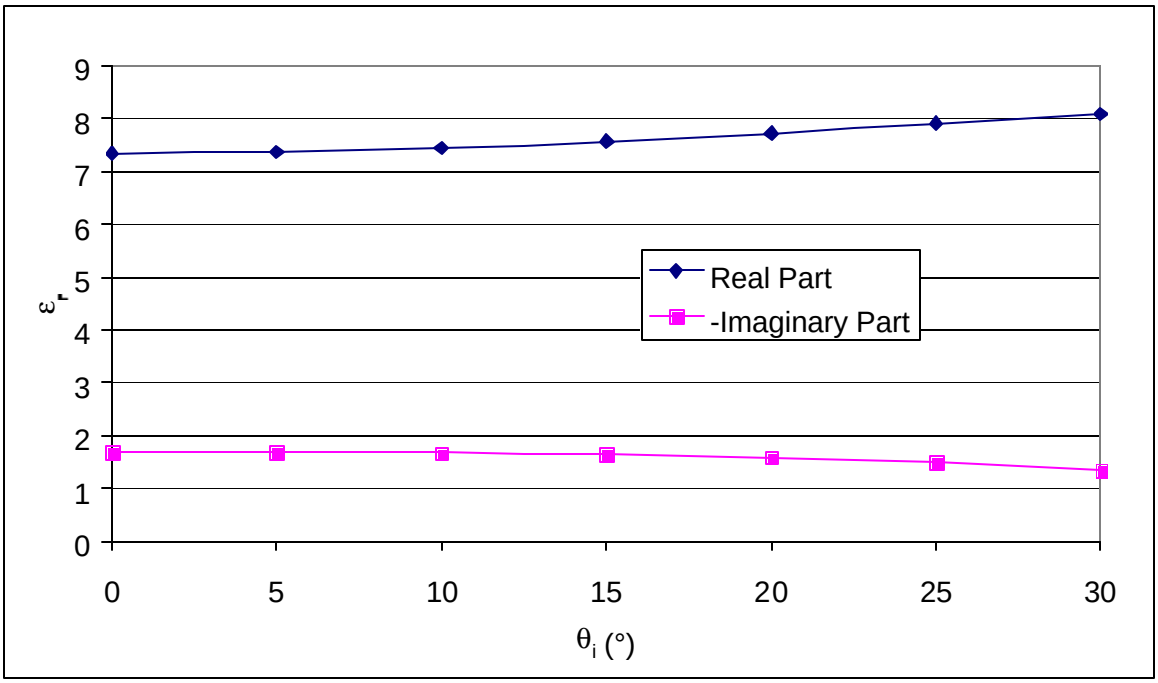

Figure 4.20 Variation of the complex dielectric constant with respect to the value of the angle of incidence at 0.75 GHz (slab M2S1)

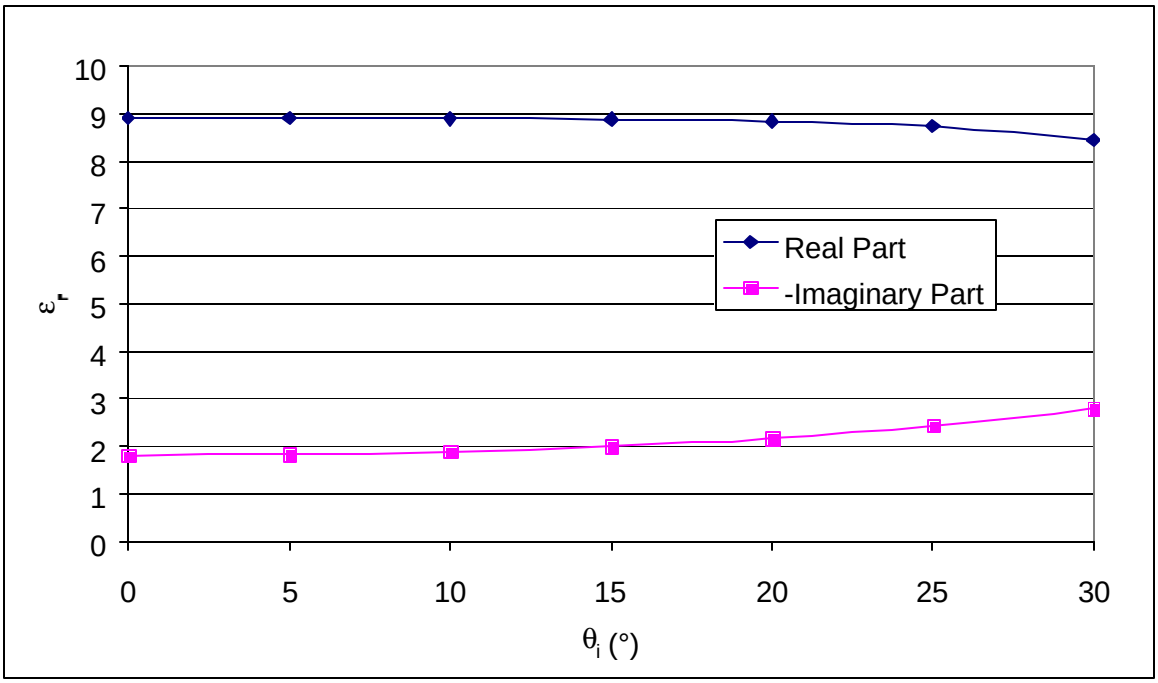

Figure 4.21 Variation of the complex dielectric constant with respect to the value of the angle of incidence at 1 GHz (slab M2S1)

4.1.3. Results

The method, described above, to determine the complex dielectric constant for concrete was used for the data taken on July 17, 2000. The 127-mm bare concrete slabs (M1S1, M2S1, M3S2, M4S1, and M5S1) were used for this purpose. Figures 4.22 to 4.26 show the chosen solution for the five concrete mixes over the frequency range of 0.5 to 1 GHz. Figures C1 to C8, in Appendix C, show all the possible solutions for the real and imaginary parts of the complex dielectric constant for all the mixes. The method was also used on the data taken on November 5, 2000. All possible solutions, as well as the chosen solutions, for all mixes are presented in Appendix C (Figures C9 to C23). Over the frequency range of 0.5 GHz to 1 GHz, the complex dielectric constant did not show any significant correlation with frequency for all the mixes.

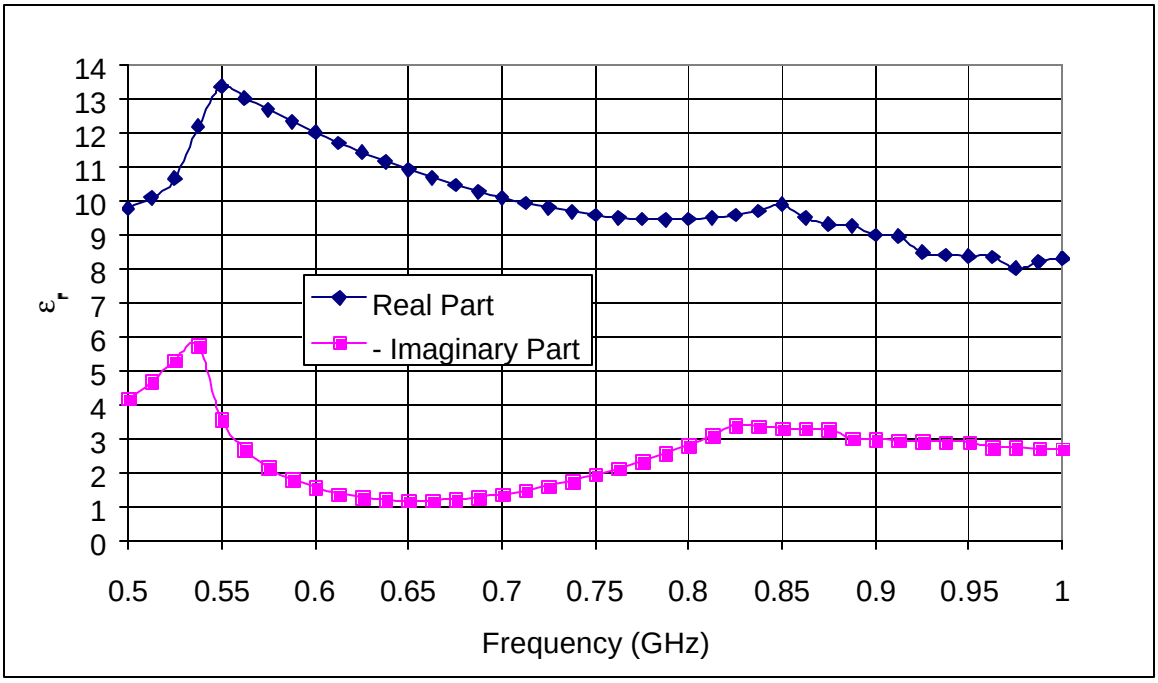

Figure 4.22 Complex dielectric constant for concrete mix M1

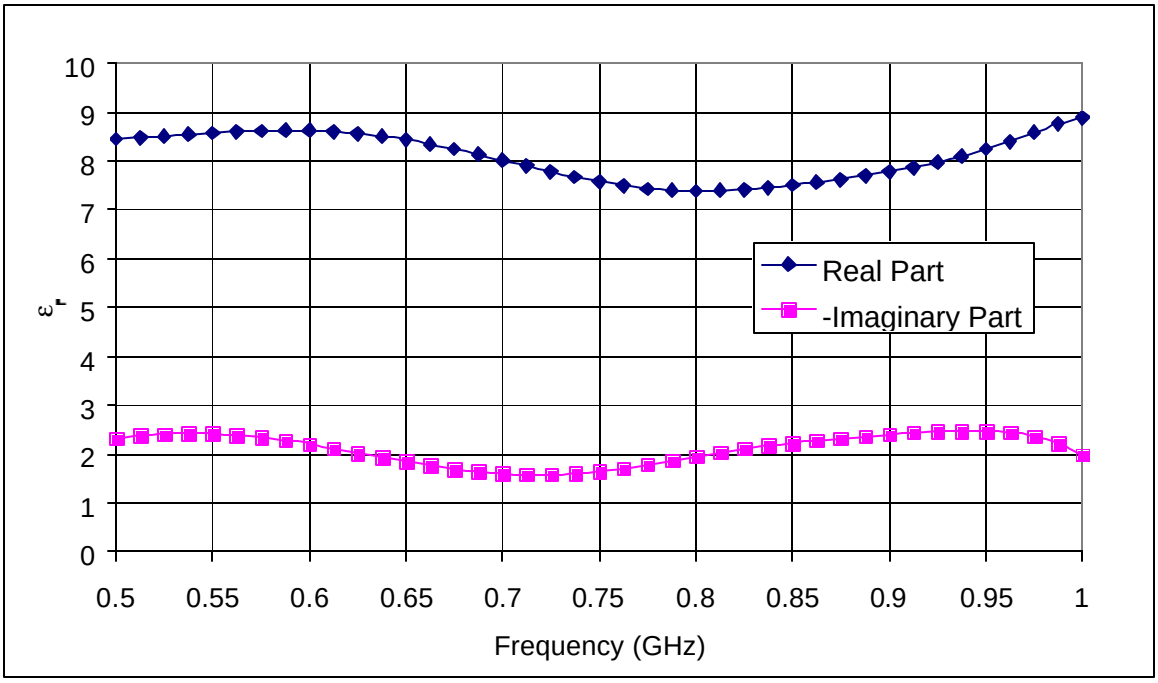

Figure 4.23 Complex dielectric constant for concrete mix M2

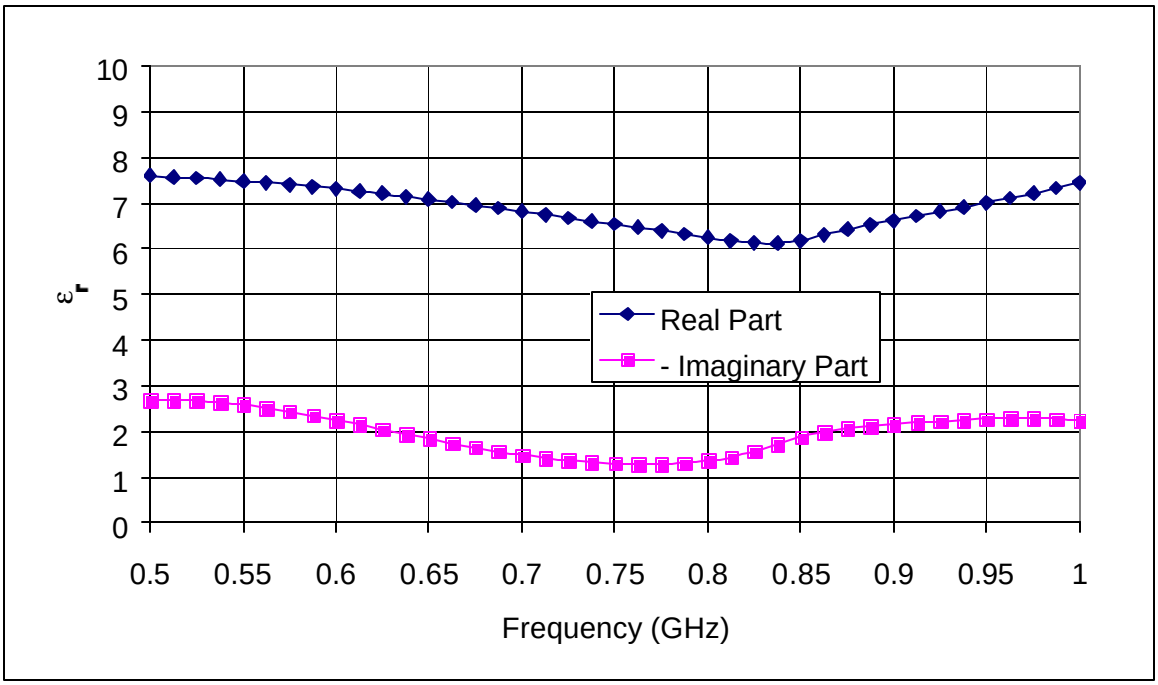

Figure 4.24 Complex dielectric constant for concrete mix M3

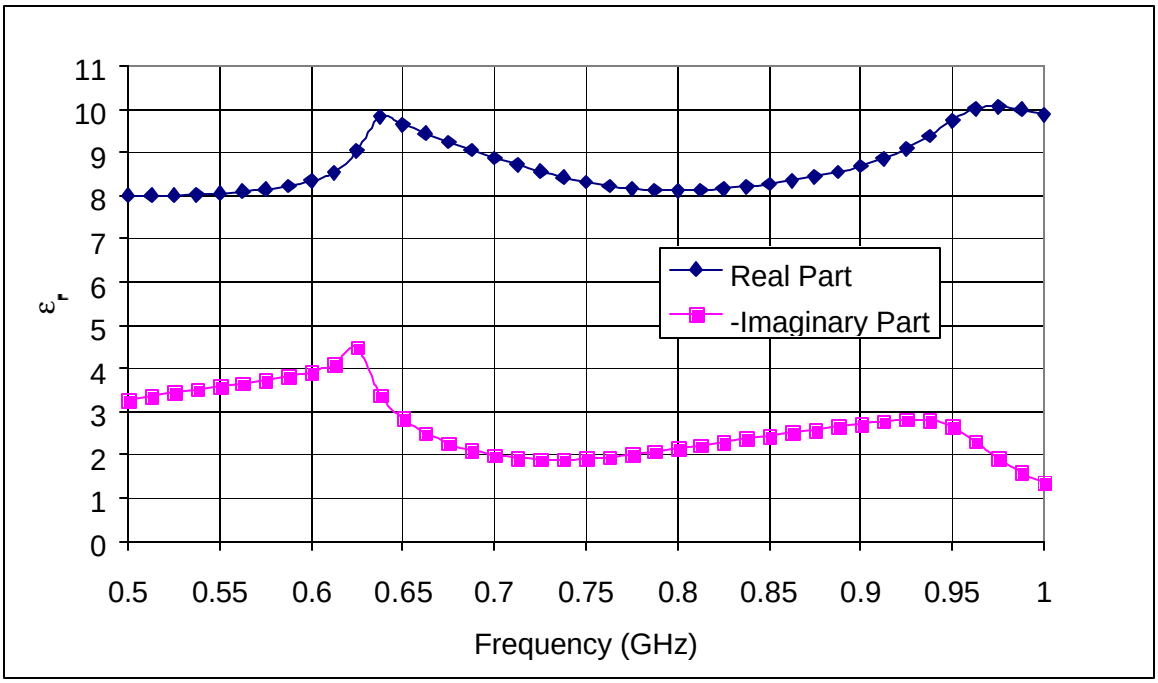

Figure 4.25 Complex dielectric constant for concrete mix M4

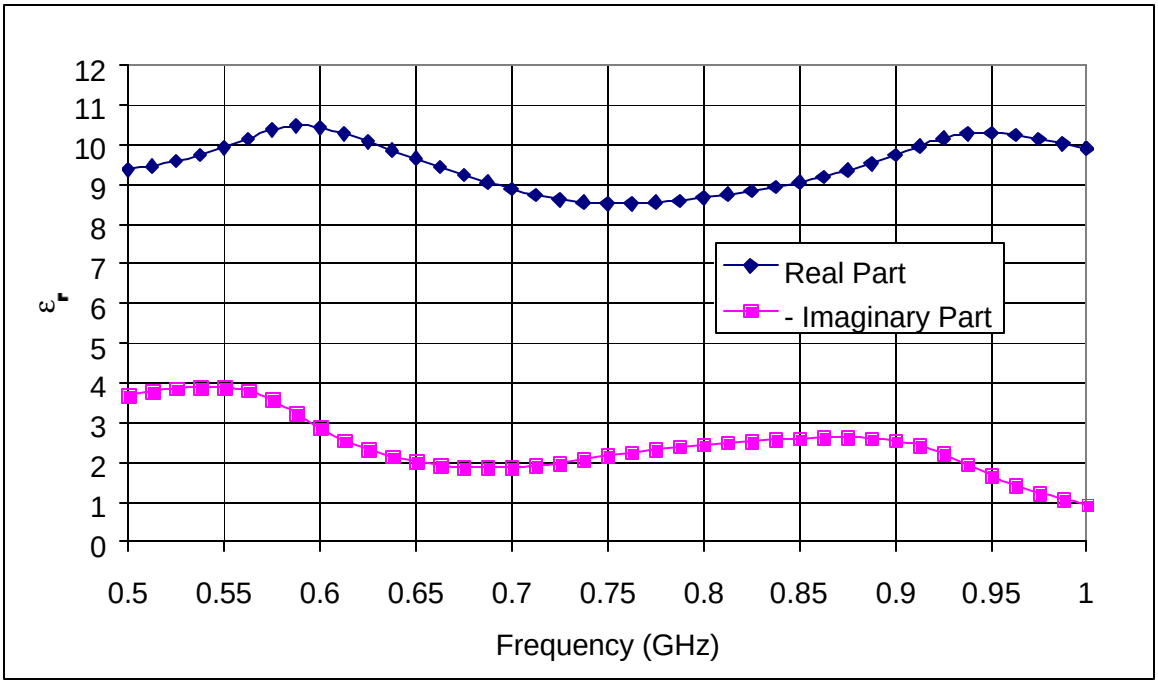

Figure 4.26 Complex dielectric constant for concrete mix M5

A statistical analysis was carried out to study the frequency dependency as well as the mix dependency of the complex dielectric constant. A two-factor ANOVA (ANalysis Of Variance) that does not include more than one sampling per group was used. The chosen level of significance was 0.05. The level of significance, known as α in statistics, represents the researcher's risk strategy and is defined as the type-I error, which is the probability to reject the null hypothesis, that is in fact true (Ott, 1993). Tables 4.1 and 4.2 show the frequency and concrete mix effects on the real part and the imaginary part of the dielectric constant, respectively. These tables present the average and variance of the complex dielectric constant at each frequency for all the mixes, as well as the average and variance of the complex dielectric constant for each mix over the entire frequency range (0.5 to 1 GHz).

Tables 4.3 and 4.4 present the ANOVA results for the real part and the imaginary part of the complex dielectric constant, respectively. The presented p-value represents the probability calculated under the null hypothesis (average means are equal). Therefore a p-value smaller than the Type-I error level (α) implies rejection of the null hypothesis (Ott, 1993). For the real part of the complex dielectric constant, the p-value for frequency as a source of variation was found to be 7.72E-05, while the p value for concrete mix as a source of variation was found to be 4.27E-48. These two p-values are smaller than the chosen α of 0.05, and therefore, both frequency and concrete mix significantly affect the real part of the complex dielectric constant. For the imaginary part of the complex dielectric constant, the p-value for frequency as a source of variation was found to be 1.37E-11, while the p value for concrete mix as a source of variation was found to be 1.16E-08. These two p-values are also smaller than the chosen α of 0.05, and therefore, both frequency and concrete mix significantly affect the imaginary part of the complex dielectric constant. The same conclusion was obtained on the data taken on November 05, 2000 as shown in Tables C1 to C4 in Appendix C.

Table 4.1 Frequency and concrete mix effects on the real part of the dielectric constant

Frequency (GHz)	Count	Average	Variance	Coef. of Var.
0.5	5	8.639527	0.837369	10.6
0.5125	5	8.720986	1.078522	11.9
0.525	5	8.859643	1.576191	14.2
0.5375	5	9.200196	3.465206	20.2
0.55	5	9.478419	5.548762	24.9
0.5625	5	9.460608	4.975634	23.6
0.575	5	9.442036	4.467174	22.4
0.5875	5	9.404204	3.991621	21.2
0.6	5	9.341825	3.497576	20.0
0.6125	5	9.275787	3.003938	18.7
0.625	5	9.261839	2.536226	17.2
0.6375	5	9.298316	2.336068	16.4
0.65	5	9.143413	2.099902	15.8
0.6625	5	8.984715	1.895741	15.3
0.675	5	8.828757	1.725104	14.9
0.6875	5	8.678724	1.585308	14.5
0.7	5	8.537004	1.473452	14.2
0.7125	5	8.405924	1.387465	14.0
0.725	5	8.288094	1.326477	13.9
0.7375	5	8.186394	1.290895	13.9
0.75	5	8.103404	1.281967	14.0
0.7625	5	8.040607	1.300534	14.2
0.775	5	7.998314	1.345779	14.5
0.7875	5	7.976195	1.415627	14.9
0.8	5	7.973433	1.508789	15.4
0.8125	5	7.989165	1.62553	16.0
0.825	5	8.024412	1.763653	16.5
0.8375	5	8.085447	1.907582	17.1
0.85	5	8.182488	2.038892	17.5
0.8625	5	8.178621	1.674392	15.8
0.875	5	8.224085	1.522183	15.0
0.8875	5	8.310458	1.505232	14.8
0.9	5	8.36387	1.446164	14.4
0.9125	5	8.469723	1.511676	14.5
0.925	5	8.498308	1.557285	14.7
0.9375	5	8.608705	1.642456	14.9
0.95	5	8.724855	1.70294	15.0
0.9625	5	8.821043	1.694061	14.8
0.975	5	8.800742	1.65095	14.6
0.9875	5	8.861554	1.358505	13.2
1	5	8.884142	1.100173	11.8
Concrete Mix	**Count**	**Average**	**Variance**	**Coef. of Var.**
M1	41	10.06216	1.901935	13.7
M2	41	8.087789	0.22722	5.9
M3	41	6.892346	0.213666	6.7
M4	41	9.487612	0.418014	6.8
M5	41	8.708632	0.44093	7.6

Table 4.2 Frequency and concrete mix effects on the imaginary part of the dielectric constant

Frequency (GHz)	Count	Sum	Variance	Coef. of Var.
0.5	5	3.230743	0.560394	23.2
0.5125	5	3.377883	0.822824	26.9
0.525	5	3.54035	1.310425	32.3
0.5375	5	3.648197	1.755334	36.3
0.55	5	3.210244	0.440958	20.7
0.5625	5	3.013947	0.451043	22.3
0.575	5	2.851477	0.560659	26.3
0.5875	5	2.694289	0.663634	30.2
0.6	5	2.558166	0.802486	35.0
0.6125	5	2.458477	1.013262	40.9
0.625	5	2.429467	1.47661	50.0
0.6375	5	2.121464	0.629161	37.4
0.65	5	1.944278	0.358791	30.8
0.6625	5	1.824923	0.226775	26.1
0.675	5	1.743296	0.148619	22.1
0.6875	5	1.691888	0.099799	18.7
0.7	5	1.66696	0.07122	16.0
0.7125	5	1.666316	0.059343	14.6
0.725	5	1.688265	0.062733	14.8
0.7375	5	1.730797	0.080191	16.4
0.75	5	1.791055	0.109478	18.5
0.7625	5	1.865624	0.147348	20.6
0.775	5	1.951424	0.191205	22.4
0.7875	5	2.046121	0.240568	24.0
0.8	5	2.148344	0.29718	25.4
0.8125	5	2.258653	0.365008	26.7
0.825	5	2.380483	0.452417	28.3
0.8375	5	2.438988	0.365684	24.8
0.85	5	2.490672	0.277301	21.1
0.8625	5	2.540659	0.236075	19.1
0.875	5	2.575745	0.204638	17.6
0.8875	5	2.548922	0.108807	12.9
0.9	5	2.564674	0.098063	12.2
0.9125	5	2.559139	0.091608	11.8
0.925	5	2.527341	0.103476	12.7
0.9375	5	2.478711	0.154285	15.8
0.95	5	2.39739	0.215393	19.4
0.9625	5	2.247292	0.242352	21.9
0.975	5	2.107388	0.32266	27.0
0.9875	5	1.978836	0.413936	32.5
1	5	1.852274	0.487109	37.7
Concrete Mix	Count	Average	Variance	Coef. Of Var.
M1	41	2.598222	1.223874	42.6
M2	41	2.105951	0.094127	14.6
M3	41	1.974338	0.205428	23.0
M4	41	2.452064	0.586276	31.2
M5	41	2.679323	0.570678	28.2

Table 4.3 ANOVA table for the real part of the dielectric constant

Source of Variation	SS	df	MS	F	P-value	F crit
Frequency	47.7479	40	1.193698	2.377803	**7.72E-05**	1.47018
Concrete Mix	250.2893	4	62.57232	124.6418	**4.27E-48**	2.428166
Error	80.32273	160	0.502017			
Total	378.3599	204				

Table 4.4 ANOVA table for the imaginary part of the dielectric constant

Source of Variation	SS	df	MS	F	P-value	F crit
Frequency	55.93835	40	1.398459	4.363622	**1.37E-11**	1.47018
Concrete Mix	15.59842	4	3.899604	12.16797	**1.16E-08**	2.428166
Error	51.27699	160	0.320481			
Total	122.8138	204				

Figure 4.27 shows the average real and imaginary parts of the complex dielectric constant over the frequency range 0.5 to 1 GHz for the data taken on July 17, 2000. Figure C24 in Appendix C shows the same graph for the data taken on November 5, 2000. Both figures show that, on average, the real part of the dielectric constant for mix M1 is the highest, followed by mixes M4, M5, M2, then M3. This could be explained by using the simple complex refractive index method, which states that the effective complex-refractive index (CRI) for a mixture is given by the volume average of the complex refractive indexes of the constituents (Feng and Sen, 1985). Since the magnetic permeability of all concrete constituents is assumed to be equal to 1, the CRI method is simplified as shown in Equation (4.17):

$$\sqrt{\varepsilon_r} = \sum_{i=1}^{n} \left(\frac{V_i}{V_t}\right)\sqrt{(\varepsilon_r)_i} \tag{4.17}$$

where ε_r is the complex dielectric constant for the material, $(\varepsilon_r)_i$ is the complex dielectric constant for constituent i, V_i is the volume of constituent i, V_t is the total volume, and n is the number of constituents in the material. As shown in Table A1, mix M1 has almost 70% by volume limestone aggregate. Since limestone has a much higher real part of the complex dielectric constant than quartzite aggregate (Al-Qadi and Riad, 1996), mix M1 has the highest real part of all mixes. On the other hand, mixes M4 and M2 have the same amount of limestone coarse aggregate and quartzite fine aggregate

(approximately 39% limestone and 27% quartzite by volume). However, mix M4 has a higher real part of the dielectric constant than mix M2. This is mainly attributed to the presence of silica fume in mix M4. Silica fume particles react with the calcium hydroxide of the concrete to form a large number of small crystals and therefore improve the microstructure of hydrated cement paste in the transition zone (Mehta and Monteiro, 1993). This results in increased strength (as shown in Table A5) and reduced permeability, which translates into a higher real part of the dielectric constant. Although mix M2 has limestone coarse aggregate, the use of only type I Portland cement as the cementitious material reduced its real part of the complex dielectric constant when compared to mix M5. Mix M5 has only quartzite aggregate, but fly ash was added as part of the cementitious material. Fly ash, like silica fume, reacts with calcium hydroxide, but at a significantly slower rate, to improve the microstructure of the hydrated cement paste, therefore increasing its strength and reducing its permeability, which increases the real part of the dielectric constant. For the imaginary part of the complex dielectric constant, the mixes did not show the same trend when tested at different times. This is because the value of the imaginary part is highly dependent on the amount of water present in the mix during testing. Even though all tests were performed when the slabs were dry (expected moisture content less than 2%), a small difference in the amount of water could significantly alter the imaginary part value of the dielectric constant.

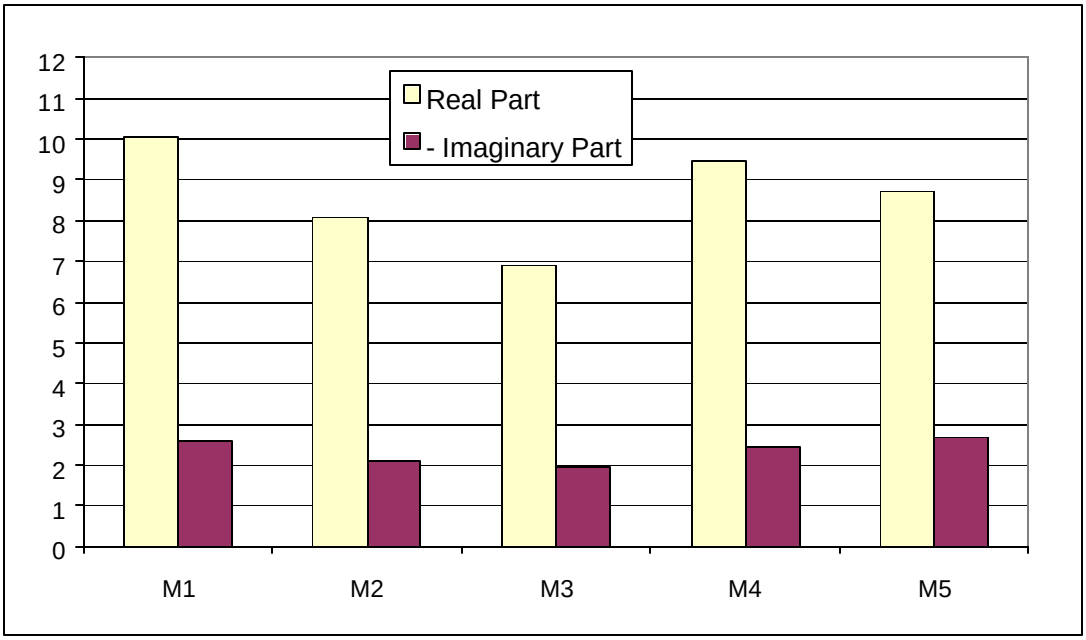

Figure 4.27 Average complex dielectric constant for all concrete mixes over the frequency range 0.5 to 1 GHz

A statistical analysis was performed to investigate whether the complex dielectric constant is affected by the testing date. A paired t-test was used for this analysis. As shown in Tables 4.5 and 4.6, the p-values for the real part and the imaginary part analyses were smaller than the α-value of 0.05. This means that the null hypothesis that the difference between the means of the real and imaginary parts of the complex dielectric constant are equal during the two testing dates could be rejected. Therefore, the testing date, meaning the microstructure state of concrete during the testing, affects the complex dielectric constant of concrete.

Table 4.5 Paired t-test for the real part of the dielectric constant

	Variable 1	*Variable 2*
Mean	8.647706933	8.188539
Variance	1.526154132	1.975172
Observations	5	5
Pearson Correlation	0.988040114	
Hypothesized Mean Difference	0	
df	4	
t Stat	3.86851722	
P(T<=t) one-tail	0.009008093	
t Critical one-tail	2.131846486	
P(T<=t) two-tail	**0.018016186**	
t Critical two-tail	2.776450856	

Table 4.6 Paired t-test for the imaginary part of the dielectric constant

	07/17/2000	11/05/2000
Mean	2.361979578	1.642262419
Variance	0.095112299	0.072142666
Observations	5	5
Pearson Correlation	0.855426735	
Hypothesized Mean Difference	0	
df	4	
t Stat	10.07090309	
P(T<=t) one-tail	0.000273418	
t Critical one-tail	2.131846486	
P(T<=t) two-tail	**0.000546836**	
t Critical two-tail	2.776450856	

The real part of the dielectric constant was also calculated using the measured two-way travel time, obtained from the time domain signals (shown in Figure 4.28), and Equation (4.18) given below:

$$\varepsilon_r = \left(\frac{ct}{2d}\right)^2 \tag{4.18}$$

where ε_r is the real dielectric constant, c is the speed of light ($3x10^8$ m/s), and d is the concrete slab thickness (0.127 m). Figure 4.29 shows the computed real part of the dielectric constant as obtained with Equation (4.18) and the average real part of the dielectric constant over the frequency range of 0.5 to 1 GHz for the data taken on July 17, 2000. Figure C25 (Appendix C) shows the same graph for the data taken on November 5, 2000. Both figures show that the time domain real part of the complex dielectric constant and the average real part over the frequency range are approximately equal. A paired t-test was performed on both sets of data to validate this conclusion. Table 4.7 and Table C5 (Appendix C) show the results for the data taken on July 17, 2000 and on November 5, 2000, respectively. The p-values for both tests were significantly higher the α-value of 0.05 (0.77 and 0.81). This means that there is not enough evidence to reject the null hypothesis, and, therefore the real part of the dielectric constant as obtained from the time domain signal is equal to the average real part of the complex dielectric constant over the frequency range of 0.5 to 1 GHz.

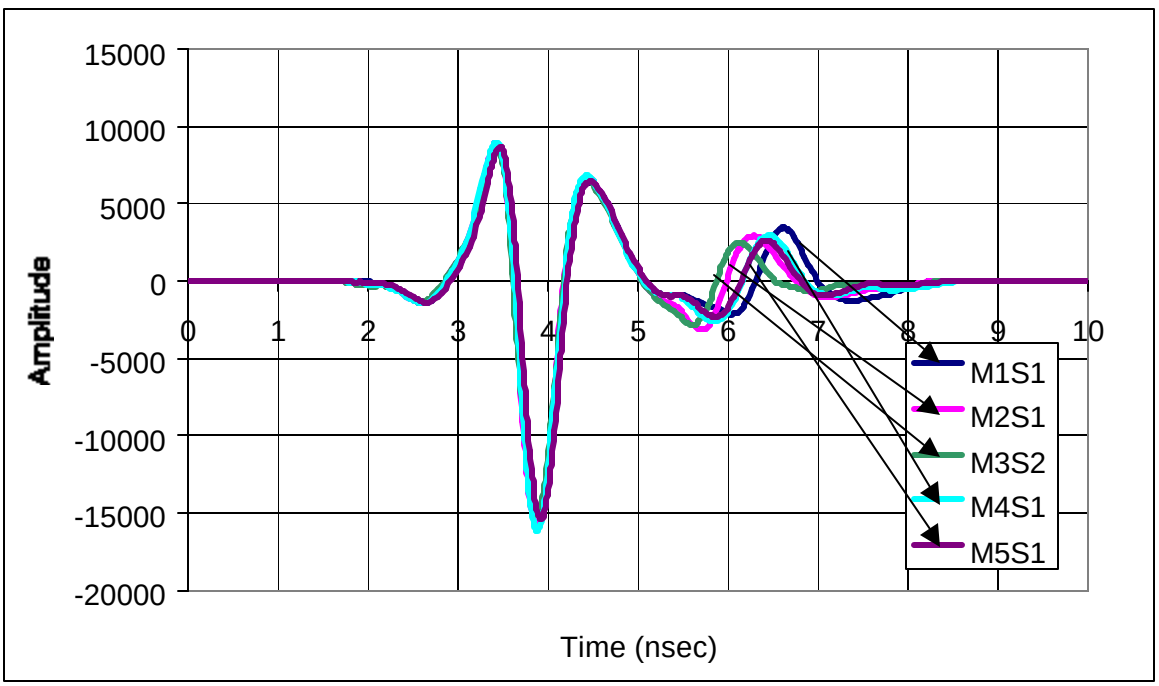

Figure 4.28 Time domain signals

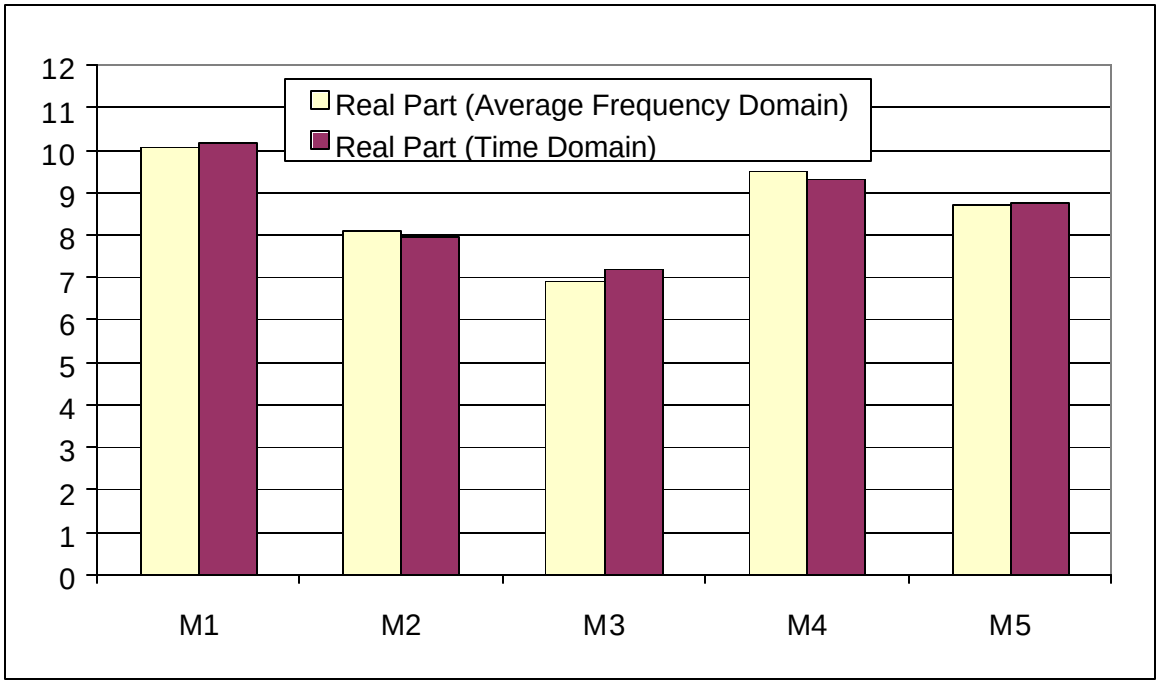

Figure 4.29. Comparison between the real parts of the complex dielectric constant as obtained by averaging the frequency domain solutions and by using the time domain signals

Table 4.7 Paired t-test for the average real part of the complex dielectric constant over the frequency range 0.5 to 1 GHz and the time domain real part of the complex dielectric constant (7/17/00)

	Average over frequency range	Time domain
Mean	8.647707	8.67514
Variance	1.526154	1.346727
Observations	5	5
Pearson Correlation	0.988952	
Hypothesized Mean Difference	0	
df	4	
t Stat	-0.31768	
P(T<=t) one-tail	0.383311	
t Critical one-tail	2.131846	
P(T<=t) two-tail	**0.766622**	
t Critical two-tail	2.776451	

4.2. Synthesis of Reflected Air-Coupled Radar Signals

A method to predict the radar signal was developed based on measurements performed on the bare 127-mm concrete slabs (M1S1, M2S1, M3S2, M4S1, and M5S1). The incident frequency spectrum, F_i, is first calculated by taking the FFT of the waveform obtained from the copper plate reflection. Zero padding is used to obtain the same frequency step as used for the case when solving for the complex dielectric constant. Originally the incident time domain waveform is 20 nesc long and consists of 512 points. With zero padding, the incident waveform is 80 nsec long and consists of 2048 points. The reflected frequency spectrum is then synthesized using Equation (4.19):

$$F_{r,syn} = [\rho_1 + \rho_2 * (1+\rho_1) * (1+\rho_2) * T^2] * F_i \tag{4.19}$$

where $F_{r,syn}$ is the synthesized frequency spectrum; ρ_1, T, and ρ_2 were previously defined by Equations (4.2), (4.4), and (4.5), respectively.

For a continuous signal, the Inverse Fourier Transform (IFT) is defined by Equation (4.20):

$$x(t) = \frac{1}{2\pi} \int_{-\infty}^{+\infty} X(\omega)\, e^{j\omega t}\, d\omega \tag{4.20}$$

where x(t) is the time domain signal, ω is the angular frequency, and $X(\omega)$ is the frequency spectrum of the signal. Equation (4.20) could be decomposed into two parts as shown by Equation (4.21):

$$x(t) = \frac{1}{2\pi} \int_{-\infty}^{0} X(\omega)\, e^{j\omega t}\, d\omega + \frac{1}{2\pi} \int_{0}^{+\infty} X(\omega)\, e^{j\omega t}\, d\omega \tag{4.21}$$

When x is real, then $X(\omega) = X^*(-\omega)$, where * denotes the conjugate of the complex number (Proakis and Manolakis, 1996). Therefore, Equation (4.21) could be written as follows:

$$x(t) = \frac{1}{2\pi}\int_{-\infty}^{0} X^*(-\omega)\, e^{j\omega t}\, d\omega + \frac{1}{2\pi}\int_{0}^{+\infty} X(\omega)\, e^{j\omega t}\, d\omega \tag{4.22}$$

Equation (4.22) is then simplified to as follows:

$$x(t) = \frac{1}{2\pi}\int_{0}^{+\infty} X^*(\omega)\, e^{-j\omega t}\, d\omega + \frac{1}{2\pi}\int_{0}^{+\infty} X(\omega)\, e^{j\omega t}\, d\omega \tag{4.23}$$

$$x(t) = \frac{1}{2\pi}\int_{0}^{+\infty} [X^*(\omega)\, e^{-j\omega t} + X(\omega)\, e^{j\omega t}]\, d\omega \tag{4.24}$$

$$x(t) = \frac{1}{2\pi}\int_{0}^{+\infty} 2\,\mathrm{Re}(X(\omega)\, e^{j\omega t})\, d\omega \tag{4.25}$$

$$x(t) = \frac{1}{2\pi} 2\,\mathrm{Re}[\int_{0}^{+\infty} X(\omega)\, e^{j\omega t}\, d\omega] \tag{4.26}$$

For the discrete form of the IFT, the integration in all the above equations is substituted with the summation. Therefore, only the positive frequencies (the first 1024 points of the synthesized frequency spectrum, $F_{r,syn}$,) are used to obtain the time domain waveform. This is achieved by using the real part of the Inverse Fast Fourier Transform (IFFT) of the synthesized frequency spectrum, as shown in Equation (4.27). All computations are performed using a MATLAB procedure, presented in Appendix B.

$$Y_{r,syn}=2*\mathrm{real}(\mathrm{IFFT}(F_{r,syn})) \tag{4.27}$$

Figure 4.30 shows the modeled and measured time domain waveforms for slab M1S1 for the data taken on November 5, 2000, while Figure 4.31 shows the synthesized and measured frequency spectrums for the same data. In both figures, the synthesized waveform and frequency spectrums were obtained using the complex dielectric constant values calculated for this slab over the frequency range 0.5 to 1 GHz; the value of ε_r for the frequency range 0 to 0.5 GHz was set constant and equal to the calculated complex

dielectric constant at 0.5 GHz, while the value of ε_r for the frequency range 1 to 3 GHz was set constant and equal to the calculated value of ε_r at 1 GHz. Values of ε_r at higher frequencies (more than 3 GHz) did not affect the synthesized waveform because the incident frequency spectrum is approximately equal to zero after 3 GHz. Therefore, $F_{r,syn}$ was set equal to zero after this frequency. The modeled waveform approximately maps the measured one. The root mean square error (RMSE) between the synthesized and the measured waveforms was found to be equal to 240.8, which is very low compared to the maximum signal amplitude of approximately 15000. The synthesized frequency spectrum exactly maps the measured one in the frequency range of 0.5 to 1 GHz, which is expected since the dielectric constant solution in that range was obtained using the inverse problem.

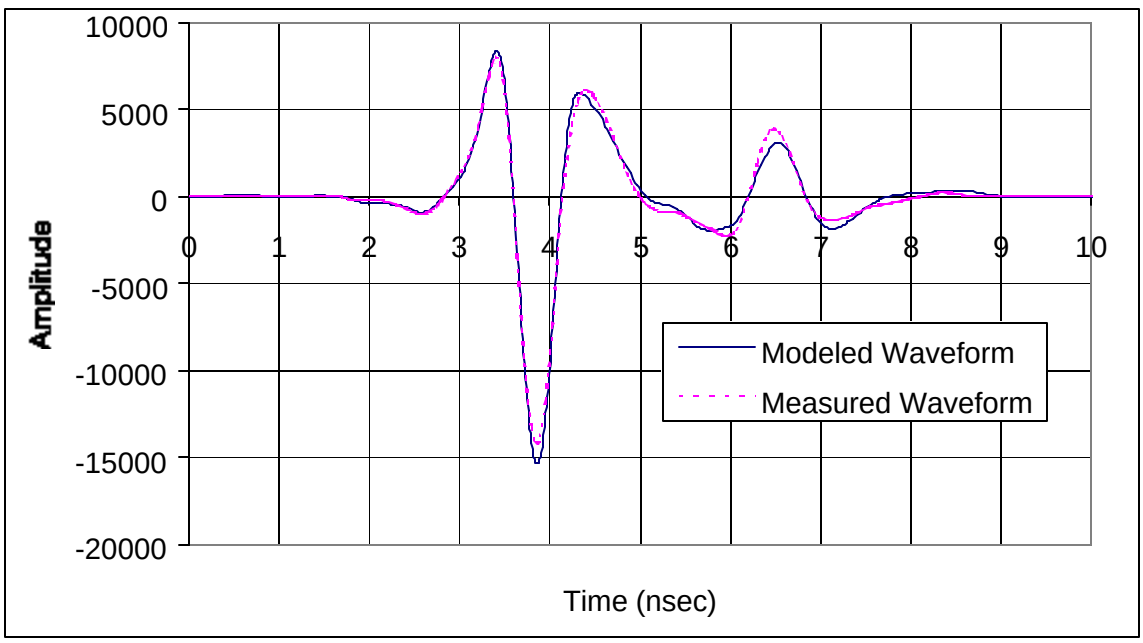

Figure 4.30 Modeled (with calculated solution for ε_r) and measured waveforms for slab M1S1

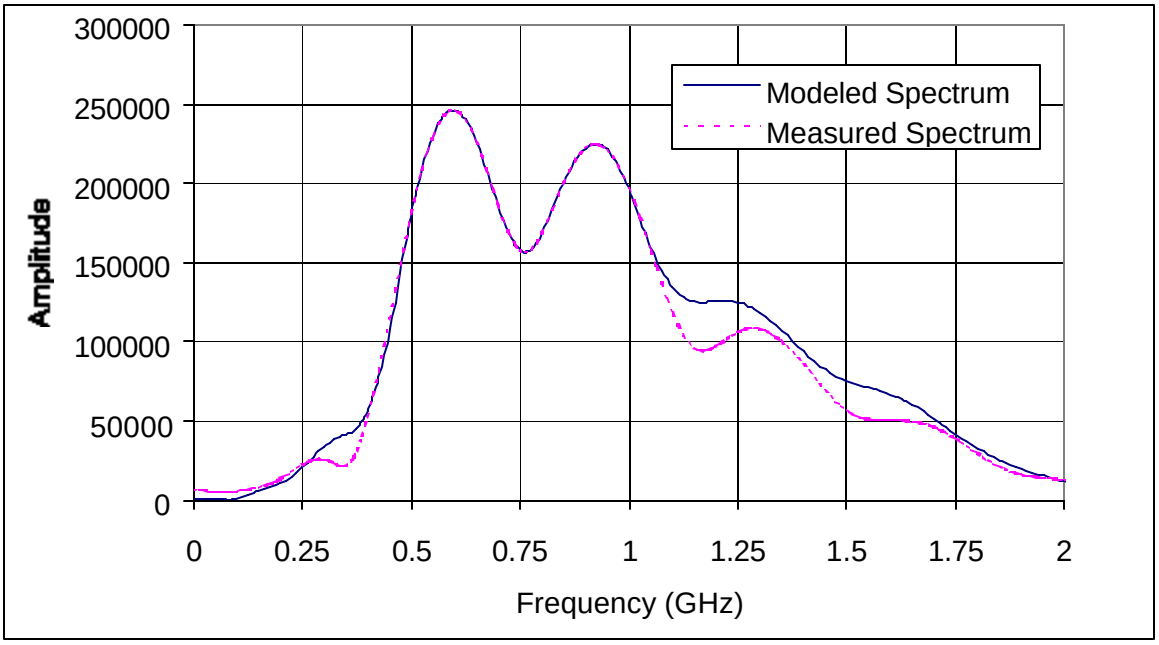

Figure 4.31 Modeled (with calculated solution for ε_r) and measured frequency spectrums for slab M1S1

Figures 4.32 and 4.33 show the synthesized waveforms and frequency spectrum for slab M1S1 when the dielectric constant is assumed not to vary over the entire frequency range, and therefore, the average calculated complex dielectric constant was used. The modeled waveform also approximately maps the measured one, with an RMSE between the synthesized and the measured waveforms of 325.7, which is still very low.

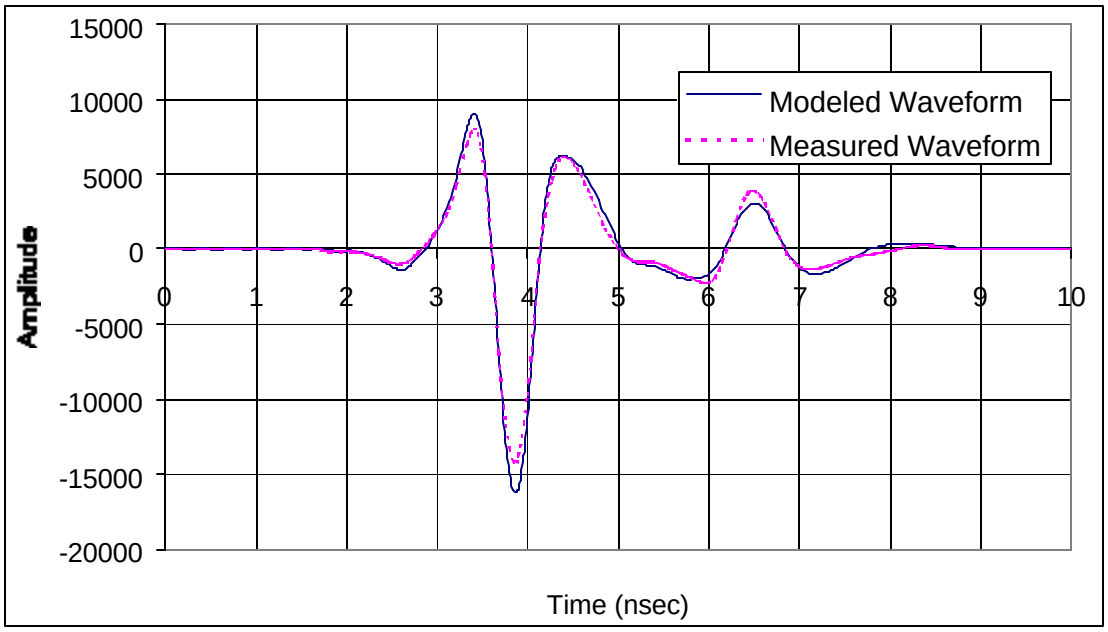

Figure 4.32 Modeled (with average ε_r) and measured waveforms for slab M1S1

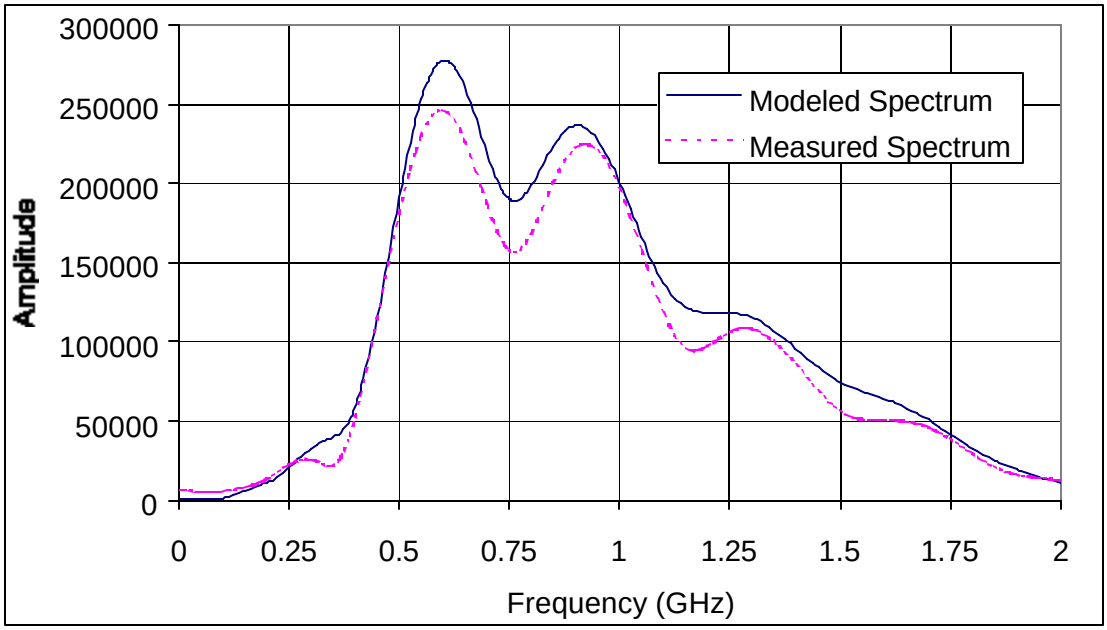

Figure 4.33 Modeled (with average ε_r) and measured frequency spectrums for slab M1S1

Figures 4.34 and 4.35 show the synthesized waveforms and frequency spectrum for slab M1S1 when the dielectric constant is assumed to be real (no loss) and not to vary over the entire frequency range. The modeled first reflection of the waveform also approximately maps the first measured reflection. However, the amplitude of the modeled second reflection is overestimated, which is expected since the assumption of a pure dielectric material is not a valid one for concrete. On the other hand, the time when the second reflection occurs is perfectly modeled. The calculated RMSE between the synthesized and the measured waveforms was 1184.5. The synthesized waveforms and frequency spectrums for all other slabs and for the data taken on July 17, 2000 are presented in Appendix C (Figures C29 to C82). Table 4.8 presents the calculated RMSE values for all the slabs. The average RMSE values between the synthesized and measured waveforms when a constant complex dielectric constant was used were 382.0 for the data taken on July 17, 2000, and 278.0 for the data taken on November 5, 2000. Both values are very small and therefore, for this GPR system, assuming a complex dielectric constant frequency independent in the frequency range of 0 to 3 GHz is a valid assumption.

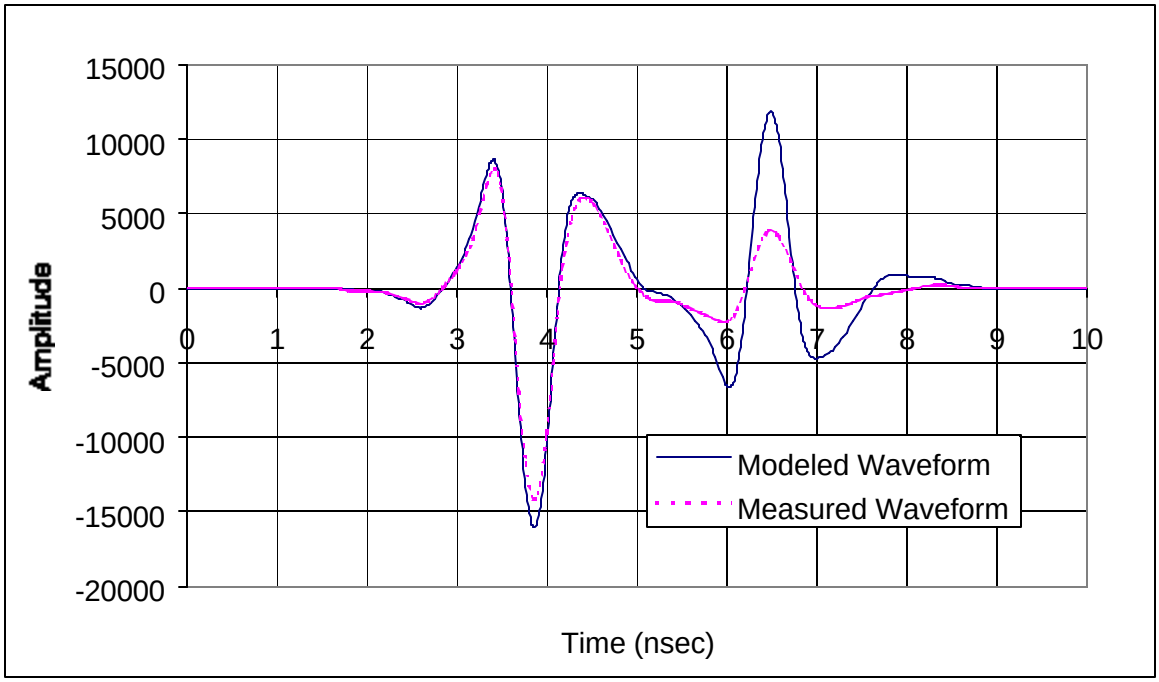

Figure 4.34 Modeled (with average real part of ε_r and zero imaginary part) and measured waveforms for slab M1S1

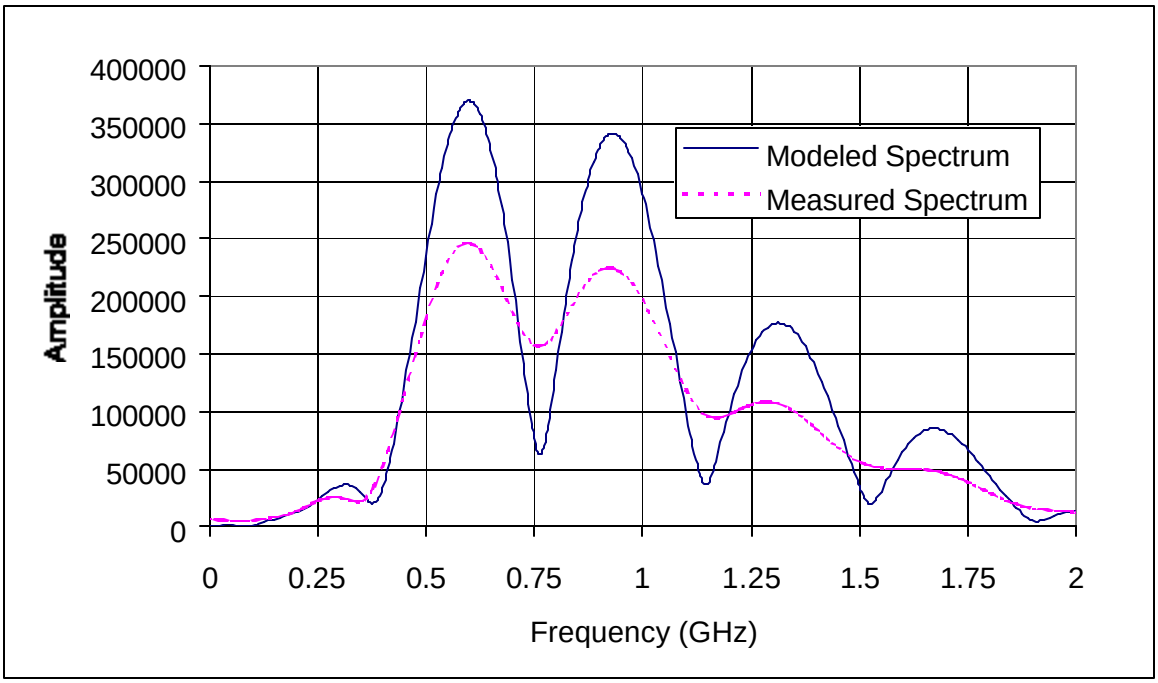

Figure 4.35 Modeled (with average real part of ε_r and zero imaginary part) and measured frequency spectrums for slab M1S1

Table 4.8 RMSE values for all synthesized waveforms for the data taken on 7/17/2000 and 11/05/2000

	7/17/00			11/5/00		
	Using Calculated Solution for ε_r	Using Average ε_r	Using Average ε_r and Zero Imaginary Part	Using Calculated Solution for ε_r	Using Average ε_r	Using Average ε_r and Zero Imaginary Part
M1	584.2	561.4	1466.7	240.8	325.7	1184.5
M2	319.4	317.1	1345.2	156.8	221.1	1067.6
M3	284.4	327.1	1325.4	150.9	202.2	1105.2
M4	429.4	352.6	1349.0	352.4	350.1	1230.8
M5	368.5	351.8	1357.1	304.7	290.7	1180.6
Average	397.2	382.0	1368.7	241.1	278.0	1153.7

4.3. Effect of Simulated Defects in Concrete on the Reflected Radar Signal

The effects of air voids and water-filled voids in concrete on the GPR signal were studied for both air-coupled and ground-coupled systems. This was achieved by comparing data from the bare concrete slabs with those that have Styrofoam embedded in them.

4.3.1. Air-coupled system

Figures 4.36 and 4.37 show the air-coupled GPR time domain waveforms and frequency spectrums, respectively, from slabs M1S1, M1S2, and M1S3 from the data taken on December 4, 1999. From the time domain signals, there was no clear reflection from the embedded Styrofoam. This is due to the fact that the air-coupled GPR system has a range resolution, as explained in Chapter 3, of approximately 43.3 mm. Since the Styrofoam is embedded at a target depth of 50 mm, its reflection is overlapped with the first reflection from the slab surface. This overlap resulted in a distortion of the first reflection. The frequency spectrum also did not show any clear relation with respect to the presence of the void and/or to its thickness. It was also expected that the time to the second reflection (reflection from the bottom of the slab) would be smaller for the slabs with embedded Styrofoam since the wave speed increases inside the Styrofoam. However, this expectation was not realized in all the data. Even though there was no visible way from either the time-domain waveform or the frequency spectrum to detect the air void located at 50 mm from the slab surface, the distorted shape of either

waveform of frequency spectrum could be used as an indication of the presence of the air-void. A similar conclusion may be drawn from the data of all other slabs as shown in Figures 4.38 to 4.45 for the data taken on December 4, 1999, or from Figures C83 to C110 in Appendix C for the data taken on May 13, 2000, July 17, 2000, and November 5, 2000. The waveforms obtained from slab M2S3 showed a very low amplitude first reflection compared to the other slabs. The reason for this was not clear until modeling of the waveform obtained from concrete with air defects was performed. The modeling, explained later in detail, showed that all Styrofoam pieces were lifted upward from their target position of 50 mm. This may have resulted from the vibration performed during the concrete consolidation to avoid segregation. The modeling has shown that the Styrofoam in slab M2S3 is only at 7 mm from the concrete surface, which lowered the first reflection significantly. For the other slabs, the Styrofoam was found to be at depths ranging from 20 to 40 mm.

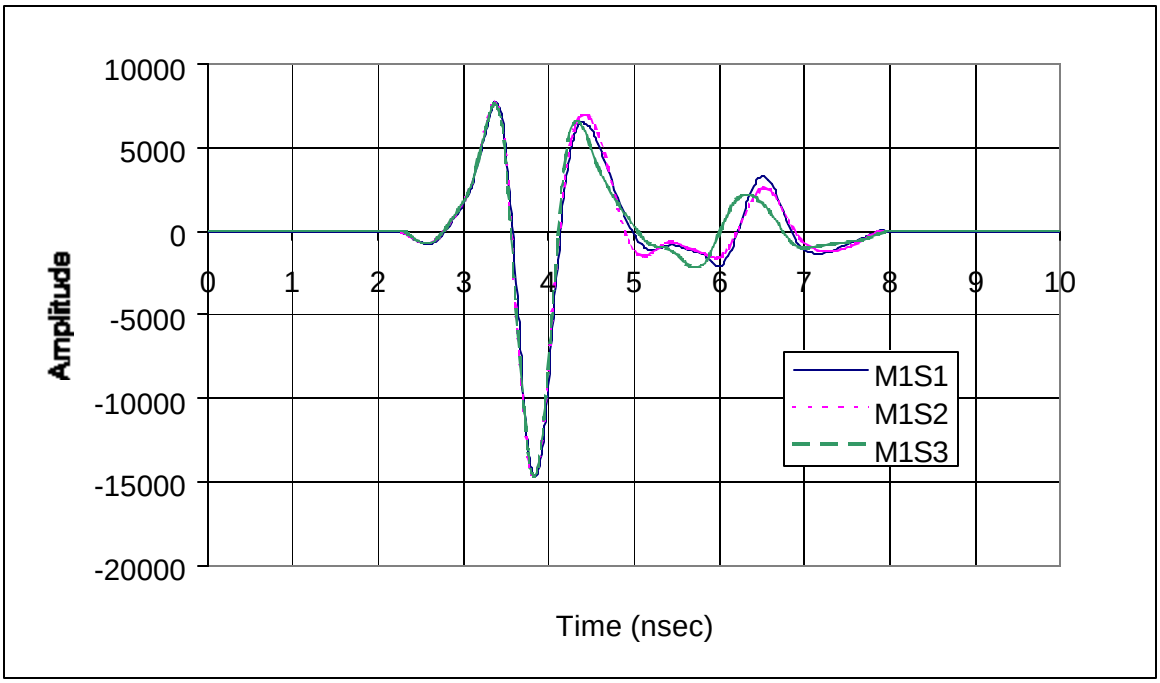

Figure 4.36 Air void effects on the time domain signal for mix M1 (12/04/99)

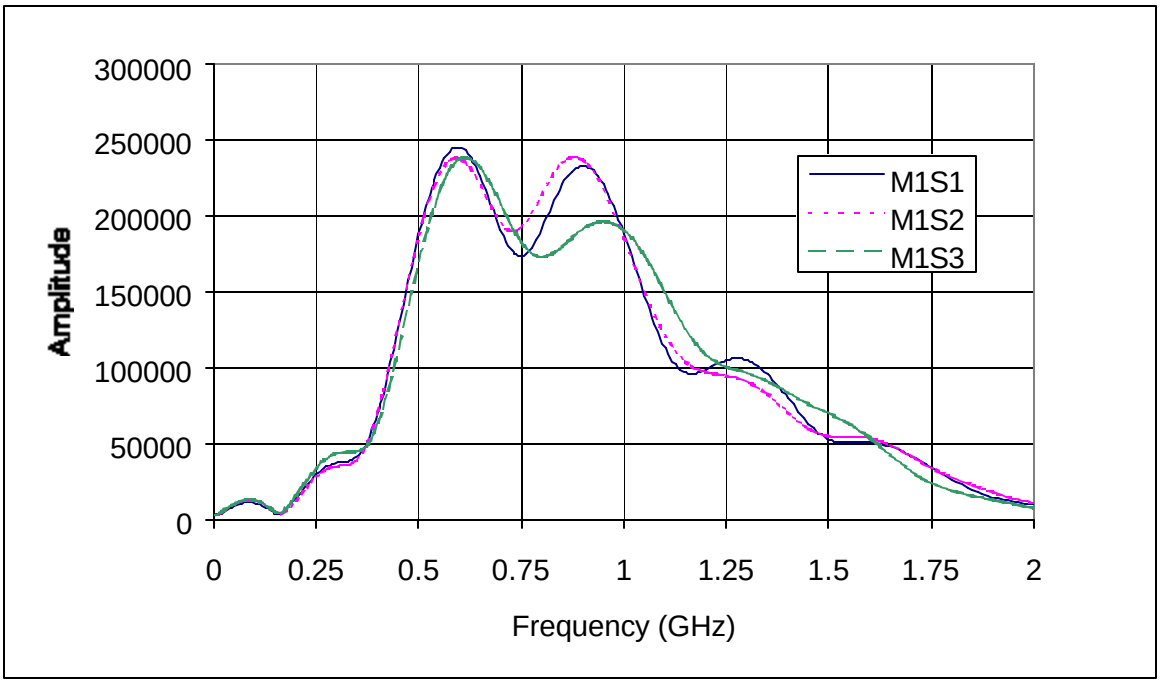

Figure 4.37 Air void effects on the frequency spectrum for mix M1 (12/04/99)

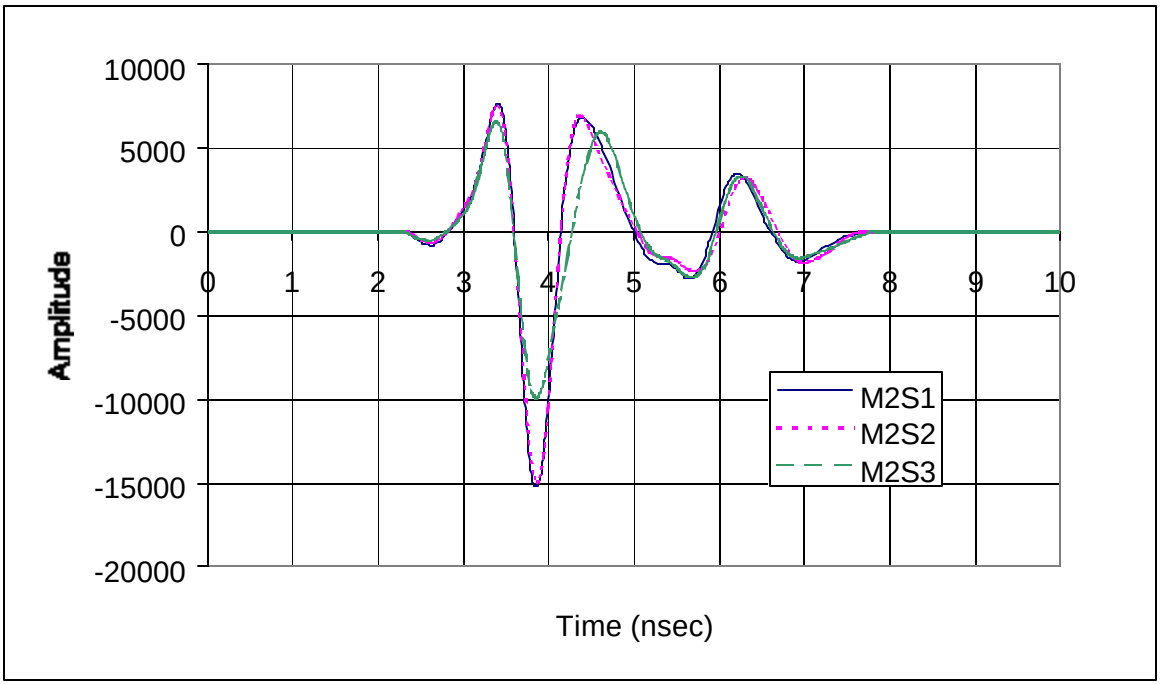

Figure 4.38 Air void effects on the time domain signal for mix M2 (12/04/99)

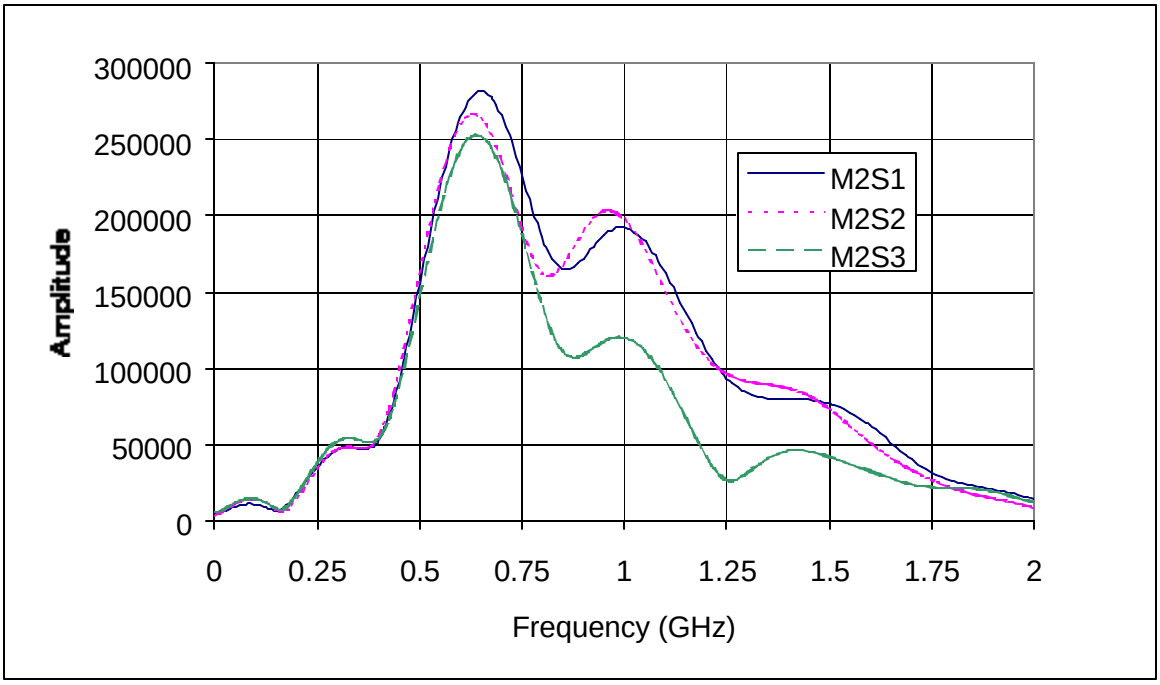

Figure 4.39 Air void effects on the frequency spectrum for mix M2 (12/04/99)

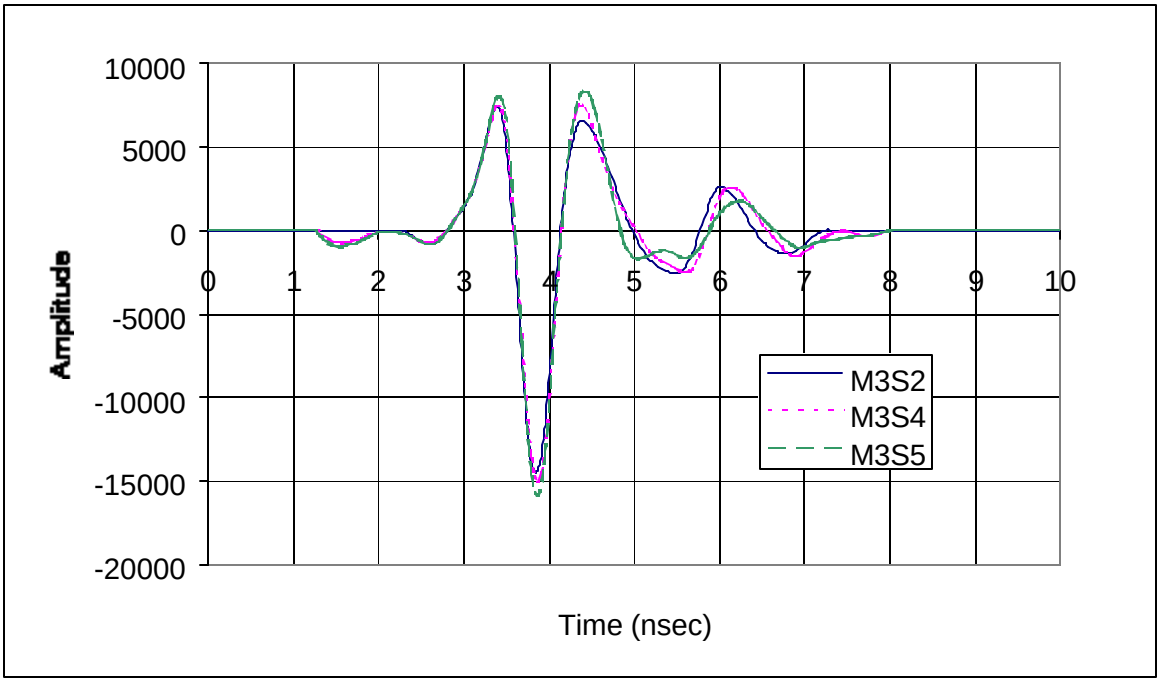

Figure 4.40 Air void effects on the time domain signal for mix M3 (12/04/99)

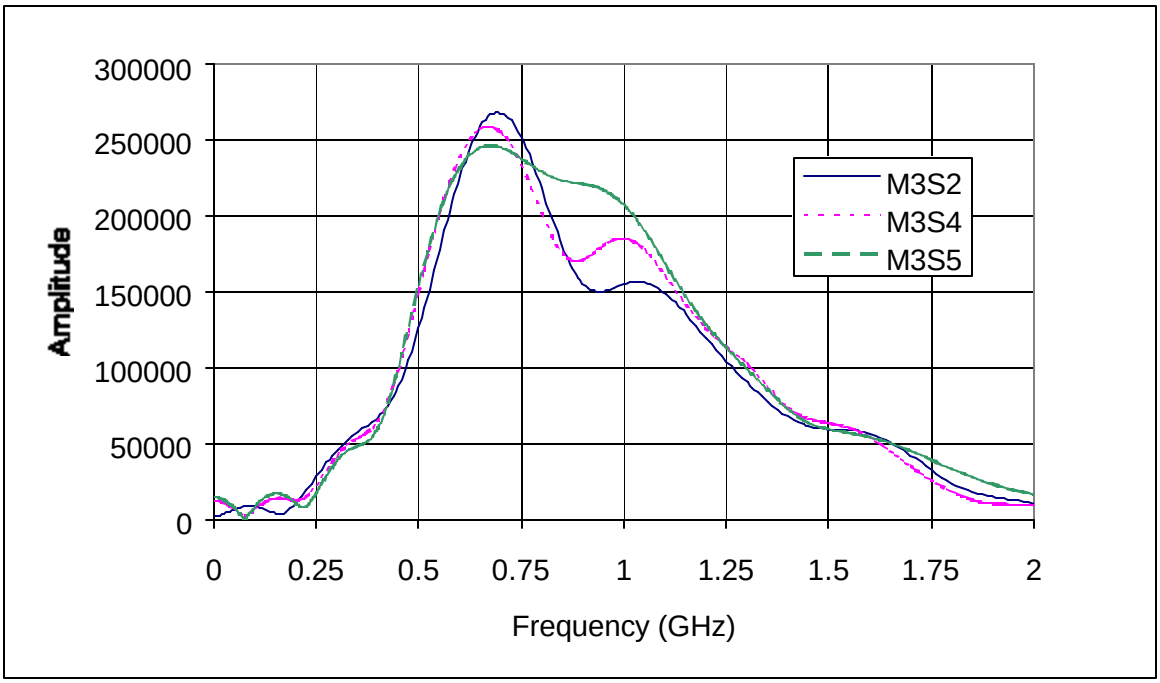

Figure 4.41 Air void effects on the frequency spectrum for mix M3 (12/04/99)

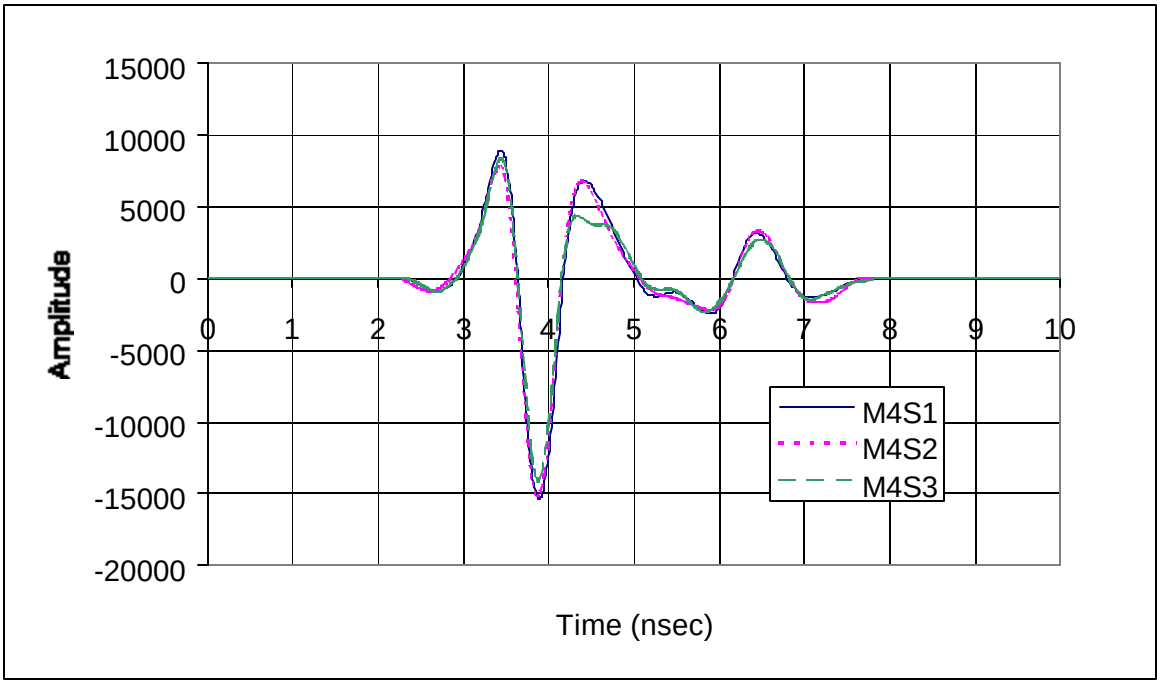

Figure 4.42 Air void effects on the time domain signal for mix M4 (12/04/99)

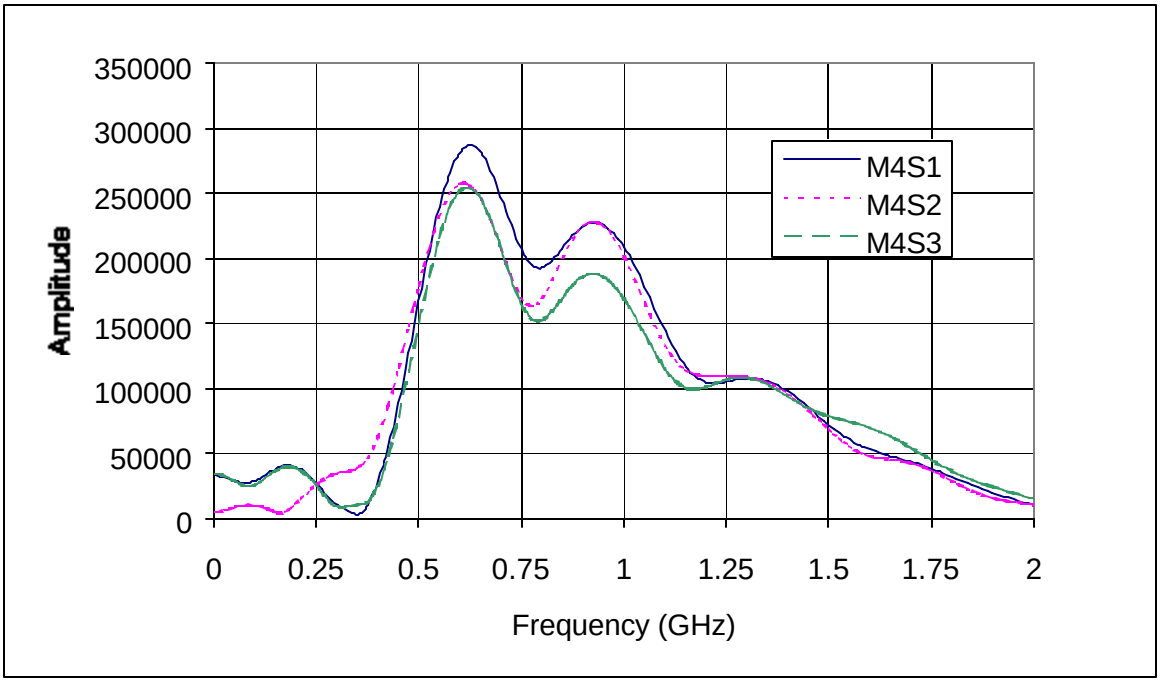

Figure 4.43 Air void effects on the frequency spectrum for mix M4 (12/04/99)

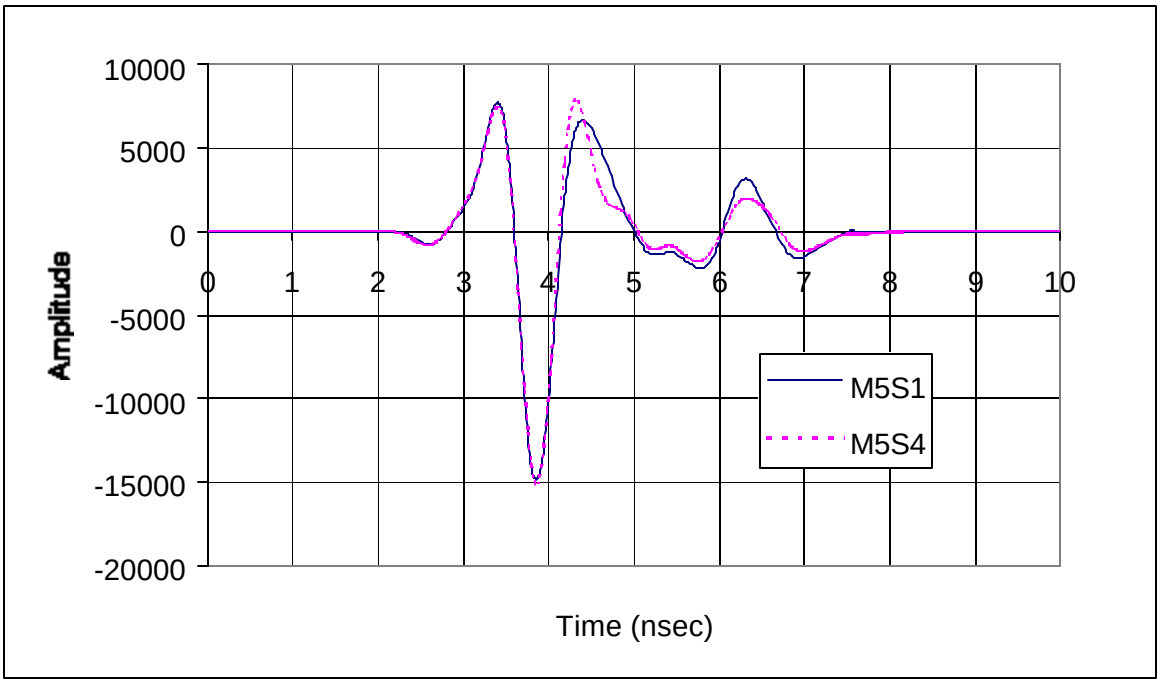

Figure 4.44 Air void effects on the time domain signal for mix M5 (12/04/99)

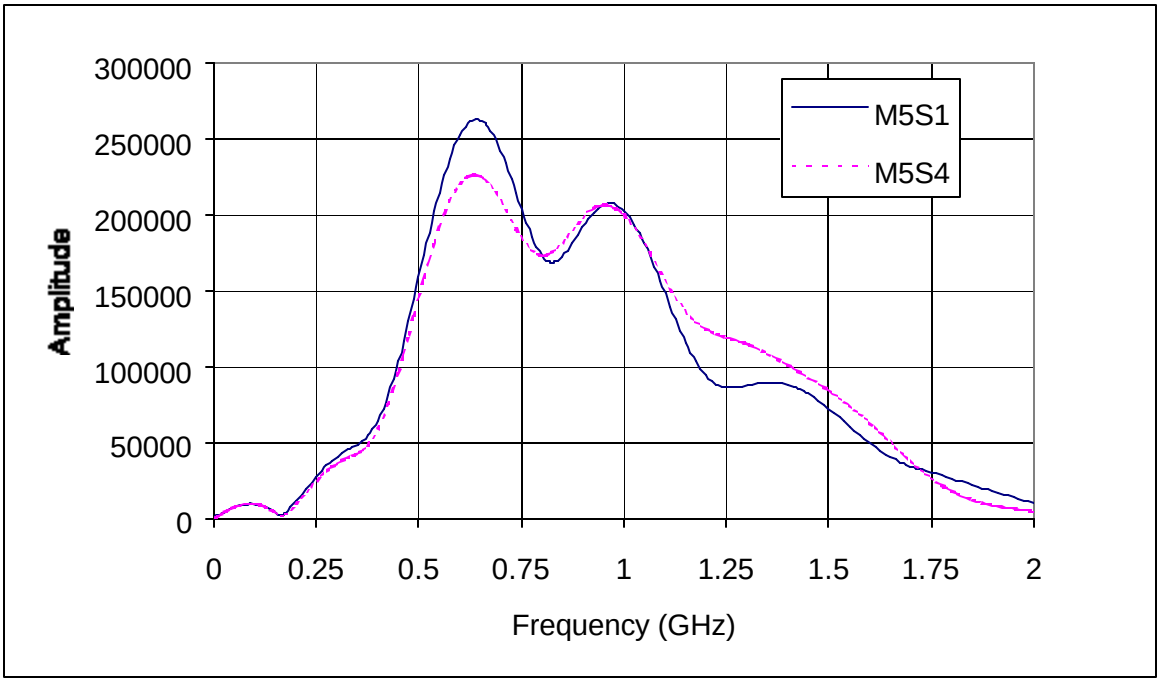

Figure 4.45 Air void effects on the frequency spectrum for mix M5 (12/04/99)

On November 5, 2000, Acetone was squeezed inside the plastic conduits to dissolve the Styrofoam pieces. Acetone was added from one side until it started to flow out from the other side. When this happened, air was squeezed inside the conduit to get the Acetone out. When no more Acetone was driven out, water was squeezed inside the plastic conduits from one side until it came out from the other side. When this was achieved for all slabs with simulated delamination, data were obtained using both air- and ground-coupled GPR systems. Figures 4.46 to 4.63 show the obtained results for the air-coupled GPR data. A significant distortion occurred to both time-domain waveforms and frequency spectrums for all the slabs. However, the signal distortion did not occur in the same manner for all slabs. Although water was added in the same manner for all slabs, its quantity, thickness, and depth from surface was not uniform for all the slabs. However, in almost all slabs, the second reflection from the bottom of the slab was delayed and its amplitude was increased. This was mainly due to the increased bulk dielectric constant of the concrete, which reduced the wave speed; however, it increased the amplitude at the bottom of the slab due to the higher dielectric contrast between air and concrete. Even though there was no quantitative way from either the time-domain waveform or frequency spectrum to detect the water-filled voids, the distorted shape of either the waveform or frequency spectrum could be used as an indication of the presence of the water-filled voids.

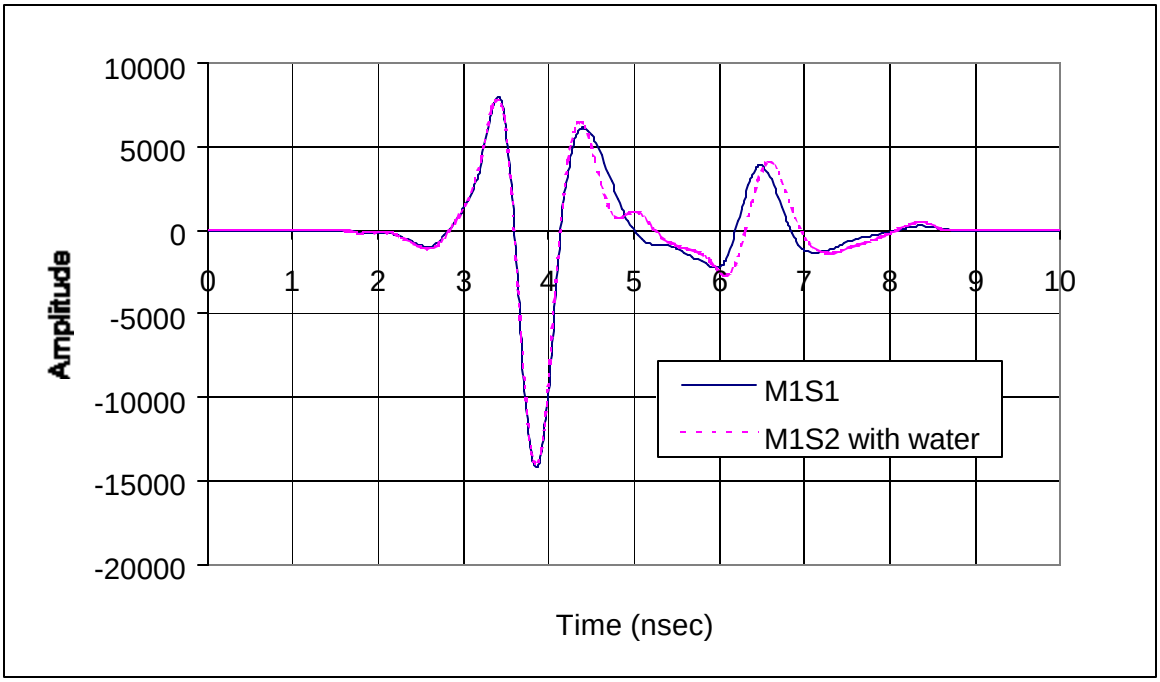

Figure 4.46 Water-filled void effects on the time domain signal for mix M1 (6.4 mm thick)

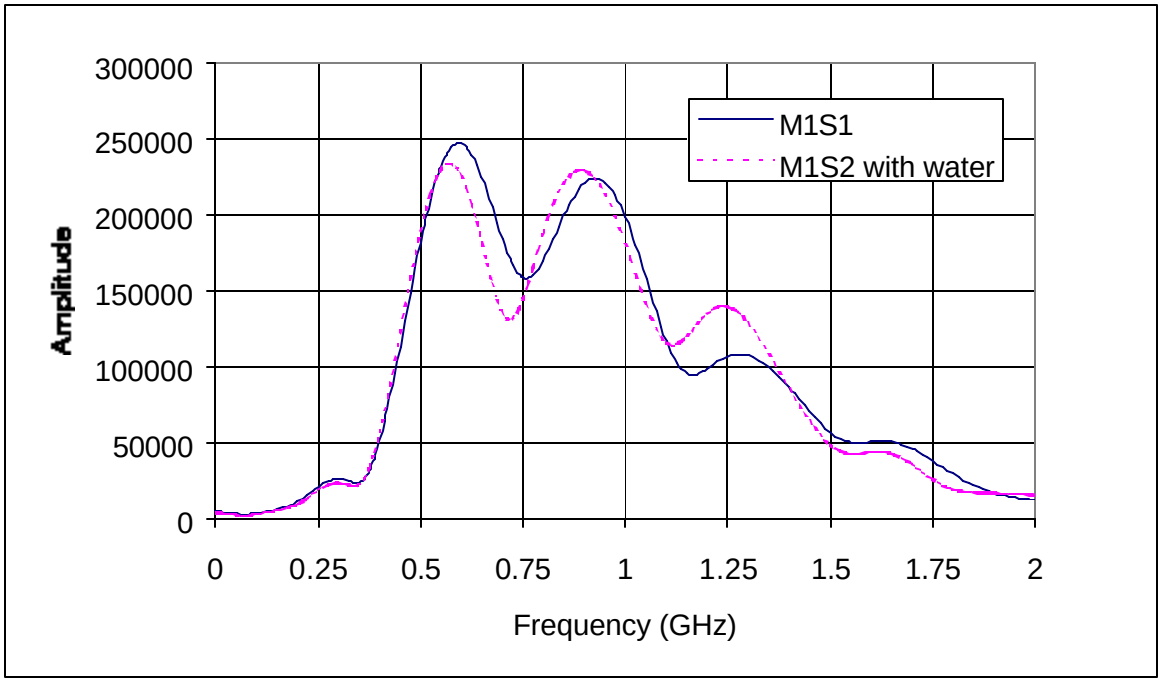

Figure 4.47 Water-filled void effects on the frequency spectrum for mix M1 (6.4 mm thick)

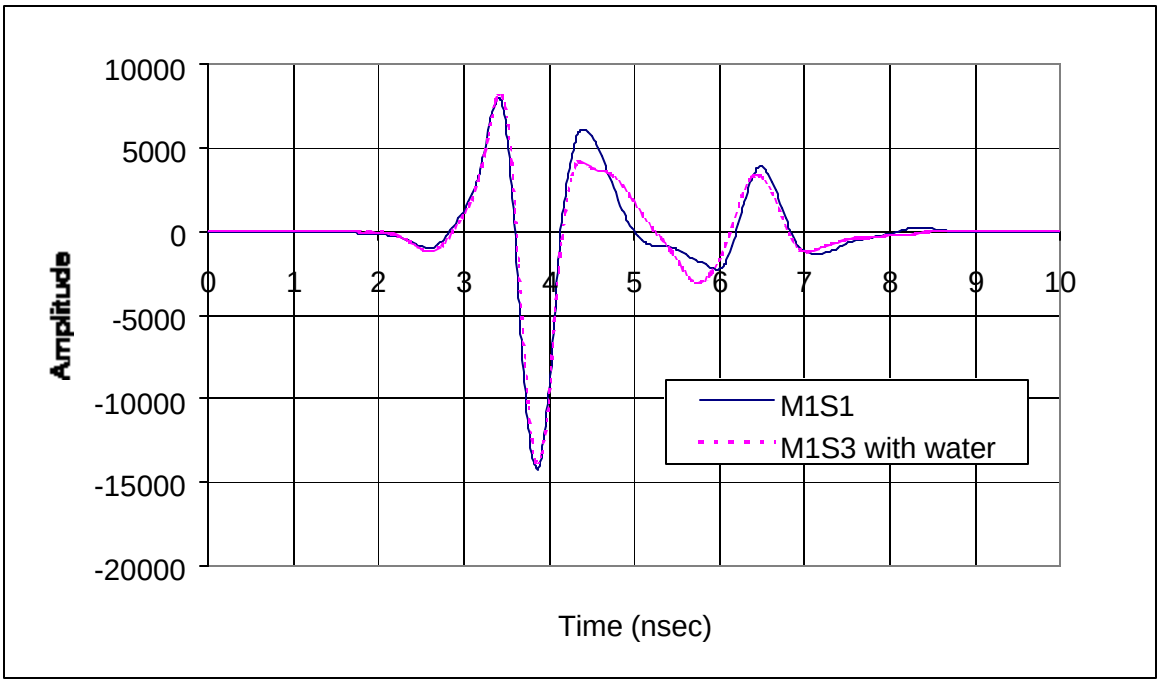

Figure 4.48 Water-filled void effects on the time domain signal for mix M1 (12.7 mm thick)

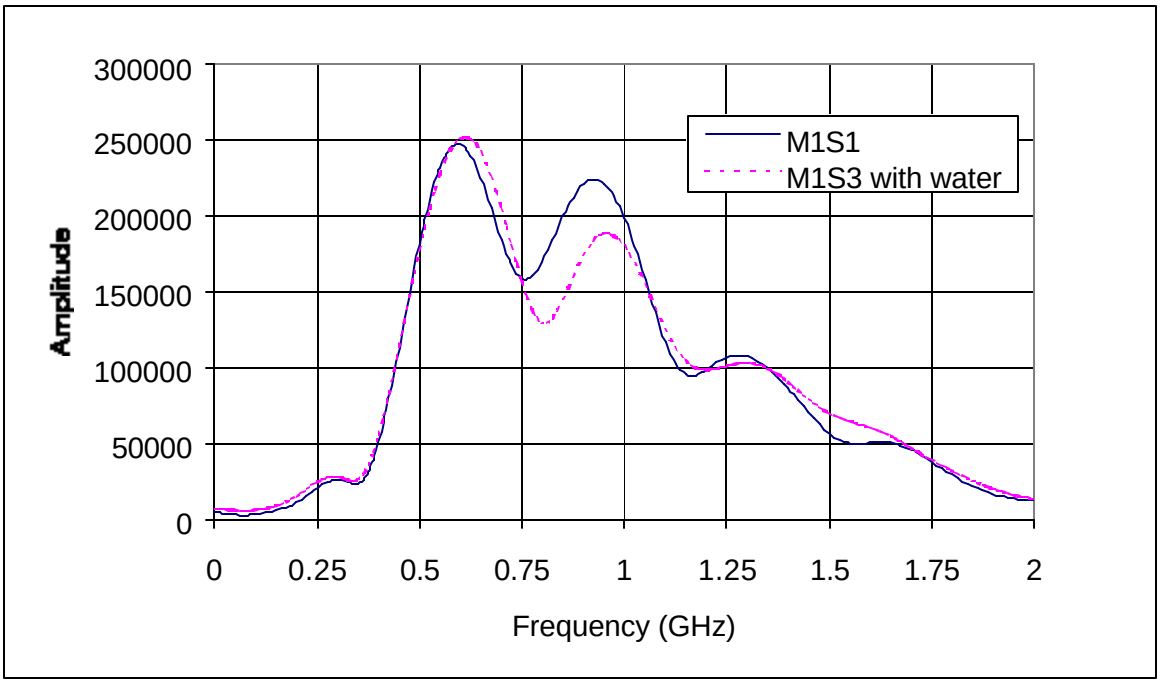

Figure 4.49 Water-filled void effects on the frequency spectrum for mix M1 (12.7 mm thick)

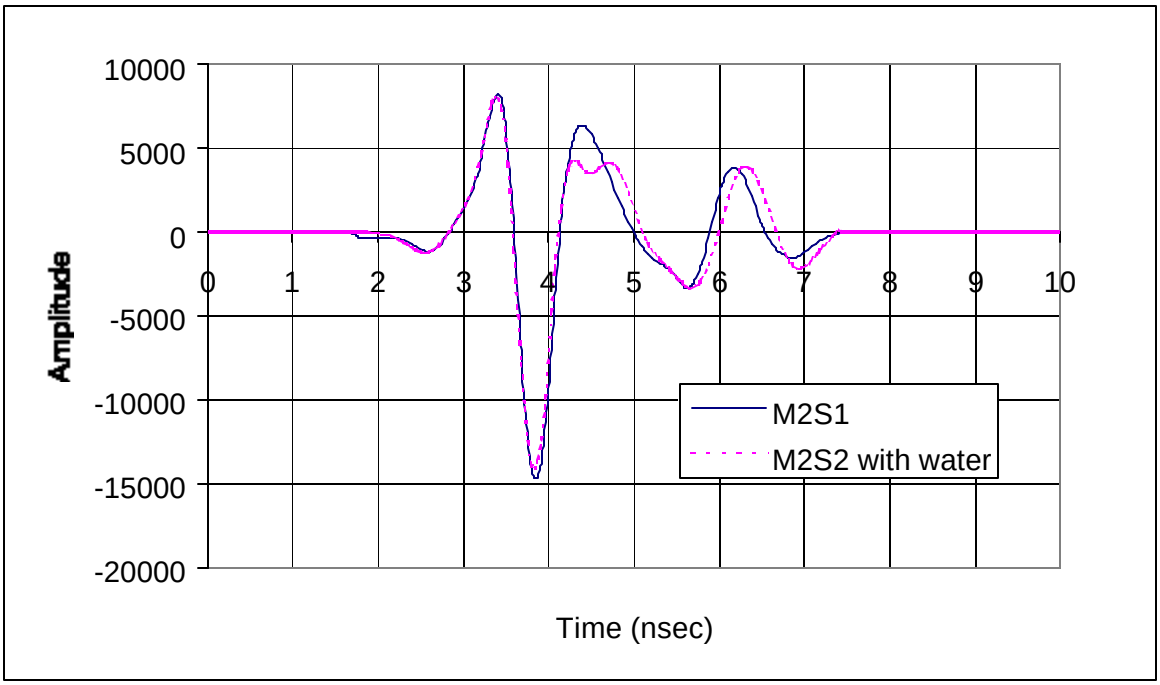

Figure 4.50 Water-filled void effects on the time domain signal for mix M2 (6.4 mm thick)

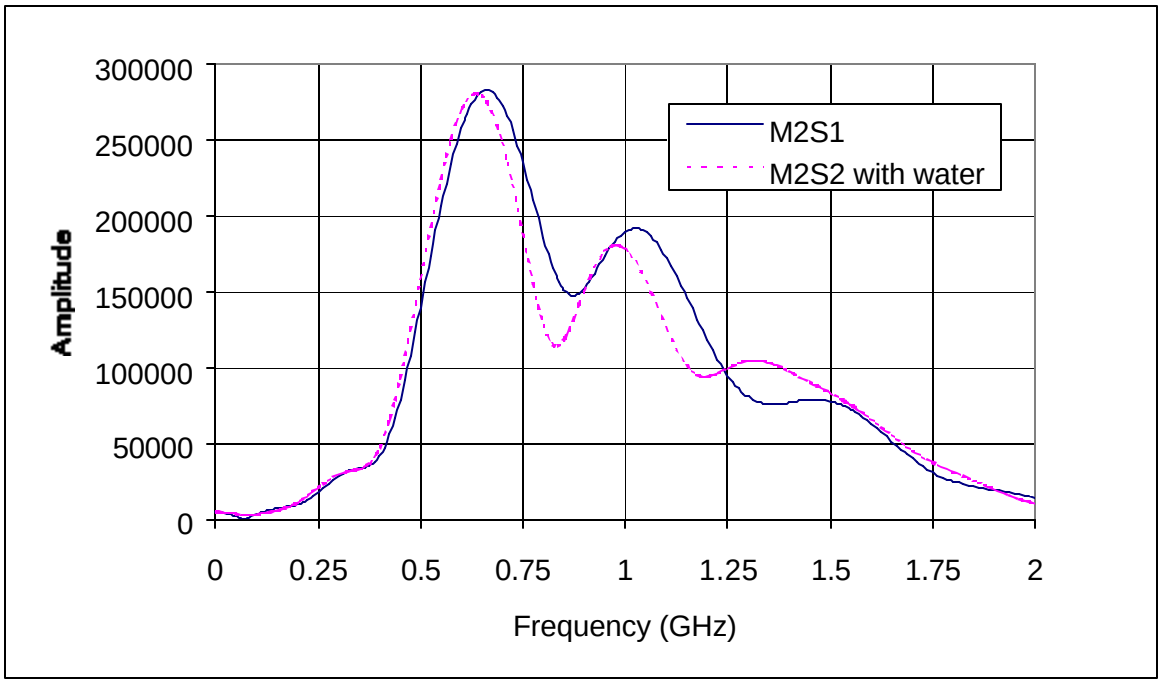

Figure 4.51 Water-filled void effects on the frequency spectrum for mix M2 (6.4 mm thick)

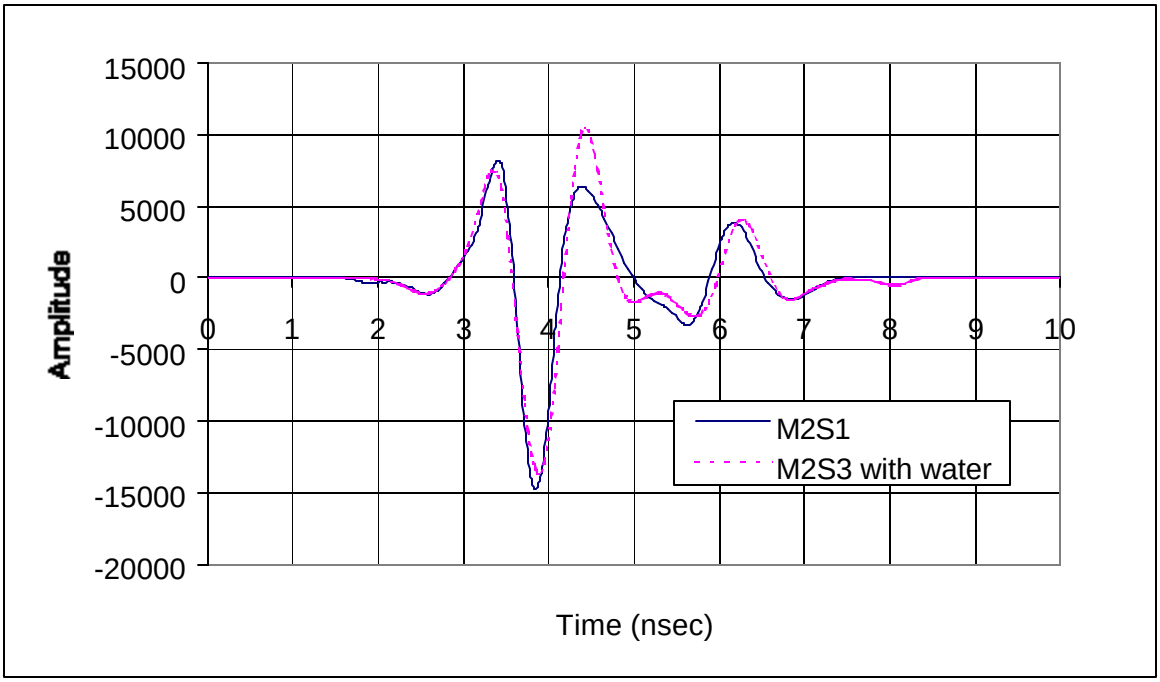

Figure 4.52 Water-filled void effects on the time domain signal for mix M2 (12.7 mm thick)

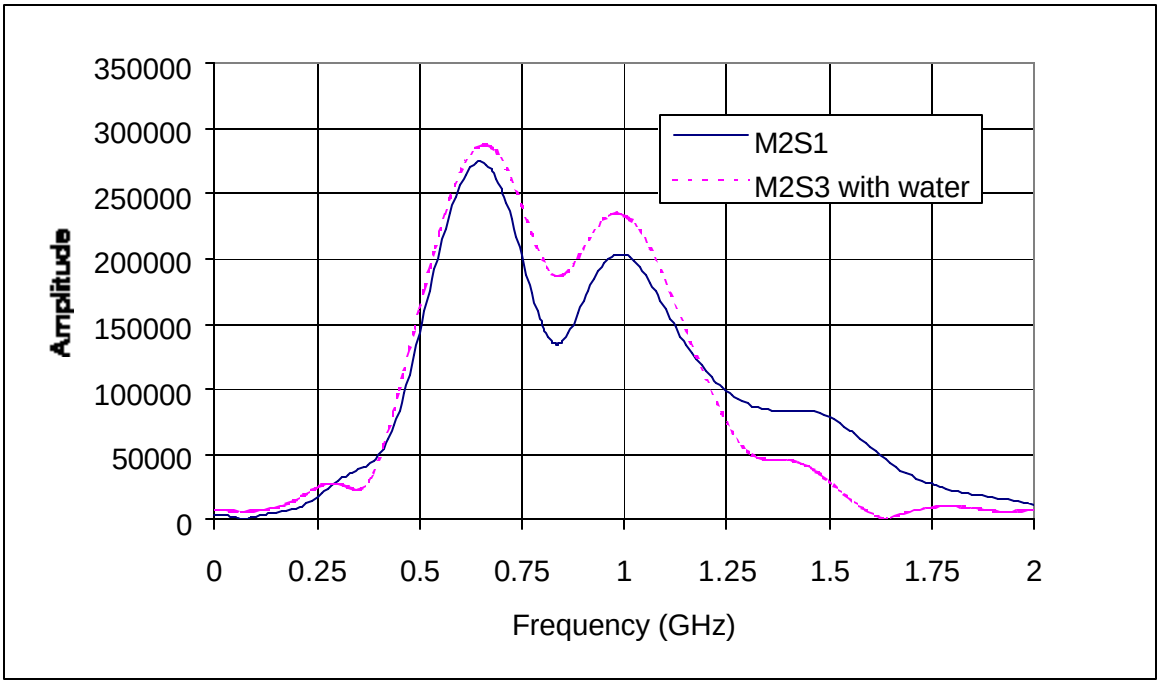

Figure 4.53 Water-filled void effects on the frequency spectrum for mix M2 (12.7 mm thick)

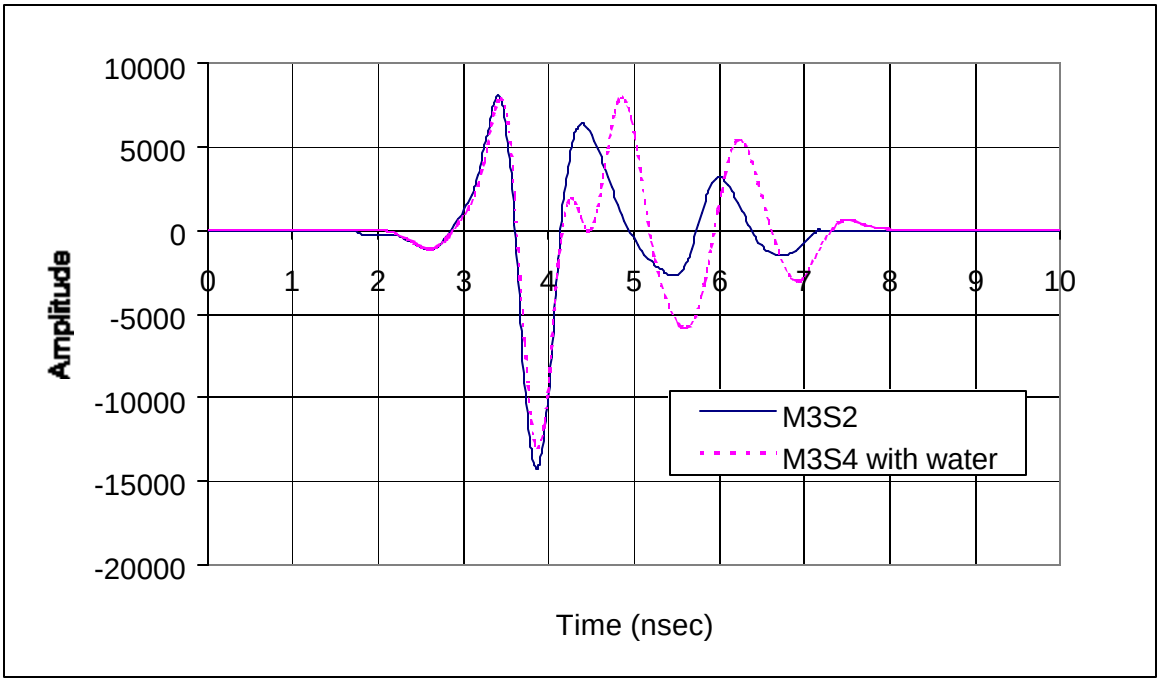

Figure 4.54 Water-filled void effects on the time domain signal for mix M3 (6.4 mm thick)

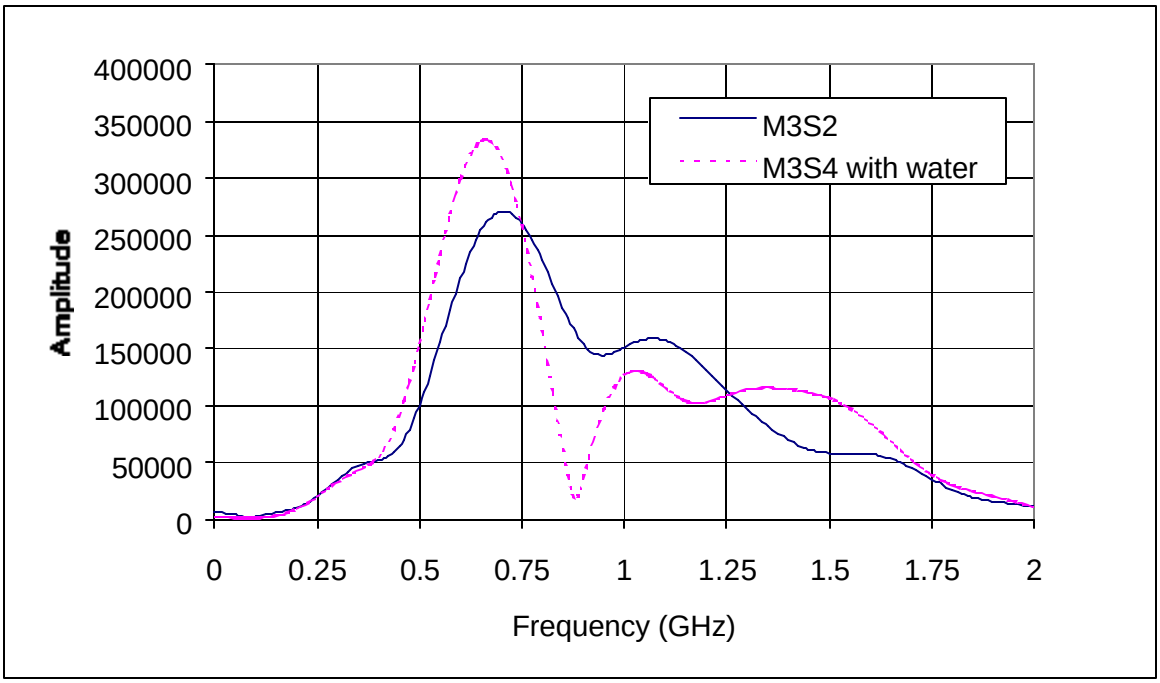

Figure 4.55 Water-filled void effects on the frequency spectrum for mix M3 (6.4 mm thick)

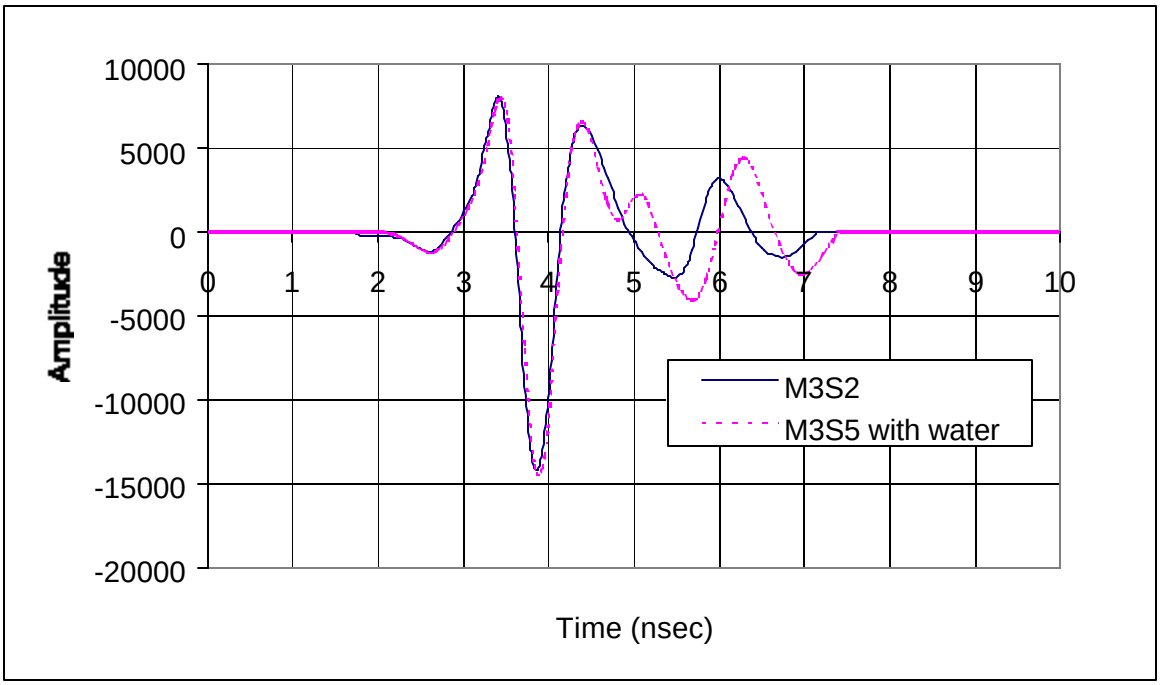

Figure 4.56 Water-filled void effects on the time domain signal for mix M3 (12.7 mm thick)

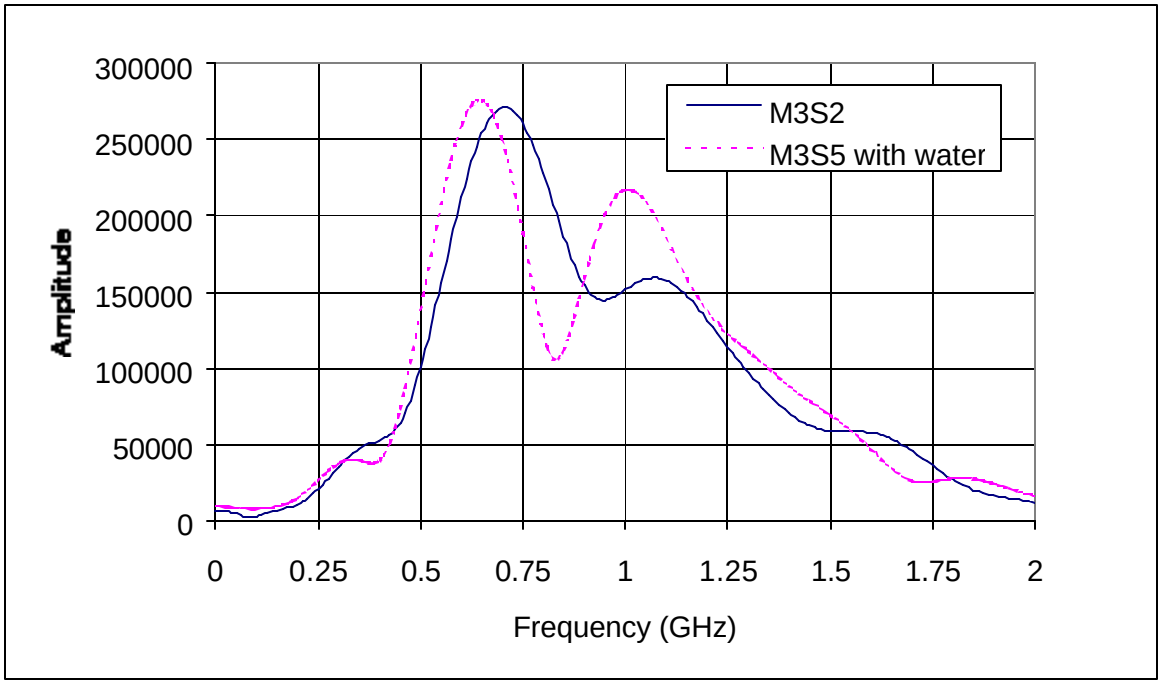

Figure 4.57 Water-filled void effects on the frequency spectrum for mix M3 (12.7 mm thick)

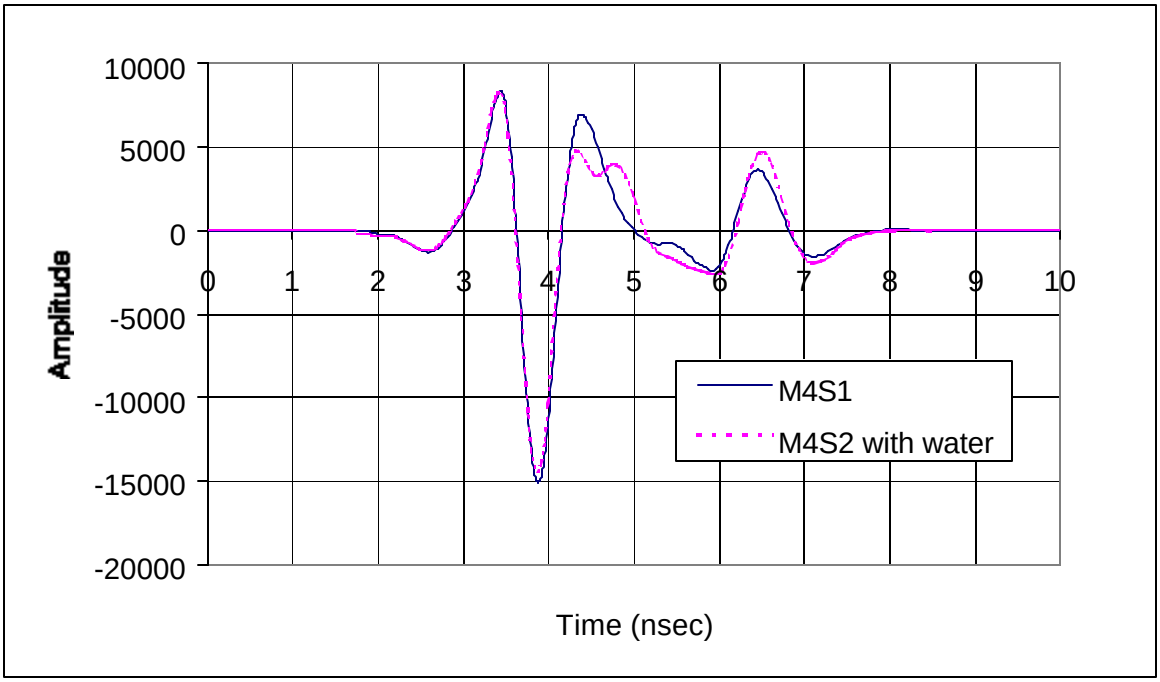

Figure 4.58 Water-filled void effects on the time domain signal for mix M4 (6.4 mm thick)

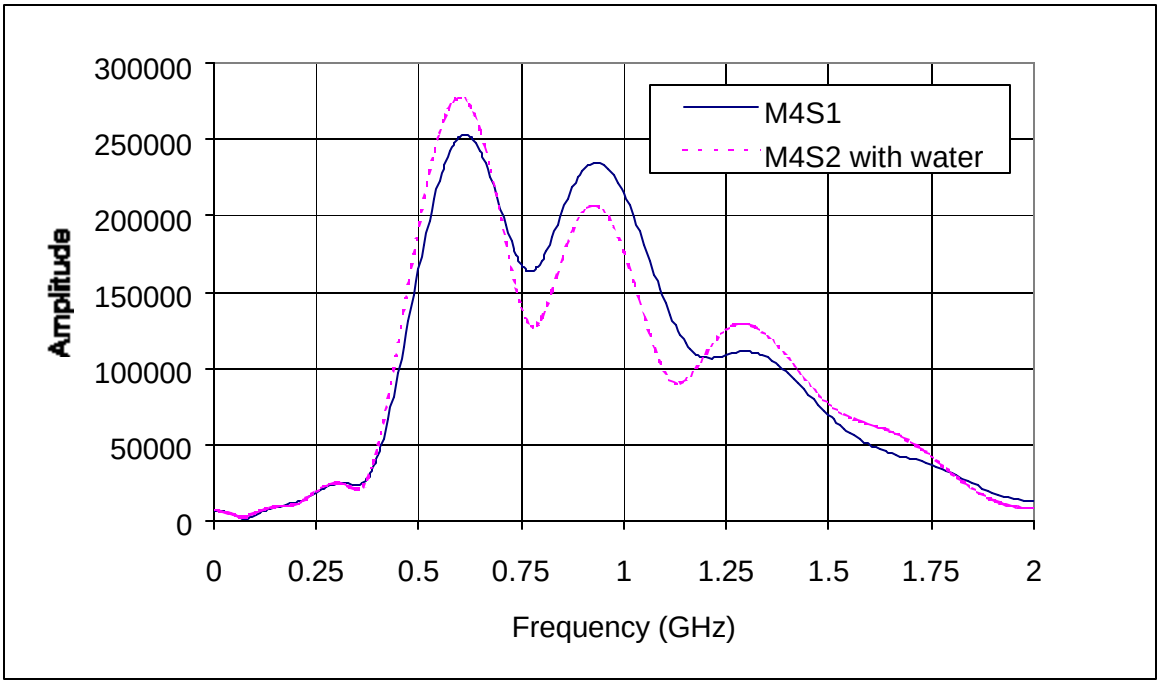

Figure 4.59 Water-filled void effects on the frequency spectrum for mix M4 (6.4 mm thick)

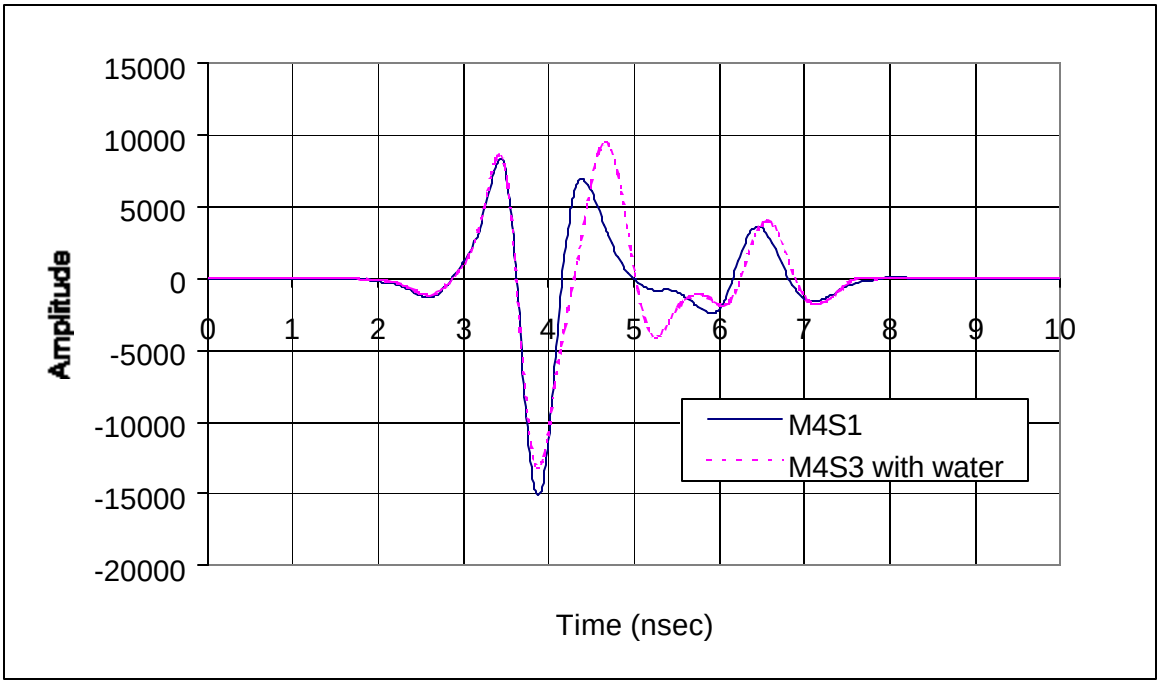

Figure 4.60 Water-filled void effects on the time domain signal for mix M4 (12.7 mm thick)

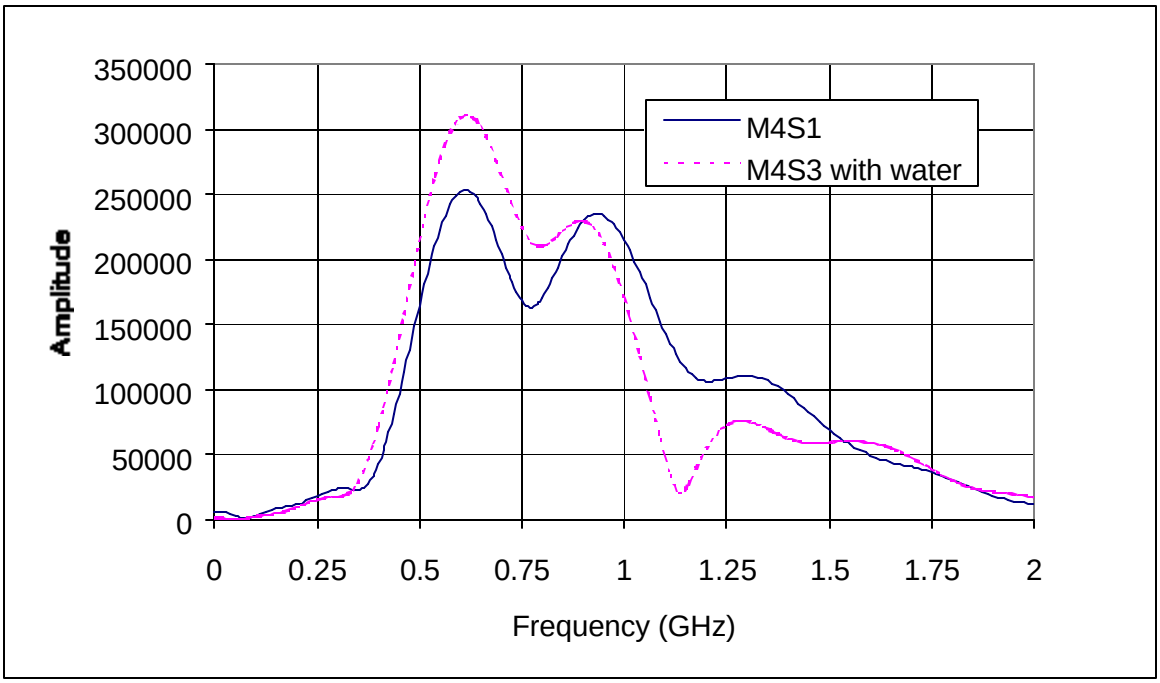

Figure 4.61 Water-filled void effects on the frequency spectrum for mix M4 (12.7 mm thick)

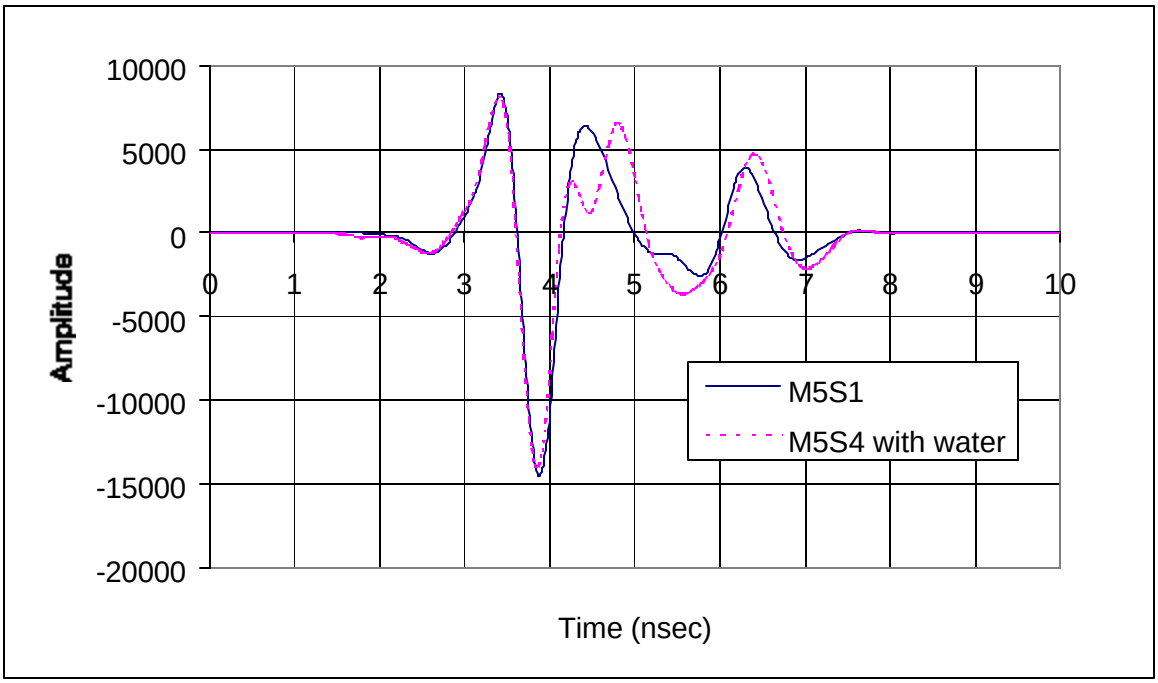

Figure 4.62 Water-filled void effects on the time domain signal for mix M5 (12.7 mm thick)

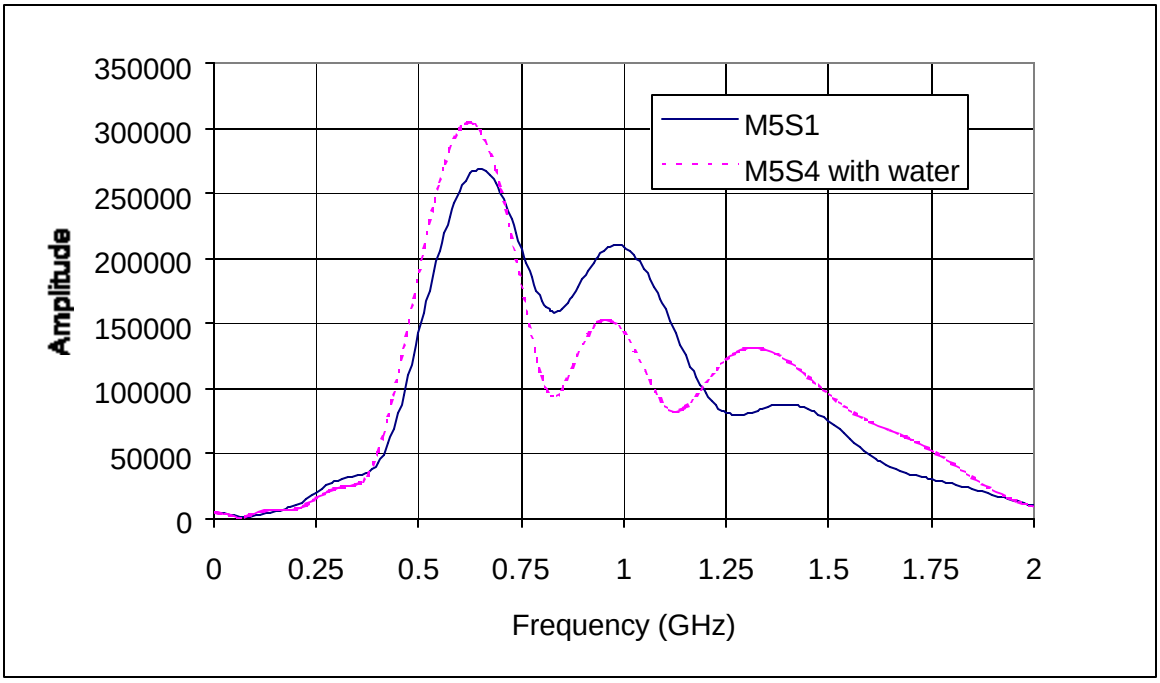

Figure 4.63 Water-filled void effects on the frequency spectrum for mix M5 (12.7 mm thick)

A method to predict the radar signal was developed for concrete with a defect inside it. The incident frequency spectrum, F_i, is first calculated by taking the FFT of the waveform obtained from the copper plate reflection and after zero padding it. Figure 4.64 presents how the prediction model was derived based on the multiple reflections. Since the defect does not cover the entire slab width, it was assumed in the model that the last reflection from the bottom of the slab will not hit the defect and will travel straight to the surface. It was also assumed for simplicity that the angle of incidence is equal to zero. The reflected frequency spectrum is therefore synthesized using Equation (4.28):

$$F_{r,syn} = [\rho_1 + \rho_2 * (1-\rho_1^2) * T1^2 - \rho_2 * (1-\rho_2^2) * (1-\rho_1^2) * T1^2 * T2^2 - \rho_1 (1-\rho_2^2) * (1-\rho_1^2) * T1 * T2 * T3 * T4] * F_i \quad (4.28)$$

where $F_{r,syn}$ is the synthesized frequency spectrum; ρ_1 was previously defined by Equation (4.9); and the other parameters are defined as follows:

$$\rho_2 = \frac{\sqrt{\varepsilon_r} - \sqrt{\varepsilon_2}}{\sqrt{\varepsilon_r} + \sqrt{\varepsilon_2}} \quad (4.29)$$

where ε_2 is the dielectric constant for the material considered as a defect.

$$T1 = e^{-j\frac{\omega}{c} d1 \sqrt{\varepsilon_r}} \quad (4.30)$$

where ω is the angular frequency, c is the speed of light, d1 is the depth to the defect, and ε_r is the complex dielectric constant for concrete.

$$T2 = e^{-j\frac{\omega}{c} d2 \sqrt{\varepsilon_2}} \quad (4.31)$$

where d2 is the defect thickness.

$$T3 = e^{-j\frac{\omega}{c} d3 \sqrt{\varepsilon_r}} \quad (4.32)$$

where d3 is the distance from the bottom of the defect to the bottom of the slab.

$$T4 = e^{-j\frac{\omega}{c}d\sqrt{\varepsilon_r}} \tag{4.33}$$

where d is the slab thickness. Once the frequency spectrum is synthesized, the modeled time domain signal is obtained using Equation (4.27). All computations were performed using a MATLAB function, presented in Appendix B.

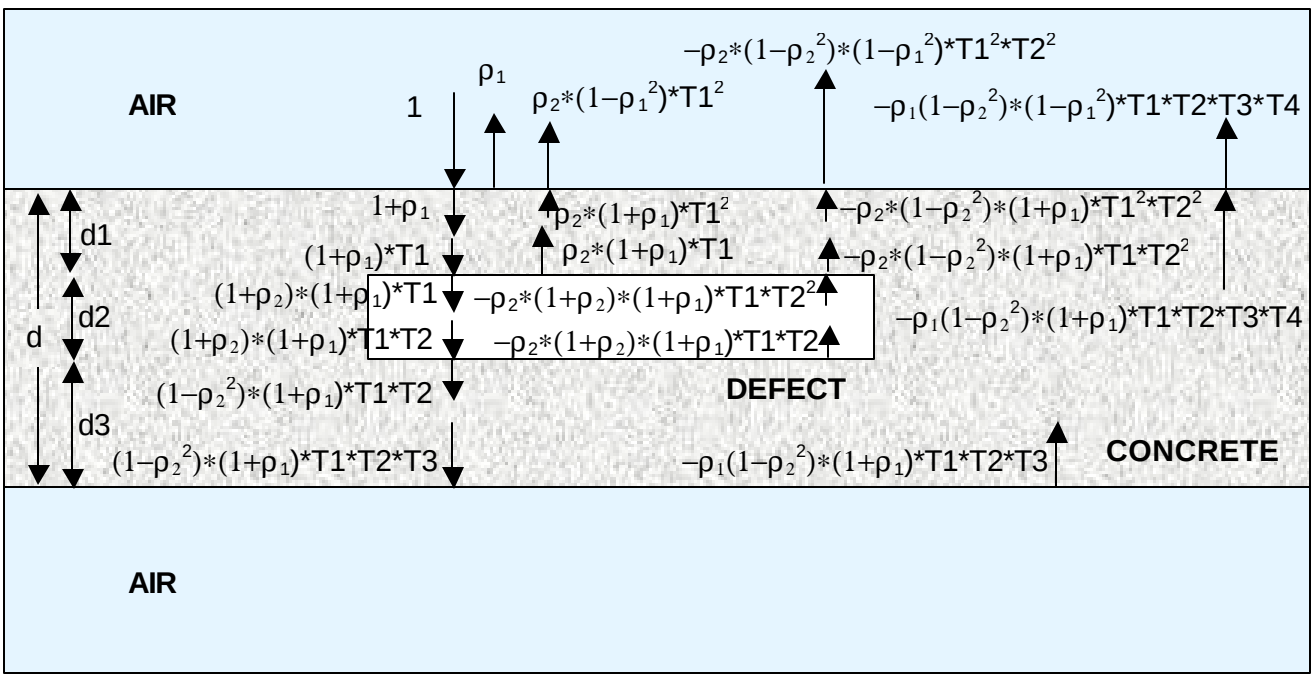

Figure 4.64 Overall reflection model for concrete with a defect

The synthesis of air-coupled GPR waveforms for concrete with defects was performed for slabs M1S2, M1S3, M2S2, and M2S3 for the data taken on November 5, 2000. Figure 4.65 shows the modeled and measured waveforms for slab M1S2. The best-modeled waveform (RMSE between modeled and measured waveforms was equal to 519.7) was found when the depth of the Styrofoam was set equal to 41 mm. Figure 4.66 shows the modeled and measured waveforms for slab M1S3. The best-modeled waveform (RMSE between modeled and measured waveforms was equal to 547.3) was found when the depth of the Styrofoam was set equal to 20 mm. Figure 4.67 shows the modeled and measured waveforms for slab M2S2. The best-modeled waveform (RMSE between modeled and measured waveforms was equal to 353.3) was found when the depth of the Styrofoam was also set equal to 20 mm. Figure 4.68 shows the modeled and measured waveforms for slab M2S3. The best-modeled waveform (RMSE between modeled and measured waveforms was equal to 409.1) was found when the depth of the Styrofoam was also set equal to only 7 mm.

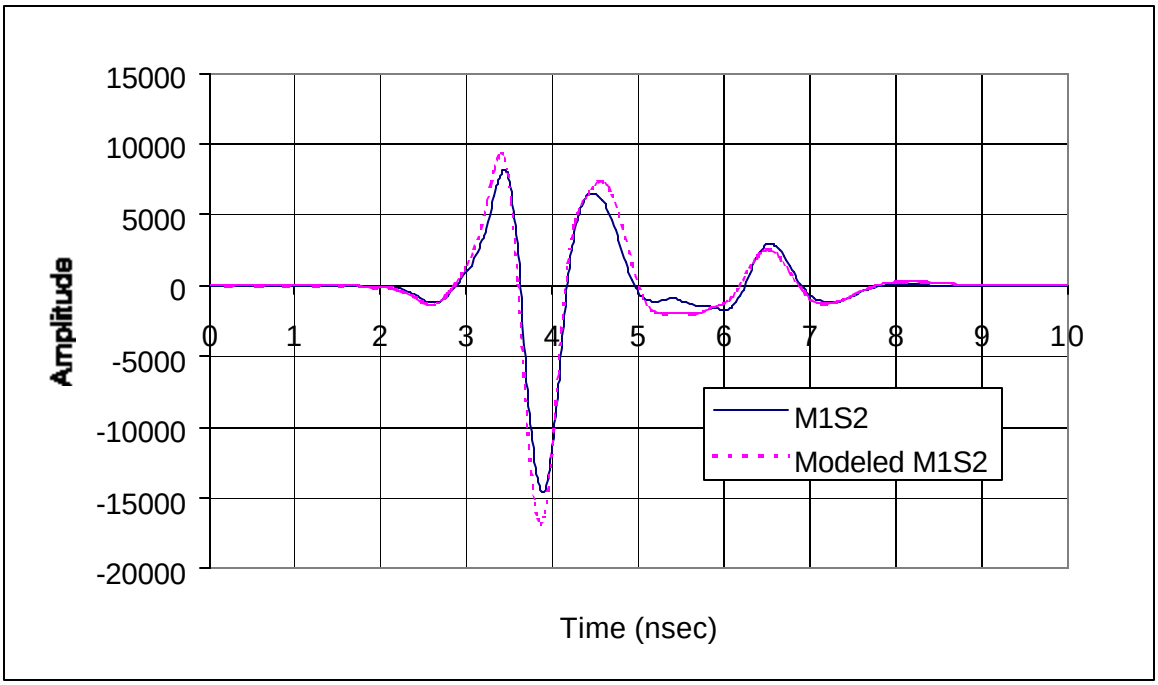

Figure 4.65 Modeled and measured waveforms for slab M1S2

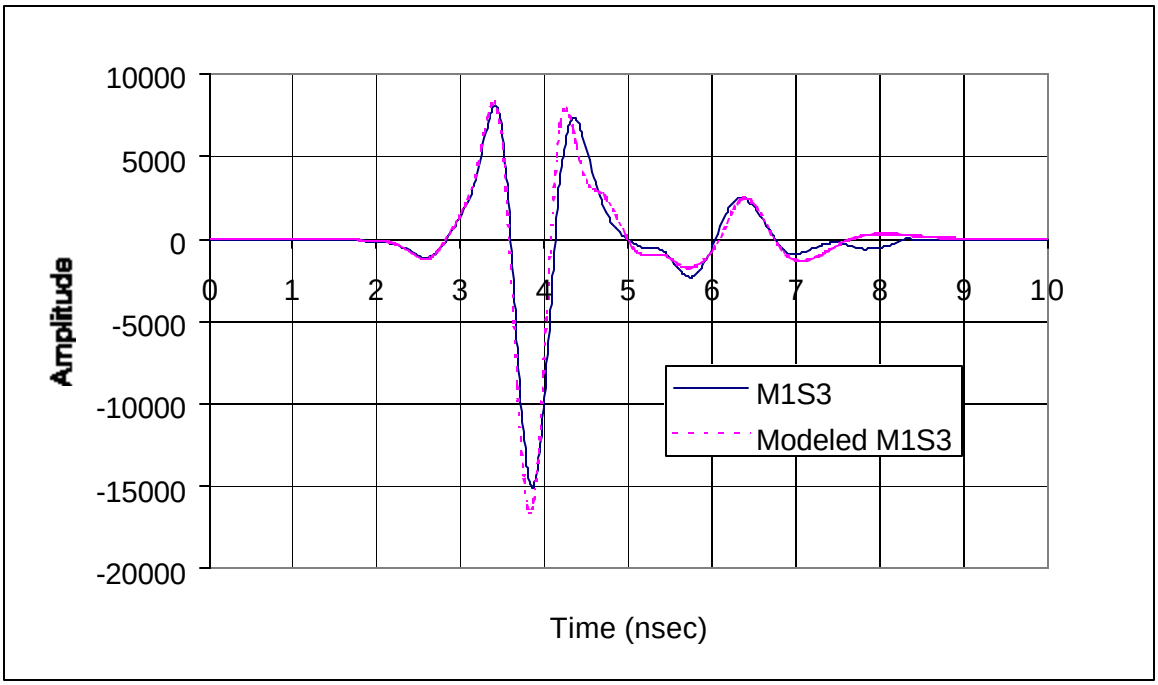

Figure 4.66 Modeled and measured waveforms for slab M1S3

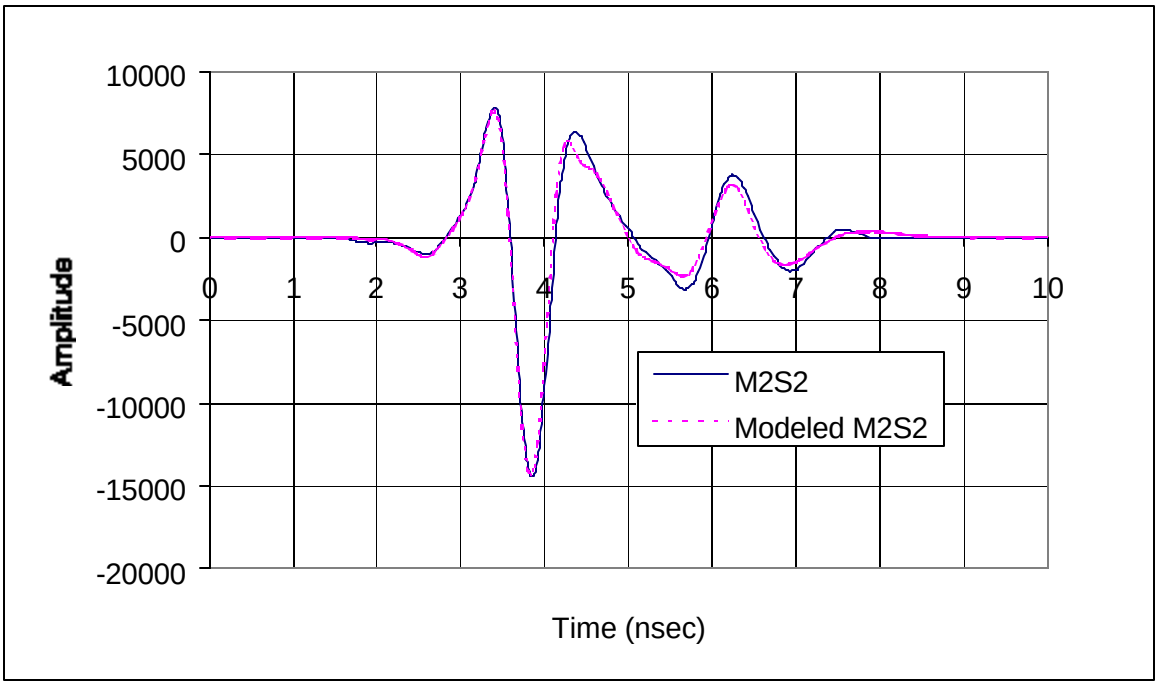

Figure 4.67 Modeled and measured waveforms for slab M2S2

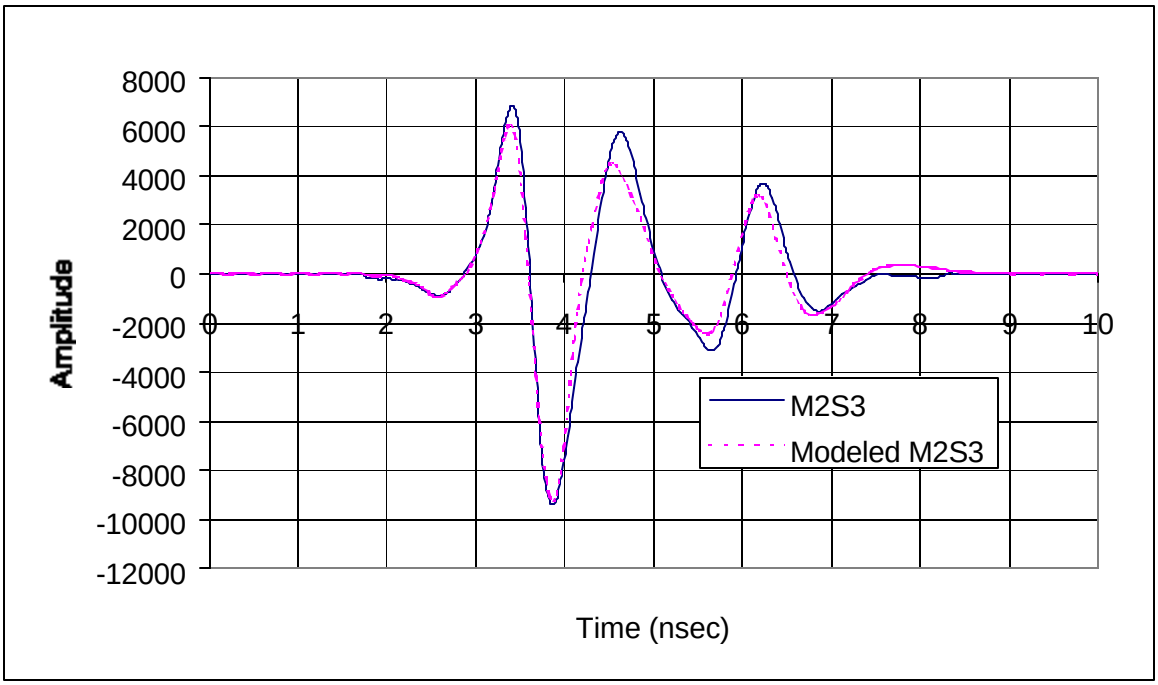

Figure 4.68 Modeled and measured waveforms for slab M2S3

Modeling the water-filled voids was not as straightforward as modeling the air voids. The dielectric constant for the air void was set equal to 1, and good fit was found between the modeled and measured waveforms. On the other hand, with the water-filled void, an initial value of 80 was used for the dielectric constant of the defect. No good model was obtained with this value for any value of the defect depth or thickness. Therefore, different models were generated by varying the dielectric constant of the water-filled defect, its depth, and thickness. Figures 4.69 to 4.71 show the modeled and measured waveforms for slabs M1S2, M1S3, and M2S2, all with water-filled voids. The best-modeled waveform for slab M1S2 was found when the defect dielectric constant was set equal to 35, its depth at 50 mm, and its thickness was 2.5 mm. With these parameters, the RMSE between modeled and measured waveforms was found to be 389.5. For slab M1S3, the best-modeled waveform was found when the defect dielectric constant was set equal to 35, its depth at 38 mm, and its thickness was 2 mm. With these parameters, the RMSE between modeled and measured waveforms was found to be 420.2. For slab M2S2, the best-modeled waveform was found when the defect dielectric constant was set equal to 35, its depth at 38 mm, and its thickness was 1.5 mm. With these parameters, the RMSE between modeled and measured waveforms was found to be 291.0.

The developed model to predict the air-coupled GPR signal over concrete with a defect was satisfactory for the air voids but was not successful for the water-filled voids. This is due to the fact that the developed model reflects well the geometry and physical properties of the slabs with air voids embedded in them. On the other hand, the physical properties and the exact geometry of the slabs with water-filled voids are not well known. In fact, adding the Acetone to dissolve the Styrofoam did not guarantee that all the Styrofoam was dissolved and that water occupied the whole void. In reality, the concrete has a mix of Acetone, water, and air (Styrofoam), which is not what the developed model reflects. Therefore, the previously synthesized waveforms for concrete with water-filled voids are those with the least calculated RMSE as compared to the measured waveforms, and do not reflect the actual physical configuration inside the concrete slab.

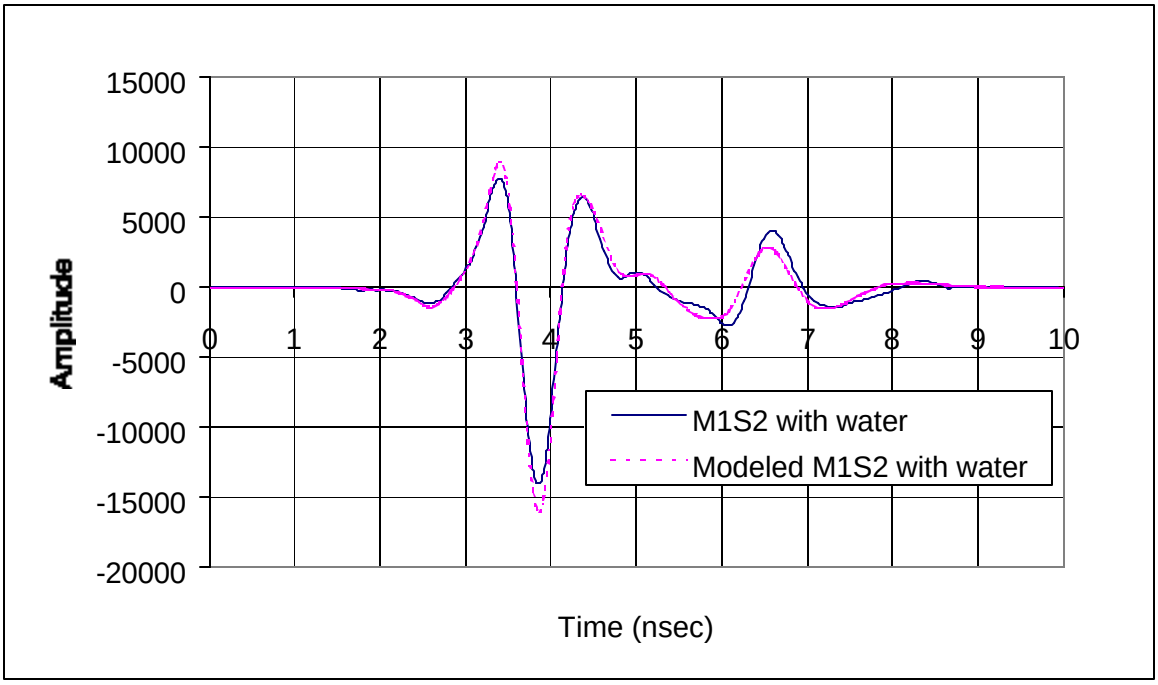

Figure 4.69 Modeled and measured waveforms for slab M1S2 with water

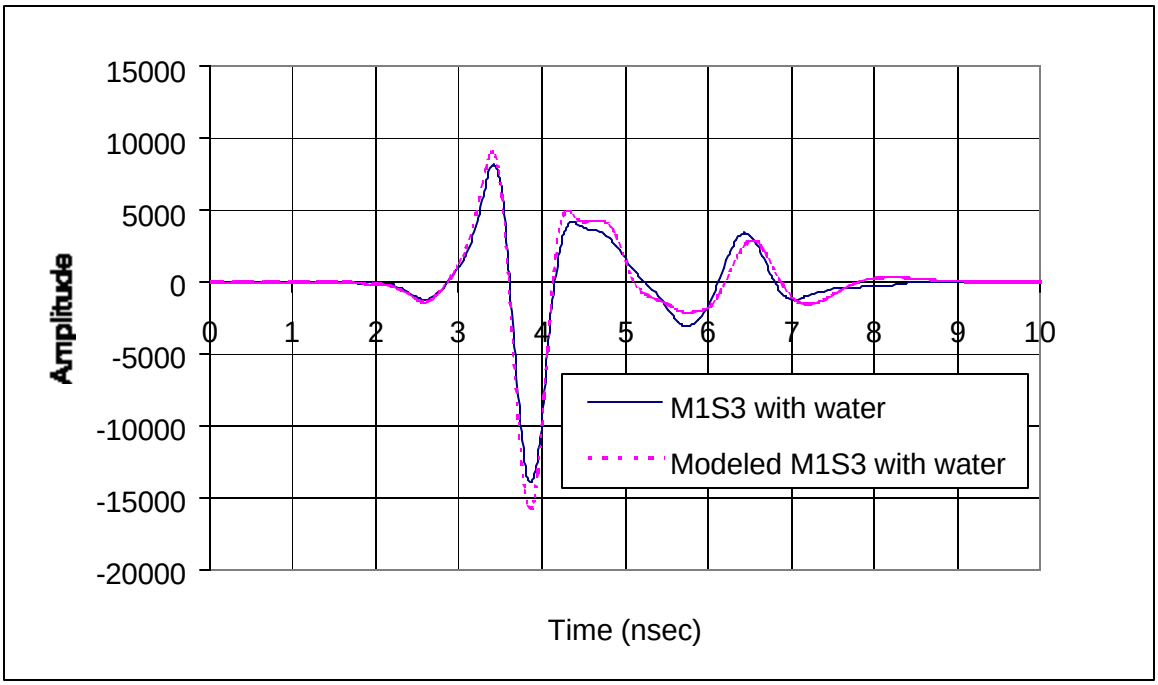

Figure 4.70 Modeled and measured waveforms for slab M1S3 with water

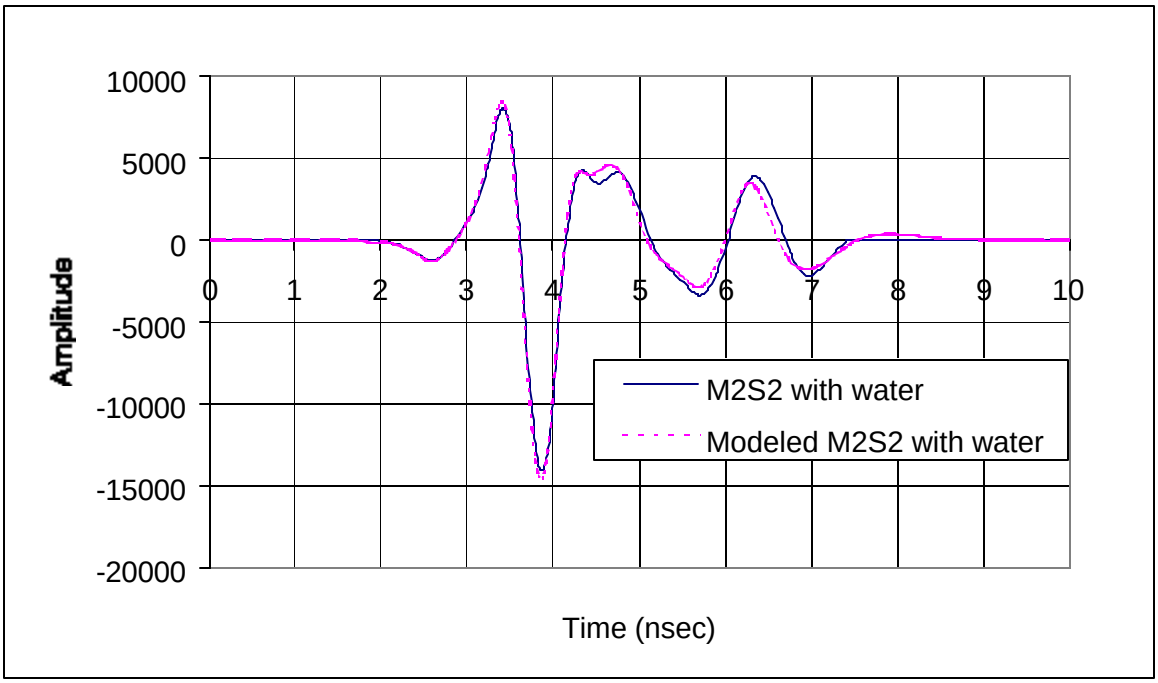

Figure 4.71 Modeled and measured waveforms for slab M2S2 with water

4.3.2. Ground-coupled system

The 900-MHz ground-coupled antenna was used to study the effect of defects inside concrete on its signal. This type of antenna has the advantage of penetrating deeper than the air-coupled antennas, however, its information, especially from near the surface, is more qualitative than quantitative (Scullion and Saarenketo, 2000). What makes the information from this system less quantitative are the surface coupling effects and the ringing problem. The surface coupling makes it difficult to know the incident pulse and to know the exact position of the surface in the reflected waveform. The incident pulse is necessary information for any modeling, while the surface position is needed for any thickness determination. The antenna ringing, also known as reverberation, is caused by the presence of a total reflective material, like steel in concrete, which causes the signal to bounce back and forth between the antenna and the reflector. Reverberation causes secondary reflection that appears deeper within the data. In reinforced concrete, for example, two or three sets of reflections are often observed, resulting from the presence of one rebar (Bungey and Millard, 1993).

Figure 4.72 shows the effect of the 6.4-mm air void on the collected ground-coupled GPR system waveform. The void presence mainly distorted the surface coupling by increasing its amplitude and decreasing the amplitude of the other reflections. The same situation occurred for slab M1S3, where a void 12.7-mm thick is present as shown in Figure 4.73. Figure 4.74 shows the linescan representation of the data. In this figure, the x-axis represents the scan number and the y-axis represents the reflection time or depth. In this representation, the amplitude of the reflected wave is quantified and then depicted using a color table (right of Figure 4.74) that maps each discrete value of the amplitude to a distinct color. The air void presence had the same effects on the other concrete mixes as presented in Figures D1 to D11 in Appendix D. For slab M2S3, where the air void was found to be very close to the surface, higher amplitude of the surface reflection was found, as shown in Figures D2 and D3 (Appendix D). Figures 4.75 and 4.76 show the linescan representation for the ground-coupled GPR data over slabs M3S4 and M3S5, respectively, from the data taken on May 13, 2000. These data were obtained by slowly moving the ground-coupled antenna over the entire slab; the x-axis represents the distance from the edge of the slab. In both figures, the air void is clearly detected from the rest of the slab due to the high surface reflection.

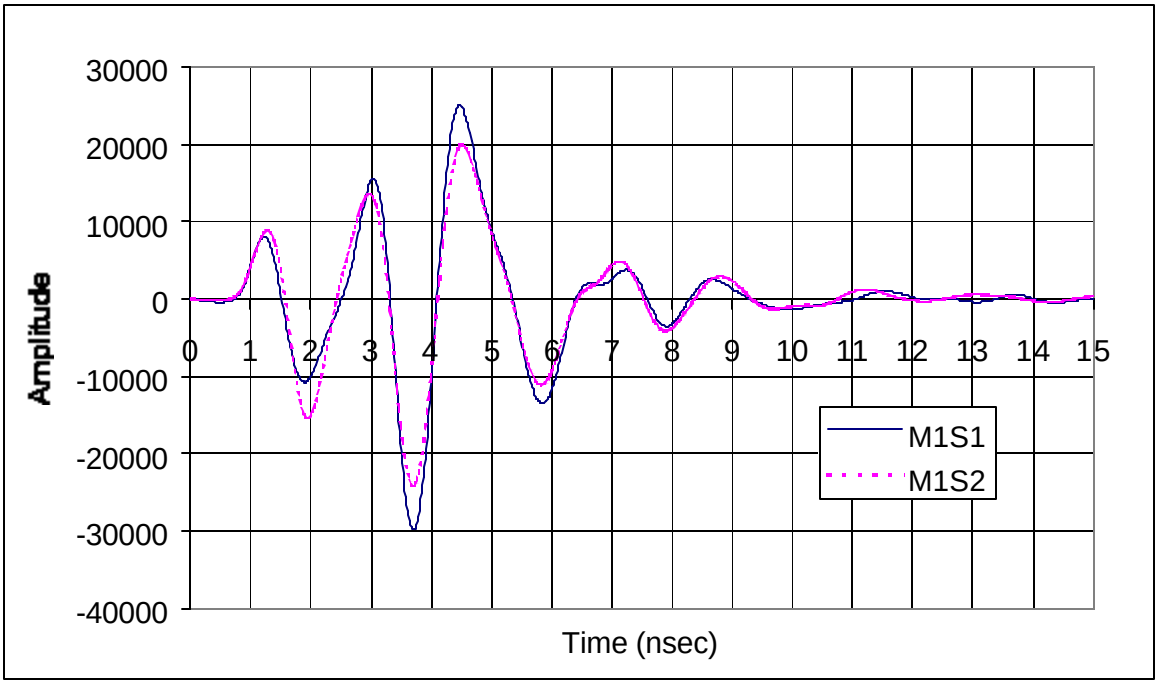

Figure 4.72 Air void effect on ground-coupled waveform for mix M1 (6.4 mm)

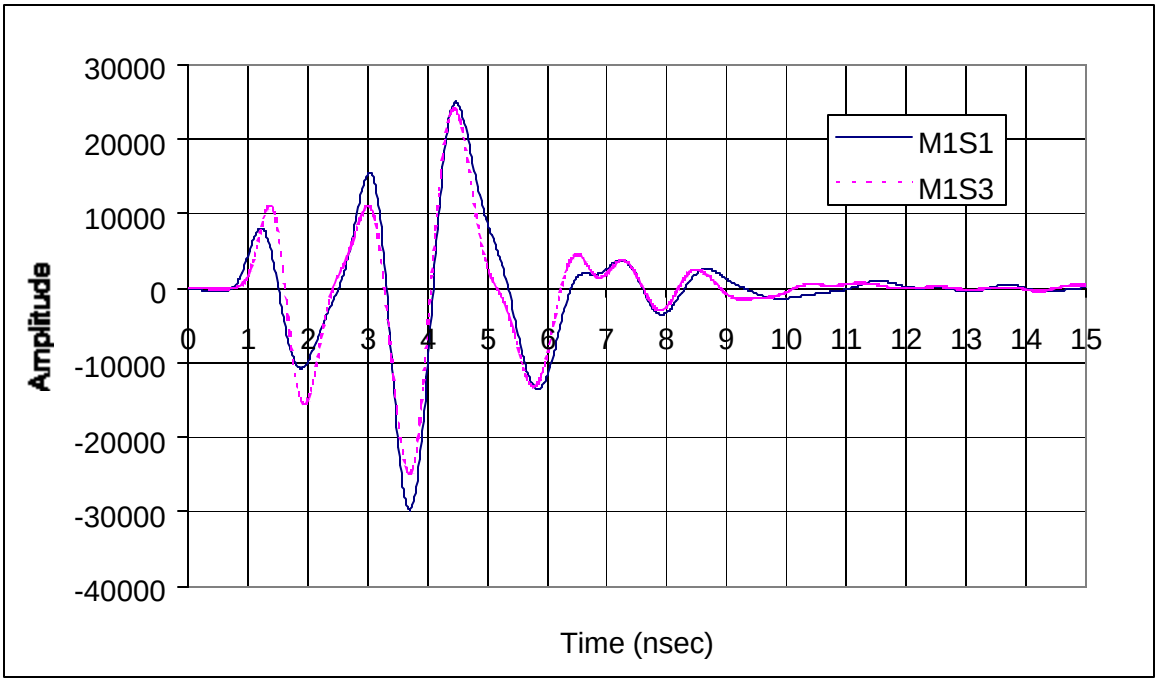

Figure 4.73 Air void effect on ground-coupled waveform for mix M1 (12.7 mm)

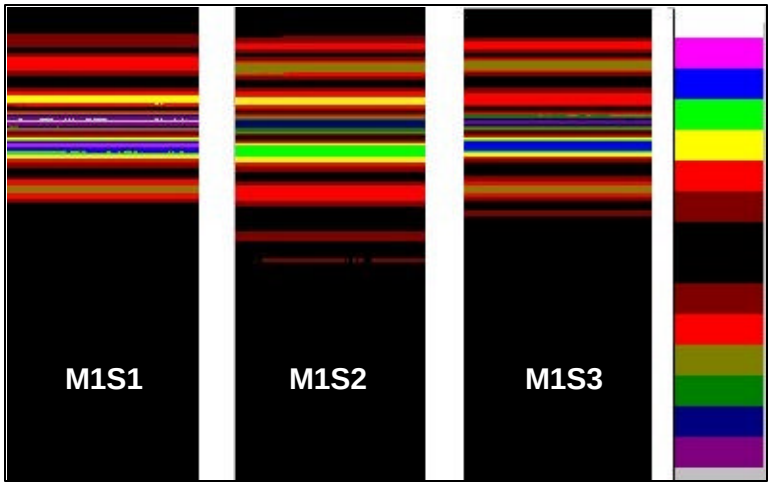

Figure 4.74 Air void effect on ground-coupled linescan representation for mix M1

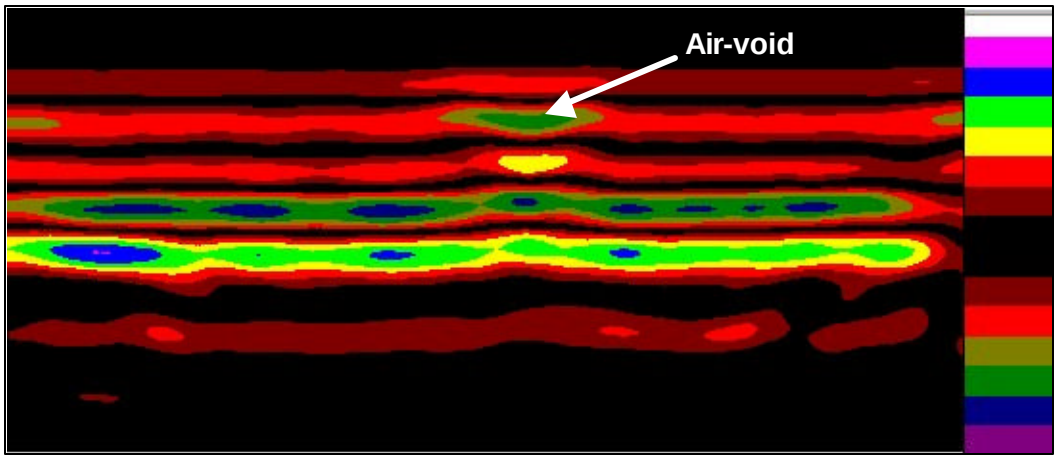

Figure 4.75 Dynamic ground-coupled linescan data for slab M3S4

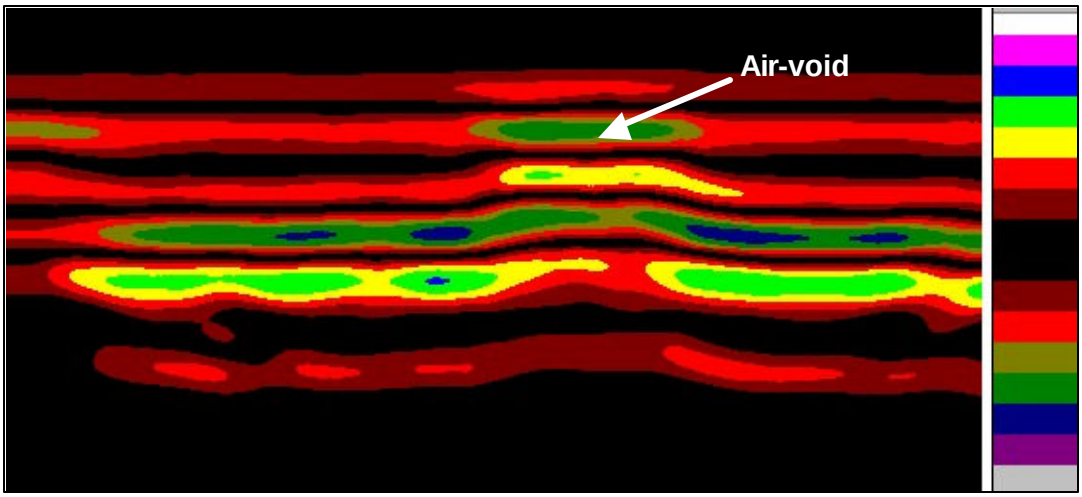

Figure 4.76 Dynamic ground-coupled linescan data for slab M3S5

On November 5, 2000, the ground-coupled GPR system was used to evaluate the effect of water-filled voids on its signal. Figure 4.77 shows the GPR signal for slabs M1S1 (no void) and M1S2 with a water-filled void. From this graph, it can be seen that the water-filled void altered the reflected waveform. The signal distortion cannot be modeled as was done for the air-coupled system because of the ground-coupled properties explained earlier. The only obvious observation is that the water-filled void did reduce the wave speed, as the time length of the waveform from the slab with a water-filled void is larger than that of the waveform obtained from the slab without a void. Similarly, Figure 4.78 shows the waveforms obtained from slab M1S1 and slab M1S3 with a water-filled void. Figure 4.79 shows the linescan representation of the data. The water-filled void presence had the same effects on the other concrete mixes as presented in Figures D12 to D22 (Appendix D).

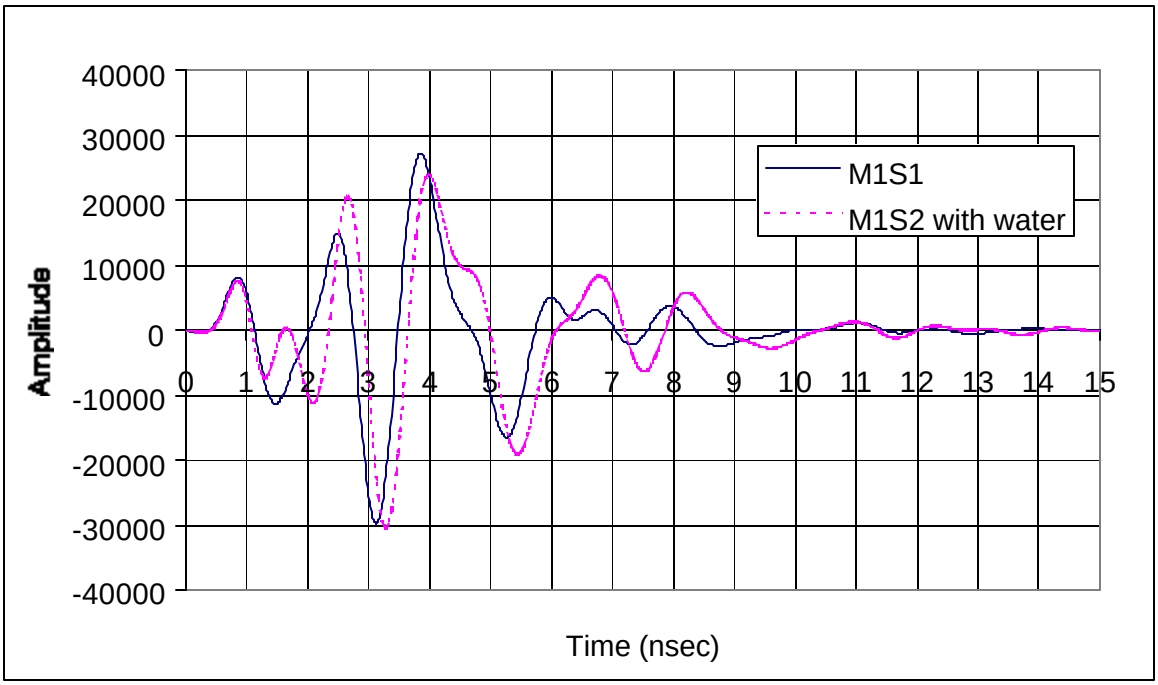

Figure 4.77 Water-filled void effect on ground-coupled waveform for mix M1 (6.4 mm)

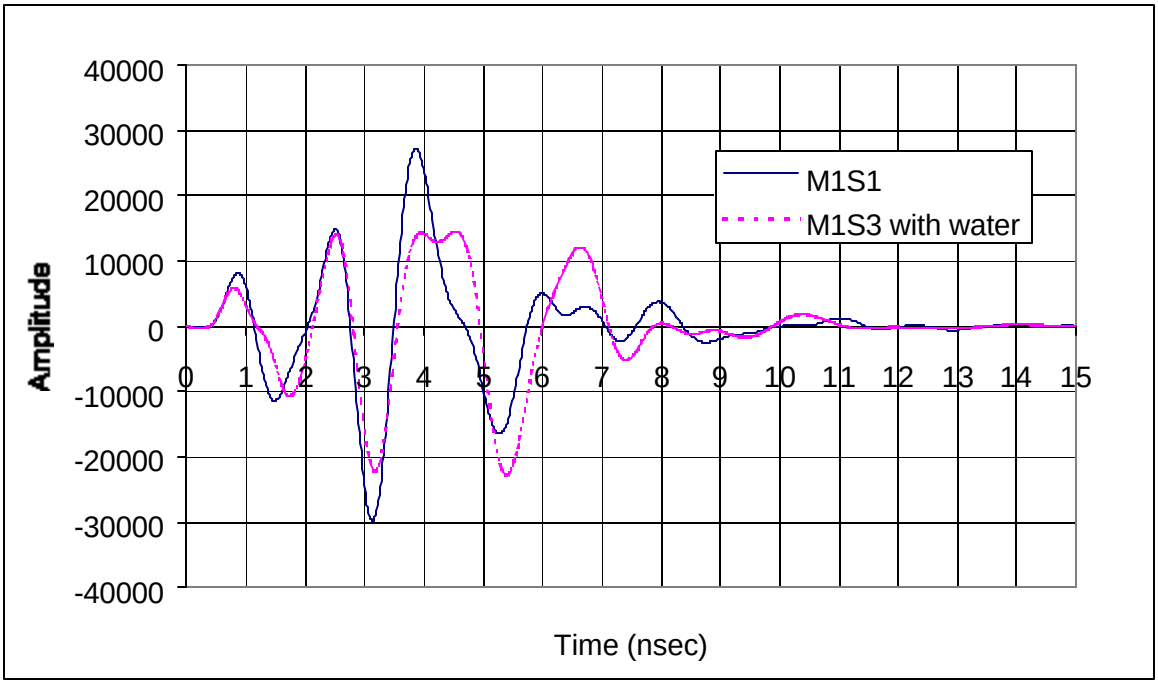

Figure 4.78 Water-filled void effect on ground-coupled waveform for mix M1 (12.7 mm)

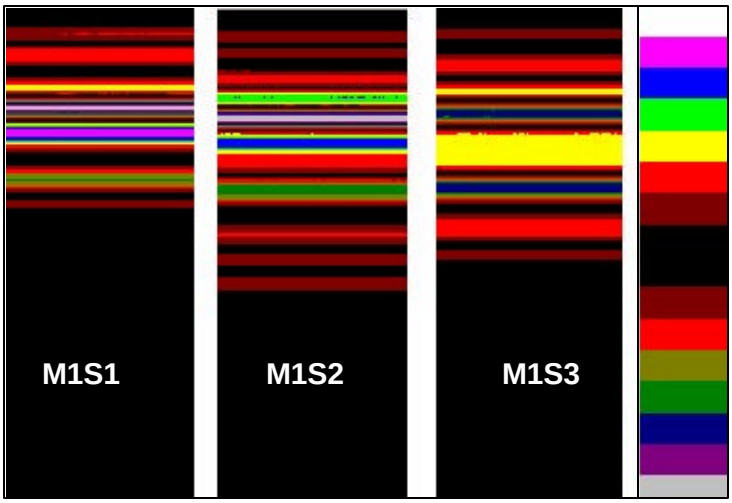

Figure 4.79 Water-filled void effect on ground-coupled linescan representation for mix M1

4.4. Effect of Reinforcement on GPR signal

The effect of steel reinforcement inside concrete on the GPR signal was studied for both air- and ground-coupled systems. For the air-coupled system, since the steel rebar is at 50 mm from the slab surface, its reflection was found to overlap the reflection from the slab surface. For the ground-coupled system, reflection from the steel rebars overlapped with the surface coupling and multiple secondary reflections occurred due to

the ringing problem. Figure 4.80 shows the air-coupled waveforms as obtained from slabs M1S1, M1S4, and M1S5 when the antennas were oriented perpendicular to the main reinforcement. As mentioned earlier, slab M1S1 had no reinforcement, M1S4 was reinforced in one direction, and M1S5 was reinforced in both directions. The waveform obtained from slab M1S5 had increased the amplitude of the first reflection and appeared also to increase the wave speed since the wave time length was smaller. The same had happened with slab M1S4. Figure 4.81 shows the frequency spectrum of the waveforms shown in Figure 4.80. From this figure, it appears that the steel reinforcement increased the amplitude in the frequency range of 550 to 800 MHz, and decreased the amplitude in the frequency range of 800 to 950 MHz. Figure 4.82 shows the waveforms obtained from slabs M1S1, M1S4, and M1S5 when the antennas were oriented in the direction of the main rebars. For slab M1S5, reflection from the longitudinal rebars has affected the GPR signal as when the antennas were oriented perpendicular to the main rebars, but in a smaller scale since the longitudinal bars are smaller in cross section compared to the main rebars. For slab M1S4, the rebars appear not to affect the GPR signal. Figure 4.83 shows the frequency spectrum for the waveforms shown in Figure 4.82. From this graph, the longitudinal reinforcement in slab M1S5 seems to increase the amplitude in the frequency range of 600 to 800 MHz, while the frequency spectrum obtained from slab M1S4 seems to increase, but not significantly, the amplitude in the frequency range of 600 to 750 MHz.

The effect of reinforcement on the air-coupled GPR system signal presented above reflects the observed behavior and was not based on any theoretical analysis. This is due to the limited number of slabs to theoretically study the effect of reinforcement. This could be achieved by making more slabs with different reinforcement spacing, diameter, and depth. Modeling the rebars using commercially available electromagnetic modeling software would help in better understanding the effect of reinforcement on the GPR signal.

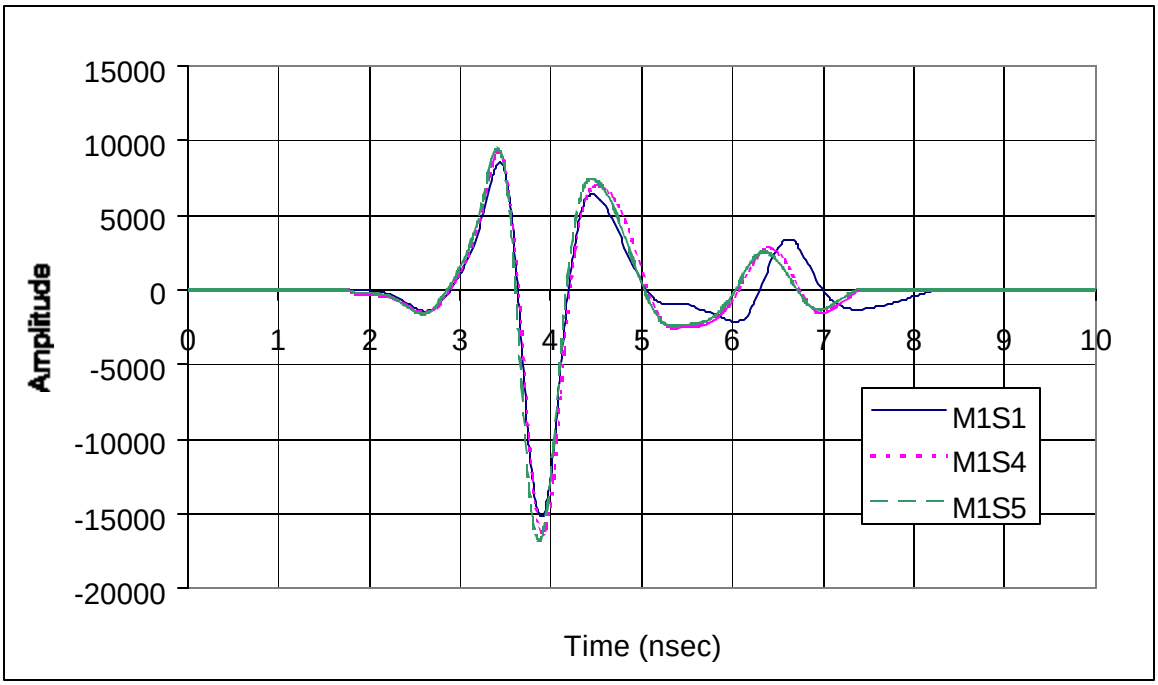

Figure 4.80 Air-coupled GPR waveforms from slabs M1S1, M1S4, and M1S5 when antennas were perpendicular to main rebars

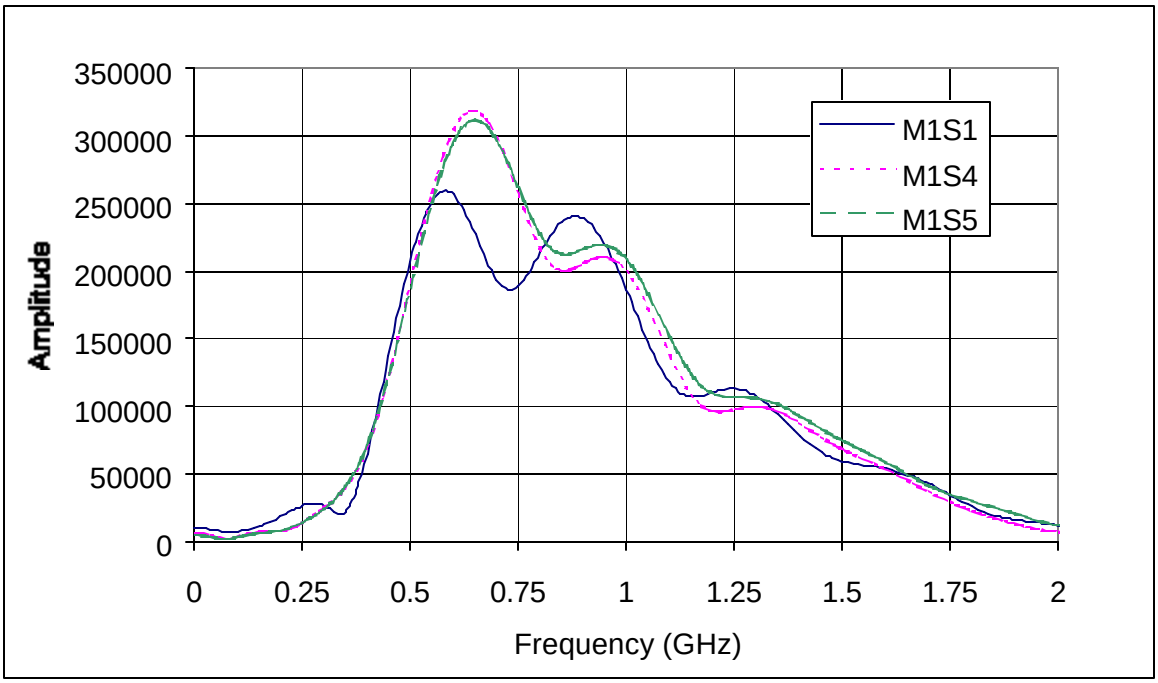

Figure 4.81 Air-coupled GPR frequency spectrums from slabs M1S1, M1S4, and M1S5 when antennas were perpendicular to main rebars

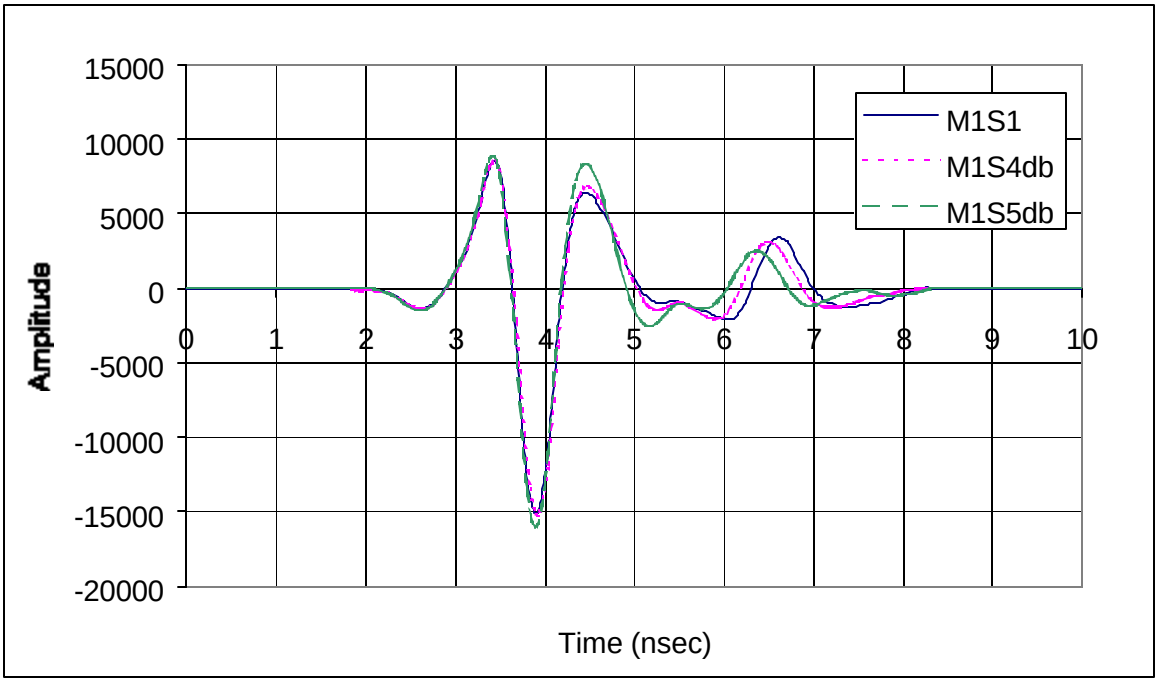

Figure 4.82 Air-coupled GPR waveforms from slabs M1S1, M1S4, and M1S5 when antennas were in the direction of the main rebars (db in legend means direction of bars)

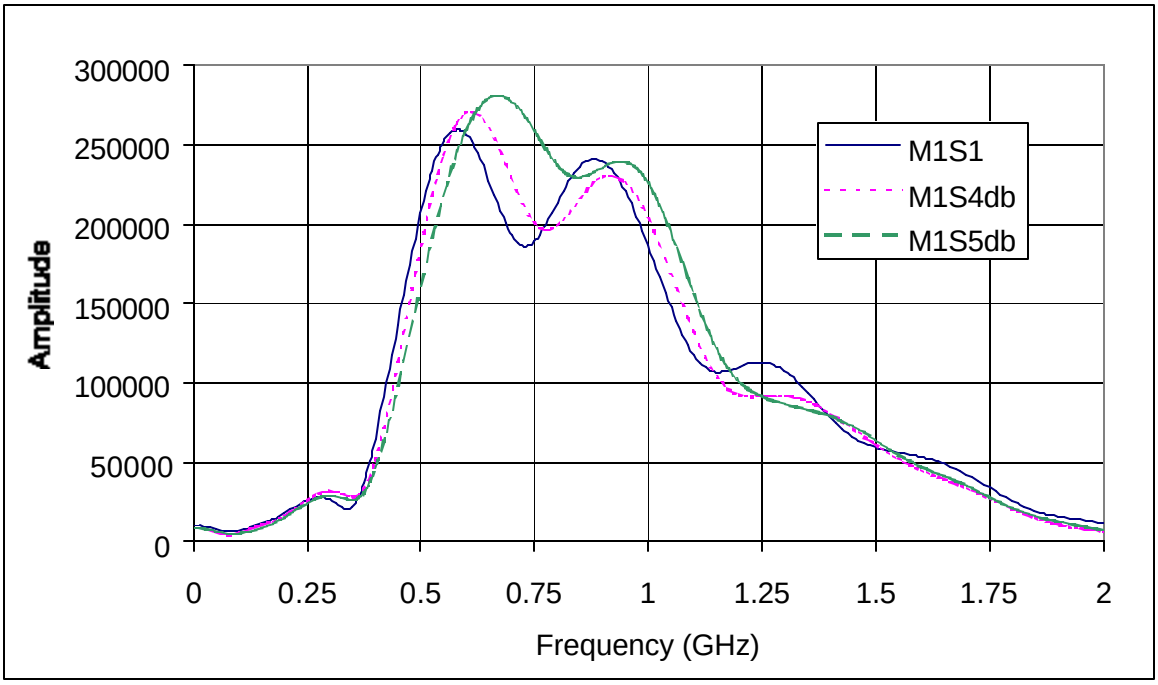

Figure 4.83 Air-coupled GPR frequency spectrums from slabs M1S1, M1S4, and M1S5 when antennas were in the direction of the main rebars (db in legend means direction of bars)

Figure 4.84 shows the waveforms obtained from slabs M1S1, M1S4, and M1S5 using the ground-coupled antenna perpendicular to the main reinforcement, while Figure 4.85 shows the waveforms from the same slabs when the antenna is oriented in the direction of the main rebars. Both figures indicate that when the antenna is perpendicular to the rebar, an increase in the surface coupling occurs followed by a decrease in the other reflections. However, when the antenna is oriented in the direction of the rebars, no significant changes occur in the ground-coupled GPR signal.

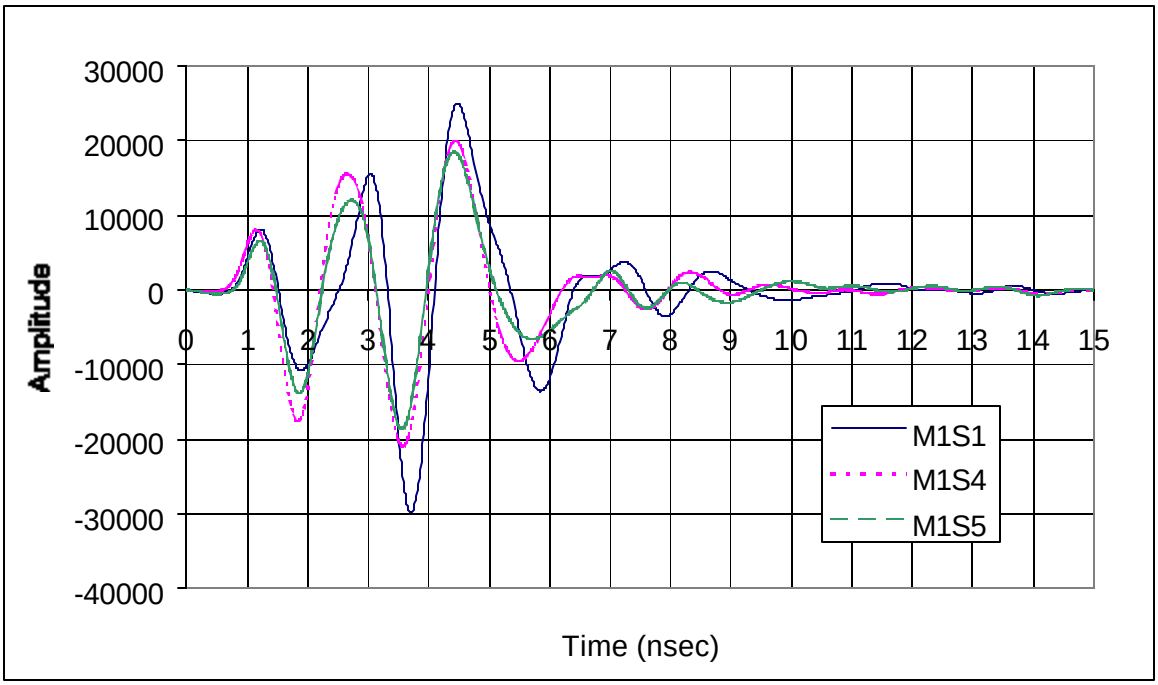

Figure 4.84 Ground-coupled GPR waveforms from slabs M1S1, M1S4, and M1S5 when the antenna was perpendicular to the main rebars

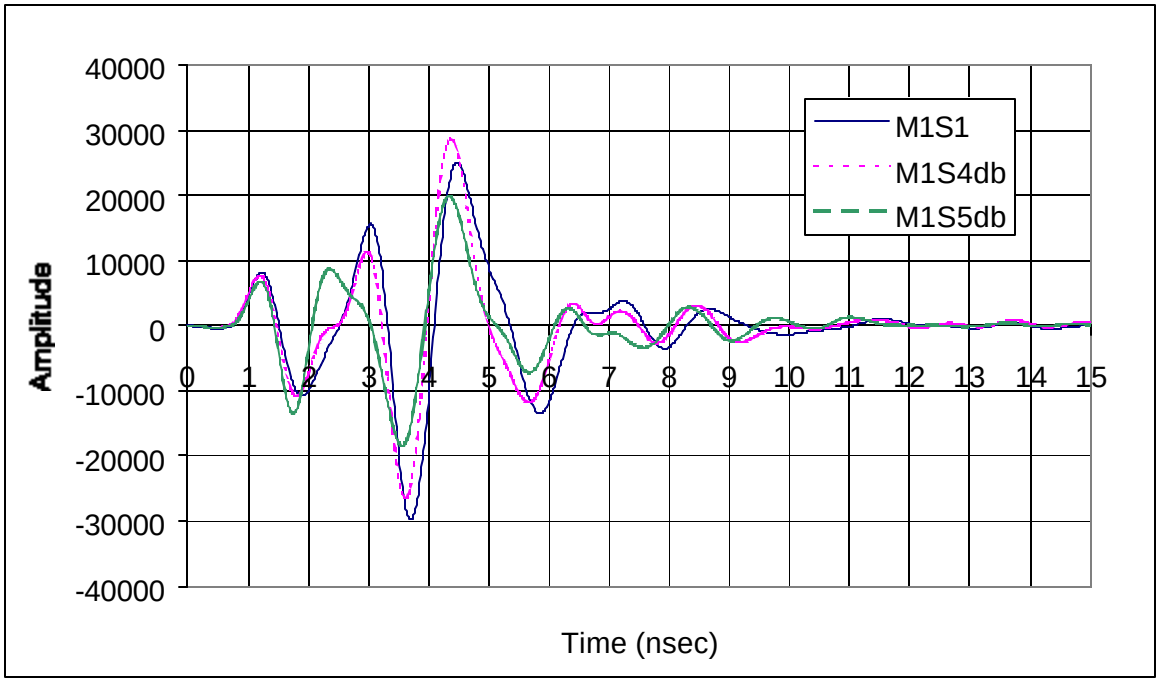

Figure 4.85 Ground-coupled GPR waveforms from slabs M1S1, M1S4, and M1S5 when the antenna was in the direction of the main rebars (db in legend means direction of bars)

Figures 4.86 and 4.87 show the data obtained over slabs M3S6 and M3S7, respectively, when the ground-coupled antenna was moved slowly perpendicular to the main rebars. In both figures, the reinforcement appears as shown by the hyperbola, the shape of which depends on the speed of the antenna. The multiple reflections are also seen in both figures. Figures 4.88 and 4.89 show the data obtained over the same slab, when the antenna was moved slowly in the direction of the main rebars. The reinforcement was not detected in the one-way slab; however, in the two-way slab, the longitudinal reinforcement was detected, but to a lesser extent than the perpendicular ones, as shown by the hyperbolas.

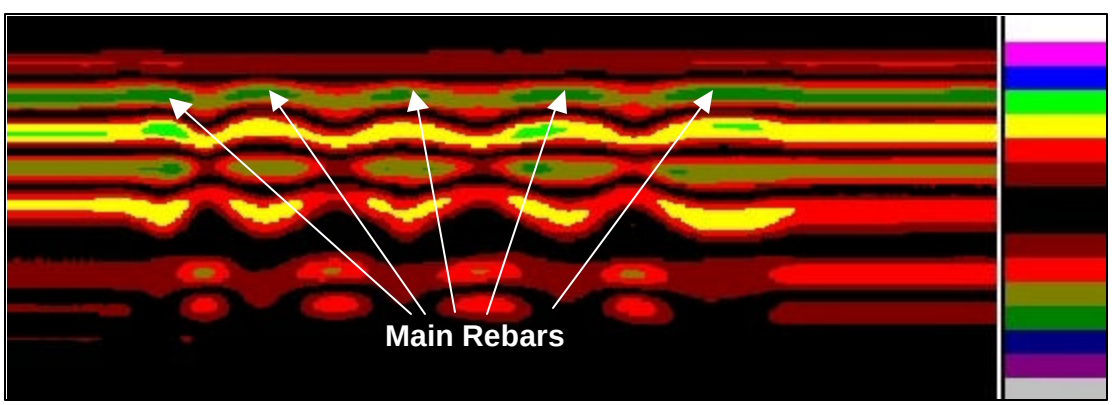

Figure 4.86 Ground-coupled scans over slab M3S6 (perpendicular to the rebars)

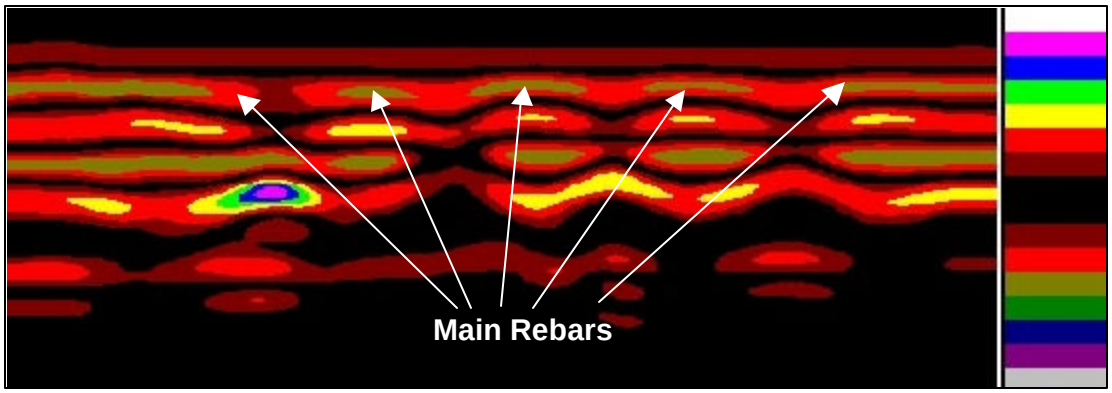

Figure 4.87 Ground-coupled scans over slab M3S7 (perpendicular to the main rebars)

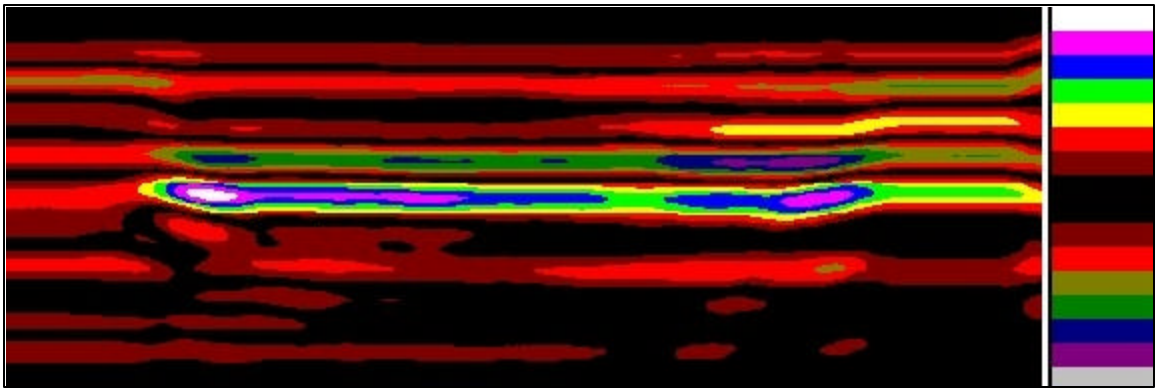

Figure 4.88 Ground-coupled scans over slab M3S6 (direction of the rebars)

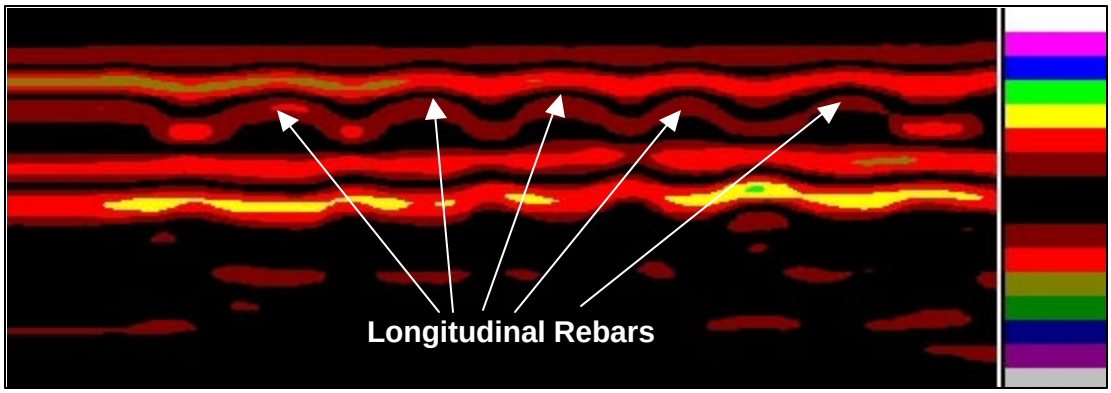

Figure 4.89 Ground-coupled scans over slab M3S7 (direction of the main rebars)

4.5. Layer Thickness Determination in Flexible Pavements

The air-coupled GPR system was used at the nine experimental sections built in Bedford, VA and described earlier in Chapter 3. Thickness measurements for the HMA and base layers were only performed in sections 1, 2, and 3 when a 600-mm strip was excavated in each of the three sections. The reported measurements for section 1 were

approximately 75 mm for the HMA layer and 124 mm for the base layer; for section 2, the reported measurements were 99 mm for the HMA layer and 124 mm for the base layer; and for section 3, the reported measurements were 110 mm for the HMA layer and 121 mm for the base layer (Bhutta, 1998).

A model was developed to predict the radar signal over a flexible pavement with two layers as shown in Figure 4.90. The predicted frequency spectrum is obtained by using Equation (4.34):

$$F_{r,syn} = [\rho_1 + \rho_2 * (1-\rho_1^2) * T1^2 + \rho_3 * (1-\rho_2^2) * (1-\rho_1^2) * T1^2 * T2^2] * F_i \qquad (4.34)$$

where $F_{r,syn}$ is the synthesized frequency spectrum; ρ_1 was previously defined by Equation (4.9); and the other parameters are defined as follows:

$$\rho_2 = \frac{\sqrt{\varepsilon_{HMA}} - \sqrt{\varepsilon_{BASE}}}{\sqrt{\varepsilon_{HMA}} + \sqrt{\varepsilon_{BASE}}} \qquad (4.35)$$

where ε_{HMA} and ε_{BASE} are the complex dielectric constants for the HMA and base layers, respectively.

$$\rho_3 = \frac{\sqrt{\varepsilon_{BASE}} - \sqrt{\varepsilon_{SUBGRADE}}}{\sqrt{\varepsilon_{BASE}} + \sqrt{\varepsilon_{SUBGRADE}}} \qquad (4.36)$$

$\varepsilon_{SUBGRADE}$ is the dielectric constant for the subgrade material.

$$T1 = e^{-j\frac{\omega}{c} d1 \sqrt{\varepsilon_{HMA}}} \qquad (4.37)$$

where d1 is the HMA layer thickness.

$$T2 = e^{-j\frac{\omega}{c} d2 \sqrt{\varepsilon_{BASE}}} \qquad (4.38)$$

where d2 is the base layer thickness. Once the frequency spectrum is synthesized, the modeled time domain signal is obtained using Equation (4.27). All computations were performed using a MATLAB function, presented in Appendix B.

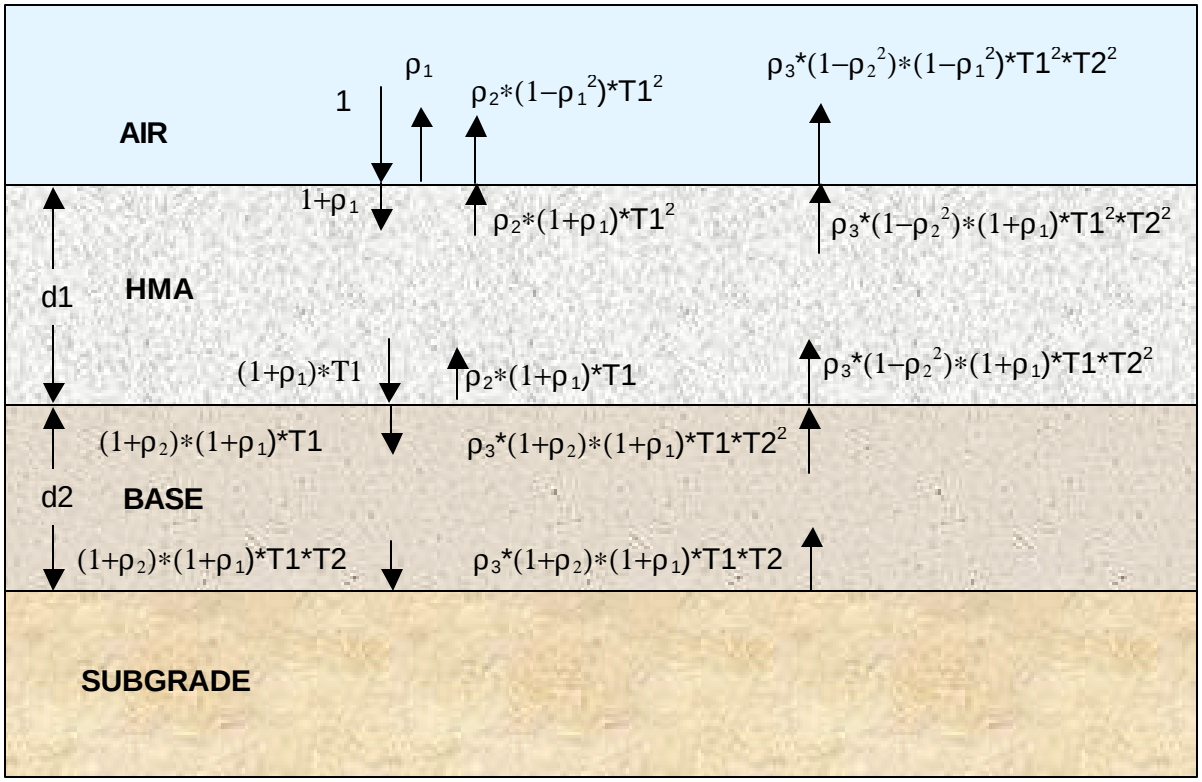

Figure 4.90 Overall reflection model for a flexible pavement with two layers

To predict the layer thicknesses of the experimental sections in Bedford, the forward modeling procedure as proposed by Lau *et al.* (1992) was modified by incorporating into it the model described earlier. The procedure, illustrated in Figure 4.91, consists of inputting ranges for the real and imaginary parts of the dielectric constants for the HMA and base layers and ranges for the expected thicknesses of the two layers. Several frequency spectrums are then generated using Equation (4.34) and the different input properties. The RMSE is then computed for all the frequency spectrums, and the model with the least RMSE is chosen as the solution.

For section 1, the best-modeled spectrum was found for an HMA with a complex dielectric constant of (5.3– 0.3j) and a thickness of 75 mm, a base layer with a complex dielectric constant of (8.5-j) and a thickness of 127 mm, and a subgrade with a real part

of the dielectric constant equal to 40. The computed RMSE between the modeled and measured waveforms, shown in Figure 4.92, with these parameters were found to be equal to 386.8. For both layers, the predicted thicknesses were very close to the reported measured thicknesses.

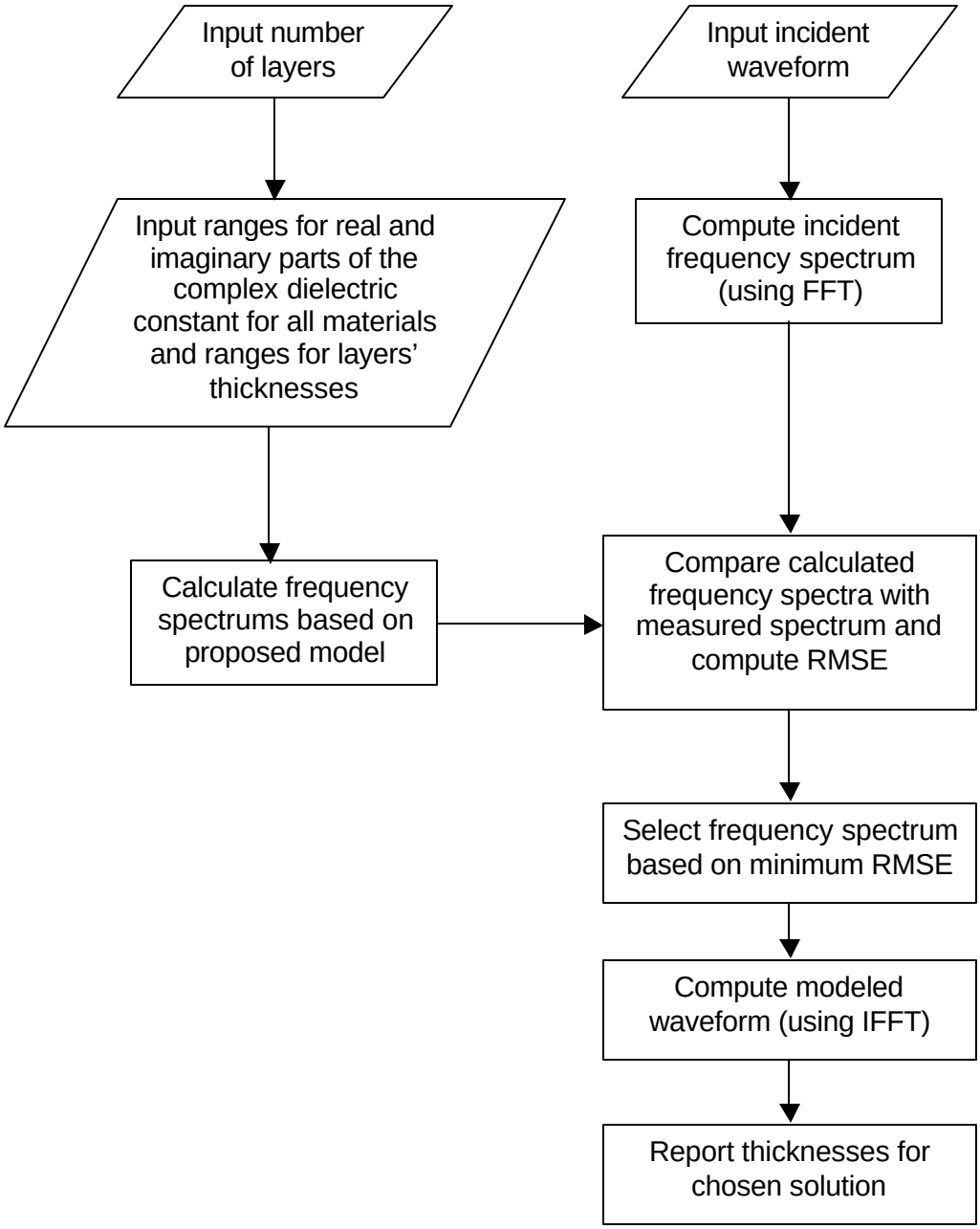

Figure 4.91 Procedure to estimate layer thicknesses in flexible pavements

For section 2, the best-modeled spectrum was found for an HMA with a complex dielectric constant of (5.3– 0.3j) and a thickness of 102 mm, a base layer with a complex dielectric constant of (8.5-j) and a thickness of 121 mm, and a subgrade with a real part of the dielectric constant equal to 40. The computed RMSE between the modeled and measured waveforms, shown in Figure 4.93, with these parameters were found to be equal to 346.7. For both layers, the predicted thicknesses were very close to the reported measured ones.

For section 3, the best-modeled spectrum was found for an HMA with a complex dielectric constant of (5.3– 0.3j) and a thickness of 114 mm, a base layer with a complex dielectric constant of (8.0-j) and a thickness of 121 mm, and a subgrade with a real part of the dielectric constant equal to 40. The computed RMSE between the modeled and measured waveforms, shown in Figure 4.94, with these parameters were found to be equal to 267.2. For both layers, the predicted thicknesses were very close to the reported measured ones.

For section 4, the best-modeled spectrum was found for an HMA with a complex dielectric constant of (5.0– 0.3j) and a thickness of 127 mm, a base layer with a complex dielectric constant of (7-j) and a thickness of 178 mm, and a subgrade with a real part of the dielectric constant equal to 20. The computed RMSE between the modeled and measured waveforms, shown in Figure 4.95, with these parameters were found to be equal to 270.4. No physical measurements for the thicknesses were available to compare with the predicted thicknesses.

For section 5, the best-modeled spectrum was found for an HMA with a complex dielectric constant of (5.3– 0.3j) and a thickness of 109 mm, a base layer with a complex dielectric constant of (7.2-j) and a thickness of 162 mm, and a subgrade with a real part of the dielectric constant equal to 40. The computed RMSE between the modeled and measured waveforms, shown in Figure 4.96, with these parameters were found to be equal to 214.7. No physical measurements for the thicknesses were available to compare with the predicted thicknesses.

For section 6, the best-modeled spectrum was found for an HMA with a complex dielectric constant of (5.3 – 0.3j) and a thickness of 109 mm, a base layer with a

complex dielectric constant of (8.0-j) and a thickness of 228 mm, and a subgrade with a real part of the dielectric constant equal to 50. The computed RMSE between the modeled and measured waveforms, shown in Figure 4.97, with these parameters were found to be equal to 294.1. No physical measurements for the thicknesses were available to compare with the predicted thicknesses.

For section 7, the best-modeled spectrum was found for an HMA with a complex dielectric constant of (5.6 – 0.3j) and a thickness of 102 mm, a base layer with a complex dielectric constant of (8.5-j) and a thickness of 188 mm, and a subgrade with a real part of the dielectric constant equal to 50. The computed RMSE between the modeled and measured waveforms, shown in Figure 4.98, with these parameters were found to be equal to 488.0. No physical measurements for the thicknesses were available to compare with the predicted thicknesses.

For section 8, the best-modeled spectrum was found for an HMA with a complex dielectric constant of (5.3 – 0.3j) and a thickness of 89 mm, a base layer with a complex dielectric constant of (9.0-j) and a thickness of 229 mm, and a subgrade with a real part of the dielectric constant equal to 50. The computed RMSE between the modeled and measured waveforms, shown in Figure 4.99, with these parameters were found to be equal to 274.9. No physical measurements for the thicknesses were available to compare with the predicted thicknesses.

For section 9, the best-modeled spectrum was found for an HMA with a complex dielectric constant of (5.3 – 0.3j) and a thickness of 102 mm, a base layer with a complex dielectric constant of (8.0-j) and a thickness of 216 mm, and a subgrade with a real part of the dielectric constant equal to 50. The computed RMSE between the modeled and measured waveforms, shown in Figure 4.100, with these parameters were found to be equal to 272.3. No physical measurements for the thicknesses were available to compare with the predicted thicknesses.

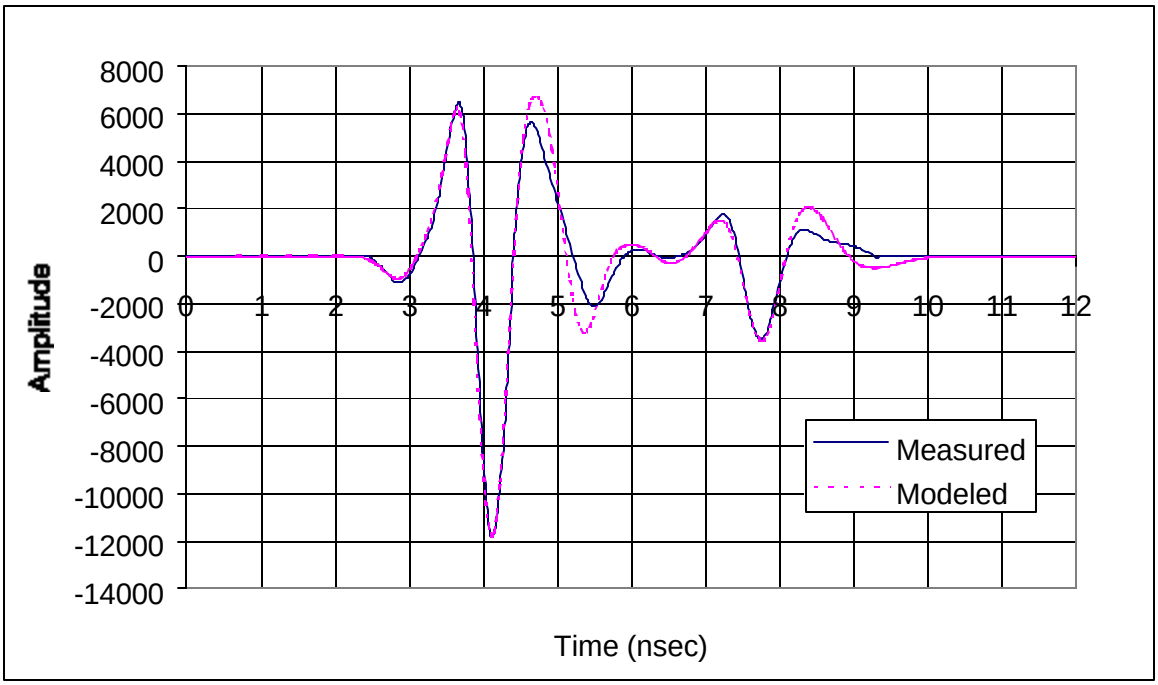

Figure 4.92 Measured and predicted waveforms for Section 1

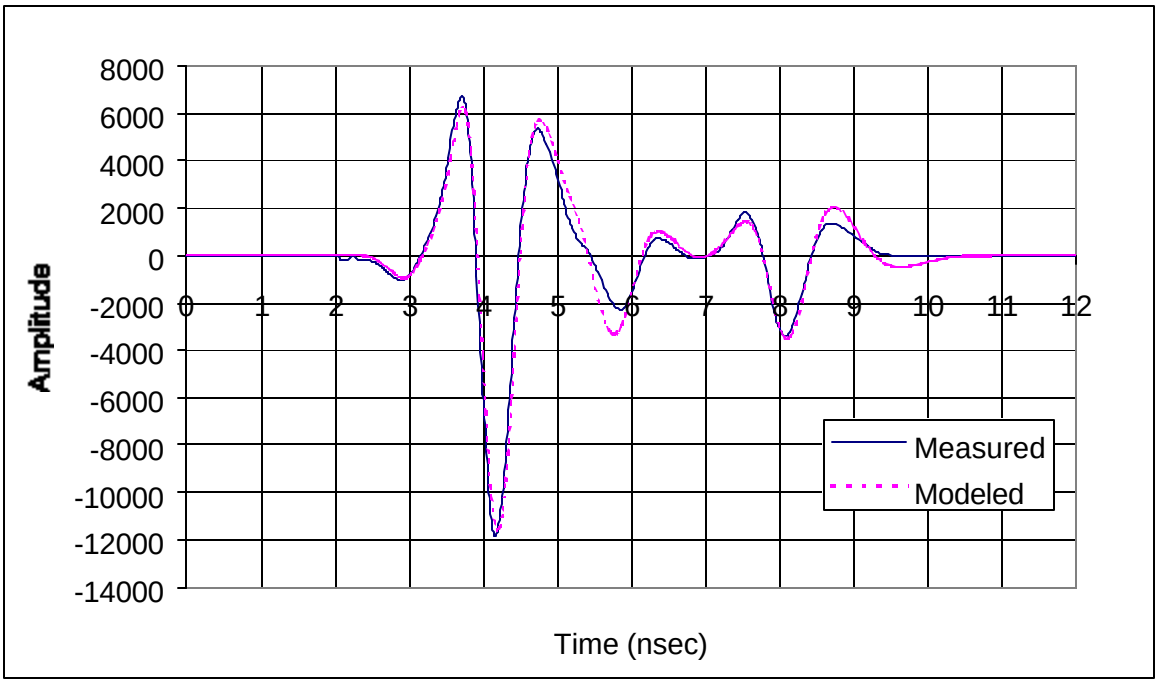

Figure 4.93 Measured and predicted waveforms for Section 2

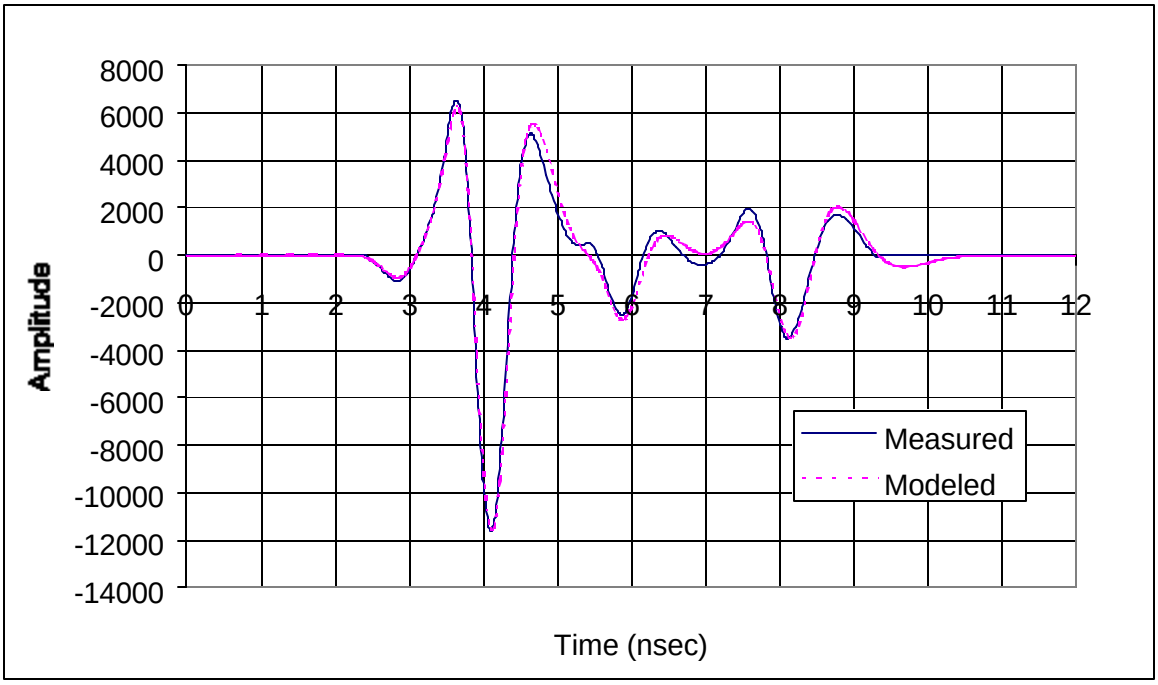

Figure 4.94 Measured and predicted waveforms for Section 3

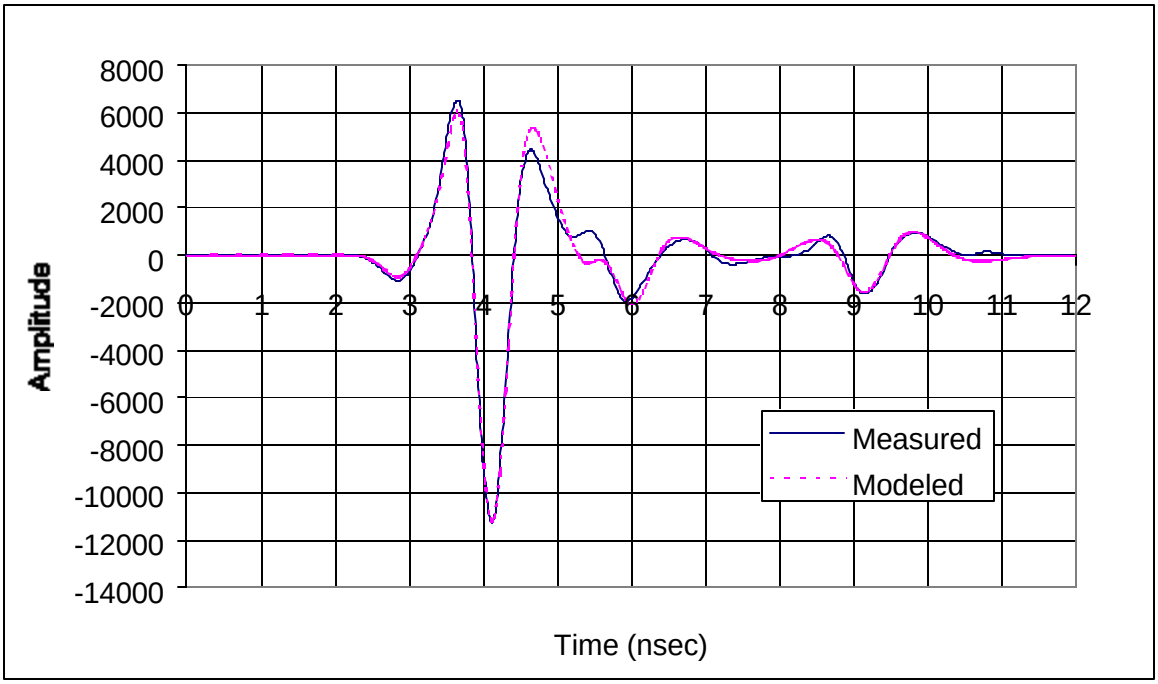

Figure 4.95 Measured and predicted waveforms for Section 4

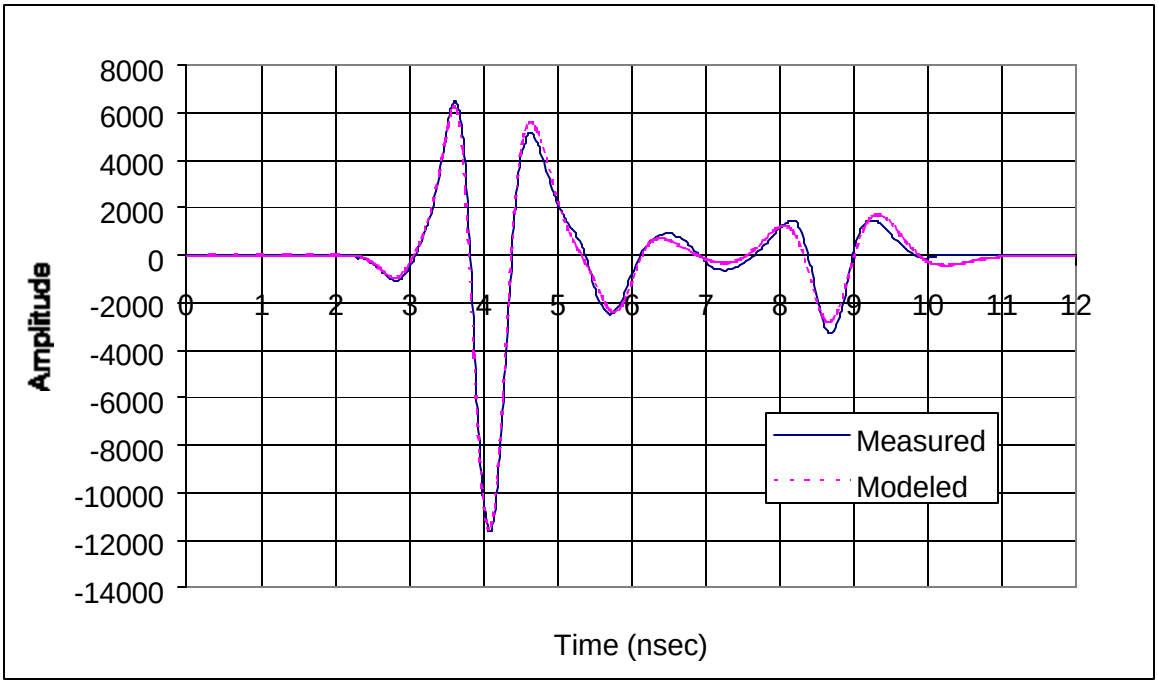

Figure 4.96 Measured and predicted waveforms for Section 5

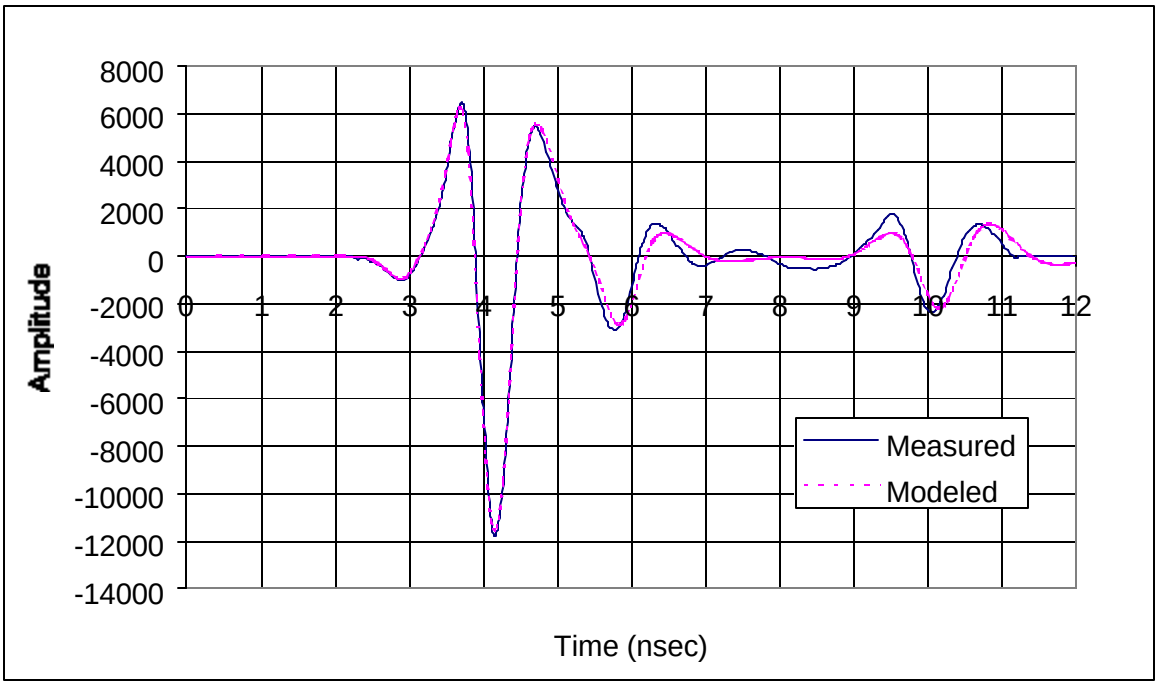

Figure 4.97 Measured and predicted waveforms for Section 6

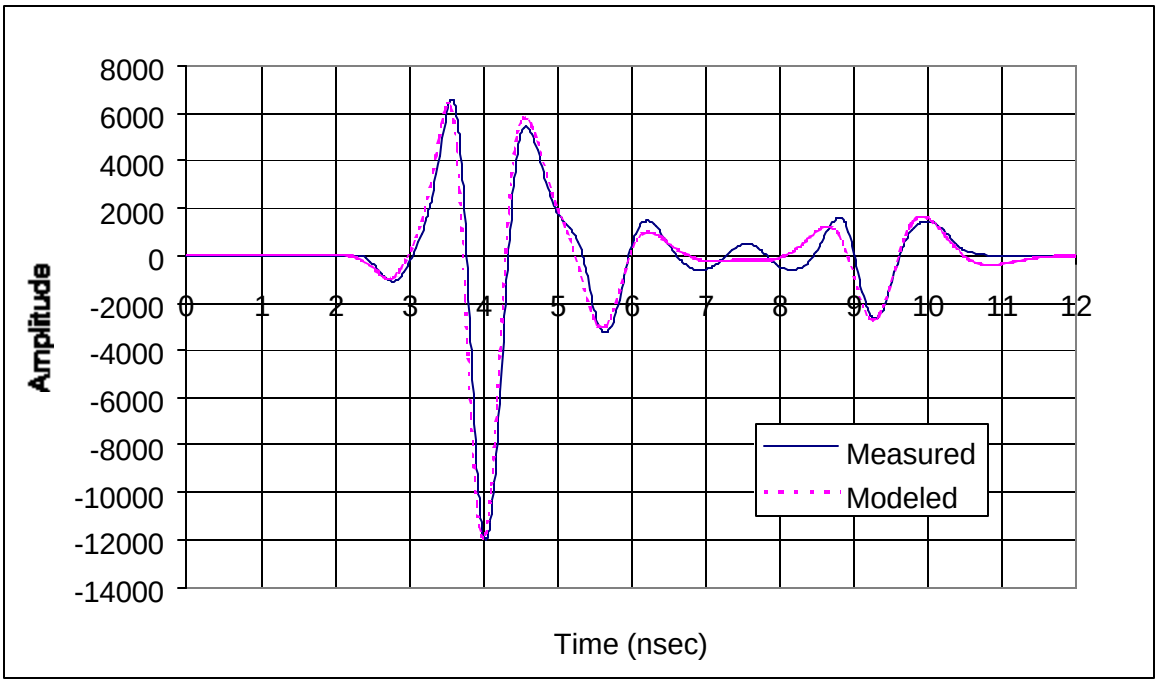

Figure 4.98 Measured and predicted waveforms for Section 7

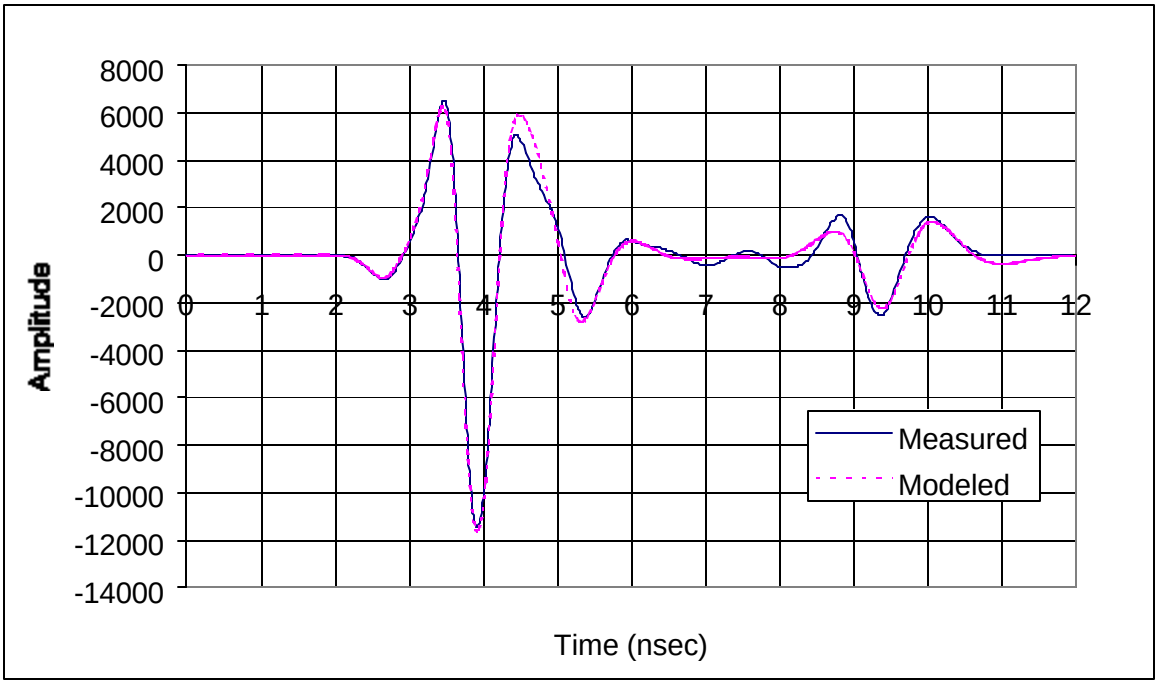

Figure 4.99 Measured and predicted waveforms for Section 8

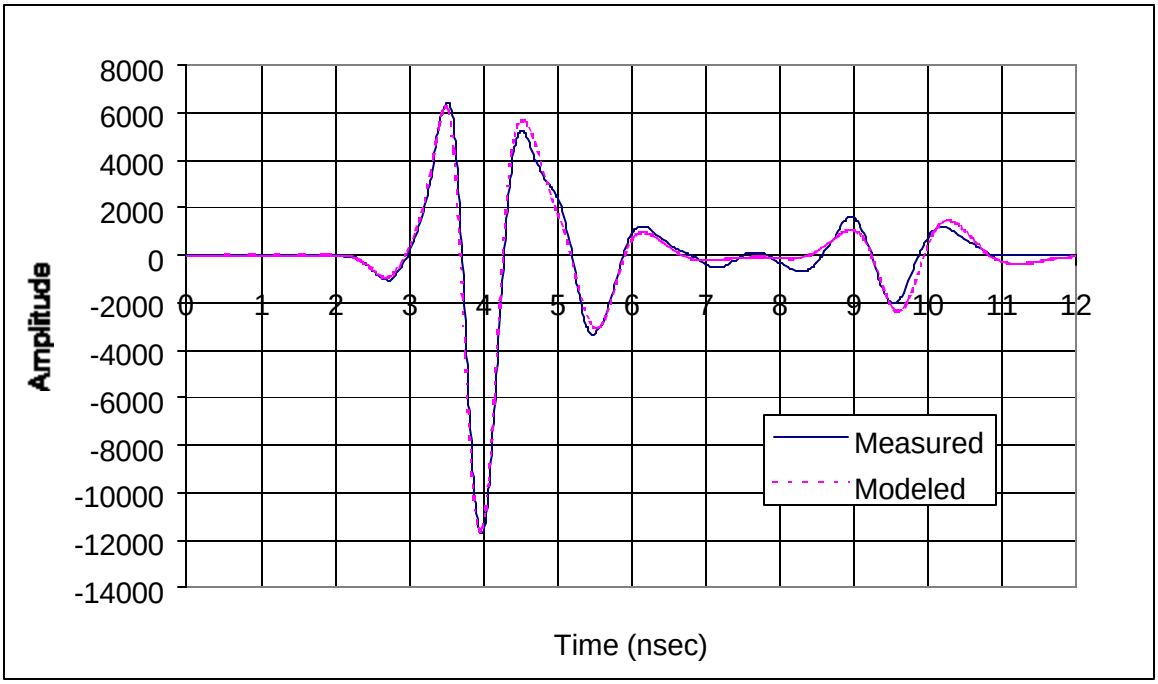

Figure 4.100 Measured and predicted waveforms for Section 9

4.6. Detection of Moisture in Pavement Systems

Drainage is considered as one of the most important factors in pavement design. This is due to the fact that moisture, when present inside a pavement system, may be the main cause of several detrimental effects. It is theoretically believed that if the base, subbase, and subgrade have a drainage capacity greater than the water infiltration rate, then there will be no need for any internal drainage system (Huang, 1993). However, because it is difficult to estimate the infiltration as well as the drainage capacity of the pavement materials over the service life of the pavement, a drainage system is recommended for any pavement structure (Huang, 1993).

4.6.1. Moisture within pavement structures

The primary sources of water in pavement structures are rainwater, high water table, and localized springs. The movement of water inside the pavement can be caused by gravity, capillarity, and/or vapor pressure. In granular materials, the flow is mainly caused by gravity. In fine-grained soils, the flow is mainly due to capillarity. Water can also move in vapor form from warmer to cooler regions due to differences in vapor pressure. The detrimental effects of high water tables have been recognized and well documented; many solutions were reported to intercept groundwater. However, it is only

recently that more attention has been given to finding solutions to intercept water infiltrating through the pavement surface. A Federal Highway Administration (FHWA) study found that 33 to 50% of precipitation water infiltrates through HMA pavements, while 50 to 67% of precipitation water could infiltrate through concrete pavements (Cedergren, 1974). Several methods have been used to limit surface water infiltration, including many types of surface treatments (e.g. chip and slurry seals) and the use of geosynthetics as moisture barriers.

4.6.2. Detrimental effects of water

The detrimental effects of water, when trapped inside a pavement structure, are numerous and could be summarized as follows:

- Water reduces the strength of granular materials and soils.
- A saturated base layer transfers the load from the surface directly to the supporting subgrade without a spreading action.
- Water causes pumping in concrete pavements, which creates voids under the slab. The presence of the void results in faulting and concrete spalling.
- Water presence increases frost/heave problems, which results in a loss of load-carrying capacity of the pavement structure after melting and a differential heaving on swelling soils.
- Deterioration of surface layer (stripping in HMA, and D-cracking in PCA).

4.6.3. Feasibility of using GPR to detect moisture inside pavements: Case studies

The 900-MHz ground-coupled GPR was used in two case studies to evaluate its feasibility as a tool to detect moisture inside the pavement system

In the first study (Al-Qadi *et al.*, 2000), the ground-coupled GPR was used to predict any internal flaws of a newly-constructed road at the National Wildlife Visitor Center in Laurel, Maryland that had failed very prematurely. The road was designed in 1990 and constructed in 1993/1994. It is a 4.3-m-wide one-way road and has a total length of approximately 2680 m. The pavement design required a stable subgrade of compacted native soils, placement and compaction of 254-mm granular base, and placement and compaction of 102-mm HMA. The road surface shows several types of increasing surface distresses with continuing use. The distresses include fatigue cracking, raveling, rutting, shoving, and mix segregation. In some areas, subgrade soils have pumped

through the pavement during wet seasons, and after ground freezing, potholes have formed. Ground penetrating radar, along with FWD testing, visual surveys, and coring, was used to examine the integrity of the structural capacity of the road in order to prepare a work plan for reconstructing the pavement to provide a 20-year design life that accommodates the anticipated traffic.

To determine if moisture exists in the pavement structure, changes in amplitude of the reflected signal were monitored. When moisture is present, the amplitude of the reflected signal becomes high due to the strong contrast between the dielectric constant of water and that of the pavement materials. When moisture is not present, the amplitude of the reflected signal would be much lower since the contrast between the dielectric constants of the pavement materials is usually small.

Figures 4.101 and 4.102 show typical data from the outer wheel path of the road. Moisture was detected by this system along the road either deep in the subgrade or at the interface between the layers. This means that there was a drainage problem, which has been verified by identifying clogged ditches. The spatial location where moisture was present was easily determined. To emphasize the areas where moisture problems exist in the pavement structure, a color code that highlights higher reflections could be used as shown in Figure 4.103. In this figure, only high reflections are presented in the GPR scans.

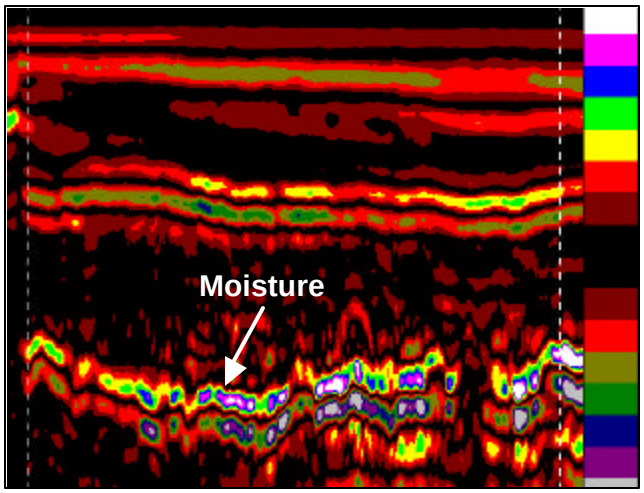

Figure 4.101 High moisture content in the subgrade

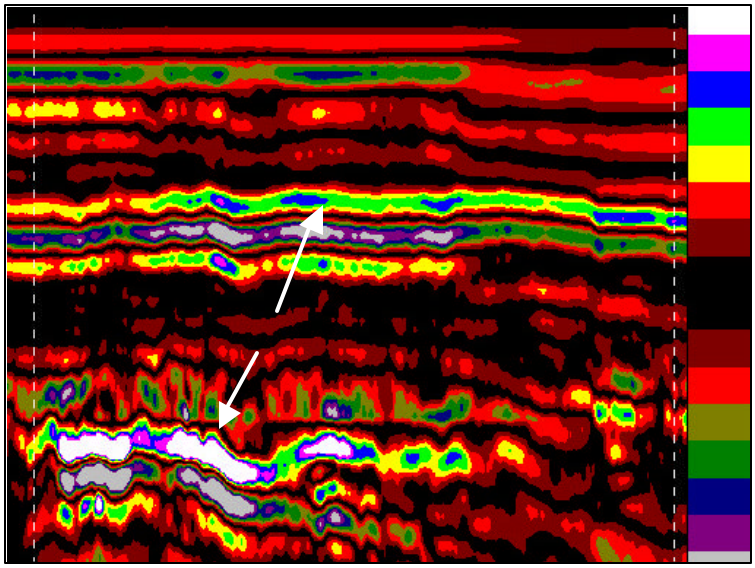

Figure 4.102 High moisture content in the HMA/base interface and in the subgrade

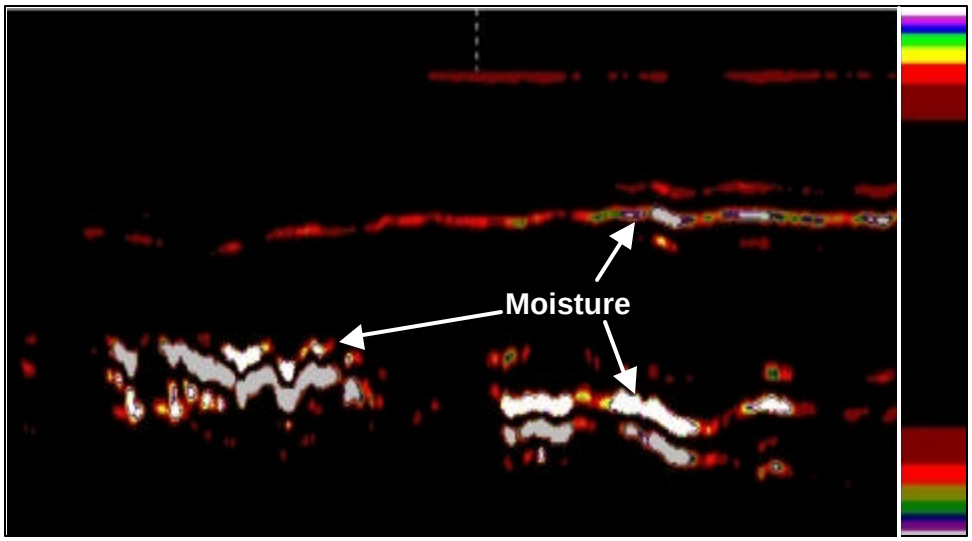

Figure 4.103 Moisture detection using a color code that highlights high reflections

In the second field study (Al-Qadi and Loulizi, 1999), the ground-coupled GPR system was used on different rehabilitated pavement sections in Kernersville, North Carolina. Two sections located at Pineview and Harrisson (urban collector two-way roads) were examined. For Pineview Road, two sections of the road were scanned. The first section is 60 m in length and had a nonwoven geosynthetic material installed prior to placement of the HMA overlay. Data were collected for this part in both traffic directions (at the lane center). The second section, which is 30.5 m in length, has not been rehabilitated. This part has no geosynthetic and shows severe cracking. Both Pineview sections were flat with no considerable longitudinal slope. For Harrisson Road, GPR data were collected in two sections as well: one section with a geosynthetic, and the other section without it. Harrisson Road is over a hill with a longitudinal slope of at least 6%. Figure 4.104 shows the location of the GPR files taken over Harrisson Road.

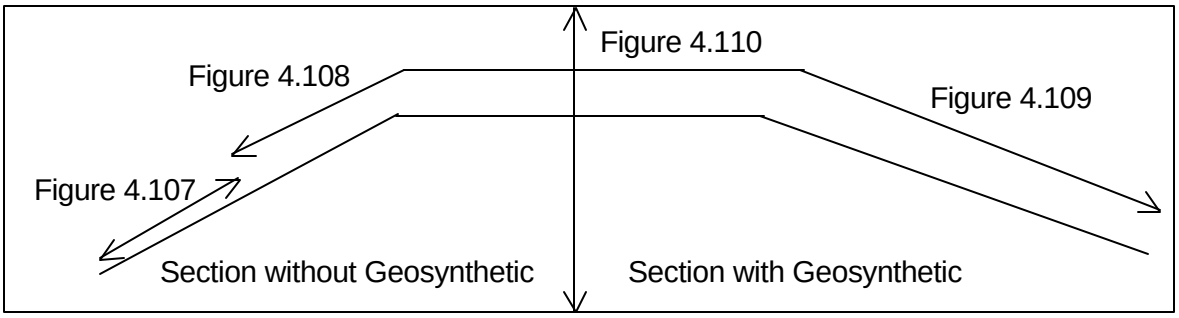

Figure 4.104 Location of GPR files over Harrisson Road

The criterion used to determine if moisture exists in the bottom of the HMA overlay is change in the amplitude of the first reflected signal. When moisture is present, the amplitude of this signal is high due to the strong contrast between the dielectric constant of water and that of the HMA material. When moisture is absent, the amplitude of the first signal would be low since there is no significant difference in the dielectric constants of the HMA overlay and the existing overlaid wearing surface.

Figure 4.105 shows a GPR profile from the first part of Pineview Road, which has the geosynthetic material. The GPR scans over this section did not show any significant presence of moisture in both directions of the road. However, the second part of Pineview Road has some cracks in the HMA and hence the GPR scans obtained from

this part showed high reflections at the pavement surface, as shown in Figure 4.106, as moisture was penetrating through and filling the cracks.

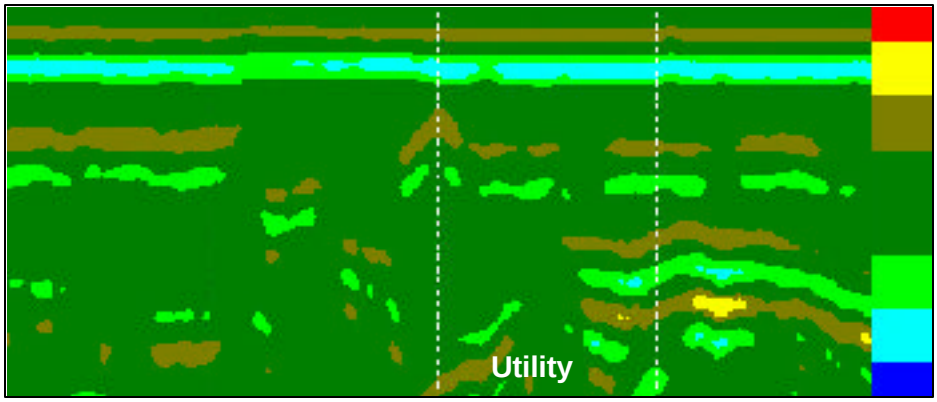

Figure 4.105 Radar scans of Pineview Road (section 1)

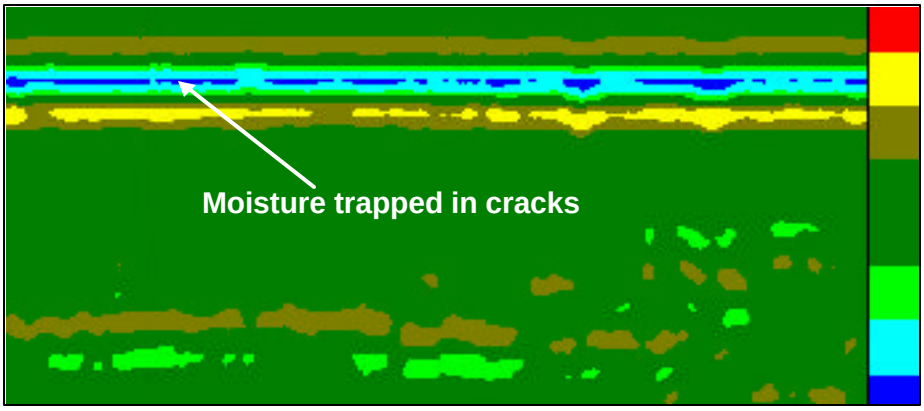

Figure 4.106 Radar scans of Pineview Road (section 2)

Figure 4.107 shows the GPR profile for the Harrisson Road section (refer to Figure 4.104) located down the hill (no geosynthetic). A significant amount of moisture accumulation was detected in the subgrade, with some in the base layer. This could be attributed to water flowing from the top of the hill. No moisture was detected between the old wearing surface and the overlay, however. Similarly, Figure 4.108 represents the pavement section located down the hill in the portion without geosynthetic. From this figure, moisture appears to be present only within the old pavement. Moisture at the bottom is due to water flowing from the top and also from infiltration. Figures 4.109 and 4.110 represent GPR scans of the portion, which has geosynthetic (refer to Figure 4.104). Figure 4.109 represents the pavement located down hill. From this figure, moisture appears to be present both at the top and bottom parts of the pavement

system. Moisture at the bottom of the pavement system is due to water flowing down the hill (as in the previous portion), while moisture in the top part is located at the top of the geosynthetic. Figure 4.110 represents the pavement at the top of the hill (flat surface). No moisture is found in the lower layers of the pavement, while there are some traces of moisture in the upper layers where the geosynthetic is present.

In both case studies, data from the ground-coupled GPR was used to establish a spatial layout of the areas where moisture is present within the pavement system by monitoring the amplitude of the reflected signal. In the first case study, the spatial layout where moisture was detected was used to properly rehabilitate the deteriorating pavement. In the second study, the GPR data have shown that moisture had accumulated in the base and the subgrade in the sections without geosynthetic material, while in the sections with geosynthetic, moisture was present above the moisture barrier. Therefore, the ground-coupled GPR has proven to be a feasible tool to detect moisture inside pavement structures.

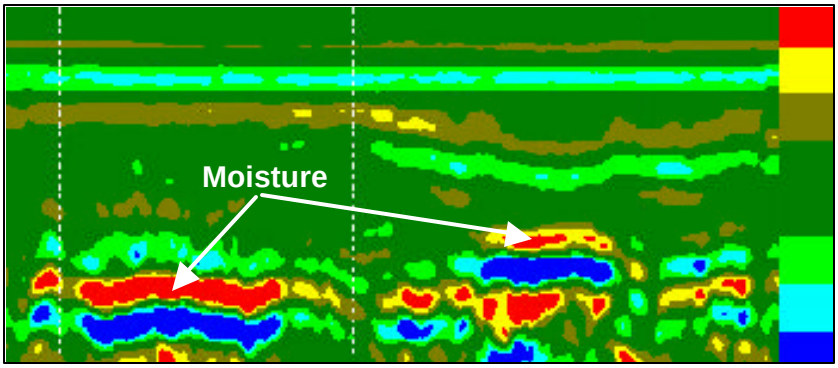

Figure 4.107 Radar scans of Harrisson Road (without geosynthetic)

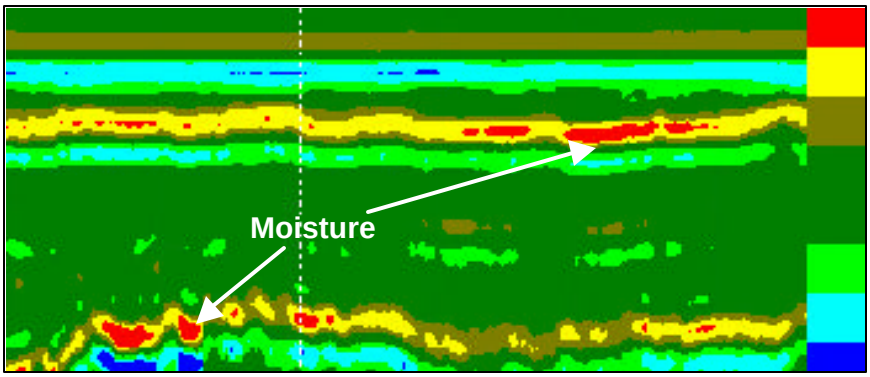

Figure 4.108 Radar scans of Harrisson Road (without geosynthetic)

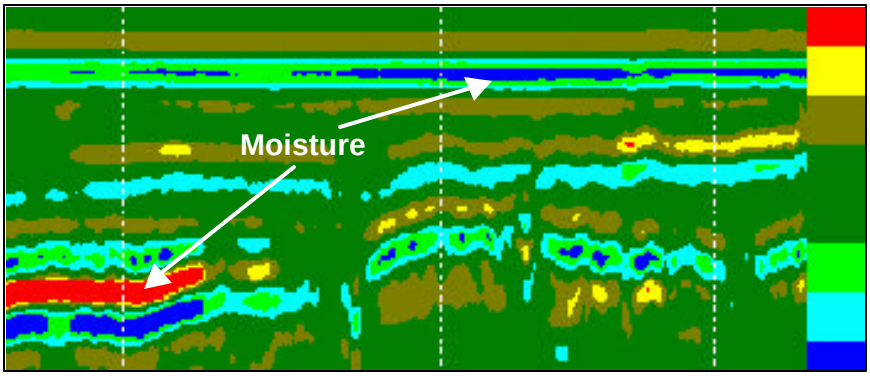

Figure 4.109 Radar scans of Harrisson Road (with geosynthetic, down the hill)

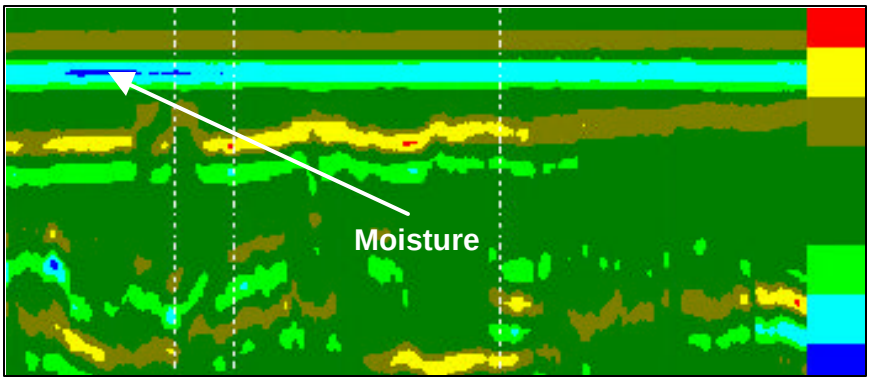

Figure 4.110 Radar scans of Harrisson Road (with geosynthetic, top of Hill)

Chapter 5. FINDINGS AND CONCLUSIONS

This research was aimed at establishing a better understanding of analyzing GPR data obtained from assessing transportation infrastructure. Two GPR systems were used: a ground-coupled system and an air-coupled system. The dielectric properties of different Portland cement concrete mixes were measured using the air-coupled system data over the frequency range of 0.5 to 1 GHz. The effect of concrete air voids and water-filled voids on both GPR systems was examined. A model to predict the air-coupled GPR system signal was developed for concrete slabs with an internal defect. The effect of reinforcement on both GPR systems was also studied. A method to measure the thicknesses of the layers in flexible pavements was developed, which incorporates the energy loss inside the pavement materials. During this research, several findings and conclusions were drawn.

5.1. Findings

During this research, reported herein, the following were found:

- The complex dielectric constant of Portland cement concrete was found to be frequency dependent in the frequency range of 0.5 to 1 GHz. However, an average complex value provided accurate predictions of the air-coupled GPR system.
- The complex dielectric constant of Portland cement concrete is dependent on the mix constituents.
- For the same moisture content, concrete with limestone aggregate has a greater real part of the dielectric constant than concrete cast with quartzite aggregate.
- Silica fume increases the real part of the complex dielectric constant of concrete.
- Reflections from air voids and water-filled voids located at 50 mm from the surface overlap with the surface reflection. However, the shape of the GPR signal is distorted.
- Reinforcing steel bars perpendicular to the air-coupled antennas distort the shape of the returned waveform by increasing the amplitude of the surface reflection. However, parallel bars do not disturb the reflected waveforms.
- The loss part of the dielectric constant should be included in any GPR modeling to assure accurate results.

- Data from ground-coupled GPR systems is mostly qualitative due to the surface coupling and antenna ringing.

5.2. Conclusions

Based on the objectives of this research, the following conclusions can be drawn:

- Modeling the expected air-coupled GPR signal is a powerful tool to better understand the measured signals.
- Current methods to measure layer thicknesses based on the assumption that there are no losses inside pavement materials do not provide accurate results. The loss part, especially in the base material, should be considered in highway assessment surveys.
- Air-coupled GPR systems operating at 1 GHz center frequency may be used on a routine basis to assess concrete bridge decks and flexible pavements, and as a quality control tool for new flexible pavements to verify the as-built thicknesses.
- Ground-coupled and air-coupled GPR systems were successfully used to detect defects in concrete slabs, including air and water-filled voids.

Chapter 6. RECOMMENDATIONS

Based on the findings of the present study, the following recommendations are made:

- The effects of overlays on the air-coupled and ground-coupled GPR system waveforms need to be studied.
- The effect of debonding between the concrete and the HMA overlay on the GPR signals may need to be investigated.
- A database of the complex dielectric constant of base materials at different moisture contents needs to be established.
- The effectiveness of GPR in detecting HMA stripping may need to be quantified.
- Further validation of the proposed modeling to measure the thicknesses of the layers on other known pavements needs to be conducted.

REFERENCES

ACI Committee 212 (1981), "Admixtures for Concrete," *Concrete International*, *Vol. 3*, No. 5, pp. 24-52.

Al-Qadi, I.L. (1992a), "The Penetration of Electromagnetic Waves Into Hot-Mix Asphalt," Proceedings of the Nondestructive Evaluation of Civil Structures and Materials, Boulder, CO, May 11-13, pp. 195-209.

Al-Qadi, I.L. (1992b), "Using Microwave Measurements to Detect Moisture in Asphaltic Concrete," *ASTM Journal of Testing and Evaluation*, *Vol. 20*, No. 1, January, pp. 43-50.

Al-Qadi, I.L., and Loulizi, A. (1999), "Using GPR to Evaluate the Effectiveness of Moisture Barriers in Pavements," Structural Faults and Repair 99, 8th International Conference, Forde, M. C., ed., London, England, July 13-15.

Al-Qadi, I.L., and Riad, S.M. (1996), Characterization of Portland Cement Concrete: Electromagnetic and Ultrasonic Measurement Techniques, Report submitted to the National Science Foundation, September.

Al-Qadi, I.L., Lahouar, S., and Loulizi, A. (2001), Assessment of I-81 Using Ground Penetrating Radar, Report submitted to the Virginia Department of Transportation, January.

Al-Qadi, I.L., Loulizi, A., and Oosterbaan, M. D. (2000), "Using Ground Penetrating Radar to Evaluate Pavement Structures," Nondestructive Testing in Civil Engineering 2000, Taketo Uomoto, ed., Tokyo, Japan, April 25-27, pp. 499-508.

Al-Qadi, I.L., Riad, S.M., Su, W.U., and Haddad, R.H. (1996), "Detecting Flaws in Portland Cement Concrete Using TEM Horn Antennae," *SPIE, Vol. 2946*, pp. 28-39.

ASTM C125, "Standard Terminology Relating to Concrete and Concrete Aggregates."

ASTM C876-91, "Standard Test Method for Half-Cell Potentials of Uncoated Reinforcing Steel in Concrete."

ASTM D1561, "Standard Practice for Preparation of Bituminous Mixture Test Specimens by Means of California Kneading Compactor."

ASTM D4580, "Standard Practice for Measuring Delaminations in Concrete Bridge Decks by Sounding."

ASTM E274, "Standard Test Method for Skid Resistance of Paved Surfaces Using a Full-Scale Tire."

ASTM E445, “Standard Test Method for Stopping Distance on Paved Surfaces Using a Passenger Vehicle equipped with Full-Scale Tires.”

ASTM E670, “Standard Test Method for Side Force Friction on Paved Surfaces Using the Mu-Meter.”

Azevedo, S. *et al.* (1996), “HERMES: a High-Speed Radar Imaging System for Inspection of Bridge Decks,” Proceedings of SPIE - The International Society for Optical Engineering, Vol. 2946, pp. 195-204.

Barnes, C.L., and Trottier, J.F. (2000), “Ground Penetrating Radar for Network Level Concrete Deck Repair Management,” *Journal of Transportation Engineering, Vol. 126,* No. 3, May-June, pp. 257-262.

Bettigole, N. and Robinson, R. (1997), *Bridge Decks*, American Society of Civil Engineers, New York.

Bhutta, S. (1998), Mechanistic-Empirical Pavement Design Procedure For Geosynthetically Stabilized Flexible Pavements, PhD Dissertation, Civil Engineering Department, Virginia Tech, April.

Bomar, L.C., Horne, W.F., Brown, D. R., and Smart, J.L. (1988), Determining Deteriorated Areas in Portland Cement Concrete Pavements Using Radar and Video Imaging, NCHRP 304, Transportation Research Board, Washington, D.C.

Bourgeois, J.M., and Smith, G.S. (1996), “A Fully Three-Dimensional Simulation of a Ground-Penetrating Radar: FDTD Theory Compared with Experiment,” *IEEE Transactions on Geoscience and Remote Sensing, Vol. 34*, No. 1, Jan., pp. 36-44.

Bungey, J.H., and Millard, S.G. (1993), “Radar Inspection of Structures,” Proceedings of the Institution of Civil Engineers Structures and Buildings, Vol. 99, pp. 173-186.

Bungey, J.H., Millard, S.G., and Shaw, M.R. (1994), “The Influence of Reinforcing Steel on Radar Surveys of Concrete Structures,” *Construction and Building Materials*, *Vol. 8,* No. 2, pp. 119-126.

Büyüköztürk, O., and Rhim, H.C. (1996), ”Detection of Delaminations in Concrete Using a Wideband Radar,” Structural Materials Technology: An NDT Conference, P. Hartbrower and P. J. Stolarski, eds., Feb., pp. 55-60.

Campbell, K.J., and Orange, A.S. (1974), “A Continuous Profile of Sea Ice and Freshwater Ice Thickness by Impulse Radar,” *Polar Rec., Vol. 17,* No. 31.

Cedergren, H.R. (1974), *Drainage of Highway and Airfield Pavements*, John Wiley and Sons, Inc., New York.

Chen, H.L.R., Halabe, U.B, Sami, Z., and Bhandarkar, V. (1994), "Impulse Radar Reflection Waveforms of Simulated Reinforced Concrete Bridge Decks," *Materials Evaluation, Vol. 52*, No. 12, Dec., pp. 1382-1388.

Clemena, G. (1983), "Nondestructive Inspection of Overlaid Bridge Decks with Ground Penetrating Radar," *Transportation Research Record*, No. 899, Transportation Research Board, Washington, D.C.

Clemena, G., Sprinkle, M., and Long, R. (1986), Use of Ground Penetrating Radar for Detecting Voids Underneath a Jointed Concrete Pavement, Final Report, Virginia Highway and Transportation Council, Charlottesville, VA..

Conway, B.V. (1995), "Bodies of Evidence: Site Surveying with Ground Radar," *IEE Colloquium (Digest)*, No. 115, Stevenage, England.

Davidson, N.C, and Chase, S.B. (1999), "Initial Testing of Advanced Ground-Penetrating Radar Technology for the Inspection of Bridge Decks – The HERMES and PERES Bridge Inspectors," Proceedings of SPIE, The International Society for Optical Engineering, S. B. Chase, ed., Newport Beach, California, Vol. 3587, March 3-5, pp. 180-185.

Davidson, N.C., Hardy, M.S.A, Broughton, K.J., Forde, M.C., and Das, P.C. (1996), "Investigation of Bridge Scour Using Digital Impulse Radar," Proceedings of 3rd Conference on Nondestructive Evaluation of Civil Structures and Materials, M. P. schuller, D. B. Woodham, and Atkinson-Noland & Associates, Inc., eds., September, pp. 69-79.

Davis, J.L., Rossiter, J.R., Mesher, D.E., and Dawley, C.B. (1994), "Quantitative Assessment of Pavement Structures Using Radar," Proceedings of the 5th International Conference on Ground Penetrating Radar, pp. 319-334.

Donohue & Associates, Inc. (1983), A Nondestructive Method for Determining the Thickness of Sound Concrete on Older Pavements, Final Report, Project HR-250, Iowa Highway Research Board.

Edde, B. (1993), *Radar: Principles, technology, applications*, PTR Prentice Hall, Englewood Cliffs, NJ.

Feng, S., and Sen, P.N. (1985), "Geometrical Model for Conductive and Dielectric Properties of Partially Saturated Rocks," *Journal of Applied Physics, Vol. 58*, No. 8, October, pp. 3236-3243.

Graves, C.R., and Drnevich, V.P. (1991), "Calculating Pavement Deflections with Velocity Transducers," *Transportation Research Record 1293*, TRB, National Research Council, Washington, D.C., pp. 12-23.

Halabe, U.D., Sotoodehnia, A., Maser, K.R., and Kausel, E.A. (1993), "Modeling the Electromagnetic Properties of Concrete," *ACI Materials Journal, Vol. 90,* No. 6, Nov.-Dec., pp. 552-563.

Halabe, U. D., Chen, H.L., Allu, M.K., and Pei, L. (1996), "Laboratory Radar Evaluation of Concrete Decks and Pavements With and Without Asphalt Overlay," Structural Materials Technology: An NDT Conference, P. E. Hartbrower and P. J. Stolarski, eds., Feb., pp. 373-377.

Horne, W.A. (1992), "Bridge Scour Detection Using Ground Penetrating Radar," Clarkson University, Potsdam, New York.

Horne, W.A. (1993), "Scour Inspection Using Ground Penetrating Radar," Hydraulic Engineering 93 Conference, W. S. Hsieh, S. T. Su, and W. Feng, eds., Vol. 2, July 25-30, pp1888-1893.

Huang,Y.H. (1993), *Pavement Analysis and Design*, Prentice Hall, Englewood Cliffs, New Jersey.

Hugenschmidt, J. (1997), "Non-Destructive Evaluation of Bridge Decks Using GPR – Benefits and Limits," Recent Advances in Bridge Engineering, Advanced Rehabilitation, Durable Materials, Nondestructive Evaluation and Management, U. Meier and R. Betti, eds., Zurich, Switzerland, July 15-16, pp. 362-367.

Koerner, R.M., Lord, A. Jr., Boweders, J., and Dougherty, W. (1982), "CW Microwave Location of Voids Beneath Paved Areas," *Journal of Geotechnical Engineering Division*, *ASCE, Vol. 108*, No. 1, pp. 133-144.

Lau, C.L., Scullion, T, and Chan, P. (1992), "Modeling of Ground-Penetrating Radar Wave Propagation in Pavement Systems," *Transportation Research Record, Nondestructive Structural Evaluation of Pavements,* No. 1355, Transportation Research Board, Washington, D.C., pp.99-107.

Liu, C. and Shen, L.C. (1991), "Numerical Simulation of Subsurface Radar for Detecting Buried Pipes," *IEEE Transactions on Geoscience and Remote Sensing, Vol. 29*, No. 5, Sep., pp. 795-797.

Loulizi, A., Al-Qadi, I.L., Bhutta, S., and Flintsch, G. (1999), "Evaluation of Geosynthetics When Used as Separators," Paper No. 99-1316, *Transportation Research Record*, Geotechnical Aspects of Pavements, No. 1687, pp. 104-111.

Manning, D.G., and Holt, F.B. (1983), "Detecting Deterioration in Asphalt-Covered Bridge Decks," *Transportation Research Record*, No. 899, transportation Research Board, Washington, D.C.

Maser, K.R. (1994), Ground Penetrating Radar Survey of Pavement Thickness on MN/ROAD Sections, Report Submitted to MN DOT, Maplewood, MN.

Maser, K.R. (1996a), "Condition Assessment of Transportation Infrastructure Using Ground Penetrating Radar," *Journal of Infrastructure Systems, Vol. 2,* No. 2, pp. 94-101.

Maser, K.R. (1996b), "Measurement of As-Built Conditions Using Ground Penetrating Radar," Structural Materials Technology: An NDT Conference, P. E Hartbrower and P. J. Stolarski, eds., Feb., pp. 61-67.

Mehta, P.K., and Monteiro, J.M. (1993), *Concrete: Structure, Properties, and Materials*, Prentice Hall, Englewood Cliffs, New Jersey.

Mesher, D.E., Dawley, C.B., Davis, J.L., and Rossiter, J.R. (1995), "Evaluation of New Ground Penetrating Radar Technology to Quantify Pavement Structures," *Transportation Research record*, No. 1505, July, pp. 17-26.

Millard, S.G., Thomas, C, Patterson, A.J., Soutsos, M.N., and Bungey, J.H. (1998), "Evaluation of Riverbed Scour Using Impulse Radar Methods," Structural Engineering World Congress, N. K. Srivastava, G. L. Fenves, R. G. Domer, and A. H. Ang, eds., Paper No. T208-2, San Fransisco, CA, July 19-23.

Moore, J.R., Echard, J.D., and Neill, C.G. (1980), "Radar Detection of Voids Under Concrete Highways," CH1493-6/80/0000-0131, Georgia Department of Transpportation, IEEE International Radar Conference, Piscataway, NJ.

Morey, R.M. (1974), "Application of Downward Looking Impulse Radar," Proceedings of the 13th Annual Canadian Hydrographic Conference, Canada Center for Inland Waters, Burlington, Ontario, Canada, March.

Morey, R.M., and Harrington, W.S.Jr. (1972), Feasibility Study of Electromagnetic Subsurface Profiling, Report EPA-R2-72-082, U. S. Environmental Protection Agency, Washington, D.C., October.

Olhoeft, G.R. (1988), "Selected Bibliography on Ground Penetrating Radar," Proceedings of the Symposium on the Applications of Geophysics to Engineering and Environmental Problems, Golden, CO, March 28-31, pp. 462-520.

Ott, R.L. (1993), *An Introduction to Statistical Methods and Data Analysis*, Duxbury Press, Belmont, California, 4th Edition.

Pollock, A.A. (1989), “Acoustic Emission Inspection,” *Nondestructive Evaluation and Quality Control, Vol. 17*, ASM handbook, ASM, pp. 278-294.

Pratt, T., and Bostian, C.W. (1986), *Satellite Communications*, John Wiley and Sons, New York.

Proakis, J.G., and Manolakis, D.G. (1996), *Digital Signal Processing: Principles, Algorithms, and Applications*, Third Edition, Prentice-Hall, Inc., Upper Saddle River, New Jersey.

Rhim, H.C., and Büyüköztürk, O. (1998), “Electromagnetic Properties of Concrete at Microwave Frequency Range,” *ACI Materials Journal, Vol. 95*, No. 3, May-June, pp. 262-271.

Rmeili, E. and Scullion, T. (1997), “Detecting stripping in asphalt concrete layers using ground penetrating radar,” Paper No. 97-0508, Submitted to Transportation Research Board, 1997.

Robert, A., Baillon, L., and Huet, C. (1995), "Design and Calibration of a Dielectric Measurement Cell for Concrete with Large Grain Heterogeneities,” International Symposium Non-Destructive Testing in Civil Engineering, Berlin, pp. 1053-1061.

Saarenketo, T. and Scullion, T. (1994), Ground Penetrating Radar Applications on Roads and Highways, Research Report 1923-2F, Texas Transportation Institute, College Station, Texas.

Sansalone, M.J. and Streett, W.B. (1997), *Impact-Echo Nondestructive Evaluation of Concrete and Masonry*, Bullbrier Press, Ithaca, NY.

Sayers, M.W., Gillespie, T.D., and Queiroz, C.A., “The International Road Roughness Experiment: Establishing Correlation and a Calibration Standard for measurements,” Technical Paper 46, The World Bank, Washington, DC.

Scaffer, J.P., Saxena, A., Antolovich, S.D, Sanders, T.H., and Warner, S.B. (1995), *The Science and Design of Engineering Materials*, Richard D. Irwin, Inc.

Scullion, T., Lau, C., and Chen, Y. (1994), Implementation of the Texas Ground Penetrating Radar System, Research Report 1233-1, Texas Transportation Institute.

Scullion, T.C., and Saarenketo, T. (2000), “Integrating Ground Penetrating Radar and Falling Weight Deflectometer Technologies in Pavement Evaluation,” Nondestructive Testing of Pavements and Backcalculation of Moduli: Third Volume, ASTM STP 1375, S. D. Tayabji, and E. O. Lukanen, eds., American Society for Testing and Materials, West Conshohcken, PA.

Seusy, F.E., Dass, W.C., and Maser, K.R. (1992), Nondestructive Layer Thickness Determination Techniques for an Advanced Pavement System Analyzer, Report No. ESL-TR-92-XX, Applied Research Associates, Panama City, Fl.

Shang, J.Q., Umana, J.A., Bartlett, F.M., and Rossiter, J.R. (1999), "Measurement of Complex Permittivity of Asphalt Pavement Materials," *Journal of the Transportation Engineering*, July-August, pp. 347-356.

Shaw, M.R., Millard, S.G., Houlde, M.A., Austin, B.A., and Bungey, J.H. (1993), "A Large Diameter Transmission Line for the Measurement of the Relative Permittivity of Construction Materials," *British Journal of NDT, Vol. 35,* No. 12, Dec., pp. 696-704.

Sheftick, D.E., and Bartoski, T.A. (1997), Study of Void Detection Methods and Slab Stabilization Procedures, Final Report, Research Project 86-102, Pennsylvania Department of Transportation, Bureau of Construction and Materials.

Smith, G.H. and Scott, W.R.Jr. (1989), "A Scale Model for Studying Ground Penetrating Radars," *IEEE Transactions on Geoscience and Remote Sensing, Vol. 27,* No. 4, July, pp. 358-363.

Smith, S.S. and Scullion, T. (1993), Development of Ground Penetrating Radar Equipment for Detecting Pavement Condition for Preventive Maintenance, Final Report Strategic Highway Research Program SHRP-672, National Research Council, Washington, DC, USA, 177pp.

Steinway, W.J., Echard, J.D., and Luke, C.M. (1981), Locating Voids Beneath Pavements Using Pulsed Electromagnetic Waves, NCHRP Report 237, Transportation Research Board, Washington, DC.

Texas Transportation Institute (1997), Specification No. TxDOT-845-49-62, Oct.

US Department of Transportation (1999)

Warhus, J.P., Mast, J.E., Johanson, E.M, and Nelson, S.D. (1994), "Advanced Ground Penetrating Radar," Proceedings of SPIE - The International Society for Optical Engineering, Nondestructive Advanced Microwave and Millimeter-Wave Detectors, S.S. Udpa and H.C. Han, eds., Vol. 2275, July 25-26, pp. 177-185.

Warhus, J.P., Mast, J.E., Johanson, E.M., and Nelson, S.D. (1995), "Imaging Radar for Bridge Deck Inspection," Proceedings of SPIE - The International Society for Optical Engineering, Nondestructive Evaluation of Aging Bridges and Highways, S. Chase, ed., Vol. 2456, June 6-7, pp. 296-305.

APPENDIX A

(MATERIAL PROPERTIES)

Table A1. Mix design per m^3 of concrete

		Mix Type				
		M1	M2	M3	M4	M5
Coarse Aggregate	Limestone (kg)	1042.2	1064.1	-	1064.1	-
	Quartzite (kg)	-	-	1028.0	-	1026.8
Fine Aggregate	Limestone (kg)	733.5	-	-	-	-
	Quartzite (kg)	-	676.1	609.1	676.1	688.5
Cementituous Materials	Cement I (kg)	418.5	418.5	339.5	389.2	300.4
	Fly Ash (kg)	-	-	80.0	-	64.6
	Silica Fume (kg)	-	-	-	29.3	-
Water	(kg)	171.3	171.3	171.8	171.3	160.0
Admixtures	AE* (liters)	0.98	0.98	0.98	0.98	0.98
	WRR** (liters)	1.27	1.27	1.27	1.27	1.27

* Air Entrainment

** Water Reducer Retarder

Table A2. Physical properties of quartzite and limestone aggregates.

	Quartzite		Limestone	
	CA*	FA**	CA	FA
Bulk Specific Gravity	2.67	2.63	2.81	2.77
Absorption (%)	0.9	0.5	0.20	0.90
Fineness Modulus	-	2.60	-	2.90
Unit Weight (kg/m^3)	1544.0	-	1581.0	-

* Coarse aggregate

** Fine aggregate

Table A3. Chemical analysis of quartzite and limestone aggregates.

	Compound (% by wt)					
	SiO_2	Al_2O_3	Fe_2O_3	$CaCO_3$	$MgCO_3$	Other
Quartzite	90.00	4.50	1.00	< 0.05	0.50	≈ 4.00
Limestone	5.00	1.50	0.15	84.00	6.00	≈ 3.35

Table A4. Chemical analysis of Portland cement, fly ash, and silica fume.

	Compound (% by wt)									
	SiO_2	Al_2O_3	Fe_2O_3	CaO	MgO	SO_3	Na_2O	K_2O	TiO_2	L. I.*
Cement	21.0	4.8	2.9	63.2	2.5	2.5	0.2	0.8	-	0.6
Fly Ash	54.7	25.9	7.3	3.3	1.3	0.7	0.3	2.6	1.5	2.0
Silica Fume	85.0	-	-	-	-	-	1.5	-	-	7.0

* Loss of Ignition

Table A5. Quality control measurements for different mixes

Mix	Unit Weight (kg/m^3)	Slump (mm)	Air Content (%)	Compressive Strength at 3 Days (MPa)	Compressive Strength at 7 Days (MPa)	Compressive Strength at 28 Days (MPa)
M1	2337.0	114.3	7.5	25.3	29.8	33.9
M2	2368.0	95.3	5.0	30.2	38.4	40.8
M3	2265.0	89.0	7.0	22.0	27.1	34.4
M4	2362.7	101.6	5.5	40.3	48.7	62.3
M5	2394.8	100.0	-	22.3	29.6	42.4

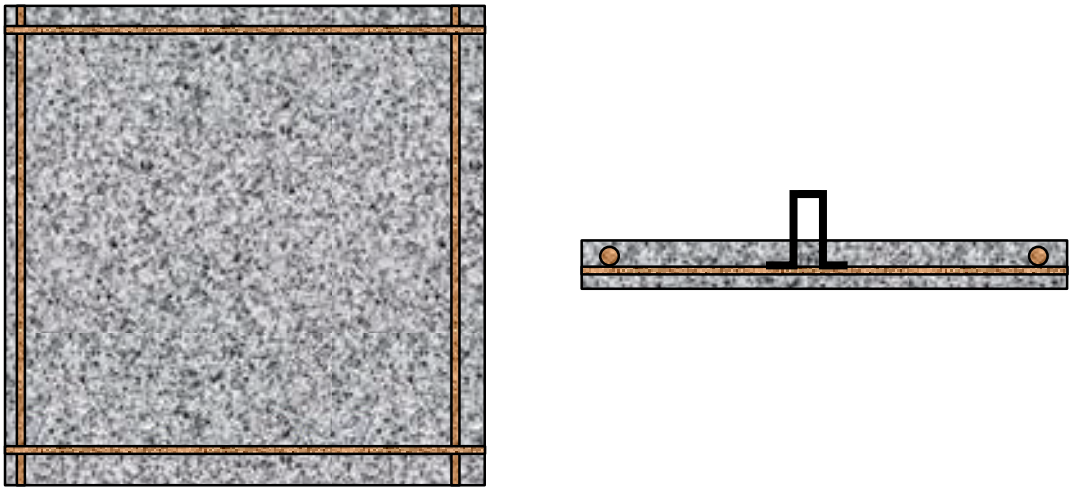

(a)

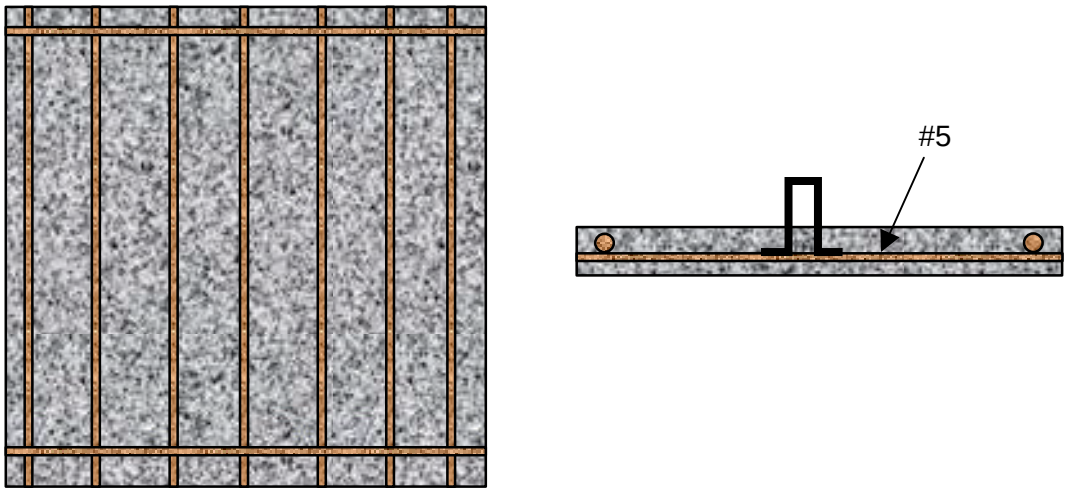

(b)

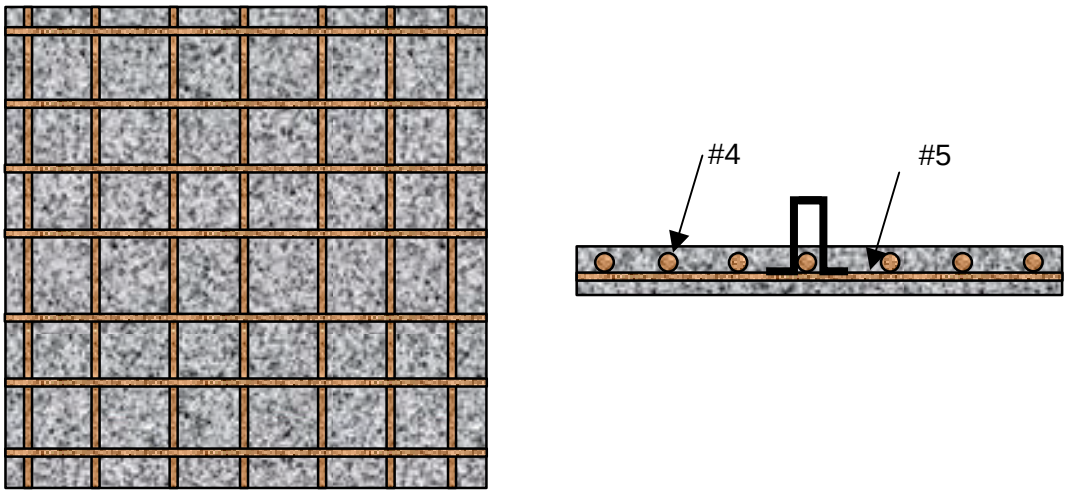

(c)

Figure A1. Schematic for (a) bare concrete slab; (b) one-way reinforced slab; and (c) two-way reinforced slab.

(a)

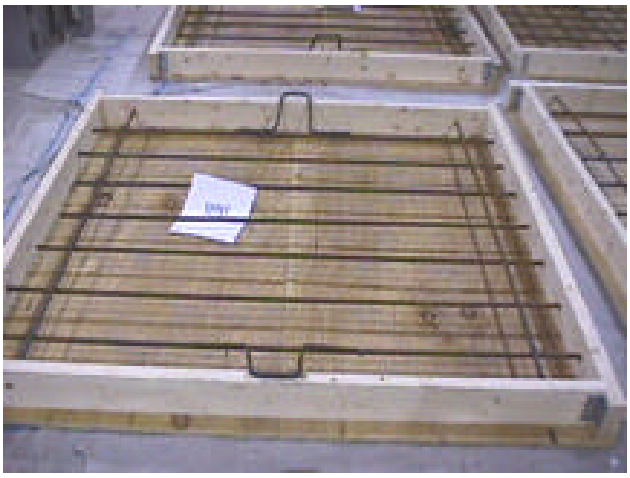

(b)

(c)

Figure A2. Forms for (a) bare concrete slab; (b) one-way reinforced slab; and (c) two-way reinforced slab.

Figure A3. Placing, finishing, and curing concrete slabs

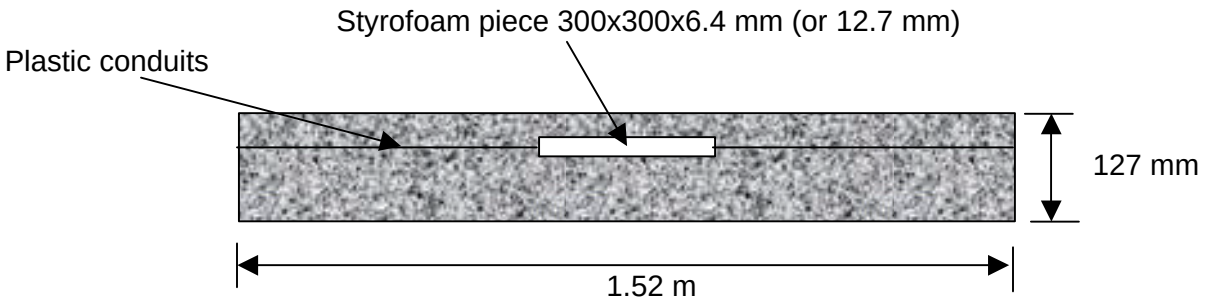

(a)

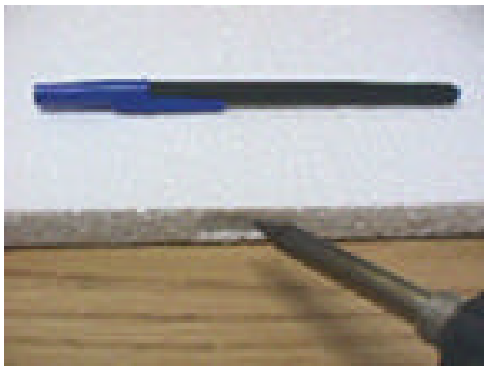

(b)

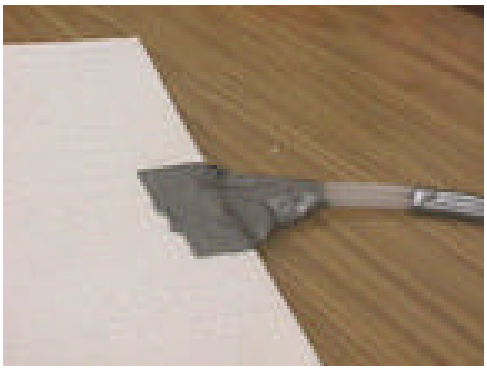

(c)

(d)

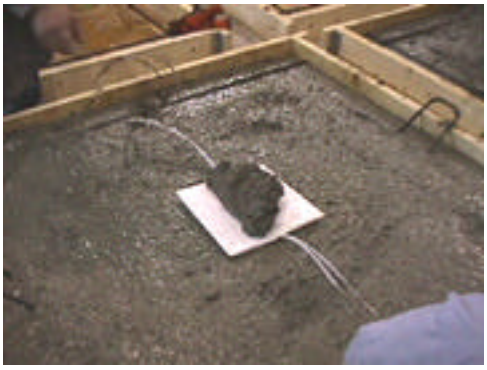

(e)

(f)

(g)

Figure A4. Simulating delamination in concrete slabs

APPENDIX B

(MATLAB LISTING)

Function DielectricslabObl

```
%epsr=DielectricslabObl(Yslabfname,d,options,fstart,fend,Yifname,Yafname) Compute
Dielectric constant
%Inputs:
%           Yslabfname:   Slab response file name (DZT file)
%           d:            Slab thickness (m)
%           options:       1 --> Plot figures
%           fstart:       Frequency start (GHz). Default 0.5 GHz
%           fend:         Frequency end (GHz). Default 3 GHz
%           Yifname:      Response from copper plate (DZT file). Default 'copper.dzt'
%           Yafname:      End reflection response (DZT file). Default 'air.dzt'
%Output:
%           epsr:         Dielectric Constant

function epsr=Dielectricslabobl(Yslabfname,d,options,fstart,fend,Yifname,Yafname)
warning off;

theta=0.2670;

if(~exist('Yafname'))
   Yafname = 'air.dzt';
end;

if(~exist('Yifname'))
   Yifname = 'copper.dzt';
end;

if (~exist('options'))
   options=0;
end;

if(~exist('fstart'))
   fstart = 0.5;
end;

if(~exist('fend'))
   fend = 3;
end;


[Yi,N,T]=LoadDZT(Yifname,1);
Yr=LoadDZT(Yslabfname,1);
Ya=LoadDZT(Yafname,1);

Yi=-RmCouple(Yi,Ya,0);       %Clean Yi
%Yi(1:134)=0.9324*Yi(1:134);
%Yi(135:512)=0.7*Yi(135:512);

Yr=RmCouple(Yr,Ya,0);        %Clean Yr
```

```
zp=4;                                                   %Zero padding
P=zp*N;                                                 %Zero padded length
t=[0:N-1]'*T/(N-1);
f=[0:N/2-1]'/(T*zp);
w=2*pi*f;

[Yic,start_idx,end_idx]=GetPulse(Yi,3,3);

Yi(1:start_idx)=0;
Yr(1:start_idx)=0;
Yi(end_idx+1:P)=0;              %Zero after pulse + zero padding

[Yrc,start_idx,end_idx]=GetPulse(Yr,0,5);

Yr(end_idx+1:P)=0;              %Zero after pulse + zero padding

if (bitand(options,1) == 1)
  figure(1)
  plot(t,Yi(1:N));
  hold on;
  plot(t,Yr(1:N),'r');
  hold off;
  grid on
  graph_title=strcat('Clean Yi, Yr, ',Yslabfname);
  title(graph_title);
  pause;
end;

%Compute fft
Fi=fft(Yi);
Fr=fft(Yr);

if (bitand(options,1) == 1)
        figure(2)
        plot(f(1:P/(2*zp)),10*log(abs(Fi(1:P/(2*zp))/max(Fi(1:P/(2*zp))))));
        hold on;
        plot(f(1:P/(2*zp)),10*log(abs(Fr(1:P/(2*zp))/max(Fi(1:P/(2*zp))))),'r');
        grid;
        axis([0 3 -30 0]);
        hold off;
  graph_title=strcat('Fi, Fr, ',Yslabfname);
  title(graph_title);
end

%Frequency range (index numbers)
fstart_idx=round(fstart*T*zp)+1
fend_idx=round(fend*T*zp)+1

x=[1:.25:30];
y=[0:0.2:10];
```

```
opt=foptions;
opt(2)=1e-12;
opt(3)=1e-16;
opt(5)=1;

max_nbr_sol_idx=fstart_idx;
max_nbr_sol=0;
for fidx=fstart_idx:1:fend_idx,
  fidx
        qo=Fr(fidx)/Fi(fidx);

  for l=1:length(x),
                for c=1:length(y),
                        z(c,l)=reflectionobl(x(l)-j*y(c),w(fidx),qo,d,theta);
          end
        end

  if (bitand(options,2) == 2)
                figure(3)
                mesh(x,y,abs(z));
          %graph_title=strcat('Solutions, ',Yslabfname,', f=',sprintf('%f',f(fidx)),' GHz');
    %title(graph_title);
    xlabel('Re(\epsilon_r)');
          ylabel('-Im(\epsilon_r)')
          zlabel('abs(f(\epsilon_r)')
    end


  stop=0;
  nbr_sol=0;
  abs_z=abs(z);
  while (stop == 0)
    [minz l]=min(min(abs_z));
    if ((minz <= 0.05) | (nbr_sol == 0))
      [minzc c]=min(abs_z);
      pos_sol=x(l)-j*y(c(l));
      bad_sol=0;
      for k=1:nbr_sol,
        mid_pt_z=abs(z((imag_idx_gma(fidx,k)+c(l))/2,(real_idx_gma(fidx,k)+l)/2));
        k_pt_z=abs(z(imag_idx_gma(fidx,k),real_idx_gma(fidx,k)));
        if (( (abs(pos_sol-gma(fidx,k)) < .75) &(k_pt_z <= mid_pt_z) & (mid_pt_z <=
minz)))
          bad_sol=1;
                break;
        end
      end
      if (bad_sol ~= 1)
        nbr_sol=nbr_sol+1;
        gma(fidx,nbr_sol)=pos_sol;
        real_idx_gma(fidx,nbr_sol)=l;
        imag_idx_gma(fidx,nbr_sol)=c(l);
```

```
        end
        abs_z(c(l),l)=200;
      else
        stop=1;
      end
    end
          nbr_sol

    if (nbr_sol >= max_nbr_sol)
      max_nbr_sol=nbr_sol;
      max_nbr_sol_idx=fidx;
    end

    if (nbr_sol ~=0)
          %   gma(fidx,1:nbr_sol)=sort(gma(fidx,1:nbr_sol));
          for sol=1:nbr_sol,
          if (gma(fidx,sol) ~= 0)
                    nbr_loops=500;
                                        stop=0;
                                        loop=nbr_loops;
                                        while ((stop == 0) & (loop > 0))

          gma(fidx,sol)=fsolve('reflectionobl',gma(fidx,sol),opt,[],w(fidx),qo,d,theta);
                                        ref=abs(reflectionobl(gma(fidx,sol),w(fidx),qo,d,theta));
                                        loop=loop-1;
                                        if (ref < 1e-10)
                                    stop = 1;
                                        end
                                end

                                        if (stop == 0)
                                                disp('Amara, malkithach');
                                        raw_epsr(fidx,sol)=0;
          else
                              raw_epsr(fidx,sol)=gma(fidx,sol);
          end
        end
      end
    else
          raw_epsr(fidx,:)=0;
    end
end

max_nbr_sol
max_nbr_sol_idx
f(max_nbr_sol_idx)

max_nbr_sol2=0;
max_nbr_sol_idx2=fstart_idx;
```

```
for fidx=fstart_idx:fend_idx,
  for pos_sol_idx=1:max_nbr_sol,                %Remove bad solutions
    if ((real(raw_epsr(fidx,pos_sol_idx)) < 0) | (imag(raw_epsr(fidx,pos_sol_idx)) > 0))
      raw_epsr(fidx,pos_sol_idx)=0;
    end
  end
  for L=1:max_nbr_sol,
    if (raw_epsr(fidx,L) ~= 0)
            for C=L+1:max_nbr_sol,
        if (abs(raw_epsr(fidx,C) - raw_epsr(fidx,L)) < 1.0e-6)                    %Remove
repeated solutions
          raw_epsr(fidx,C)=0;
        end
      end
    end
  end
        %Shift NULL solutions to the right
  for L=1:max_nbr_sol,
    if (raw_epsr(fidx,L) == 0)
            for C=L+1:max_nbr_sol,
        if (raw_epsr(fidx,C) ~= 0)
          raw_epsr(fidx,L)=raw_epsr(fidx,C);
          raw_epsr(fidx,C)=0;
          break;
        end
      end
    end
  end
end


%Find maximum number of non zero solutions
for fidx=fstart_idx:fend_idx,
  nbr_non_zero_sol=0;
  for L=1:max_nbr_sol,
    if (raw_epsr(fidx,L) ~= 0)
      nbr_non_zero_sol=nbr_non_zero_sol+1;
    end
  end
  if (nbr_non_zero_sol >= max_nbr_sol2)
    max_nbr_sol2=nbr_non_zero_sol;
    max_nbr_sol_idx2=fidx;
  end
end

max_nbr_sol2
max_nbr_sol_idx2
f(max_nbr_sol_idx2)

max_nbr_sol=max_nbr_sol2;
```

```
max_nbr_sol_idx=max_nbr_sol_idx2;

epsr=zeros(size(raw_epsr));
prev_sols=raw_epsr(max_nbr_sol_idx,:);
epsr(max_nbr_sol_idx,:)=raw_epsr(max_nbr_sol_idx,:);

min_all_err=1.05;

for fidx=max_nbr_sol_idx-1:-1:fstart_idx,
  for sol_idx=1:max_nbr_sol,
    if (raw_epsr(fidx,sol_idx) ~= 0)
                        min_error=dist(raw_epsr(fidx,sol_idx),prev_sols(1));
                        min_err_idx=1;
      for prev_sol_idx=2:max_nbr_sol2,
                              err=dist(raw_epsr(fidx,sol_idx),prev_sols(prev_sol_idx));
                              if ((err < min_error) & (epsr(fidx,prev_sol_idx)==0))
              min_error=err;
                min_err_idx=prev_sol_idx;
      end
          end
     if (min_error > min_all_err)      %Add new column to the solutions
       max_nbr_sol2=max_nbr_sol2+1;
       epsr(fidx,max_nbr_sol2)=raw_epsr(fidx,sol_idx);
      prev_sols(max_nbr_sol2)=raw_epsr(fidx,sol_idx);
     else
              epsr(fidx,min_err_idx)=raw_epsr(fidx,sol_idx);
     end
    end
  end
  %Compute new previous epsr vector
  for sol_idx=1:max_nbr_sol2,
    if (epsr(fidx,sol_idx) ~=  0)
                  prev_sols(sol_idx)=epsr(fidx,sol_idx);
    end
  end
end
max_nbr_sol2
prev_sols;
prev_sols(1:max_nbr_sol)=raw_epsr(max_nbr_sol_idx,1:max_nbr_sol);

for fidx=max_nbr_sol_idx+1:fend_idx,
  for sol_idx=1:max_nbr_sol,
    if (raw_epsr(fidx,sol_idx) ~= 0)
                        min_error=dist(raw_epsr(fidx,sol_idx),prev_sols(1));
                        min_err_idx=1;
      for prev_sol_idx=2:max_nbr_sol2,
                              err=dist(raw_epsr(fidx,sol_idx),prev_sols(prev_sol_idx));
                              if ((err < min_error) & (epsr(fidx,prev_sol_idx)==0))
              min_error=err;
                min_err_idx=prev_sol_idx;
      end
```

```
                end
        if (min_error > min_all_err)       %Add new column to the solutions
           max_nbr_sol2=max_nbr_sol2+1;
           epsr(fidx,max_nbr_sol2)=raw_epsr(fidx,sol_idx);
           prev_sols(max_nbr_sol2)=raw_epsr(fidx,sol_idx);
        else
                epsr(fidx,min_err_idx)=raw_epsr(fidx,sol_idx);
        end
      end
   end
   %Compute new previous epsr vector
   for sol_idx=1:max_nbr_sol2,
      if (epsr(fidx,sol_idx) ~=  0)
                        prev_sols(sol_idx)=epsr(fidx,sol_idx);
      end
   end
end

if (bitand(options,1) == 1)
           figure(4);
   subplot(2,1,1)
 % plot(f(fstart_idx:fend_idx),real(epsr(fstart_idx:fend_idx,:)));
  % hold on
   plot(f(fstart_idx:fend_idx),real(epsr(fstart_idx:fend_idx,:)),'o');
   hold off
   graph_title=strcat('Real(epsr)',Yslabfname);
   title(graph_title);
   grid;

   subplot(2,1,2)
%        plot(f(fstart_idx:fend_idx),-imag(epsr(fstart_idx:fend_idx,:)));
 %  hold on
   plot(f(fstart_idx:fend_idx),-imag(epsr(fstart_idx:fend_idx,:)),'o');
   hold off
   graph_title=strcat('-Imag(epsr)',Yslabfname);
   title(graph_title);
           grid;
end
max_nbr_sol2
return
```

Function Reflectionobl

```
function [output]=reflectionobl(eps,w,qo,d,theta)
ro1=(cos(theta)-sqrt(eps-sin(theta)^2))/(cos(theta)+sqrt(eps-sin(theta)^2));
thetat=asin(sin(theta)/real(eps));
ro2=(cos(thetat)-sqrt(1/eps-sin(thetat)^2))/(cos(thetat)+sqrt(1/eps-sin(thetat)^2));
T=exp(-j*(w/(.3))*sqrt(eps)*d/cos(thetat));
output=ro1+ro2*(1+ro2)*(1+ro1)*T^2-qo;
```

Function LoadDZT

```
%[Y,N,T]=LoadDZT(fname,average,scan_start,scan_end): Load a binary DZT file
%Inputs:
%       fname: DZT file name (for now you need to include .dzt)
%       average (optioanl, default 0):
%               0 -> don't average: load all waves
%               1 -> average waves
%       scan_start (optional, default 1): first scan to read (starting from 1)
%       scan_end (optional, default EOF): last scan to read
%Outputs:
%       Y: matrix containing all the waves
%       N: Number of samples in each wave
%       T: signal length (ns)

function [Y,N,T]=LoadDZT(fname,average,scan_start,scan_end)

if(~exist('average'))
  average = 0;
end;

if(~exist('scan_start'))
  scan_start = 1;
end;

fid=fopen(fname,'r');

if (fid ~= -1)
        fseek(fid,4,-1);
  N=fread(fid,1,'ushort');
        fseek(fid,20,0);
  T=fread(fid,1,'float');

  fseek(fid,1024*scan_start,-1);

  if (exist('scan_end'))
    Y=fread(fid,[N,(scan_end-scan_start+1)],'ushort')-32768;
  else
    Y=fread(fid,[N,inf],'ushort')-32768;
  end
  Y(1,:)=0;
  Y(2,:)=0;
  if (average == 1)
    Y=sum(Y,2)/size(Y,2);
  end
  fclose(fid);
else
  disp('Cannot open DZT file')
        Y=0;N=0;T=0;
end
```

Function RmCouple

```
%RmCouple(Ys,Yc,clean): Remove Coupling
%Inputs:
%	Ys: original input wave
%	Yc: Coupling wave
%	clean (optional, default 1):
%		0 -> Yc is not clean; GetPulse will be performed first
%		1 -> Yc is already clean
%Output:
%	Y: signal without coupling

function [Y]=RmCouple(Ys,Yc,clean)
if (~exist('clean'))
  clean=1;
end
if (clean == 0)
  Ycc=GetPulse(Yc,0,4,0);
else
	Ycc=Yc;
end
NYcc=length(Ycc);
max_corr_idx=max_corr(Ys,Ycc,NYcc,round(1.2*NYcc),-round(.2*NYcc));
Y=Ys;
if (max_corr_idx < 0)
	Y(1:NYcc+max_corr_idx)=Y(1:NYcc+max_corr_idx)-Ycc(-max_corr_idx+1:NYcc);
else
  if (max_corr_idx ~= 0)
    Y(1:length(Y)-max_corr_idx)=Y(max_corr_idx:length(Y)-1);
    Y(1:NYcc)=Y(1:NYcc)-Ycc;
  end
end
```

Function max_corr

```
%max_cor_idx=max_corr(Yi,Ys,sig_len,corr_len,orig): Finds the best position of a signal
in another
%Inputs:
%       Yi: Searched Signal
%       Ys: Signal to find
%       sig_len: length of Ys
%       corr_len: Searched length of Yi
%       orig (optional, default 1): correlation starting point in Yi; Can be < 0
%Output:
%       max_cor_idx: position of Ys in Yi

function [max_cor_idx,max_cor]=max_corr(Yi,Ys,sig_len,corr_len,orig)
if (~exist('orig'))
  orig=1;
end
if (orig < 0)
  Yim(1:-orig,1)=0;                                    %Modified Yim
  Yim(-orig+1:corr_len-orig,1)=Yi(1:corr_len);
        corr_len_m=corr_len-orig;     %Modified correlation length
else
  if ((orig+corr_len) > length(Yi))
    corr_len_m=length(Yi)-orig;
  else
                corr_len_m=corr_len;
  end
  Yim=Yi(orig:orig+corr_len_m-1);
end
max_cor=0;
max_cor_idx=0;
for i=1:corr_len_m-sig_len,
  cur_cor=0;
  cur_cor=Yim(i:i+sig_len-1)'*Ys(1:sig_len);
  if (cur_cor > max_cor)
    max_cor=cur_cor;
    max_cor_idx=i;
  end
end
max_cor_idx=max_cor_idx+orig;
```

Function Dielectricslab

```
%epsr=DielectricSlab(Yslabfname,d,options,fstart,fend,Yifname,Yafname) Compute
Dielectric constant
%Inputs:
%		Yslabfname:	Slab response file name (DZT file)
%		d:				Slab thickness (m)
%		options:		1 --> Plot figures
%		fstart:		Frequency start (GHz). Default 0.5 GHz
%		fend:		Frequency end (GHz). Default 3 GHz
%		Yifname:		Response from copper plate (DZT file). Default
'copper.dzt'
%		Yafname:		End reflection response (DZT file). Default 'air.dzt'
%Output:
%		epsr:		Dielectric Constant

function epsr=DielectricSlab(Yslabfname,d,options,fstart,fend,Yifname,Yafname)
warning off;

theta=0;%0.267;


if(~exist('Yafname'))
   Yafname = 'air.dzt';
end;

if(~exist('Yifname'))
   Yifname = 'copper.dzt';
end;

if (~exist('options'))
   options=0;
end;

if(~exist('fstart'))
   fstart = 0.5;
end;

if(~exist('fend'))
   fend = 3;
end;



[Yi,N,T]=LoadDZT(Yifname,1);
Yr=LoadDZT(Yslabfname,1);
Ya=LoadDZT(Yafname,1);

Yi=-RmCouple(Yi,Ya,0);	%Clean Yi
Yr=RmCouple(Yr,Ya,0);	%Clean Yr
```

```
zp=4;                                                   %Zero padding
P=zp*N;                                                 %Zero padded length
t=[0:N-1]'*T/(N-1);
f=[0:N/2-1]'/(T*zp);
w=2*pi*f;

[Yic,start_idx,end_idx]=GetPulse(Yi,3,3);

Yi(1:start_idx)=0;
Yr(1:start_idx)=0;

Yi(end_idx+1:P)=0;              %Zero after pulse + zero padding

[Yrc,start_idx,end_idx]=GetPulse(Yr,0,5);

Yr(end_idx+1:P)=0;              %Zero after pulse + zero padding

if (bitand(options,1) == 1)
   figure(1)
   plot(t,Yi(1:N));
   hold on;
   plot(t,Yr(1:N),'r');
   hold off;
   grid on
   graph_title=strcat('Clean Yi, Yr, ',Yslabfname);
   title(graph_title);
   pause
end;

%Compute fft
Fi=fft(Yi);
Fr=fft(Yr);

if (bitand(options,1) == 1)
          figure(2)
          plot(f(1:P/(2*zp)),10*log(abs(Fi(1:P/(2*zp))/max(Fi(1:P/(2*zp))))));
   hold on;
          plot(f(1:P/(2*zp)),10*log(abs(Fr(1:P/(2*zp))/max(Fi(1:P/(2*zp))))),'r');
          grid;
          axis([0 3 -30 0]);
          hold off;
   graph_title=strcat('Fi, Fr, ',Yslabfname);
   title(graph_title);

end

%Frequency range (index numbers)
fstart_idx=round(fstart*T*zp)+1
fend_idx=round(fend*T*zp)+1
```

```
x=[-0.6429:1/100:0];
y=[0:1/200:0.3003];

opt=foptions;
opt(2)=1e-12;
opt(3)=1e-16;
opt(5)=1;

max_nbr_sol_idx=fstart_idx;
max_nbr_sol=0;
for fidx=fstart_idx:1:fend_idx,
  fidx
        qo=Fr(fidx)/Fi(fidx);

  for l=1:length(x),
                for c=1:length(y),
                        z(c,l)=reflection(x(l)+j*y(c),w(fidx),qo,d);
          end
        end

  if (bitand(options,2) == 2)
                figure(3)
                mesh(x,y,abs(z));
         % graph_title=strcat('Solutions, ',Yslabfname,', f=',sprintf('%f',f(fidx)),' GHz');
    %title(graph_title);
    xlabel('Re(\rho)');
    ylabel('-Im(\rho)');
    zlabel('abs(f(\rho)');


        end

  stop=0;
  nbr_sol=0;
  abs_z=abs(z);
  while (stop == 0)
    [minz l]=min(min(abs_z));
    if (minz <= 4.0e-1)
      [minzc c]=min(abs_z);
      pos_sol=x(l)+j*y(c(l));
      bad_sol=0;
      for k=1:nbr_sol,
        mid_pt_z=abs(z((imag_idx_gma(fidx,k)+c(l))/2,(real_idx_gma(fidx,k)+l)/2));
        k_pt_z=abs(z(imag_idx_gma(fidx,k),real_idx_gma(fidx,k)));
        if (( (abs(pos_sol-gma(fidx,k)) < 0.2) &(k_pt_z <= mid_pt_z) & (mid_pt_z <=
minz)))
          bad_sol=1;
                break;
        end
      end
      if (bad_sol ~= 1)
```

```
            nbr_sol=nbr_sol+1;
            gma(fidx,nbr_sol)=pos_sol;
            real_idx_gma(fidx,nbr_sol)=l;
            imag_idx_gma(fidx,nbr_sol)=c(l);
          end
          abs_z(c(l),l)=200;
        else
          stop=1;
        end
      end
            nbr_sol

      if (nbr_sol >= max_nbr_sol)
        max_nbr_sol=nbr_sol;
        max_nbr_sol_idx=fidx;
      end

      if (nbr_sol ~=0)
            %   gma(fidx,1:nbr_sol)=sort(gma(fidx,1:nbr_sol));
            for sol=1:nbr_sol,
            if (gma(fidx,sol) ~= 0)
                    nbr_loops=500;
                                    stop=0;
                                    loop=nbr_loops;
                                    while ((stop == 0) & (loop > 0))

            gma(fidx,sol)=fsolve('reflection',gma(fidx,sol),opt,[],w(fidx),qo,d);
                                    ref=abs(reflection(gma(fidx,sol),w(fidx),qo,d));
                                    loop=loop-1;
                                    if (ref < 1e-10)
                                  stop = 1;
                                    end
                                end

                                    if (stop == 0)
                                            disp('Amara, malkithach');
                                    raw_epsr(fidx,sol)=0;
            else
                            raw_epsr(fidx,sol) = cos(theta)^2*((1-
gma(fidx,sol))/(1+gma(fidx,sol)))^2+sin(theta)^2;
            end
          end
        end
      else
            raw_epsr(fidx,:)=0;
      end
end

max_nbr_sol
max_nbr_sol_idx
f(max_nbr_sol_idx)
```

```
max_nbr_sol2=0;
max_nbr_sol_idx2=fstart_idx;


for fidx=fstart_idx:fend_idx,
  for pos_sol_idx=1:max_nbr_sol,                %Remove bad solutions
    if ((real(raw_epsr(fidx,pos_sol_idx)) < 0) | (imag(raw_epsr(fidx,pos_sol_idx)) > 0))
      raw_epsr(fidx,pos_sol_idx)=0;
    end
  end
  for L=1:max_nbr_sol,
    if (raw_epsr(fidx,L) ~= 0)
            for C=L+1:max_nbr_sol,
        if (abs(raw_epsr(fidx,C) - raw_epsr(fidx,L)) < 1.0e-6)                    %Remove
repeated solutions
          raw_epsr(fidx,C)=0;
        end
      end
    end
  end
        %Shift NULL solutions to the right
  for L=1:max_nbr_sol,
    if (raw_epsr(fidx,L) == 0)
            for C=L+1:max_nbr_sol,
        if (raw_epsr(fidx,C) ~= 0)
          raw_epsr(fidx,L)=raw_epsr(fidx,C);
          raw_epsr(fidx,C)=0;
          break;
        end
      end
    end
  end
end

%Find maximum number of non zero solutions
for fidx=fstart_idx:fend_idx,
  nbr_non_zero_sol=0;
  for L=1:max_nbr_sol,
    if (raw_epsr(fidx,L) ~= 0)
      nbr_non_zero_sol=nbr_non_zero_sol+1;
    end
  end
  if (nbr_non_zero_sol >= max_nbr_sol2)
    max_nbr_sol2=nbr_non_zero_sol;
    max_nbr_sol_idx2=fidx;
  end
end

max_nbr_sol2
max_nbr_sol_idx2
```

```
f(max_nbr_sol_idx2)

max_nbr_sol=max_nbr_sol2;
max_nbr_sol_idx=max_nbr_sol_idx2;

epsr=zeros(size(raw_epsr));
prev_sols=raw_epsr(max_nbr_sol_idx,:);
epsr(max_nbr_sol_idx,:)=raw_epsr(max_nbr_sol_idx,:);

min_all_err=2;

for fidx=max_nbr_sol_idx-1:-1:fstart_idx,
  for sol_idx=1:max_nbr_sol,
    if (raw_epsr(fidx,sol_idx) ~= 0)
                        min_error=dist(raw_epsr(fidx,sol_idx),prev_sols(1));
                        min_err_idx=1;
      for prev_sol_idx=2:max_nbr_sol2,
                              err=dist(raw_epsr(fidx,sol_idx),prev_sols(prev_sol_idx));
                              if ((err < min_error) & (epsr(fidx,prev_sol_idx)==0))
              min_error=err;
                min_err_idx=prev_sol_idx;
      end
          end
     if (min_error > min_all_err)      %Add new column to the solutions
       max_nbr_sol2=max_nbr_sol2+1;
       epsr(fidx,max_nbr_sol2)=raw_epsr(fidx,sol_idx);
       prev_sols(max_nbr_sol2)=raw_epsr(fidx,sol_idx);
     else
              epsr(fidx,min_err_idx)=raw_epsr(fidx,sol_idx);
     end
    end
  end
  %Compute new previous epsr vector
  for sol_idx=1:max_nbr_sol2,
    if (epsr(fidx,sol_idx) ~=  0)
                  prev_sols(sol_idx)=epsr(fidx,sol_idx);
    end
  end
end
max_nbr_sol2
prev_sols;
prev_sols(1:max_nbr_sol)=raw_epsr(max_nbr_sol_idx,1:max_nbr_sol);

for fidx=max_nbr_sol_idx+1:fend_idx,
  for sol_idx=1:max_nbr_sol,
    if (raw_epsr(fidx,sol_idx) ~= 0)
                        min_error=dist(raw_epsr(fidx,sol_idx),prev_sols(1));
                        min_err_idx=1;
      for prev_sol_idx=2:max_nbr_sol2,
                              err=dist(raw_epsr(fidx,sol_idx),prev_sols(prev_sol_idx));
                              if ((err < min_error) & (epsr(fidx,prev_sol_idx)==0))
```

```
                min_error=err;
                  min_err_idx=prev_sol_idx;
          end
               end
        if (min_error > min_all_err)       %Add new column to the solutions
           max_nbr_sol2=max_nbr_sol2+1;
           epsr(fidx,max_nbr_sol2)=raw_epsr(fidx,sol_idx);
          prev_sols(max_nbr_sol2)=raw_epsr(fidx,sol_idx);
        else
                epsr(fidx,min_err_idx)=raw_epsr(fidx,sol_idx);
        end
      end
   end
   %Compute new previous epsr vector
   for sol_idx=1:max_nbr_sol2,
      if (epsr(fidx,sol_idx) ~=  0)
                      prev_sols(sol_idx)=epsr(fidx,sol_idx);
      end
   end
end
%raw_epsr(51:65,:)

if (bitand(options,1) == 1)
          figure(4);
   subplot(2,1,1)
 %  plot(f(fstart_idx:fend_idx),real(epsr(fstart_idx:fend_idx,:)));
 %  hold on
   plot(f(fstart_idx:fend_idx),real(epsr(fstart_idx:fend_idx,:)),'o');
   hold off
   graph_title=strcat('Real(epsr)',Yslabfname);
   title(graph_title);
   grid;

   subplot(2,1,2)
%        plot(f(fstart_idx:fend_idx),-imag(epsr(fstart_idx:fend_idx,:)));
%   hold on
   plot(f(fstart_idx:fend_idx),-imag(epsr(fstart_idx:fend_idx,:)),'o');
   hold off
   graph_title=strcat('-Imag(epsr)',Yslabfname);
   title(graph_title);
          grid;
end
max_nbr_sol2
```

Function Reflection

```
function [output]=reflection(g,w,qo,d)
if (real((g)) >= -1.1 & real((g)) <= -.9)
   output=10;
else
   e=((1-g)/(1+g))^2;

   T=exp(-j*(w/(.3))*sqrt(e)*d);
   output=g*(1+(g^2-1)*T^2)-qo;

end
```

Function Synthesis

```
%[Yrsyn,t]=synthesis(epsrfname,Yifname,Yslabfname,Yafname,d,options)
%options: (default 0)
%       0: no options
%       1: Draw figures
function [Yrsyn,t]=synthesis(epsrfname,Yifname,Yslabfname,Yafname,d,options)
warning off;

theta=0.267;


if(~exist('Yafname'))
   Yafname = 'air.dzt';
end;

if(~exist('Yifname'))
   Yifname = 'copper.dzt';
end;

if (~exist('options'))
   options=0;
end;

close all

[Yi,N,T]=LoadDZT(Yifname,1);
Ya=LoadDZT(Yafname,1);
Yr=LoadDZT(Yslabfname,1);

Yr=RmCouple(Yr,Ya,0);       %Clean Yr
Yi=-RmCouple(Yi,Ya,0);      %Clean Yi

zp=4;                                                   %Zero padding
P=zp*N;                                                 %Zero padded length
t=[0:N-1]'*T/(N-1);
f=[0:N/2-1]'/(T*zp);
w=2*pi*[0:2*N-1]'/(T*zp);

[Yic,start_idx,end_idx]=GetPulse(Yi,3,3);

Yi(1:start_idx)=0;
Yi(end_idx+1:P)=0;          %Zero after pulse + zero padding

Yr(1:start_idx)=0;
[Yrc,start_idx,end_idx]=GetPulse(Yr,0,5);

Yr(end_idx+1:P)=0;          %Zero after pulse + zero padding

if (bitand(options,1) == 1)
   figure(1)
```

```
   plot(t,Yi(1:N));
   hold on
   plot(t,Yr(1:N),'r')
   hold off
   grid on
   title('Clean Yi');
end;

load(epsrfname);
epsrall=eval(strtok(epsrfname,'.'));
epsr_idx=epsrall(:,1)*T*zp+1;
epsr=epsrall(:,2)-j*epsrall(:,3);

if (bitand(options,1) == 1)
          figure(2)
   subplot(2,1,1);
   plot(epsrall(:,1),epsrall(:,2));
   subplot(2,1,2);
   plot(epsrall(:,1),epsrall(:,3));

end

%Compute fft
Fi=fft(Yi);
Fr=fft(Yr);
Frsyn(1:epsr_idx(1)-1)=0;
Frsyn(epsr_idx(end):P/2)=0;


ro1=(cos(theta)-sqrt(epsr-sin(theta)^2))/(cos(theta)+sqrt(epsr-sin(theta)^2));
thetat=asin(sin(theta)/real(epsr));
ro2=(cos(thetat)-sqrt(1/epsr-sin(thetat).^2))./(cos(thetat)+sqrt(1/epsr-sin(thetat).^2));
T=exp(-j*(w(epsr_idx)/(.3)).*sqrt(epsr)*d./cos(thetat));
Frsyn(epsr_idx)=(ro1+ro2.*(1+ro2).*(1+ro1).*T.^2).* Fi(epsr_idx);


Frsyn(P/2+1:P)=0;

if (bitand(options,1) == 1)
          figure(3)
          plot(f(1:P/(2*zp)),abs(Fi(1:P/(2*zp))));
   hold on;
          plot(f(1:P/(2*zp)),abs(Fr(1:P/(2*zp))),'r');
          plot(f(1:P/(2*zp)),abs(Frsyn(1:P/(2*zp))),'m');
          grid;
          %axis([0 3 -30 0]);
          hold off;
   graph_title=strcat('Fi, Fr,');
   title(graph_title);

end
```

```
Yrsyn=2*real(ifft(Frsyn));
Yrsyn=Yrsyn(1:N)';
if (bitand(options,1) == 1)
        figure(4);
        plot(t,Yrsyn);
        hold on
        plot(t,Yr(1:N),'r');
        hold off
end
x=t;
x(:,2)=Yrsyn;
x(1:length(f),3)=f;
x(1:length(f),4)=abs(Frsyn(1,1:length(f))');
x(1:length(f),5)=abs(Fr(1:length(f)));
fname=strcat(strtok(Yslabfname,'.'),'-synth','.txt');

save(fname,'x','-ascii','-tabs');
```

Function SynthesisDefect

```
%[Yrsyn,t]=synthesisdefect(epsrfname,Yifname,Yslabfname,Yafname,d,options)
%options: (default 0)
%        0: no options
%        1: Draw figures
function [Yrsyn,t]=synthesisdefect(epsrfname,Yifname,Yslabfname,Yafname,d,options)
warning off;
theta=0;%0.267;

d1=0.8*0.0254;
d2=0.25*0.0254;
d3=d-(d1+d2);
e2=1;



if(~exist('Yafname'))
   Yafname = 'air.dzt';
end;

if(~exist('Yifname'))
   Yifname = 'copper.dzt';
end;

if (~exist('options'))
   options=0;
end;

close all

[Yi,N,T]=LoadDZT(Yifname,1);
Ya=LoadDZT(Yafname,1);
Yr=LoadDZT(Yslabfname,1);

Yr=RmCouple(Yr,Ya,0);        %Clean Yr
Yi=-RmCouple(Yi,Ya,0);       %Clean Yi

zp=4;                                                    %Zero padding
P=zp*N;                                                  %Zero padded length
t=[0:N-1]'*T/(N-1);
f=[0:N/2-1]'/(T*zp);
w=2*pi*[0:2*N-1]'/(T*zp);

[Yic,start_idx,end_idx]=GetPulse(Yi,3,3);

Yi(1:start_idx)=0;
Yi(end_idx+1:P)=0;           %Zero after pulse + zero padding

Yr(1:start_idx)=0;
```

```
[Yrc,start_idx,end_idx]=GetPulse(Yr,0,5);

Yr(end_idx+1:P)=0;              %Zero after pulse + zero padding

if (bitand(options,1) == 1)
   figure(1)
   plot(t,Yi(1:N));
   hold on
   plot(t,Yr(1:N),'r')
   hold off
   grid on
   title('Clean Yi');
end;

load(epsrfname);
epsrall=eval(strtok(epsrfname,'.'));
epsr_idx=epsrall(:,1)*T*zp+1;
epsr=epsrall(:,2)-j*epsrall(:,3);

if (bitand(options,1) == 1)
          figure(2)
   subplot(2,1,1);
   plot(epsrall(:,1),epsrall(:,2));
   subplot(2,1,2);
   plot(epsrall(:,1),epsrall(:,3));

end

%Compute fft
Fi=fft(Yi);
Fr=fft(Yr);
Frsyn(1:epsr_idx(1)-1)=0;
Frsyn(epsr_idx(end):P/2)=0;


rho1=(1-sqrt(epsr))./(1+sqrt(epsr));
rho2=(sqrt(epsr)-sqrt(e2))./(sqrt(epsr)+sqrt(e2));
T1=exp(-j*(w(epsr_idx)/(.3)).*sqrt(epsr)*d1);
T2=exp(-j*(w(epsr_idx)/(.3)).*sqrt(e2)*d2);
T3=exp(-j*(w(epsr_idx)/(.3)).*sqrt(epsr)*d3);
T4=exp(-j*(w(epsr_idx)/(.3)).*sqrt(epsr)*d);


Frsyn(epsr_idx)=(rho1+rho2.*(1-rho1.^2).*T1.^2-rho2.*(1-rho2.^2).*(1-
rho1.^2).*T1.^2.*T2.^2-rho1.*(1-rho2.^2).*(1-rho1.^2).*T1.*T2.*T3.*T4).*Fi(epsr_idx);


Frsyn(P/2+1:P)=0;

if (bitand(options,1) == 1)
          figure(3)
```

```
        plot(f(1:P/(2*zp)),abs(Fi(1:P/(2*zp))));
  hold on;
        plot(f(1:P/(2*zp)),abs(Fr(1:P/(2*zp))),'r');
        plot(f(1:P/(2*zp)),abs(Frsyn(1:P/(2*zp))),'m');
        grid;
        %axis([0 3 -30 0]);
        hold off;
  graph_title=strcat('Fi, Fr,');
  title(graph_title);

end

Yrsyn=2*real(ifft(Frsyn));
Yrsyn=Yrsyn(1:N)';
if (bitand(options,1) == 1)
        figure(4);
        plot(t,Yrsyn);
        hold on
        plot(t,Yr(1:N),'r');
        hold off
end
x=t;
x(:,2)=Yrsyn;
x(1:length(f),3)=f;
x(1:length(f),4)=abs(Frsyn(1,1:length(f))');
x(1:length(f),5)=abs(Fr(1:length(f)));
fname=strcat(strtok(Yslabfname,'.'),'-synth','.txt');

save(fname,'x','-ascii','-tabs');
```

Function SynthesisFlexible

```
%[Yrsyn,t]=synthesisflexible(epsrfname,Yifname,Yslabfname,Yafname,d,options)
%options: (default 0)
%       0: no options
%       1: Draw figures
function [Yrsyn,t]=synthesisflexible(epsrfname,Yifname,Yslabfname,Yafname,d,options)
warning off;
theta=0;%0.267;

d1=3*0.0254;
d2=5*0.0254;
d3=d-(d1+d2);
e2=8.5-0*j;
e3=15;


if(~exist('Yafname'))
   Yafname = 'air.dzt';
end;

if(~exist('Yifname'))
   Yifname = 'copper.dzt';
end;

if (~exist('options'))
   options=0;
end;

close all

[Yi,N,T]=LoadDZT(Yifname,1);
Ya=LoadDZT(Yafname,1);
Yr=LoadDZT(Yslabfname,1);

Yr=RmCouple(Yr,Ya,0);       %Clean Yr
Yi=-RmCouple(Yi,Ya,0);      %Clean Yi

zp=4;                                                   %Zero padding
P=zp*N;                                                 %Zero padded length
t=[0:N-1]'*T/(N-1);
f=[0:N/2-1]'/(T*zp);
w=2*pi*[0:2*N-1]'/(T*zp);

[Yic,start_idx,end_idx]=GetPulse(Yi,3,3);

Yi(1:start_idx)=0;
Yi(end_idx+1:P)=0;          %Zero after pulse + zero padding

Yr(1:start_idx)=0;
```

```
[Yrc,start_idx,end_idx]=GetPulse(Yr,0,10);

Yr(end_idx+1:P)=0;              %Zero after pulse + zero padding

if (bitand(options,1) == 1)
   figure(1)
   plot(t,Yi(1:N));
   hold on
   plot(t,Yr(1:N),'r')
   hold off
   grid on
   title('Clean Yi');
end;

load(epsrfname);
epsrall=eval(strtok(epsrfname,'.'));
epsr_idx=epsrall(:,1)*T*zp+1;
epsr=epsrall(:,2)-j*epsrall(:,3);

if (bitand(options,1) == 1)
          figure(2)
   subplot(2,1,1);
   plot(epsrall(:,1),epsrall(:,2));
   subplot(2,1,2);
   plot(epsrall(:,1),epsrall(:,3));

end

%Compute fft
Fi=fft(Yi);
Fr=fft(Yr);
Frsyn(1:epsr_idx(1)-1)=0;
Frsyn(epsr_idx(end):P/2)=0;



rho1=(1-sqrt(epsr))./(1+sqrt(epsr));
rho2=(sqrt(epsr)-sqrt(e2))./(sqrt(epsr)+sqrt(e2));
rho3=(sqrt(e2)-sqrt(e3))./(sqrt(e2)+sqrt(e3));

T1=exp(-j*(w(epsr_idx)/(.3)).*sqrt(epsr)*d1);
T2=exp(-j*(w(epsr_idx)/(.3)).*sqrt(e2)*d2);


Frsyn(epsr_idx)=(rho1+rho2.*(1-rho1.^2).*T1.^2+rho3.*(1-rho2.^2).*(1-
rho1.^2).*T1.^2.*T2.^2).*Fi(epsr_idx);


Frsyn(P/2+1:P)=0;

if (bitand(options,1) == 1)
```

```
        figure(3)
        plot(f(1:P/(2*zp)),abs(Fi(1:P/(2*zp))));
  hold on;
        plot(f(1:P/(2*zp)),abs(Fr(1:P/(2*zp))),'r');
        plot(f(1:P/(2*zp)),abs(Frsyn(1:P/(2*zp))),'m');
        grid;
        %axis([0 3 -30 0]);
        hold off;
  graph_title=strcat('Fi, Fr,');
  title(graph_title);

end

Yrsyn=2*real(ifft(Frsyn));
Yrsyn=Yrsyn(1:N)';
if (bitand(options,1) == 1)
        figure(4);
        plot(t,Yrsyn);
        hold on
        plot(t,Yr(1:N),'r');
        hold off
end
x=t;
x(:,2)=Yrsyn;
x(1:length(f),3)=f;
x(1:length(f),4)=abs(Frsyn(1,1:length(f))');
x(1:length(f),5)=abs(Fr(1:length(f)));
fname=strcat(strtok(Yslabfname,'.'),'-synth','.txt');

save(fname,'x','-ascii','-tabs');
zoom on;
grid on;
```

APPENDIX C
(AIR-COUPLED GPR DATA)

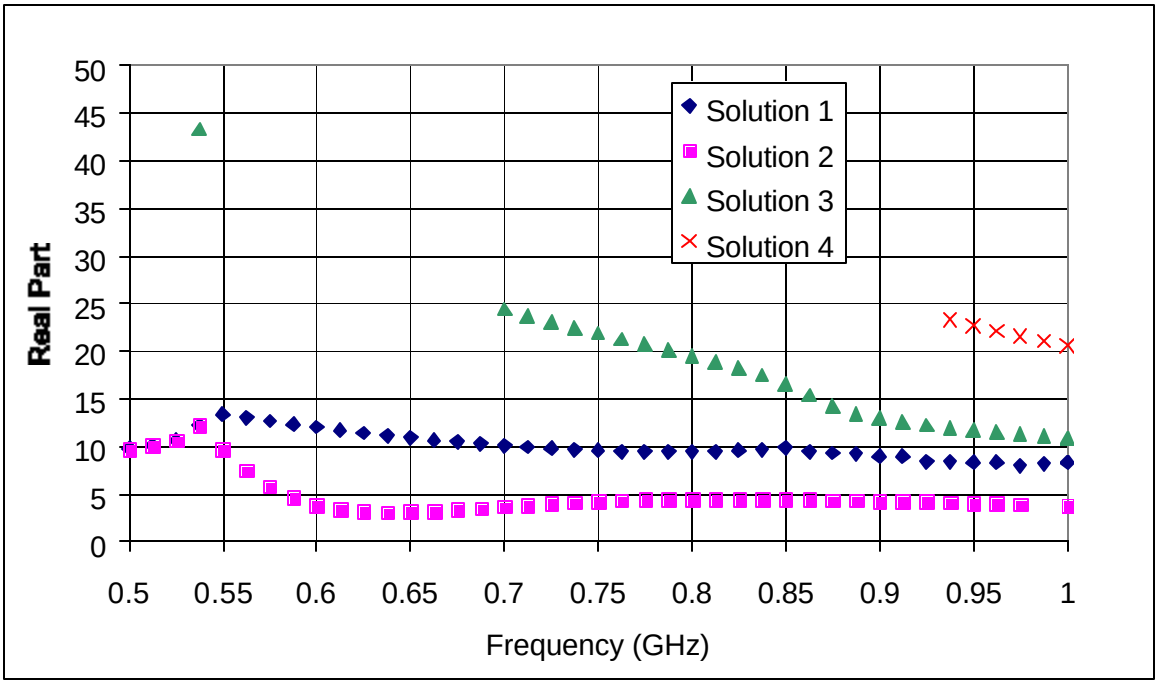

Figure C1 Solutions for the real part of ε_r from 0.5 to 1 GHz for slab M1S1 (07/17/00)

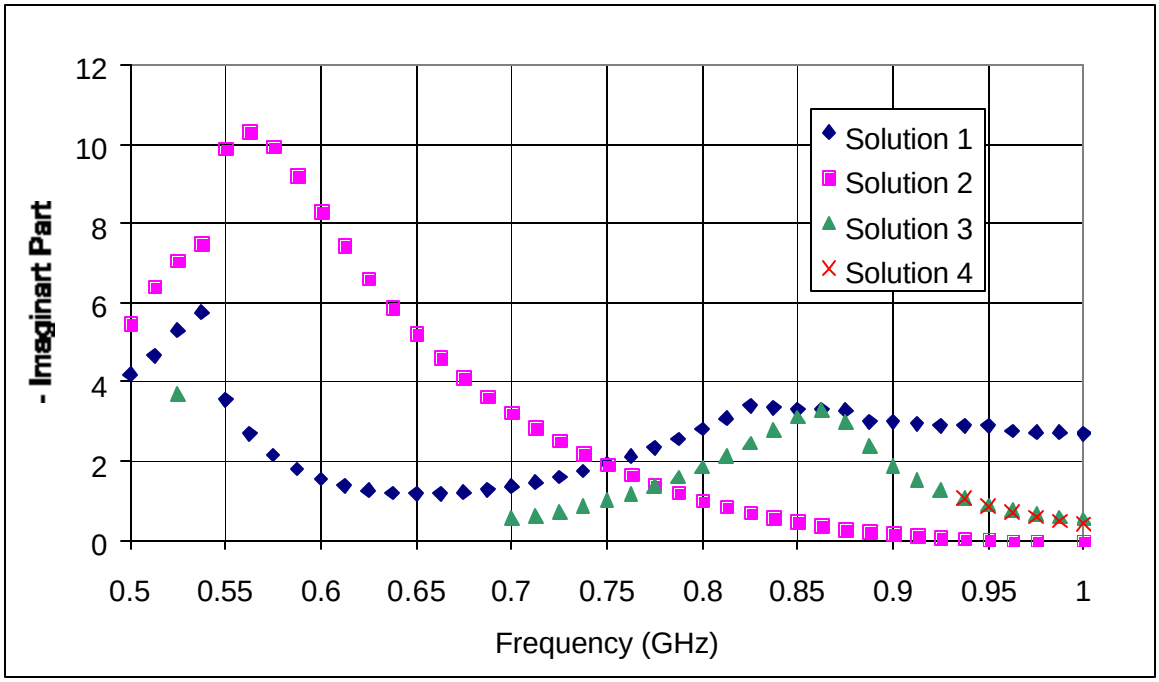

Figure C2 Solutions for the imaginary part of ε_r from 0.5 to 1 GHz for slab M1S1 (07/17/00)

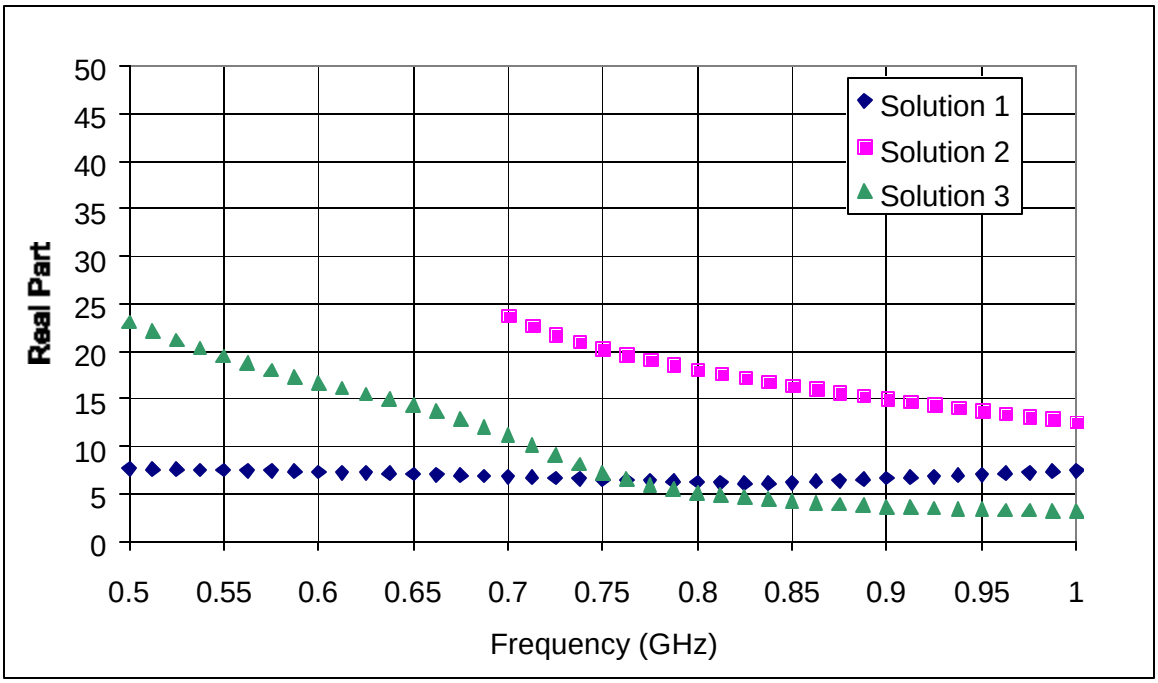

Figure C3 Solutions for the real part of ε_r from 0.5 to 1 GHz for slab M3S2 (07/17/00)

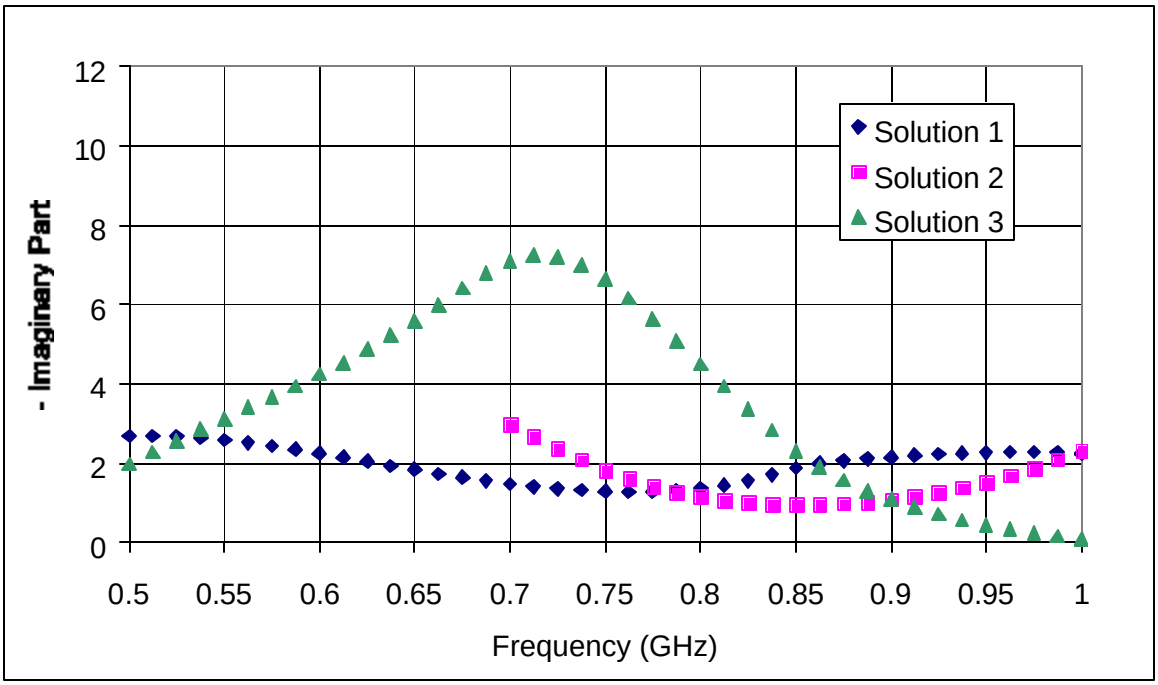

Figure C4 Solutions for the imaginary part of ε_r from 0.5 to 1 GHz for slab M2S1 (07/17/00)

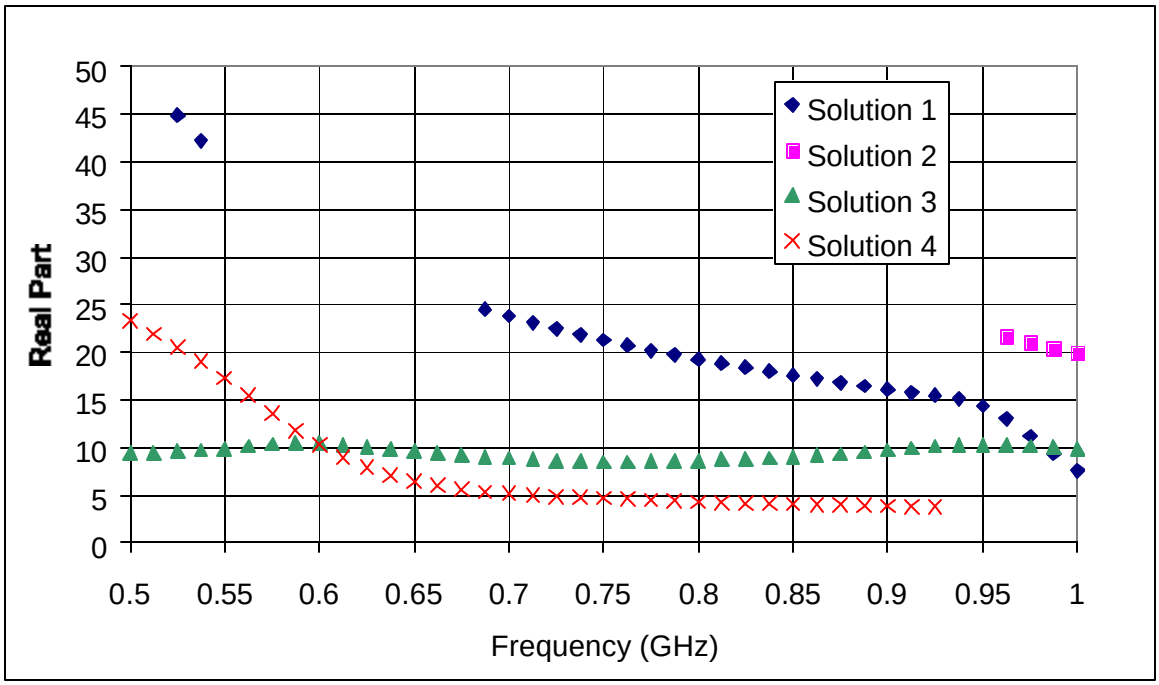

Figure C5 Solutions for the real part of ε_r from 0.5 to 1 GHz for slab M4S1 (07/17/00)

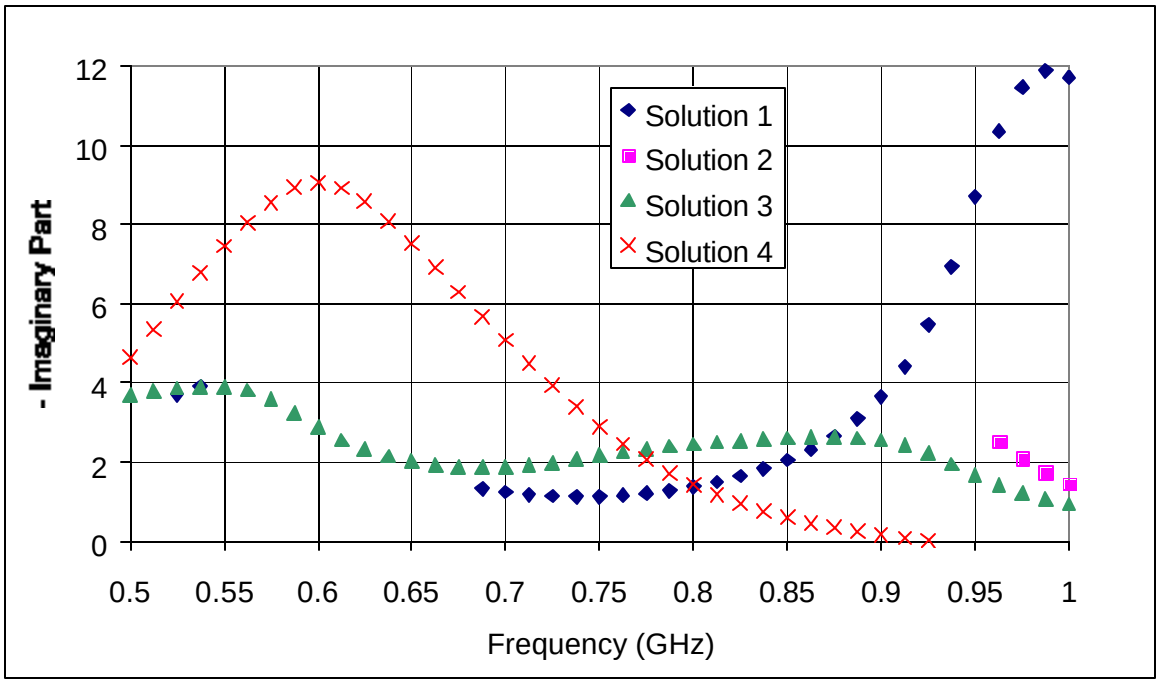

Figure C6 Solutions for the imaginary part of ε_r from 0.5 to 1 GHz for slab M4S1 (07/17/00)

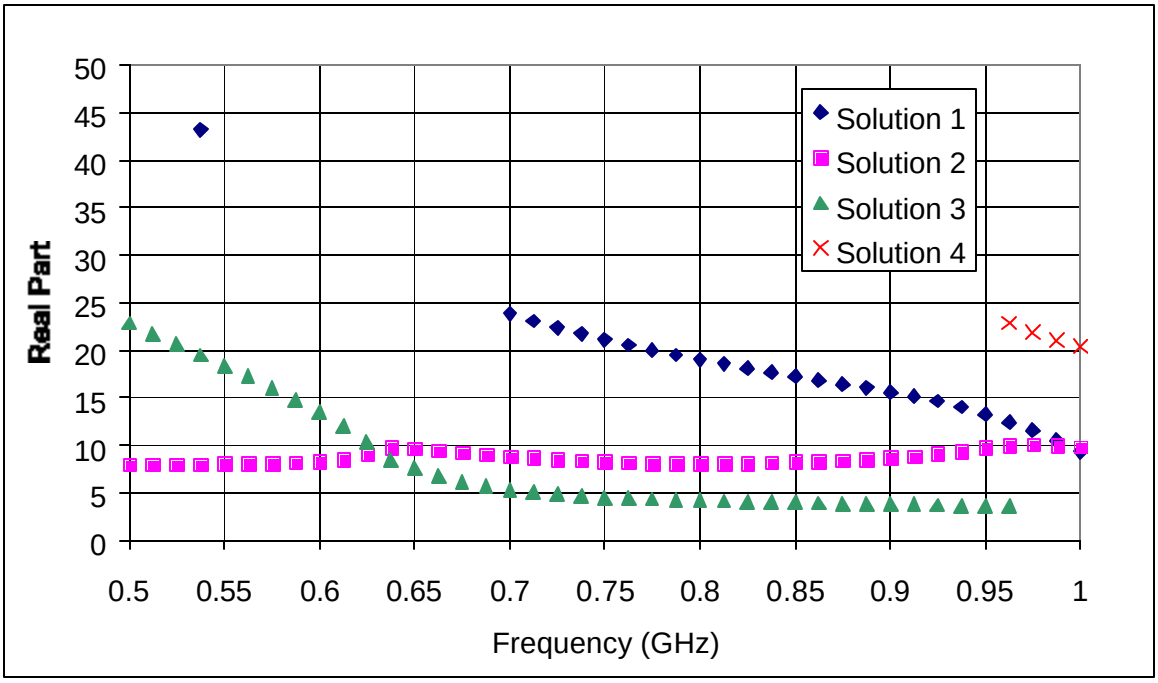

Figure C7 Solutions for the real part of ε_r from 0.5 to 1 GHz for slab M5S1 (07/17/00)

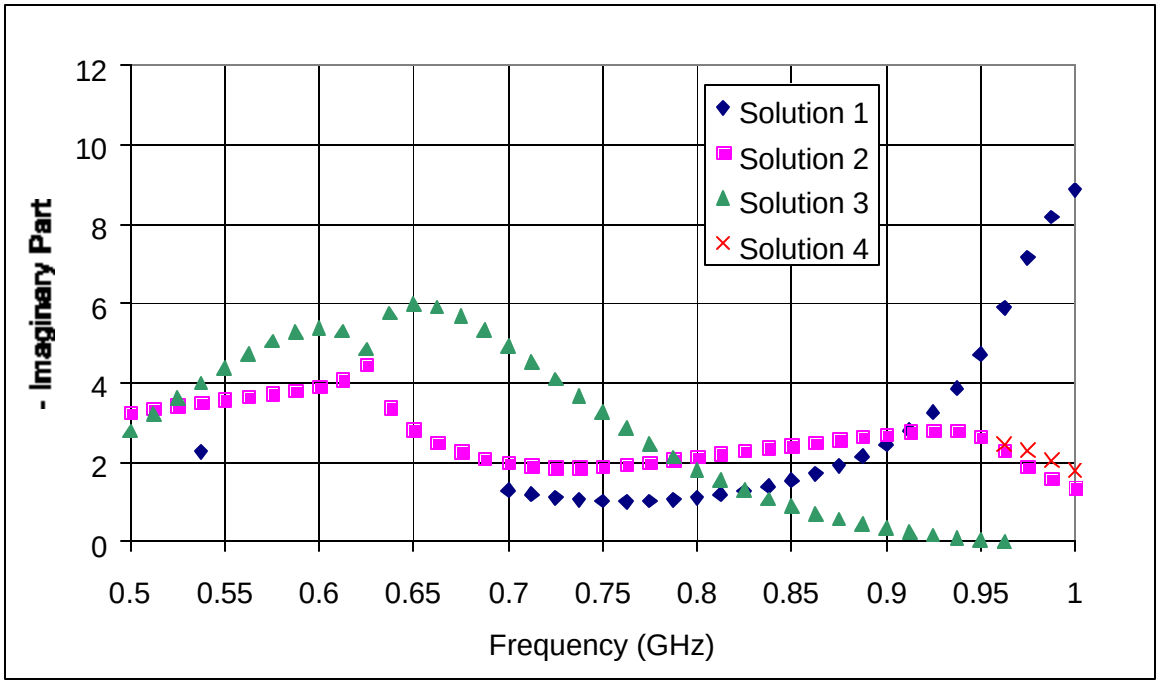

Figure C8 Solutions for the imaginary part of ε_r from 0.5 to 1 GHz for slab M5S1 (07/17/00)

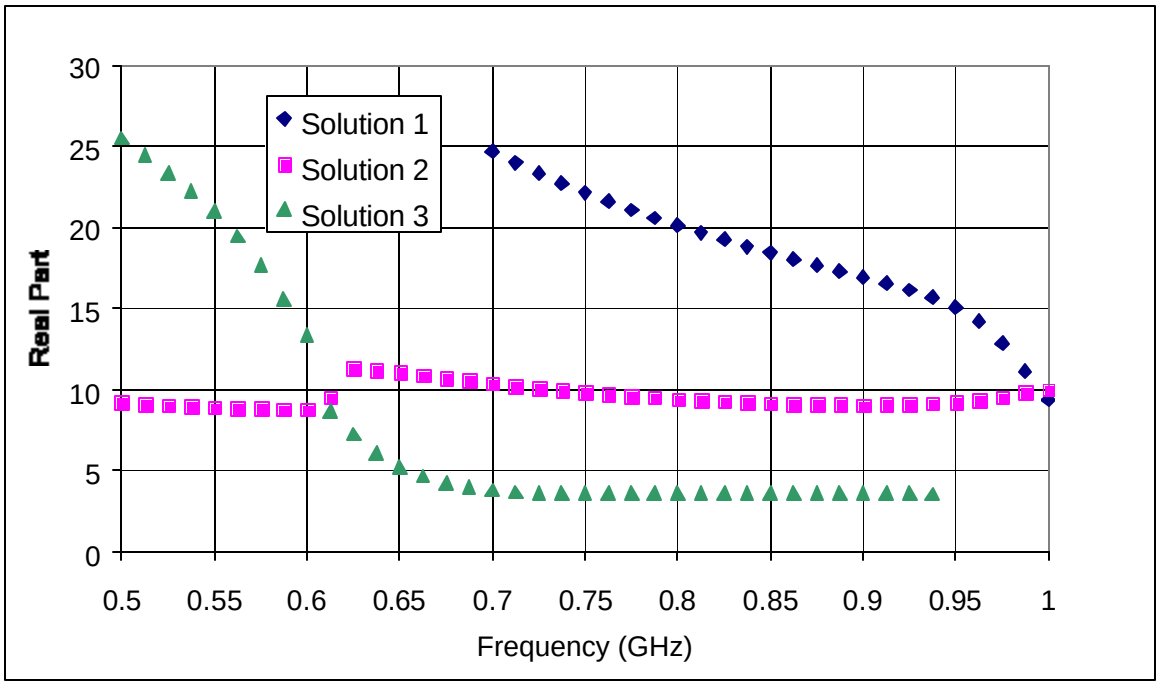

Figure C9 Solutions for the real part of ε_r from 0.5 to 1 GHz for slab M1S1 (11/05/00)

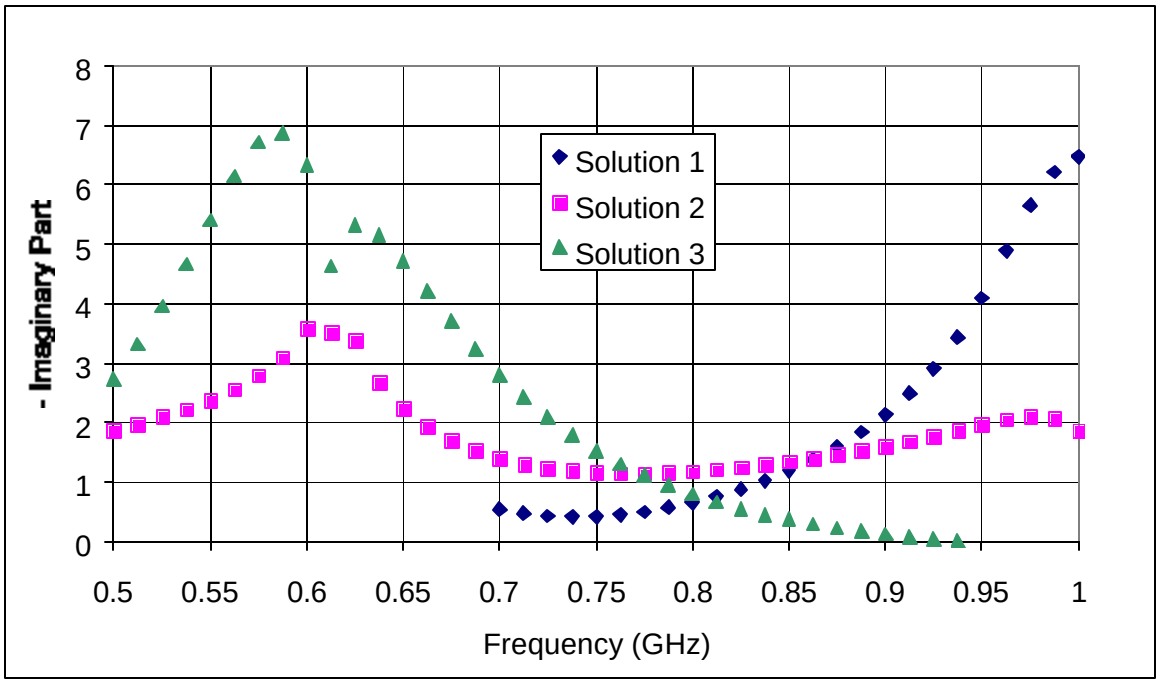

Figure C10 Solutions for the imaginary part of ε_r from 0.5 to 1 GHz for slab M1S1 (11/05/00)

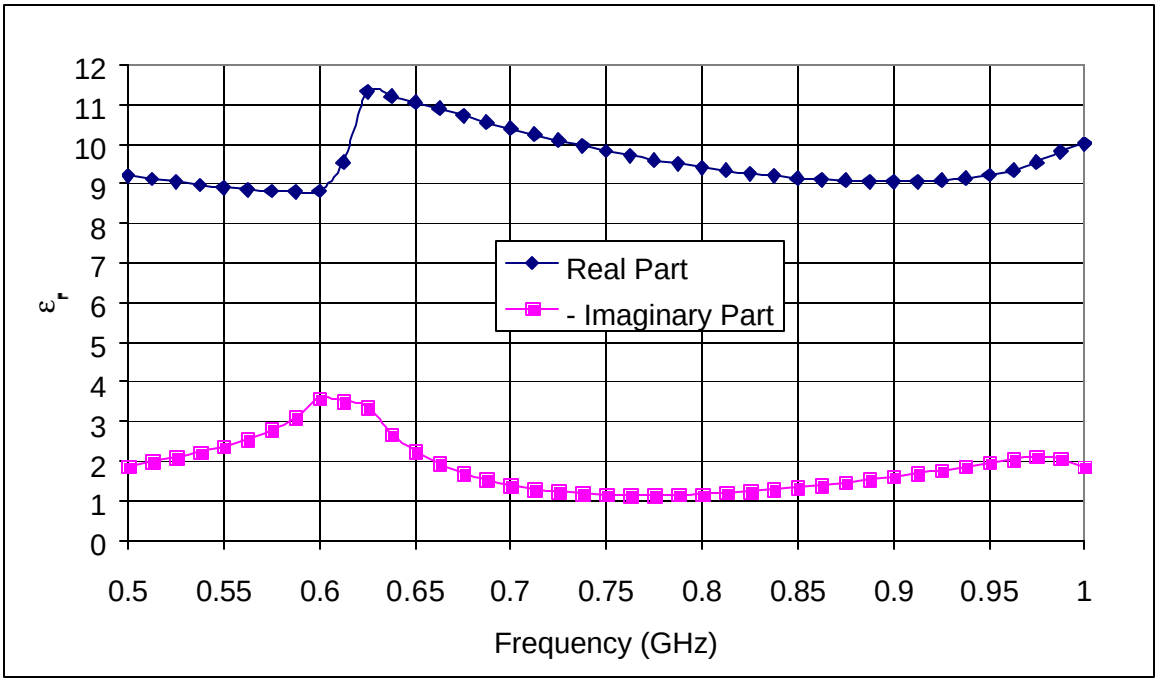

Figure C11 Complex dielectric constant for concrete mix M1 (11/05/00)

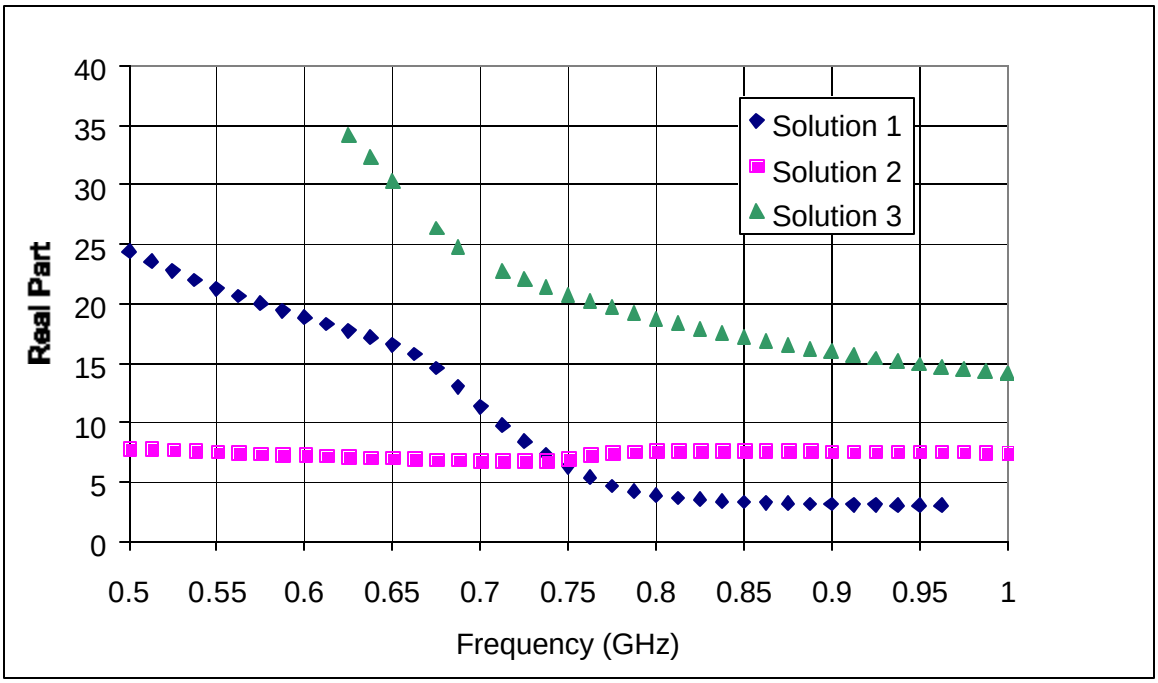

Figure C12 Solutions for the real part of ε_r from 0.5 to 1 GHz for slab M2S1 (11/05/00)

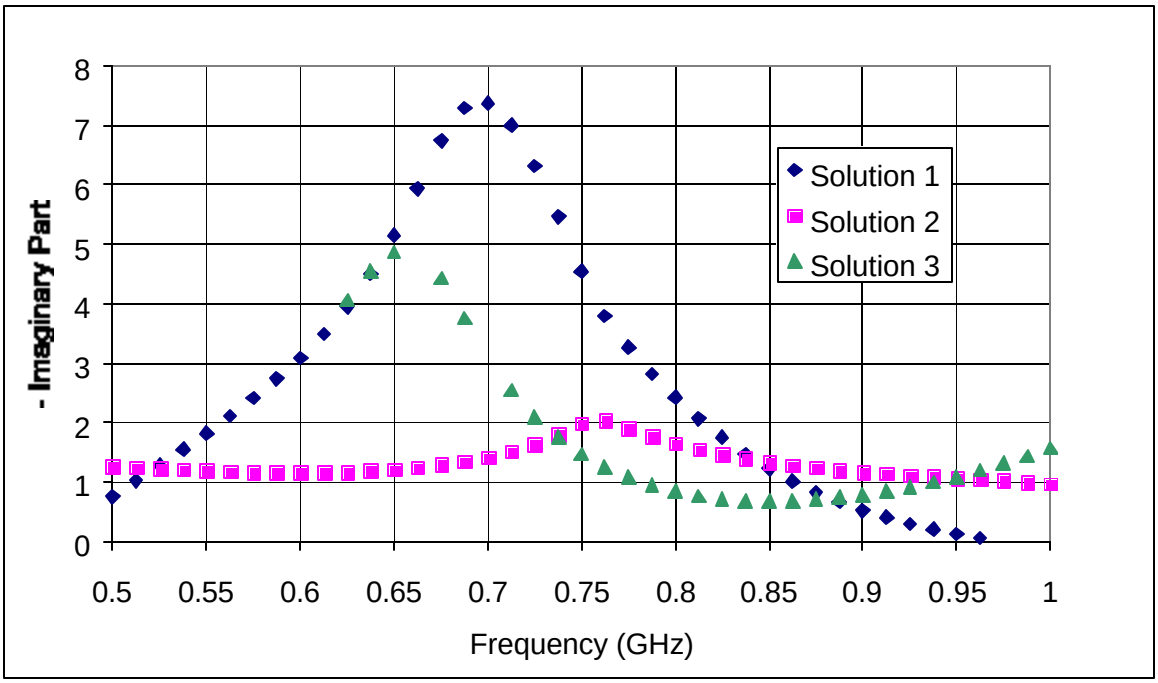

Figure C13 Solutions for the imaginary part of ε_r from 0.5 to 1 GHz for slab M2S1 (11/05/00)

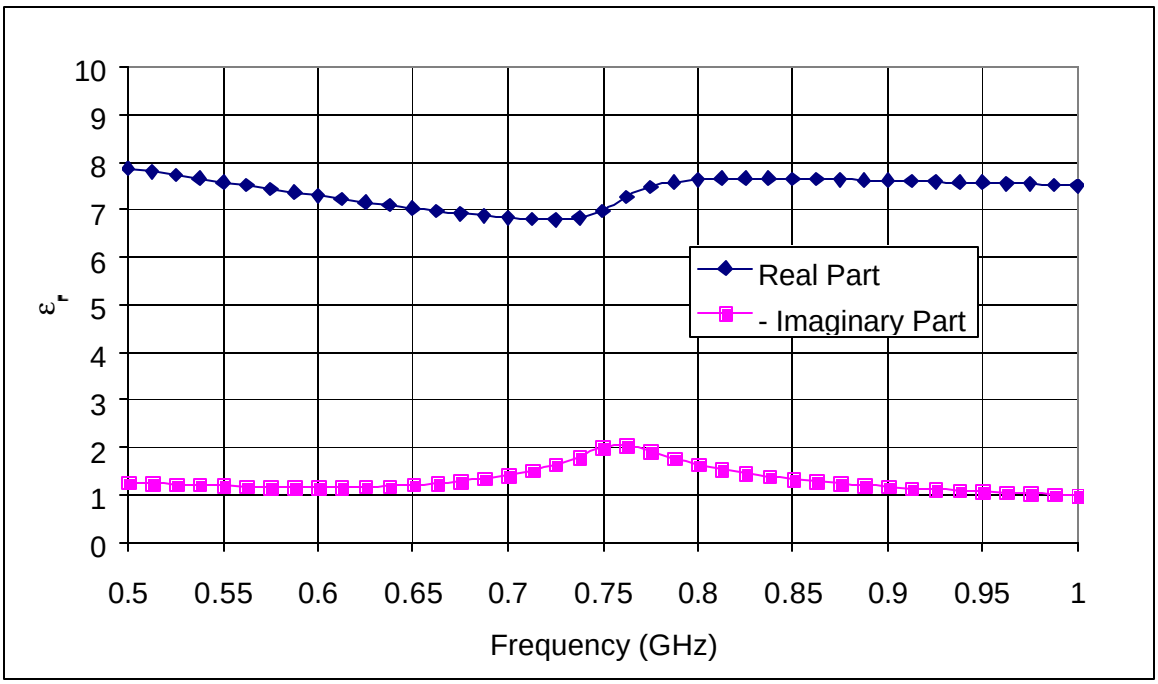

Figure C14 Complex dielectric constant for concrete mix M2 (11/05/00)

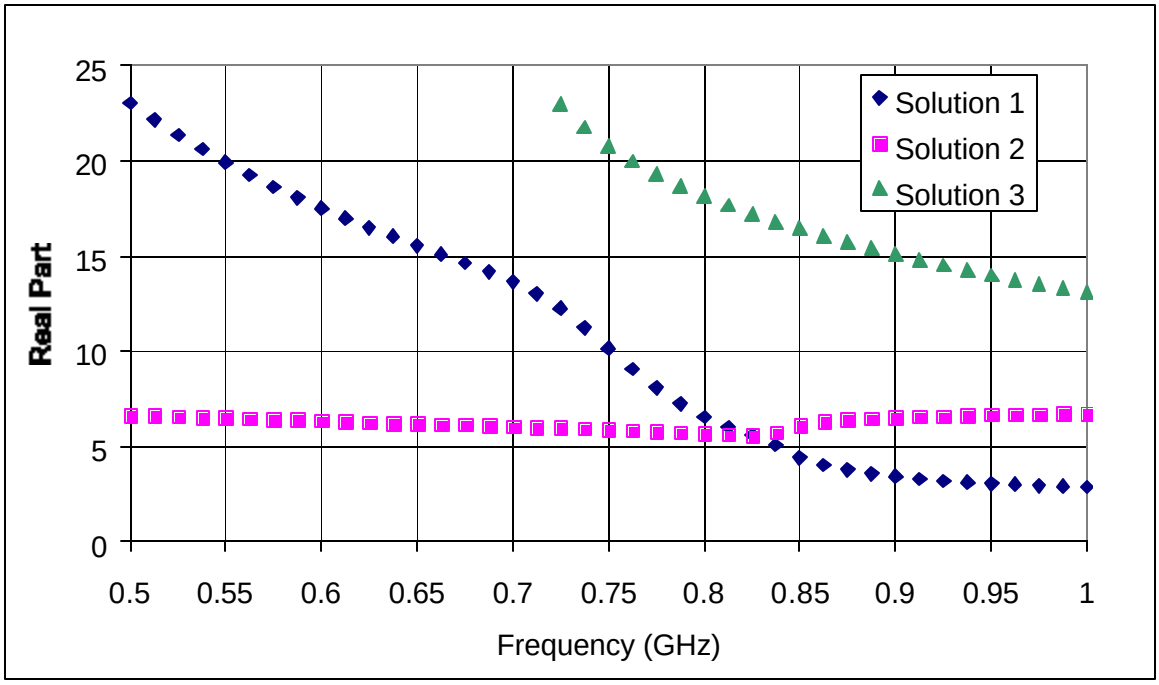

Figure C15 Solutions for the real part of ε_r from 0.5 to 1 GHz for slab M3S2 (11/05/00)

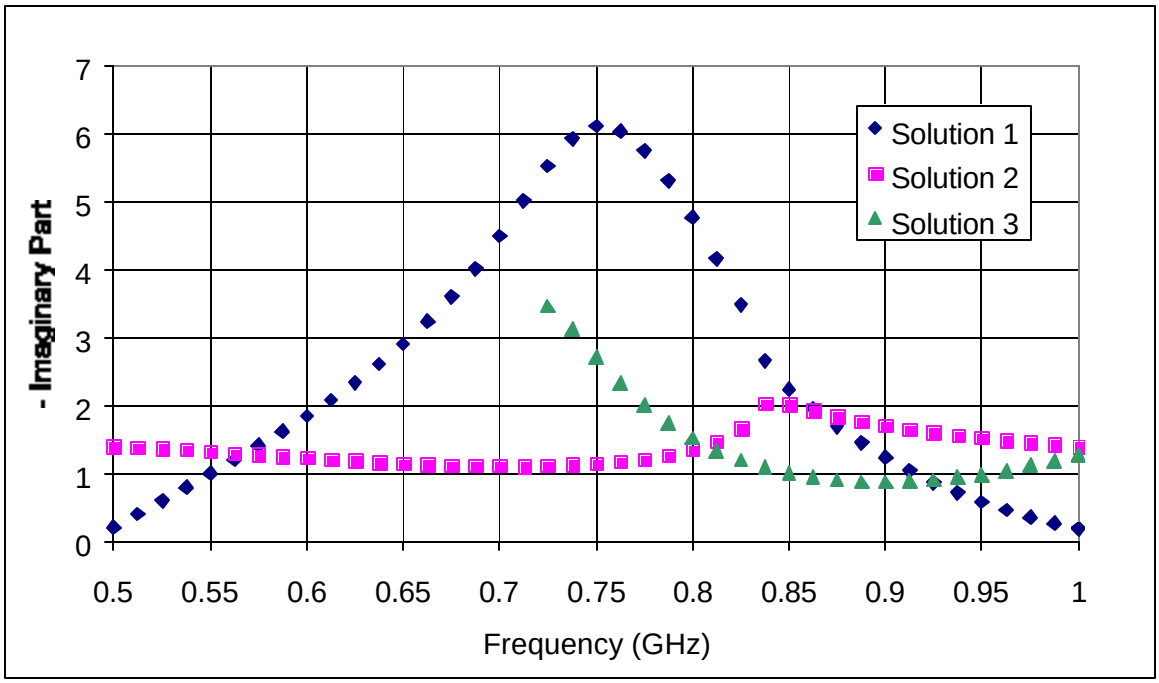

Figure C16 Solutions for the imaginary part of ε_r from 0.5 to 1 GHz for slab M3S2 (11/05/00)

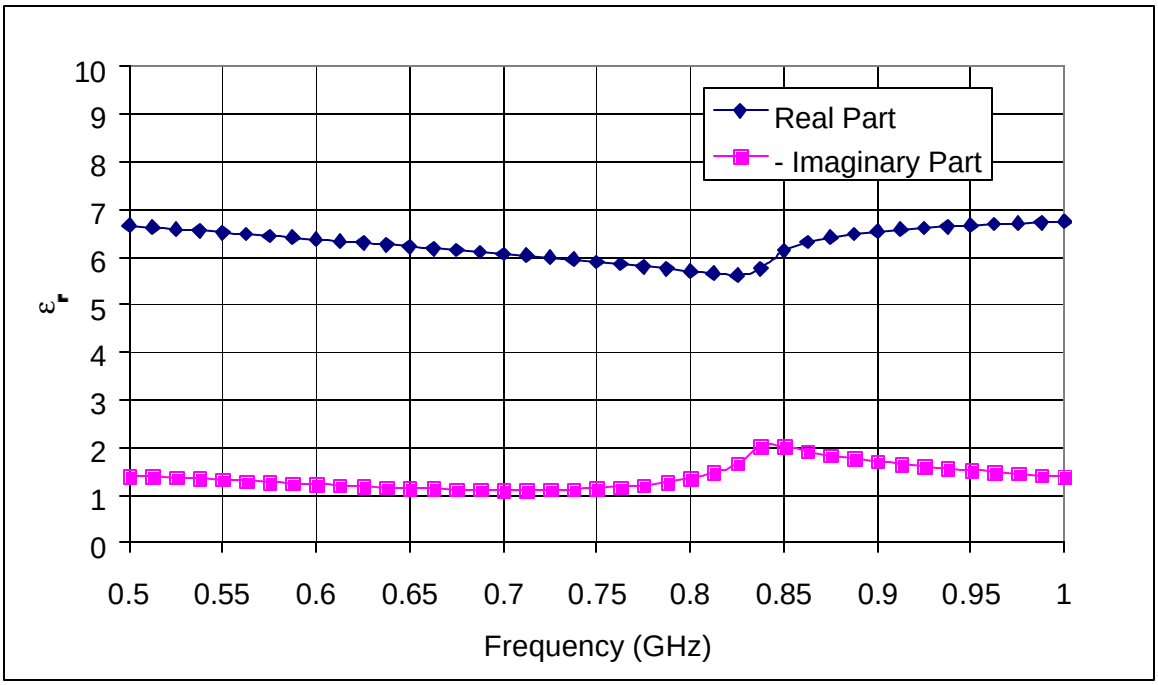

Figure C17 Complex dielectric constant for concrete mix M3 (11/05/00)

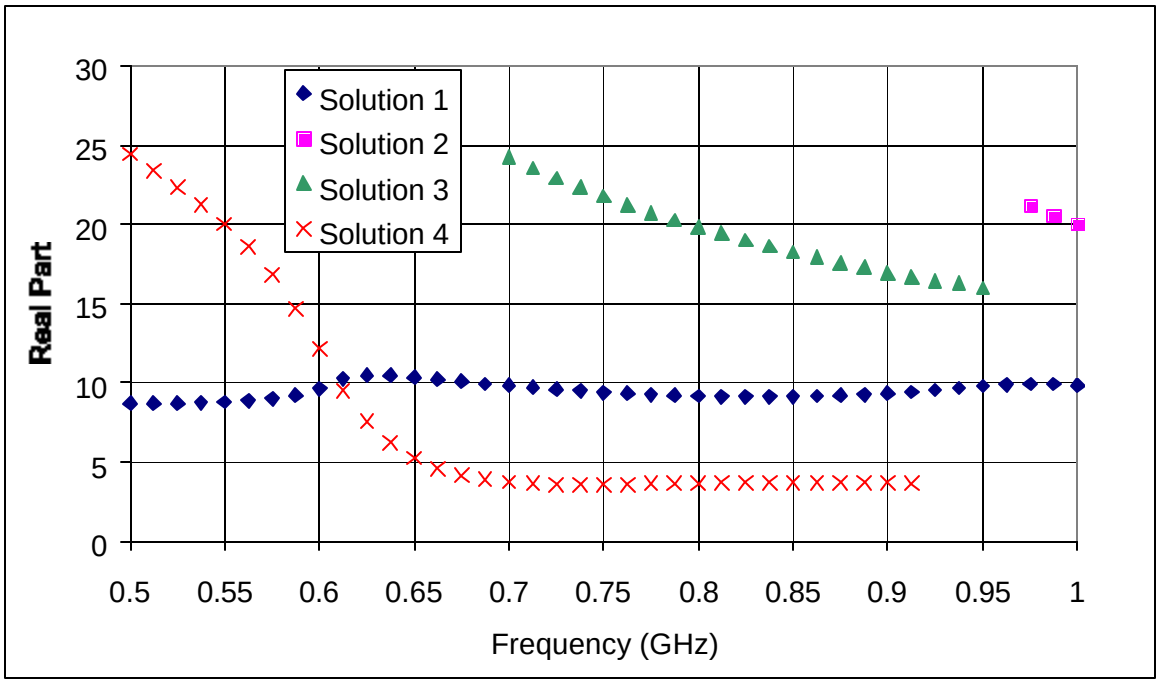

Figure C18 Solutions for the real part of ε_r from 0.5 to 1 GHz for slab M4S1 (11/05/00)

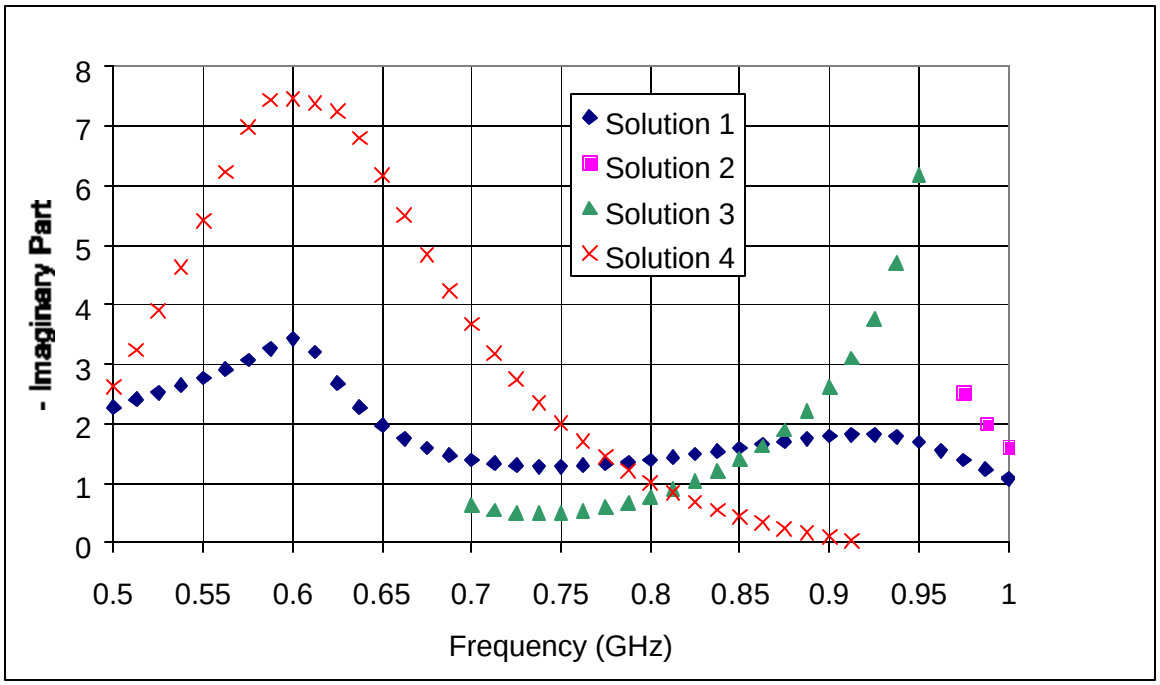

Figure C19 Solutions for the imaginary part of ε_r from 0.5 to 1 GHz for slab M4S1 (11/05/00)

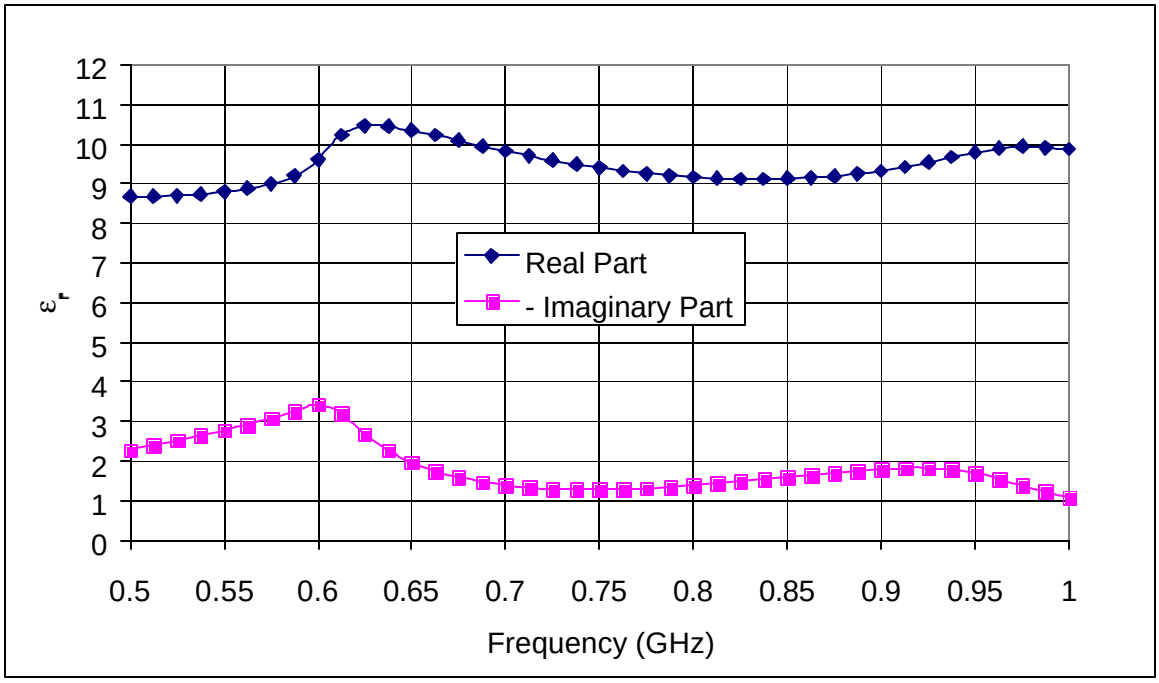

Figure C20 Complex dielectric constant for concrete mix M4 (11/05/00)

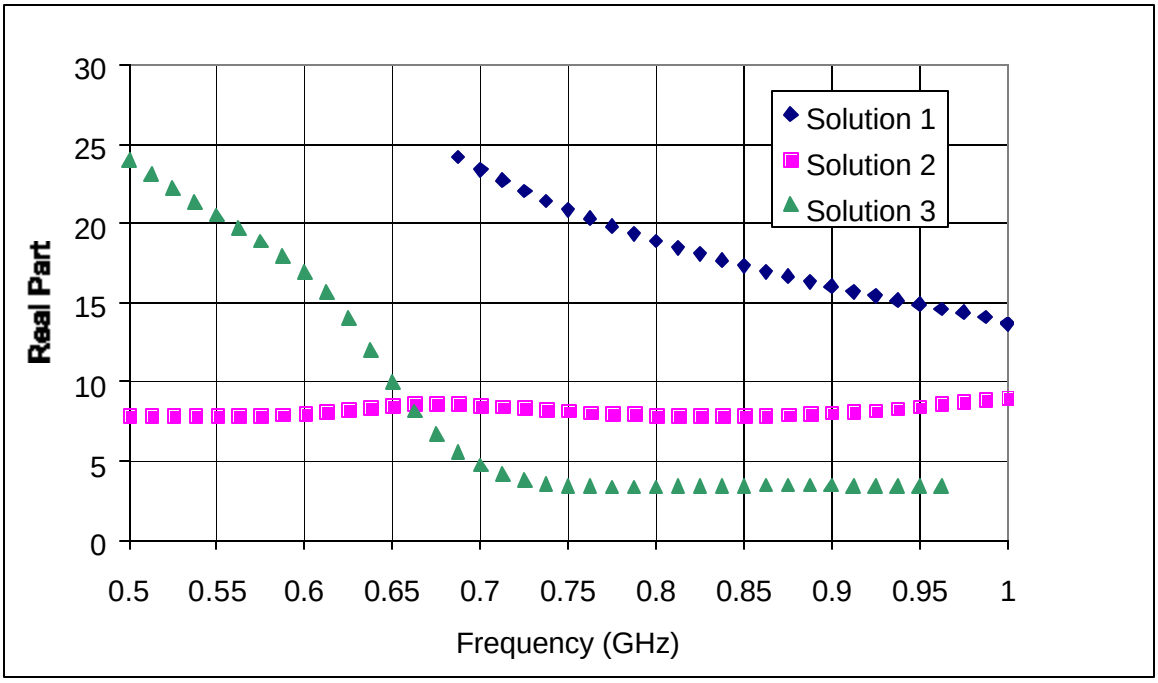

Figure C21 Solutions for the real part of ε_r from 0.5 to 1 GHz for slab M5S1 (11/05/00)

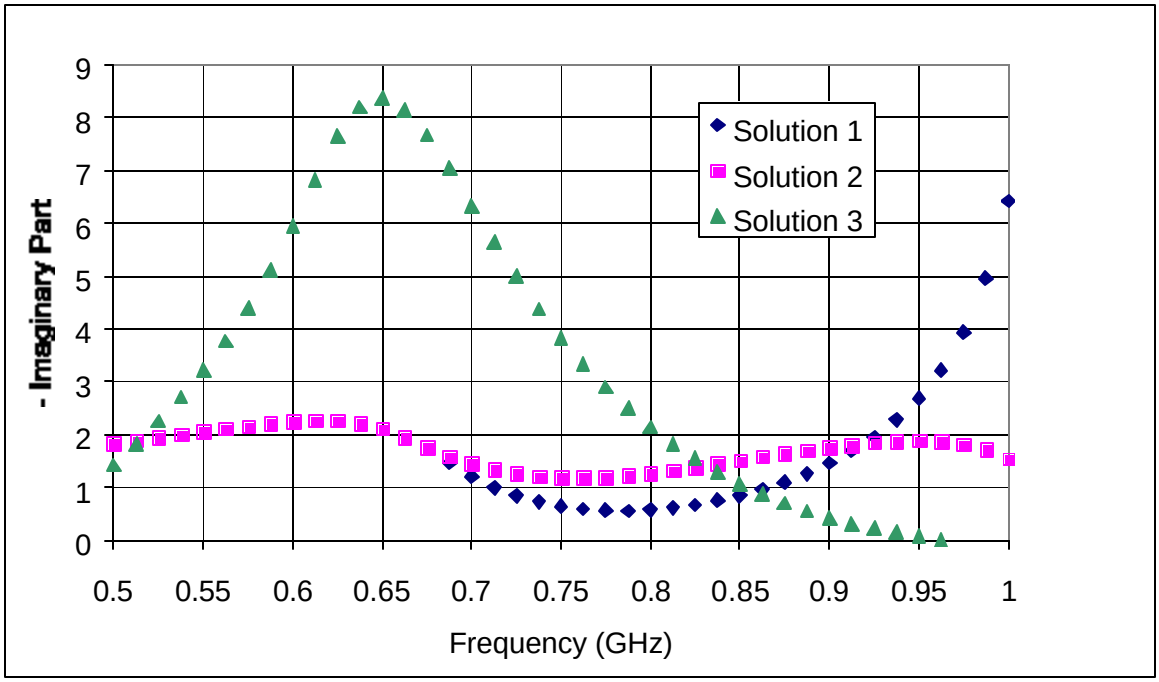

Figure C22 Solutions for the imaginary part of ε_r from 0.5 to 1 GHz for slab M5S1 (11/05/00)

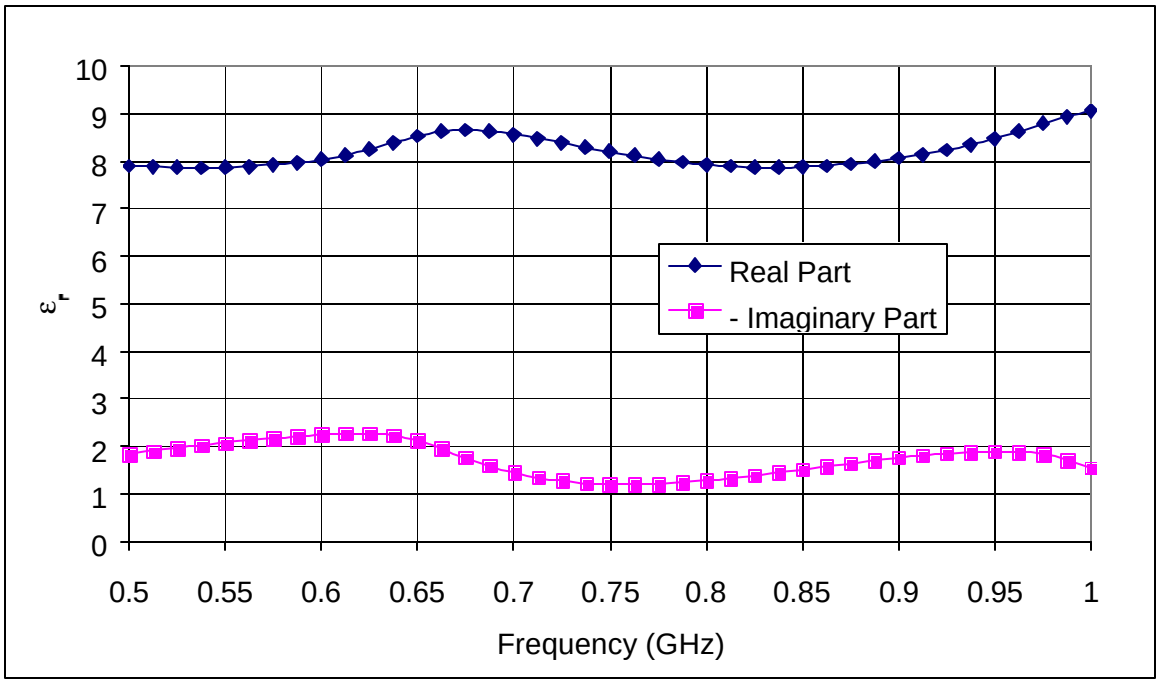

Figure C23 Complex dielectric constant for concrete mix M5 (11/05/00)

Table C1 Frequency and concrete mix effects on the real part of the dielectric constant (11/05/00)

Frequency	Count	Average	Variance	Coef. of Var.
0.5	5	8.065089	0.933694	12.0
0.5125	5	8.02372	0.924039	12.0
0.525	5	7.987632	0.923682	12.0
0.5375	5	7.957525	0.935174	12.2
0.55	5	7.934763	0.962566	12.4
0.5625	5	7.921823	1.01308	12.7
0.575	5	7.923401	1.101406	13.2
0.5875	5	7.949552	1.26343	14.1
0.6	5	8.024828	1.610088	15.8
0.6125	5	8.292584	2.597816	19.4
0.625	5	8.696355	4.597751	24.7
0.6375	5	8.679425	4.508715	24.5
0.65	5	8.638984	4.319196	24.1
0.6625	5	8.58054	4.108108	23.6
0.675	5	8.506241	3.896498	23.2
0.6875	5	8.422205	3.689558	22.8
0.7	5	8.334779	3.490699	22.4
0.7125	5	8.248889	3.301177	22.0
0.725	5	8.168936	3.117972	21.6
0.7375	5	8.101295	2.929077	21.1
0.75	5	8.060812	2.703049	20.4
0.7625	5	8.054333	2.458764	19.5
0.775	5	8.036368	2.312037	18.9
0.7875	5	8.003925	2.234465	18.7
0.8	5	7.967364	2.19355	18.6
0.8125	5	7.932544	2.174764	18.6
0.825	5	7.904592	2.160068	18.6
0.8375	5	7.918295	1.961924	17.7
0.85	5	7.987683	1.550671	15.6
0.8625	5	8.022277	1.386598	14.7
0.875	5	8.050596	1.306309	14.2
0.8875	5	8.080703	1.272414	14.0
0.9	5	8.116242	1.273295	13.9
0.9125	5	8.159495	1.305788	14.0
0.925	5	8.212014	1.369808	14.3
0.9375	5	8.274292	1.464055	14.6
0.95	5	8.344978	1.580873	15.1
0.9625	5	8.42154	1.708019	15.5
0.975	5	8.503288	1.847214	16.0
0.9875	5	8.584682	2.008479	16.5
1	5	8.635528	2.124216	16.9
Concrete Mix	**Count**	**Average**	**Variance**	**Coef. of Var.**
M1	41	9.589538	0.497414	7.4
M2	41	7.395939	0.099836	4.3
M3	41	6.278186	0.115424	5.4
M4	41	9.476966	0.2503	5.3
M5	41	8.202068	0.11177	4.1

Table C2 Frequency and concrete mix effects on the imaginary part of the dielectric constant (11/05/00)

Frequency	Count	Average	Variance	Coef. of Var.
0.5	5	1.730801	0.1652	23.5
0.5125	5	1.783377	0.219765	26.3
0.525	5	1.835429	0.284894	29.1
0.5375	5	1.889368	0.363265	31.9
0.55	5	1.947948	0.459453	34.8
0.5625	5	2.014674	0.581482	37.8
0.575	5	2.09456	0.744196	41.2
0.5875	5	2.195552	0.977249	45.0
0.6	5	2.328293	1.342628	49.8
0.6125	5	2.273297	1.202061	48.2
0.625	5	2.136069	0.920481	44.9
0.6375	5	1.907522	0.4773	36.2
0.65	5	1.739421	0.270486	29.9
0.6625	5	1.602935	0.149727	24.1
0.675	5	1.493495	0.075992	18.5
0.6875	5	1.411076	0.035552	13.4
0.7	5	1.354249	0.019028	10.2
0.7125	5	1.321167	0.020376	10.8
0.725	5	1.310732	0.037605	14.8
0.7375	5	1.322885	0.073374	20.5
0.75	5	1.353576	0.12811	26.4
0.7625	5	1.3675	0.14195	27.6
0.775	5	1.358464	0.099516	23.2
0.7875	5	1.356311	0.0587	17.9
0.8	5	1.368438	0.031066	12.9
0.8125	5	1.397115	0.017422	9.4
0.825	5	1.447942	0.023128	10.5
0.8375	5	1.540114	0.083977	18.8
0.85	5	1.561259	0.080056	18.1
0.8625	5	1.567157	0.061553	15.8
0.875	5	1.577539	0.05426	14.8
0.8875	5	1.591453	0.056103	14.9
0.9	5	1.607024	0.064597	15.8
0.9125	5	1.621957	0.077539	17.2
0.925	5	1.633244	0.092947	18.7
0.9375	5	1.636897	0.109561	20.2
0.95	5	1.628518	0.128383	22.0
0.9625	5	1.604835	0.152497	24.3
0.975	5	1.561701	0.177093	26.9
0.9875	5	1.485625	0.172689	28.0
1	5	1.373243	0.126843	25.9
Concrete Mix	**Count**	**Average**	**Variance**	**Coef. of Var.**
M1	41	1.877177	0.458293	36.1
M2	41	1.321511	0.072607	20.4
M3	41	1.394098	0.068337	18.8
M4	41	1.890318	0.418041	34.2
M5	41	1.728208	0.118583	19.9

Table C3 ANOVA table for the real part of the dielectric constant (11/05/00)

Source of Variation	SS	df	MS	F	P-value	F crit
Frequency	12.43768	40	0.310942	1.62839	0.018464	1.47018
Concrete Mix	323.9283	4	80.98207	424.0997	5.08E-84	2.428166
Error	30.55209	160	0.190951			
Total	366.918	204				

Table C4 ANOVA table for the imaginary part of the dielectric constant (11/05/00)

Source of Variation	SS	df	MS	F	P-value	F crit
Frequency	15.83343	40	0.395836	2.139578	0.000481	1.47018
Concrete Mix	11.8314	4	2.957849	15.98782	4.95E-11	2.428166
Error	29.60103	160	0.185006			
Total	57.26586	204				

Table C5 Paired t-test for the average real part of the complex dielectric constant over the frequency range 0.5 to 1 GHz and the time domain real part of the complex dielectric constant (11/05/00)

	Average over frequency range	Time Domain
Mean	8.188539447	8.20800668
Variance	1.97517235	1.825295555
Observations	5	5
Pearson Correlation	0.993070844	
Hypothesized Mean Difference	0	
Df	4	
t Stat	-0.254435587	
P(T<=t) one-tail	0.405851997	
t Critical one-tail	2.131846486	
P(T<=t) two-tail	**0.811703994**	
t Critical two-tail	2.776450856	

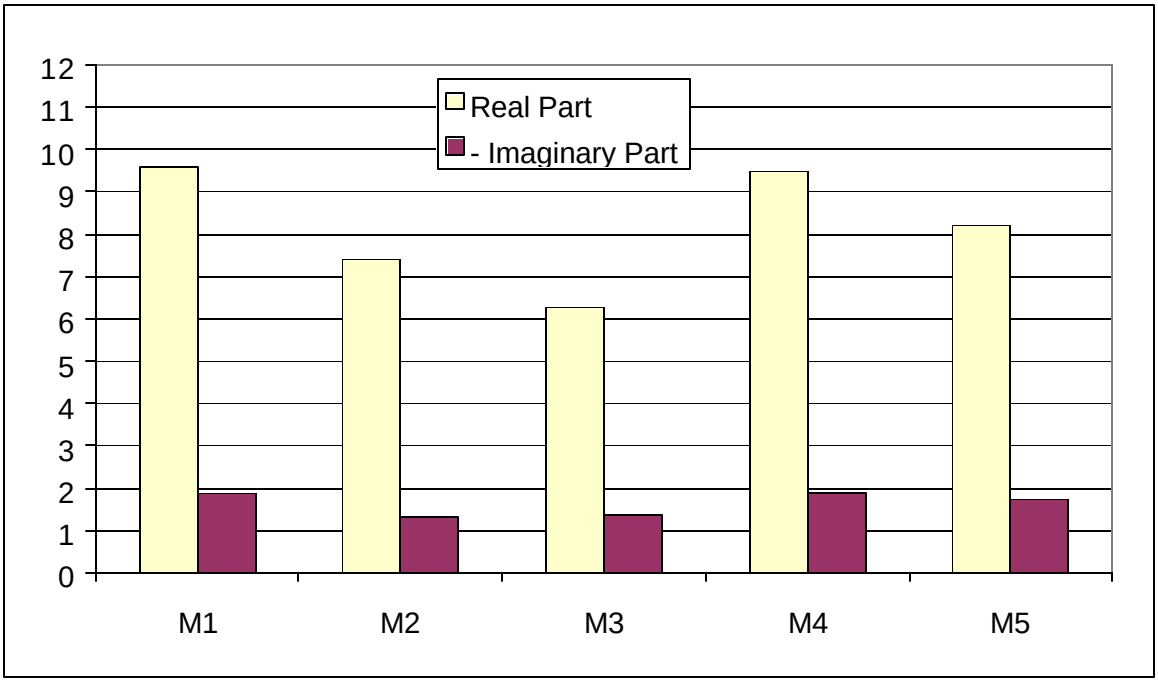

Figure C24 Average complex dielectric constant for all concrete mixes over the frequency range 0.5 to 1 GHz (11/05/00)

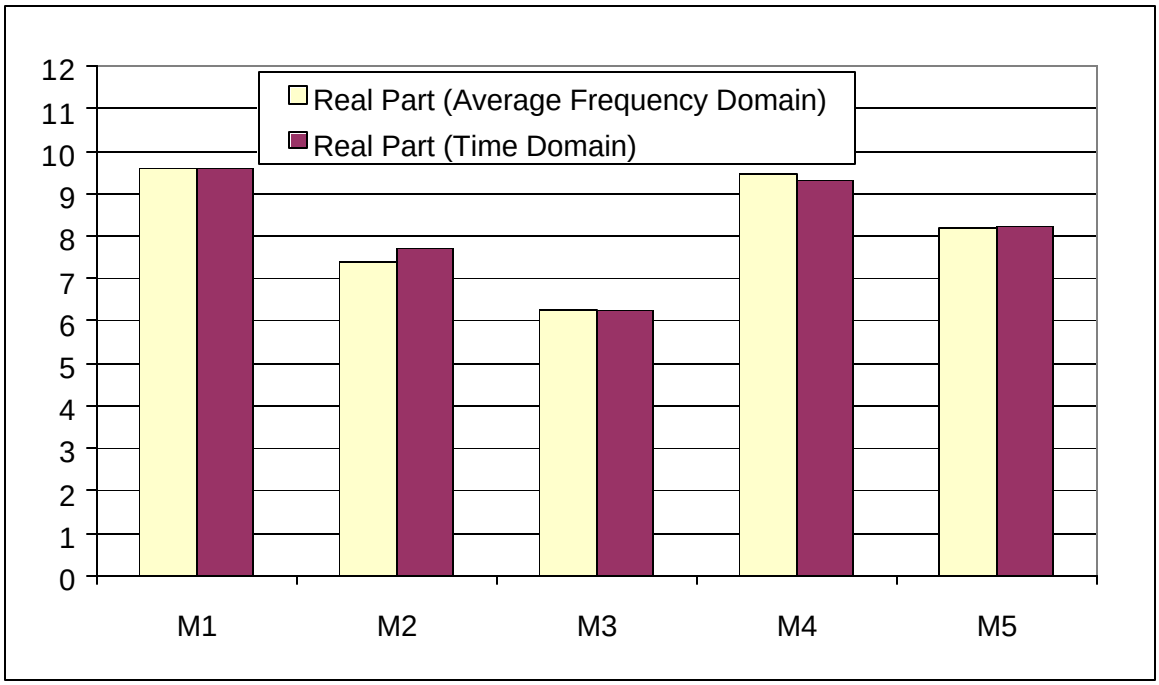

Figure C25 Comparison between the real parts of the complex dielectric constant as obtained by averaging the frequency domain solutions and by using the time domain signals (11/05/00)

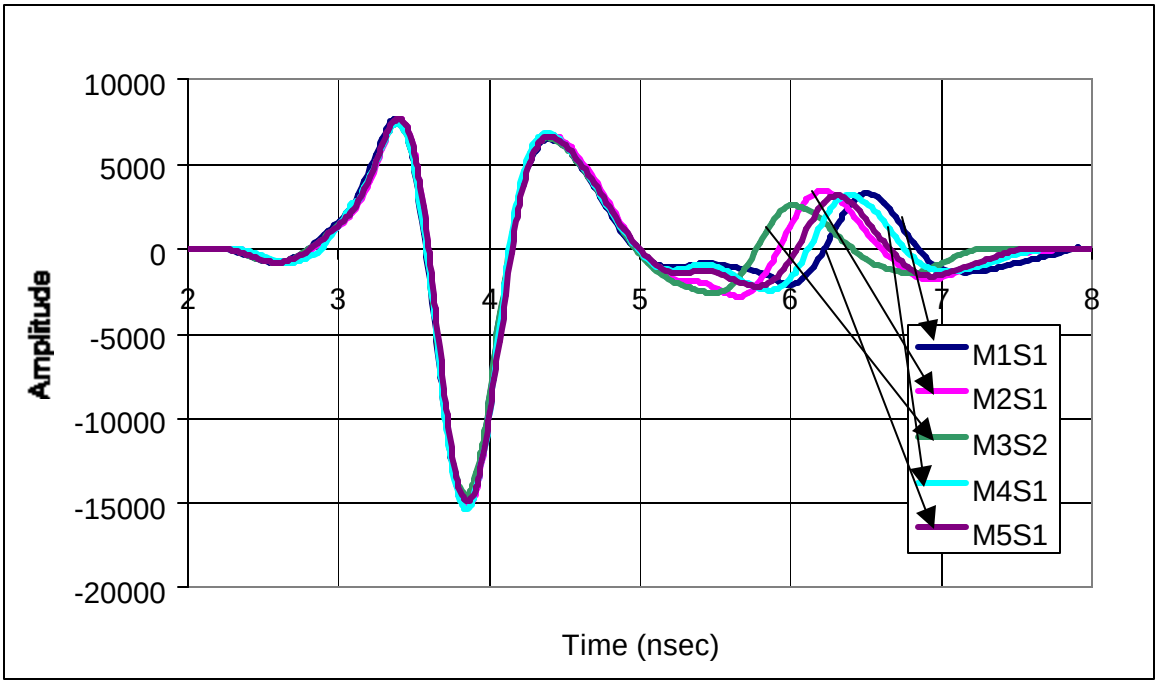

Figure C26 Time domain signals (12/04/99)

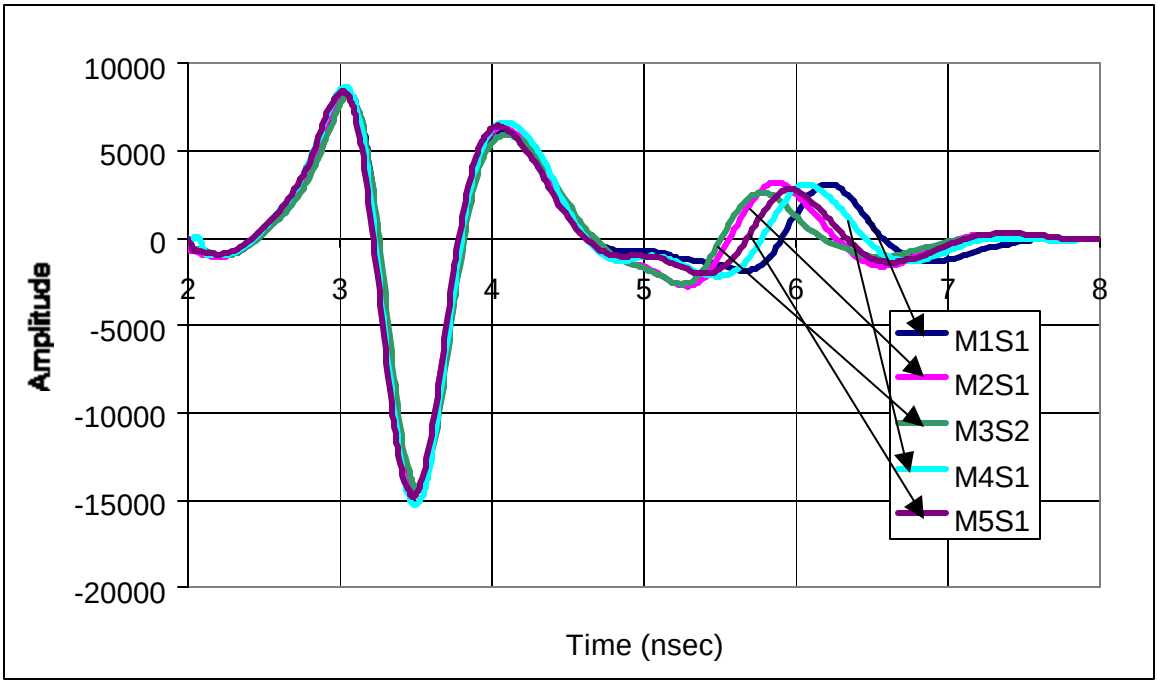

Figure C27 Time domain signals (05/13/00)

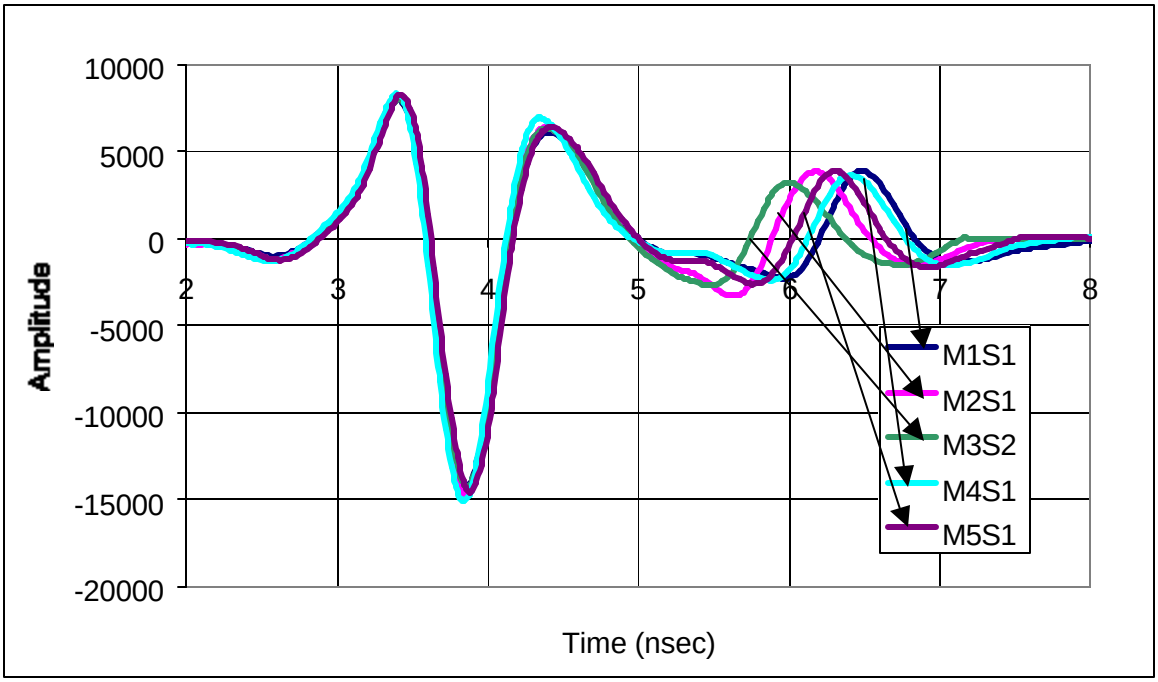

Figure C28 Time domain signals (11/05/00)

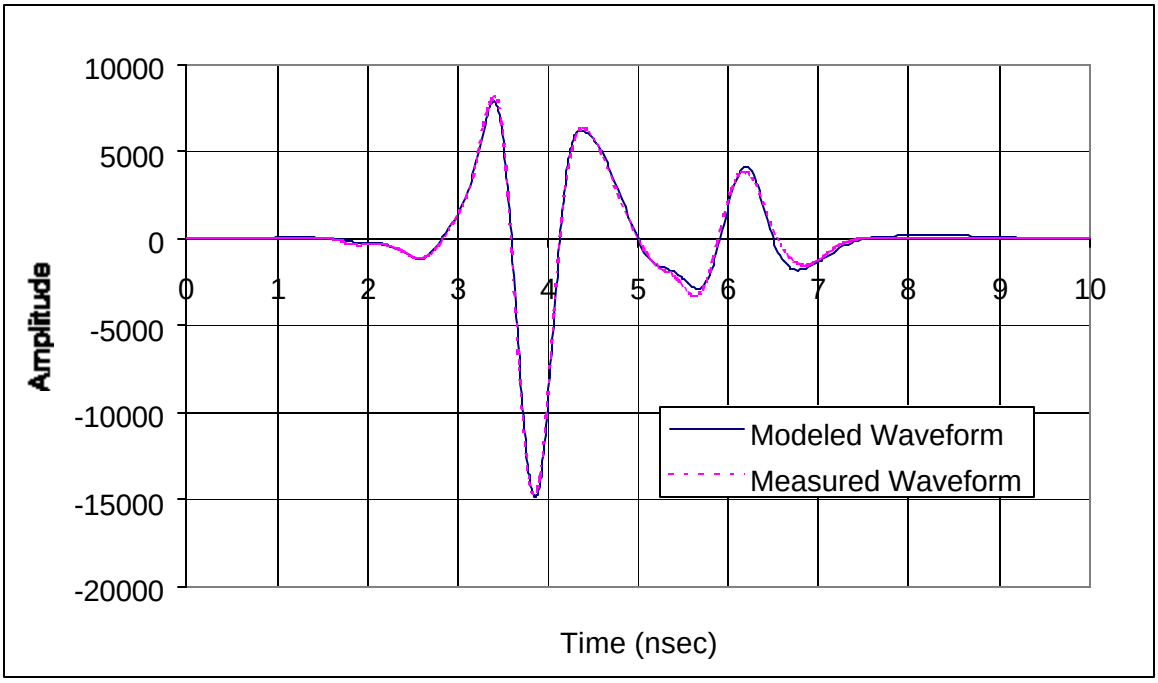

Figure C29 Modeled (with calculated solution for ε_r) and measured waveforms for slab M2S1 (11/05/00)

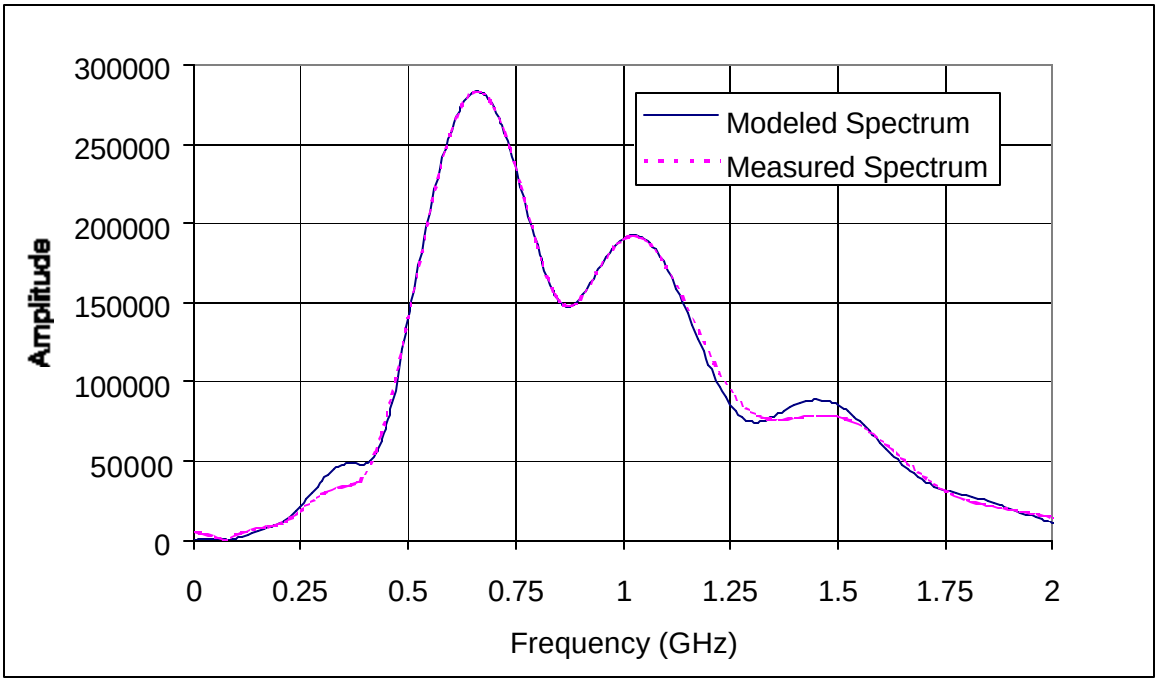

Figure C30 Modeled (with calculated solution for ε_r) and measured frequency spectrums for slab M2S1 (11/05/00)

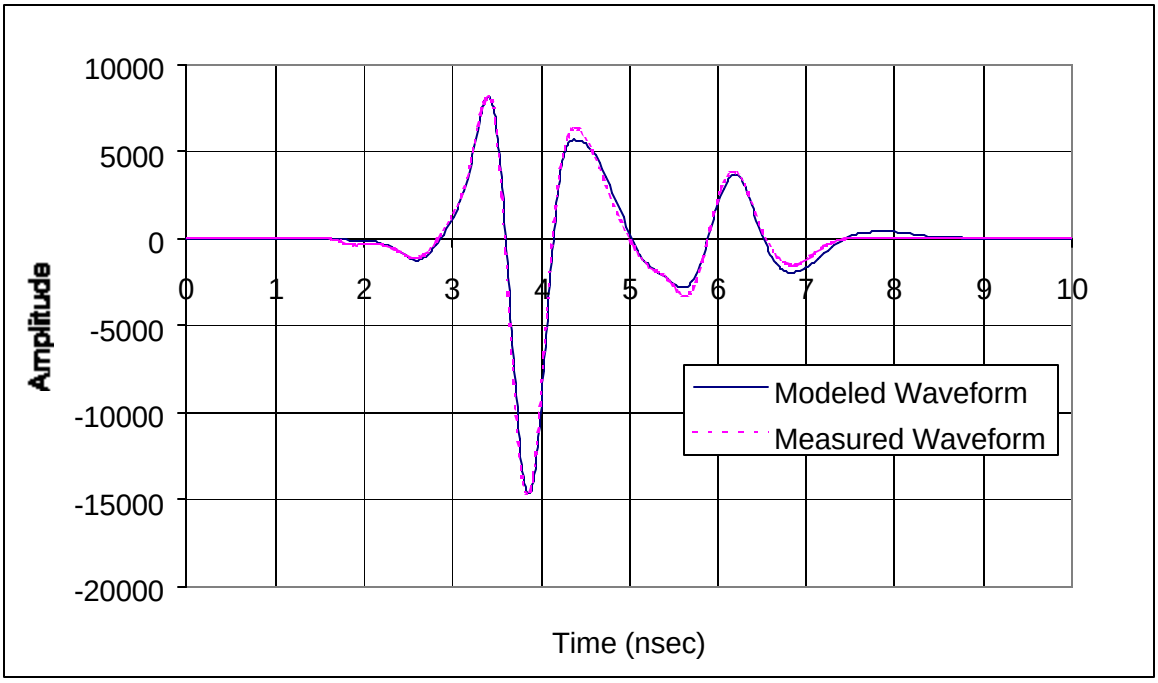

Figure C31 Modeled (with average ε_r) and measured Waveforms for slab M2S1 (11/05/00)

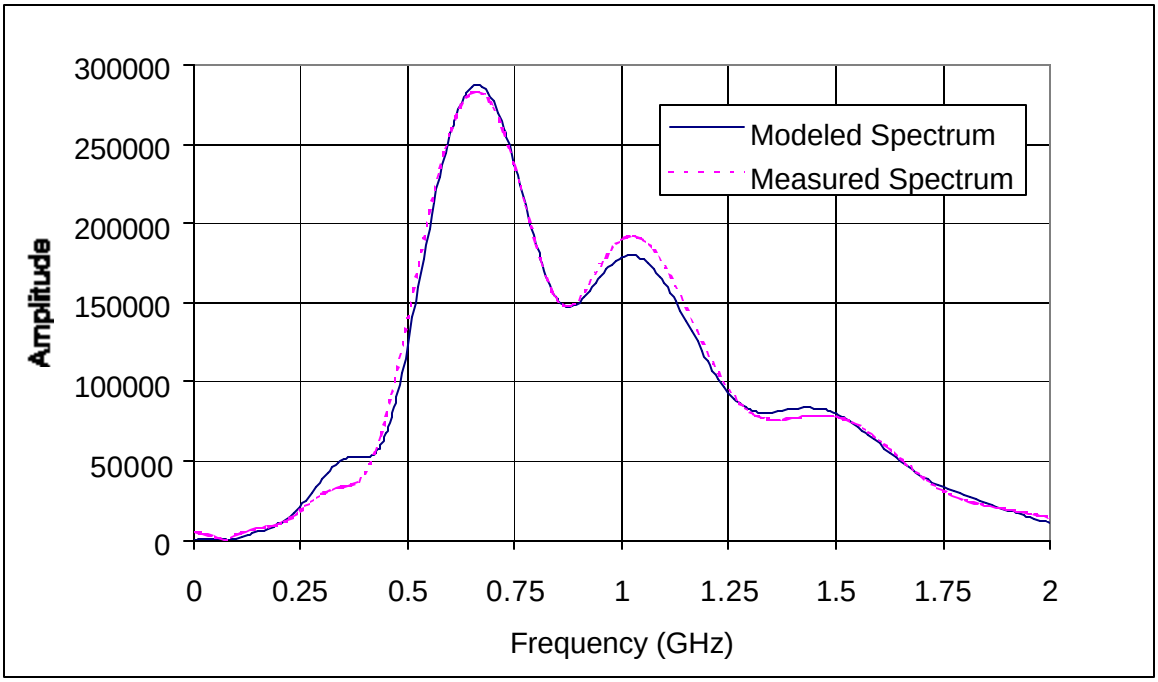

Figure C32 Modeled (with average ε_r) and measured frequency spectrums for slab M2S1 (11/05/00)

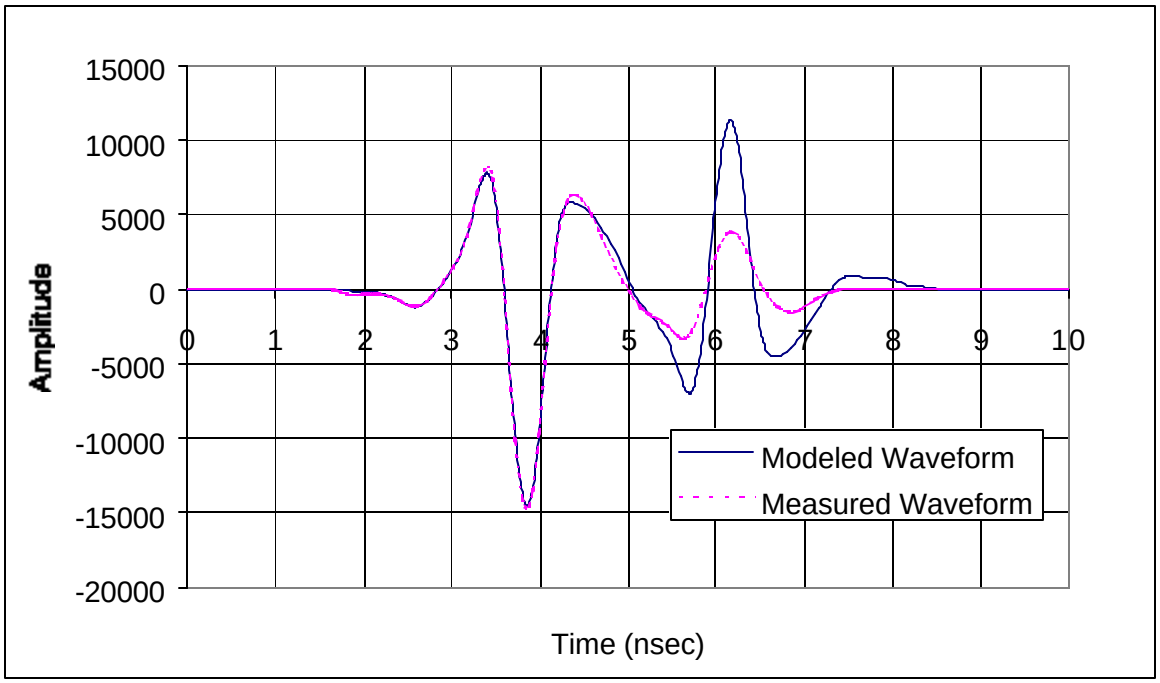

Figure C33 Modeled (with average real part of ε_r and zero imaginary part) and measured waveforms for slab M2S1 (11/05/00)

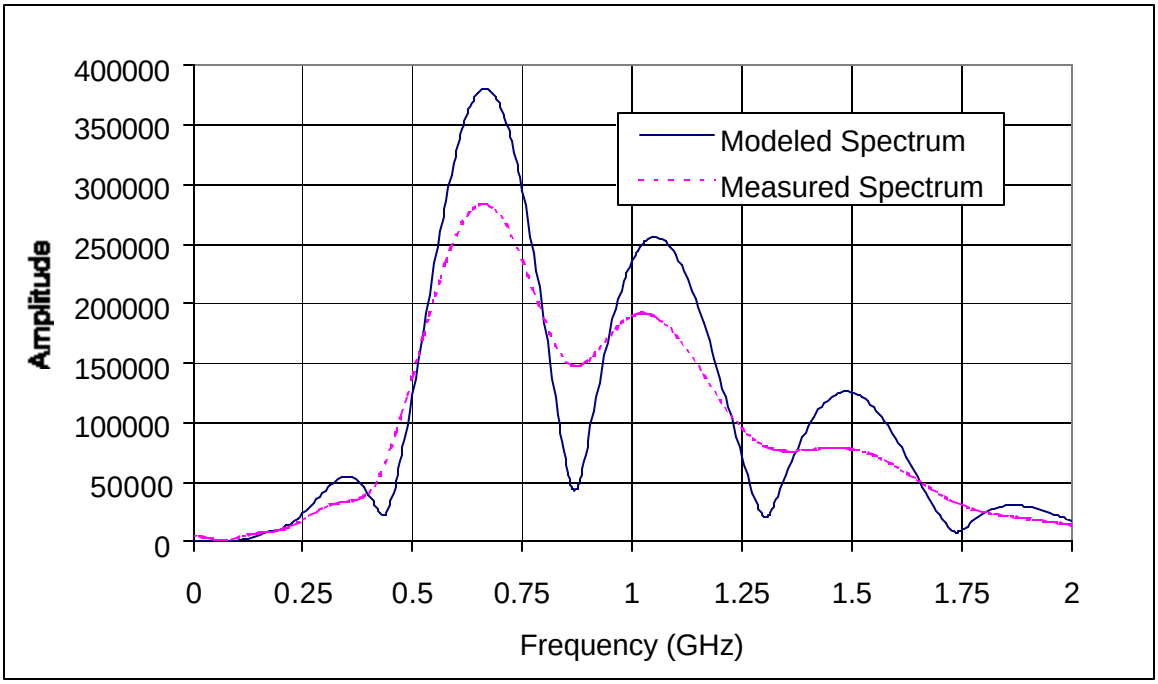

Figure C34 Modeled (with average real part of ε_r and zero imaginary part) and measured frequency spectrums for slab M2S1 (11/05/00)

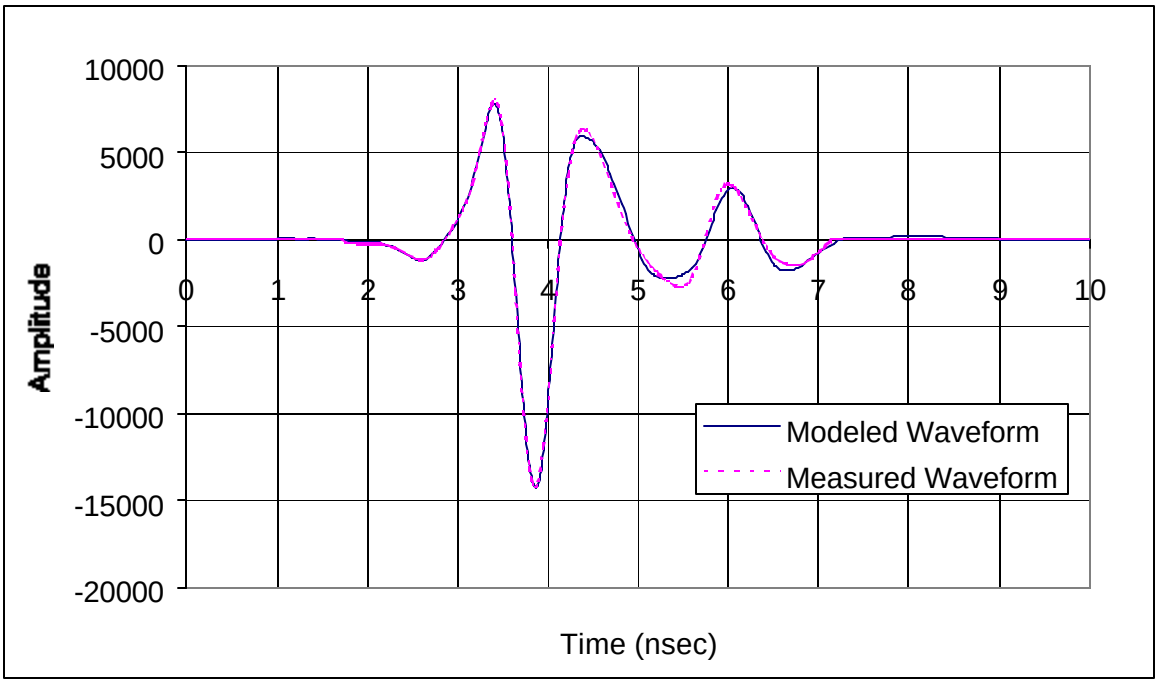

Figure C35 Modeled (with calculated solution for ε_r) and measured waveforms for slab M3S2 (11/05/00)

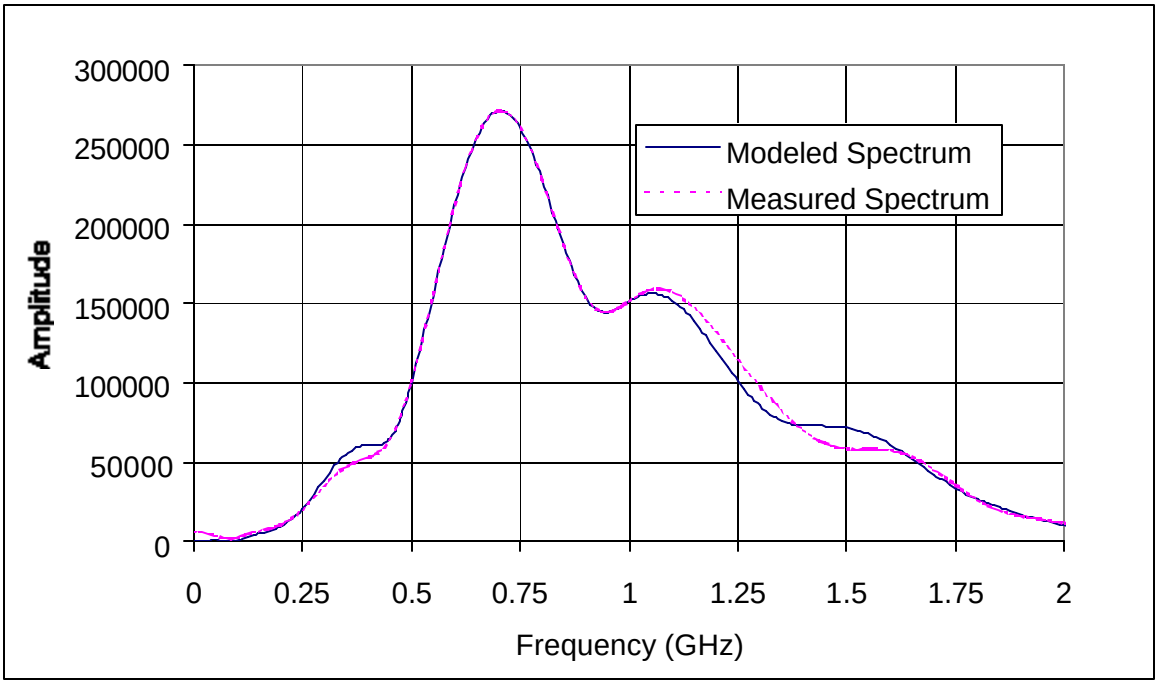

Figure C36 Modeled (with calculated solution for ε_r) and measured frequency spectrums for slab M3S2 (11/05/00)

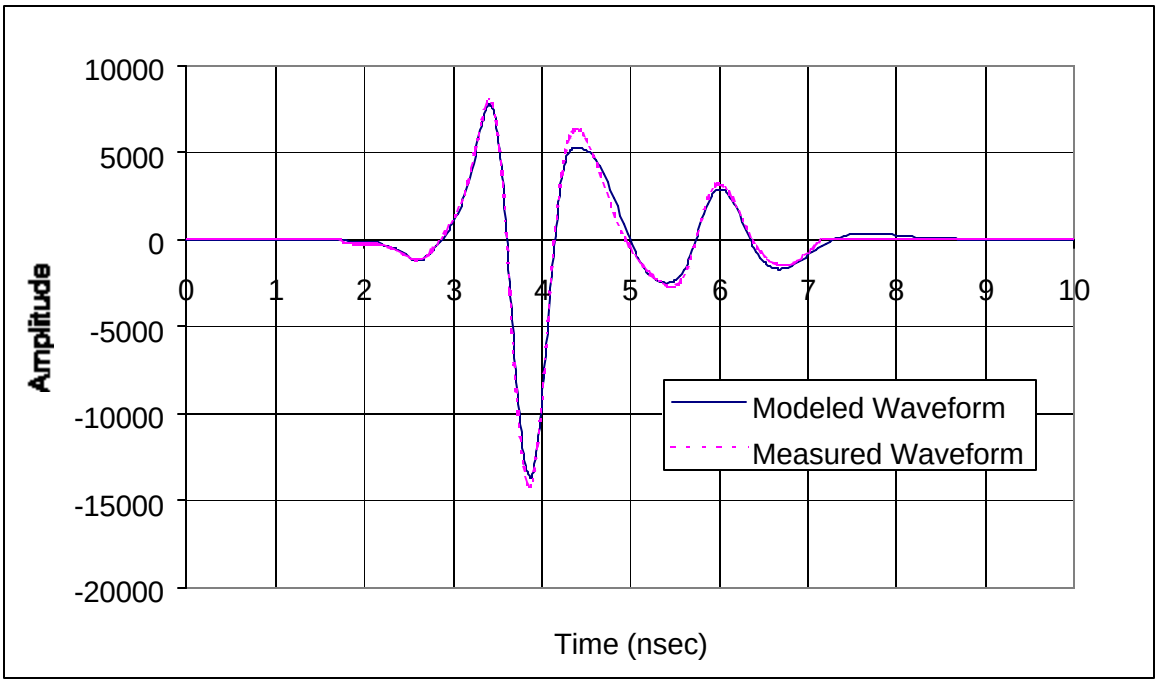

Figure C37 Modeled (with average ε_r) and measured Waveforms for slab M3S2 (11/05/00)

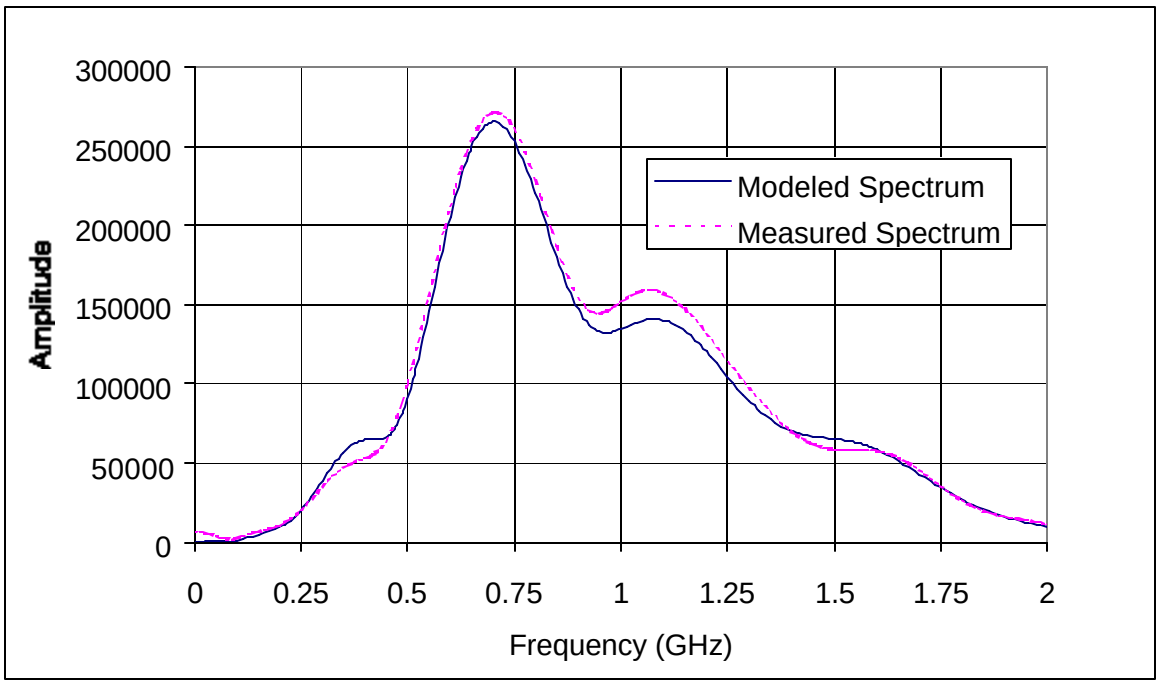

Figure C38 Modeled (with average ε_r) and measured frequency spectrums for slab M3S2 (11/05/00)

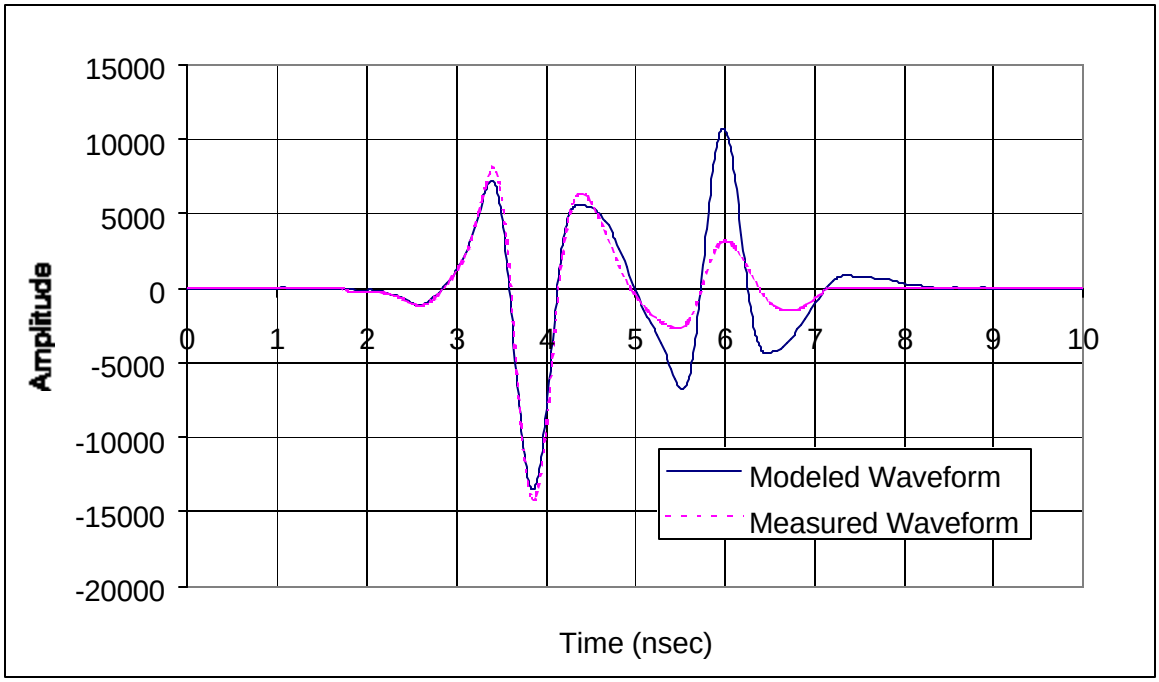

Figure C39 Modeled (with average real part of ε_r and zero imaginary part) and measured waveforms for slab M3S2 (11/05/00)

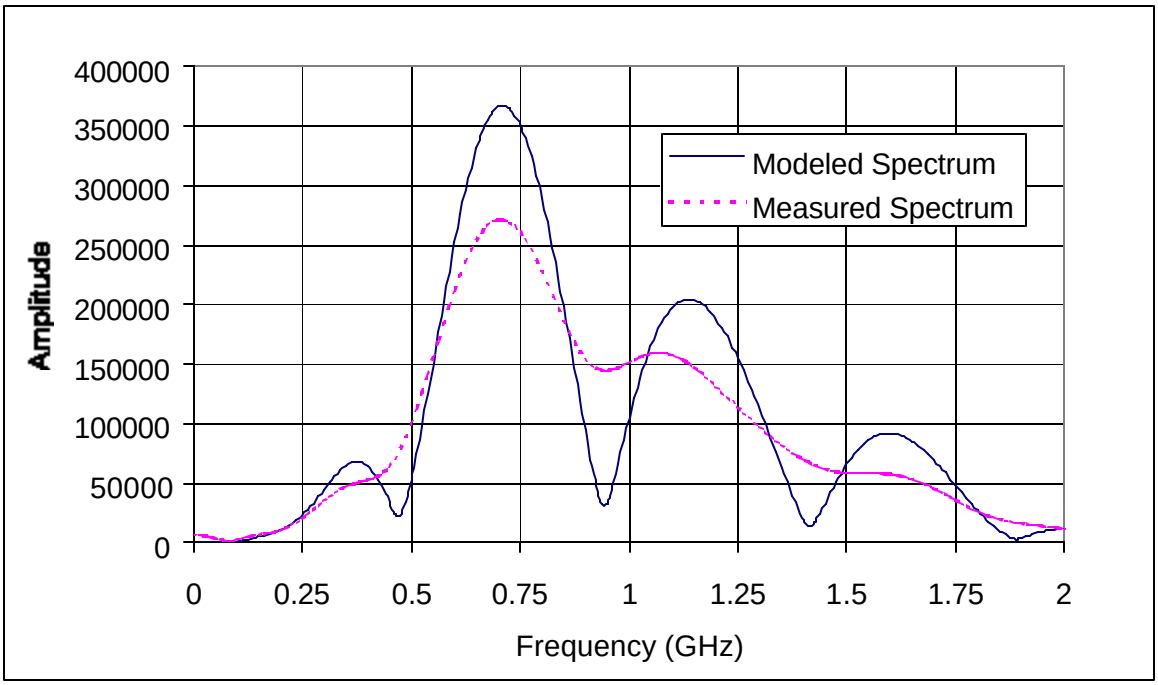

Figure C40 Modeled (with average real part of ε_r and zero imaginary part) and measured frequency spectrums for slab M3S2 (11/05/00)

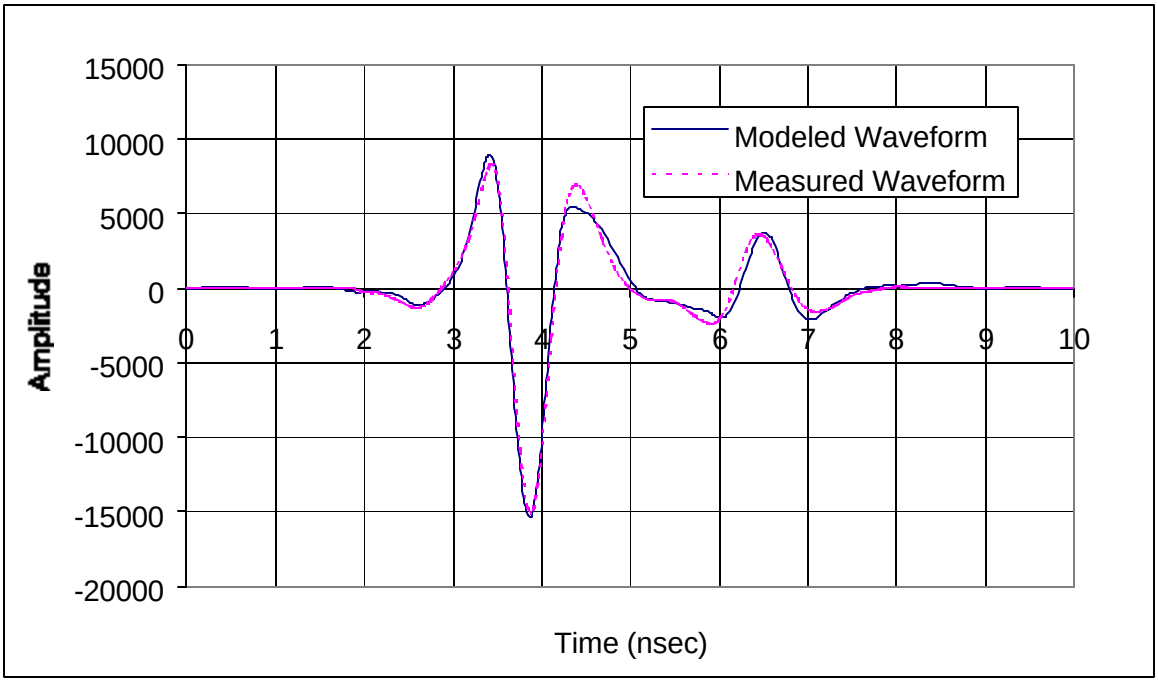

Figure C41 Modeled (with calculated solution for ε_r) and measured waveforms for slab M4S1 (11/05/00)

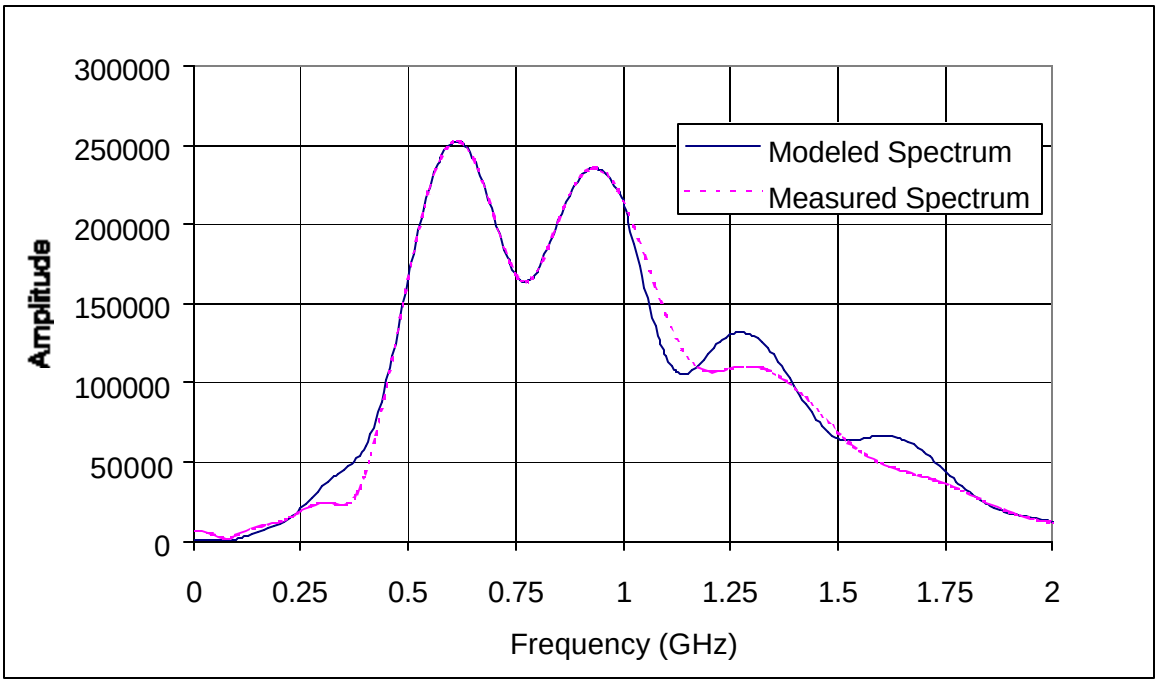

Figure C42 Modeled (with calculated solution for ε_r) and measured frequency spectrums for slab M4S1 (11/05/00)

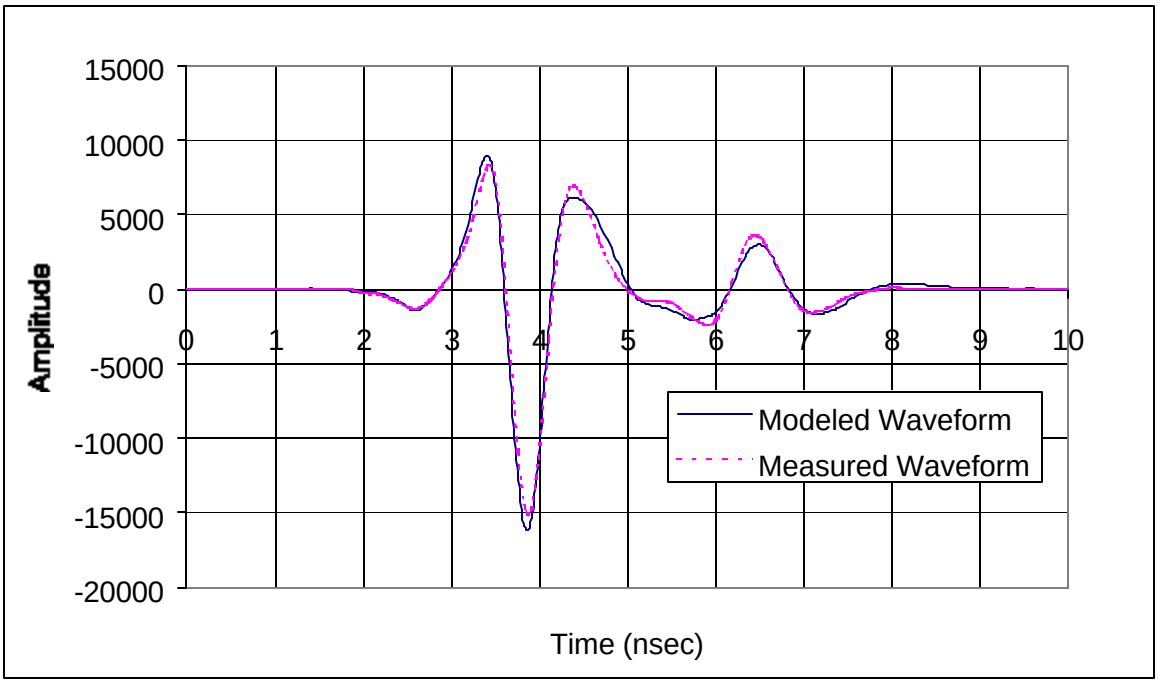

Figure C43 Modeled (with average ε_r) and measured Waveforms for slab M4S1 (11/05/00)

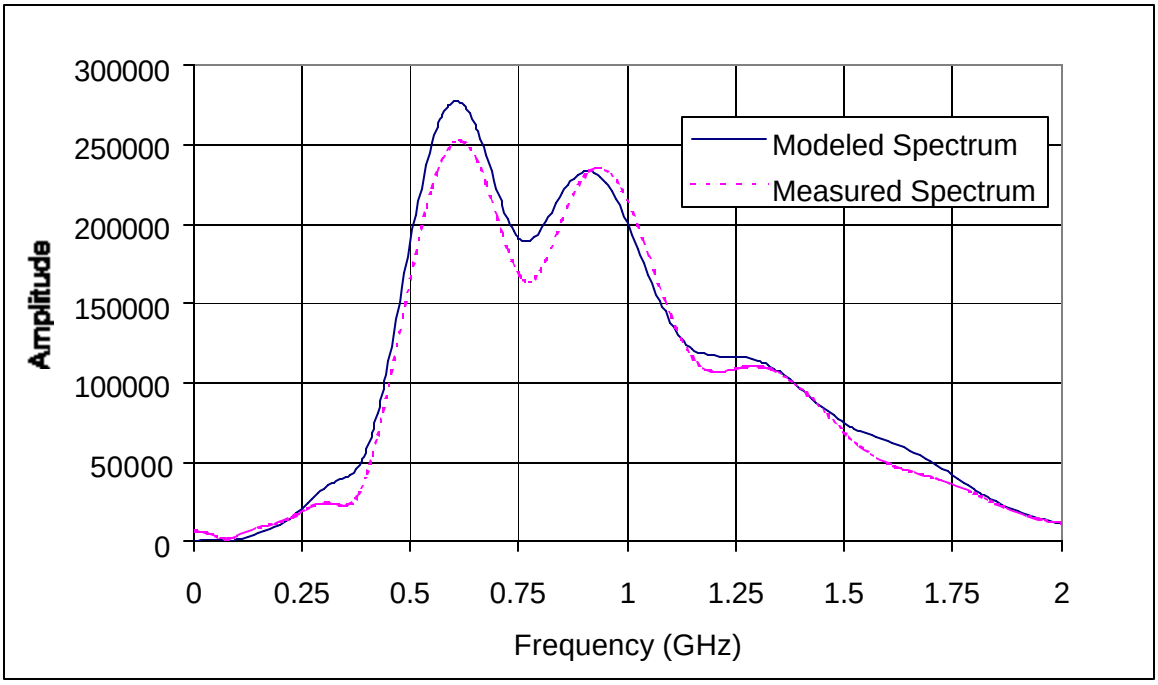

Figure C44 Modeled (with average ε_r) and measured frequency spectrums for slab M4S1 (11/05/00)

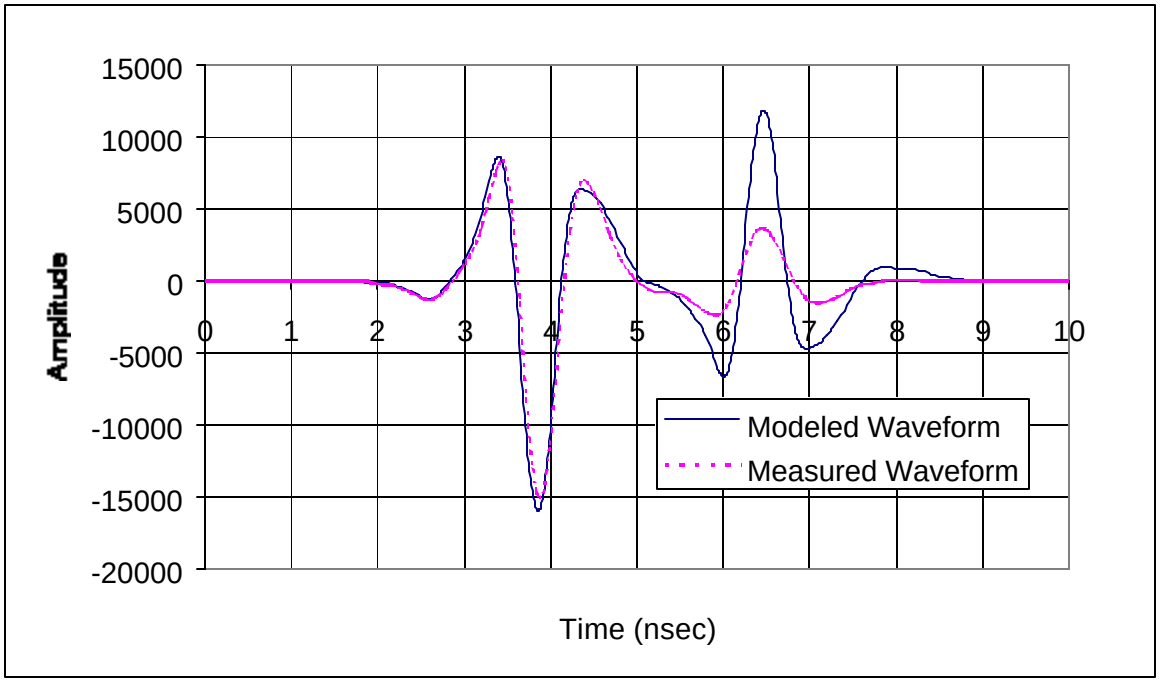

Figure C45 Modeled (with average real part of ε_r and zero imaginary part) and measured waveforms for slab M4S1 (11/05/00)

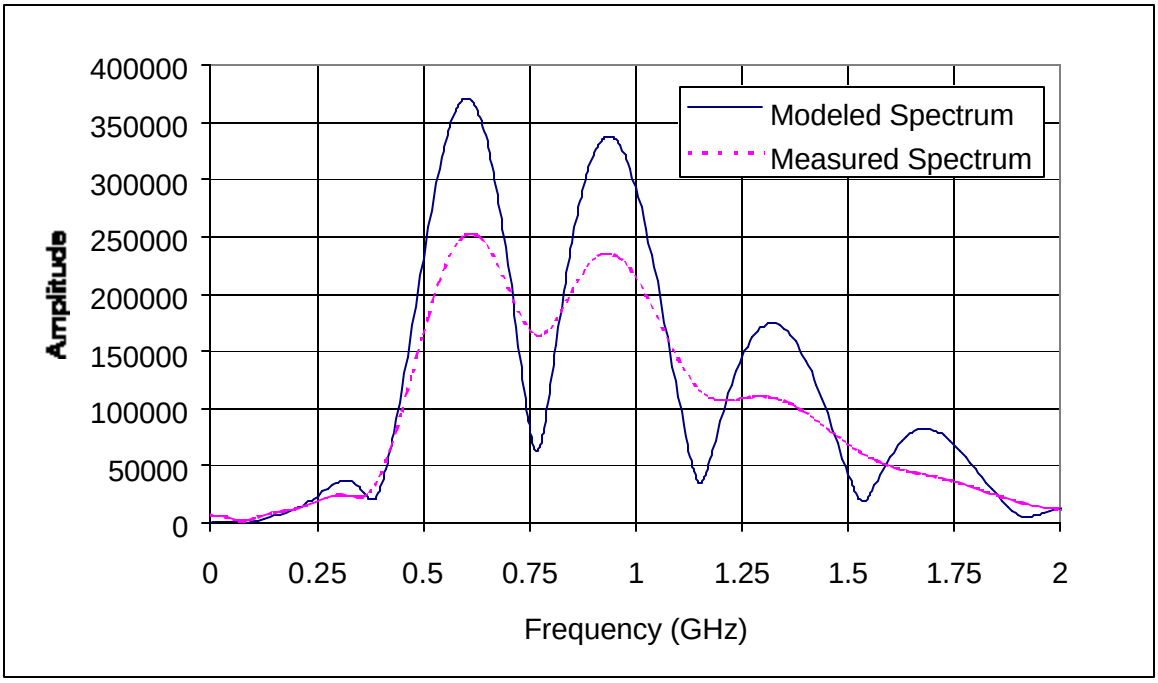

Figure C46 Modeled (with average real part of ε_r and zero imaginary part) and measured frequency spectrums for slab M4S1 (11/05/00)

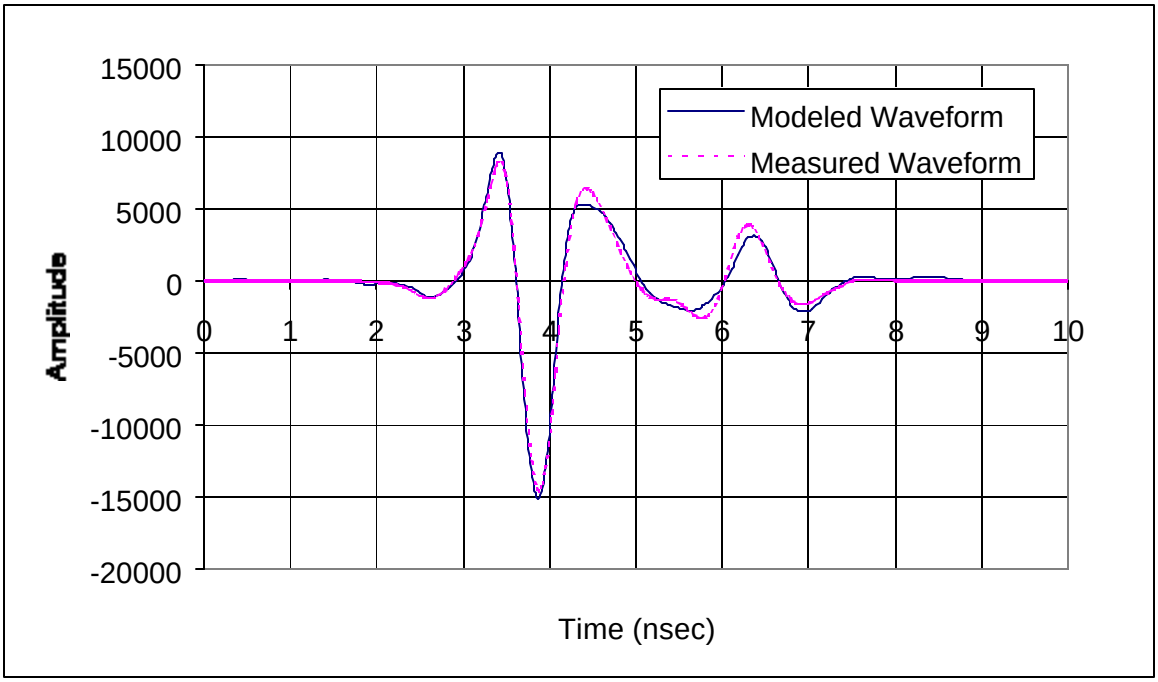

Figure C47 Modeled (with calculated solution for ε_r) and measured waveforms for slab M5S1 (11/05/00)

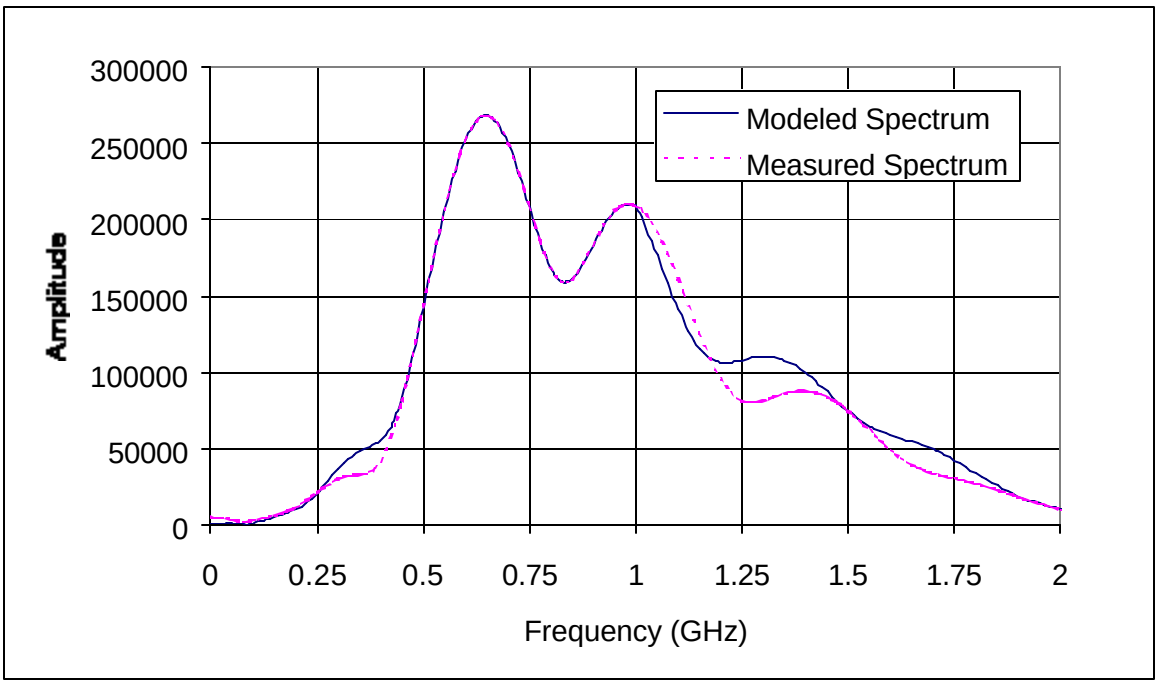

Figure C48 Modeled (with calculated solution for ε_r) and measured frequency spectrums for slab M5S1 (11/05/00)

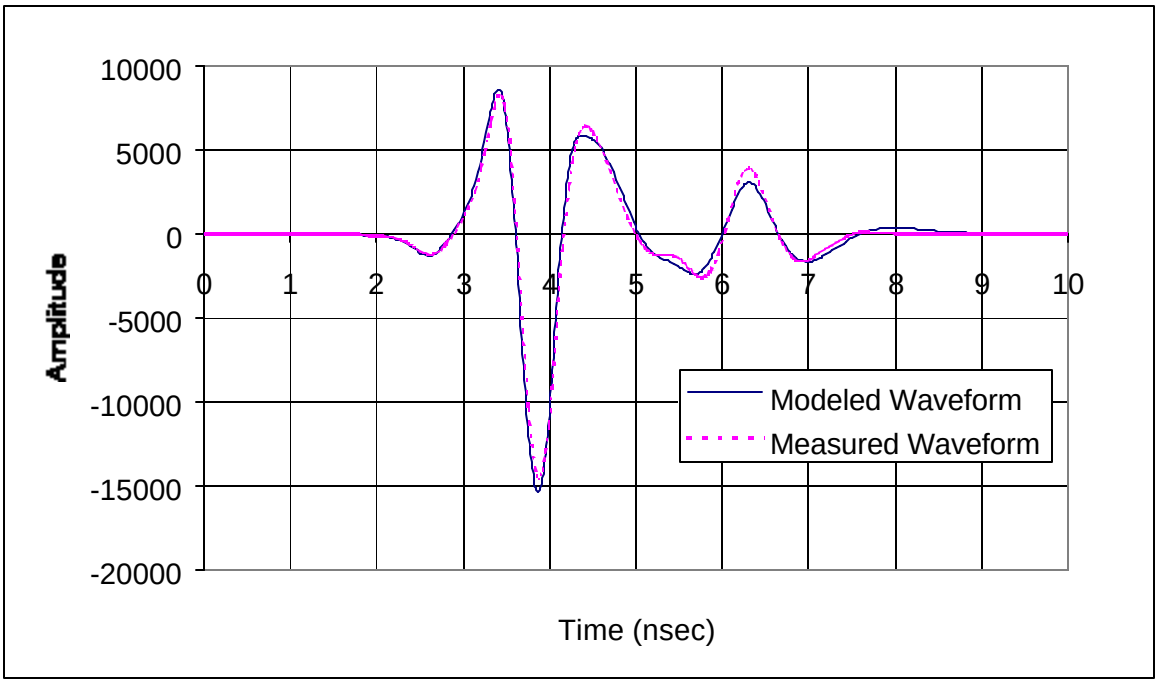

Figure C49 Modeled (with average ε_r) and measured Waveforms for slab M5S1 (11/05/00)

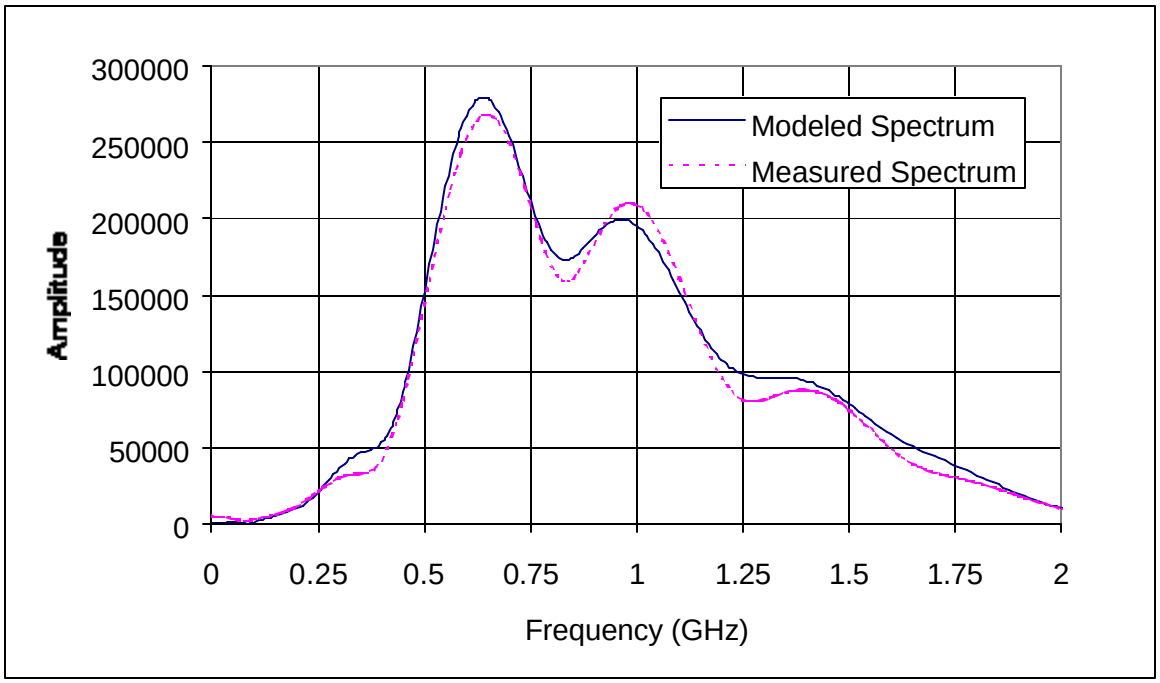

Figure C50 Modeled (with average ε_r) and measured frequency spectrums for slab M5S1 (11/05/00)

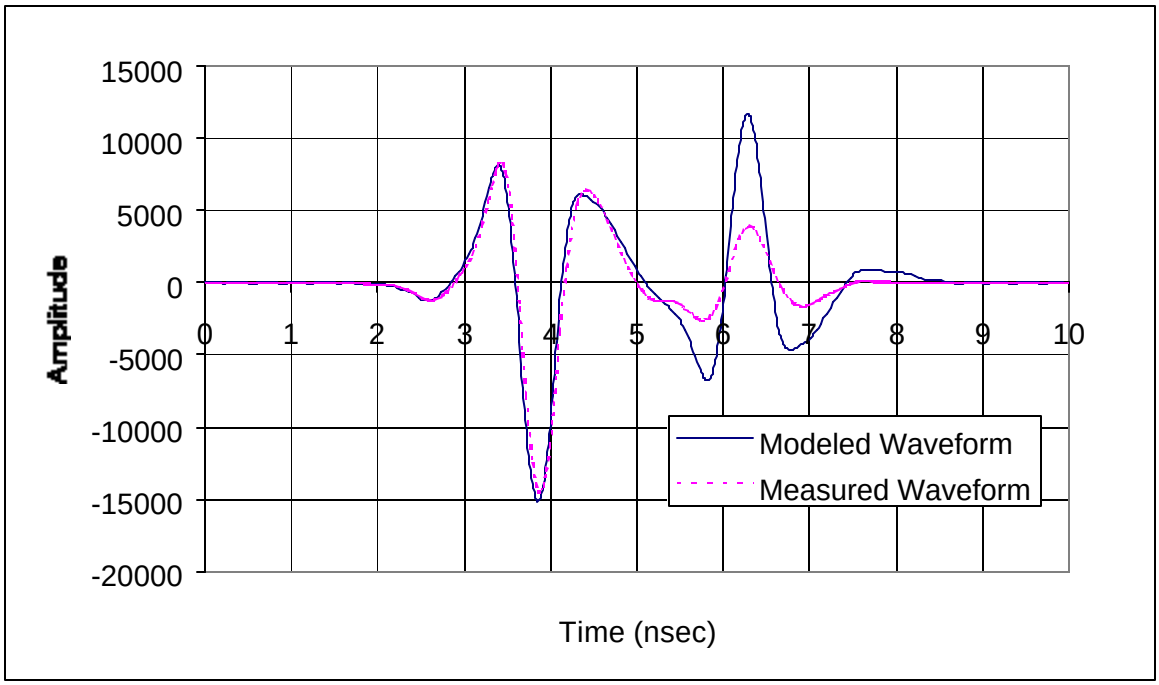

Figure C51 Modeled (with average real part of ε_r and zero imaginary part) and measured waveforms for slab M5S1 (11/05/00)

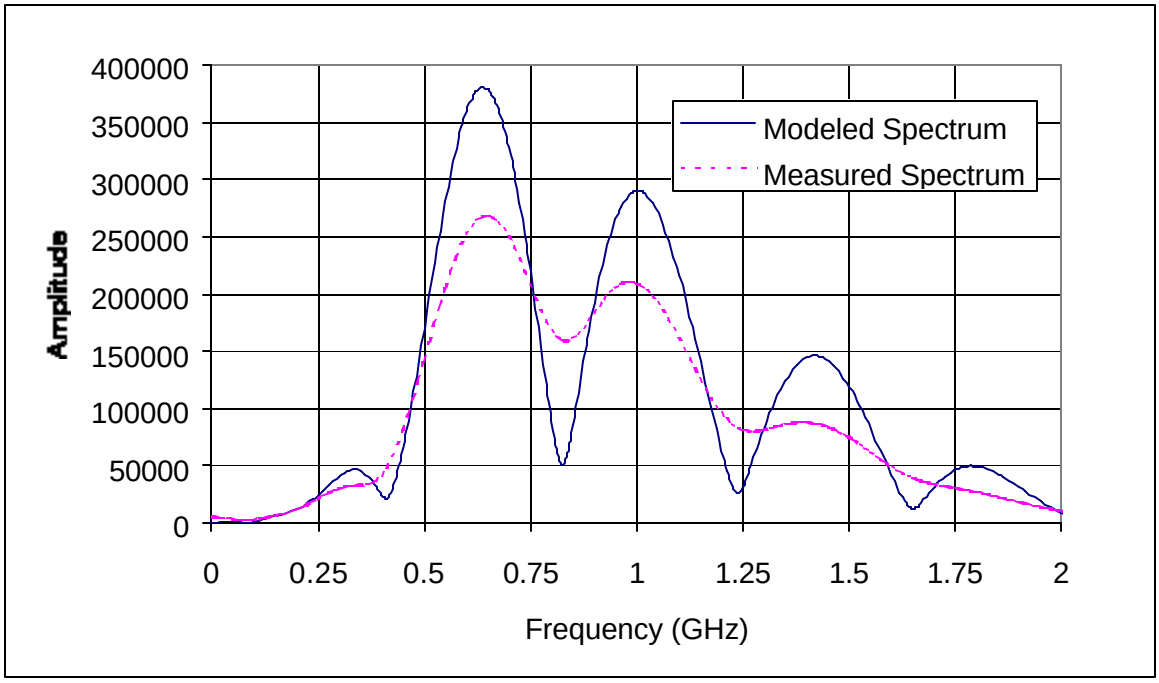

Figure C52 Modeled (with average real part of ε_r and zero imaginary part) and measured frequency spectrums for slab M5S1 (11/05/00)

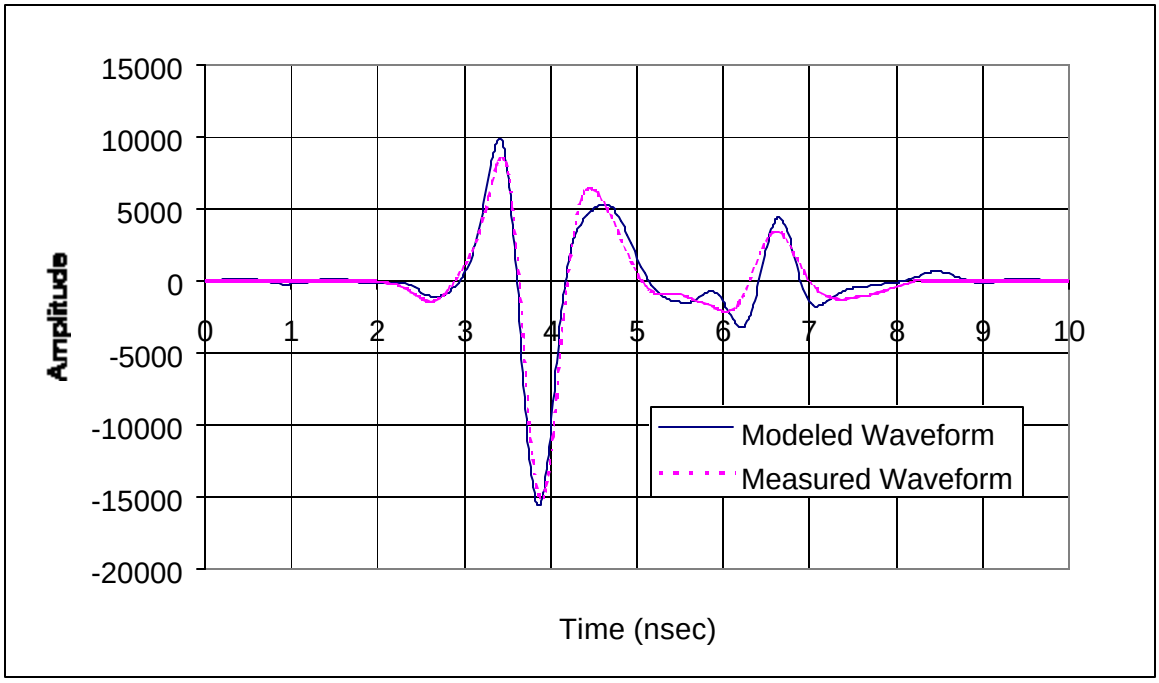

Figure C53 Modeled (with calculated solution for ε_r) and measured waveforms for slab M1S1 (07/17/00)

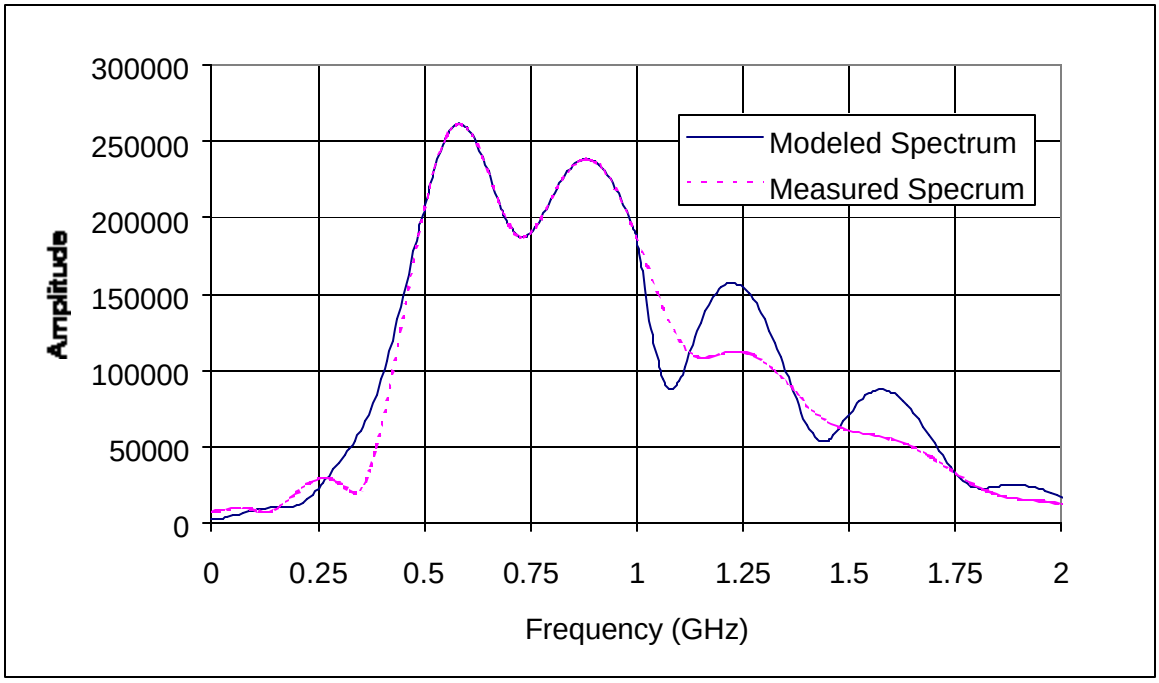

Figure C54 Modeled (with calculated solution for ε_r) and measured frequency spectrums for slab M1S1 (07/17/00)

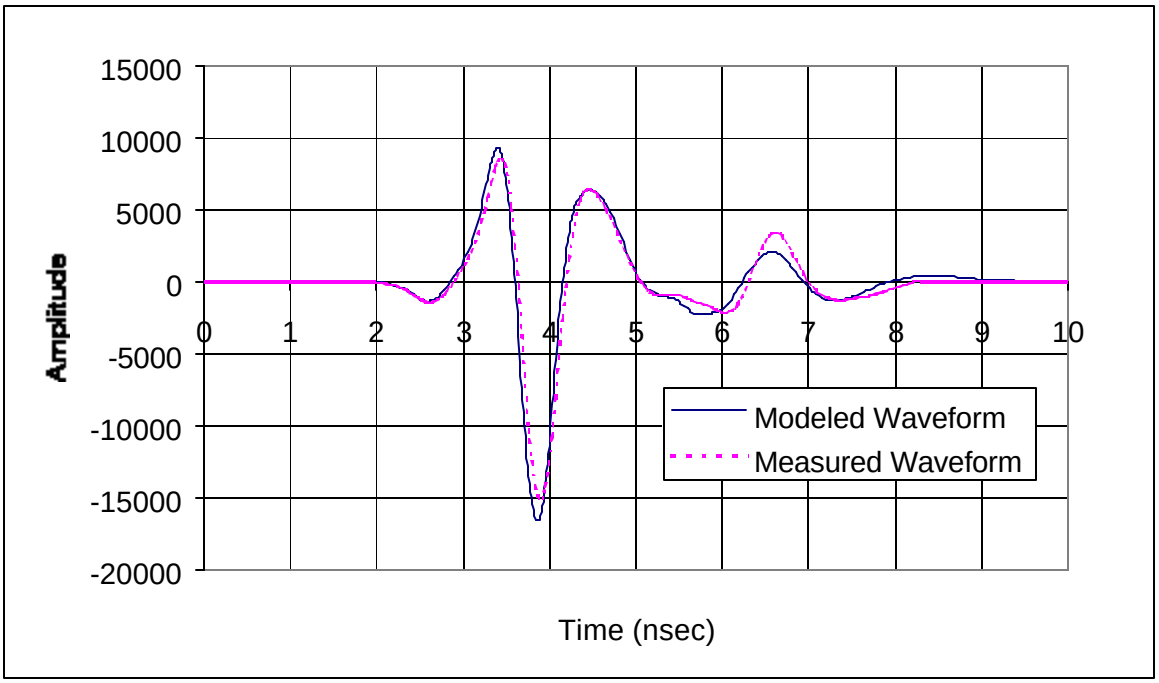

Figure C55 Modeled (with average ε_r) and measured Waveforms for slab M1S1 (07/17/00)

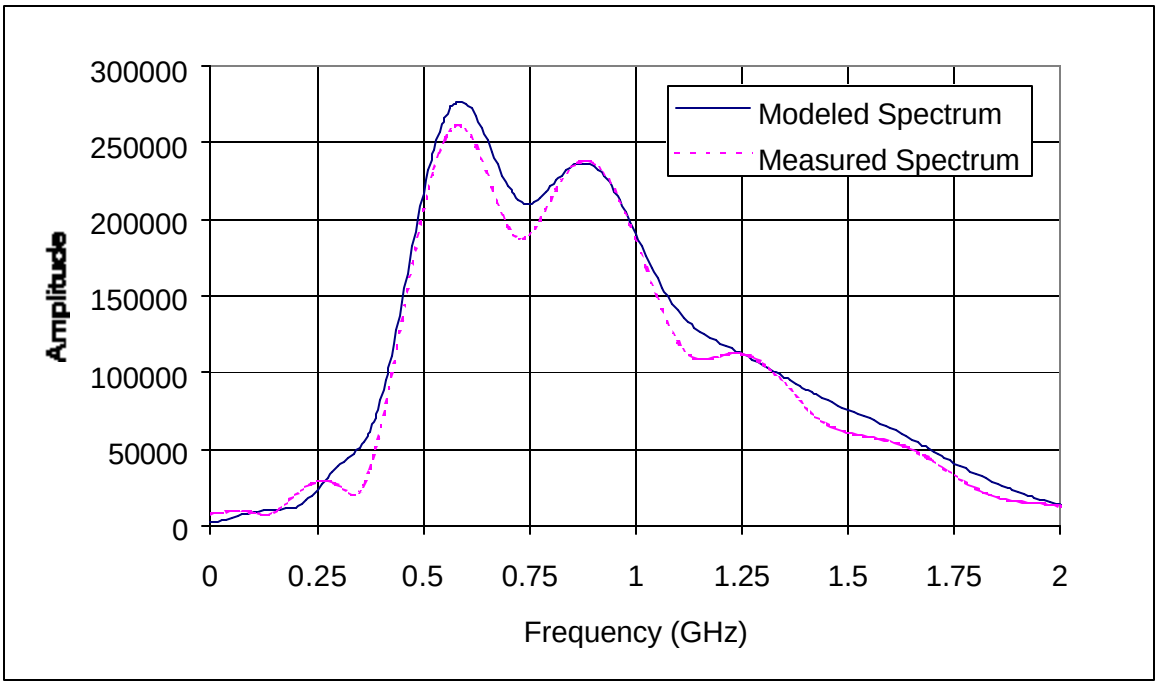

Figure C56 Modeled (with average ε_r) and measured frequency spectrums for slab M1S1 (07/17/00)

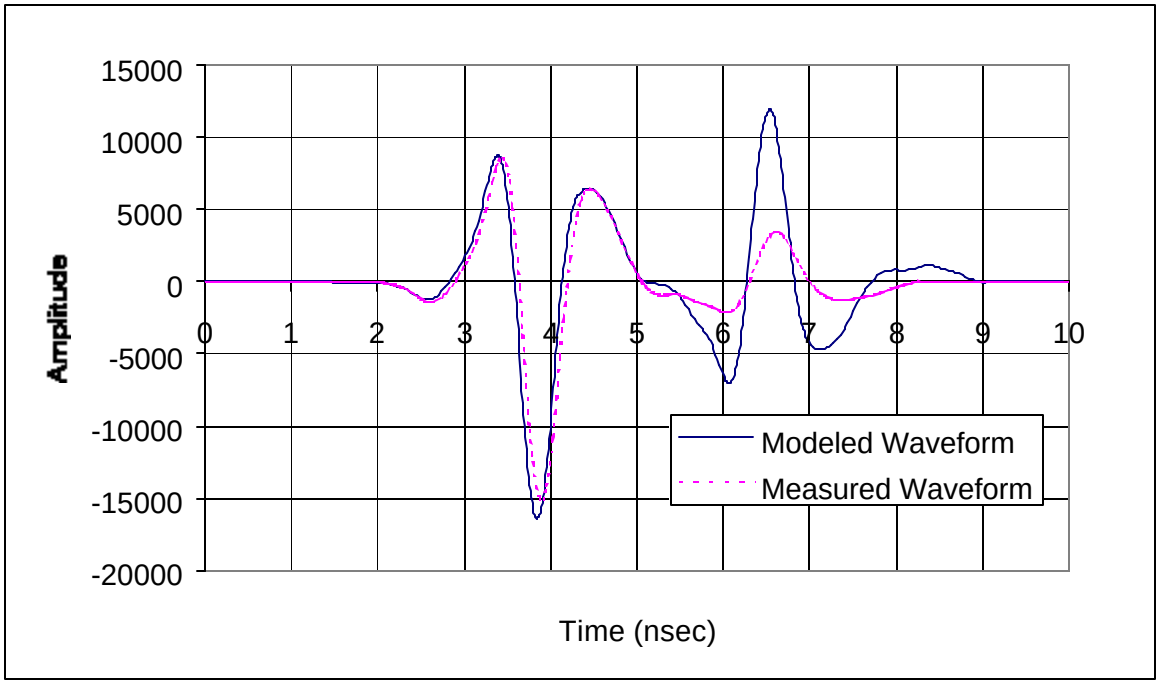

Figure C57 Modeled (with average real part of ε_r and zero imaginary part) and measured waveforms for slab M1S1 (07/17/00)

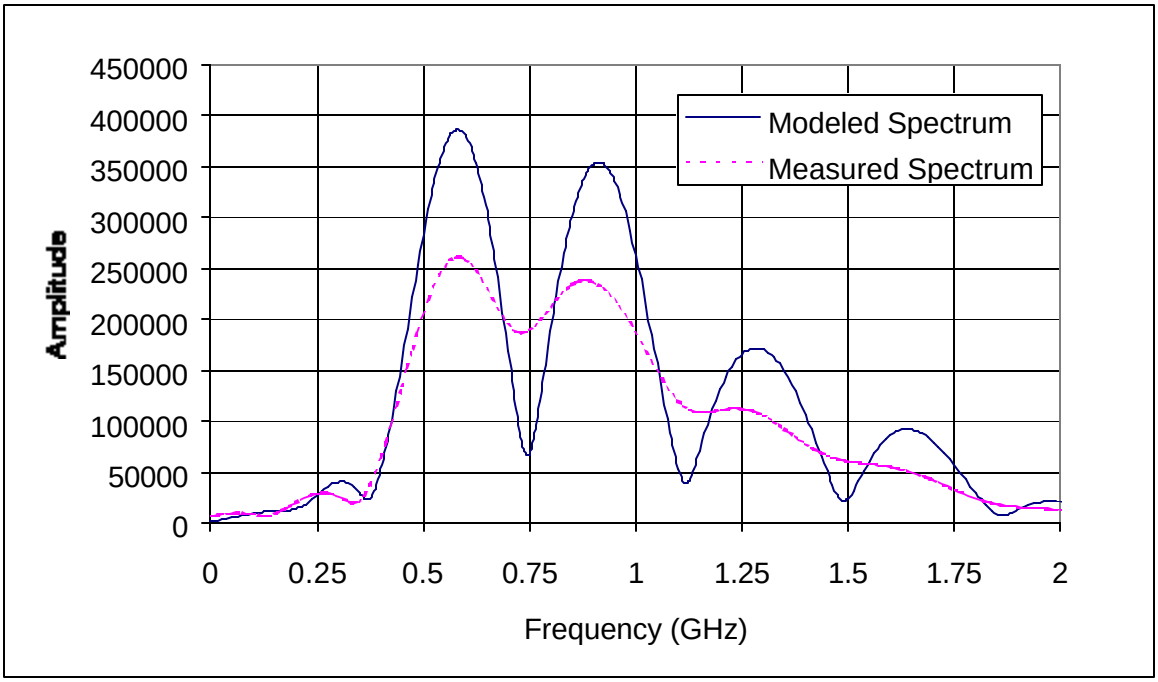

Figure C58 Modeled (with average real part of ε_r and zero imaginary part) and measured frequency spectrums for slab M1S1 (07/17/00)

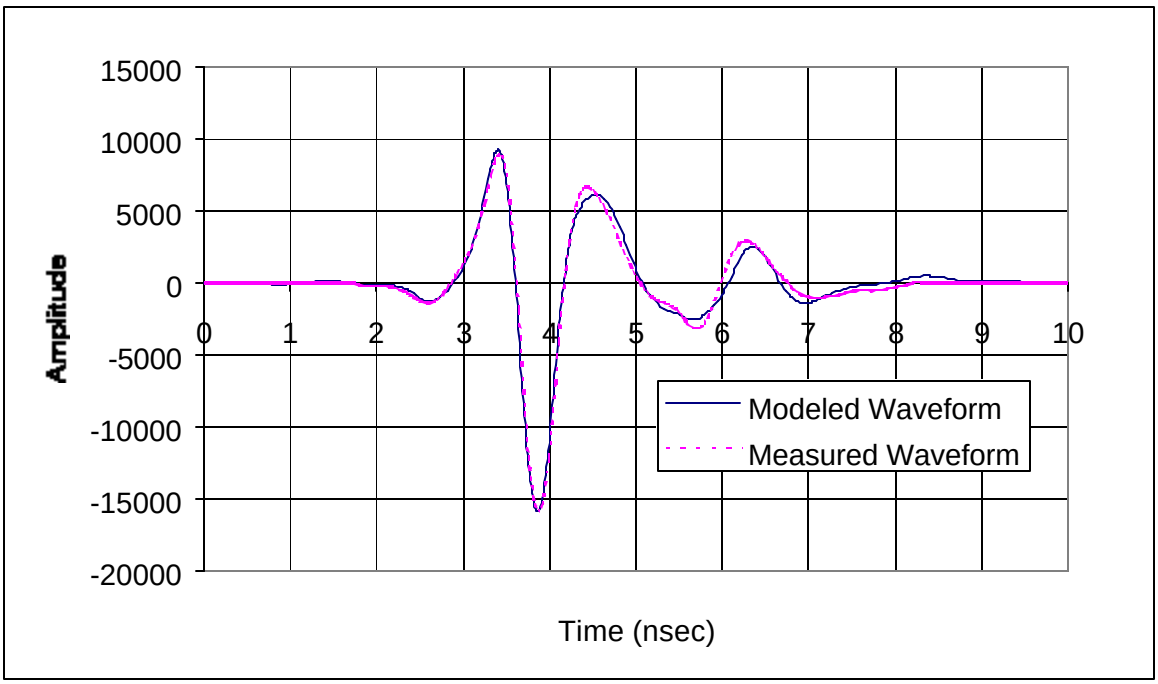

Figure C59 Modeled (with calculated solution for ε_r) and measured waveforms for slab M2S1 (07/17/00)

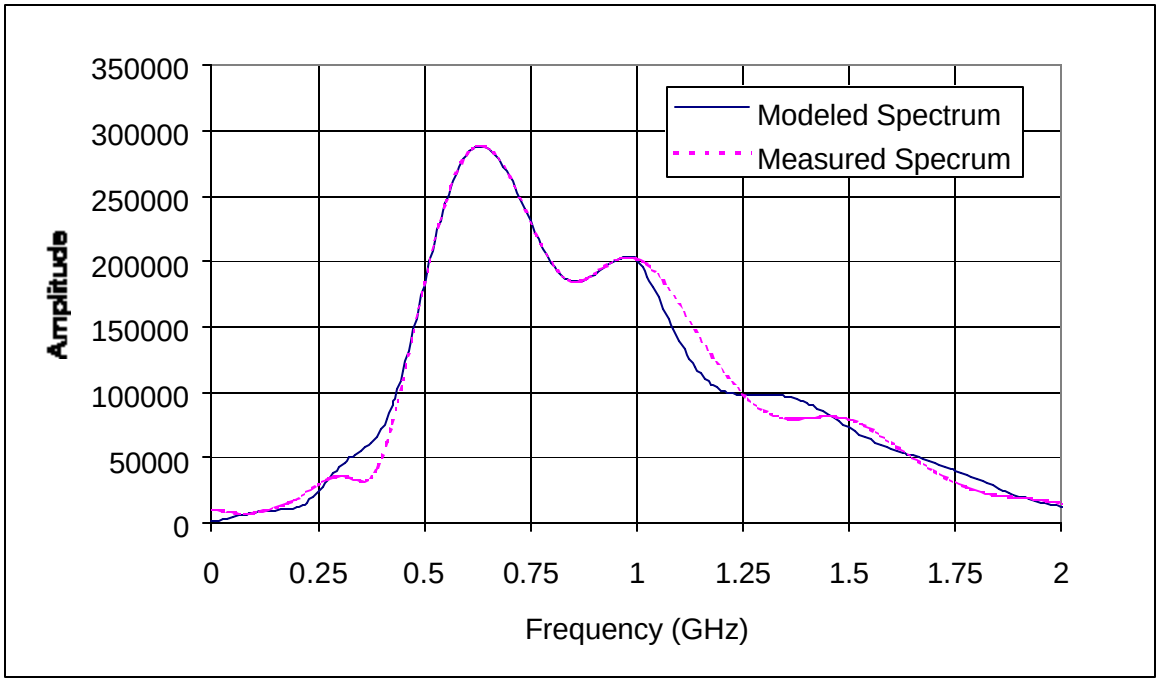

Figure C60 Modeled (with calculated solution for ε_r) and measured frequency spectrums for slab M2S1 (07/17/00)

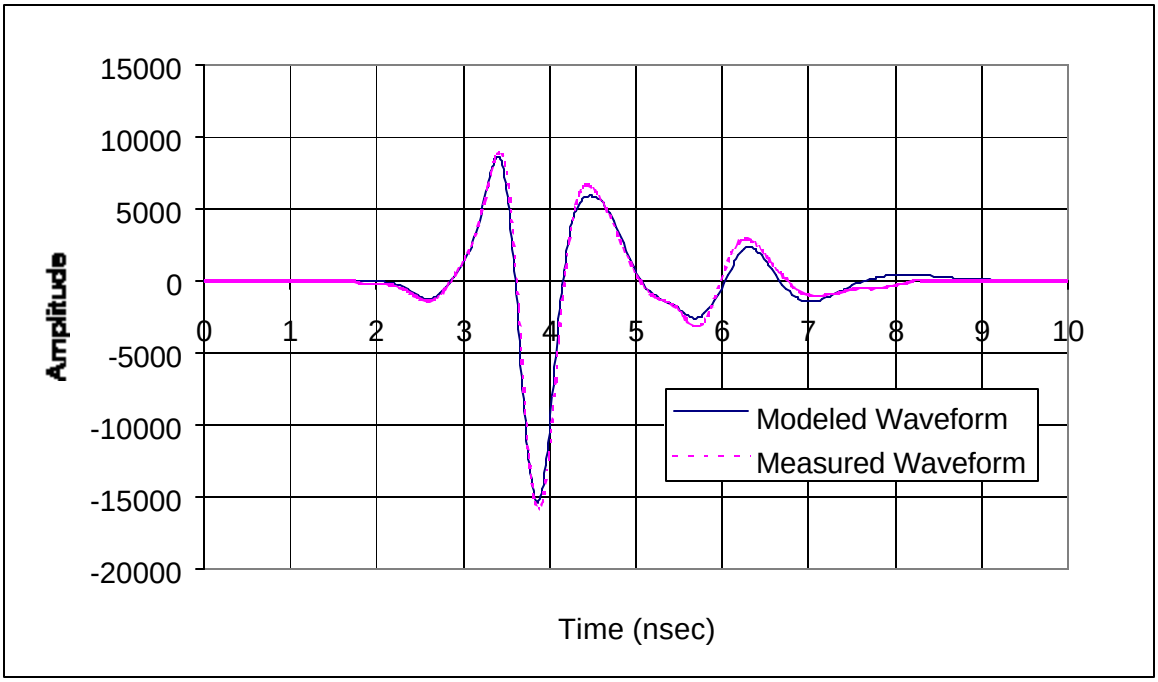

Figure C61 Modeled (with average ε_r) and measured Waveforms for slab M2S1 (07/17/00)

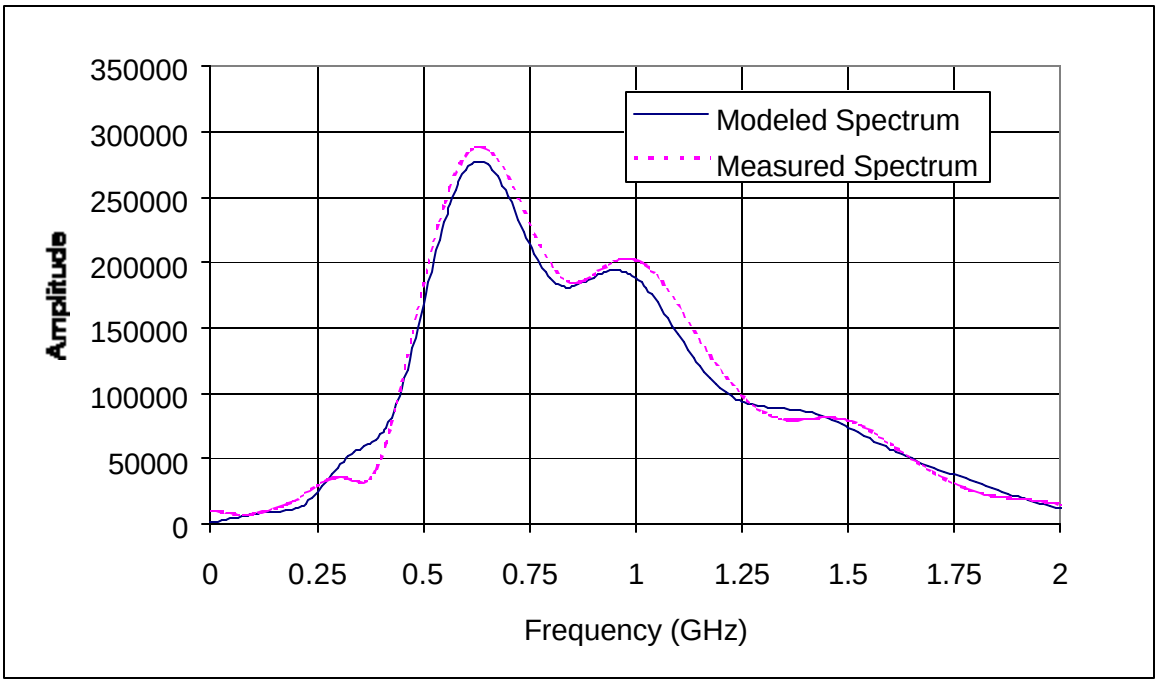

Figure C62 Modeled (with average ε_r) and measured frequency spectrums for slab M2S1 (07/17/00)

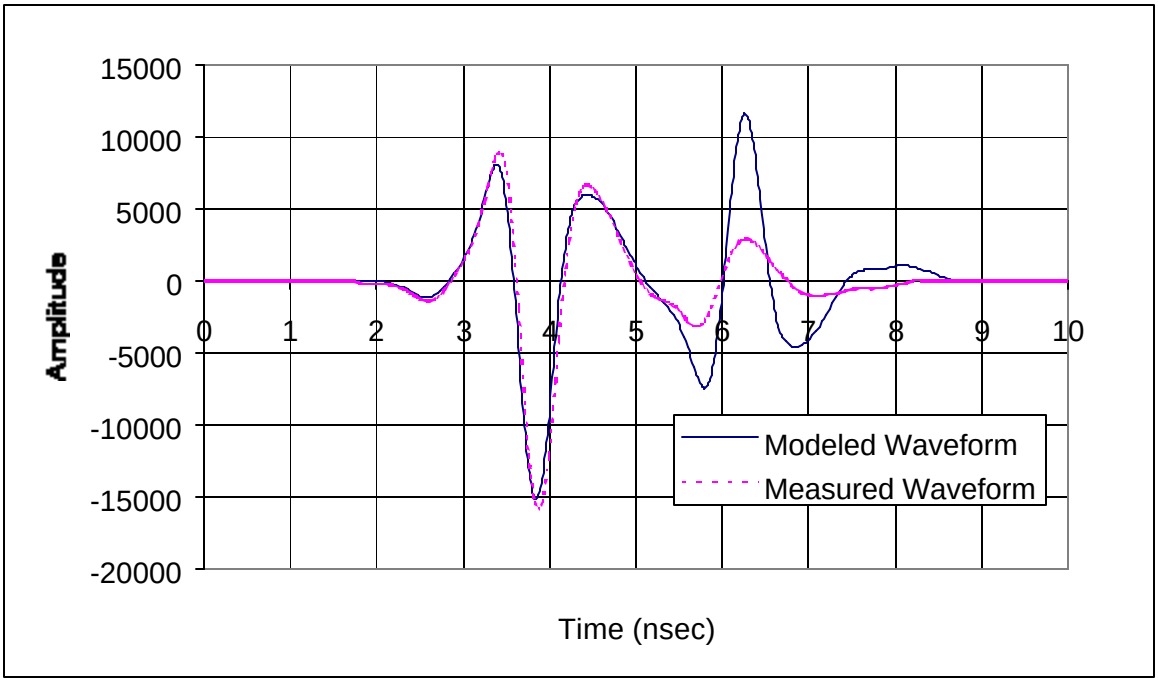

Figure C63 Modeled (with average real part of ε_r and zero imaginary part) and measured waveforms for slab M2S1 (07/17/00)

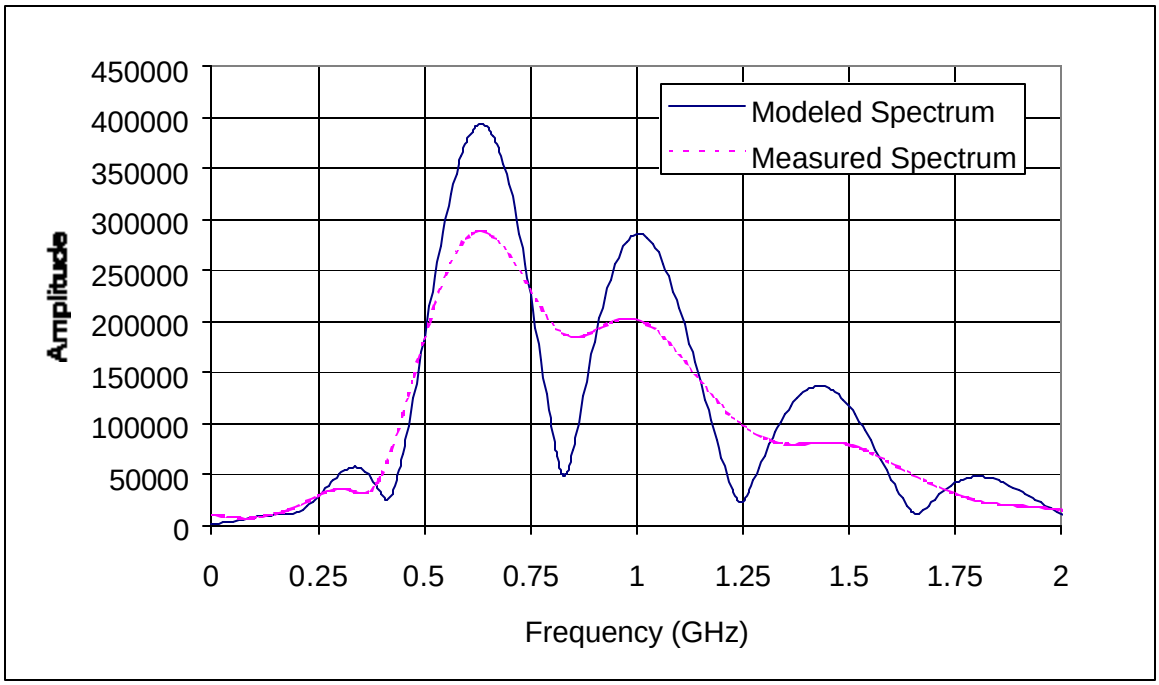

Figure C64 Modeled (with average real part of ε_r and zero imaginary part) and measured frequency spectrums for slab M2S1 (07/17/00)

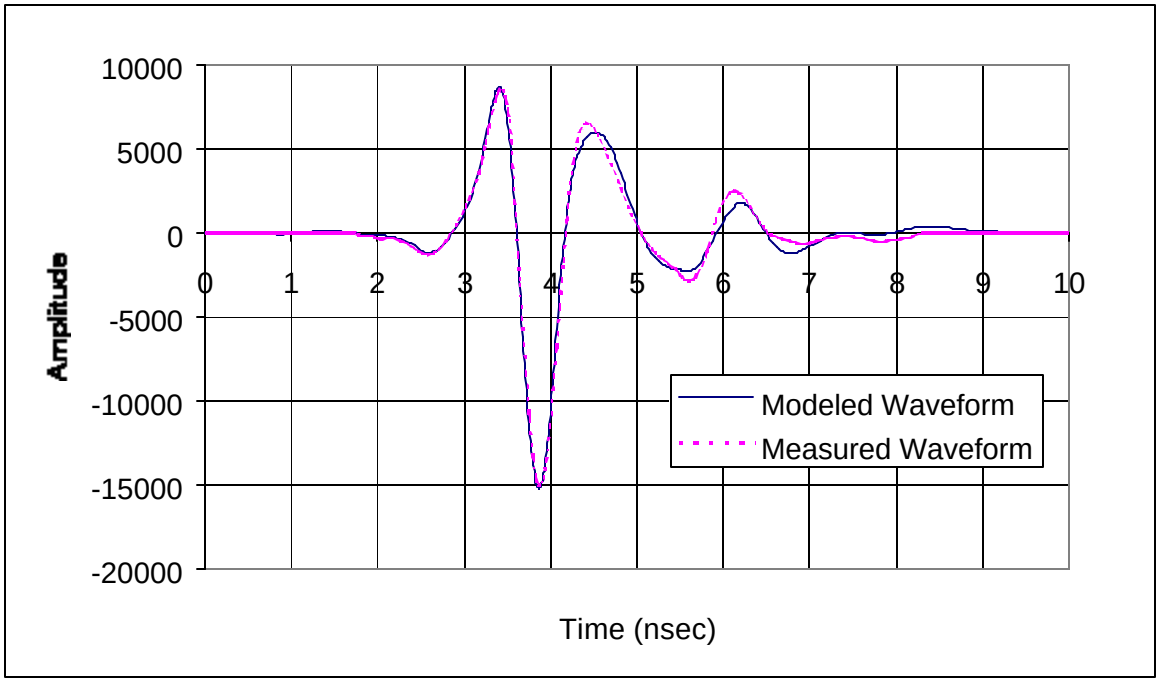

Figure C65 Modeled (with calculated solution for ε_r) and measured waveforms for slab M3S2 (07/17/00)

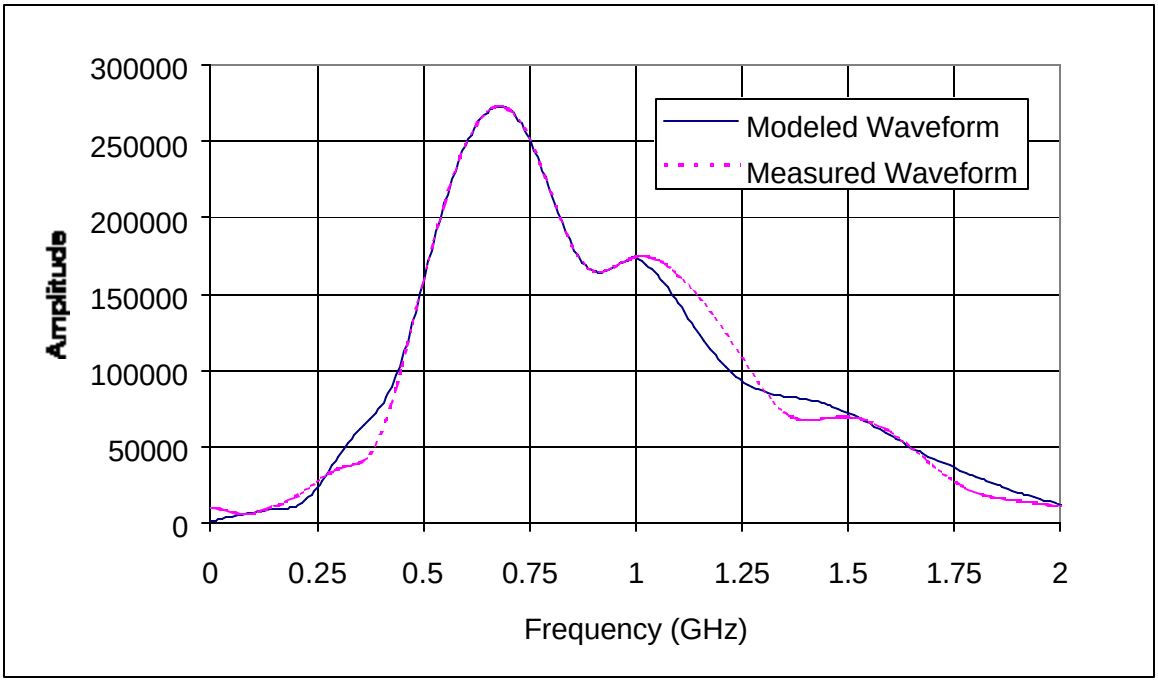

Figure C66 Modeled (with calculated solution for ε_r) and measured frequency spectrums for slab M3S2 (07/17/00)

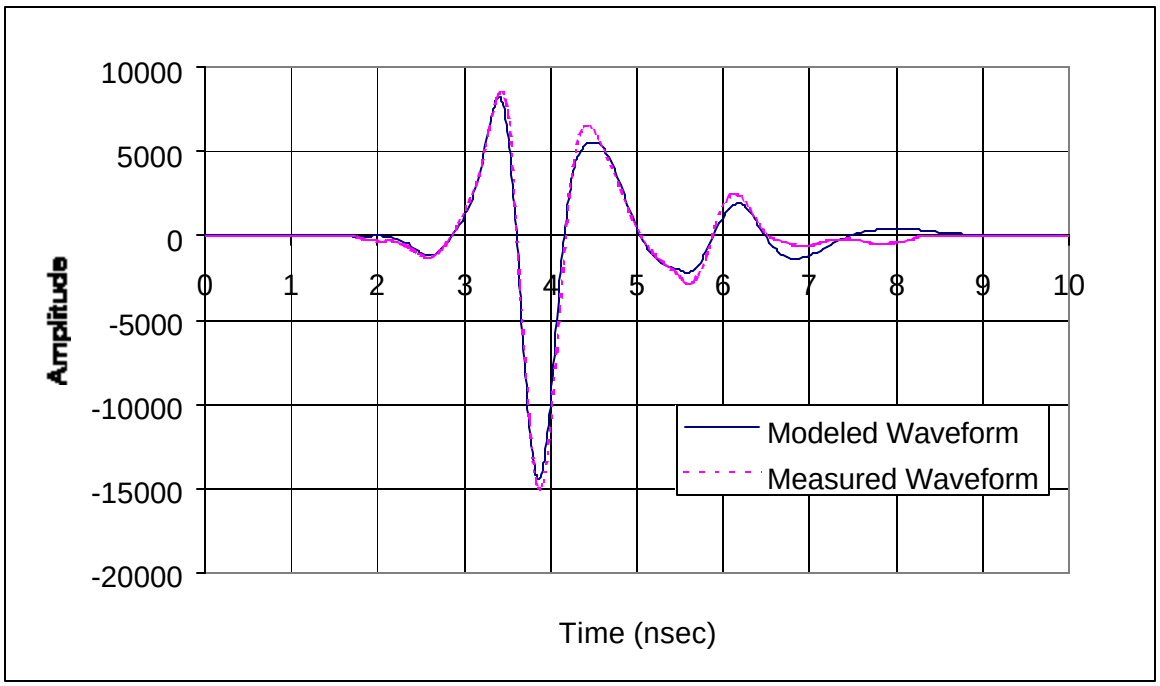

Figure C67 Modeled (with average ε_r) and measured Waveforms for slab M3S2 (07/17/00)

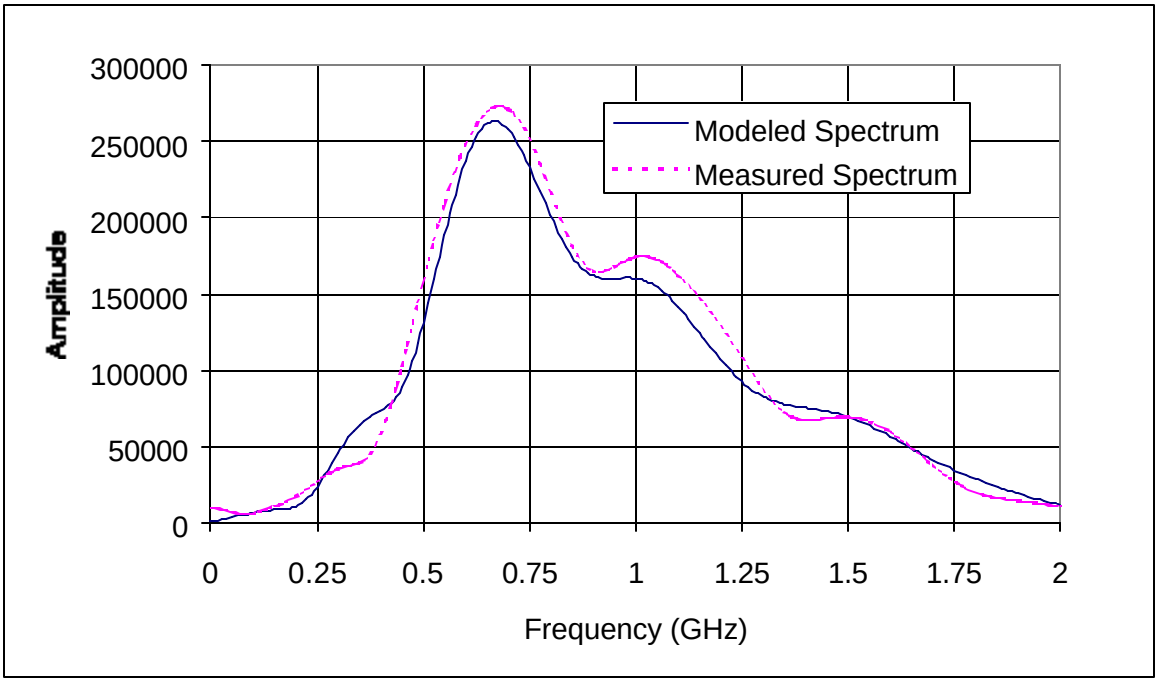

Figure C68 Modeled (with average ε_r) and measured frequency spectrums for slab M3S2 (07/17/00)

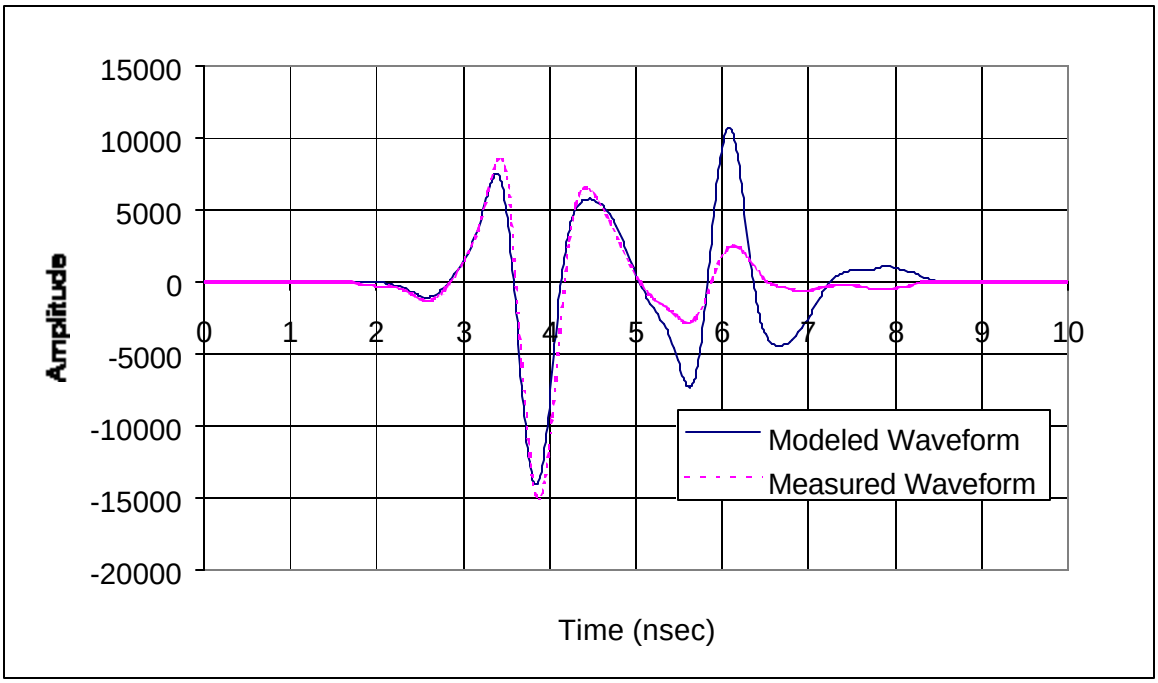

Figure C69 Modeled (with average real part of ε_r and zero imaginary part) and measured waveforms for slab M3S2 (07/17/00)

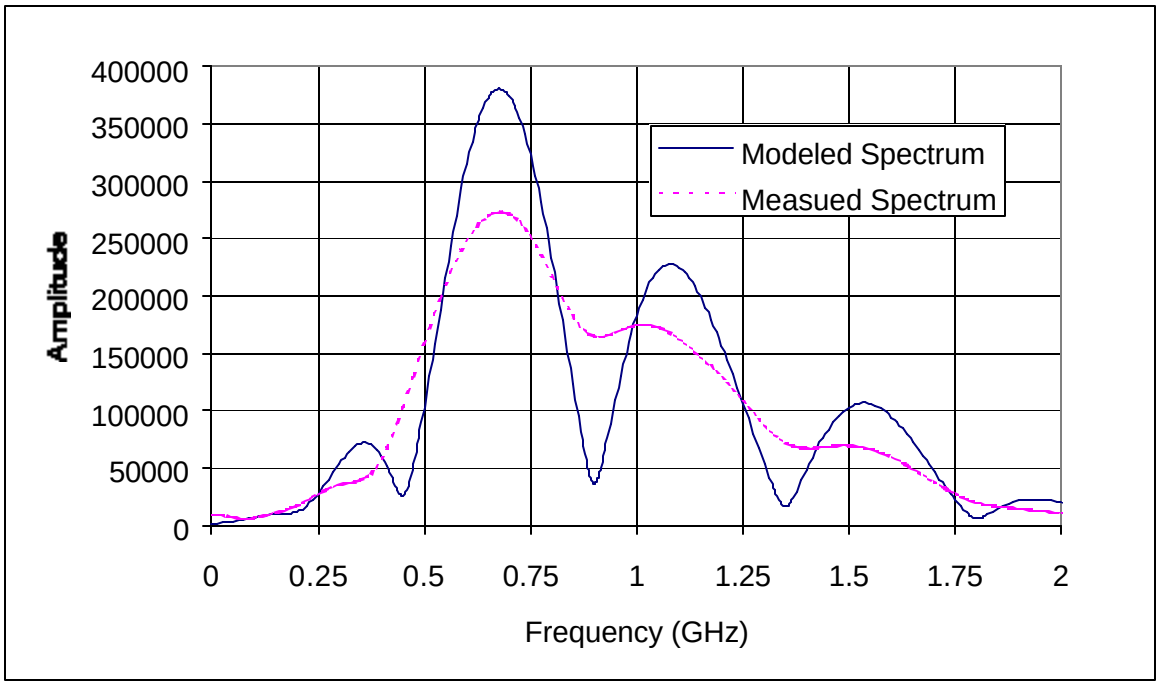

Figure C70 Modeled (with average real part of ε_r and zero imaginary part) and measured frequency spectrums for slab M3S2 (07/17/00)

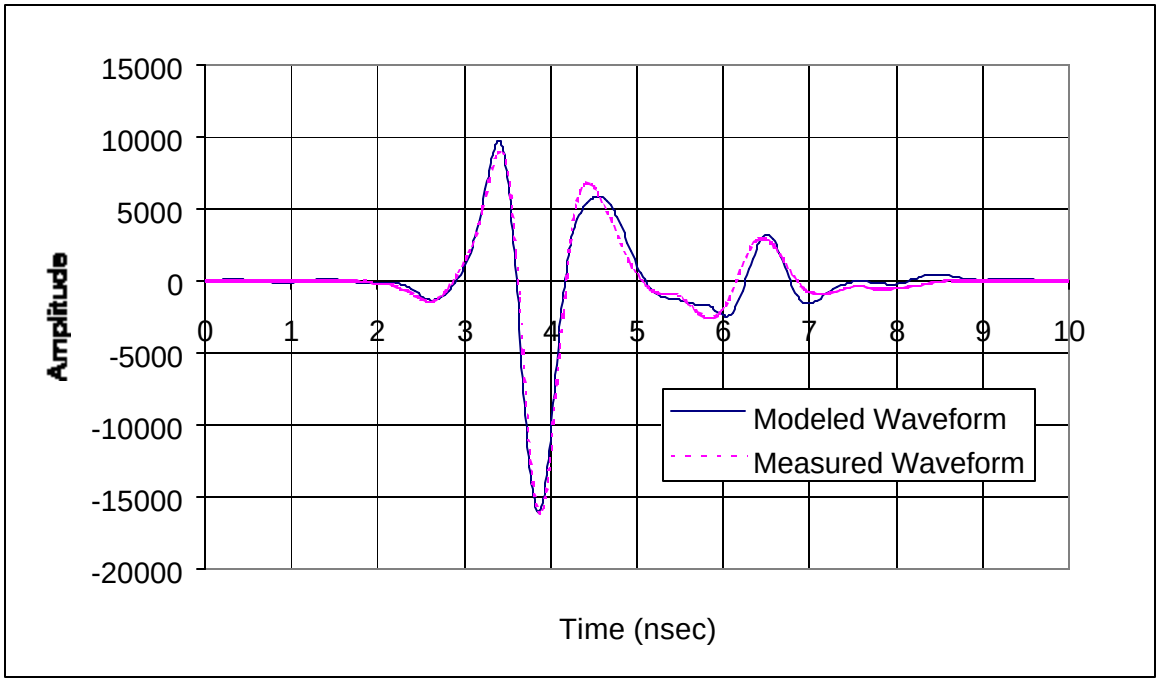

Figure C71 Modeled (with calculated solution for ε_r) and measured waveforms for slab M4S1 (07/17/00)

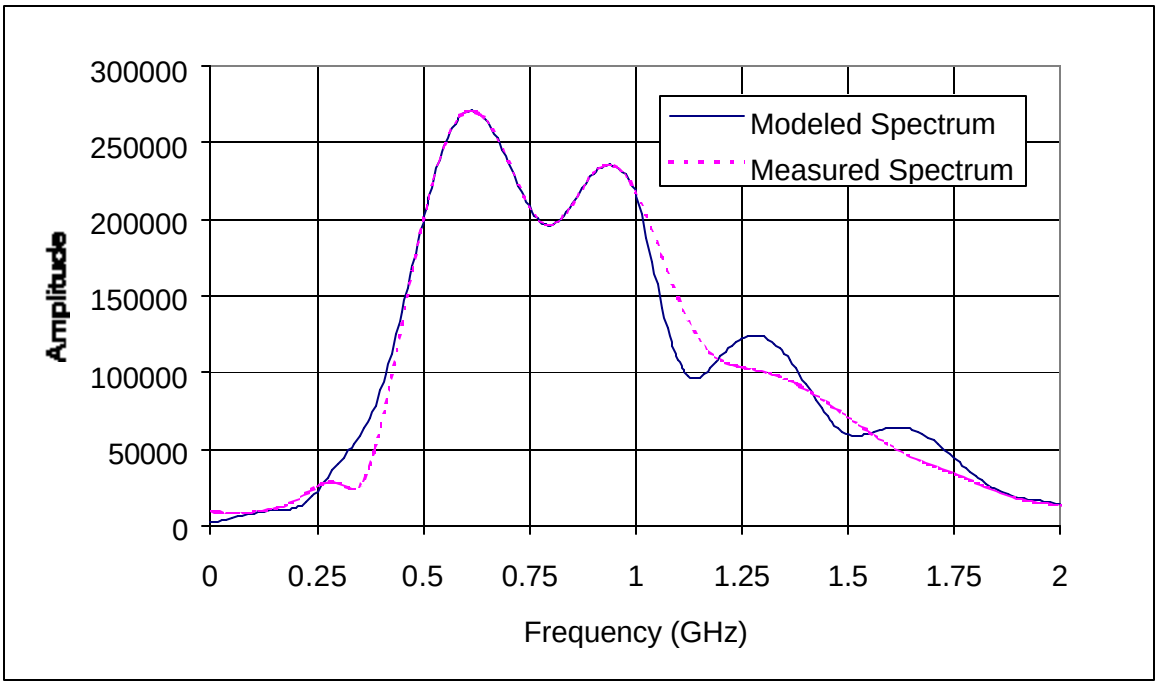

Figure C72 Modeled (with calculated solution for ε_r) and measured frequency spectrums for slab M4S1 (07/17/00)

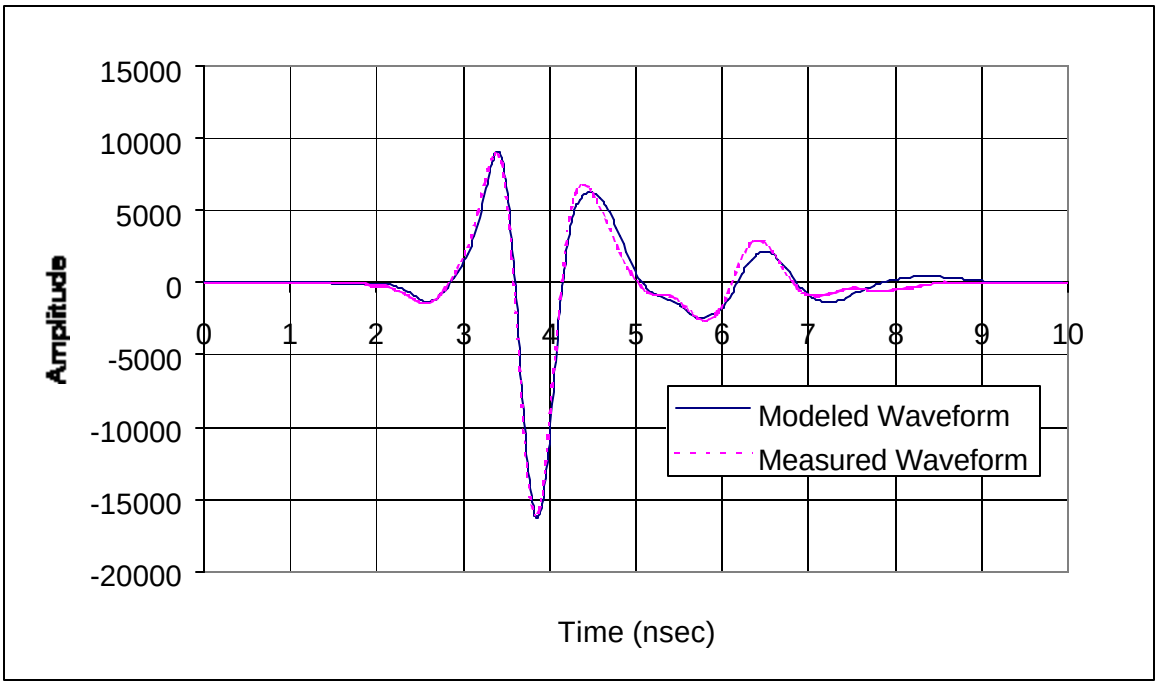

Figure C73 Modeled (with average ε_r) and measured Waveforms for slab M4S1 (07/17/00)

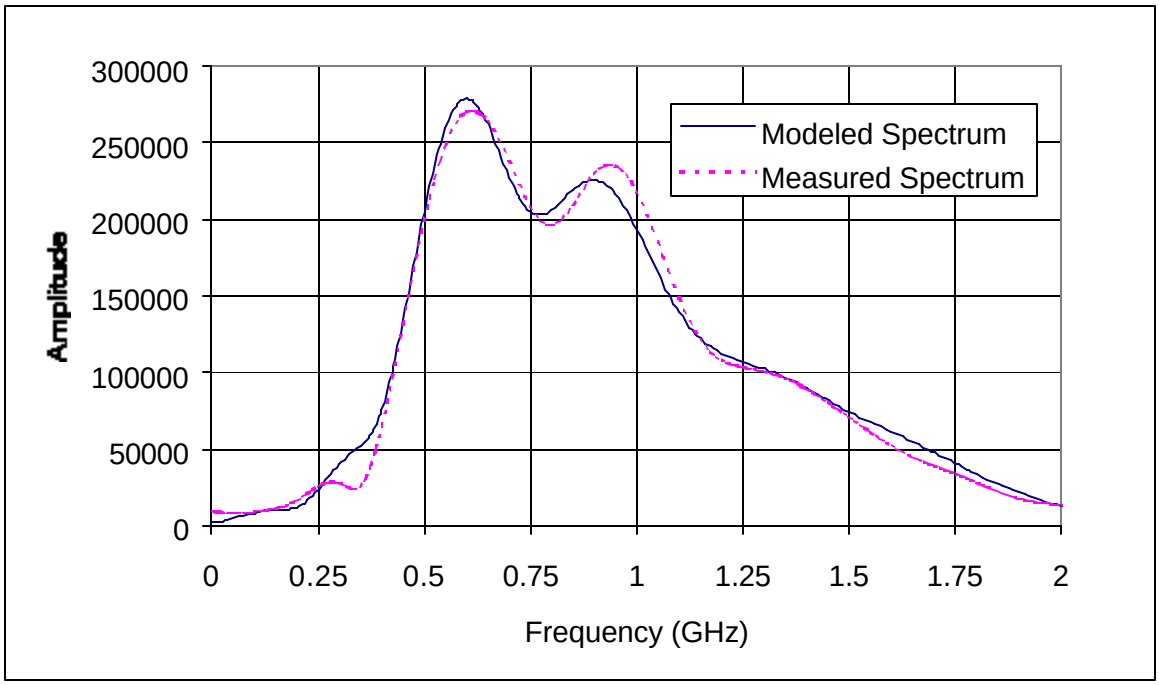

Figure C74 Modeled (with average ε_r) and measured frequency spectrums for slab M4S1 (07/17/00)

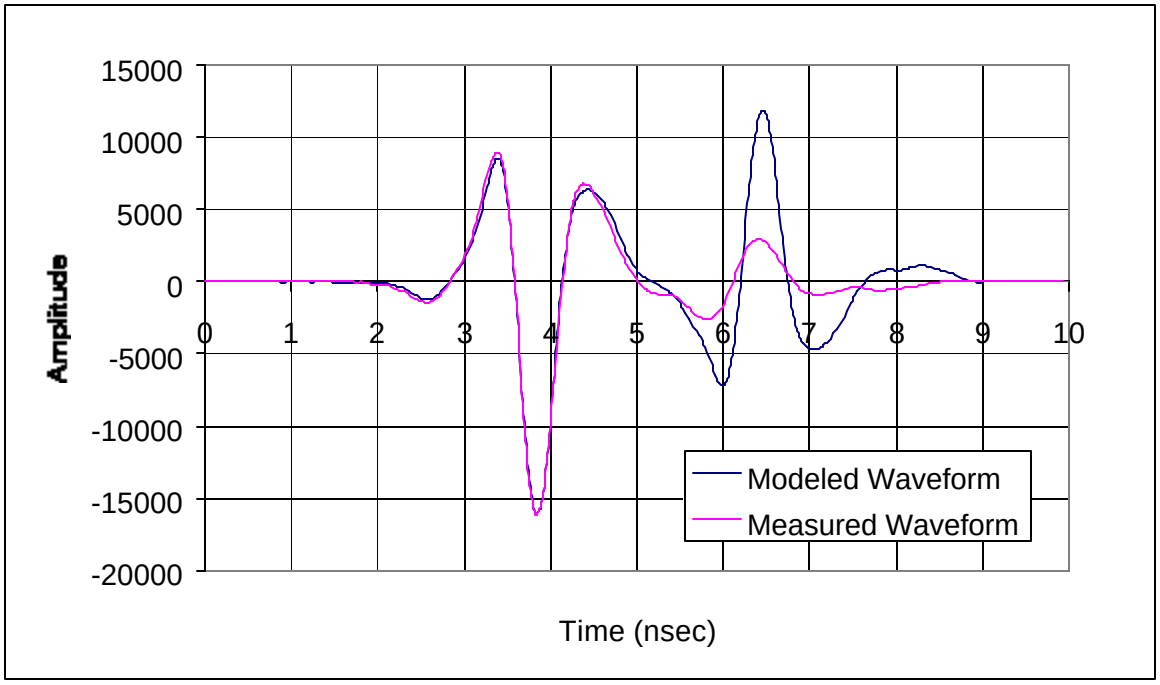

Figure C75 Modeled (with average real part of ε_r and zero imaginary part) and measured waveforms for slab M4S1 (07/17/00)

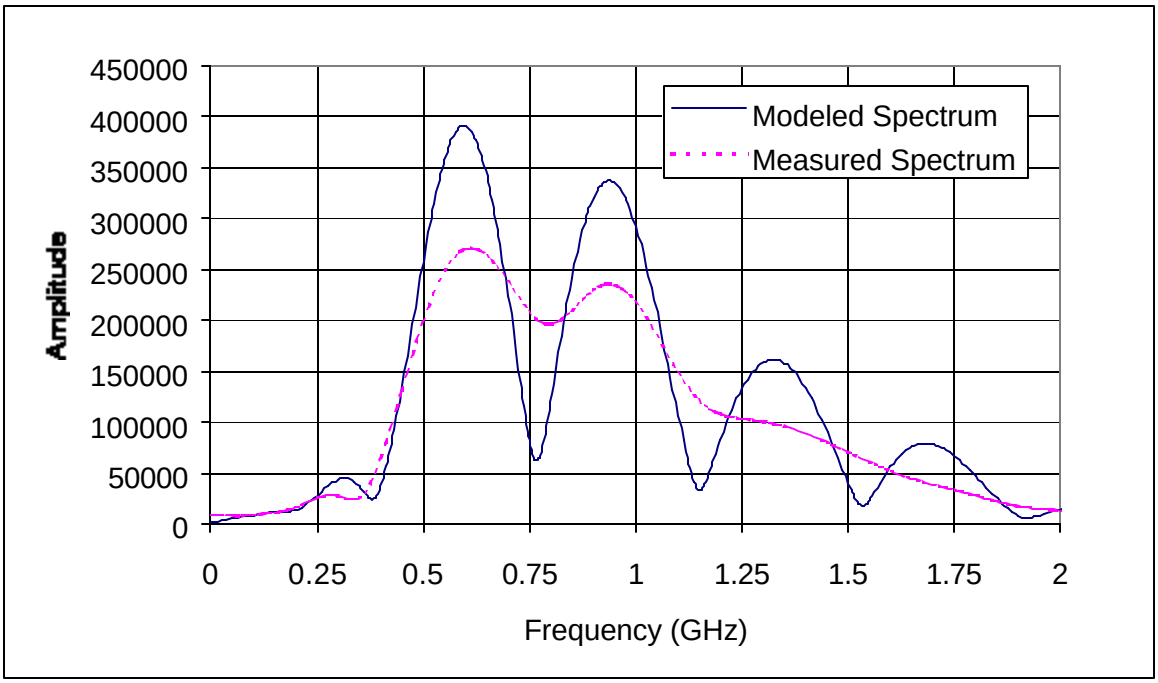

Figure C76 Modeled (with average real part of ε_r and zero imaginary part) and measured frequency spectrums for slab M4S1 (07/17/00)

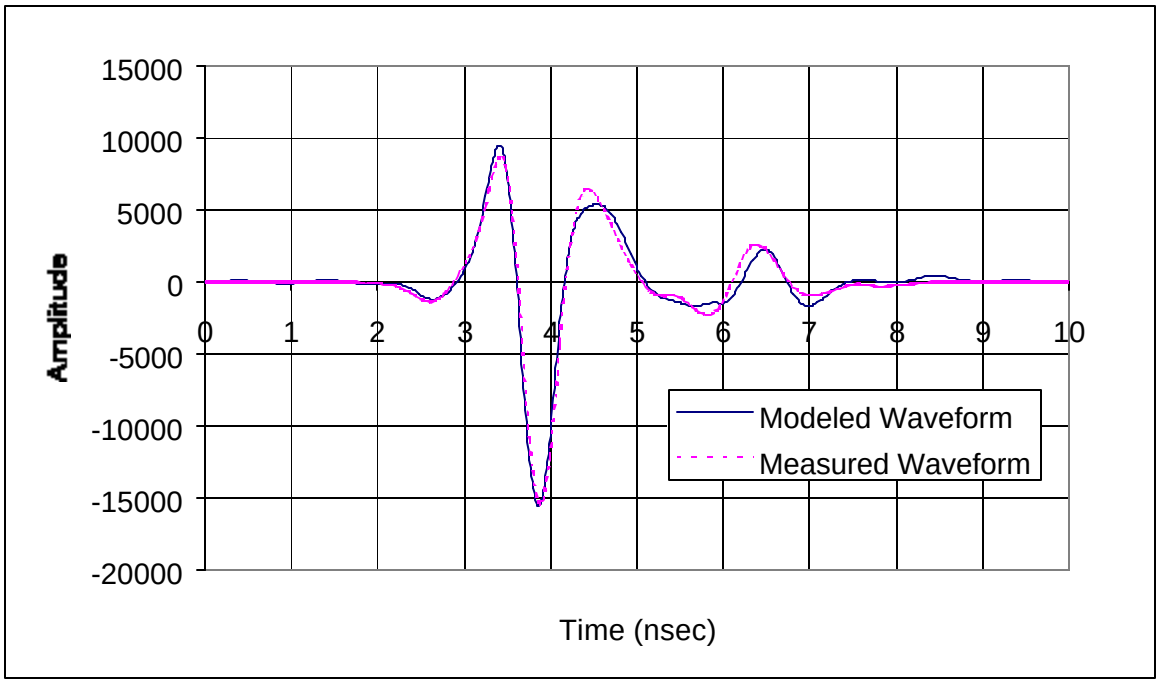

Figure C77 Modeled (with calculated solution for ε_r) and measured waveforms for slab M5S1 (07/17/00)

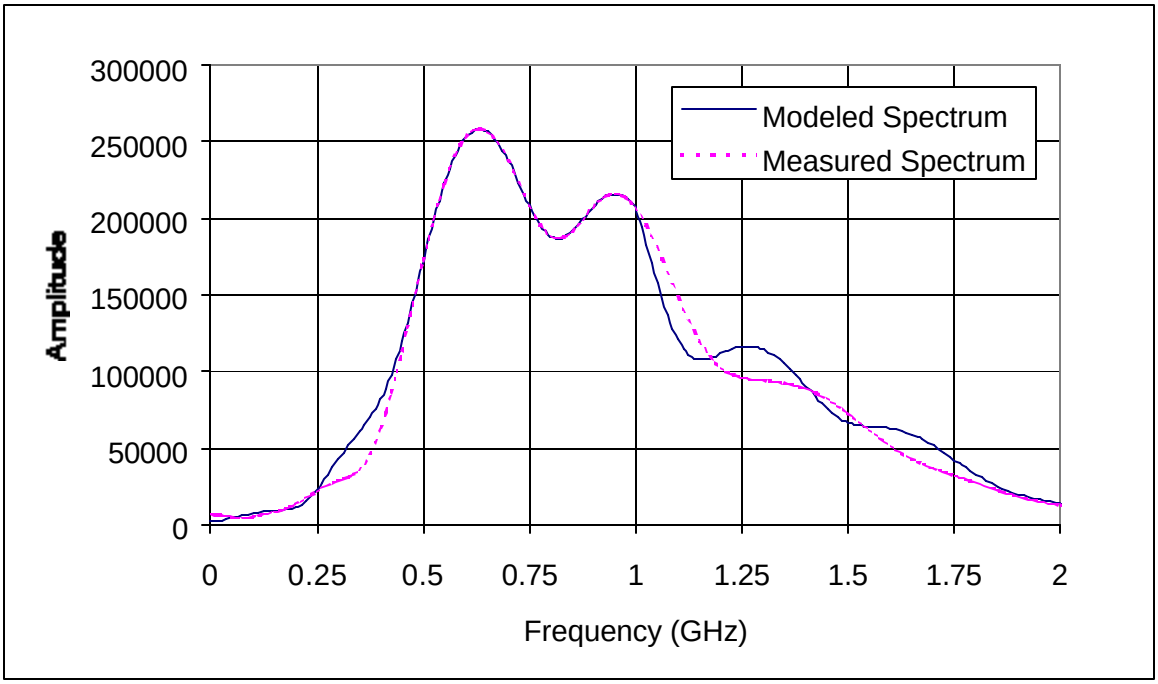

Figure C78 Modeled (with calculated solution for ε_r) and measured frequency spectrums for slab M5S1 (07/17/00)

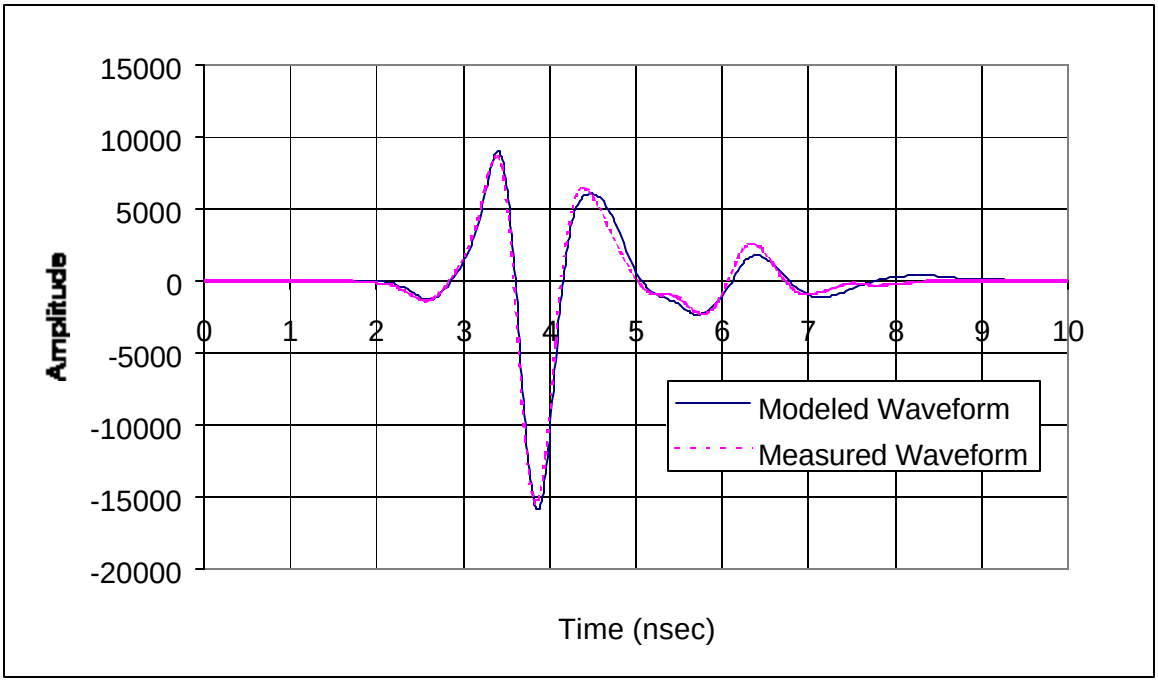

Figure C79 Modeled (with average ε_r) and measured Waveforms for slab M5S1 (07/17/00)

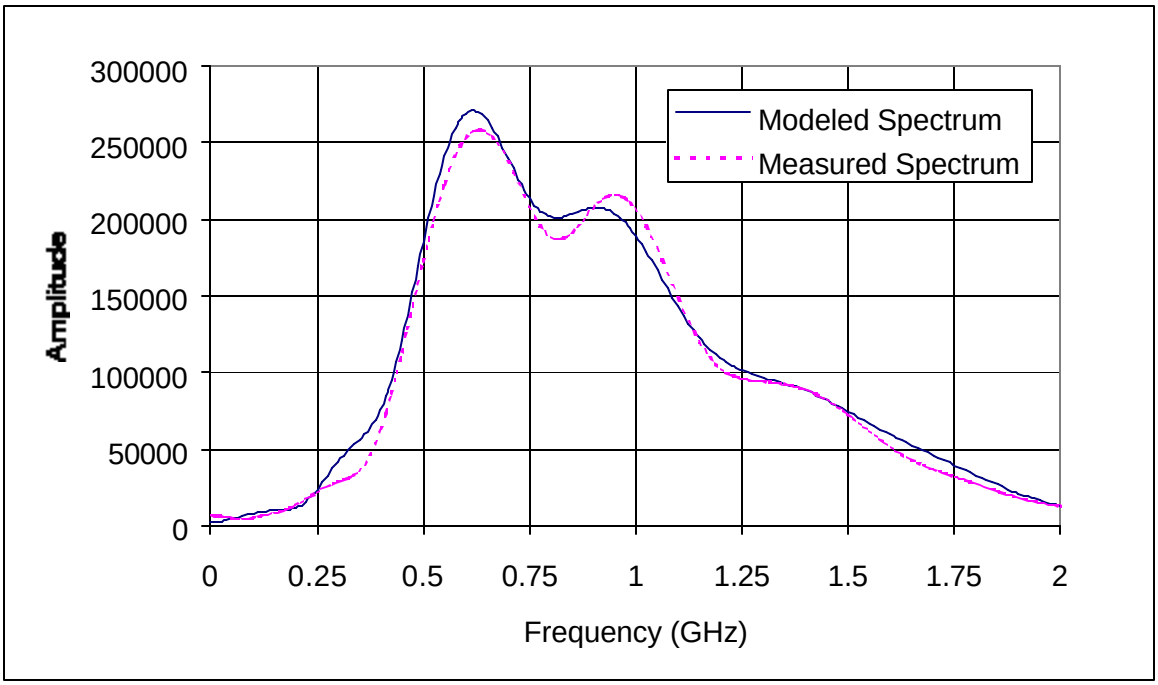

Figure C80 Modeled (with average ε_r) and measured frequency spectrums for slab M5S1 (07/17/00)

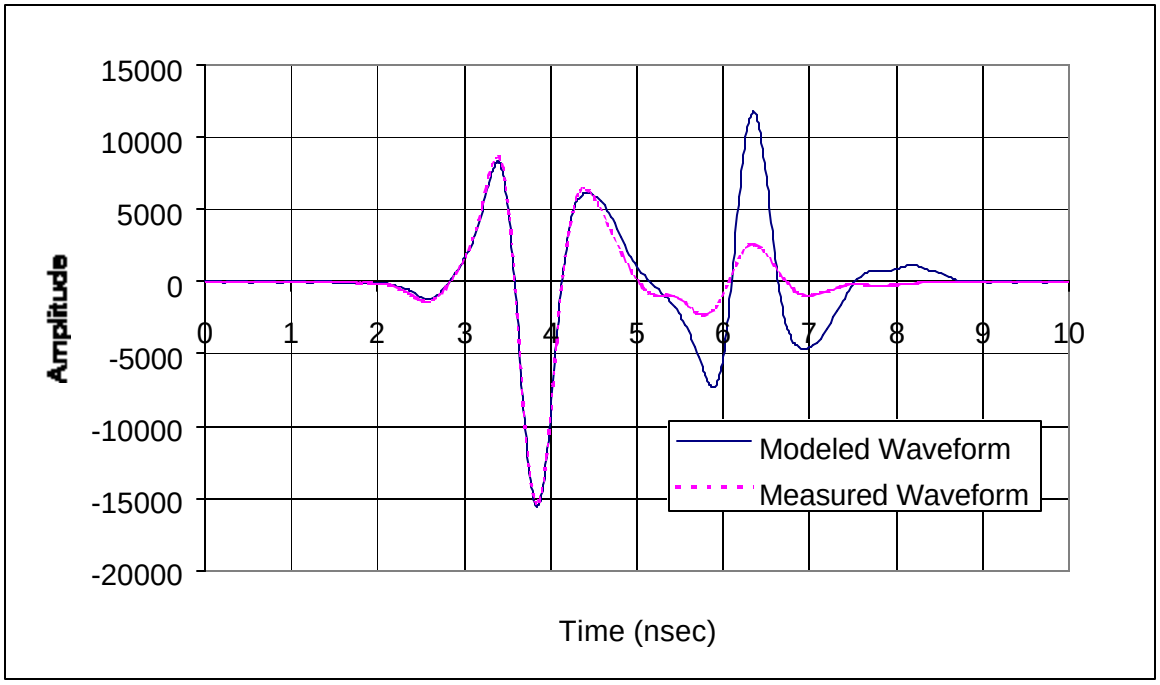

Figure C81 Modeled (with average real part of ε_r and zero imaginary part) and measured waveforms for slab M5S1 (07/17/00)

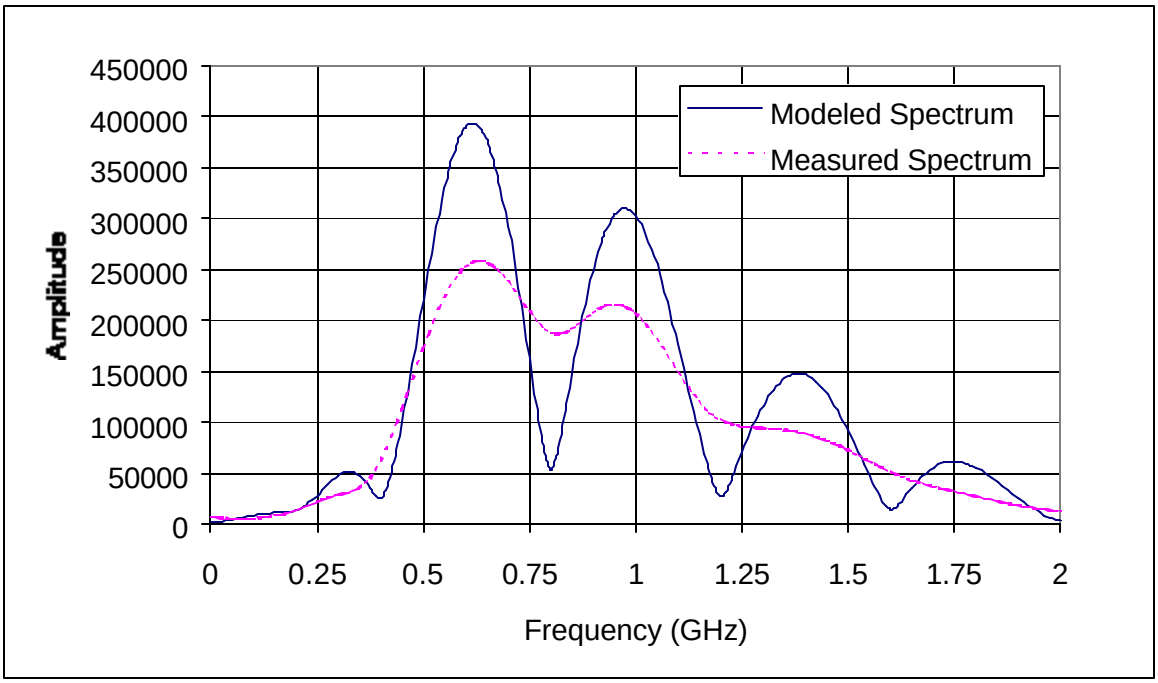

Figure C82 Modeled (with average real part of ε_r and zero imaginary part) and measured frequency spectrums for slab M5S1 (07/17/00)

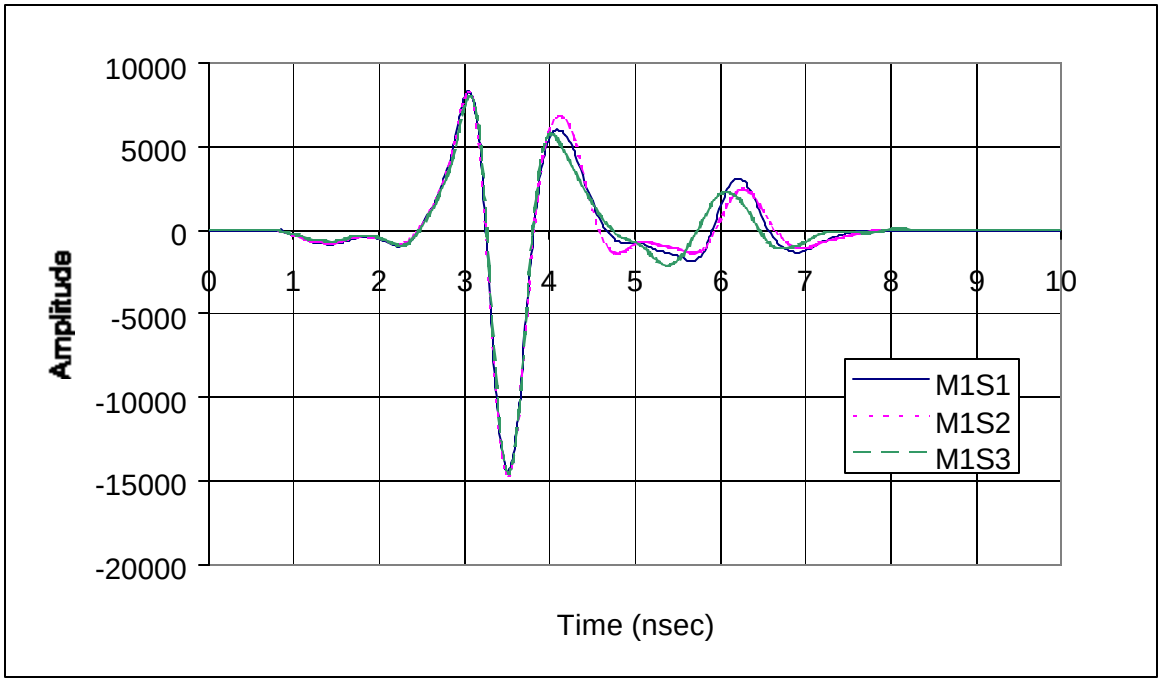

Figure C83 Air void effects on the time domain signal for mix M1 (05/13/00)

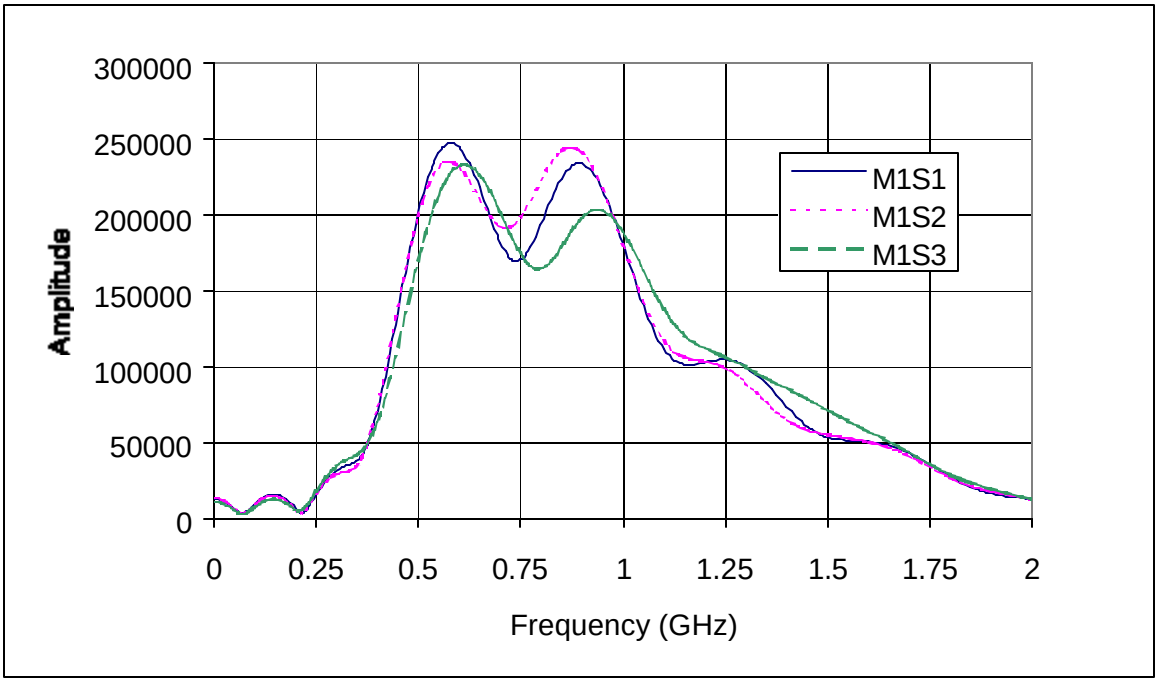

Figure C84 Air void effects on the frequency spectrum for mix M1 (05/13/00)

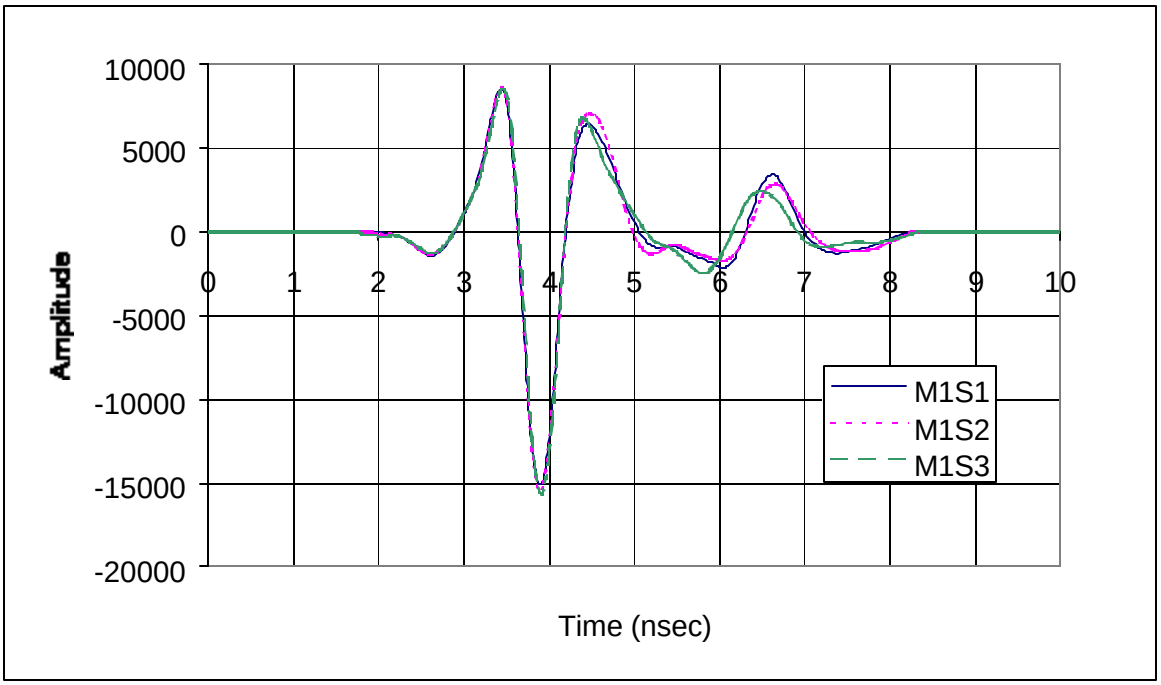

Figure C85 Air void effects on the time domain signal for mix M1 (07/17/00)

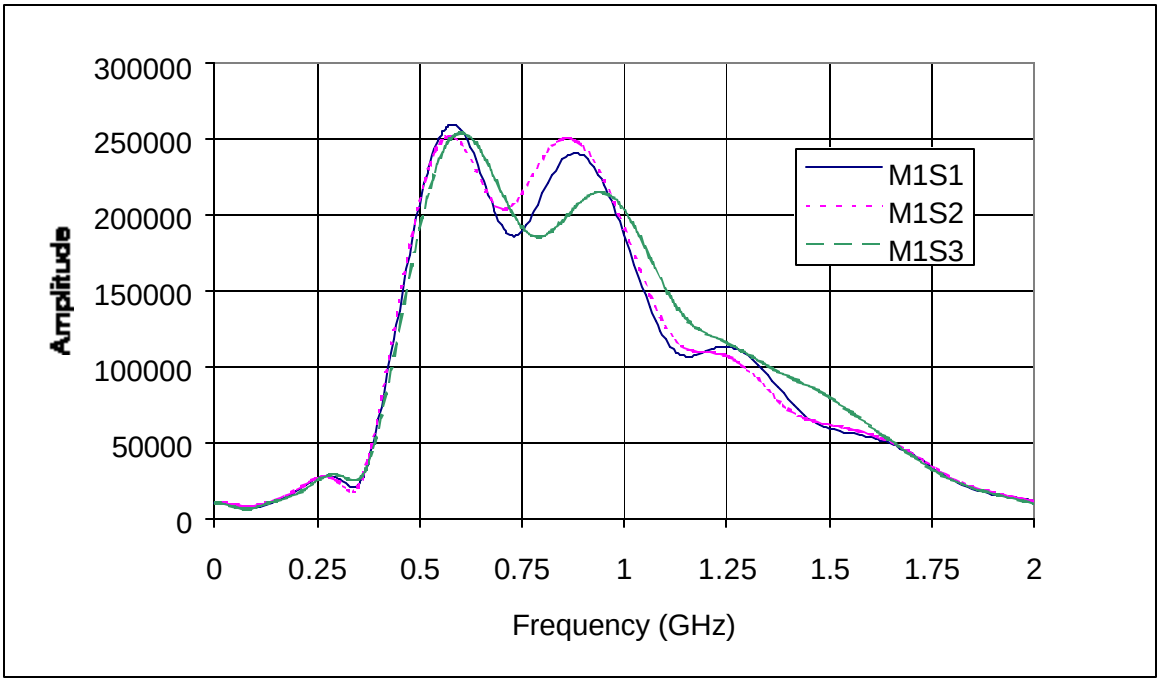

Figure C86 Air void effects on the frequency spectrum for mix M1 (07/17/00)

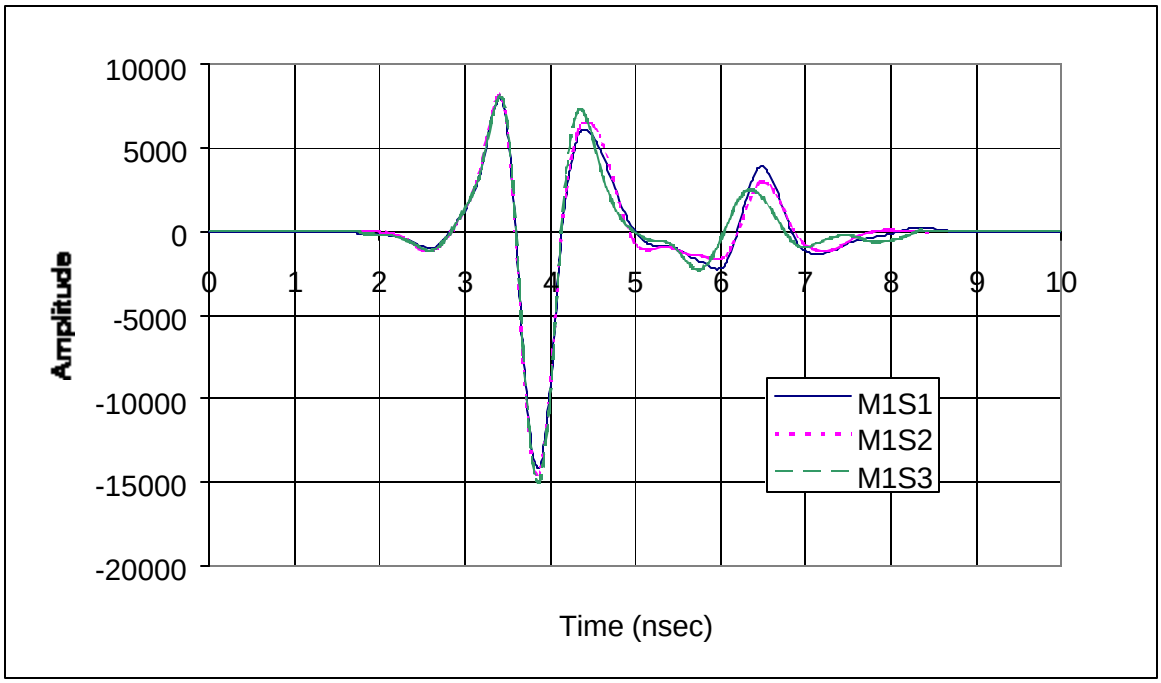

Figure C87 Air void effects on the time domain signal for mix M1 (11/05/00)

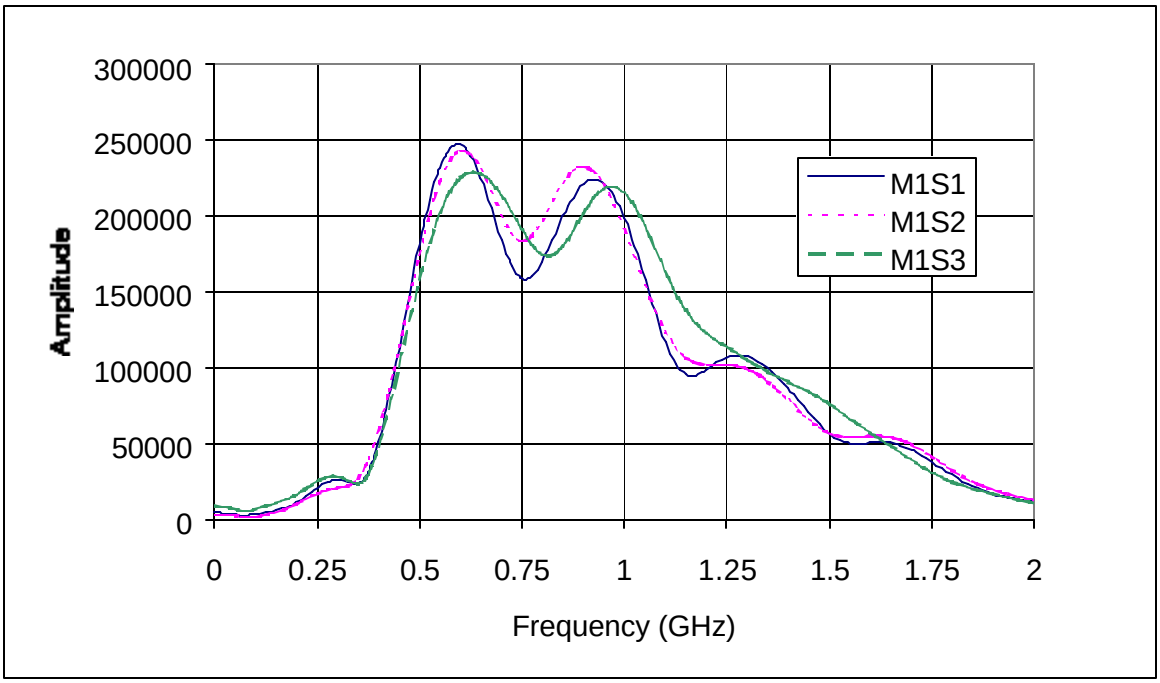

Figure C88 Air void effects on the frequency spectrum for mix M1 (11/05/00)

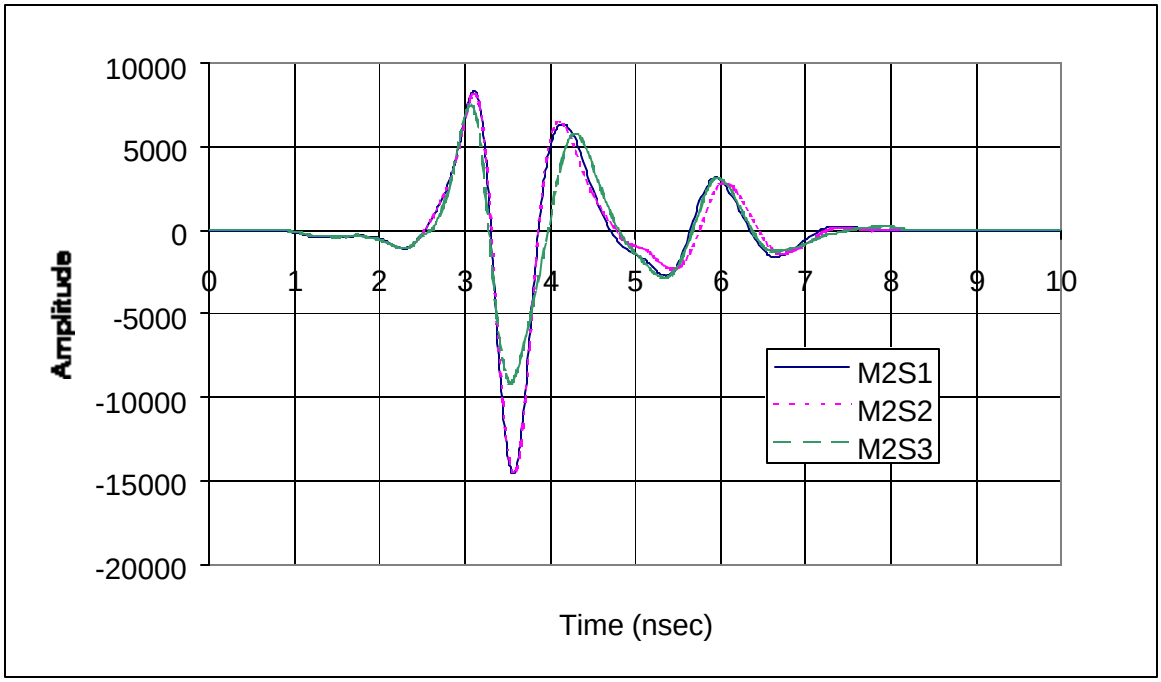

Figure C89 Air void effects on the time domain signal for mix M2 (05/13/00)

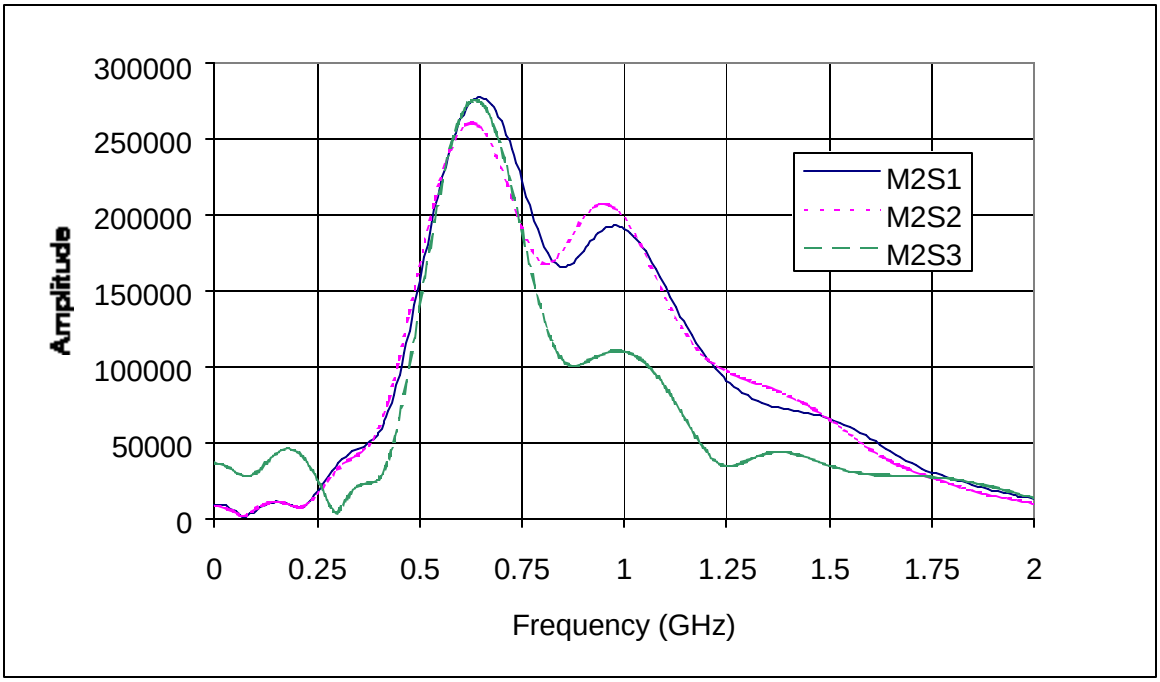

Figure C90 Air void effects on the frequency spectrum for mix M2 (05/13/00)

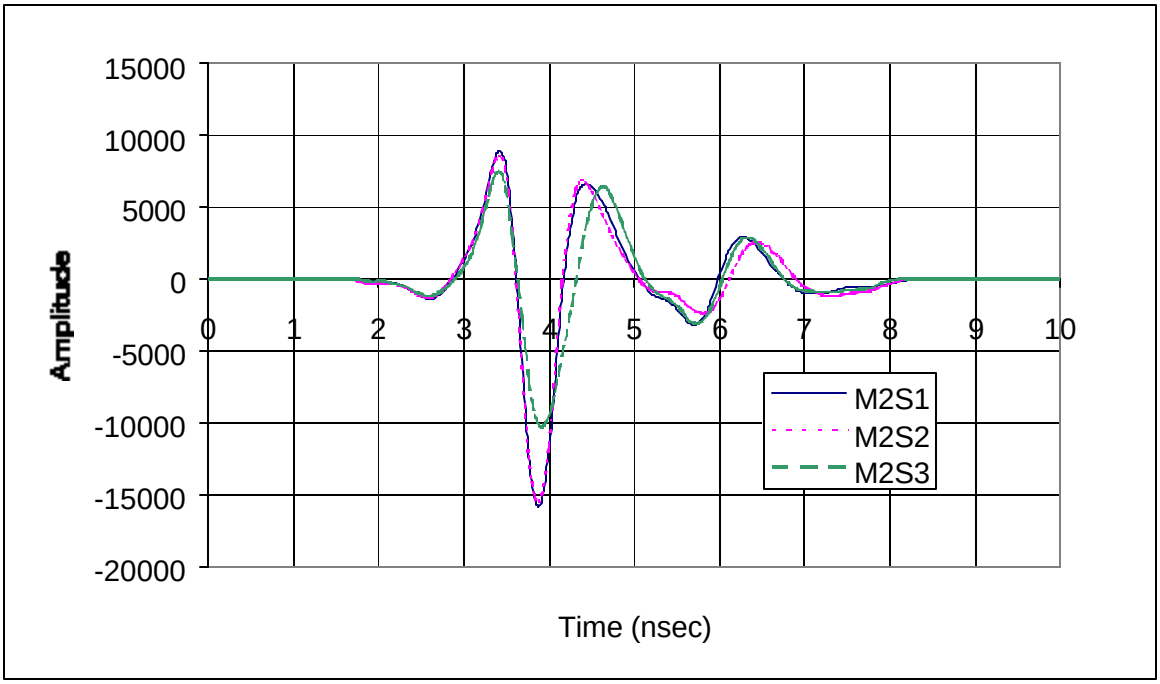

Figure C91 Air void effects on the time domain signal for mix M2 (07/17/00)

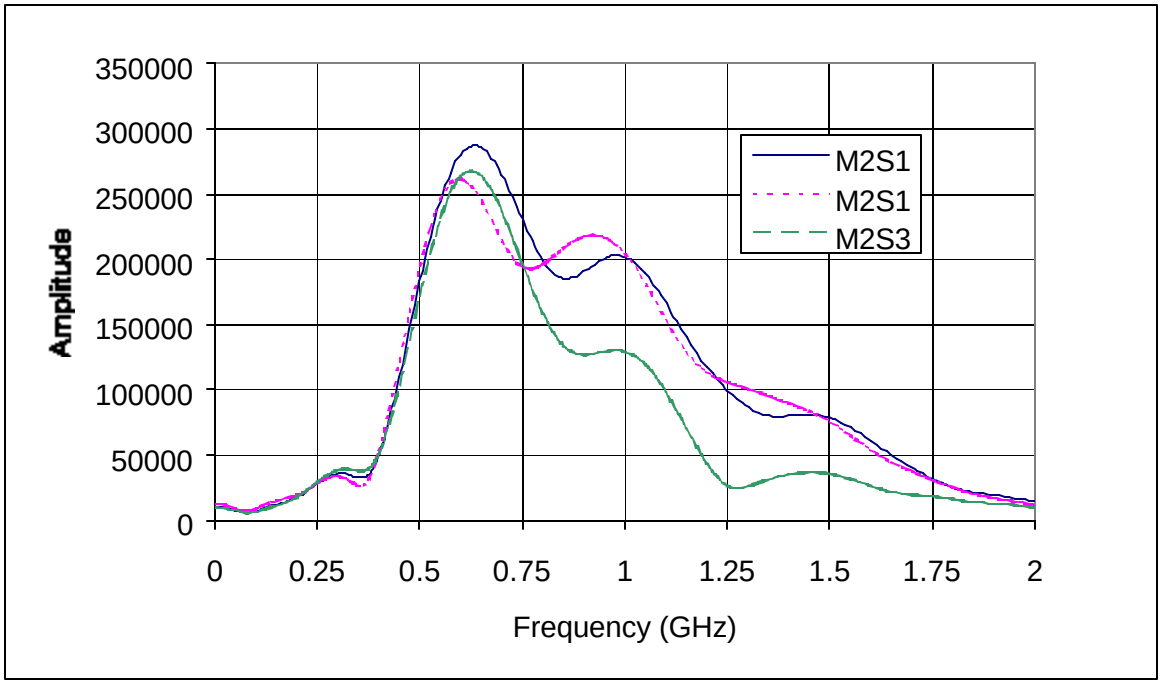

Figure C92 Air void effects on the frequency spectrum for mix M2 (07/17/00)

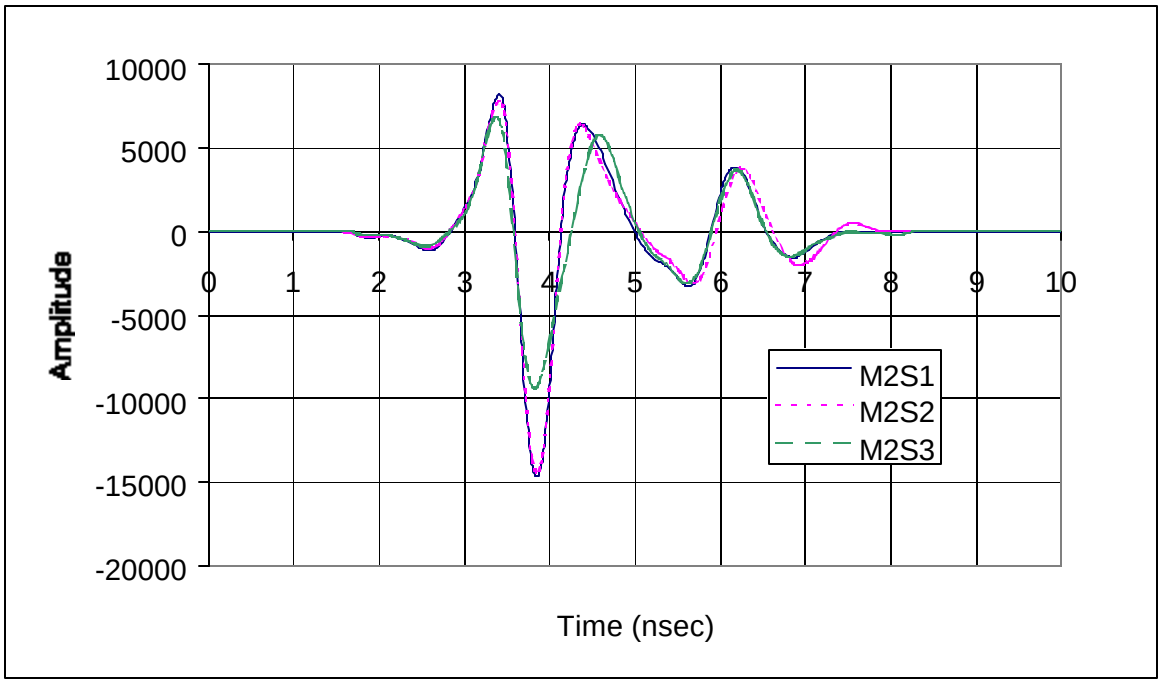

Figure C93 Air void effects on the time domain signal for mix M2 (11/05/00)

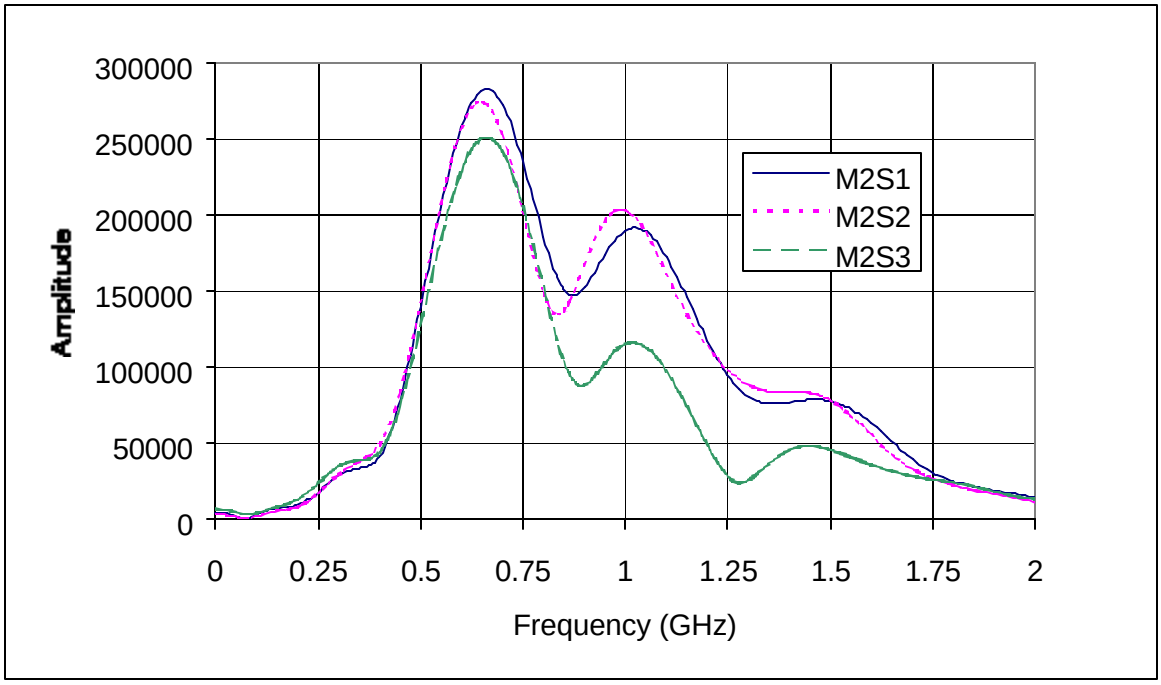

Figure C94 Air void effects on the frequency spectrum for mix M2 (11/05/00)

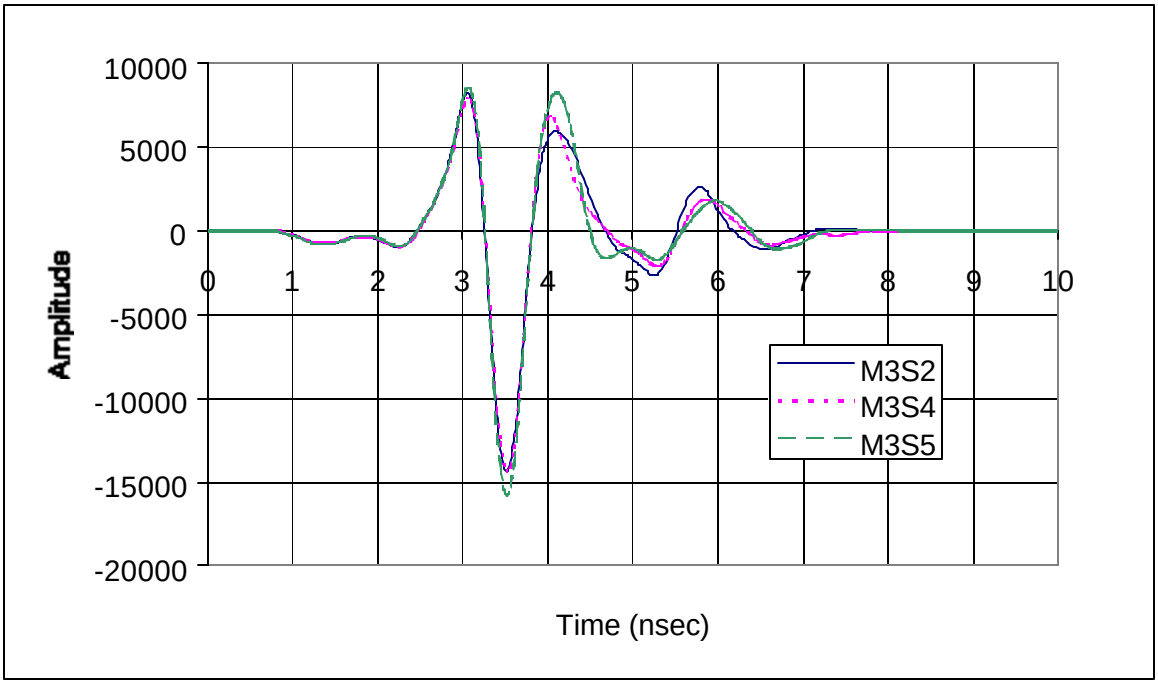

Figure C95 Air void effects on the time domain signal for mix M3 (05/13/00)

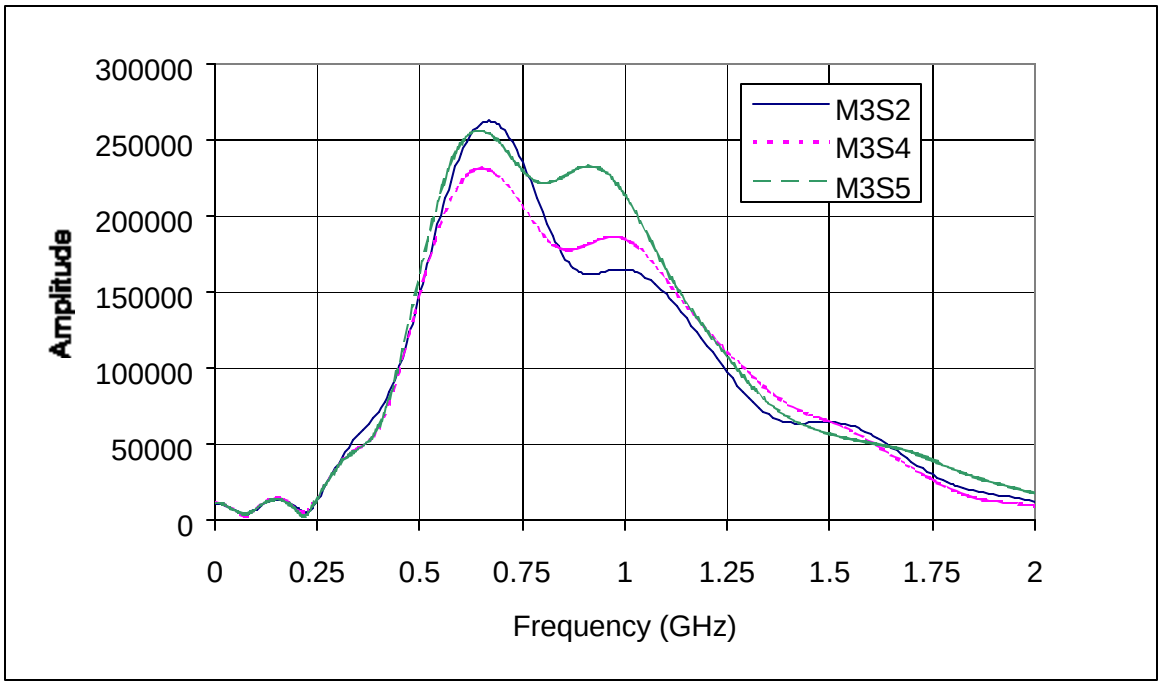

Figure C96 Air void effects on the frequency spectrum for mix M3 (05/13/00)

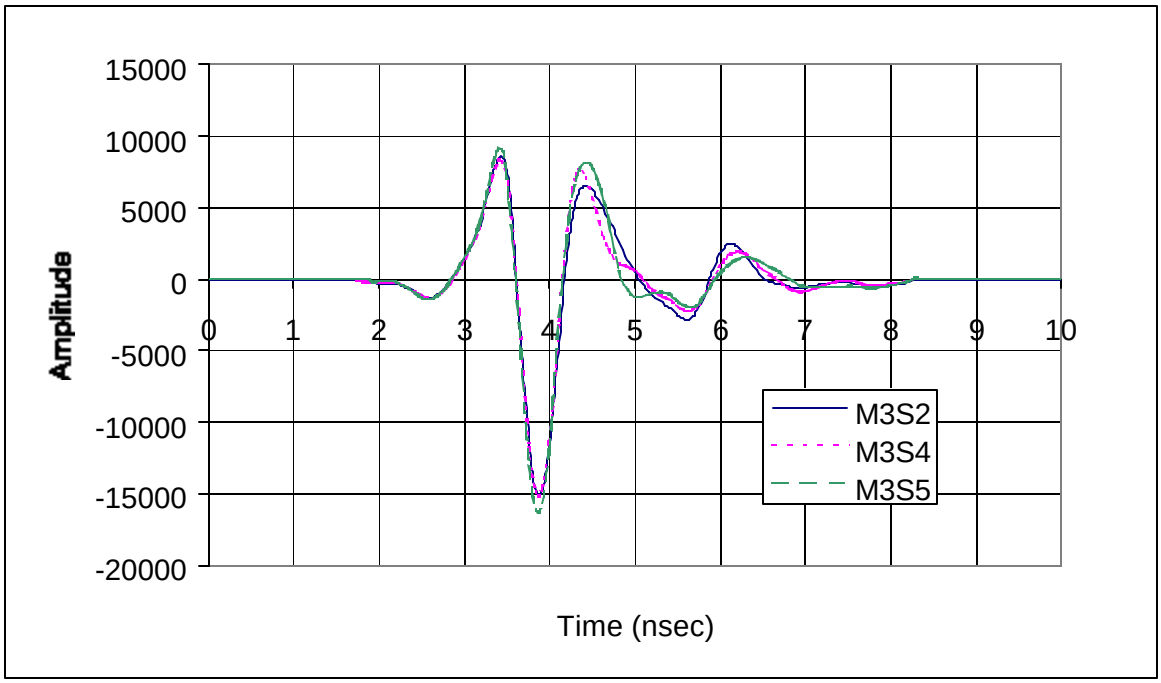

Figure C97 Air void effects on the time domain signal for mix M3 (07/17/00)

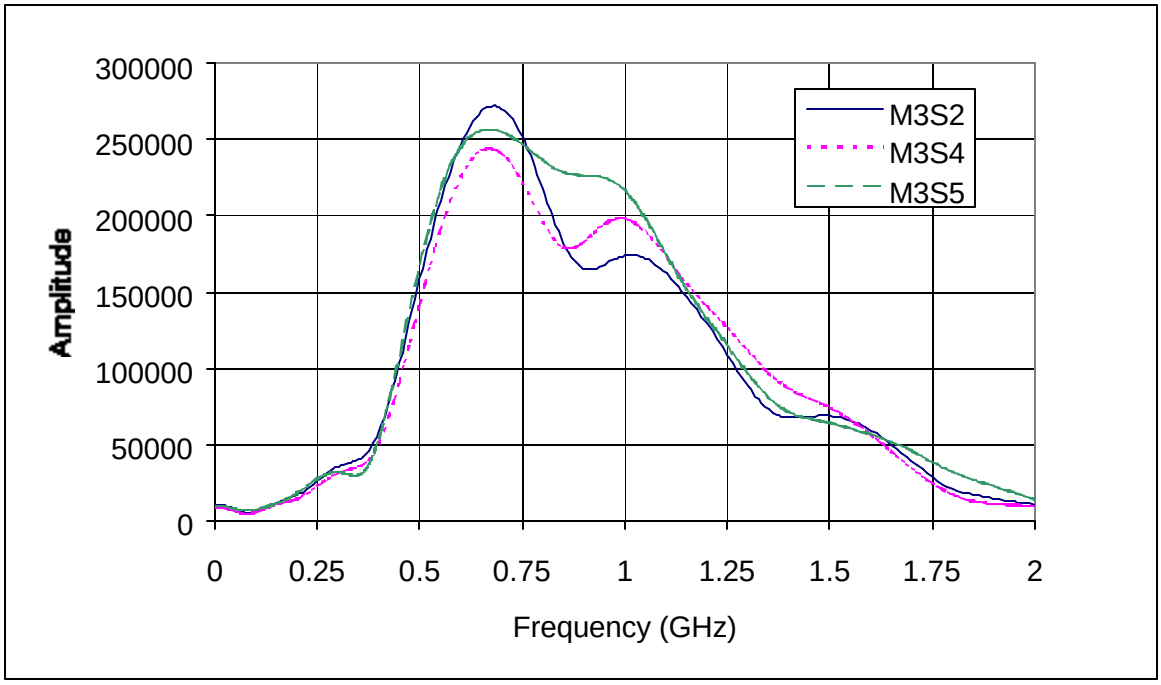

Figure C98 Air void effects on the frequency spectrum for mix M3 (07/17/00)

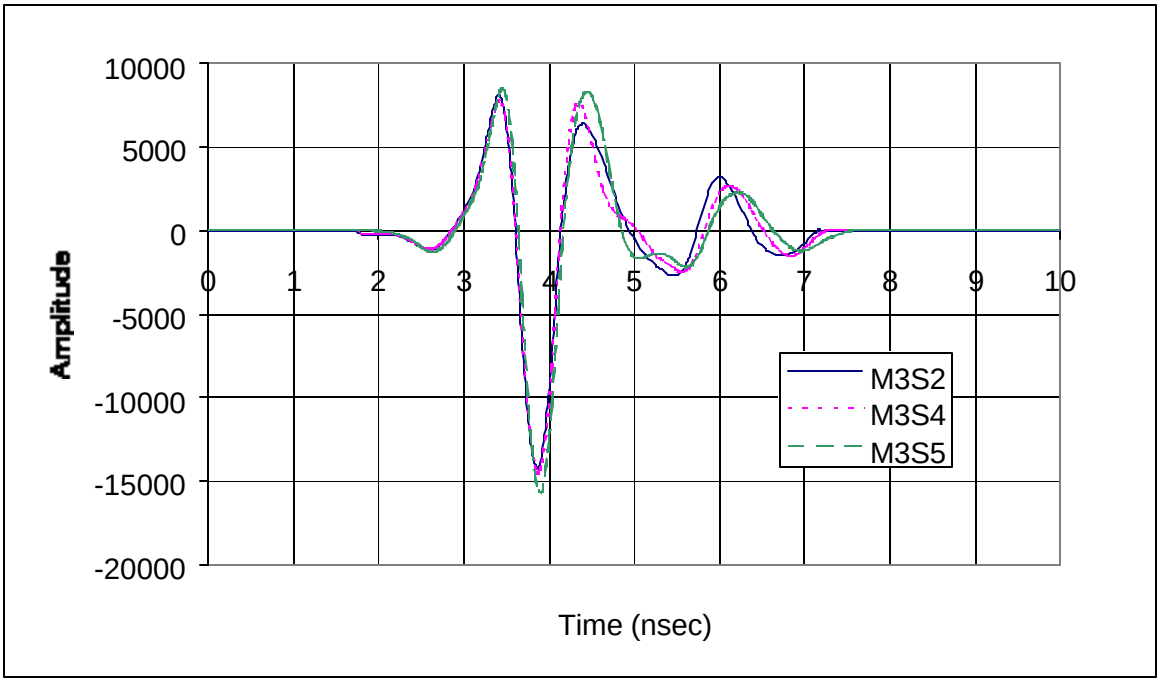

Figure C99 Air void effects on the time domain signal for mix M3 (11/05/00)

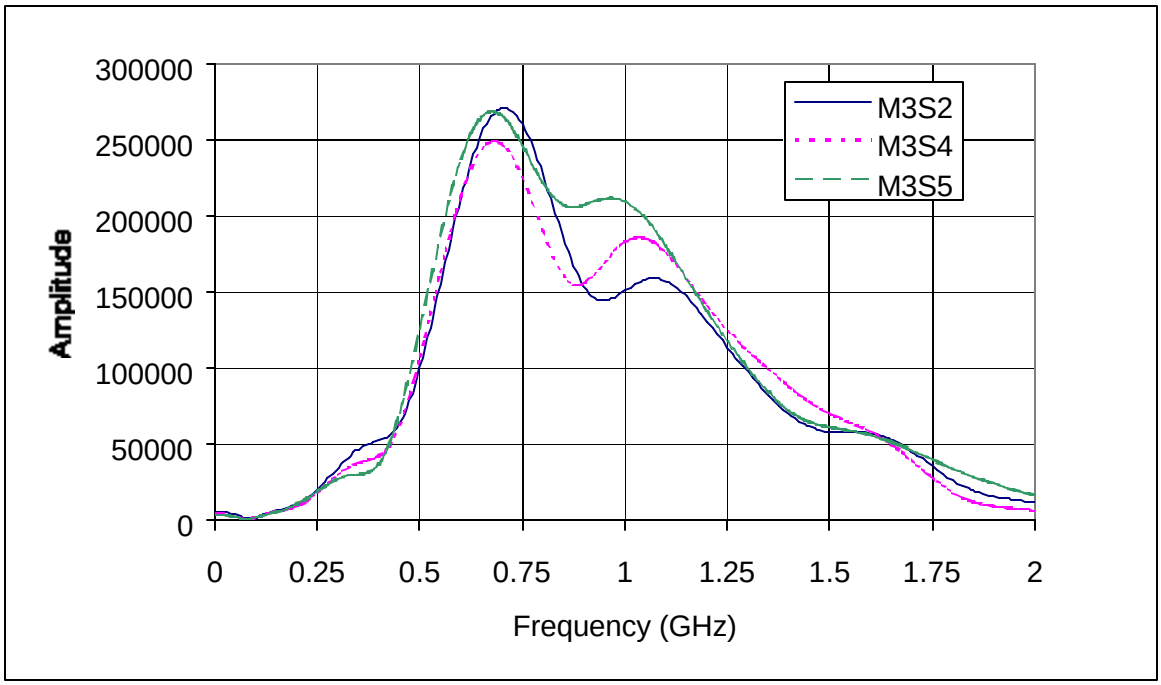

Figure C100 Air void effects on the frequency spectrum for mix M3 (11/05/00)

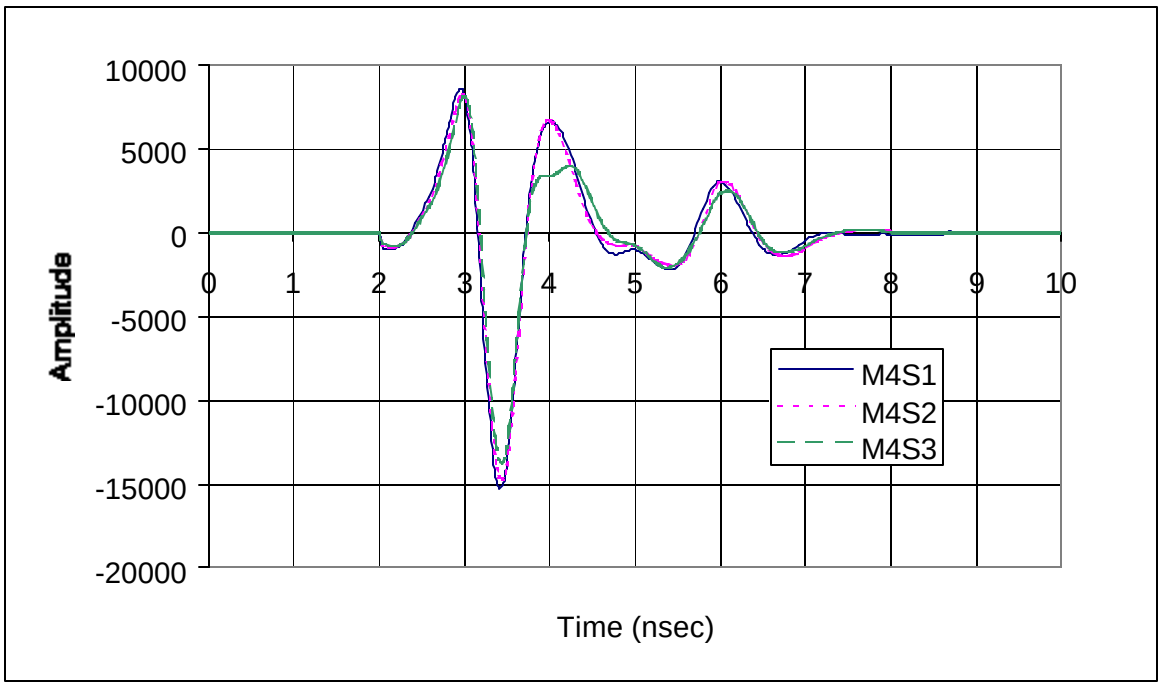

Figure C101 Air void effects on the time domain signal for mix M4 (05/13/00)

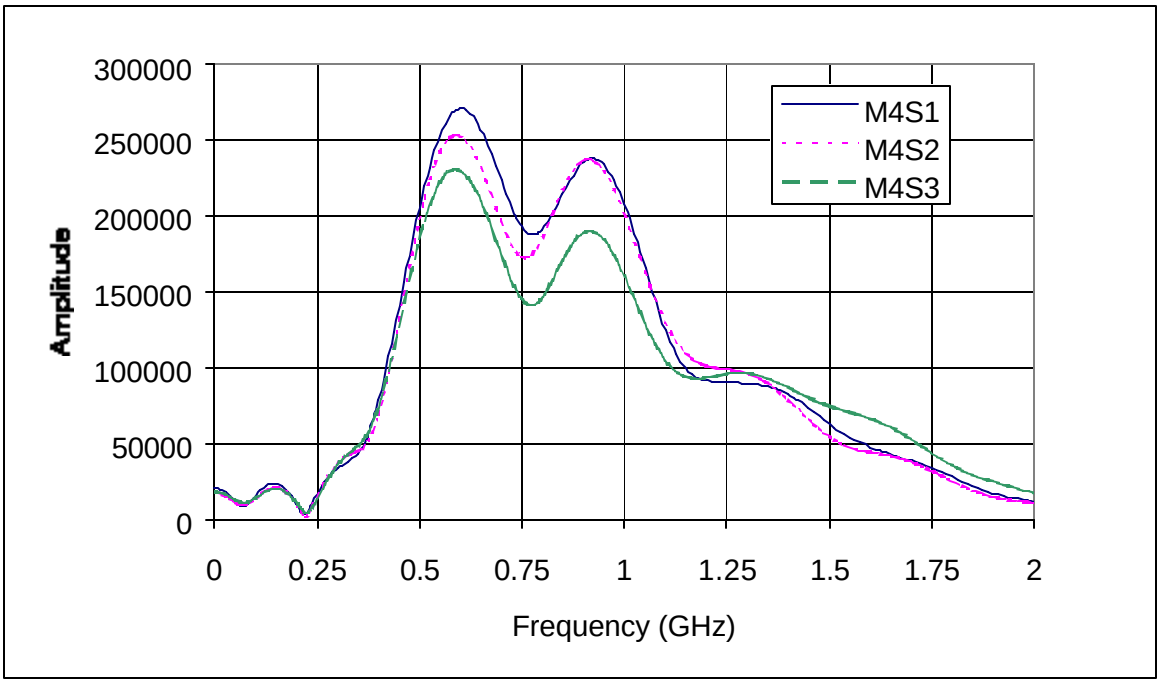

Figure C102 Air void effects on the frequency spectrum for mix M4 (05/13/00)

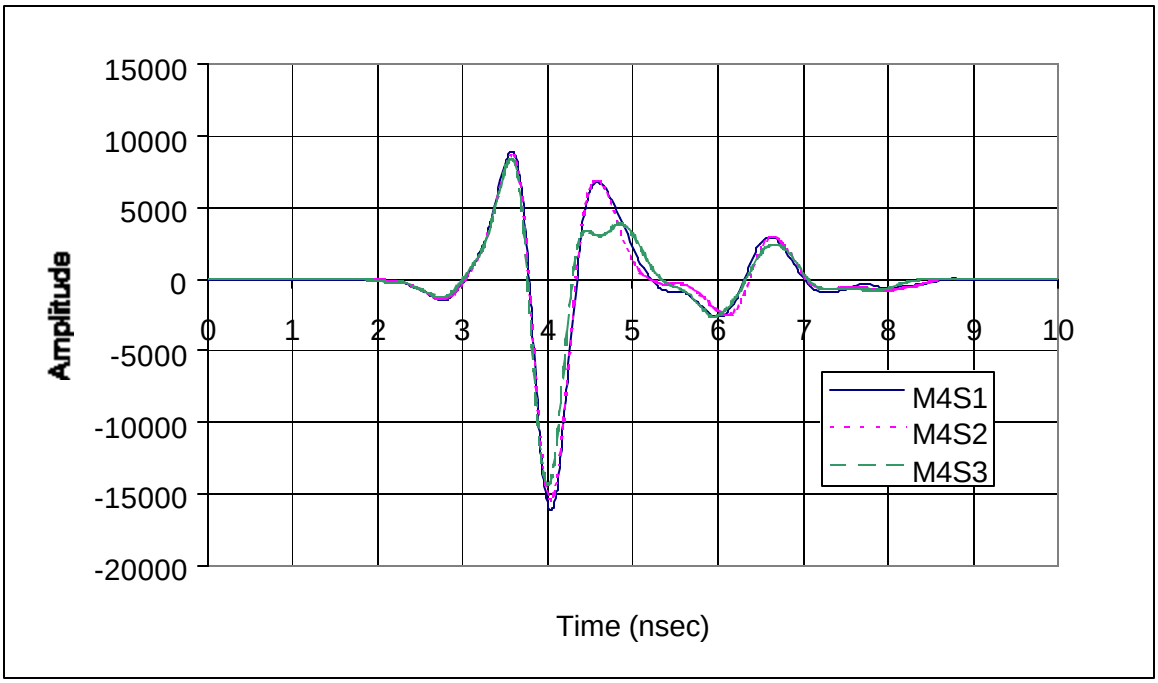

Figure C103 Air void effects on the time domain signal for mix M4 (07/17/00)

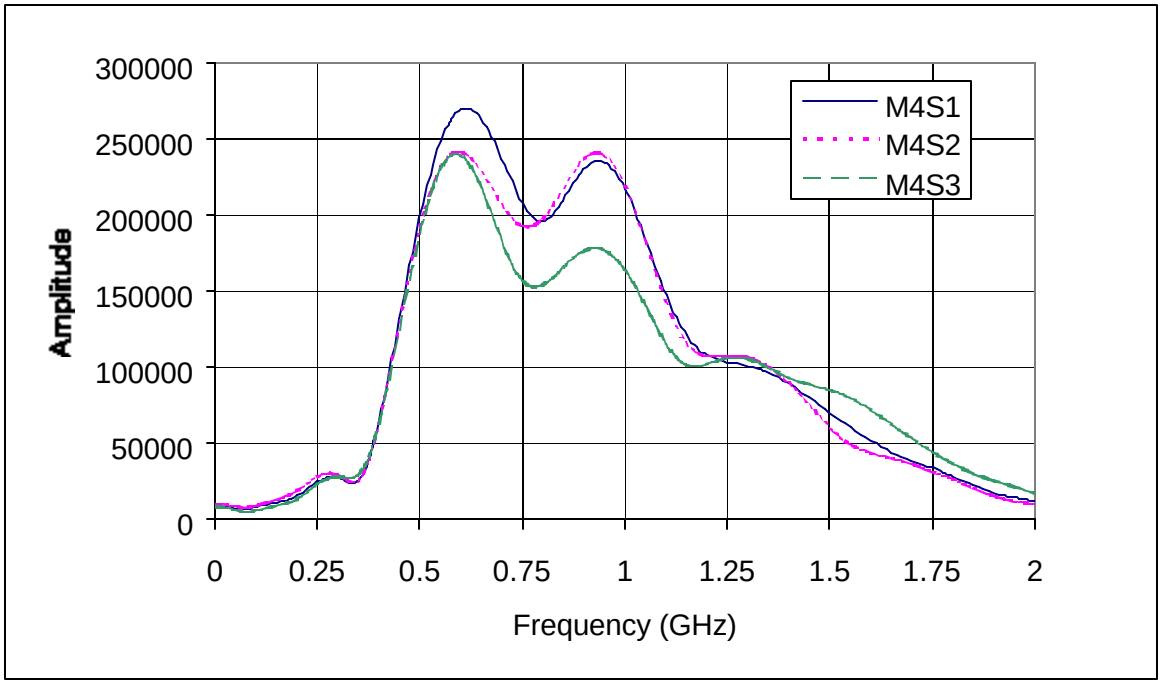

Figure C104 Air void effects on the frequency spectrum for mix M4 (07/17/00)

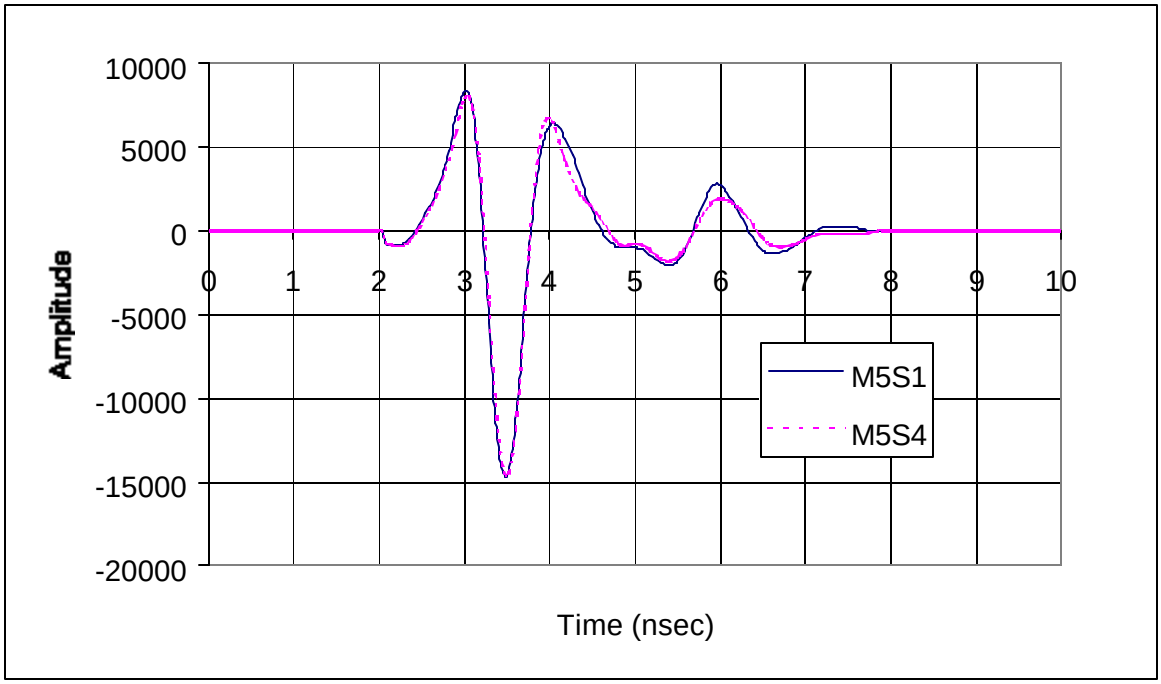

Figure C105 Air void effects on the time domain signal for mix M5 (05/13/00)

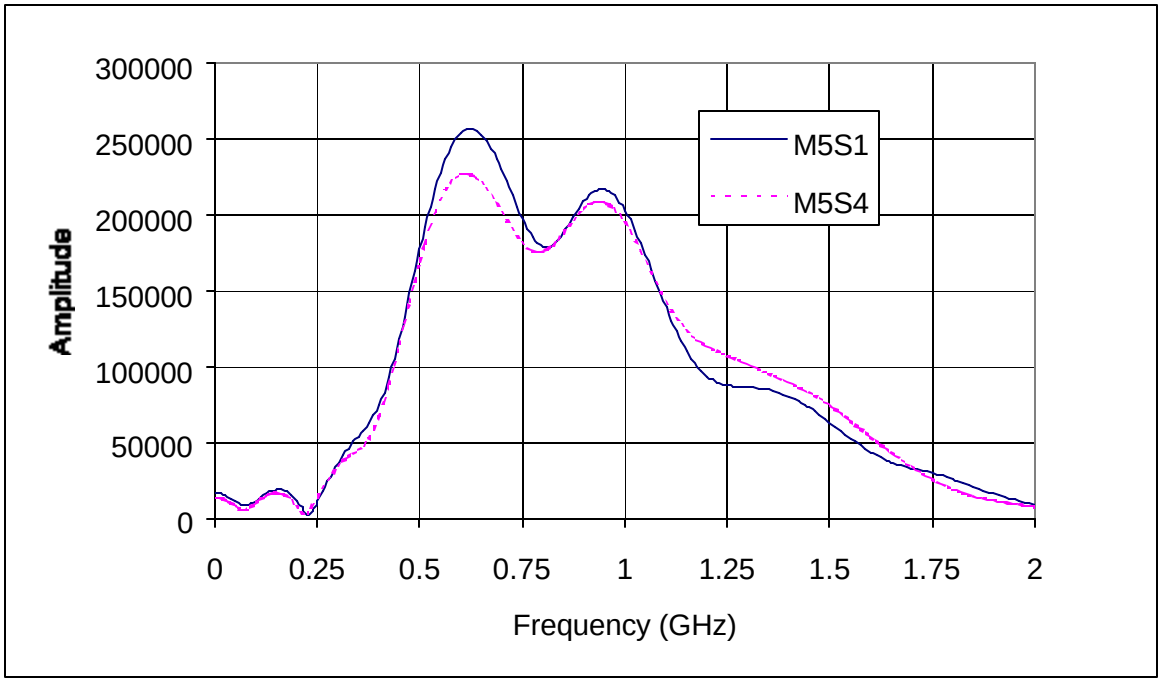

Figure C106 Air void effects on the frequency spectrum for mix M5 (05/13/00)

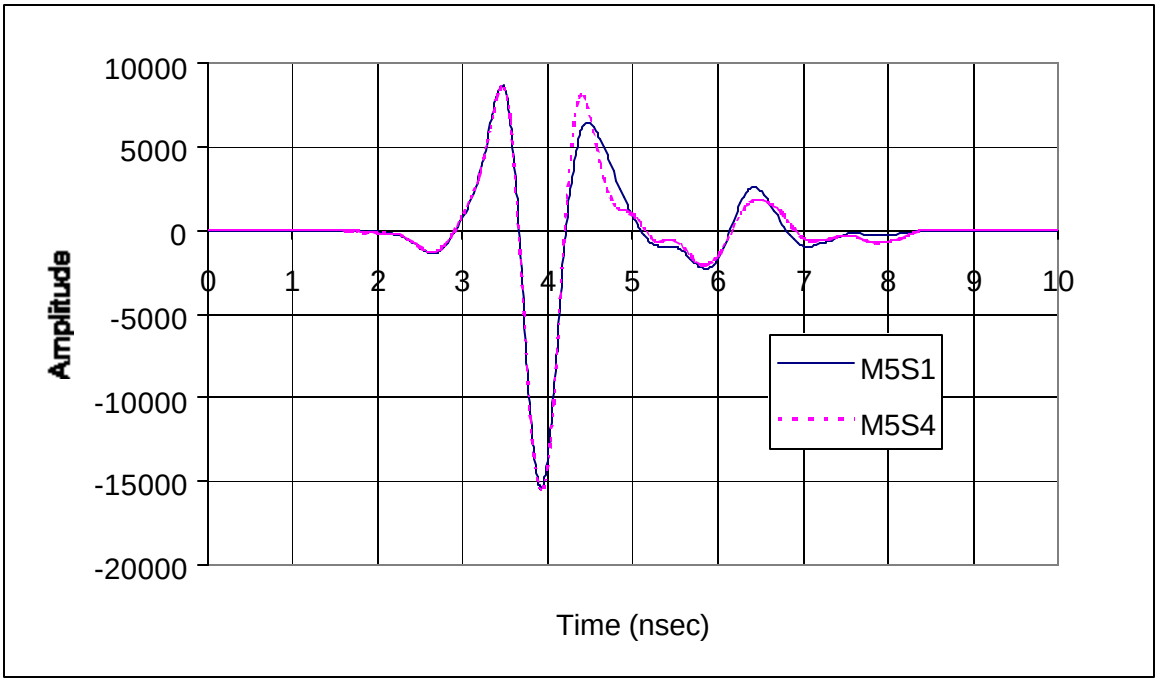

Figure C107 Air void effects on the time domain signal for mix M5 (07/17/00)

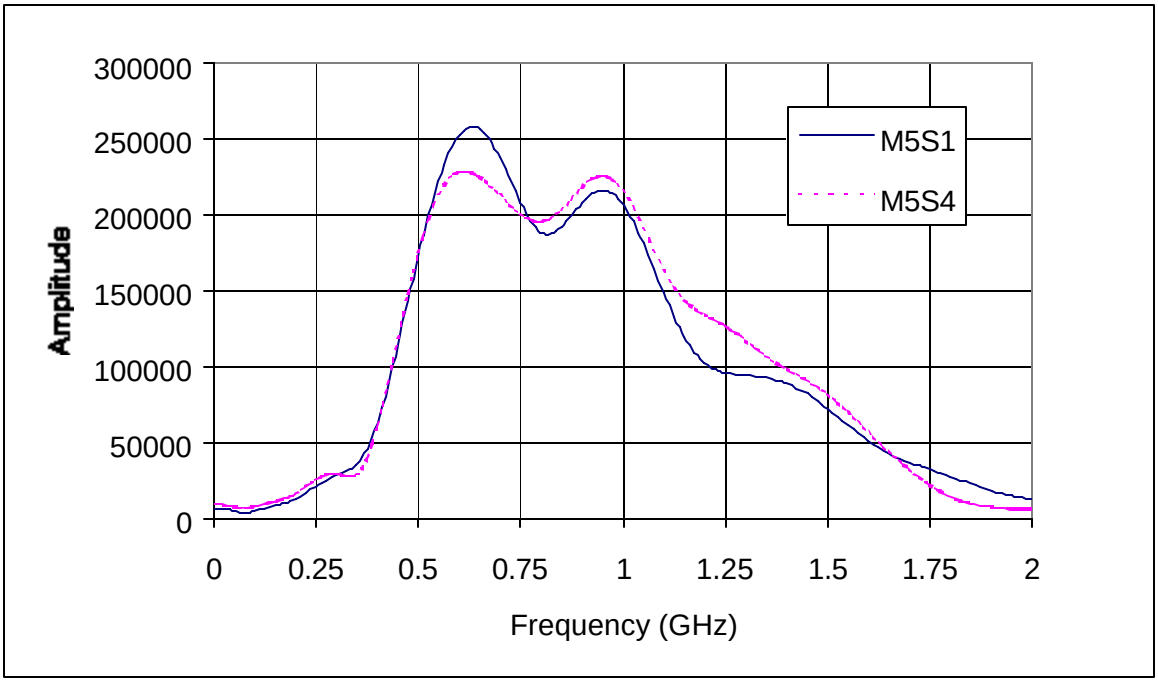

Figure C108 Air void effects on the frequency spectrum for mix M5 (07/17/00)

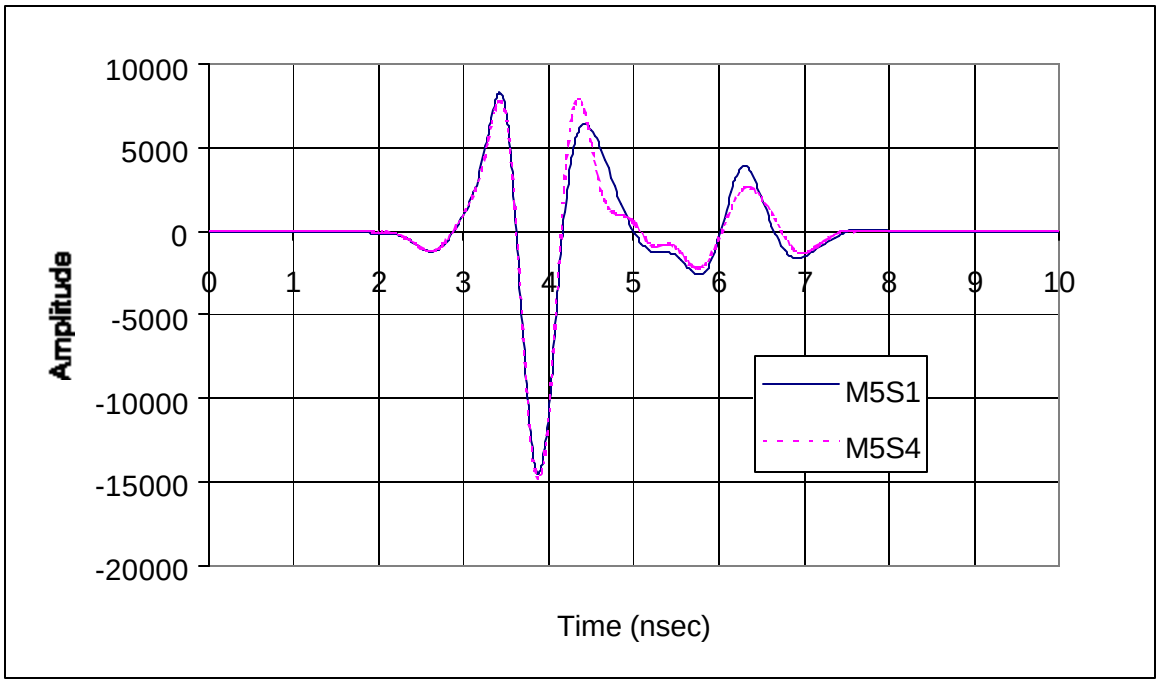

Figure C109 Air void effects on the time domain signal for mix M5 (11/05/00)

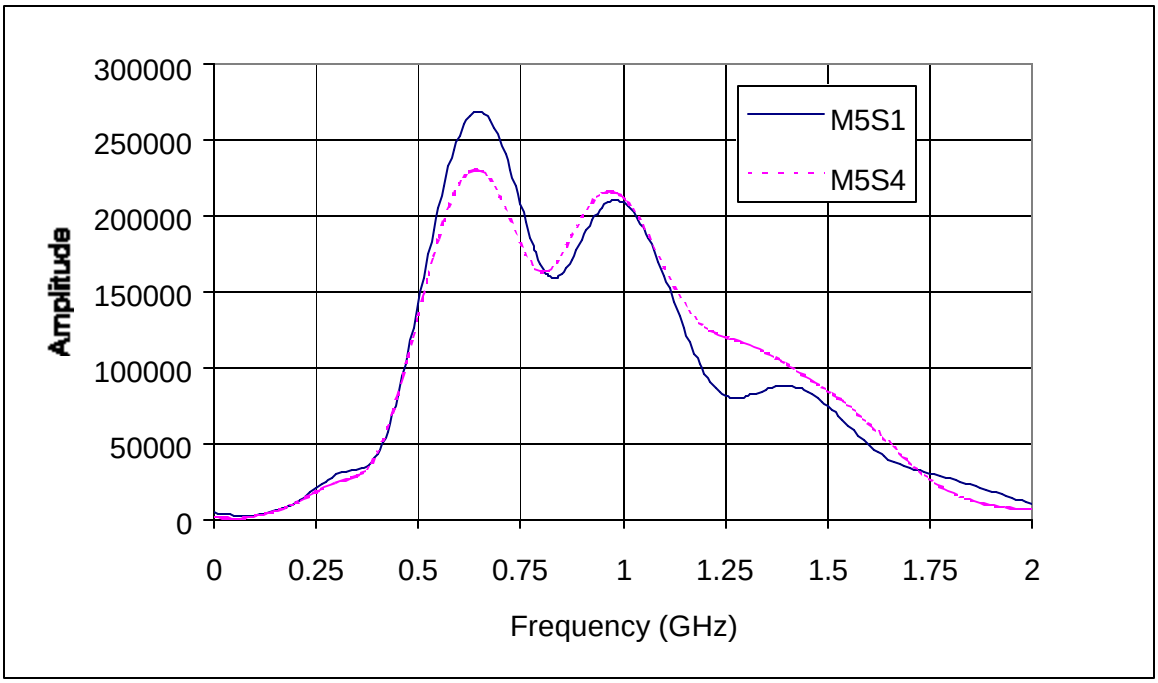

Figure C110 Air void effects on the frequency spectrum for mix M5 (11/05/00)

APPENDIX D

(GROUND-COUPLED GPR DATA)

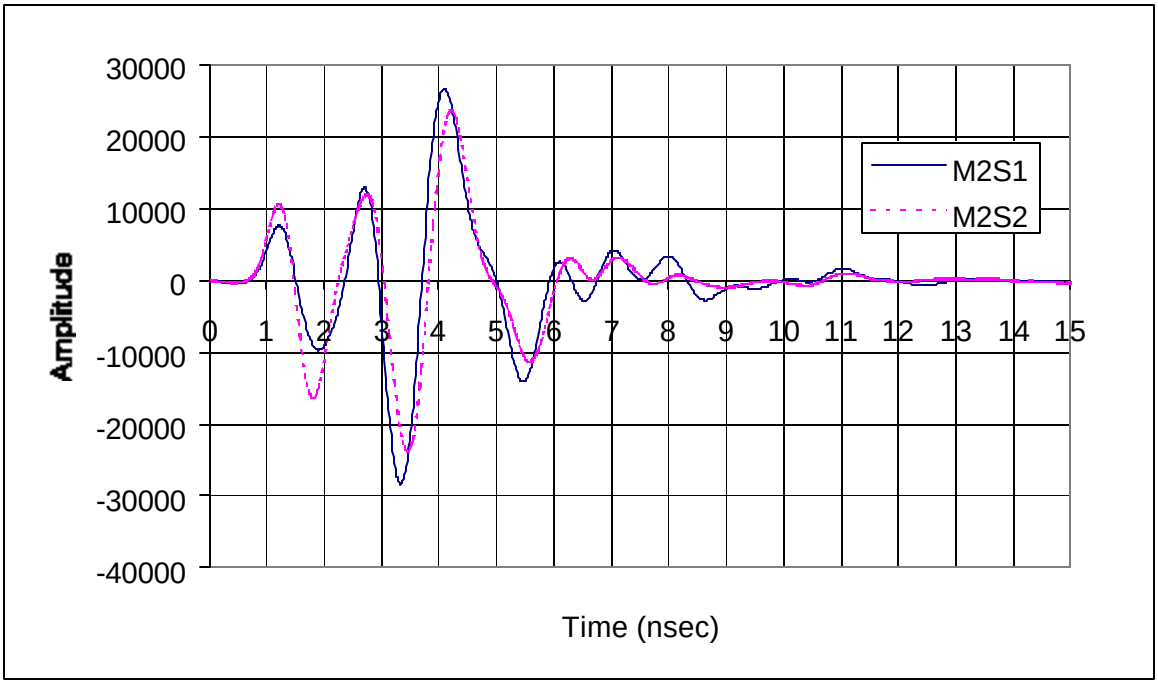

Figure D1 Air void effect on ground-coupled waveform for mix M2 (6.4 mm)

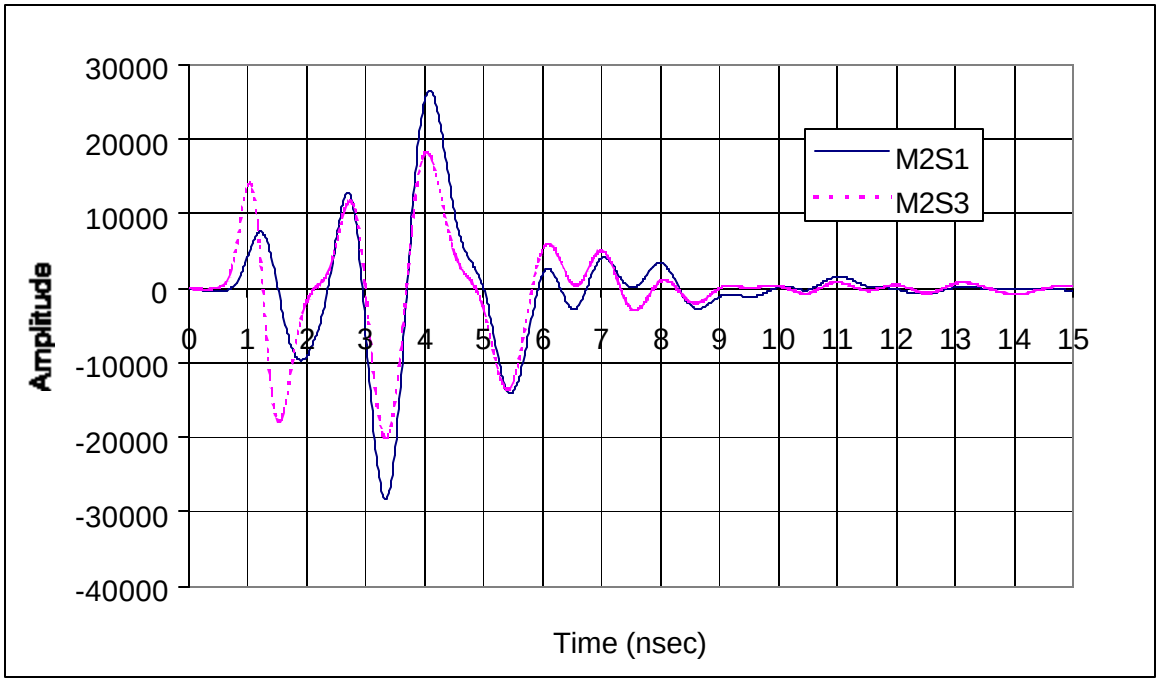

Figure D2 Air void effect on ground-coupled waveform for mix M2 (12.7 mm)

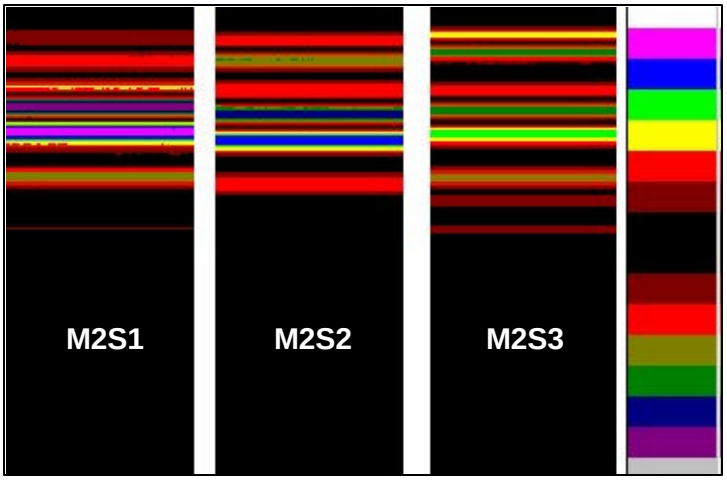

Figure D3 Air void effect on ground-coupled linescan representation for mix M2

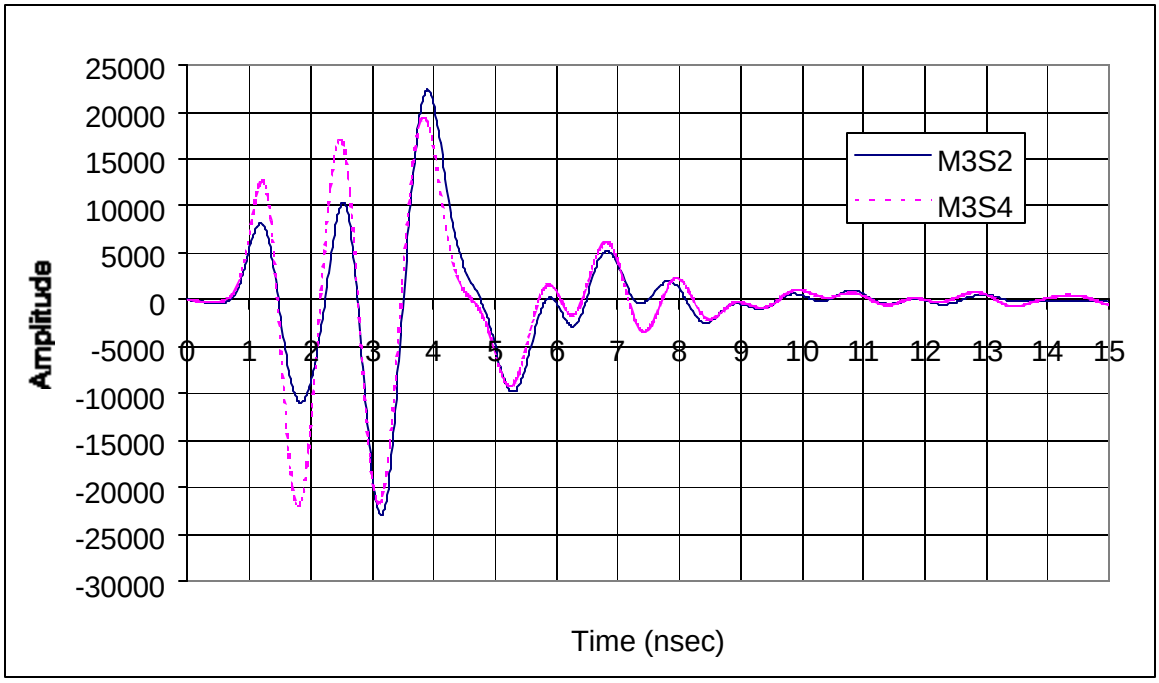

Figure D4 Air void effect on ground-coupled waveform for mix M3 (6.4 mm)

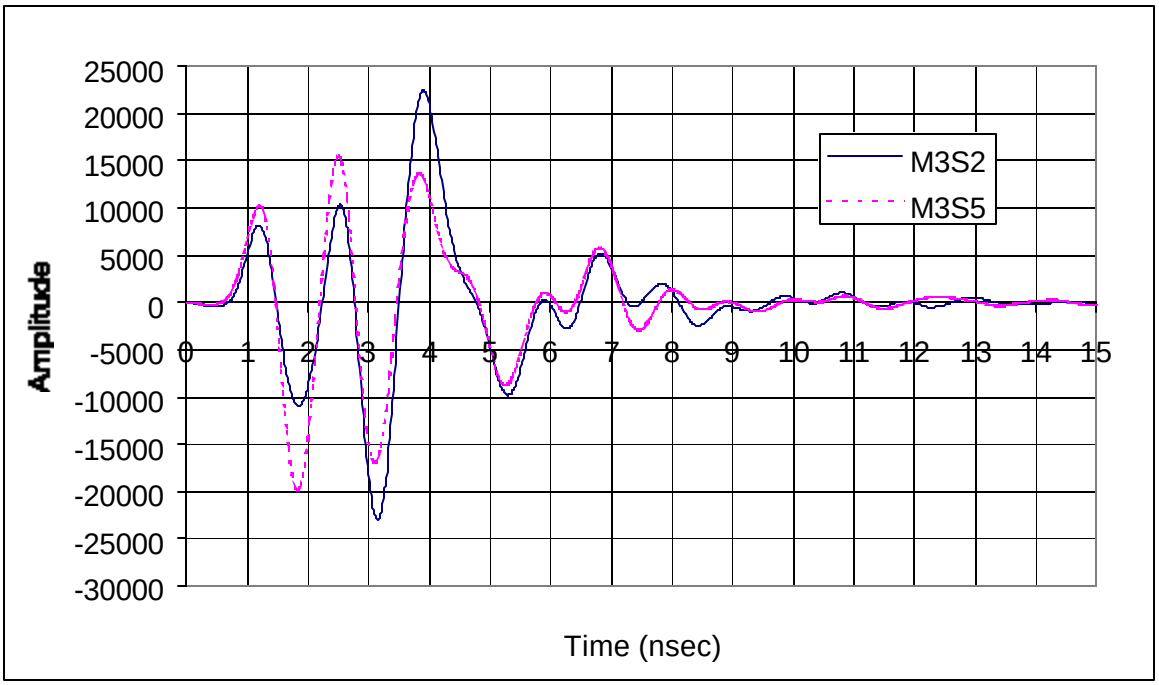

Figure D5 Air void effect on ground-coupled waveform for mix M3 (12.7 mm)

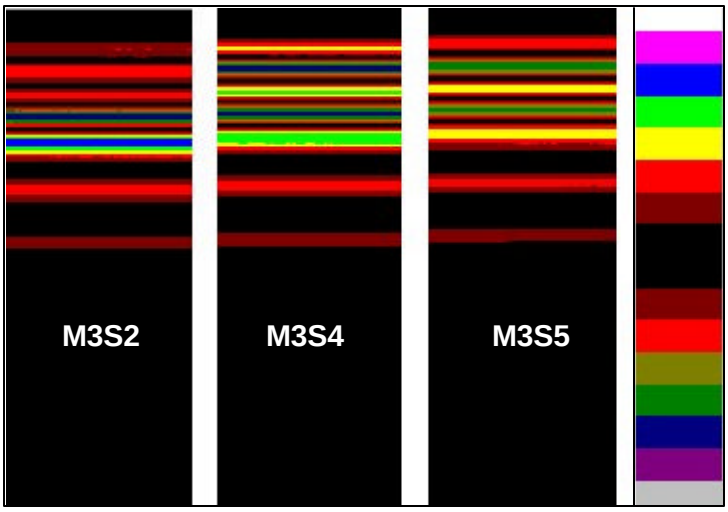

Figure D6 Air void effect on ground-coupled linescan representation for mix M3

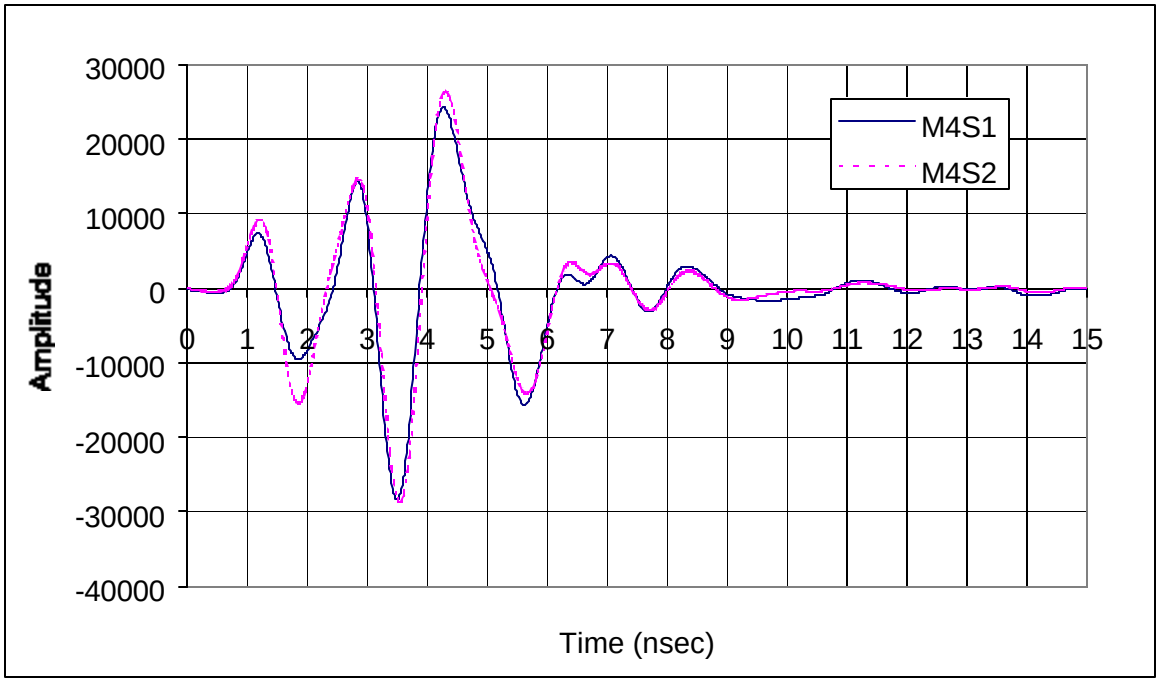

Figure D7 Air void effect on ground-coupled waveform for mix M4 (6.4 mm)

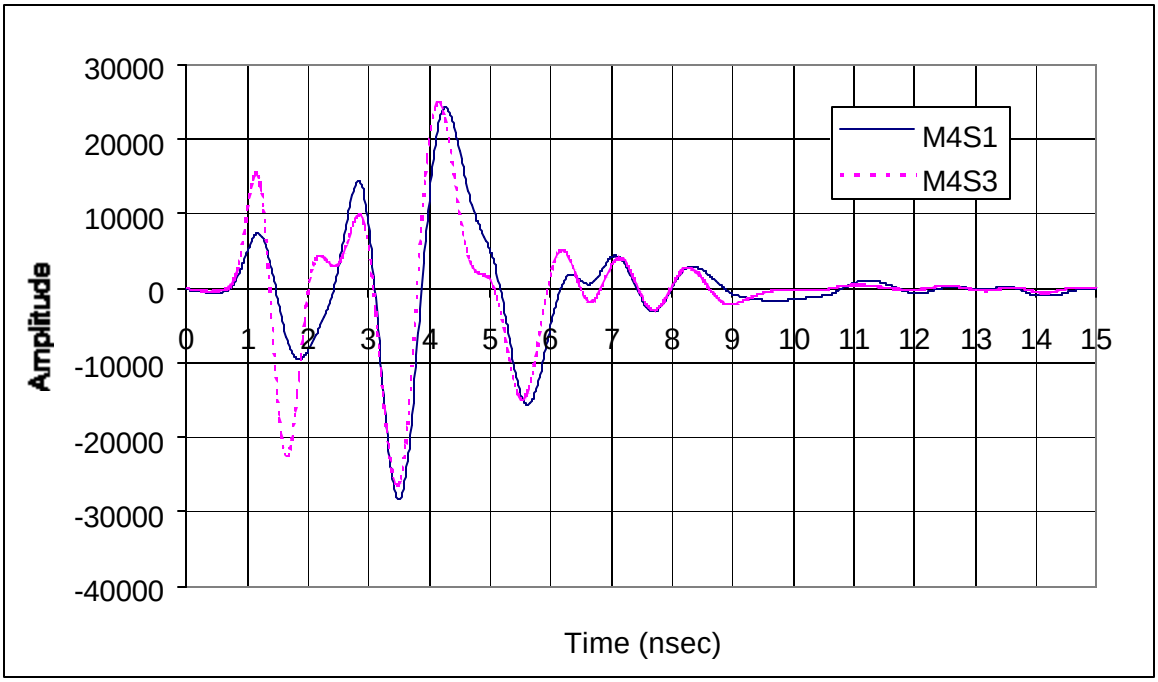

Figure D8 Air void effect on ground-coupled waveform for mix M4 (12.7 mm)

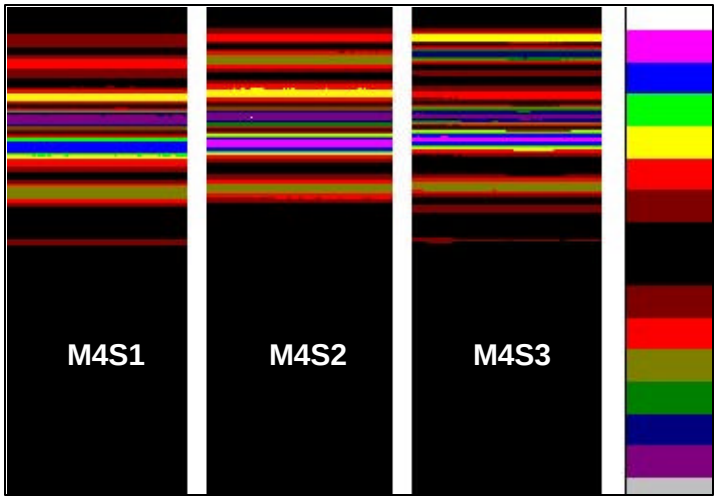

Figure D9 Air void effect on ground-coupled linescan representation for mix M4

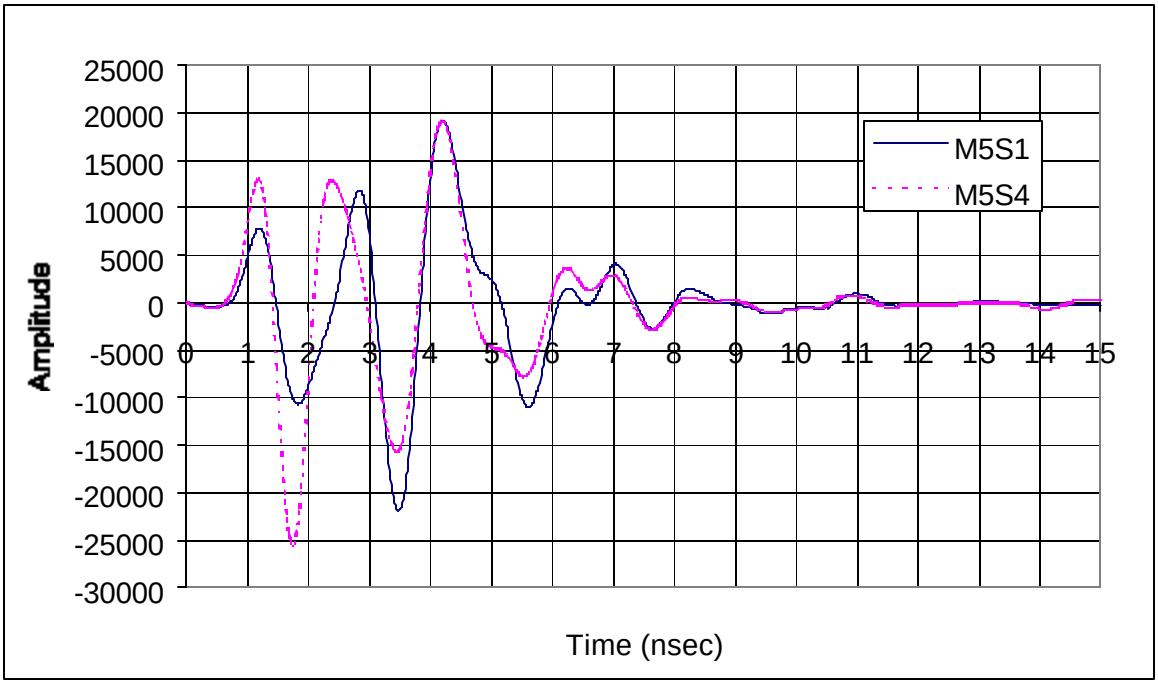

Figure D10 Air void effect on ground-coupled waveform for mix M5 (12.7 mm)

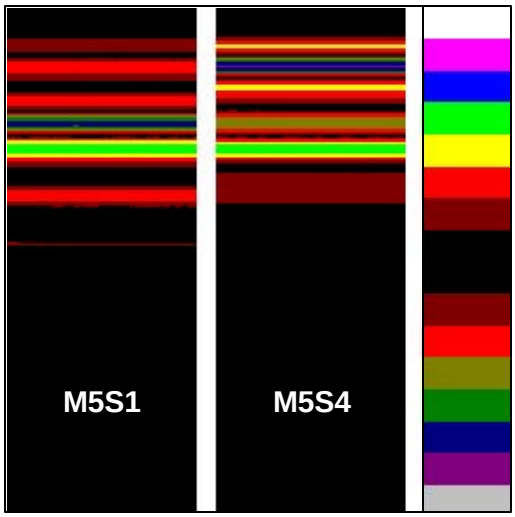

Figure D11 Air void effect on ground-coupled linescan representation for mix M5

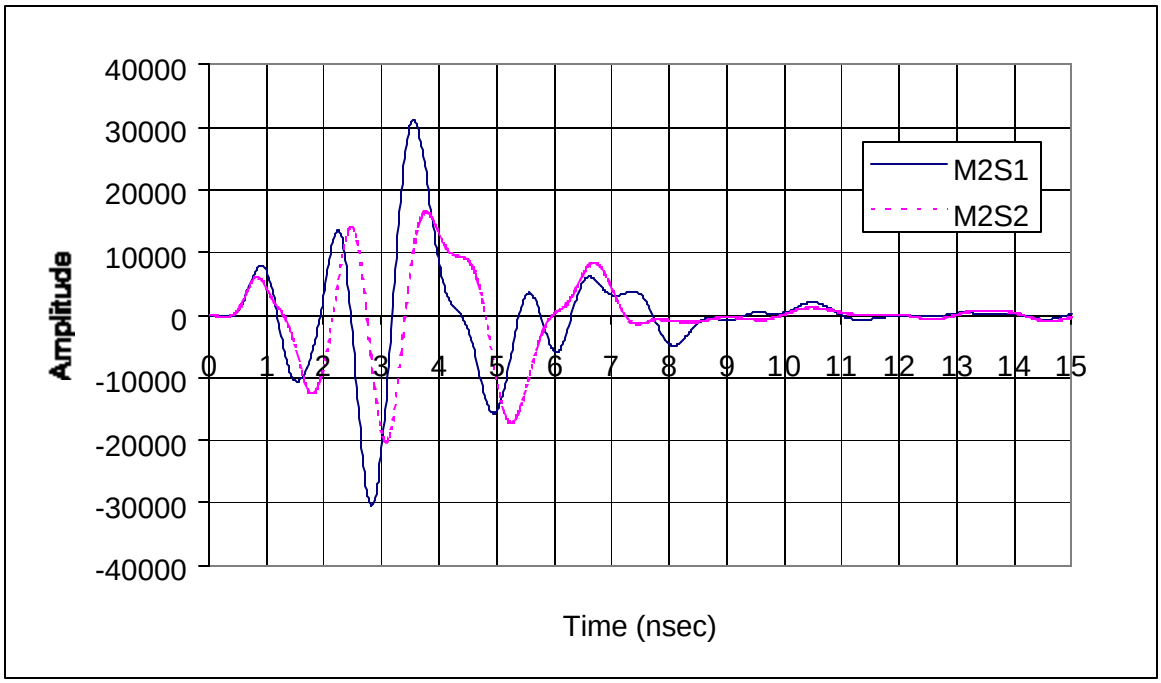

Figure D12 Water-filled void effect on ground-coupled waveform for mix M2 (6.4 mm)

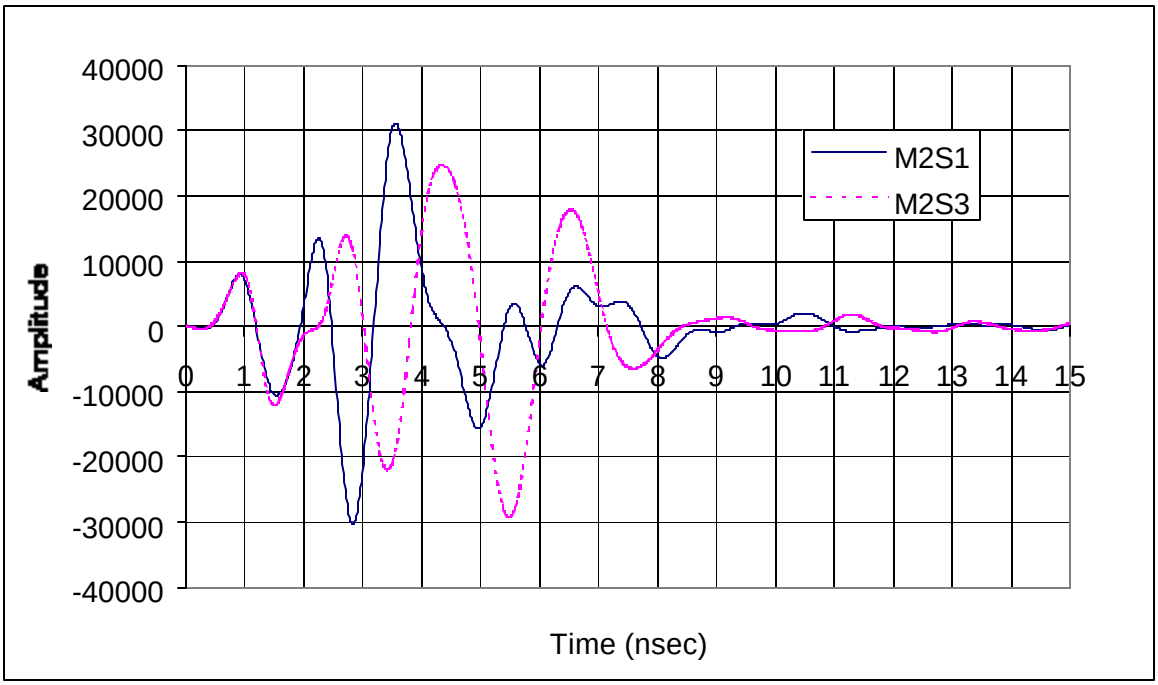

Figure D13 Water-filled void effect on ground-coupled waveform for mix M2 (12.7 mm)

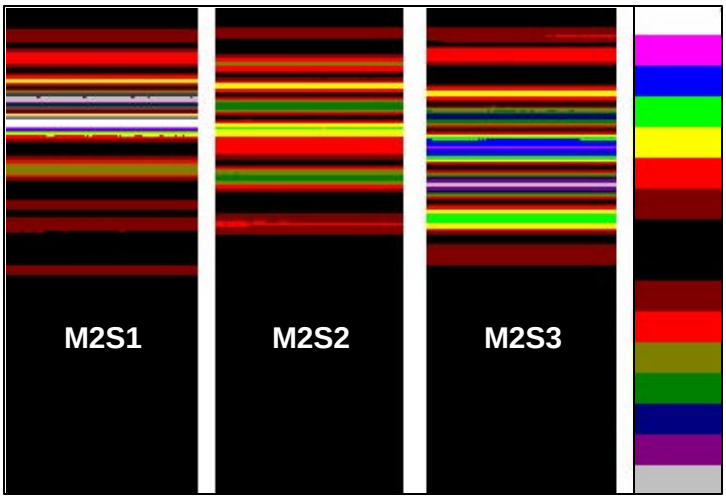

Figure D14 Water-filled void effect on ground-coupled linescan representation for mix M2

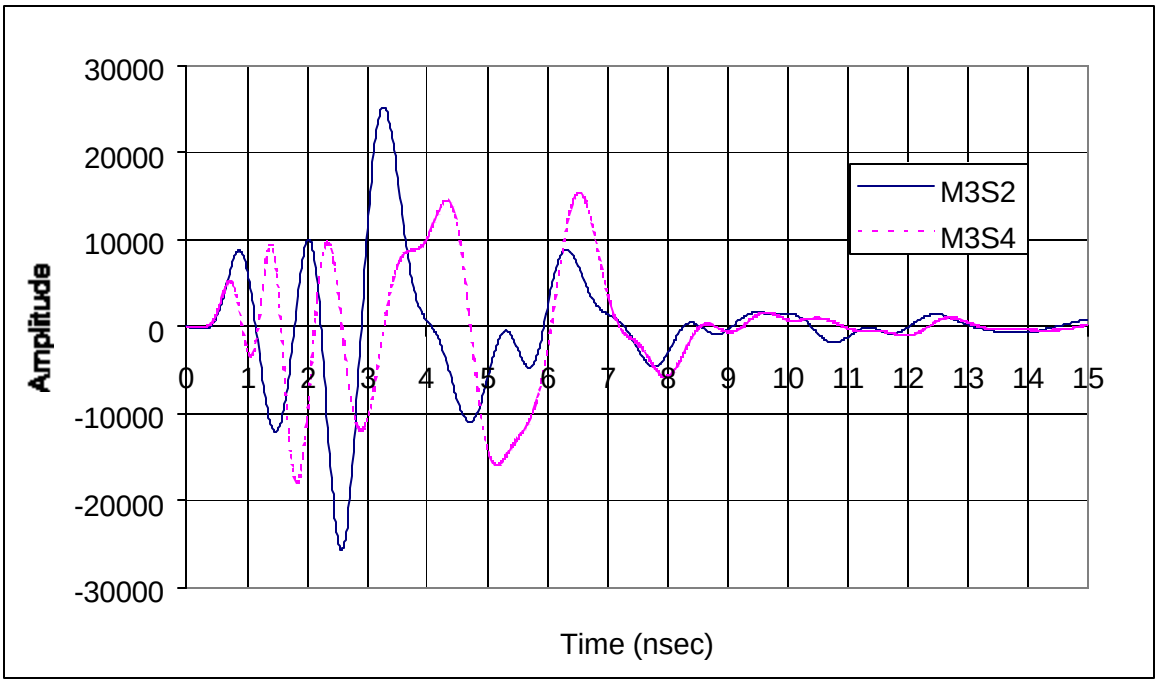

Figure D15 Water-filled void effect on ground-coupled waveform for mix M3 (6.4 mm)

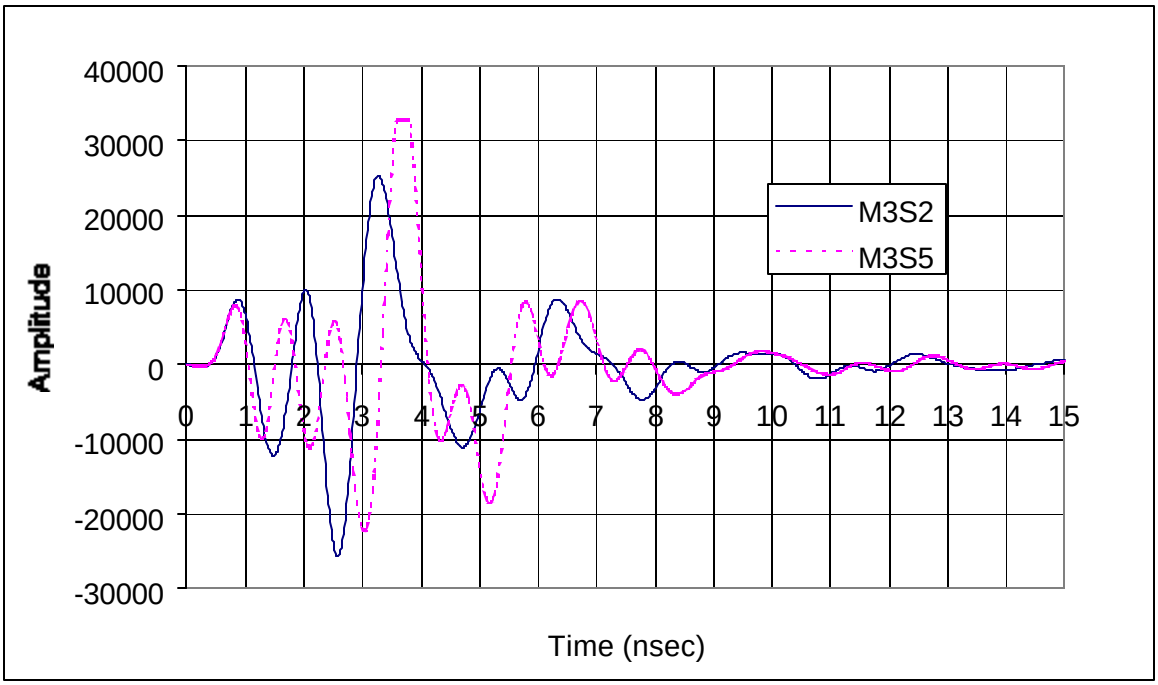

Figure D16 Water-filled void effect on ground-coupled waveform for mix M3 (12.7 mm)

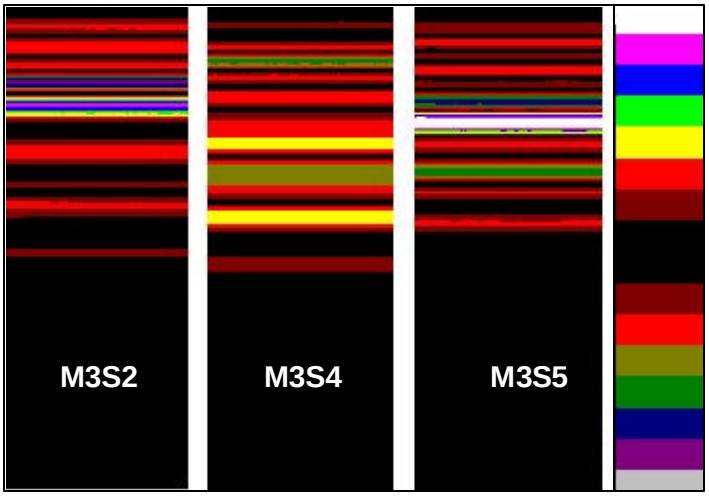

Figure D17 Water-filled void effect on ground-coupled linescan representation for mix M3

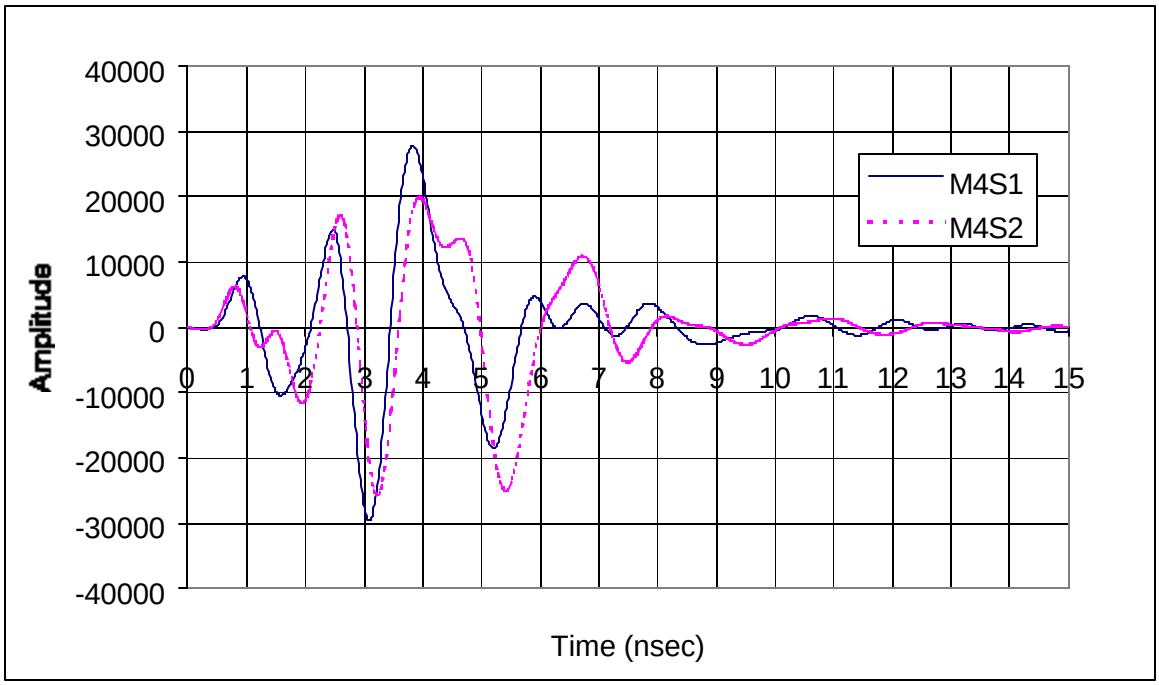

Figure D18 Water-filled void effect on ground-coupled waveform for mix M4 (6.4 mm)

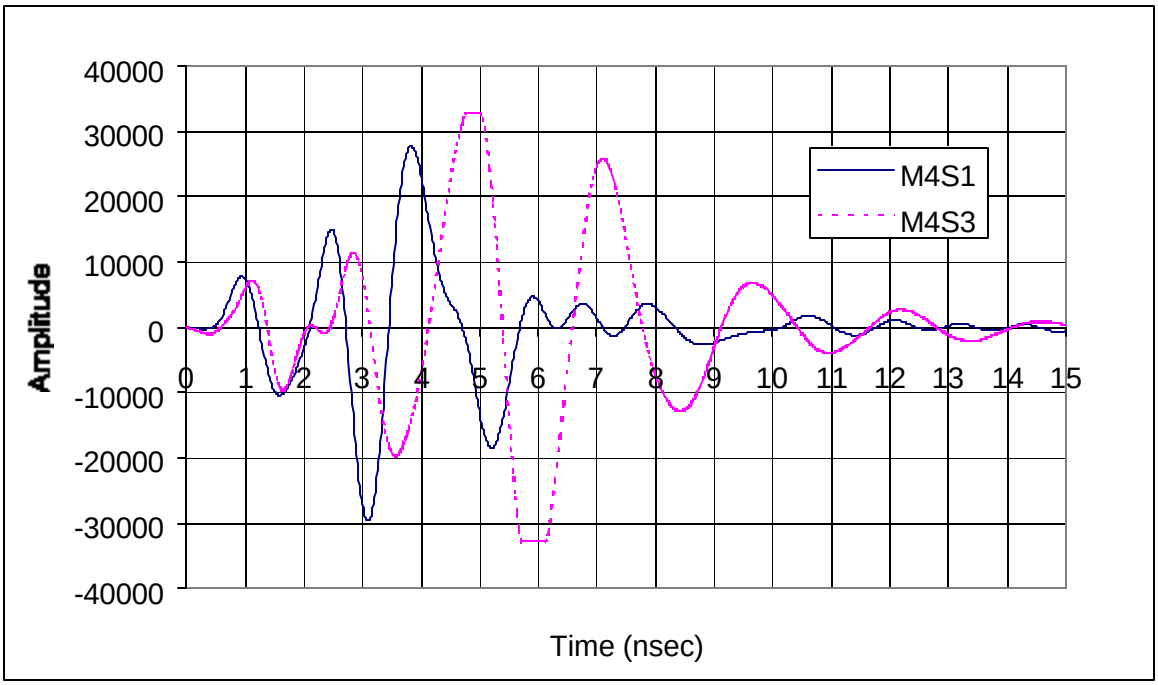

Figure D19 Water-filled void effect on ground-coupled waveform for mix M4 (12.7 mm)

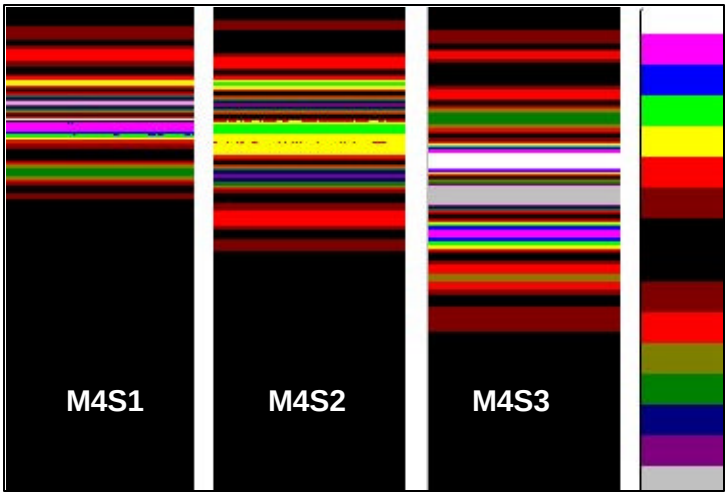

Figure D20 Water-filled void effect on ground-coupled linescan representation for mix M4

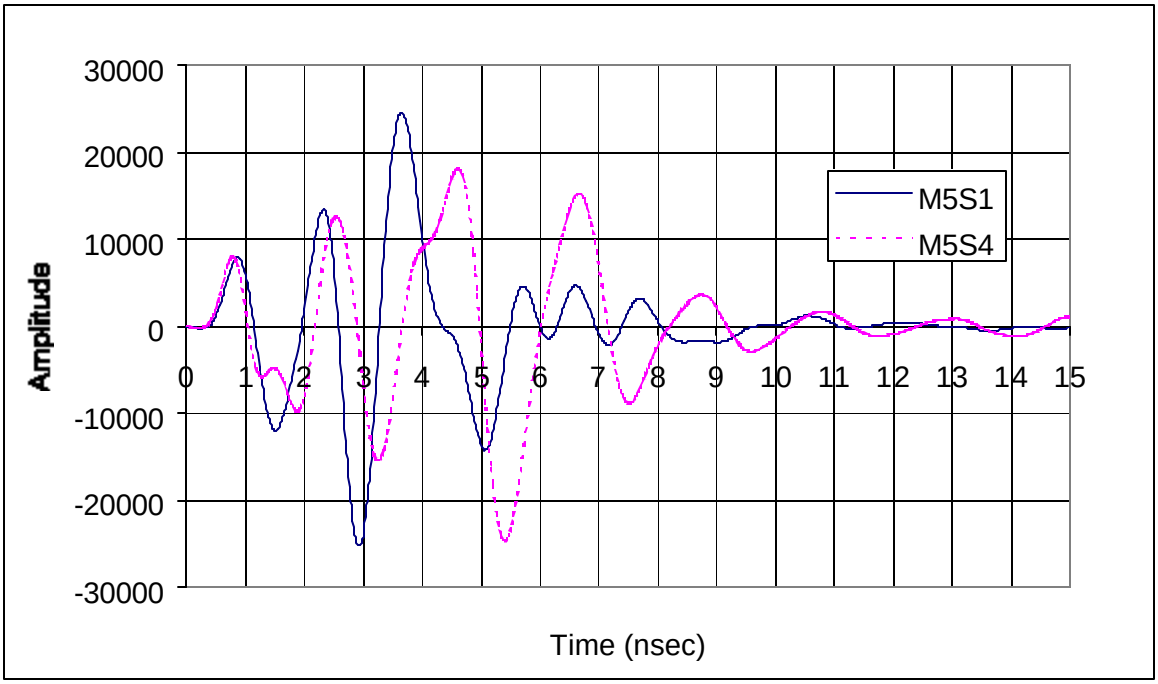

Figure D21 Water-filled void effect on ground-coupled waveform for mix M5 (12.7 mm)

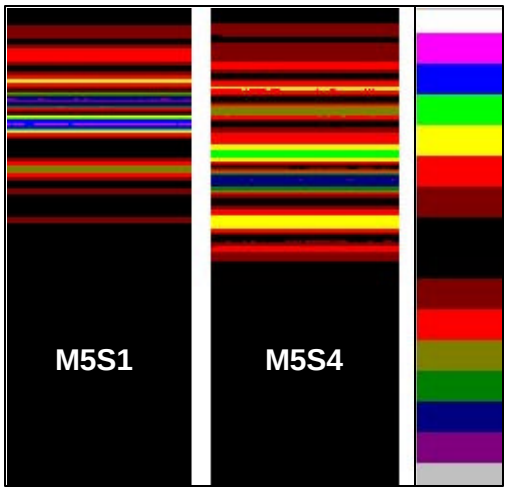

Figure D22 Water-filled void effect on ground-coupled linescan representation for mix M5

VITAE

Amara Loulizi was born in 1967 in the beautiful island of Djerba, surrounded by the Mediterranean Sea, in the south of Tunisia. He received his high school diplomat (Baccalauréat) in 1986 from the "Lycée Secondaire d'Hammam Lif" with honors, which earned him a scholarship to study Civil Engineering at Michigan State University. He received a Bachelor of Science from the home of the Spartans in 1990. He joined the Structures Division of the Civil Engineering Department of Virginia Tech for his MS degree, which he earned in 1992 under the supervision of Dr. Richard M. Barker. In that year, he left the States to work as a structural engineer with "TECI," an engineering firm located in Tunis, Tunisia. After working for TECI for three years, he joined "SOCEAHF" to work as a project engineer for one year. In January 1996, he decided to go back to the home of the Hokies to work on a PhD program with the Transportation Division of the Civil Engineering Department under the supervision of Dr. Imad L. Al-Qadi. In July 1998, he was married to his beautiful, smart, and caring wife, Sonia. In August 1999, he joined the Virginia Tech Transportation Institute, where he now works as a Senior Research Associate with the Roadway Infrastructure Group.